Proton Conducting Membrane Fuel Cells III

The Electrochemical Society
Founded in Philadelphia 1902
Incorporated 1930

The Electrochemical Society
100
1902-2002

Edited by
M. Murthy
T. F. Fuller
J. W. Van Zee
S. Gottesfeld

PV 2002-31

Editors
Murthy
Fuller
Van Zee
Gottesfeld

Proton Conducting Membrane Fuel Cells III

PV
2002-31

ISBN
1-56677-
455-1

ISBN 1-56677-455-1

Proton Conducting Membrane Fuel Cells III

Proceedings of the International Symposium

Editors

M. Murthy
Gore Fuel Cell Technologies
Newark, DE, USA

T. F. Fuller
School of Chemical and Biomolecular Engineering
Georgia Institute of Technology
Atlanta, GA, USA

J. W. Van Zee
Dept. of Chemical Engineering
University of South Carolina
South Carolina, USA

S. Gottesfeld
MTI Microfuel Cells
431 New Karner Road
Albany, NY, USA

Sponsoring Divisions:
Industrial Electrolysis and Electrochemical Engineering, Energy Technology, Physical Electrochemistry

Proceedings Volume 2002-31

THE ELECTROCHEMICAL SOCIETY, INC.
65 South Main St., Pennington, NJ 08534-2839, USA

Published by:

The Electrochemical Society, Inc.
65 South Main Street
Pennington, New Jersey 08534-2839, USA

Telephone 609.737.1902
Fax 609.737.2743
e-mail: ecs@electrochem.org
Web: www.electrochem.org

Library of Congress Catalogue Number: 2004117397

ISBN 1-56677-455-1

Printed in the United States of America

Preface

This volume contains papers presented at the 3rd Symposium on Proton Conducting Membrane Fuel Cells, which took place at the Salt Lake City ECS meeting in the fall of 2002.

The field of polymer electrolyte fuel cells continues to be a major area of activity in electrochemistry and electrochemical engineering. And with recent declared plans to make hydrogen a future fuel for transportation, attention to polymer electrolyte fuel cells has further increased for more reasons than one.

With the ultimate goal of the research activity in this area being a power source of superior efficiency, ultra-low emissions and, last but not least, effective cost, burdens of technical viability and overall techno-economic relevance have to be considered in any chapter of work devoted to fuel cell science and engineering. This in addition to the fundamental criteria of high scientific quality. These combined demands of scientific value and technical relevance, have been well reflected by the series of these Electrochemical Society PEFC symposia , and maintaining this quality, now and in the future, becomes more and more important as the number of fuel cell meetings of all kinds has increased exponentially. Members of The Electrochemical Society should not only recognize "ownership" of the PEFC and DMFC fields, but should secure such ownership by continuously maintaining the highest scientific quality in papers published under the auspices of the ECS, while serving, at the same time, as a central forum for meshing the key science and technology disciplines required to achieve technical success and, ultimately, market entry.

Finally, handling of this Volume has, unfortunately, been less than efficient, and, as result, it is to be published as late as two years after the Salt Lake City meeting. We feel an apology is due to both the authors and the readers for this long delay. In spite of this delay, however, there is little doubt that this collection of papers, divided into the five sections of "Overview", "Electrocatalysis", "Mass Transport & Spatial Distribution" , "Membranes" and "Direct Methanol Fuel Cells" , have maintained good degree of freshness two years after their presentation. They address a wide variety of science and technology aspects, covering fabrication, testing, characterization and modeling of PEFC and DMFC components and systems. And so, with a feeling of "(much) better later than never", here is the collection of the Symposium papers for you to read, learn and use as baseline for further advancements.

Table of Contents

Overview

Electrocatalysis

Transport Processes and Spatial Distributions

Proton Conducting Membranes

Direct Methanol Fuel Cells

Facts about ECS

The Electrochemical Society (ECS) is an international, nonprofit, scientific, educational organization founded for the advancement of the theory and practice of electrochemistry, electrothermics, electronics, and allied subjects. The Society was founded in Philadelphia in 1902 and incorporated in 1930. There are currently over 7,000 scientists and engineers from more than 70 countries who hold individual membership; the Society is also supported by more than 100 corporations through Contributing Memberships.

The technical activities of the Society are carried on by its Divisions. Sections of the Society have been organized in a number of cities and regions. Major international meetings of the Society are held in the spring and fall of each year. At these meetings, the Divisions hold general sessions and sponsor symposia on specialized subjects.

The Society has an active publications program that includes the following:

Journal of The Electrochemical Society — The *Journal* is the peer-reviewed leader in the field of electrochemical and solid-state science and technology. Articles are posted online as soon as they become available for publication. This archival journal is also available in a paper edition, published monthly following electronic publication.

Electrochemical and Solid-State Letters — *Letters* is the first and only rapid-publication electronic journal covering the same technical areas as the ECS *Journal*. Articles are posted online as soon as they become available for publication. This peer-reviewed, archival journal is also available in a paper edition, published monthly following electronic publication. It is a joint publication of ECS and the IEEE Electron Devices Society.

Interface — *Interface* is ECS's quarterly news magazine. It provides a forum for the lively exchange of ideas and news among members of ECS and the international scientific community at large. Published online (with free access to all) and in paper, issues highlight special features on the state of electrochemical and solid-state science and technology. The paper edition is automatically sent to all ECS members.

Meeting Abstracts *(formerly Extended Abstracts)* — Meeting Abstracts of the technical papers presented at the spring and fall meetings of the Society are published on CD-ROM.

Proceedings Series — Papers presented in symposia at Society and topical meetings are published as serialized Proceedings Volumes. These provide up-to-date views of specialized topics and frequently offer comprehensive treatment of rapidly developing areas.

Monograph Volumes — The Society sponsors the publication of hardbound monograph volumes, which provide authoritative accounts of specific topics in electrochemistry, solid-state science, and related disciplines.

For more information on these and other Society activities, visit the ECS website:

www.electrochem.org

Proceedings of The Electrochemical Society, PV 2002-31, 1-24 (2002)
DOI: 10.1149/200231.0001PV © The Electrochemical Society

FUNDAMENTAL RESEARCH AND DEVELOPMENT CHALLENGES IN POLYMER ELECTROLYTE FUEL CELL TECHNOLOGY

Hubert A. Gasteiger, Mark F. Mathias

General Motors Corporation – Fuel Cell Activities
10 Carriage Street, Honeoye Falls, NY 14472

ABSTRACT

The purpose of this paper is to define needs for improved membrane and catalyst materials that would accelerate commercialization of Polymer Electrolyte Fuel Cells (PEFCs) in automobiles. Starting with system and cost considerations, we define targets for membrane operating temperature, conductivity vs. relative humidity, gas permeability, and water uptake. To consider the catalysts needs, we examine the polarization losses in state-of-the-art membrane electrode assemblies (MEAs) and demonstrate that approximately 2-3 fold improvement in electrocatalyst activity is needed to enable achievement of automotive Pt targets of <0.2 g_{Pt}/kW.

INTRODUCTION

Many companies are diligently working to bring hydrogen, reformate, and methanol fed polymer electrolyte fuel cell (PEFC) products to a variety of markets. It appears that currently available fuel cell materials and designs will be adequate for near-term markets with the highest cost ($/kW) entry points. In these cases, challenges in engineering, manufacturing, and marketing must be overcome prior to successful market penetration. However, there are also more technically demanding and lower-cost markets (e.g., automotive) for which current materials and designs may not be sufficient. In this paper, we attempt to identify key automotive system and cost issues and show how they lead to specific materials development challenges.

Current PEFCs systems run at a maximum of 80°C because operation above that temperature requires too much system support of the membrane as will be explored further below. Also, current membranes have glass transition temperatures in the range of 80-120°C and are thus subject to creep and hole-formation at temperatures in that range. Unfortunately, it turns out that the heat rejection rate of automotive radiators is insufficient to reject continuous full power waste heat loads with the 80°C source temperature. Although fuel cell vehicles are inherently more efficient than the internal combustion engine (ICE), the ICE has a thermal system packaging advantage. This is because the ICE rejects approximately one-third of its waste heat in the exhaust stream (vs. <10% for the PEFC), and the ICE-system coolant temperature reach approximately 120°C (vs. 80°C for the PEFC) (1). This system problem has given rise to a need for development of a "high-temperature membrane". In this paper, we will begin with system considerations and define targets for membrane operating temperature, conductivity vs. relative humidity, gas permeability, and water uptake.

State-of-the-art catalysts comprise Pt-containing metals or alloys supported on carbon. We will consider Pt-containing catalyst cost in automotive applications for both state-of-the-art and projected performance. This is a particularly critical question in light of the probable upward pressure on Pt price, a limited natural resource, as volume increases; this is in contrast to the membrane material cost which would be expected to benefit from economies of scale. To do this analysis, we examine the polarization losses in state-of-the-art MEAs and demonstrate the degree of improvement in electrocatalysts needed to achieve automotive Pt targets of $<0.2\ g_{Pt}/kW$.

HIGH-TEMPERATURE POLYMER ELECTROLYTE NEEDS

The High-Temperature Target:

GM automotive system analysis suggests a reasonable target for high-temperature membrane operation is between 110-120°C for H_2-fueled fuel cell vehicles (2). At this temperature, heat rejection with conventional packaging becomes feasible. Furthermore, CO tolerance improves to approximately 50 ppmv CO without air bleed at low anode catalyst loading (0.1-0.2 $mg_{noble\ metal}/cm^2$) (3), thereby reducing the purity requirement for on-board stored H_2. For stationary systems with reduced dynamic load-following requirements and operating with hydrocarbon-based H_2-reformate, system operation at ca. 140-160°C would offer an increase of the CO-tolerance level to ca. 0.1-0.5%, thereby allowing for a simpler Preferential Oxidation (PROX) reactor, or even PROX elimination. Whereas some gains in oxygen reduction activity would be realized at 160°C, these would probably have small impact on system size and mass since they would be counteracted by a loss in equilibrium voltage. (E_{equil} ca. 70±5 mV lower at 160°C compared to 80°C, i.e., approximately one Tafel-slope (4)). At temperatures >160°C, carbon-support material stability becomes problematic (5). For H_2–fueled automotive fuel cell systems, the focus of this paper, we conclude that 120°C is the best target temperature to guide high-temperature membrane development efforts.

Proton Conductivity Requirements:

In this section, we define targets relevant to high-temperature ionomer development. In order to provide material property targets that can be directly measured in *ex-situ* tests, we assume electrode and membrane structures similar to what we have today. Specifically, we assume membranes in the neighborhood of 20-50 μm and electrode structures with thickness of 10-20 μm in which 15-25 volume percent ionomer ($\varepsilon_{ionomer}$) is incorporated to provide proton conductivity (6). The ionomer requirements are different for membrane vs. electrode application, and we consider this in setting targets. Of course, more radical departures from current MEA architectures are welcome, and the targets we provide here can readily be generalized to evaluate alternative MEA constructions.

Conductivity of Ionomer in Membrane – The operating conditions of current PEFC technology are dictated by the properties of the perfluorosulfonic acid (PFSA) ionomers that are used in the membrane and the catalyst layers. Figure 1 shows the proton conductivity (σ_{H+}) vs. relative humidity for 1100 EW Nafion® as measured by Alberti (7, through-plane), a relationship he found to be roughly independent of temperature in the 80-120°C temperature range. The conductivity is above 0.1 S/cm for relative humidity (RH) values greater than 90%, but drops to 0.01 S/cm at 40% RH. Also represented on the right-hand axis of the plot is the ohmic loss for a 25 µm membrane at 1 A/cm^2. At 0.1 S/cm, the loss is 25 mV, a voltage efficiency penalty of about 2%. Whereas this loss appears relatively small, overall voltage efficiency is a critical issue due to sluggish cathode kinetics. Thus, assuming a membrane thickness, $\delta_{membrane}$, in the neighborhood of 20-25 µm we suggest a 0.1 S/cm target be adopted for ionomer development directed at membrane application. Alternatively, one could target an overall membrane sheet resistance, R_{sheet}, of less than 25 mΩ cm^2 (i.e., $R_{sheet} = \delta_{membrane} / \sigma_{H+}$).

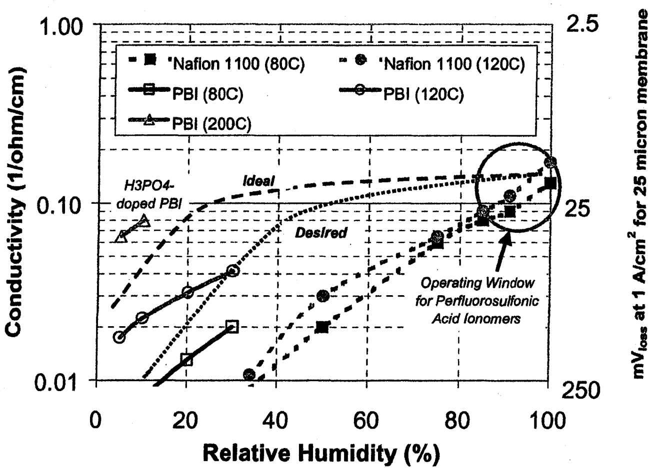

Figure 1: Relationship between proton conductivity and adjoining gas stream relative humidity at various temperatures for perfluorosulfonic acid (1100 EW) (7) and phosphoric-acid-doped polybenzimidazole (8). Curves are also shown for materials that would enable and be ideal for system simplification.

Conductivity of Ionomer in Electrode – In current PEFC electrode configurations, ionomer dispersed throughout the electrodes also contributes a resistance. The voltage-loss ratio between the electrolyte phase in the electrode and the membrane can be estimated using simple geometric arguments and typical values for state-of-the-art electrodes based on optimal cathode performance, assuming the membrane ionomer has the same intrinsic conductivity in both phases.

$$\frac{\Delta V_{\text{ionomer,electrode}}}{\Delta V_{\text{membrane}}} = \left(\frac{\delta_{\text{electrode}}}{\delta_{\text{membrane}}}\right)\cdot\frac{\tau}{2\cdot\varepsilon_{\text{ionomer}}} = \left(\frac{15\mu\text{m}}{25\mu\text{m}}\right)\cdot\frac{1}{2\cdot 0.20} = 1.5 \qquad [1]$$

The factor of 2 in the denominator accounts for conduction of protons halfway, on average, through the catalyst layer thickness. The tortuosity, τ, is not well known but was assumed to be unity to provide a lower-limit estimate of the voltage-loss ratio. We assumed electrode and membrane thickness of 15 and 25 µm, respectively, and ionomer volume fraction in the electrode of 0.2. Thus, the total electrolyte phase voltage losses in a single electrode are approximated to be at least 1.5 times those in the membrane.

For fuel cell systems with pure H_2-feed, the electrode ionomer-phase loss is expected to be present mainly in the cathode and could be reduced by designing thinner cathode electrode structures (note that it is unlikely to achieve electrodes with good gas-diffusion properties using significantly larger values of $\varepsilon_{ionomer}$). Thinner cathode structures are enabled by the development of either *i)* higher-loaded Pt-catalysts (> 50%wt. Pt/carbon) without compromising Pt-dispersion and/or *ii)* more active cathode catalysts which would allow operation at significantly reduced catalyst loading resulting in thinner electrodes. In the case of fuel cell system operation with CO-contaminated reformate, the very much reduced anode kinetics would produce similar comparable voltage losses on the anode and the same development goals as stated for cathode catalysts would apply. In summary, it is reasonable to set an ionomer conductivity target of 0.1 S/cm at 120°C for high-temperature ionomers that are developed for use in electrodes, i.e., identical to the membrane conductivity target.

System-Imposed RH Requirements:

Because of the rapid drop-off in conductivity with decreasing relative humidity for PFSA ionomers, they are typically operated in the high-RH window as shown in Figure 1. The role of the system built around such a membrane is to provide the 100% RH environment so that the membrane/electrode can efficiently conduct protons with minimum voltage loss. However, maintaining 100% RH in the gas streams is problematic from the system point-of-view. The membrane RH requirement drives high-pressure operation (resulting in higher compressor auxiliary loads), low temperature operation (resulting in lower system heat-rejection rates), and increased RH in inlet streams (resulting in higher complexity and cost due to humidification/condensation requirements). Although Figure 1 indicates that PFSA conductivity at 120°C for current ionomers is above 0.1 S/cm at 100%RH, we will next show that this is an impractical operating region from a system point-of-view. We will also seek to define a suitable target RH at 120°C at which the 0.1 S/cm target developed above should be applied.

To define a target RH-value at 120°C, we will assume a dead-ended H_2 system running at air stoichiometry of 2 as shown in Figure 2:

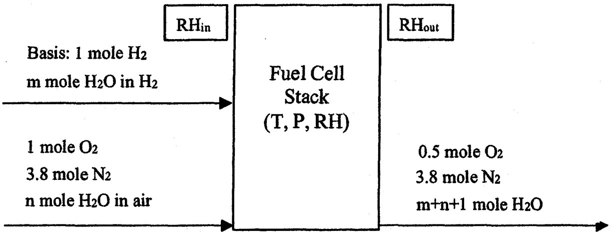

Figure 2: Dead-ended H2/air fuel cell system with air stoichiometry of 2 on a one-mole$_{H2}$ basis.

A state-of-the-art system using conventional PFSA membranes is indicated in Table 1 as System 1. For such a low pressure system (ca. 150kPa$_{absolute}$) at 80°C, fuel and air streams must be (nearly) fully humidified to achieve high conductivity in the membrane and in the catalyst layers. Since the water vapor pressure at 80°C is ca. 50kPa, the effective gas pressure (fuel and air) is ca. 100kPa. To fully humidify the fuel and air inlet streams at 100%RH at 80°C and 150kPa$_{abs}$, 0.5 and 2.4 moles of H_2O per moles of H_2 consumed, respectively, must be added, and this total water-flux of 2.9 moles$_{H2O}$/mole$_{H2\text{-}consumed}$ (last column in Table 1) must be recirculated to avoid net consumption of water on the vehicle.

For a high-temperature system to be feasible, we can set the following system guidelines:

- No more humidification water-recirculation, i.e., $(m+n)_{H2O}$ (Table 1), to the fuel cell stack than for 80°C/150 kPa$_{abs}$ system, with 100% RH requirement (current systems are already too complex and costly).
- Operation near 150kPa$_{abs}$, otherwise parasitic compressor power is excessive.
- Retain fuel/air partial pressures of $\geq$100kPa$_{gas}$ (dry-basis) to avoid performance losses compared to current systems. This is particularly critical to avoid excessive cathode kinetics losses.

Table 1: Four potential system operating conditions based on Figure 2 (dead-ended H_2, air stoichiometry of 2), illustrating the effect of membrane RH requirement on system pressure and water supply requirements. System 1 is feasible with conventional PFSA membranes, Systems 3 and 4 are target high-temperature membrane systems with membrane conductivity requirements as shown in Figure 1 (lines labeled "Desired" and "Ideal").

System	System Description	RH_{in}	RH_{out}	P_{total}	P_{air}, P_{H2}	P_{H2O}	$m_{H2O,an}$	$n_{H2O,ca}$	$(m+n)_{H2O}$
		[%]	[%]	[kPa$_{abs}$]	[kPa$_{abs}$]	[kPa$_{abs}$]	[mole$_{H2O}$/mole$_{H2\text{-}consumed}$]		
1	Current **80°C**-System	100	135	150	100	50	0.5	2.4	**2.9**
2	**120°C**-System, *Current Membrane*	100	135	300	100	200	2	9.6	**11.6**
3	**120°C**-System, *Desired Membrane*	50	67	200	100	100	1	4.8	**5.8**
4	**120°C**-System, *Ideal Membrane*	25	33	150	100	50	0.5	2.4	**2.9**

We now consider a future system running at 120°C, System 2 in Table 1. Membranes which require 100%RH for optimal operation would require 300kPa$_{abs}$ total system pressure to maintain 100kPa fuel/air pressure, since the water vapor pressure at 120°C is ca. 200kPa. In addition, the amount of water to be recirculated would be four times (!) that of the currently used systems at 80°C, i.e., $(m+n)_{H2O} = 11.6$. We conclude that a 120°C system with current membranes is not feasible due to undesirably high system pressure and water recirculation requirements.

System 3 in Table 1 represents a 120°C system if one had a membrane maintaining ca. 0.1 S/cm at 50%RH (see Figure 1). The water partial pressure of 100 kPa in addition to the reactant partial pressure of 100 kPa results in a total system pressure requirement of

200 kPa_{abs}, higher than the target of 150 kPa_{abs}. Furthermore, the required water recirculation rate would be approximately twice the requirement for 80°C systems, i.e., $(m+n)_{H2O} = 5.8$. System 4 represents the ideal case, enabled by a 120°C membrane requiring 25% RH to provide a conductivity of 0.1 S/cm (see Figure 1). The system pressure (50 kPa water plus 100 kPa fuel/air) and the water recirculation rate are equivalent to those of the baseline 80°C system, i.e., $(m+n)_{H2O} = 2.9$.

We conclude that demonstration of ca. 0.1S /cm at 25%RH (80-120°C), is a necessary condition for a high-temperature membrane which would operate in a 120°C system. Long term, the system would obviously benefit from membranes that required no external humidification. Membranes can be screened for this necessary condition without fuel cell testing and MEA preparation.

Available High-Temperature Membrane – Phosphoric-acid doped polybenzimidazole (PBI), first identified by Case Western Reserve University and now under development by Celanese, is a high-temperature membrane that does allow operation at temperatures up to approximately 200°C (8). Available data for PBI membrane conductivity vs. RH and temperature are included in Figure 1. At 200°C, its conductivity is 0.06-0.08 S/cm with an RH of 5-10%. Whereas this is interesting performance, the reported conductivity drops rapidly as a function of temperature reaching 0.01-0.02 S/cm at 15-30% RH and 80°C. This is problematic from an automotive system start-up point-of-view. However, recently presented data indicate significant improvements in low temperature conductivity with this material (9). Additional issues with PBI have been stability in the presence of liquid water and inefficient cathode structures resulting in low areal power density. Whereas the material is not yet suitable for use in automotive systems, its potential for high proton conductivity at low RH is attractive. Hopefully, further development will overcome these shortcomings and enable its use in automotive applications.

Hydrogen/Oxygen Permeability Requirement:

In addition to proton conductivity, other critical ionomer properties include the H_2 and O_2 permeability. The membrane material must not be too permeable to the reactive gases to avoid excessive gas crossover and resulting fuel efficiency loss. On the other extreme, the ionomer in the electrode must have sufficient gas permeability so that the reactant transport through it occurs without significant concentration gradients and associated mass transfer losses. In this section, we present simple calculations to roughly estimate the maximum and minimum H_2 and O_2 permeability requirements.

Gas Permeability through the Membrane – PFSA-based membranes allow permeation of gases at a rate proportional to the product of a permeability coefficient (dependent on temperature and RH, normalized by membrane thickness) multiplied by a partial pressure driving force and divided by the membrane thickness. This permeation leads to a fuel cell crossover efficiency loss with two components: direct reaction at the anode determined by the O_2 crossover rate and direct reaction at the cathode determined by the H_2 crossover rate. This crossover loss can be expressed in terms of an equivalent current that would be observed externally if the H_2 consumed by crossover had been reacted electrochemically:

$$i_{\text{Fuel Loss}}[A/cm^2] = \frac{2F\cdot k_{H_2}(T,P)\cdot \Delta p_{H_2}}{\delta_{\text{membrane}}} + \frac{4F\cdot k_{O_2}(T,P)\cdot \Delta p_{O_2}}{\delta_{\text{membrane}}} \qquad [2]$$

where k_i indicates the H_2 or O_2 permeability coefficient, Δp_i is the partial pressure difference driving force of H_2 or O_2 from one face of the membrane to the other, and δ_{membrane} is the membrane thickness. Knowing this "crossover current density" one can calculate the fuel efficiency loss from the following

$$\eta_{\text{Loss, Crossover}} = \frac{i_{\text{Fuel Loss}}}{i_{\text{External}} + i_{\text{Fuel Loss}}}\cdot 100\% \qquad [3]$$

where i_{External} is the current observed in the external circuit divided by the electrode active area.

Rather than conduct a more complicated analysis involving a drive cycle and transients in the stack load/temperature/pressure profile, we will set criteria at the low and high current density points on the load curve and calculate the permeability requirements at those two extremes. The assumptions are listed in Table 2. The fuel cell stack temperature is assumed to instantaneously vary with load: 60°C at 0.05 A/cm^2 and 120°C at 2 A/cm^2 (high-temperature stack at high-current-density rating point). The gas partial pressures reflect average conditions of Systems 1 and 4 in Table 1.

Table 2: Basic assumptions for the determination of the permeability requirements for high-temperature ionomers to be used in the membrane and in the electrodes.

Quantity	Units	Low Load	High Load
Load vs. Temperature -- Partial Pressures			
Current Density	A/cm^2	0.05	2
Temperature	C	60	120
Avg. H_2 Partial Press. (Absolute/ Anode to Cath. Difference)	kPa abs	100	
Avg. O_2 Partial Press. (Absolute/ Anode to Cath. Difference)	kPa abs	15	
Membrane Crossover			
Membrane Thickness	micron	25	
Fuel Efficiency Loss due to Crossover (a)	**%**	**<10**	**<1**
Electrode Permeabilty			
Ionomer Film Thickness	nm	2	
Roughness Factor	cm^2(Pt)/cm^2	100	
H_2 Tafel Slope (Ref. 10)	V/decade	0.03	
O_2 Tafel Slope (Ref. 6)	V/decade	0.065	
Efficiency Loss Due to Film (a)	**%**	**<1.6 (20 mV)**	

(a) criterion applied separately to O_2 and H_2, so total crossover loss can be twice these values

The calculated membrane-permeability limits based on Table 2 and calculated using Eq. [2] are shown as endpoints of the solid lines in Figure 3 for H_2 and Figure 4 for O_2. Permeability values above the lines would be unacceptably high based on the criteria. Measured permeability values from a variety of sources are also shown in the figures. The data extend to lower temperatures than assumed to be present in the system operating

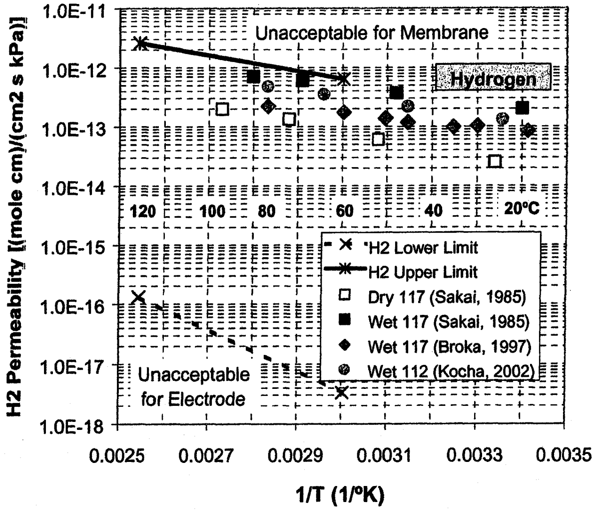

Figure 3: H_2 Permeability as a function of temperature and RH. Upper limit (solid line) defined by crossover losses (assuming no contribution from O_2 crossover), lower limit (dotted line) defined by electrode ionomer film transport requirements, and data is for wet and dry Nafion 1100 EW based membranes (11,12,13).

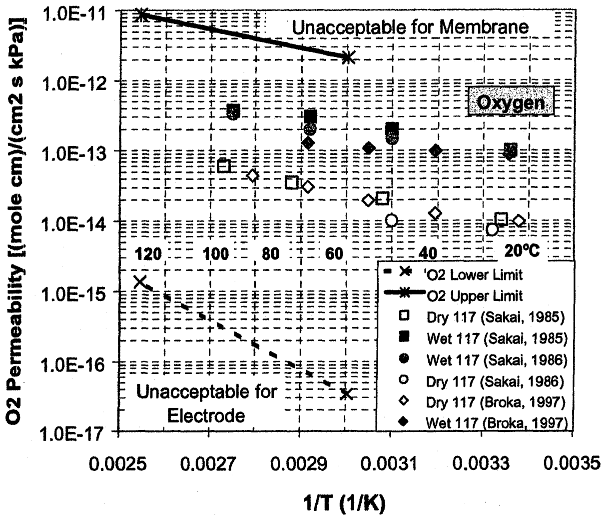

Figure 4: O_2 Permeability as a function of temperature and RH. Upper limit (solid line) defined by crossover losses (assuming no contribution from H_2 crossover), lower limit (dotted line) defined by electrode ionomer film transport requirements, and data is for wet and dry Nafion 1100 EW based membranes (11,12,14).

at steady state. In the 60-90°C region, the H_2 data approach the limit, suggesting that a high-temperature membrane, if implemented at 25 μm, cannot be any more permeable than a conventional PFSA-based membrane. The data show that the permeability of wet PFSA membranes is as much as an order of magnitude higher than dry membranes at a given temperature.

Gas Permeability through the Ionomer in the Electrode – Although the architecture of state-of-the-art electrode layers is still a matter of debate, one can reasonably postulate a structure like that shown in Figure 5. The average thickness of the ionomer film can be estimated by assuming that the ionomer volume is spread uniformly over the Pt and carbon surface area:

$$\delta_{film} = \frac{m_C \cdot \left(\frac{m_{ionomer}}{m_C}\right)}{(m_{Pt} \cdot A_{Pt} + m_C \cdot A_C) \cdot \rho_{ionomer}} \qquad [4a]$$

where $(m_{ionomer}/m_C)$ is the weight ratio of dry ionomer to dry carbon (values from 0.8/1.0 (6) to 1.7/1.0 (15), m_{Pt} is the Pt-loading in $[g_{Pt}/cm^2]$ of the catalyst characterized by a Pt-specific surface area A_{Pt} (typically $5 \cdot 10^5$-$1 \cdot 10^6$ cm^2/g_{Pt} (16), m_C is the carbon-loading in $[g_C/cm^2]$ of a catalyst characterized by a carbon-specific surface area A_C (typically $2.5 \cdot 10^6$-$8 \cdot 10^6$ cm^2/g_{Pt} (17), and $\rho_{ionomer}$ is the ionomer density (≈ 2 g/cm^3). For state-of-the-art catalysts, the Pt-loading is typically on the order of 50%wt Pt/(carbon+Pt) (generally ranging from 40-60%wt Pt/(carbon+Pt), in which case Equation 4a reduces to:

$$\delta_{film} = \frac{\left(\frac{m_{ionomer}}{m_C}\right)}{(A_{Pt} + A_C) \cdot \rho_{ionomer}} \qquad [4b]$$

This yields a range of values for the film thickness between 0.5 and 3 nm. Experimental support for this electrode structure comes from double layer capacitance measurements using cyclic voltammetry and AC impedance techniques. We have observed values on the order of 20 μF/cm^2 total surface area independent of $m_{ionomer}/m_{carbon}$ between 0.4/1.0 and 0.8/1.0 for Vulcan XC-72 (18). This capacitance is characteristic of Pt and carbon interfaces with electrolyte and implies that the entire solid surface was in contact with electrolyte for these electrodes.

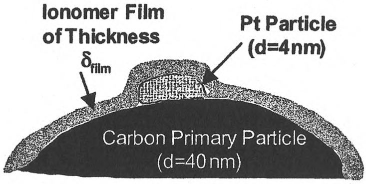

Figure 5: Schematic of carbon primary particle supporting a Pt particle. These electronically conducting phases are considered to be uniformly coated by an ionomer film.

One can estimate the mass transport overpotential associated with transport loss in the ionomer film adjacent to the Pt catalyst. We derive below the relationship for the O_2 transport losses through the ionomer film; the losses due to hydrogen transport are directly analogous. The IR-free cell voltage ($E_{IR\text{-}Free}$) is related to the ionomer-film O_2 concentration at the Pt surface (c_{O2}^{o}) at constant current density (i), surface H_2 concentration on the anode (c_{H2}^{o}), and temperature (T) as

$$\left.\frac{\partial E_{IR-free}}{\partial \log(c_{O_2}^{o})}\right|_{i,c_{H_2}^{o},T} = m \cdot b \qquad [5]$$

where m is the O_2 reaction order at constant IR-free cell voltage (approximately 1) and b is the Tafel slope (V/decade) observed in the kinetically controlled region (6). Integrating Eq. [5] and taking m=1 gives the following equation for the transport overpotential due to dissolved gas transport through the ionomer ($\eta_{O2,ionomer}$)

$$\eta_{O_2,ionomer} = -b \cdot \log\left(\frac{c_{O_2}^{o}}{c_{O_2}^{\delta}}\right) \qquad [6]$$

where concentrations at the Pt/ionomer interface and the ionomer/gas interface are designated with superscript o and δ, respectively. The flux through the film adjacent to the Pt surfaces is proportional to the average current density based on the active area (i) divided by Pt roughness factor (f_{rough} with units of cm^2 Pt/(cm^2 active area)). This flux is proportional to the diffusion coefficient and the concentration driving force across the film

$$N_{O_2} = \frac{i}{nFf_{rough}} = \frac{D_{O_2}(c_{O_2}^{\delta} - c_{O_2}^{o})}{\delta_{film}} \qquad [7]$$

Combining Eqs. [6] and [7] to eliminate the unknown surface concentration, we arrive at

$$\eta_{O_2,ionomer} = -b \cdot \log\left(1 - \frac{i \cdot \delta_{film}}{nF \cdot f_{rough} \cdot D_{O_2} \cdot c_{O_2}^{\delta}}\right) \qquad [8]$$

We assume that the O_2 concentration in the ionomer phase is related to the O_2 partial pressure (p_{O2}) through Henry's law

$$c_{O_2}^{\delta} = H_{O_2} p_{O_2} \qquad [9]$$

where H_{O2} is the Henry's law constant. The permeability coefficient, introduced in Eq. [2], is related to the diffusion coefficient as

$$k_{O_2} = H_{O_2} D_{O_2} \qquad [10]$$

Combining Eqs. [8], [9], and [10], we find

$$\eta_{O_2,\text{ionomer}} = -b \cdot \log\left(1 - \frac{i \cdot \delta_{\text{film}}}{nF \cdot f_{\text{rough}} \cdot k_{O_2} \cdot p^{\delta}_{O_2}}\right) \qquad [11]$$

the relationship that predicts the voltage loss as a function of operating conditions and film properties. An analogous relationship applies for the H_2 transport on the anode side. The value of n is 2 and 4 for H_2 and O_2, respectively.

To estimate the lower permeability limit, we assume the values shown in Table 2: a 2 nm thick film and an electrode roughness factor, f_{rough}, of 100 cm^2_{Pt}/cm^2_{MEA} (ca. 0.15 $mg_{Pt}/cm^2_{electrode}$ with 65 m^2/g_{Pt}). Based on a criterion of no more than 20 mV loss due to ionomer phase gas transport, we calculate the low permeability limits shown in Figures 3 and 4. The permeability window is approximately 3 to 4 orders of magnitude for both H_2 and O_2. PFSA materials represented by Nafion 1100 are orders of magnitude higher than the limit defined here, so we conclude that losses due to ionomer-phase reactant transport are negligible with current materials and structures, consistent with the literature (13). For initial screening purposes, we suggest measurements at 80°C and use of the following criteria taken from Figures 3 and 4 (note: permeability, k_{gas}, in units of (mole cm)/(cm^2 sec kPa)):

i) H_2 permeability of $k_{H2}<1\cdot 10^{-12}$ for the ionomer used in the membrane and $k_{H2}>1\cdot 10^{-17}$ for the ionomer used in the electrode;

ii) O_2 permeability of $k_{O2}<3\cdot 10^{-12}$ for the ionomer used in the membrane and $k_{O2}>1\cdot 10^{-16}$ for the ionomer used in the electrode.

Water Interaction Requirements:

Solubility – Many new materials are being considered as next generation ionomers. Even for systems that run at low RH, we anticipate that ionomers could come in contact with liquid water during automotive system start-up and shutdowns. Therefore, we require insolubility of the ionomer in the liquid water. One could try to avoid liquid water formation with an engineering solution, but this would add undesirable system complexity. A reasonable screening test is <1% ionomer loss when held in liquid water at 150°C in an autoclave for 24 hours.

Swelling – PFSA materials uptake about 50% of their dry weight when boiled in liquid water, and some alternative ionomers take up even more. For example, versions of sulfonated poly ether ketone (PEEK) membranes can exhibit over 100% (i.e., $100\%\cdot m_{H2O}/m_{dry\text{-}polymer}$) water uptake (19). One can estimate the wet thickness relative to the dry thickness of a membrane as a function of water uptake by assuming conservation of volume and zero in-plane expansion for MEAs sandwiched between diffusion media under relatively high compressive forces:

$$\frac{\delta_{wet}}{\delta_{dry}} = 1 + \frac{\rho_{dry}}{\rho_{H_2O}} \left(\frac{m_{H_2O}}{m_{dry\ polymer}} \right) \qquad [12]$$

where the $m_{H2O}/m_{dry\ polymer}$ is the water uptake (wt/wt). For PEEK (ρ_{dry}=1.5 gm/cc) and 100% water uptake the membrane would swell by a factor of 2.5. This creates a practical issue in that, assuming state-of-the art PEFC construction, the diffusion media would compress in response to the membrane swelling. Assuming constant total thickness for the components before and after swelling, a scenario like that shown in Table 3 could occur. In this case, each diffusion media is forced to compress by 22 µm to accommodate the swollen membrane.

Table 3: Component thicknesses before and after swelling with liquid water ($\rho_{dry\ polyjmer}$=1.5 g/cm^3, 100% water uptake, initial membrane thickness of 30 µm). Based on stress-strain data of Toray paper shown in Figure 6.

Layer	Initial –Dry [µm]	Final –Wet [µm]
Anode Diffusion Media Thickness [µm]	170	148
Anode Catalyst Layer Thickness [µm]	15	15
Membrane Thickness [µm]	30	75
Cathode Catalyst Layer Thickness [µm]	15	15
Cathode Diffusion Media Thickness [µm]	170	148
Total Thickness [µm]	400	400

This membrane expansion will apply pressure on the diffusion media which can be estimated using the stress-strain data for carbon fiber paper (Toray TGPH-060) in Figure 6. We assume an initial uncompressed thickness of 200 µm. Each diffusion media compresses to 170 µm in the cell build, resulting in 30 µm of strain and a stress of about 180 psi. Upon further strain of an additional 22 µm, the stress more than doubles.

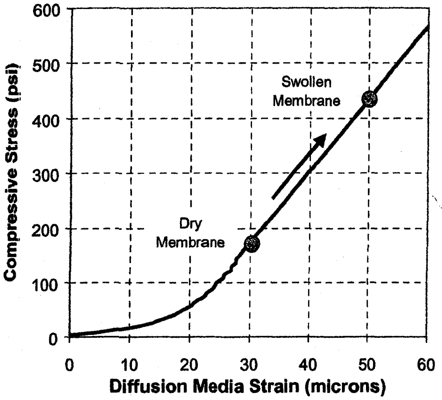

Figure 6: Stress-strain data for Toray TGPH-060 taken at Southwest Research Institute. Effect of membrane swelling in this scenario (Table 3) is to more than double the compressive force on diffusion media.

It is possible to handle this issue using a more compressive element in the stack. However, to avoid impractical requirements for that material, we set a criterion of less than 100% water uptake for the membrane ionomer when boiled in water. This criterion does not apply to the electrode ionomer (since it is embedded in a highly porous structure), although we project that water uptake of >200% for that material would be impractical from the point-of-view of long-term electrode stability.

Chemical Stability of Membranes/Ionomers:

Chemical degradation of current PFSA materials is believed to proceed via peroxide radical attack, whereby fluoride ions and low-molecular-weight perfluorosulfonic acid species are the major decomposition products which can be found in the water exiting fuel cell stacks (20). Peroxide radicals are mainly produced by the permeation of oxygen through the membrane followed by partial electrochemical reduction to H_2O_2 on the anode catalyst (21); the presence of adsorbed CO (from CO-contaminated H_2-reformate) further increases the yield of H_2O_2 under these conditions (22).

Accelerated chemical stability tests of candidate ionomer/membrane materials have been conducted by exposing membranes to an aqueous solution of 3%wt H_2O_2 and 4 ppm of Fe^{+2} at 68°C (Fenton's reagent). Ionomer degradation is determined from fluoride analysis of the solution, assuming that the major degradation product is HF; the percent degradation represents that amount of fluoride released relative to that in the original membrane. Under these conditions, the degradation of current PFSA membranes is ca. 0.5% in an 8 hour period compared to a value of ca. 5% in the case of cross-linked polyphospazene membranes and ca. 50% in the case of cross-linked sulfonated polystyrene (20). In general it has been found that ionomers which contain hydrogen bonded to aliphatic carbon atoms are not sufficiently stable in the PEFC environment (e.g., sulfonated polystyrene).

Based on our current understanding, this accelerated degradation test is a reasonable predictive method to determine whether certain ionomeric materials may be stable in the fuel cell environment. Nevertheless, there is a small but finite chance that ionomeric materials which fail this test may still be suitable fuel cell materials and consequently this criterion is less stringent than the above presented requirements on conductivity, permeability, solubility, and swelling in the presence of water.

Mechanical Stability of Membranes/Ionomers:

In addition to the requirements described above, there are requirements on ionomer mechanical properties. However, we are not yet able to suggest screening criteria for these properties since the mechanical stresses experienced by the membrane in operating fuel cells are still poorly understood. We have set up such equipment at Giner Electrochemical Systems, LLC (Newton, Massachussets) where we regularly screen high-temperature membrane candidates for the all of these properties.

Summary of the Requirements for High-Temperature Ionomers/Membranes:

In the above analysis we have attempted to describe the required physical-chemical properties of high-temperature membranes/ionomers, all of which can be determined in *ex-situ* tests so that no fuel cell testing (and MEA preparation) is necessary for the screening of candidate materials. Even though our analysis has been based on simplified assumptions on the design of fuel cell systems, the numerical values of the required properties should be largely independent of the specific fuel cell system design based on our premise that a fuel cell system be as simple as possible in order to be reliable, economical, and efficient.

For a better overview, the physical-chemical and mechanical requirements on high-temperature membranes/ionomers are listed together in Table 4, starting with the most clearly specified requirements on the top and the least well-defined requirements toward the bottom to the table. It should be mentioned that these requirements are necessary but not sufficient conditions for high-temperature membranes/ionomers and we do believe that MEA preparation and fuel cell testing are of limited use unless at least conductivity and permeability of candidate materials fall within the required ranges.

Table 4: Summary of physical-chemical and mechanical property requirements of high-temperature membranes/ionomers and possible testing methods. All properties can be measured *ex-situ* and do not require fuel cell testing.

Property	**Membrane**	**Electrode**[(a)]	**Methods**
Conductivity at 25%RH (see Figure 1)	>0.1 S/cm at 120°C >0.03 S/cm at 25°C	>0.1 S/cm at 120°C >0.03 S/cm at 25°C	2- or 4-point methods (e.g., (7))
H_2-Permeability	below solid black line in Figure 3	above dashed black line in Figure 3	via GC methods (e.g., (12))
O_2-Permeability	below solid black line in Figure 4	above dashed black line in Figure 4	via GC methods (e.g., (12))
Solubility in H_2O	<1% at 150°C for 24h	<1% at 150°C for 24h	Autoclave in H_2O
Swelling in H_2O	<100% H_2O uptake in boiling water	<200% H_2O uptake in boiling water	weight-gain meas. (e.g., (23)
Chemical Stability	stable in presence of peroxyl species	stable in presence of peroxyl species	test with Fenton's reagent (e.g., (20))
Mechanical Stability	critical	less critical	specifications and requirements not yet determined

[(a)] note that the ionomer in the membrane my be different from the ionomer used in the electrodes.

CATALYST DEVELOPMENT NEEDS

Over the past decades, volumetric (kW/liter) and gravimetric (kW/kg) power densities have been the most commonly used indicators for tracking the progress of PEFC development, particularly in industry. Having exceeded the initially defined automotive stack power density requirements of 1 kW/liter and 1 kW/kg (e.g., 1.7 kW/liter and 1.2 kW/kg published by GM/Opel (24)), the focus of PEFC R&D in the automotive industry is now shifting toward both an increase in stack operating temperature (see above discussion) and a reduction of the platinum-specific stack-power density (g_{Pt}/kW). The latter significantly impacts the final cost of the membrane electrode assembly (MEA) and, equally important, determines the feasibility of a large-scale automotive PEFC market in view of platinum supply constraints.

Assuming a stack peak-power requirement of ca. 75 kW for an average automotive fuel cell vehicle (see reference 1), a Pt-specific stack-power-density of 0.2 g_{Pt}/kW would translate into a consumption of 15 g_{Pt}/vehicle, a value which may be compared to the Pt-metals loading of catalytic-converters in current vehicles of ca. 3-5 g. The production of 10 million vehicles/year would therefore require 150 $tons_{Pt}$/year, which at a current platinum mining rate of 170 $tons_{Pt}$/year (25) is obviously only feasible if the rate of platinum mining can be increased significantly. According to Jaffray and Hards (25), the latter can be accomplished if the platinum requirements can be forecast reliably 3 to 4 years into the future, an argument based on the time required for a significant expansion of current platinum mines. In conclusion, if Pt-specific stack-power-densities of 0.2 g_{Pt}/kW can be achieved, both platinum cost (ca. <\$5/kW at <\$25/g_{Pt} (i.e., <\$780/troy-ounce of Pt)) and platinum supply requirements can be met for a large-scale penetration of the automotive market (currently 52 million vehicles/year (25)) with PEFC-based vehicles.

In the following we will outline the three principal approaches toward increasing the Pt-specific power density: *i)* reduction of the mass-transport losses observed at high current densities in order to maximize the MEA power density; *ii)* reduction of anode and cathode catalyst loadings at minimized voltage losses (i.e., Pt-thrifting); *iii)* implementation of improved cathode catalysts. Based on the analysis of 50 cm^2 active-area MEA fuel cell measurements, it will be shown that the above stated requirement of 0.2 g_{Pt}/kW can be met if Pt-alloy cathode catalysts with a claimed 2-3 times improved Pt-mass-activity ((16, 22, 26) or other yet-to-be-developed catalysts can be implemented successfully into PEFCs.

<u>Experimental Details/Procedures:</u>

MEA Preparation – 50 cm^2 active-area catalyst-coated membranes (CCM) were prepared in-house (6). Carbon-supported 47%wt Pt/carbon (Tanaka, Japan) and organic-solvent based ionomer solutions (ca. 900 EW (equivalent weight)) were used to fabricate thin-layer electrodes which were transferred *via* a decal method onto ca. 25 µm thick low-EW membranes (ca. 900 EW). An ionomer/carbon ratio of approximately 0.8/1 (weight ratio) was maintained in the electrodes of all prepared CCMs using ionomers identical to the ones used in the membrane. CCMs with various catalyst loadings were produced and loadings are referred to as anode-loading/cathode-loading (*e.g.*, 0.05/0.4 mg_{Pt}/cm^2 refers to a 0.05 mg_{Pt}/cm^2 anode and a 0.4 mg_{Pt}/cm^2 cathode loading). Gas-diffusion media (DM) were treated in-house and are based on carbon-fiber-paper substrates (Toray Inc., Japan). Both anode and cathode DMs were teflonated and additionally processed using a proprietary surface treatment. Single cells (50 cm^2) were assembled by sandwiching CCMs between the appropriate DMs and applying an average compressive load of ca. 1500 kPa_{abs} to the active-area.

Fuel Cell Testing – Fuel cell stations from Fuel Cell Technology (Los Alamos, NM) were used to test 50 cm^2 active-area MEAs. Pure oxygen or air were used as cathode reactants and pure H_2 as anode reactant (all gases of 99.99% purity). Stoichiometric flow rates were used for current densities ≥ 0.2 A/cm^2, while at lower current densities constant flows based on the stoichiometric flows at 0.2 A/cm^2 were used. Reactant humidification was achieved by water-bubblers, the temperature of which was calibrated to yield the quoted relative humidity (RH) values. Cell resistances as a function of current density (*i.e.*, the sum of the proton-conduction resistance in the membrane and the various electronic resistances (bulk and contact resistances)) were determined using an AC perturbation of 1 kHz. For each data point, the cell voltage was stabilized over 15 minutes and data were averaged over the last 5 minutes; it should be noted at this point that measurement times of this order are imperative if one desires to obtain meaningful steady-state fuel cell performance and kinetic data. Kinetic analysis was conducted on the basis of H_2-crossover-corrected effective current densities, $i_{eff} = i + i_x$, whereby the value of the H_2-crossover current density, i_x, was measured according to reference (13).

Multiple-path serpentine flow-fields (2 and 3 parallel channels for the anode and cathode, respectively) machined into sealed graphite blocks (Poco) were used. The flow-field channel width was approximately 0.8 mm with a channel/land width ratio of 1.3/1.

Analysis of Voltage-Loss Terms in State-of-the-Art MEAs:

H_2/O_2 performance – Figure 7 shows the resistance-corrected cell voltage versus the logarithm of the effective current density with fully humidified pure H_2/O_2 (stoichiometric flows of s=2.0/9.5) at 150 kPa_{abs} and 80°C. The fact that a straight Tafel-line with a constant slope of 70 mV/decade is obtained for current densities ranging from ca. 0.02 to 2 A/cm^2, suggests pure kinetic control by the oxygen reduction reaction (ORR). The overpotential of the ORR, η_{ORR}, can therefore be modeled by a simple Tafel-relation

$$\eta_{ORR} \approx 70\,mV/decade \cdot \log(i_{eff}) \qquad [13]$$

Analysis of the H_2/O_2 data in Figure 7 in combination with the *in-situ* determined accessible platinum surface area of ca. 60 m^2_{Pt}/g_{Pt} (measured in the so-called driven cell mode (see reference 13)) results in a value for the exchange-current density of $1.7 \cdot 10^{-8}$ A/cm^2_{Pt} (normalized to p_{O2}=100 kPa_{abs} and assuming an equilibrium voltage of E_{eq}=1.184 V (4); for details see reference 6). This is slightly larger than the exchange-current densities at 80°C published in the literature, ranging from $0.2 \cdot 10^{-8}$ A/cm^2_{Pt} to $0.9 \cdot 10^{-8}$ A/cm^2_{Pt} (6, 27, 28, 29), a discrepancy which we associate with the large error in extrapolating the H_2/O_2-Tafel-line over many orders of magnitude in current density. Consequently, much better consistency is found by comparing the intrinsic activity at 0.90 V which is obtained directly from Figure 7 without extrapolaton. Clearly, the value of $i_{0.9V} = 44$ $mA/cm^2 = 0.18$ mA/cm^2_{Pt} (at 100 kPa O_2) extracted from Figure 7 falls now within the rather narrow range of 0.14 to 0.32 mA/cm^2_{Pt} reported in the literature (6, 27, 28, 29). Therefore, the evaluation and benchmarking of new or modified catalysts is achieved most precisely via evaluating values of $i_{0.9V}$ rather than the exchange-current density; however, it is critical to use steady-state data (>5 mins./point) rather than voltammetric sweep data as the latter would result in much higher non-steady-state values.

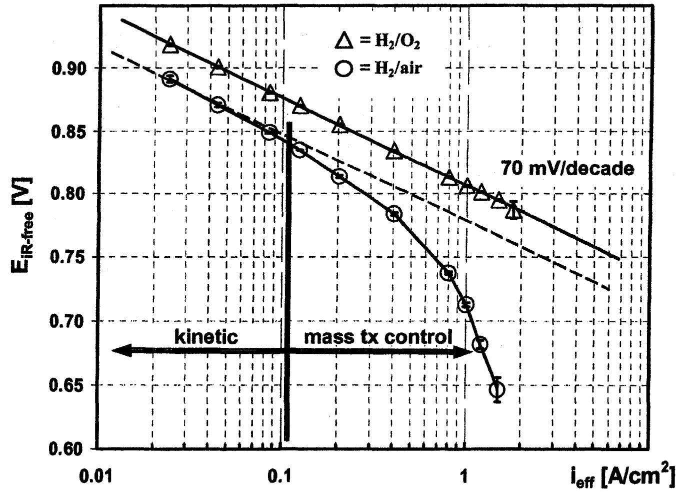

Figure 7: Resistance-corrected single-cell voltage, $E_{iR\text{-free}}$, versus H_2-crossover corrected effective current density, i_{eff}, with H_2/O_2 and H_2/air for a 50 cm^2 active-area MEA using a ca. 25 μm low-EW membrane (ca. 900 EW) coated with electrodes consisting of ca. 50%wt. Pt/carbon (0.4/0.4 mg_{Pt}/cm^2 (anode/cathode)) and a low-EW ionomer (ca. 900 EW; ionomer/carbon ratio=0.8/1). Data were recorded at a cell temperature of 80°C with fully-humidified reactants (80°C dewpoints, i.e., 100% RH) at a total pressure of 150 kPa_{abs} and stoichiometric flows of s=2.0/9.5 (H_2/O_2) and s=2.0/2.0 (H_2/air), respectively (controlled stoichiometric flows for $i_{eff} \geq 0.2$ A/cm^2; 0.2 A/cm^2 flows at $i_{eff} < 0.2$ A/cm^2). The dashed line is a parallel-shifted guide-to-the-eye, following the same Tafel-slope as for pure O_2 (solid regression line). Voltages were averaged between 10 and 15 mins. holding time at each current density (measured current densities are corrected for H_2-crossover of 2.5 mA/cm^2).

H_2/air performance – Based on the above findings one would expect a similarly straight Tafel-line for fuel cell operation with air instead of O_2, but offset toward lower cell voltages due to the reduced oxygen partial pressure in air. As is shown in Figure 7, this is indeed true for very low current densities where H_2/O_2 and H_2/air Tafel-curves are parallel and offset in the expected direction. At current densities above 0.1 A/cm^2, however, the H_2/air curve begins to deviate from the kinetically-controlled Tafel-line of 70 mV/decade and displays an increase in the apparent Tafel-slope with increasing current density, indicative of additional mass-transport related resistances (due to diffusion-overpotentials at the cathode and possibly potential gradients in the electrolyte phase of the electrode). Since the purely ohmic resistance losses, ΔE_{ohmic}, are measured *in-situ*, the mass-transport related overpotential, η_{tx}, can be evaluted via:

$$\eta_{tx} = E_{eq} - E_{cell} - \eta_{ORR} - \Delta E_{ohmic} \qquad [14]$$

where the η_{ORR}-term is calculated by assuming that the resistance-free H_2/air cell voltage at current densities <<0.1 A/cm^2 is purely controlled by the ORR kinetics with a Tafel-slope of 70 mV/decade (for details see reference 6). The mass-transport induced voltage losses may be visualized in Figure 7 by the voltage difference between the extrapolated kinetically-controlled Tafel-line (dashed line) and the reistance-corrected air-curve (circles). Overall it may be stated that the mass-transport induced voltage losses are negligible below 0.2 A/cm^2 and amount to ca. 65 mV at 1 A/cm^2. Based on comparative experiments with helox (21% O_2 in He), the majority of these mass-transport related losses seem to be due to flooding of the diffusion medium (6) and data in the literature (30) suggest that this can be alleviated by proper design of the flow-field/diffusion medium interface.

Figure 8 presents the polarization curve (not IR-corrected) shown in Figure 7 and indicates the various losses determined from the analysis described above, and the results reveal the various possibilities for performance improvements.

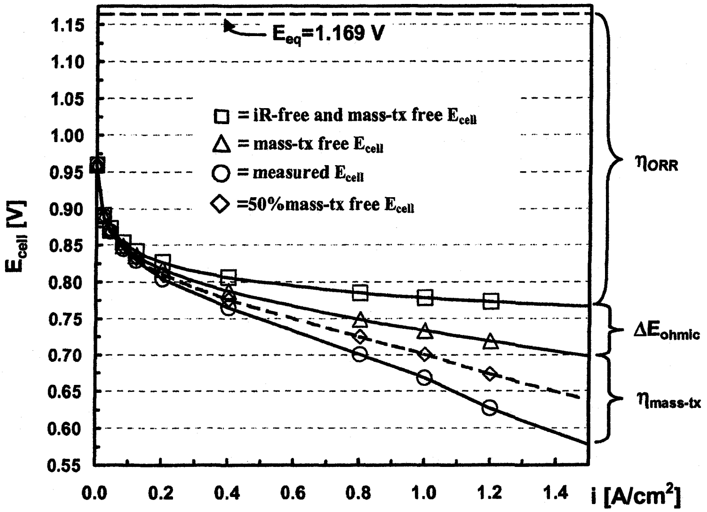

Figure 8: a) circular symbols: 50 cm^2 single-cell voltage, E_{cell}, versus current density, i, with H_2/air (s=2.0/2.0) for a 50 cm^2 MEA at a cell temperature of 80°C with fully-humidified reactants at a total pressure of 150 kPa$_{abs}$ (same experimental conditions and MEA as in Figure 7).
b) triangular symbols: E_{cell} vs. i for the mass-transport-free E_{cell}/i-curve shown in a).
c) square symbols: iR-correction of the E_{cell}/i-curve shown in b) using *in-situ* high-frequency resistance measurements at 1 kHz (ranging from 45 to 55 mΩcm^2).
d) diamond symbols: E_{cell}/i-curve shown in a) corrected for 50% of the mass-transport losses.

The experimentally measured polarization curve achieves approx. 0.58 V at 1.5 A/cm^2 (circles in Figure 8), but could potentially reach 0.70 V at the same current density if one were able to reduce mass-transport related voltage losses to zero (triangles in Figure 8). Yi *et al.* have shown recently (30), that voltage losses due to "flooding" phenomena can be reduced significantly by an optimized design of the MEA/diffusion-medium/flow-field interfaces and it is not implausible to assume that at least 50% of the currently observed mass-transport related voltage losses might be recovered (diamonds in Figure 8) by proper interface design. The ohmic resistances in the graphite hardware used in these experiments are 0.050±0.005 Ωcm^2 (measured *in-situ*), whereby the contributions from contact resistance (mainly between the flow-field and the diffusion medium) and from the proton conduction resistance in the membrane are of approximately equal value (6). Thinner or more conductive membranes and lower contact-resistance DM/flow-filed configurations would reduce these losses, but the potential for improvement is clearly less than in the case of the mass-transport losses. Clearly the biggest voltage-loss is due to sluggish oxygen reduction kinetics and besides modest improvements over pure Pt reported for Pt-alloy cathode catalysts (ca. 20-40 mV at constant current density, equivalent to a factor of 2 to 3 in current density at constant cell voltage (16, 22, 26)), no other material options have ever been reported

Current and Projected MEA Performance and Pt-Specific Power Densities:

We now analyze the consequence of the above deconvolution of the various voltage-loss contributions and the significance with regards to the long-term automotive requirement to obtain platinum-specific stack-power densities of $\leq 0.2\ g_{Pt}/kW$. A further consideration in defining this goal is that a cell voltage significantly above 0.60 V is required in order to both effectively harvest the higher energy conversion efficiency of fuel cell systems compared to internal combustion engines and to reduce the amount of heat which needs to be rejected by the system via the radiator (1).

The following analysis is based on the polarization curves shown in Figure 8, obtained with MEAs having a Pt-loading of 0.40/0.40 mg_{Pt}/cm^2 (anode/cathode). In a recent study (31) we have shown, however, that the Pt-loading of the anode electrode can be reduced to 0.05 mg_{Pt}/cm^2 without significant voltage loss in the case of H_2/air fuel cell operation with pure H_2 (rather than CO-contaminated reformate), a fact related to the very facile H_2 oxidation kinetics on Pt in the absence of CO (32). With this in mind, the current state-of-the-art MEA performance shown in Figure 8 (line a), circular symbols) can be analyzed in terms of Pt-specific power density vs. cell voltage, assuming a total MEA Pt-loading of 0.45 mg_{Pt}/cm^2 (i.e., 0.05/0.40 $mgPt/cm^2$ (anode/cathode)). This is shown by the first line from the top in Figure 9 (line a), circular symbols), clearly demonstrating the trade-off between voltage efficiency (i.e., cell voltage) and Pt-specific power density. Quite obviously, the automotive requirement of $<0.2\ g_{Pt}/kW$ at $E_{cell}>0.6$ V is missed by a factor of three with this MEA/cell-design technology and approaches need to be developed with which this requirement can be met.

Higher Pt-specific power densities can be achieved by reducing the mass-transport related voltage-losses via improving the MEA/DM/flow-field interfaces, as was demonstrated in a recent article by Yi *et al.* (30). Assuming that ca. 50% of the observed mass-transport related voltage losses can be recovered by optimized design, the power density of the MEA at 0.65 V can be increased by approx. 25% (circles vs. diamonds in Figure 8), thereby increasing both the volumetric and the gravimetric power density of the fuel cell stack. This also translates to a similar improvement of the Pt-specific power density (see diamond symbols, line b) in Figure 9), but still falls short by more than a factor 2 of the desired goal of $<0.2\ g_{Pt}/kW$.

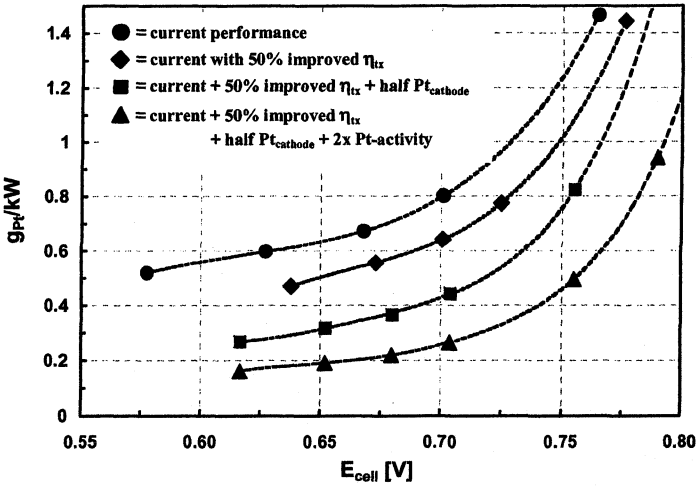

Figure 9: Pt-specific power-density [g_{Pt}/kW] vs. cell voltage, E_{cell}, based on the performance data shown in Figure 8 both for the uncorrected cell voltage (see a) in Figure 8) and the performance curve projected for a 50% reduction of mass-transport losses (see d) in Figure 8). It is assumed that the cell performance can be maintained at a reduced anode loading of 0.05 mg_{Pt}/cm^2 (see text).
a) circular symbols: g_{Pt}/kW vs. E_{cell} for the uncorrected cell performance curve in Figure 8 (a).
b) diamond symbols: g_{Pt}/kW vs. E_{cell} for the cell performance curve in Figure 8 (d) for which the mass-transport losses were assumed to be reduced by 50%.
c) square symbols: g_{Pt}/kW vs. E_{cell} for the above curve (b), assuming a two-fold reduction of the Pt-cathode loading to a total loading of 0.05/0.2 mg_{Pt}/cm^2 (anode/cathode), accompanied by a cell voltage loss of 21 mV independent of current density (see text).
d) triangular symbols: g_{Pt}/kW vs. E_{cell} for the above curve (c), assuming a doubling of the Pt-specific cathode-catalyst activity without cell voltage loss, resulting in a total Pt loading of 0.05/0.1 mg_{Pt}/cm^2 (anode/cathode).

A more significant step toward approaching the above automotive requirements is achieved by a two-fold reduction of the platinum cathode-loading, if the associated cell voltage loss can be minimized. Considering that the PEFC performance is largely controlled by the O_2 reduction reaction kinetics (see Figure 8), a reduction of the platinum cathode-loading is expected to definitely lead to a cell voltage loss. The best-case scenario, i.e., the minimum achievable voltage loss, would be the kinetic limit described by the Tafel-relation for the ORR (see reference 6 for a detailed analysis):

$$\Delta E_{loss-ORR} \approx 70\,\mathrm{mV/decade} \cdot \log(L_1/L_2) \qquad [15]$$

where $\Delta E_{loss\text{-}ORR}$ describes the kinetically-limited voltage loss if the cathode Pt-loading is reduced from a value of L_1 to L_2. For a cathode loading reduction by a factor of two, this would translate into a minimum voltage loss of 21 mV across the entire current density range or, in other words, into a down-shift of the polarization curves in Figure 8 by 20 mV. For most available non-optimized MEAs, a cathode loading reduction from 0.40 to 0.20 mg_{Pt}/cm^2) leads to cell voltage losses on the order of 40 to 60 mV, i.e., far beyond the above prediction based on ORR kinetics (31). In the case of specifically optimized low-Pt-loading MEAs, however, the predicted kinetically-limited cell voltage loss of ca.

20 mV can indeed be observed over the entire current density range (31). In this case, an optimized MEA/DM/flow-field configuration with 50% improved mass-transport losses (diamond symbols in Figure 9) and a reduced MEA loading of 0.05/0.20 mg_{Pt}/cm^2 will produce Pt-specific power densities very closely approaching the <0.2 g_{Pt}/kW target (see square symbols, line c) in Figure 9).

Any further improvements via MEA/DM/flow-field interface optimization or Pt-thrifting are unlikely to further approach the Pt-specific power density requirement, if a cell voltage of >0.60 V is demanded. This most likely can only be achieved by an improvement of the intrinsic cathode catalyst activity by a factor of at least two, i.e., by at least doubling the mass-specific activity of platinum (in terms of A/mg_{Pt}). There are quite a few reports in the literature that this can be accomplished by the implementation of Pt-alloy cathode catalysts, e.g., PtCo, PtNi, PtCr (16, 22, 26), for which voltage gains on the order of 25 to 40 mV have been reported, consistent with a factor of two to three increase in Pt mass-specific activity. This intrinsic kinetic gain for Pt-alloys was also confirmed in our laboratory (33), and MEA implementation would allow the Pt-loading to be reduced from 0.25 mg_{Pt}/cm^2 (0.05/0.20 mg_{Pt}/cm^2 anode/cathode) to 0.15 mg_{Pt}/cm^2 (0.05/0.10 mg_{Pt}/cm^2 anode/cathode) without any loss in cell voltage. In this scenario, a Pt-specific power density of <0.2 g_{Pt}/kW could be achieved at a cell voltage of 0.65 V as is shown in Figure 9 (triangular symbols, line d)).

In summary, the very stringent automotive requirements in terms of Pt-specific power density combined with high voltage efficiency can be met only if the mass-specific activity of Pt-based cathode catalysts can be at least doubled. Initial data with Pt-alloys seem to satisfy this criterion, but significant fundamental research efforts are still required to both optimize their performance and to demonstrate the long-term durability of Pt-alloys which until now is unknown. So far, no Pt-free cathode catalysts have been demonstrated to achieve significant current densities at cell voltages comparable to what is obtained with platinum, but world-wide research efforts in cathode catalyst development have been very limited over the past twenty years and other catalysts may be found in the future if a focused effort is placed in this area.

SUMMARY AND CONCLUSIONS

As PEFC commercialization approaches, the need for product and manufacturing engineering is obviously increasing. However, the need remains for aggressive research and development focussed on new fuel cell materials, particularly if the technology is to meet demanding automotive requirements. Improved polymer electrolyte and catalyst materials will have the largest impact on PEFC commercialization. The development of these new materials will be most efficient if end-users attempt to define material requirements in terms of properties than can be measured in well-defined *ex-situ* characterization tests. The process of materials discovery will be most efficient if materials developers focus on making materials and obtaining *ex-situ* data. Once promising materials have been identified, projects involving implementation in MEAs can then be launched, ideally involving experts in MEA preparation. This approach will allow polymer scientists and electrocatalyst experts to focus their efforts on discovering materials and avoid wasting their efforts on the time consuming and potentially misleading process of MEA preparation.

We determine that an ideal automotive fuel cell polymer electrolyte would exhibit an ionic conductivity of 0.1 S/cm (at 25% relative humidity and 120°C). We identified upper (set by fuel efficiency constraints) and lower (set by electrode requirements) oxygen and hydrogen permeability limits of the electrolyte. More work is needed to identify reliable electrolyte chemical stability and mechanical property requirements. To reach automotive cost targets, cathode catalysts with mass specific activity twice that of those available today are needed. Promising approaches to achieve this include a combination of improved dispersion and improved intrinsic activities (e.g. stable Pt alloys).

REFERENCES

1. D.A. Masten, and A.D. Bosco, "System Design for Vehicle Applications (GM/Opel)" in *Handbook of Fuel Cells: Fundamentals, Technology, and Applications, Vol. 3*, W. Vielstich, A. Lamm, and H.A. Gasteiger, Editors, Wiley (to be published Spring 2003).
2. D.A. Masten, Unpublished results.
3. T. Springer, T. Zawodzinski, and S. Gottesfeld, in *Electrode Materials and Processes for Energy Conversion and Storage,* J. McBreen, S. Mukerjee, S. Srinivasan, Editors, PV 97-13, pp. 15-24, The Electrochemical Society Proceedings Series, Pennington, NJ, (1997).
4. D.M. Bernardi and M.W. Verbrugge, *J. Electrochem. Soc.*, **139**, 2477 (1992).
5. R.D. Breault, "PAFC Stack Materials and Stack Design" in *Handbook of Fuel Cells: Fundamentals, Technology, and Applications, Vol. 3*, W. Vielstich, A. Lamm, and H.A. Gasteiger, Editors, Wiley (to be published Spring 2003); b) C. Reiser and M. Landau, U.S. Patent 4,202,933 (1980).
6. H.A. Gasteiger, W. Gu, R. Makharia, M.F. Mathias, and B. Sompalli, "Beginning-of-Life MEA Performance – Efficiency Loss Contributions" in *Handbook of Fuel Cells: Fundamentals, Technology, and Applications, Vol. 3*, W. Vielstich, A. Lamm, and H.A. Gasteiger, Editors, Wiley (to be published Spring 2003).
7. G. Alberti, M. Casciola, L. Massinelli, and B. Bauer, *J. Membrane Science*, **185**, 73 (2001).
8. J.S. Wainright, M.H. Litt, and R.F. Savinell, "High-Temperature Membranes" in *Handbook of Fuel Cells: Fundamentals, Technology, and Applications, Vol. 3*, W. Vielstich, A. Lamm, and H.A. Gasteiger, Editors, Wiley (to be published Spring 2003).
9. E.W. Choe, B. Krishnamurthy, L. Xiao, H. Zhang, G. Calundann, and B. Benicewicz, "PBI Membranes for Fuel Cells", *This Proceedings Volume.*
10. N.M. Markovic, B.N. Grgur and P.N. Ross, *J. Phys. Chem. B*, **101**, 5405 (1997).
11. T. Sakai, N. Takenaka, Y. Wakabayashi, Y. Kawami, and E. Torikai, *J. Electrochem. Soc.*, **132**, 1328 (1985).
12. K. Broka and P. Ekdunge, *J. App. Electrochem.*, **27**, 117 (1997).
13. S. Kocha, "Principles of MEA Preparation for PEM Fuel Cells" in *Handbook of Fuel Cells: Fundamentals, Technology, and Applications* (eds.: W. Vielstich, A. Lamm, and H.A. Gasteiger), Wiley: vol. 3, to be published spring of 2003.
14. T. Sakai, H. Takenaka, and E. Torikai, *J. Electrochem. Soc.*, **133**, 88 (1986)
15. S.J. Lee, S. Mukerjee, J. McBreen, Y.W. Rho, Y.T. Kho, and T.H. Lee, *Electrochim. Acta*, **43**, 3693 (1998).
16. T.R. Ralph and M.P. Hogarth, *Platinum Metals Rev.*, **46**, 3 (2002).
17. T. Tada, "High Dispersion Catalysts Including Novel Carbon Supports for PEM Fuel Cells" in *Handbook of Fuel Cells: Fundamentals, Technology, and Applications, Vol. 3*, W. Vielstich, A. Lamm, and H.A. Gasteiger, Editors, Wiley (to be published Spring 2003).

18. R. Makharia, M.F. Mathias, D.R. Baker, J. Iaculli, M.W. Murphy, "Electrolyte Resistance Measurement in the Catalyst Layer of Polymer Electrolyte Fuel Cells using Electrochemical Impedance Spectroscopy", *This Proceedings Volume.*
19. K.D. Kreuer, "Hydrocarbon Based Membranes for PEM Fuel Cells" in *Handbook of Fuel Cells: Fundamentals, Technology, and Applications, Vol. 3*, W. Vielstich, A. Lamm, and H.A. Gasteiger, Editors, Wiley (to be published Spring 2003).
20. A.B. LaConti, M. Hamdan, and R.C. McDonald, "Mechanisms of Membrane Degradation for PEMFCs" *Handbook of Fuel Cells: Fundamentals, Technology, and Applications, Vol. 3*, W. Vielstich, A. Lamm, and H.A. Gasteiger, Editors, Wiley (to be published Spring 2003).
21. U.A. Paulus, T.J. Schmidt, H.A. Gasteiger, R.J. Behm; *J. Electroanal. Chem.*, **495**, 134 (2001).
22. N.M. Markovic, T.J. Schmidt, V. Stamenkovic and P.N. Ross (Jr.), *Fuel Cells*, **1**, 105 (2001).
23. K.D. Kreuer, *J. Membrane Science*, **185**, 29 (2001).
24 A. Rodrigues, M. Fronk and B. McCormick, "General Motors/Opel Fuel Cell Activities – Driving Toward a Successful Future" in *Handbook of Fuel Cells: Fundamentals, Technology, and Applications, Vol. 3*, W. Vielstich, A. Lamm, and H.A. Gasteiger, Editors, Wiley (to be published Spring 2003).
25 C. Jaffray and G. Hards, "Precious Metal Supply Requirements" in *Handbook of Fuel Cells: Fundamentals, Technology, and Applications, Vol. 3*, W. Vielstich, A. Lamm, and H.A. Gasteiger, Editors, Wiley (to be published Spring 2003).
26 D. Thompsett, "Platinum Alloys as Oxygen Reduction Catalysts" in *Handbook of Fuel Cells: Fundamentals, Technology, and Applications, Vol. 3*, W. Vielstich, A. Lamm, and H.A. Gasteiger, Editors, Wiley (to be published Spring 2003).
27 S. Mukerjee and S. Srinivasan, *J. Electroanal. Chem.*, **357**, 201 (1993).
28 E.A. Ticianelli, C.R. Derouin and S. Srinivasan, *J. Electroanal. Chem.*, **251**, 275 (1988).
29 S. Hirano, J. Kim and S. Srinivasan, *Electrochim. Acta.*, **42**, 1587 (1997).
30 J.S. Yi, J. Puhalski and C. King, in: *Abstracts of the 202nd Meeting of The Electrochemical Society*, Salt Lake City, October 2002, volume MA 2002-2, abstract number 812.
31 H.A. Gasteiger, J.E. Panels and S.G. Yan, submitted to *J. Power Sources*.
32 N.M. Markovic B.N. Grgur and P.N. Ross, *J. Phys. Chem. B*, **101**, 5405 (1997).
33 S. Kocha, General Motors Fuel Cell Activities, unpublished results.

Proceedings of The Electrochemical Society, PV 2002-31, 25-43 (2002)
DOI: 10.1149/200231.0025PV © The Electrochemical Society

ADVANCED ELECTRODE DEVELOPMENT AT W. L. GORE & ASSOCIATES, INC. VACUUM COATED CATALYZED / INKING HYBRID ELECTRODES

Carlos Cavalca, Mahesh Murthy and Daniel Frydrych
W. L. Gore & Associates, Inc. - Fuel Cell Technologies
201 Airport Road, Elkton MD 21922

James Arps and Kevin Walter*
Southwest Research Institute - Materials Engineering Department
6220 Culebra Road, San Antonio TX 78238
* *Current address: Technanogy 2146 Michelson Drive, Suite B, Irvine CA 92612*

ABSTRACT

One aspect of advanced electrode development at Gore Fuel Cell Technologies is presented and discussed: Membrane Electrode Assemblies (MEAs) with improved power output by concentration of a vacuum-deposited catalyst metal at the electrode/membrane interface.

These MEAs have electrodes exhibiting a gradient in the concentration of catalyst metal at the catalyzed electrode/membrane interface. The gradient can be formed by various vacuum-deposition techniques including electron-beam physical vapor deposition, EB-PVD, and dc sputtering. The process can be performed on the outer surface of a catalyzed electrode, on the surface on the PEM membrane or onto appropriate backings, which can be used to transfer the metal deposit to the membrane surface or electrode surface. The purpose of this structure is to enhance the performance of the electrode by concentrating the metal catalyst at the electrode/membrane interface, where the highest level of electrochemical activity takes place.

INTRODUCTION

Fuel cells show great commercial promise throughout the world as an alternative high efficiency energy source. Despite improvements in fuel cell technology key challenges still remain in the development of PEM fuel cells that need to be addressed. Improvements in power output, reduction of noble metal catalyst loading, improvements in water management, and lengthening of operational lifetimes are key technological challenges being addressed by numerous industrial and academic fuel cell developers.

The electrode technology development presented in this paper addresses the first two needs: improvement in power density and decrease in electrode Pt loading by modification of composite cathode electrodes. Good reviews on the state of the art in PEMFC science and technology have been published by Srinivasan and coworkers [1, 2], Appleby [3] and by Gottesfeld and Zawodzinski [4].

It is widely recognized that the cathode overpotential loss (activation, ohmic, and concentration) is mainly responsible for the polarization behavior in a H_2/air PEMFC. This controlling polarization is mainly due to the electrocatalytic sluggishness of the oxygen reduction reaction (ORR). It then follows that electrode design variables such as catalyst crystallite size and catalyst intrinsic loading, electrode loading, and electrode structure/architecture will have a significant impact on the electrode activity. Electrode formulation variables, such as type of process, ionomer and PTFE levels, solvent nature, etc. will also play a key role in overall electrode performance. Examples of development addressing the latter group of variables are the interesting work of Uchida [5] and Oh [6].

Addressing the first group of electrode design variables, one general approach to optimize electrode activity and minimize loading of expensive catalytic metal has been to use smaller catalyst particles. However, long operational lifetimes may be particularly difficult to achieve with low catalyst loadings. Also, catalyst particle size may be unstable and increase by agglomeration or sintering [7]. From another electrode design strategy, the pioneering work of LANL [8] is a nice example of cathode performance optimization by modifying electrode architecture. In this work the performance of MEAs with cathodes with catalyst layers of variable thickness (but same loading) are compared. This work demonstrated that thinner catalyst layers (using higher intrinsic loading electrocatalyst) of comparable electrode Pt loading are relatively more active than thicker ones (when one takes in consideration the difference in crystallite size between low and high intrinsic loading catalysts).

An alternative strategy to improve electrode performance by changing its architecture has also been to selectively elevate electrode Pt loading at its surface by concentration of relatively large amounts of metal catalyst at the gas diffusion electrode surface [8, 9]. Typically 500 Å (ca. 0.1 mg Pt cm^{-2} equivalent loading range) dense layers of metal catalyst have been sputtered onto gas diffusion electrodes. Improved electrode performance was reported for all three regions of the polarization curve (activation, ohmic and mass transport).

EXPERIMENTAL

For this study, ink-based composite ionomer/carbon-supported Pt catalyst electrodes compatible with PRIMEA® membrane electrode assembly technology were used. All the reference and modified MEAs were prepared with 20 μm GORE-SELECT® membranes. The MEAs used double-sided ELAT® as gas diffusion media for their fuel cell characterization.

The vacuum catalyst deposition was carried out using two techniques: electron-beam physical vapor deposition (EB-PVD) and magnetron sputtering. These deposition processes take place in-vacuum at pressures below 10^{-4} torr. The catalyzed substrates (15.24 cm x 15.24 cm swatches) were coated in batch mode using a double-rotation 4 point-holder carousel to assure uniformity of the coating. For the EB-PVD process, the evaporator consisted of a 5.08cm x 5.08 cm crucible loaded with high purity Pt slugs (99.95%). The Pt source was first re-melted and then evaporated using an electron beam source. For the sputtering deposition runs, a 15.24 cm diameter DC magnetron unit was used, which was loaded with a Pt foil target (0.127 mm thickness, 99.9%, Alfa). Typical deposition rates for both processes were kept comparable and ranged from 1 – 0.1 Å/sec.

All the testing was done using a standard 25 cm^2 single cell fixture (Fuel Cell Technologies) with triple-channel serpentine flow field using appropriate gasketing and cell compression. The assembled cells were loaded in Globetech fuel cell testing plants interfaced with Scribner & Assoc. electronic load units (500 W, 10 A Model 890B). The testing plant allowed for reactant flowrate (stoichiometric control), reactant saturation, cell temperature, and backpressure control. Polarization curves were obtained potentiostatically after ca. 1-day cell break-in. The polarization curves were taken using stability criteria, i.e., steady-state current per selected (controlled) voltage level. Current-interrupt techniques built in the Scribner load allowed the measurement of cell resistance and extraction of IR-compensated cell voltage.

To measure the cathode electrochemical active area and cell H_2 crossover, a galvanostat-potentiostat and function generator setup (Amel high-power galvanostat/potentiostat, Model 2055 interfaced with an AMEL function generator, Model 568) was used in conjunction with the gas unit during cell diagnostics.

RESULTS AND DISCUSSION

Part I - Vacuum Catalyzation process characterization: EB-PVD vs. sputtering

Although there are many well known vacuum deposition technologies, for this work two general deposition technologies were selected and compared as catalyzation strategies: thermal evaporation and sputter deposition.

In thermal evaporation or physical vapor deposition (PVD), a vaporized catalyst phase is obtained by direct heating and concomitant evaporation (sublimation) of a metal source. The choice of heating is dependent of several factors, including melting point, thermal resistance, etc. Examples include the use of ovens, resistance heater and electron-beam (EB). For the case of evaporation (sublimation) of noble metals (Pt, Pd, Ir, etc.), their high melting point forces the use of EB heating. Figure 1 depicts the EB-PVD process. An electron beam heats a Pt source and the resulting evaporated flux of catalyst physically condenses on MEA components, which are used as substrates, forming electrochemically active catalyst deposits. Fuel cell MEA components used as substrates include the exposed surface of electrodes, the exposed surface of proton-conducting membranes and the exposed surface of decal layers, such as skived PTFE.

Sputter deposition of metals is also a well-known technique in the art of metallization. Sputtering deposition can typically be done by direct ion bombardment or magnetron sputtering. Figure 2 depicts the sputtering process using a magnetron for a bimetallic system using a dual target array (i.e., two targets: Pt and Ru).

There are some key distinctions between these two processes that may direct their selection as catalyzation processes. First, the vaporized atom or cluster energy is higher for magnetron sputtering than thermal (typically 100 eV for magnetron vs. 10 eV for thermal). Second, alloys can be sputtered but not thermally evaporated. And third, one can typically expect more substrate heating from thermal evaporation.

In order to characterize the morphological and electrochemical behavior of EB-PVD and sputtered electrocatalysts, vacuum-coated catalyzed gas diffusion electrodes were prepared. Swatches of ELAT® gas diffusion media were catalyzed to a loading of 0.1 mg Pt cm^{-2} (ca. 500 Å equivalent thickness) via EB-PVD and magnetron sputtering. Figures 3a and 3b show field emission SEM conducted on the samples to achieve a deposition morphology characterization. Although the macro-morphology is mainly controlled by the GDM substrate roughness (vacuum deposition is a line-of-sight process that forms conformational coatings on a substrate), the micro-morphology between samples (which is of interest in catalysis) is clearly different and dependent on the vacuum catalyzation process used.

Analysis of the micrographs indicates that relatively uniform zones of the vaporized metal phase are formed. Electron-beam evaporated catalyzed samples exhibit a greater degree of surface micro-texture, characterized by high dispersion spherical nodules or clusters approximately 25 nm to about 100 nm in diameter, as well as the presence of rod-shaped structures. On the other hand, sputter deposition provided more dense catalyst layers with larger clusters. One possible explanation for this difference in micro-morphology could be attributed to the difference in energy between vaporized samples. Sputtered Pt atoms are more energetic than evaporated ones, thus it is possible that upon deposition, sputtered atoms or clusters relax (i.e., thermalize) the excess energy via surface migration, exhibiting cluster-to-cluster collision and concomitant sintering.

Electrochemical characterization of the above vacuum catalyzed GDEs was conducted next. MEAs were prepared bonding these catalyzed GDEs to 20 μm GORE-SELECT® membranes. Prior to bonding, the electrodes were impregnated with perfluorinated ionomer solution via brushing at a level of ca. 0.05 mg dry ionomer cm^{-2}. The cells were conditioned in H_2/air at $T_{cell} = 65$ °C with saturated reactants, and their polarization performance was then measured. Figure 4 shows a Tafel analysis for both prototype cathodes. The Tafel performance indicates that the EB-PVD catalyzed electrode offers superior electrocatalytic performance in comparison with the sputtered sample. Curve fitting of the data to the semi-empirical relation:

$$E_c = E(i) + iR = E_o - b \log i \quad \text{with } E_o = OCV + b \log i_o \qquad (1)$$

suggests that the evaporation process yields electrodes with improved exchange current density i_o, i.e., less polarizabilily of catalyst/electrolyte interface with overall improvement in ORR electrocatalytic activity.

The above finding clearly depicts a structure-performance relationship: EB-PVD catalyzed GDEs, which show more dispersed and abundant catalyst micro-structure yields superior electrodic performance when compared to the more agglomerated and denser Pt sputtered active phase formed by magnetron sputtering.

Part II - Pt EB-PVD Pt/C-ionomer composite hybrid electrode

This section describes how EB-PVD is used to modify standard inking-based Pt/C-ionomer composite electrodes to obtain higher performance hybrid structures.

Figure 5 depicts the concept: Pt EB-PVD is used to place a gradient in the concentration of catalyst metal at the electrode/membrane interface using very low levels of vaporized catalyst. The equivalent loading of vaporized Pt is very low, typically ranging from 0.001 mg Pt cm^{-2} (5 Å) up to 0.03 mg Pt cm^{-2} (150 Å). It should be noted that at the Pt loading levels used for the evaporated phase, it is expected that its effect on electrode activity due to increased metal loading in itself should be very small or negligible (depending upon the Pt loading of the base composite electrode).

This gradient in the concentration of Pt at the electrode/membrane interface can be implemented using diverse strategies, each one more or less appropriate to the electrode technology used: Pt EB-PVD of exposed surface of Gas Diffusion Electrodes (GDEs), Pt EB-PVD of the exposed surface of proton-conducting membranes and Pt EB-PVD of the exposed surface of decal layers, like skived PTFE.

MEAs containing modified cathodes and reference MEAs were electrochemically characterized by polarization performance, Tafel analysis and cyclic voltammetry. Figure 6 shows a Tafel analysis comparing the specific activity (as cathode mass activity) for the MEA containing the hybrid cathode versus a reference MEA. The MEA with the hybrid air electrode contained a total loading of 0.11 mg Pt cm^{-2}, formed by 0.1 mg Pt cm^{-2} at the electrode and 0.01 mg Pt cm^{-2} (ca. 50 Å) EB-PVD at the membrane electrode interface. The reference MEA had a cathode loading of 0.1 mg cm^{-2}. The data clearly shows that the hybrid cathode exhibits superior specific activity than the reference cathode at the overall same Pt loading.

Cathode Electrochemical Active area (ECA) titration was done on the hybrid cathodes consisting of 0.1 mg Pt cm^{-2} at the composite electrode and 0.03 (150 Å) and 0.01 (50 Å) mg Pt cm^{-2} EB-PVD at the interface. The ECA was then compared to the one of a reference 0.1 mg Pt cm^{-2} composite electrode. The cyclic voltammetry analysis showed that adding 0.01-0.03 (i.e., 50 - 150 Å) mg Pt cm^{-2} PVD at the interface results in a significant (non linear) increase in cathode specific ECA (cm^2/mg Pt). This increase in number of electrochemically-active sites is possibly due to the combined effect of the highly dispersed evaporated Pt deposition and the concomitant increase in electrode Pt utilization (Figure 7).

The effect of Pt vaporized phase loading at the membrane/electrode interface on the hybrid electrode performance can be seen in Figures 8a and b. This data demonstrates that the addition of more Pt at the interface does not guarantee an increase in performance. It may instead cause an adverse effect on electrode activity, as it can be seen for "larger" PVD loadings of 0.03 (150 Å) and 0.1 (500 Å) using a 0.3 mg Pt cm^{-2} composite cathode. This adverse effect on performance with high PVD loadings could be due to the formation of blocking electrode structures that reduce the proton ionic continuity between electrode and membrane.

It is interesting to note that the vaporized catalyst phase, at the loading levels applied of ca. 0.01 mg Pt cm^{-2}, displays very little activity in itself when tested as the only source of Pt in the electrode (Figure 8c). The poor activity level is due to the catalyst-intensive nature of ORR and the low loading magnitude for this electrode. On the other hand, when the ultra-low loading PVD phase is used in conjunction with a composite catalyzed structure, it forms a hybrid structure, and the effect is synergetic, thereby improving the activity of the base composite electrode. It will be seen in the coming section that this improvement is beyond the performance gain that may be obtained just by increasing the electrode loading (using conventional methods) by an amount comparable to the PVD deposition. The intrinsic activity Tafel analysis presented in Figure 6 and mass activity polarization curves presented in Figures 11 and 13 are in agreement with the above explanation.

Hybrid cathode performance – medium Pt loading range

Figure 9 shows data for a MEA using a hybrid cathode: 0.3 mg Pt cm^{-2} loading composite base electrode and 0.01 mg Pt cm^{-2} (50Å) EB-PVD at the electrode/membrane interface. The performance is compared to the one of a reference MEA using a standard composite electrode (0.3 mg Pt cm^{-2} loading). Polarization analysis shows that the MEA using the hybrid cathode offers superior performance compared to a reference MEA with standard electrocatalyst layers at the same loading. For example, at 0/0 psig and 65°C cell temperature the hybrid electrode containing MEA yields ca. 1200 mA cm^{-2} versus ca. 820 for the reference.

Figure 10 shows data for the same system, but at 15 psig and higher cell temperature (75°C). The same improvement can again be observed. The improvement in performance extends throughout the entire region of the polarization curve, showing at 0.6 V 1600 mA cm^{-2} versus 1200 mA cm^{-2} for the reference MEA. In the right axis, power density is also plotted. The system displays an improvement in power density with a displacement of the peak power to larger current densities.

Figure 11 shows an electrocatalyst mass activity analysis for the same system. For practicality reasons, and to get an idea of overall MEA Pt utilization economy, mass activity is here defined as current density (or power density) normalized by the overall MEA electrocatalyst loading (Pt at anode, Pt at cathode and vaporized Pt at the interface). The figure shows the improvement in electrocatalyst mass activity obtained when using hybrid cathodes, observing an improvement in mass activity almost proportional to the improvement in power density.

Hybrid cathode performance – low Pt loading range

Figure 12 depicts performance for a low loading MEA comprising a 0.1 mg Pt cm^{-2} composite cathode and 0.001 mg Pt cm^{-2} (5Å) EB-PVD Pt at the cathode/membrane interface. The anode was a standard composite electrode, 0.05 mg Pt cm^{-2}. The performance of this MEA using a hybrid low loading cathode is again compared against the one of a reference MEA having a standard composite cathode with 0.1 mg Pt cm^{-2} (same anode). Performance was evaluated at 15 psig cell backpressure and 65°C cell temperature. The data indicates that the low loading MEA using the hybrid cathode achieves an increase in current density of a factor of 2 at 0.6 V (from 440 mA cm^{-2} up to 860 mA cm^{-2}) with a substantial increase in peak power density.

The same graph also shows iR-free polarization performance (compensated potential), that, for the conditions of our test, mostly reflects cathode overpotential losses. All the tests are conducted with pure H_2 in the anode, thus it is expected that activation polarization losses at the anode, at the loading level of 0.05 mg Pt cm^{-2}, if any, may show up as linear overpotential contributions which are extractable by the current interrupt technique. It is observed that the compensated potential polarization curve perfectly tracks with the polarization curve expressed as a function of total cell potential. This behavior indicates that the enhancement in performance is solely due to the cathode, i.e. due the evaporated gradient at the cathode/membrane interface.

The mass activity behavior for the above MEA is showed in Figure 13. It is again observed that the enhancement in electrocatalyst utilization is mostly proportional to the measured enhancement in current/power density.

Part III - Spectroscopic characterization of electrode Pt distribution: RBS characterization

In order to characterize the Pt distribution on the hybrid inking/EB-PVD electrode, Rutherford Backscattering Spectrometry (RBS) was used. RBS has been successfully used in the past for post-mortem analysis and confirmation of Pt migration in PAFC gas diffusion electrode assemblies [10].

During RBS, an energetic ion beam (typically 2 MeV alpha particles) is directed onto the sample to be characterized. Some of the ions elastically scatter from the atoms on the sample surface and from atoms beneath the sample surface. These ions are said to backscatter from the sample. The ions that pass by the surface loose energy inelastically while traversing the sample, thus showing a shift in their energy. The energy and number of backscattered ions is measured by a detector and displayed as a plot of intensity versus channel (energy). This RBS spectrum can then be qualitatively and quantitatively interpreted to determine the concentration and depth distribution of an element (or elements) in a material. The backscattered ion energy is proportional to the mass of the atom from which the ion scattered and the amount of an element can be determined quantitatively by measuring the area under the part of the RBS spectrum that is due to the presence of that element. The profile is extracted by analysis of RBS signal with energy. The analysis depth is proportional to ion energy, that is, higher energy ions allow analysis to greater depths, but depth resolution is inversely proportional to ion energy. A more in-depth explanation of backscattering spectrometry can be found in reference [11].

Cells containing the hybrid cathode technology (0.1 mg Pt cm^{-2} composite electrode and ca. 0.01 mg Pt cm^{-2} (50 Å) at the electrode/membrane interface) and reference cells containing only 0.1 mg Pt cm^{-2} composite electrodes were characterized using RBS. Experiments were performed at the ion beam analysis (IBA) facility at Los Alamos National Laboratory. Two energies were used to perform the analysis (2 and 5.6 MeV). The RBS spectra were analyzed using RUMP computer program.

The RBS spectra presented in Figure 14 compare a hybrid electrode to a reference electrode. The data indicates that RBS can be successfully used to measure and quantify Pt distribution in a MEA half-cell. The Pt EB-PBD gradient at the electrode/membrane interface of the hybrid electrode technology is clearly visible: the Pt-portion of the RBS spectrum shows a very pronounced, highly localized distribution, mostly "spike" or delta-function in shape.

Simulation of the spectra was also done to confirm the loading of the PVD-applied phase. The quantitative analysis shows very good agreement with the targeted loading measured during the evaporation/catalyzation process using catalyst evaporation rates, dosing time and a vibrating micro-crystal balance placed in-situ the vacuum chamber.

CONCLUSIONS

Advanced high power density PEMFC MEA architectures from W. L. Gore & Associates, Inc. that have hybrid inking/vacuum deposited catalyzed electrodes have been characterized electrochemically and spectroscopically. These electrodes are compatible with PRIMEA® membrane electrode assembly technology.

These hybrid electrodes exhibit a gradient in the concentration of catalyst metal at the catalyzed composite electrode/membrane interface, where the highest level of electrochemical activity takes place. This interfacial gradient in catalyst concentration is formed by vacuum deposition using electron-beam physical vapor deposition (EB-PVD), and/or dc magnetron sputtering. The amount of vacuum-deposited catalyst metal that forms such gradient is very low (ca. 0.001 – 0.03 mg Pt cm^{-2}), thus not affecting, nor effectively increasing, the overall Pt loading of the cathode. This hybrid electrode architecture improves the current density distribution and overall electrode Pt utilization, yielding improved electrode performance and a concomitant increase in electrode Pt mass activity. It is found that EB-PVD yields catalytically more active microstructures both when tested as GDEs (i.e., vaporized layer as only catalytic metal) and as hybrid structures.

MEAs containing hybrid cathodes show improved single-cell polarization performance both at medium (ca. 0.3 mg Pt cm^{-2}) and low cathode loadings (ca. 0.1 mg Pt cm^{-2}) when compared to standard composite cathode. Concomitant almost-proportional enhancements in catalyst mass activity are also found, thus suggesting overall improvement in cathode electrodic activity. Cell diagnostics indicates that the concentration of this ultra-low loading Pt evaporated gradient at the Pt/C-ionomer composite electrode/membrane interface improves both the cathode specific electrochemical active area (i.e., cm^2/mg Pt) and specific activity (mA/mg Pt).

Rutherford Backscattering Spectroscopy (RBS) was successfully used to characterize the Pt distribution on the hybrid electrode. The Pt portion of the RBS spectra clearly shows a very pronounced gradient of catalyst at the electrode/membrane interface for the hybrid cathode due to the vacuum catalyzation step. Quantification of the interfacial PVD-gradient was successfully done via modeling of the spectra.

ACKNOWLEDGMENTS

The authors would like to thank the following associates on the Gore Fuel Cell Technologies team for their contribution during this work: Connie Gibson (MEA prototype preparation), Will Johnson (intellectual property), Nick Sisofo and Dave Everson (fuel cell station set-up and qualification), Judy Rudolph and Tsueychen Long (SEM characterization), Carole Baczkowski (fuel cell testing), and Bonnie Sue Heist (manuscript preparation).

The following personnel at SwRI also deserve special recognition: Dr. Richard Page, Steve Clay, and Jim Riggs.

REFERENCES

1. P. Costamagna and S. Srinivasan *J. Power Sources* **102** 242-252 (2001)
2. P. Costamagna and S. Srinivasan *J. Power Sources* **102** 253-269 (2001)
3. S. Gamburzev and A. Appleby *J. Power Sources* **107** 5-12 (2002)
4. S. Gottesfeld and T. Zawodzinski *Adv. Electrochem. Sci. Eng.* **5** 195-301 (1997)
5. M. Uchida, Y. Aoyama, N. Eda and A. Ohta *J. Electrochem. Soc.* **142** No. 12 (1995)
6. S. Shin, J. Lee, H. Ha, S. Hong, H. Chun and I. Oh *J. Power Sources* **106** 146-152 (2002)
7. M. Wilson, F. Garzon, K. Sickafus and S. Gottesfeld *J. Electrochem. Soc.* **140** No. 10 (1993)
8. E. A. Ticianelli, C. R. Derouin, A. Redondo and S. Srinivasan *J. Electroanal. Chem.* **251**, 257 (1988)
9. S. Mukerjee, S. Srinivasan and A. Appleby *Electrochimica Acta* **38**, No.12 (1993)
10. L. Borodovsky, J. Beery and M. Paffett *Nuclear Instruments and Methods in Physics Research* **B24/25** 568 (1987)
11. W. Chu, J. Mayer and M. Nicolet in "Backscattering Spectrometry", Academic Press

FIGURES

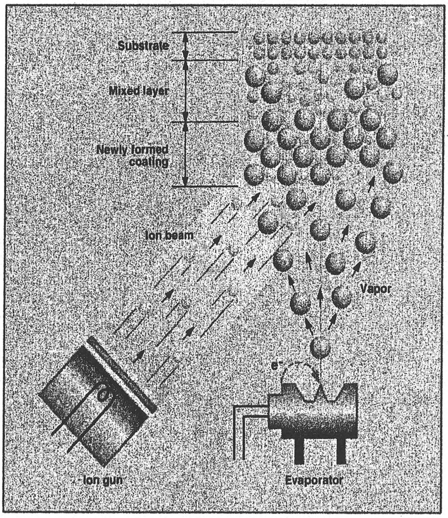

Figure 1: Electron-Beam Physical Vapor Deposition (EB-PVD) vacuum deposition / catalyzation process.

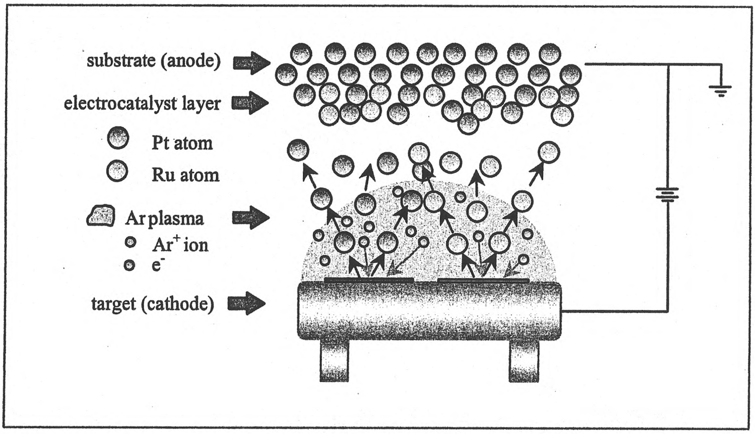

Figure 2: Dual-target magnetron sputtering deposition.

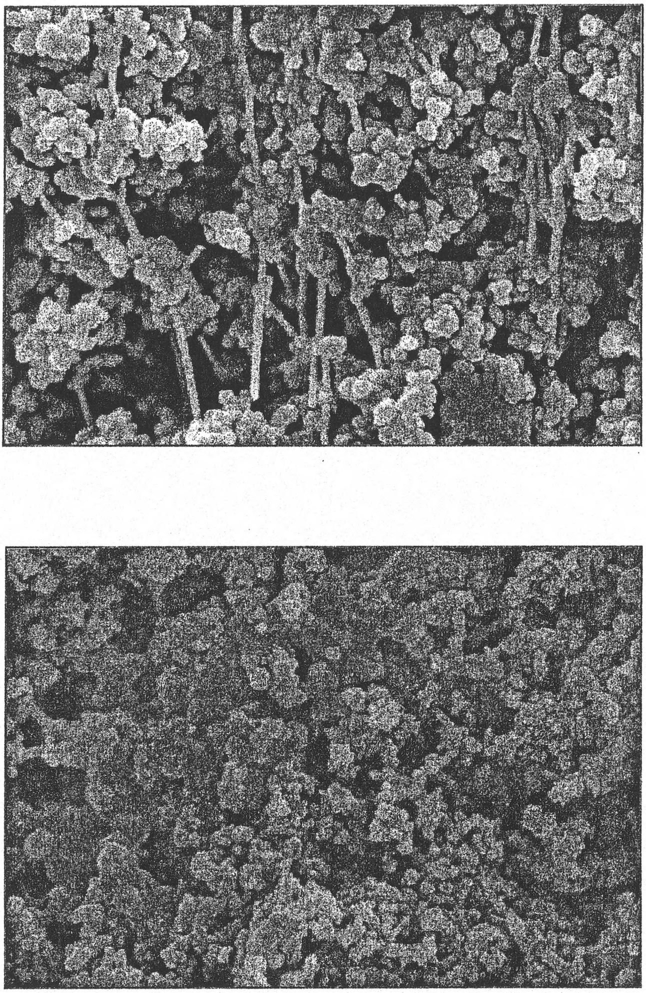

Figures 3 a & b: Field emission SEM micrographs (x 25k magnification) of **a:** (top) Pt EB-PVD catalyzed ELAT® gas diffusion media and **b:** (bottom) Magnetron sputtering catalyzed ELAT® gas diffusion media showing difference in electrocatalyst microstructure. Electrode loading is 0.1 mg Pt cm^{-2} (500 Å equivalent PVD thickness). Micrographs are of electrodes prior to ionomer impregnation.

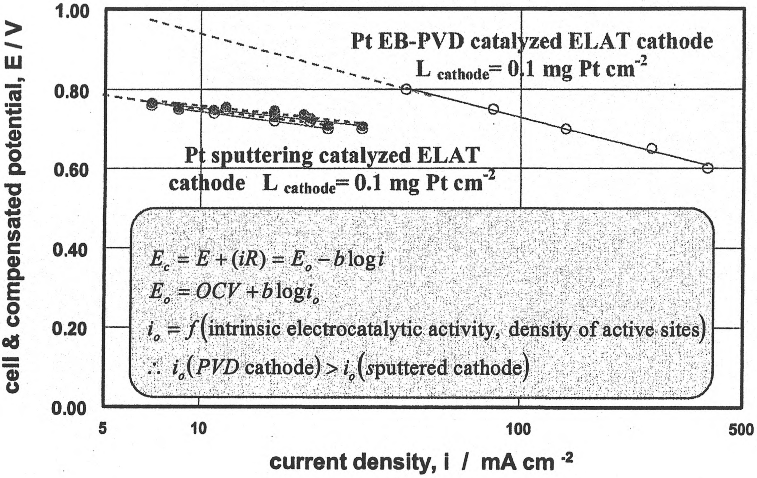

Figure 4: Tafel analysis for Pt EB-PVD and sputtering catalyzed ELAT® GDEs. The vaporized phase is the only source of cathode electrocatalyst.

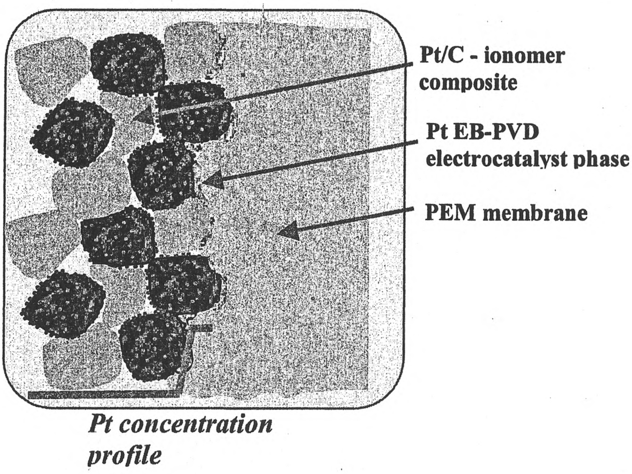

Figure 5: Vacuum coated catalyzed / composite (inking) hybrid electrode concept. The vaporized catalyst phase is of ultra-low loading in nature (ca. 0.001 – 0.03 mg cm^{-2}), and forms a highly localized gradient of catalyst at the composite electrode/membrane interface.

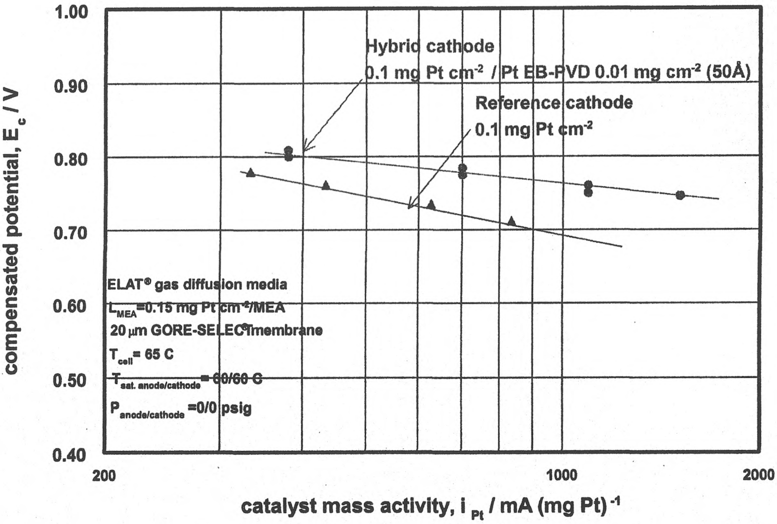

Figure 6: Specific activity (as electrocatalyst mass activity) for the hybrid cathode versus a composite reference electrode. The hybrid cathode structure shows superior specific activity (i.e., activity per catalyst mass) than the reference.

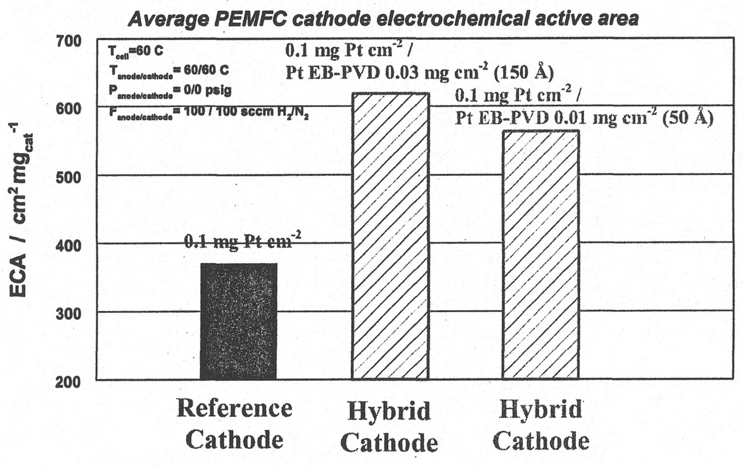

Figure 7: Cathode specific electrochemical active area titration. Hybrid electrodes are shown versus a reference. Both modified structures yield improved number of active sites per gram of catalyst.

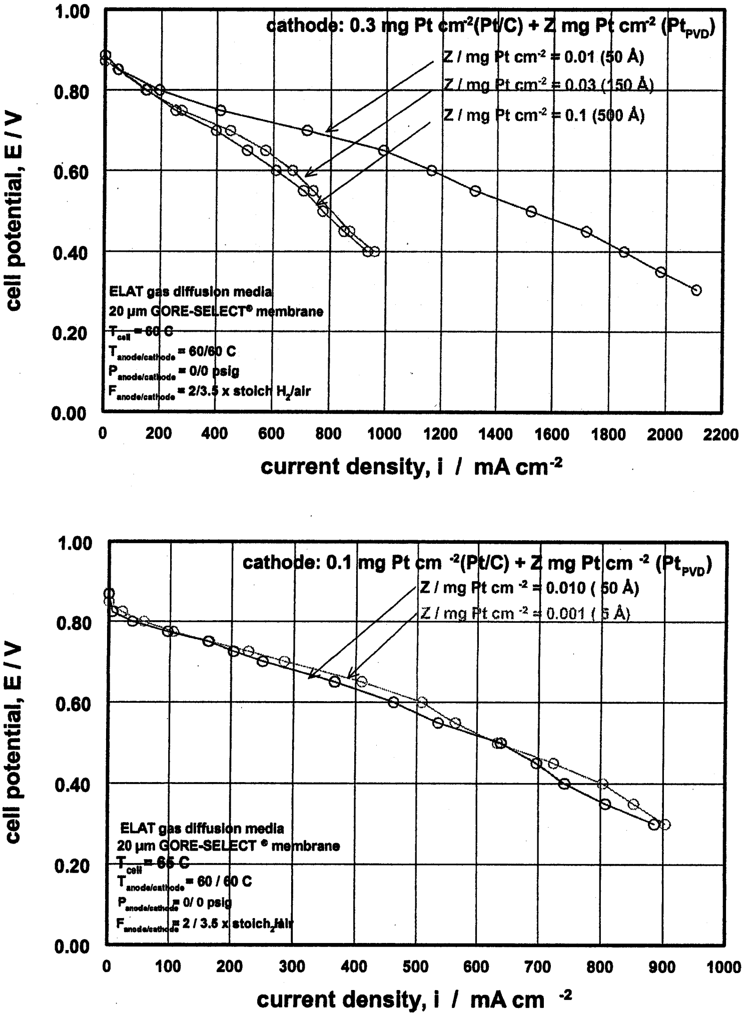

Figures 8 a & b: Effect of Pt vaporized phase loading at the membrane/electrode interface on the hybrid electrode performance. **a:** (top) Effect of incremental PVD loadings using a medium loading composite cathode. **b:** (bottom) Effect of decreasing PVD loadings using a low loading composite cathode.

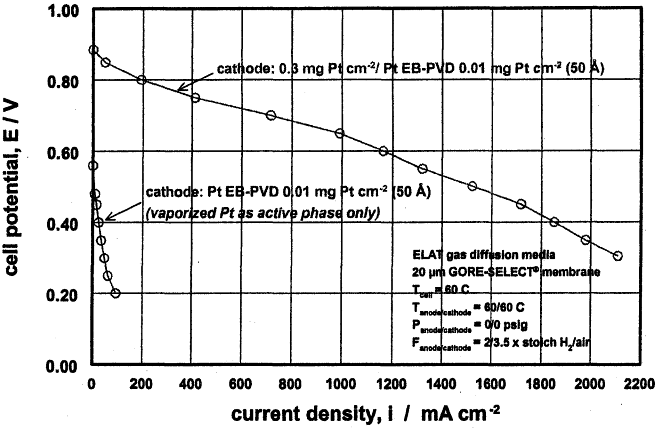

Figure 8 c: Electrodic activity of Pt vaporized phase (i.e., Pt PVD phase at 0.01 mg cm^{-2} loading level as the only source of electrode catalyst) versus activity of the hybrid electrode counterpart (0.1 mg Pt cm^{-2} base composite electrode / 0.01 mg cm^{-2} Pt EB-PVD at interface).

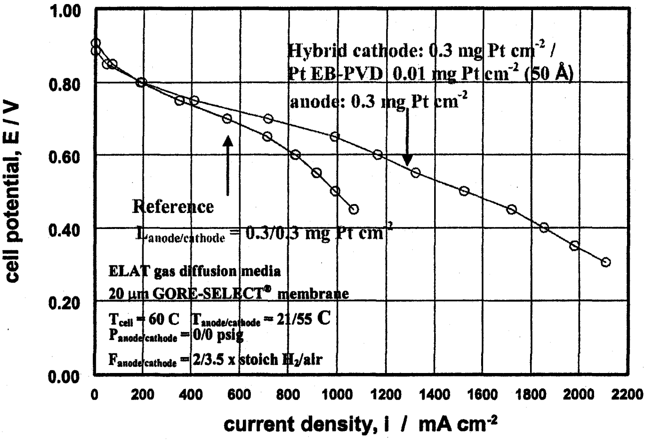

Figure 9: Performance of MEA using a hybrid cathode: 0.3 mg Pt cm^{-2} loading composite base electrode and 0.01 mg Pt cm^{-2} (50 Å) EB-PVD at the electrode/membrane interface. Performance compared to reference MEA using standard composite cathode of same loading. $T_{cell} = 60$ °C, $P_{cell} = 0$ psig.

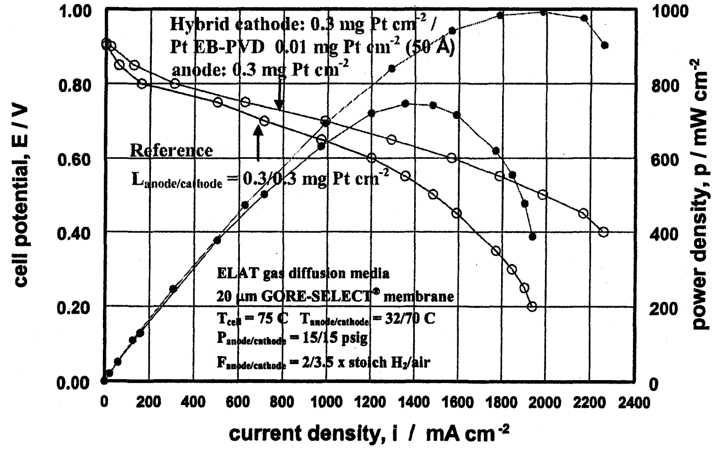

Figure 10: Performance of MEA using a hybrid cathode: 0.3 mg Pt cm^{-2} loading composite base electrode and 0.01 mg Pt cm^{-2} (50 Å) EB-PVD at the electrode/membrane interface. Performance compared to reference MEA using standard composite cathode of same loading. T_{cell} = 75°C, P_{cell} = 15 psig.

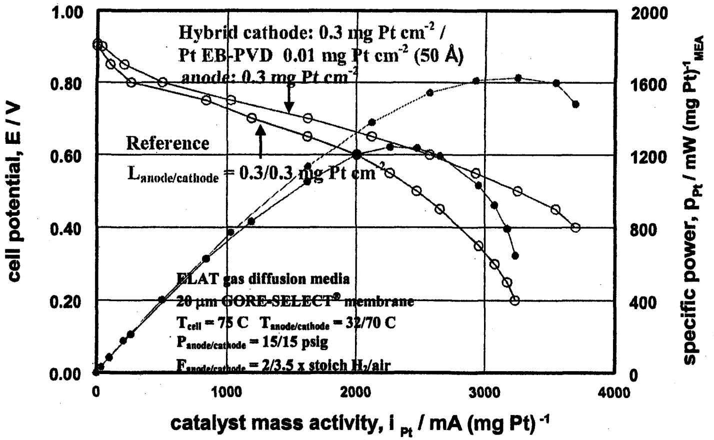

Figure 11: Electrocatalyst mass activity for MEA using a hybrid cathode: 0.3 mg Pt cm^{-2} loading composite base electrode and 0.01 mg Pt cm^{-2} (50 Å) EB-PVD at the electrode/membrane interface. Performance compared to reference MEA using standard composite cathode of same loading. T_{cell} = 75 °C, P_{cell} = 15 psig.

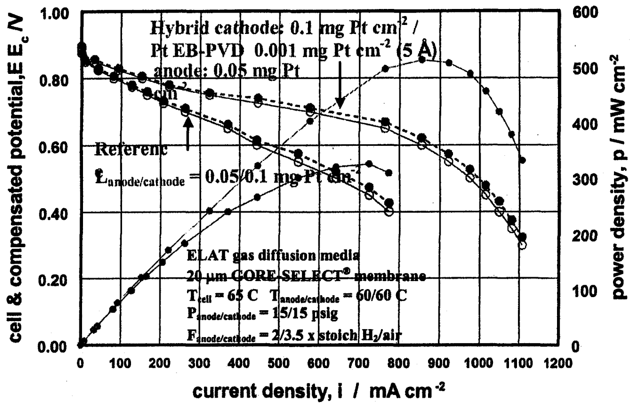

Figure 12: Performance of low loading MEA using a hybrid cathode: 0.1 mg Pt cm^{-2} loading composite base electrode and 0.001 mg Pt cm^{-2} (5 Å) EB-PVD at the electrode/membrane interface. Performance compared to reference MEA using standard composite cathode of same loading. All anodes contain 0.05 mg Pt cm^{-2} T_{cell} = 65 °C, P_{cell} = 15 psig. Solid lines correspond to total cell potential and dashed lines to iR-free (compensated) potential.

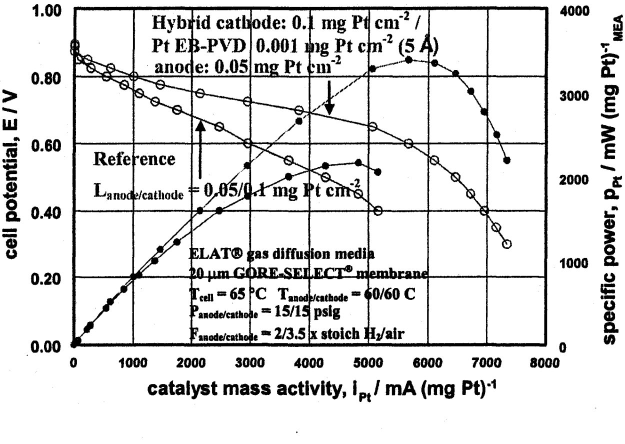

Figure 13: Electrocatalyst mass activity of low loading MEA using a hybrid cathode: 0.1 mg Pt cm^{-2} loading composite base electrode and 0.001 mg Pt cm^{-2} (5 Å) EB-PVD at the electrode/membrane interface. Performance compared to reference MEA using standard composite cathode of same loading. All anodes contain 0.05 mg Pt cm^{-2} T_{cell} = 65 °C, P_{cell} = 15 psig.

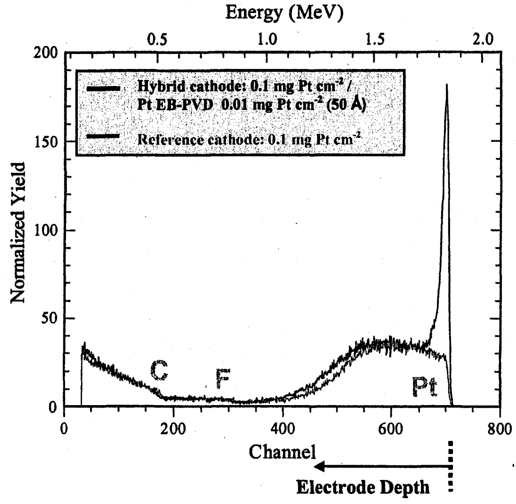

Figure 14: Rutherford Backscattering Spectroscopy (RBS) characterization of hybrid half cell structure consisting of 0.1 mg Pt cm^{-2} composite base electrode and 0.01 mg Pt cm^{-2} (50Å) EB-PVD at the electrode/membrane interface (versus a reference cell). Along the spectral Pt edge, the electrode Pt distribution for the hybrid structure clearly shows the steep highly localized gradient in Pt due to the PVD catalyzation.

Proceedings of The Electrochemical Society, PV 2002-31, 44-53 (2002)
DOI: 10.1149/200231.0044PV © The Electrochemical Society

KINETIC MODEL OF PLATINUM DISSOLUTION IN PEM FUEL CELLS

Robert M. Darling and Jeremy P. Meyers
UTC Fuel Cells
195 Governor's Highway
South Windsor, Ct 06040

ABSTRACT

This paper presents a mathematical model of oxidation and dissolution of supported platinum catalysts in polymer-electrolyte fuel cells. Kinetic expressions for the oxidation and dissolution reactions are developed and compared to available experimental data. The model is used to investigate the influences of electrode potential and particle size on catalyst stability.

INTRODUCTION

The principle source of inefficiency in PEM fuel cells is sluggish oxygen-reduction reaction (ORR) kinetics at the cathode. Carbon-supported platinum catalyst is commonly used to enhance the rate of the ORR. In such catalysts, the high surface-to-volume ratio of the platinum particles maximizes the area of the surfaces available for reaction. If the platinum particles cannot maintain their structure over the lifetime of the fuel cell, changes in the morphology of the catalyst layer from the initial state will result in a loss of electrochemical activity. It has been established experimentally that platinum dissolves in PEM fuel cells.[1,2] In this paper, we develop a mathematical model for the kinetics of platinum dissolution and examine model predictions under a range of PEM fuel cell operating conditions.

The model described in this paper is a spatially lumped model that treats a single, porous platinum electrode and the ionomeric solution that fills the pores of the electrode. The model includes spherical platinum particles that can grow and shrink as platinum plates and dissolves; a platinum oxide layer; and an ionic platinum species in solution (Pt^{2+}). This model contains the basic interfacial reactions and material balances, without including the mass-transport and reaction-rate distributions that come into play in a more detailed electrode model to be published later.

MODEL EQUATIONS

Electrochemistry

We consider three electrochemical reactions: platinum dissolution

$$Pt = Pt^{2+} + 2e^{-}, \tag{1}$$

platinum oxide film formation

$$Pt + H_2O = PtO + 2H^{+} + 2e^{-}\ , \tag{2}$$

and chemical dissolution of platinum oxide

$$\mathrm{PtO} + 2\mathrm{H}^{+} = \mathrm{Pt}^{2+} + \mathrm{H_2O}. \qquad (3)$$

In a purely thermodynamic analysis, one of these equations could be discarded; only two of them are thermodynamically independent. For example, reaction (3) could be obtained by subtracting reaction (2) from reaction (1). However, we assume that the ion-exchange reaction (3) occurs by a chemical pathway that is distinct from any combination of the two charge transfer reactions. Thus, it is included in the kinetic analysis of the system. Pt^{2+} is assumed to be the only ionic platinum species present in significant amounts. Other ionic species with higher oxidation states are reported by Pourbaix[3], but they are not expected to be important in the region of interest. In the literature the oxide species was often regarded to be $\mathrm{Pt(OH)_2}$, however, recent quartz microbalance measurements show that the film is not hydrated.[4] This distinction is probably not critical in this work. Further oxidation of the PtO film is not considered explicitly in this work. There are two methods by which we could lose platinum to the solution. The first is by the electrochemical dissolution of Pt to Pt^{2+} according to reaction (1), and the second is by the chemical dissolution of the PtO film according to reaction (3).

Rate equations

The platinum dissolution reaction is treated as a single elementary step. We propose a rate expression of the following form:

$$r_1 = \frac{i_1}{n_1 F} = k_1 \theta_{\mathrm{vac}} \left[\exp\left(\frac{\alpha_{a,1} n_1 F}{RT} (\Phi_1 - \Phi_2 - U_1) \right) - \left(\frac{c_{Pt^{2+}}}{c_{Pt^{2+},ref}} \right) \exp\left(-\frac{\alpha_{c,1} n_1 F}{RT} (\Phi_1 - \Phi_2 - U_1) \right) \right]$$

where $\theta_{vac}=1-\theta_{PtO}$ is the fraction of the platinum surface that is not covered by oxides. This term is included in the forward rate expression to allow oxide on the surface to insulate the particle and prevent platinum dissolution from beneath the oxide film. θ_{vac} is included in the reverse term to prevent Pt^{2+} from plating on Pt through a PtO film.

$$U_1 = U_1^{\theta} - \frac{\Delta\mu_{Pt}}{2F}$$

is the standard equilibrium potential of reaction (1). This potential is shifted away from the literature value for bulk platinum by the factor

$$\Delta\mu_{Pt} = \frac{\sigma_{Pt} M_{Pt}}{r \rho_{Pt}}.$$

This factor accounts for the effect of the surface tension of the platinum crystallite on the equilibrium potential. As the platinum particle becomes larger, the shift in the chemical potential of platinum diminishes.

The kinetic expression for platinum oxidation was adapted from the models of Harrington and Heyd,[4,5] and Conway and co-workers.[6] The anodic term, which describes the formation of the oxide, is equivalent to their models. The cathodic term was added in order to describe the reduction of PtO back to platinum metal. The original model of Conway and co-workers allows for unlimited growth of PtO on the Pt surface; our expression reaches equilibrium coverage when the forward and reverse rates are equal in magnitude. The equilibrium coverage may exceed a monolayer.

$$r_2 = k_2\left[\exp\left(-\frac{\omega\theta_{\mathrm{PtO}}}{RT}\right)\exp\left(\frac{\alpha_{a,2}n_2F}{RT}(\Phi_1-\Phi_2-U_2)\right)-\theta_{\mathrm{PtO}}\left(\frac{c_{H^+}^2}{c_{H^+,ref}^2}\right)\exp\left(-\frac{\alpha_{c,2}n_2F}{RT}(\Phi_1-\Phi_2-U_2)\right)\right]$$

As in reaction (1), the equilibrium potential for this reaction is shifted to account for the surface energy of the platinum crystallite. We also shifted the chemical potential of PtO from the value reported by Pourbaix.[3] In order to match the onset of platinum oxidation observed in cyclic voltammetry data, the platinum oxide must begin to form at lower potentials than would be predicted by using the chemical potential of bulk platinum oxide. Thus, one must assume that the oxide formed on the surface of a platinum crystallite is somehow stabilized by its interactions with the platinum metal and, hence, has a lower chemical potential than a bulk oxide. Alternatively, one might ascribe adsorption at low potentials to PtOH, which further oxidizes to PtO at higher potentials.

$$U_2 = U_2^{\theta} + \frac{\Delta\mu_{PtO}}{2F} - \frac{\Delta\mu_{Pt}}{2F}.$$

where

$$\Delta\mu_{PtO} = \Delta\mu_{PtO}^{0} + \frac{\sigma_{PtO}M_{PtO}}{r\rho_{PtO}}.$$

U_2 may either increase or decrease with particle size depending upon the magnitudes of σ_{Pt} and σ_{PtO}. The value of σ_{Pt} used in this work exceeds the value of σ_{PtO}, which means that U_2 increases with particle size.

Finally, the rate of the chemical reaction is

$$r_3 = k_3\left(\theta_{\mathrm{PtO}}\, c_{\mathrm{H^+}}^2 - \frac{c_{\mathrm{Pt^{2+}}}}{K_3}\right),$$

where the equilibrium constant, K_3, is again shifted from what one would calculate for bulk platinum oxide. The equilibrium constant, K_3, is related to U_1 and U_2 by the equation,

$$K_3 = \exp\left[\frac{F}{RT}(n_1U_1 - n_2U_2)\right].$$

The proton concentration is related to the water content of the membrane material by the equation,

$$c_{H^+} = \frac{EW}{\lambda}$$

where EW is the equivalent weight of the membrane and λ is the number of water molecules per acid site.

Material balances

To complete the development of the mathematical model, we need an appropriate set of material balances. The kinetic equations involve five species: Pt, PtO, Pt^{2+}, H^+, and H_2O. We assume that the concentrations of protons and water are fixed, and write material balances on the three remaining species. Assuming spherical platinum crystallites we get the following:

For PtO,

$$\frac{d\theta_{PtO}}{dt}=\left(\frac{r_2-r_3}{\Gamma_{\max}}\right)-\left(\frac{2\theta_{PtO}}{r}\right)\frac{dr}{dt}$$

where r is the particle radius, and Γ_{max} is the number of moles of active sites per unit of platinum area. This number is taken to be constant in this work, and is calculated assuming a specific charge of 220 μC/cm^2 in the hydrogen adsorption region. This equation indicates that PtO grows as a film of uniform thickness, on the surface of the platinum crystallites.

For Pt we obtain

$$\frac{dr}{dt}=-\frac{M}{\rho}(r_1+r_2)$$

where M and ρ are the molecular weight and density of platinum, respectively. Again, r_1 and r_2 refer to the reaction rates, in moles per second per square centimeter of Pt surface area.

Finally, a balance on Pt^{2+} in solution yields

$$\varepsilon\frac{dc_{Pt^{2+}}}{dt}=4\pi r^2 N(r_1+r_3)$$

where ε is the porosity of the electrode, which is assumed to be constant. N is the number of platinum crystallites per unit electrode volume,

$$N=\frac{a}{4\pi r^2},$$

Where a specific surface area of the electrode and r is the mean particle radius measured after initial electrode formation, before cycling alters the particle-size distribution.
The current density is

$$i=8\pi r^2 NFL(r_1+r_2)$$

where L is the thickness of the catalyst layer. Reaction 3 does not directly affect the current density, as it is a chemical reaction, not an electrochemical reaction.

RESULTS AND DISCUSSION

Figure 1 shows an experimental cyclic voltammogram taken on a commercially available Gore 5510 MEA, and simulations run with the model described above, at a scan rate of 10 mV/s and a temperature of 50°C. Hydrogen adsorption on the platinum surface occurs below 0.4 V. This region of the voltammogram is used to measure the electrochemical area (ECA) of platinum catalysts. Between 0.4 and 0.6 V, no significant electrochemical reactions occur, and the response is dominated by the double-layer capacitance. Finally, above 0.6 V, platinum is oxidized. This is the region of interest in this work, as it corresponds to typical operating potentials in fuel-cell cathodes. The goal of the modeling work is to fit parameters for reactions 1 through 3 at typical cathode potentials. As stated above, the dominant reaction is 2, platinum oxidation. Thus, the fit of the model to the experimental cyclic voltammograms is essentially determined by this reaction. However, platinum dissolution is the mechanism that we are ultimately interested in describing. The rate constant for the dissolution reaction was fit to unpublished data. The chemical dissolution of the platinum oxide film via reaction 3 is more difficult to account for because it is not electrochemical, and so its rate cannot be determined by current measurements. Its rate was arbitrarily set to a low value.

The shape of the voltammogram at high potentials is unusual. On the anodic sweep there is a plateau beginning at approximately 0.85 V and extending to at least 1.5 V (not shown in this set of experimental data, but established in the literature). On the cathodic sweep there is a distinct peak centered at approximately 0.75 V. The long plateau on the cathodic sweep happens because platinum oxide is not limited to monolayer coverage. Rather, multilayers of PtO may formThe onset of PtO formation predicted by the model, using the parameters in table 1, on the anodic sweep is approximately 25 mV too high. The location of the reduction peak predicted by the model matches the experiment, but the shape is different. The model particles discharge much of the film at a higher potential than what is observed experimentally.Table 1 lists the model parameters. Available literature values are given for comparison.

Figure 2 shows the surface coverage and platinum-ion concentration during the potential sweep experiments. The broad loops are the surface coverage, while the dashed lines are the Pt^{2+} concentration. The surface coverage begins to increase rapidly at a potential of approximately 0.8 V, and reaches values that vary from 0.6 at 1 V to 1.6 at 1.4 V. The maximum in surface concentration actually occurs after the sweep is reversed, because the reaction is slow. The system is not quick to come to equilibrium, and so, for finite sweep rates, the oxide coverage is lower than the thermodynamic equilibrium coverage. Figure 3 clarifies this effect. Even as the potential sweep reverses and starts to decrease, the oxide coverage is in equilibrium with a lower potential. Eventually, the decreasing potential and the lagging equilibrium potential cross, and the oxide layer is reduced.

The Pt^{2+} concentration increases rapidly at 1.1 V, but it plateaus at a concentration of 7×10^{-4} M because, at this sweep rate, it is at this concentration that the surface coverage of PtO reaches a monolayer, blocking off the surface from either further dissolution or plating. The Pt^{2+} concentration drops on the reverse sweep once the PtO coverage falls below a monolayer and exposes the surface for platinum plating. The Pt^{2+} is kinetically stable at the high potentials seen in this work, but it is not thermodynamically stable. Given enough time, the Pt^{2+} would tend to convert to PtO chemically according to reaction 3. We have assumed, however, that this reaction is slow.

Figure 4 shows the predicted equilibrium Pt^{2+} concentration as a function of potential and temperature. The data of Bindra *et al.*[8] is included for the sake of comparison. The slope of the experimental data, taken in 96% H_3PO_4 at 176 and 196°C, agrees well with the simulations at 176°C. The simulations and experimental data are offset because temperature dependence of the standard equilibrium potentials was neglected , due to a lack of experimental data on PtO. The slopes of the measured and simulated data below 1 V are consistent with the Nernst equation for reaction (1). The solubility of platinum should be lower in a polymer-electrolyte fuel cell than in a high temperature fuel cell. The striking feature in the simulated data is the rapid drop in equilibrium concentration at approximately 1.1 V. At this point, the platinum surface is completely covered with platinum oxide, and the equilibrium is determined by reactions 2 and 3. These simulations show the thermodynamic equilibrium concentrations (as defined by the three reactions), as well as the kinetically stable branch. As the sweeps proceed at higher sweep rates, the concentration of Pt^{2+} in solution at more positive potentials can increase beyond the concentration in equilibrium with the PtO layer, as the Pt dissolution reaction continues as long as the surface is not completely covered. As stated above, the rate of the chemical reaction was assumed to be slow, for lack of better information. Thus, the approach to equilibrium at high potentials is slow.

This slow approach to equilibrium has a rather serious implication for Pt stability: Pt is stable at low potentials due to the low equilibrium concentration of Pt^{2+} at these potentials, and Pt is fairly stable at higher potentials due to the protective oxide layer. Transitions between two potentials, however, can undermine the stability of the Pt crystallites, as the concentration of Pt^{2+} in solution can increase by orders of magnitude over that which is stable at either low or high potentials. It is worth noting that this window of instability occurs between the H_2-air open-circuit mixed potential at the cathode (~0.95 V) and the air-air open circuit potential (~1.229 V). Once the Pt^{2+} dissolves into solution, it can be recaptured by the electrode from which it was liberated, but it can also diffuse to other regions of the membrane-electrode assembly and permanently lower Pt content within the cathode. Thus, these transitions at start-up and shutdown can have profound implications on electrochemical area and performance of PEMFC cathodes.

Figure 5 compares, approximately, the platinum dissolution predictions of the model to the triangular-wave potential cycles of Kinoshita *et al.*[2] Kinoshita and co-workers measured platinum dissolution from sheet electrodes subjected to triangular cycles in 1 M H_2SO_4 at 23°C between 0.4 and 1.4 V at a rate of 1 cycle per minute and found an initial dissolution rate of 4.5 ng/cm^2_{Pt}-cycle*.. The rate was essentially unchanged when the upper potential limit was dropped to 1.2 V, but the rate fell to

---

* The numbers reported in the text of reference 2 are 1000 times too large; the correct numbers may be determined from the figures.

approximately 0.8 $\mathrm{ng/cm^2_{Pt}}$-cycle when the upper potential limit was dropped to 1.0 V. The model predicts initial dissolution rates of 0.5, 0.16, and 3.5×10^{-4} $\mathrm{ng/cm^2_{Pt}}$-cycle for these three cases, respectively. The measured dissolution rates at these potentials are approximately 10 times the predicted rates at 1.2 and 1.4 V. The shapes of the experimental and simulated dissolution curves are similar, although the simulations appear to be shifted to higher potentials by approximately 100 mV. This is probably related to the onset potential for platinum oxidation in the two acids. The experimentally observed plateau in dissolution rate at high potentials appears to confirm the assumption that reaction 3 is slow.

Figure 6 shows model predictions of initial platinum dissolution rate versus initial particle radius. The model predicts that the solubility of platinum changes dramatically in the range of 1.5 to 5 nm, well within the range of commercially available catalyst particle sizes. This figure suggests that gains in ORR activity obtained by fabricating smaller catalyst particles may come at the expense of decreased catalyst stability.

CONCLUSIONS

The model presented in this document describes the oxidation and dissolution of platinum in a PEM fuel cell. Parameters describing the oxidation of platinum were fit to cyclic voltammograms taken on commercially available supported platinum electrodes. The fit is reasonably good. The description of platinum oxidation differs from that proposed in the literature by the inclusion of the cathodic term, which is necessary to describe the reduction of platinum oxide to platinum. This leads to an equilibrium oxide coverage, which differs from the unlimited oxide growth predicted by the literature models. The platinum dissolution kinetics and solubility compare reasonably well with the data available in the literature.

ACKNOWLEDGEMENTS

Thanks to M. Perry, T. Patterson, and J. Bett for their careful reviews of this document, and to UTC Fuel Cells for assistance with publication costs.

LIST OF SYMBOLS

Alphabetical

c_i	concentration of species *i*, $\mathrm{mol/cm^3}$
C_{dl}	double-layer capacitance, $\mathrm{F/cm^2}$
F	Faraday's constant, 96487 C/eq
i	current density, $\mathrm{A/cm^2}$
k_i	rate constant for reaction *i* in the forward direction, units
k_{-i}	rate constant for reaction *i* in the reverse direction, units [used?]
M	molecular weight of Pt, 195 g/mol
n_i	number of electrons in reaction i
N	number of Pt particles per unit volume, $\mathrm{cm^{-3}}$
r	particle radius, cm
r_i	rate of reaction *i*, $\mathrm{mol/cm^2 s}$

R	universal gas constant, J/mol K
t	time, s
T	temperature, K
U_i	thermodynamically reversible potential for reaction i, V

Greek

$\alpha_{a,i}$	anodic transfer coefficient for reaction i
$\alpha_{c,i}$	cathodic transfer coefficient for reaction i
β_i	symmetry coefficient for reaction i
ε	electrode porosity
Φ_1	solid-phase potential, V
Φ_2	membrane-phase potential, V
Γ_{max}	maximum surface coverage on Platinum, 2.18×10^{-9} mol/cm^2
μ_i	electrochemical potential of i, J/mol
θ_{PtO}	fraction of Platinum surface covered by PtO
θ_{vac}	fraction of Platinum surface not covered by PtO
ρ_{Pt}	density of Platinum, 21.0 g/cm^3
ρ_{PtO}	density of Platinum, 14.1 g/cm^3
σ_{Pt}	surface tension, J/cm^2
σ_{PtO}	surface tension, J/cm^2
ω	PtO-PtO interaction parameter, J

REFERENCES

1) T. Patterson, "Effect of Potential Cycling on Loss of Electrochemical Surface Area of Platinum Catalyst in Polymer Electrolyte Membrane Fuel Cell," *Fuel Cell Technology Topical Conference Proceedings,* 2002 AIChE Spring National Meeting, March 10-14, 2002.
2) K. Kinoshita, J. T. Lundquist, and P. Stonehart, "Potential cycling effects on platinum electrocatalyst surfaces", *Electroanal Chem. and Interfacial Electrochem.*, **48**, 157-166 (1973).
3) Marcel Pourbaix, *Atlas of Electrochemical Equilibria in Aqueous Solutions,* Pergamon Press, Oxford, 1966.
4) D. V. Heyd and D. A. Harrington, "Platinum oxide growth kinetics for cyclic voltammetry", *J. Electroanal. Chem.*, **335**, 19-31 (1992).
5) D. A. Harrington, "Simulation of anodic Pt oxide growth", *J. Electroanal. Chem.*, **420**, 101-109 (1997).
6) B. E. Conway, B. Barnett, H. Angerstein-Kozlowska, B. V. Tilak, "A surface-electrochemical basis for the direct logarithmic growth law for initial stages of extension of anodic oxide films formed at noble metals", *J. Chem. Phys.*, **93**, 8361-8373 (1990).
7) J. Bett, personal communication.
8) P. Bindra, S. Clouser, and E. Yeager, "Platinum dissolution in concentrated phosporic acid", *J. Electrochem. Soc.,* **126,** 1631 (1979).

Table 1: Fitting parameters

Parameter	Fitted value	Literature value	Reference
U_1^θ	1.188 V		
$\alpha_{a,1}$	0.5		
$\alpha_{c,1}$	0.5		
k_1	3.4×10^{-13} mol/cm^2-s		
U_2^θ	0.98 V		
$\alpha_{a,2}$	0.35	0.2-0.45	4
$\alpha_{c,2}$	0.15		
ω	30 kJ/mol	24-35 kJ/mol	4
σ_{Pt}	0.237 mJ/cm^2	0.237 mJ/cm^2	7
σ_{PtO}	0.1 mJ/cm^2	0.1 mJ/cm^2	7
$\Delta\mu_{PtO}{}^0$	-42.3 kJ/mol		
k_2	1.36×10^{-11} mol/cm^2-s		
k_3	3.2×10^{-24} mol/cm^2-s		
r	3×10^{-7} cm		
C_{dl}	7×10^{-2} F/cm^2		

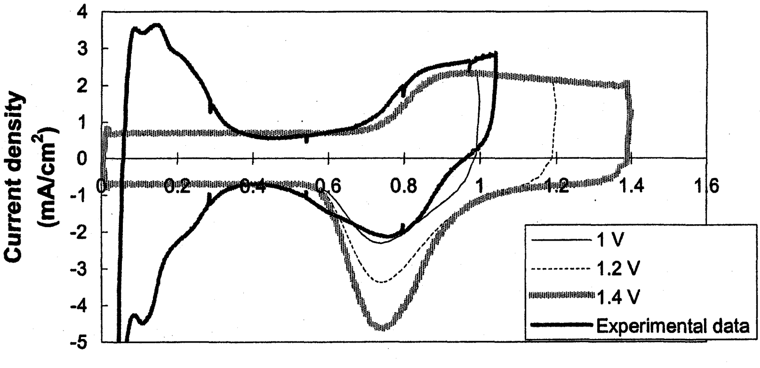

Figure 1. Cyclic voltammograms of MEA to different upper potential-sweep limits.

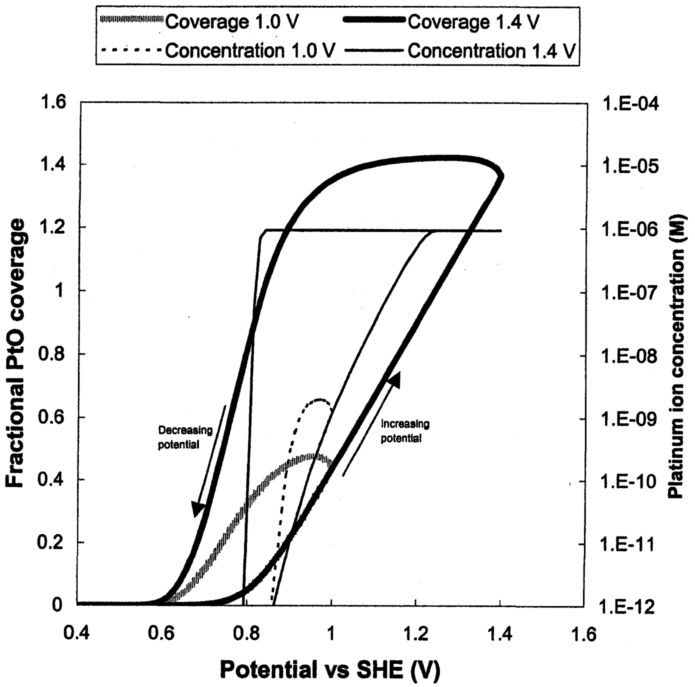

Figure 2. Coverage and concentration during potential-sweep experiments.

Proceedings of The Electrochemical Society, PV 2002-31, 54-66 (2002)
DOI: 10.1149/200231.0054PV © The Electrochemical Society

Effect of Water Content on Oxygen Reduction Reaction (ORR) Kinetics on Supported Pt Catalyst: A Rotating Disk Electrode Study

R. CRAIG URIAN, VIVEK SRINIVASAMURTHI and SANJEEV MUKERJEE*

Department of Chemistry, Northeastern University
360 Huntington Avenue, Boston, MA 02115

Abstract

The oxidation of water at potentials above 0.7V has been viewed as a potential problem for Pt on the cathode side of a Proton Exchange Membrane Fuel Cell (PEMFC). Pt alloys have shown a minimization or shift to higher potentials the oxide formation due to water oxidation. As a result, an increase in the Oxygen Reduction Reaction (ORR) activity has been observed. Not all of the Pt alloys show the same improvement in ORR activity which raises the question of what role does an alloy play in improving the cathodic overpotential losses. If the minimization of PtOH formation was the primary reason for poor ORR activity, then substantial improvement should be seen for Pt if the water content of the electrolyte was reduced and/or the activity of water and thus its interaction with Pt was also decreased. By looking at how much ORR activity improves for Pt in a more anhydrous environment would help explain the role different alloying metals play with Pt but also suggest new directions for new Pt based alloys, particularly in tailoring the electronic properties of Pt. This is also a chance to get preliminary information on how cathode catalysts will behave in elevated temperature fuel cells where the relative humidity is expected to be lower.

INTRODUCTION

The principle cause of the poor kinetics of the four-electron oxygen reduction reaction (ORR) can be attributed to the low exchange current density. Even with the current state of the art low Pt loading electrocatalysts, there is still a substantial high cathodic overpotential loss of ~ 220mV. This loss which appears even at open circuit potential (OCP) is attributed to a mixed potential at the cathode electrode.

In the late 1970's and early 80's, this issue was addressed with the approach of alloying Pt with other transition elements (see following reviews of the early efforts and references their in [1-3]). The early alloy development was targeted for Phosphoric Acid Fuel Cells (PAFCs) which differ from Proton Exchange Membrane Fuel Cells (PEMFCs) in the following ways: PAFCs operate at higher temperatures, the mechanism for proton conduction is different, the water content of the acid electrolyte is much lower than what is required for PEMFC system, oxygen solubility is much higher in the fluorinated PEMFC system, and the overpotential loss due to anion adsorption is substantial in the PAFC system. Mukerjee *et. al.*[4-6] was the first to show that many of the catalysts originally developed for the enhancement of ORR in the PAFC also showed improved ORR activity in the low temperature, fully hydrated PEMFC system. Watanabe *et. al.*[7, 8] have also shown that alloys prepared as thin films showed enhanced ORR activity.

Reasons that have been reported for the observed enhancement in ORR activity start with enhanced surface Pt features due to alloy leaching, changes in the surface structure of the Pt skin surface, particle size effect, changes in the short range atomic order (Pt-Pt bond distance), changes in the electronic states, particularly Pt, and the minimization/potential shift of PtOH formation. The more recent works [9-11] have started to support the shift/minimization of PtOH formation as the rational for the improved ORR activity Pt alloys have shown. But following this rational of developing new Pt alloys to reduce or shift the potential of Pt hydroxyl formation may be a misleading direction for future catalyst development efforts.

In PAFC, the main source of surface poisoning was the phosphate anion. In the fully hydrated PEMFC, the source of Pt poisoning/ORR hindrance on the cathode side is the oxide layer that results from the oxidation of water over Pt.

$$H_2O + Pt \rightarrow Pt\text{-}OH_{(ads)} + H^+ + e^-$$

Pt alloys have shown the ability to impede this process. The means by which this is achieved still needs to be further investigated. It could be purely the result of increasing the Pt 5d-band vacancy above a certain level or it could be attributed to the alloying metal that may lie below the surface of the Pt skin but yet has surface accessibility which may have a higher affinity for water than Pt (see Anderson's work on water binding energy [12]). Paulus and Ross [11] have also offered a speculation along this line citing solution chemistry and the "common ion" effect to explain that OH formation on the non Pt atoms could hinder the OH formation on Pt.

There is one trend that can be seen thus far in the list of actively, studied alloys, which deserves further attention. This trend emanates from the order of increasing ORR activity reported by Mukerjee *et. al.* [4-6] (PtNi, PtCo, PtFe, PtCr). The reported order in improved ORR activity follows the reverse order for increasing Pt 5d-band vacancy which will be presented again in this work. Toda and Watanabe[8] has also looked at changes in the electronic state of Pt and has proposed an ORR mechanism were in it is postulated that the Pt-O bond becomes stronger with increasing Pt 5d-band vacancy. As the Pt 5d-band vacancy is increased; the ability of that metal to give up an electron also becomes more difficult. So looking back at the trend in ORR enhancement and d-band vacancy, it could be suggested that the reason why PtCr performs the best is: 1) there is minimal PtOH formation in the potential range of 0.7 to 1.0V, thus sufficient Pt sites and 2) the charge transfer process is not significantly impeded, as may be the case with PtNi which shows the lease improvement in ORR activity and the larges Pt 5d-band vacancy. Thus, the following question is posed: what would happen if the environmental water content or the activity of water around Pt were significantly reduced without causing any other detrimental effects to the electrolyte or any other transport properties which could impact the Oxygen Reduction Reaction?

The objective of this work is to evaluate the role Pt alloys play in a fully hydrated full cell; the specific focus being the minimization of the oxide layer, PtOH formation, that results from the oxidation of water in the 0.8 to 1.0 V range. If the main role of Pt alloys is to change the electronic state of Pt so as to cause impediment of PtOH formation, then the ORR kinetics for Pt in an acid electrolyte will improve with decreasing the water content and/or water activity so long as the conductivity of the acid is still substantial, and the oxygen permeability (product of solubility and diffusion) is not significantly decreased. Water activity is not a major issue and does not necessarily need to be kept constant. The idea is to minimize the interaction water has with Pt thus decreasing the oxide layer that begins to form at 0.7V. By decreasing this pre-formed oxide layer, the ORR kinetics for Pt are expected to improve substantially.

EXPERIMENTAL

The following supported cathode designated catalysts were synthesized and evaluated for fuel cell performance, kinetics, electrochemical characteristics and electronic and structural properties: Pt, PtCo, PtCr, PtCoCr, PtNi, and PtFe. The catalyst loading on Cabot carbon Vulcan XC-72 was 20%. The cathode electrodes were fabricated using Single-Sided ELAT obtained from DeNora N.A. E-TEK Division at a medal loading of 0.4mg/cm^2. The anode electrode used was a commercially available 20% Pt/C with 0.4mg/cm^2 metal loading on Single-Sided ELAT obtained also from DeNora N.A. E-TEK Division. The MEAs with 5 cm^2 electrodes were fabricated with DuPont Nafion® 1135 membrane using a hot pressing technique.

Fuel cell testing was carried out on a home built multi-channel test station which used an Agilent Technology load bank and modules. Data acquisition was done with a home designed program which utilized LabVIEW™ software. For general screening purposes the fuel cells were run under oxygen or air on the cathode side and hydrogen on the anode side. The cathode/anode backpressures were 60/50 psig respectfully. The cells were operated at 85°C were the gasses were at 100% relativehumidity. To ascertain kinetic information such as energy of activation, the temperature of the fuel cell was varied from 40°C to 90°C in 10°C increments. To obtain the reaction order, the fuel cell was kept at 85°C and the backpressure was varied from 5 to 1 atm in increments of 1 atm. After all fuel cell testing had been completed, cyclic voltammetry was performed on the fuel cells to obtain the electrochemical profile of the catalysts in the following manner.

The cathode was purged with N_2 to displace the O_2. Once the OCP had reached a potential of ~ 0.1V, the cathode electrode acted as the working electrode while the anode with H_2 still passing through doubled as the counter and reference electrode. The fuel cells were kept at 85°C with backpressures of 50 psig under 100% relativehumidity. The cyclic voltammetry was performed using an Eco Chemie Auto Lab system.

X-ray Adsorption Spectroscopy (XAS) measurements were conducted at the National Synchrotron Light Source (NSLS) at Brookhaven National Laboratory (BNL) at the following beam lines: X11A, X18B and X23A2. Measurements were conducted at the Pt L_3 & L_2 edges and the K edge of the alloying elements. All of the experiments were conducted at room temperature in 1M $HClO_4$ in transmission mode. Details of the spectroelectrochemical cell, data acquisition, monochrometer design & resolution and electrode preparation are described elsewhere[4, 5]. Cyclic voltammetry and thus the potential control of the electrodes for the *in-situ* XAS was done with an Eco Chemie Auto Lab system.

Rotating Disk Electrode experiments were conducted using a Pine Instrument Analytical Rotator and Eco Chemie Auto Lab system. A Pt plug electrode (0.283 cm^2) polished to a mirror finished with $0.05\mu m$ alumina acted as the working electrode with a Pt flag as the counter electrode. The reference electrode was a Reversible Hydrogen Electrode. The Trifluoromethane Sulfonic Acid was obtained from 3M Inc. and triply distilled under vacuum. The monohydrate (9.5M) was then prepared. The pure white crystalline material was re-crystallized two more times prior to the preparation of the 6M and 1M solutions used for this investigation. The solutions were first purged with N_2 and the electrode was cycled continuously until a clean reproducible Pt profile was obtained. The solutions were then purged with O_2 were the electrode was rotated at speeds of 400, 625, 900, 1225, 1600, & 2500 rpms. The potential sweep rate was 10mV/s. Oxygen permeability measurements of the electrolytes was also measured using a micro-electrode technique described else where.

RESULTS AND DISCUSSION

Electrocatalyst Specification & Characterization

One of the most powerful aspects of XANES analysis is the ability to determine the Pt 5 *d*-band vacancies. The Pt 5 *d*-band vacancies were determined by integrating the Pt L_3 and L_2 peak intensities of the XANES spectra which represent the $2p_{3/2}$ and $2p_{1/2}$ to $5d_{5/2}$ transitions. The theoretical aspects and the methodology of this analysis are described else where[4, 5]. Figure 1 shows that as the electro negativity of the alloying metal to Pt increases, the Pt-Pt bond distance decreases and the Pt 5 *d*-band vacancy increases. This is further exemplified in Figure 2 which shows that as the potential of the electrode is changed, the Pt 5 *d*-band vacancy does not significantly change for the alloys. The large change observed for Pt is attributed to the charge transfer process for PtOH formation. Thus, one would expect not to see a charge transfer process at 0.84V and possibly higher if the interaction of water with Pt is minimized and the Pt 5 *d*-band vacancy for a Pt catalyst would stay constant over a larger potential range and it would be smaller than those shown for the currently studied alloys. The more interesting question to answer would be: what would happen to the Pt 5 *d*-band vacancy in an anhydrous electrolyte that was saturated with oxygen? Table I is a summary of the electrocatalyst specifics. In addition to the Pt 5 *d*-band vacancies at 0.54V for the different catalysts, and the Pt-Pt bond distances, it can be seen that the particle size for all of the catalyst, determined by both XRD and XAS, are in the 3 nm range.

The catalysts that have been studied have been characterized by XAS to consist predominantly of a Pt skin. Figure 3a & 3b shows the XANES of PtNi taken at the Ni K edge for an acid washed catalyst and a non-washed catalyst. It can be seen for the non-washed sample that the Ni shows changes in the oxidation state as a function of potential. With washing the sample, all of the non-alloyed Ni is removed from the surface and the oxidation state of Ni is stable with change in the potential. To answer the question of whether or not the nickel has access to the surface and if a nickel oxide is formed due to the presence of water, XANES should be performed again on the two sets of catalyst in an electrolyte with low water content and that is deprived of oxygen. If the XANES of the Ni K edge does not change with change in water content of the electrolyte then Ni oxide formation due to water is not a factor to consider for ORR on Pt.

For some of the catalysts studied such as an acid washed PtCo, XAS has shown that the Pt and the Co are both stable at 0.9V for prolong periods of time (Figure 4a & 4b). Figure 4c shows the dissolution of Ru from PtRu with increasing potential. Alloy stability may be a function of synthesis methodology. Watanabe *et. al.*[13] has shown the effects of ordered and disordered phases on supported catalyst stability. Alloy stability may also be a function of the alloying metal itself due to segregation energies [14, 15] and whether it is present on the surface of the catalyst or in the bulk. It was observed in Paffett's and Gottesfeld's[16] work which looked at changes in the cyclic voltammetery of bulk PtCr as the Cr is removed from the catalyst that with the removal of the Cr, there was an increase in the PtOH formation in addition to the hydrogen evolution features. This use of cyclic voltammetry applied to fuel cells would be a good means to monitor alloy stability over time. The removal of non-alloyed metals or surface metals may not necessarily show major changes in the cyclic voltammetry, particularly in the PtOH region but, the oxygen/hydrogen polarization curve would improve with the exposure of more Pt sites. This we have seen with other studied Pt alloys and will be the subject of future discussions. Only when the core alloy begins to breakdown, would the cyclic voltammetry of the alloy begin to show PtOH formation.

Steady State Polarization & Kinetics

Steady state polarization curves have been acquired for many Pt alloy cathode catalysts. Figure 5 represents a selection of iR corrected Tafel plots taken from fuel cell data. Relative to Pt, it can be seen that there is a significant improvement in ORR activity for PtCo and PtCr with the later being the best. This trend has also been observed in other reports[4-11] which include data not shown here. Table II shows a summary of the results presented in Figure 5. All of the results are comparable because the catalyst utilization for all of the studies has been a consistent 50%. The catalyst utilization was determined by the hydrogen desorption and also by the hydrogen adsorption peaks from the fuel cell cyclic voltammograms. The significant decrease in the energy of activation for all of the Pt alloys is attributed to the decrease in PtOH formation which can be observed via cyclic voltammetry and re-affirmed by XAS as shown in Figures 6a & 6b. Even though the energy of activation for ORR is decreased for all of the Pt alloys, the reaction order does not change because the reduction of oxygen is still taking place on Pt sites and the means by which the reaction occurs has not changed. What has been achieved with Pt alloys is the creation of more Pt sites by the minimization of the oxide layer attributed to PtOH formation and the possibility of the Pt hydroxyl groups from interfering with the ORR process. This may be related to a statement by Yeager *et. al.*[17] suggesting that O_2 adsorption will increase with a decrease in the dielectric constant of the interface. This statement was in reference to the use of additives and the formation of a self-assembled film in the PAFC system.

The ternary alloy PtCoCr represents a case in which the electronic properties of the Pt would suggest that the performance should be closer to that of PtCr (Figure 2). The performance of the ternary although resembled that of PtCo but was found not to be as good at larger current densities. Part of the reason why the ternary behaved the way it did may be due in part to observations that the Cr was not that well alloyed. The Co was found to be well alloyed. The instability of the Cr was the primary reason why the alloy composition could not be soundly confirmed via XAS and reported in Table II. In addition to what Watanabe *et. al.* have shown [13], the ternary alloy may be another example of the role synthesis methodology and composition may play in acquiring top performing Pt alloys. It may also hint at new variables such as new segregation energies that arise from a ternary system that may not otherwise be present in the individual binary systems. The presence and instability of the Cr on/near the surface and possible resulting Cr-oxides may have also increased the dielectric constant of the surface, thus decreasing the adsorption of O_2 to the surface.

In the past a relationship has been demonstrated correlating current density with Pt-Pt bond distance and Pt 5 *d*-band vacancies [4-6]. This type of relationship does not separate out principle reasons for why certain Pt alloys perform better than others. This issue is only more complicated by the notion that Pt alloys involving first row transition metals show a minimization/disappearance/shift in PtOH formation in the 0.85V region. The relationship does not afford the room to say that the principle reason for the improved ORR observed from Pt-alloys involving first row transition metals is primarily due to the impingement of PtOH formation in the potential range of 0.7 to 1.0V. Thus it could be inferred that if the environmental water content could be controlled/minimized, or the activity of the surrounding water decreased, with out consequence to other aspects such as proton conduction and resistance as demonstrated by Uribe and Gottesfeld[18], the Oxygen Reduction Reaction on Pt could show significant improvement. It may even be shown that Pt could out perform any currently studied alloy. This type of result would suggests that the Pt 5 *d*-band vacancy plays a more significant role in ORR than the Pt-Pt bond distance where the later may be a consequence of the electronic state changes in Pt due to alloying. This would also indicate that the parameter that needs to be controlled for improving cathodic overpotential loss is to minimize the Pt oxide layer that results from the oxidation of water but without increasing the Pt 5 *d*-band vacancies because of consequence to the electron charge transfer steps.

Rotating Disk Electrode

Novak and Conway have looked at the oxide formation on Pt as a function of water content [19]. They showed that as the water content in trifluoroacetic acid was decreased the oxide film growth due to the oxidation of water also decreased. Even with increasing the time held at the anodic end potential, the oxide film still decreased with less water present in the electrolyte. The anhydrous electrolyte showed no PtOH formation or oxide reduction features attributable to an oxide layer. This result was analogous to what has been observed for Pt alloys in a fully hydrated full cell and in 1M $HClO_4$ using cyclic voltammetry and XAS (Figures 6a & 6b).

To the best of our knowledge, no one has published results specifically looking at the water content effect on ORR for Pt in the absence of Nafion® and without attributing ORR enhancement to the addition of surfactants to the electrolyte or catalyst. Inferences have been made but never specifically shown. Groups such as Yeager's[20] have used the term "dry cave" but this normally referred to the use of perfluorinated additives in phosphoric acid to increased O_2 solubility in the electrolyte and at the electrode surface because of the physical adsorption seen by the additive to the catalyst. As a consequence one can also infer the impingement of water to the reaction site because of the hrydrophobicity of the additives but also because the adsorbed layer could lead to size restrictions for water and other acid anions as demonstrated by Collman, Durant, Anson et. al.[21, 22] in their porphyrin work. Other works which look at the use of surfactants [23, 24] allude to the creation of a hydrophobic shell and increased O_2 solubility to the catalyst surface but show more evidence for decreased anion adsorption.

Figure 7a shows the current density / cell potential results for a Pt plug electrode in 1M and 6M TFMSA. In the potential range of 0.6 to 0.8V, it can be seen that the currents increase faster for the 6M TFMSA case compared to the 1M TFMSA case. This type of trend has also been observed in fuel cell polarization curves when comparing Pt to Pt alloys in the low current density region and this is also clearly shown in the iR corrected Tafel plots of Figure 5. The reason why the diffusion limiting currents for 6M TFMSA are not larger is attributed to the low oxygen permeability which is the product of oxygen solubility and diffusion. Oxygen permeability results were obtain via micro-electrode technique and are reported in Table III.

Figure 7b shows the Tafel plots that were generated from the initial RDE data. The 1M TFMSA case showed a classic two Tafel slope behavior (59 mV/dec & 112 mV/dec). The 6M TFMSA case showed only one Tafel slope. This 110 mV/dec slope which spans both the high over potential and low over potential ranges is analogous to a Pt surface that is free of adsorbed species, mainly the oxide layer which are formed in the low over potential range because of the oxidation of water over Pt. These results coincide with the cyclic voltamograms shown by Novak and Conway[19] which showed that as the water content of the acid electrolyte is decreased, and/or as the activity of water is decreased, so is the adsorbed oxide layer due to the oxidation of water on Pt to PtOH.

Table III summarizes the kinetic information found for the RDE experiment of a Pt plug in 1M and 6M TFMSA. In addition to Tafel slopes and oxygen permeability results, it can be seen that the kinetic current at given potentials is much higher for the 6M TFMSA case than the 1M TFMSA case. Also the exchange current density is at least a factor of 1000 greater in 6M TFMSA than in 1M TFMSA.

Based on the earlier discussion that revolved around the strong influence the Pt 5 *d*-band vacancies could play in the Oxygen Reduction Reaction, particularly when trying to understand why some Pt alloys perform better than others, the improvement seen in the ORR for the Pt plug going from 1M to 6M TFMSA suggests that as the water content of the electrolyte media is decreased and the more filled the Pt 5 *d*-band vacancy is the better the ORR could be. This though can only be answered by comparing RDE results of Pt and a Pt alloy such as PtCo run in 1M and 6M TFMSA.

CONCLUSION

We have focused on the shift/minimization of PtOH formation that has been observed with Pt alloys in a fully hydrated fuel cell and mimicked this phenomenon for Pt in an acid electrolyte by decreasing the water content. The result of decreasing the water content on the oxygen reduction kinetics for Pt was significant. Only one Tafel slope of 110mV/dec could be found, the kinetic currents at 0.8V and 0.7V were nearly doubled, and the exchange current density was a factor of 1000 higher for the 6M TFMSA compared to the 1M TFMSA. In observing the improved ORR activity for Pt in electrolytes with different water contents suggests that the primary achievement gained with the current Pt alloys is the minimization/shift in oxide formation due to the oxidation of water over Pt. This is achieved by increasing the Pt 5 *d*-band vacancy above a certain level. By decreasing the ability of Pt to oxidize water a penalty is incurred. This sacrifice is a decrease in the charge transfer process necessary for greater enhancement in ORR activity. The results of this work suggest the following new directions for fuel cell research.

The development of new membranes and/or fuel cell operating systems should focus on decreasing either the relative humidity and/or the amount of water necessary for proton conduction or the activity of water. With the achievement of this Pt may surpass the best Pt alloy currently available. The new direction for catalyst development would then be to develop Pt alloys with a lower Pt 5 *d*-band vacancy.

ACKNOLEDGEMNT

The authors wish to thank Lei Zhang for oxygen permeability measurements and Mohammad Enayetullah of Protonex for his helpful input and experience with TFMSA preparation, historical input and rotating disk electrode experiments. The authors would also whish to thank the Dept. of Education for a GAAN fellowship. The following funding agencies are also great fully acknowledged for their financial support of the work: DOE for their infrastructure support at NSLS at BNL, Army Research Office, UTC Fuel Cells and DeNora N.A. ETEK Division.

1. A. J. Appleby, in 'Assessment of Research Needs for Advanced Fuel Cells' (Department of Energy, USA, Advanced Working Group Report, (S.S. Penner editor) U. S. Department of Energy, Office of Energy Research (Contract # DE-AC01-84ER30060) (1985).
2. P. Stonehart, J. Appl. Electrochem., 22, 995 (1992).
3. P. Stonehart, ber.Bunsengos, Phys.Chem., 94, 913 (1990).
4. S. Mukerjee, S. Srinivasan, M. P. Soriaga, and J. McBreen, J. Electrochem. Soc., 142, 1409 (1995).
5. S. Mukerjee, S. Srinivasan, M. P. Soriaga, and J. McBreen, J. Phys. Chem., 99, 4577 (1995).
6. S. Mukerjee and S. Srinivasan, J. Electroanal. Chem., 357, 210 (1993).
7. T. Toda, H. Igarashi, and M. Watanabe, J. Electrochem. Soc., 145, 4185 (1998).
8. T. Toda, H. Igarashi, H. Uchida, and M. Watanabe, J. Electrochem. Soc., 146, 3751 (1999).
9. F. A. Uribe and T. A. Zawodzinski, Electrochim. Acta, 47, 3799 (2002).

10. U. A. Paulus, A. Wokaun, G. G. Schere, T. J. Schmit, V. Stamenkovic, N. M. Markovic, and P. N Ross, Electrochim. Acta, 47, 3787 (2002).
11. U. A. Paulus, A. Wokaun, G. G. Schere, T. J. Schmit, V. Stamenkovic, V. Radmilovic, N. M. Markovic, and P. N. Ross, J. Phys. Chem. B, 106, 4181 (2002).
12. A. B. Anderson, E. Grantscharova, and S. Seong, J. Electrochem. Soc., 143, 2075 (1996).
13. M. Watanabe, K. Tsurumi, T. Mizukami, T. Nakamura, and P. Stonehart, J. Electrochem. Soc., 141, 2659 (1994).
14. A. V. Ruban, H. L. Skriver, and J. K. Norskov, Phys. Rev. B, 59, 15990 (1999).
15. S. Mukherjee and J.L. Moran-Lopez, Surface Sci., 189, 1135 (1987).
16. M. T. Paffett, J. G. Beery, and S. Gottesfeld, J. Electrochem. Soc., 135, 1431 (1988).
17. E. Yeager, M. Razaq, D. Gervasio, R. A, and D. Tryk, in D. Scherson, D. Tryk, M. Daroux, X. Xing, eds., Structure Effects in Electrocatalysis and Oxygen Electrochemistry, Proc. Vol. 92-11. Pennington NJ: The Electrochem. Soc. Inc., (1992), p. 440.
18. F. A. Uribe, M. S. Wilson, T. E. Springer, and S. Gottesfeld, in D. Scherson, D. Tryk, M. Daroux, X. Xing, eds., Structure Effects in Electrocatalysis and Oxygen Electrochemistry, Proc. Vol. 92-11. Pennington NJ: The Electrochem. Soc. Inc., (1992), p. 494.
19. B. E. Conway and D. M. Novak, J. Electrochem. Soc., 128, 956 (1981).
20. M. Razaq, A. Razaq, E. Yeager, D. D. DesMarteau, and S. Singh, J. Electrochem. Soc., 136, 385 (1989).
21. J. P. Collman, P. Denisovich, Y. Konai, M. Marroco, C. Koval, and F. Anson, J. Am. Chem. Soc., 103, 6027 (1980).
22. R.R. Durant, J., C. S. Bencosme, J. P. Collman, and F. C. Anson, J. Am. Chem. Soc., 105, 2710 (1983).
23. H. M. Saffarian, R. Srinivasan, D. Chu, and S. Gilman, J. Electroanal. Chem., 504, 217 (2001).
24. H. M. Saffarian, R. Srinivasan, D. Chu, and S. Gilman, J. Electrochem. Soc., 148, A559 (2001).

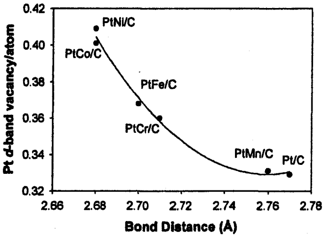

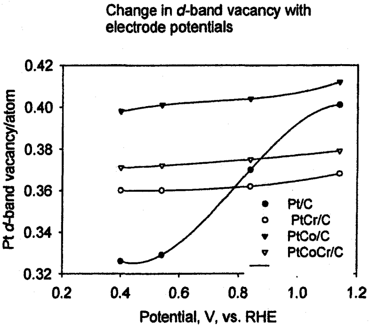

Figure 1. Pt d-band vacancy vs. Pt-Pt bond distance

Figure 2. Pt d-band vacancy vs. Cell potential

Electrocatalyst	Pt *d*-band vacancy/atom @ 0.54 V (XANES)	Atomic Ratio (a/o) (XANES)	Pt-Pt bond distance (Å)		CN (Pt) (from EXAFS) @ 0.54 V (first shell)	Particle Size (Å)	
			XRD (as received)	EXAFS @ 0.54 V		XRD (line broadening)	EXAFS @ 0.54 V
Pt/C	0.329		2.77	2.77	10.05	25	27
PtCr/C	0.360	74/26	2.74	2.71	10.48	32	33
PtCo/C	0.401	72/28	2.72	2.68	10.67	36	35
PtCoCr/C	0.372		2.72	2.70	10.85	35	42

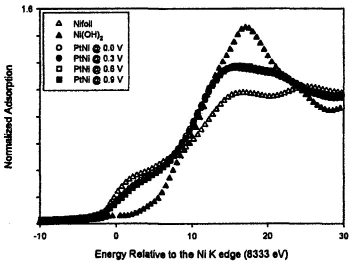

Figure 3a. XANES of acid washed PtNi/C at Ni K edge

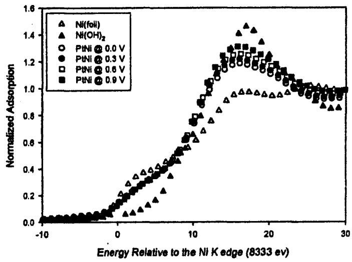

Figure 3b. XANES of non acid washed PtNi/C at Ni K edge

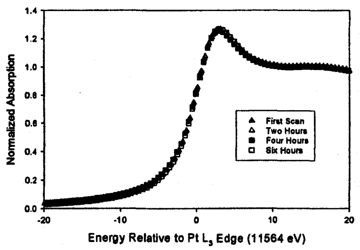

Figure 4a. XANES of PtCo at Pt L3 edge polarized at 0.9V

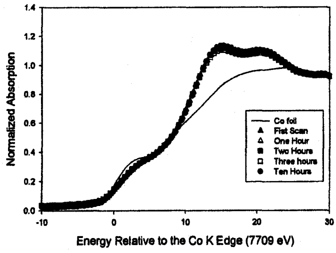

Figure 4b. XANES of PtCo at Co K edge polarized at 0.9V

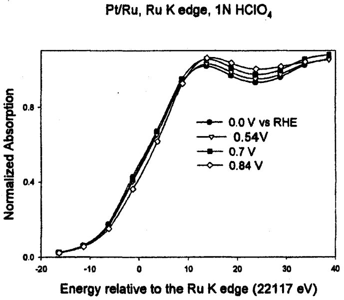

Figure 4c. XANES of PtRu at Ru K edge

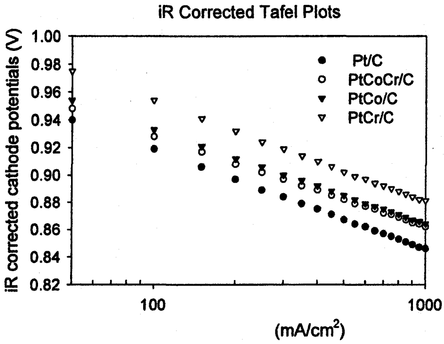

	E_o (V)	b (mV/dec)	R Ω cm²	io (10^{4}) mA/cm²	$I_{900\ mV}$ (mA/cm²)	$E_{100mA/cm2}$	Roughness Factor (cm²/cm²)	Utilization	E_{act} (kJ/mol)	Reaction Order
Pt	1.064	72.85	0.2	26.39	182	0.918	182	45.45%	62.17	0.96
PtCoCr	1.06	65.87	0.2	15.61	270	0.93	136	48.70%	20.14	1.04
PtCo	1.071	68.97	0.2	27.17	300	0.935	180	51.43%	29.59	0.785
PtCr/C	1.095	65.45	0.18	34.5	680	0.953	180	51.40%	28.18	1.028

Table II. Summary of kinetic data from fuel cell polarization curves

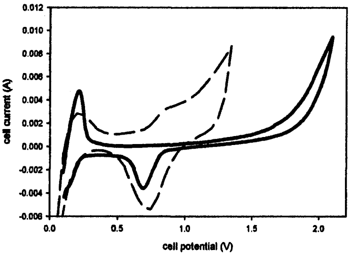

Figure 6a. Cyclicvoltammograms of Pt and PtCo in fully hydrated fuel cells

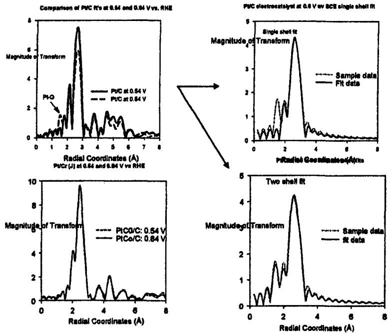

Figure 6b. Fouier transforms of Pt @ 0.54V & 0.84V showing PtOH formation and PtCo @ 0.54V & 0.84V showing no change and no Pt oxide formation

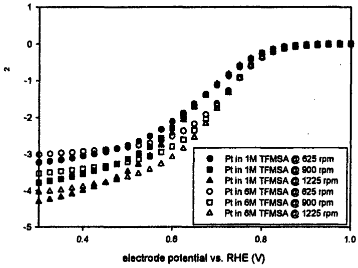

Figure 7a. I-V curves of Pt plug in oxygen saturated 1M & 6M TFMSA @ different rotational speeds

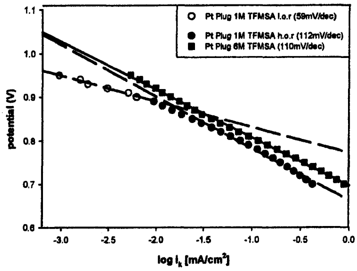

Figure 7b. Tafel plots of Pt plug in oxygen saturated 1M & 6M TFMSA @ 1225 rpm

	I_k @ 0.8V (mA/cm^2)	I_k @ 0.7V (mA/cm^2)	$b_{\text{l.o.p.}}$ (mV/dec)	$b_{\text{h.o.p.}}$ (mV/dec)	$I_o \times 10^{-6}$ (mol/cc)	C x 10^{-6} (mol/cc)	D x 10^{-6} (cm^2/s)	CD x10^{-12} (mol/cm s)
1M TFMSA	0.076	0.425	59	112	0.056	0.63	9.68	6.09
6M TFMSA	0.114	0.884	110		26	6.88	0.29	2.00

Table III. Summary of kinetic data for Pt plug in 1M & 6M TFMSA. Oxygen permeability also included.

Proceedings of The Electrochemical Society, PV 2002-31, 67-73 (2002)
DOI: 10.1149/200231.0067PV © The Electrochemical Society

LOW-PLATINUM TIN-OXIDE ELECTROCATALYSTS FOR PEM FUEL CELL CATHODES

Norma P. Ugarte and Karen E. Swider-Lyons
Naval Research Laboratory
Surface Chemistry Branch, Code 6171
Washington, DC 20375-5342 USA

ABSTRACT

Proton-exchange membrane fuel cells (PEMFCs) can be made more affordable by reducing their noble metal (platinum) content. Traditional fuel cells often use 10 wt% Pt on Vulcan carbon (10% Pt/VC), but we show that this platinum content can be lowered by the utilization of metal oxide supports for the Pt at the cathode. New low-Pt catalysts of hydrous tin oxide (Pt-SnO_x) are compared to 10% Pt/VC in both half-cell and PEMFC measurements. Half-cell voltammetric evaluation with a rotating disk electrode shows that Pt-SnO_x/VC has higher activity for oxygen reduction than the standard 10% Pt/VC even though it contains 5× less Pt. Preliminary PEMFC measurements are made using a Pt-SnO_x/VC cathode and a Pt/VC anode at room temperature using humidified hydrogen and oxygen. The Pt-SnO_x/VC catalyst performs well in PEMFCs compared to 10% Pt/VC catalysts, despite having a 23× lower platinum loading.

INTRODUCTION

Proton-exchange membrane fuel cells (PEMFCs) are under development as high-efficiency fuel conversion devices, however several technological problems must be solved before they are available for wide-scale consumer use. For instance, the PEMFC electrodes contain platinum, which makes the fuel cells costly and subject to fluctuations in the market availability of the noble metal. The Pt content of the electrodes is lowered by dispersing nanoscale particles on Vulcan carbon (VC), but the amount of Pt is still too high (ca. 0.1 mg Pt cm^{-2}) for fuel cells to be affordable to consumers (1).

Our goal is to further lower the platinum content of PEMFCs by dispersing the Pt on an oxide support, and then supporting that oxide on VC. We are targeting the fuel-cell cathode, where oxygen is reduced by protons and electrons to yield water via the oxygen reduction reaction (ORR) in Eq. [1]. The kinetics limitations of this four-electron reaction are alleviated by the catalytic properties of the platinum. The slow transport of molecular oxygen and/or protons can also hinder the ORR at high current densities, (2, 3, 4).

$$O_2 + 4H^+ + 4e^- = 2\,H_2O \qquad [1]$$

Hydrous transition-metal oxides are ideal supports for platinum in PEMFCs, because they are good proton and water conductors (5). Oxides are also less prone to poisoning than metals, and some oxide catalysts are resistant to dissolution under the highly corrosive conditions at the PEMFC cathode. More importantly, the catalytic activity of platinum can be improved by using the appropriate oxide support.

Our previous electrochemical and structural studies on hydrous Pt-FeO_x indicate that the catalysts having the highest ORR activities have open-framework structures (6,7). The ~0.5-nm micropores in the FeO_x structure are ideal for rapid proton conduction. Unfortunately the Fe-based catalysts are prone to corrosion and therefore are not viable PEMFC catalysts.

In this paper, we discuss new catalysts for PEMFC cathodes comprising hydrous tin oxides that are loaded with low amounts of Pt. These hydrous metal oxides are targeted due to their stability in acidic environments plus their likelyhood for catalytic activity. Pt-SnO_x catalysts have already been recognized for their high ORR activity in alkaline solutions (8). The chemical, physical, and structural properties of our catalysts are determined via characterization with inductively coupled plasma (ICP) analysis, Brunauer-Emmett-Teller (BET) analysis, and powder X-ray diffraction (XRD). The oxygen reduction activity of the Pt-SnO_x catalysts is evaluated using a rotating disk electrode (RDE) in argon- and oxygen-saturated H_2SO_4 at 60 °C and compared to a 10% Pt/VC standard catalyst. The ORR activity of the catalysts is noted from the difference in their voltammetric sweeps under Ar and O_2 and in Tafel plots of the ORR. The performance of these catalysts is also compared in a PEMFC operated on humidified H_2 and O_2 at room temperature.

EXPERIMENTAL

The standard electrocatalyst is 10 wt% Pt on Vulcan carbon (Alfa Aesar) having approximately 2.5 nm Pt particles. This Pt/VC is used as received.

Hydrous SnO_x is prepared by dissolving $SnSO_4$ (Alfa) in 18 MΩ•cm H_2O and then neutralizing the solution with NH_4OH. The resulting precipitate is vacuum filtered and air dried. The hydrous SnO_x powder is stirred in a solution of Pt in H_2SO_4, filtered, and dried at 150 °C. The material has 7.12 wt% Pt and 59.95 wt% Sn, according to ICP (Galbraith Lab, Knoxville TN). The surface area and pore size distribution of the Pt-SnO_x is determined via BET analysis under N_2 to 77K (Micromeretics ASAP 2010). The crystal phase composition of the powders is surveyed with XRD (Bruker D-8 Advance with Göbel mirrors and Cu Kα radiation).

For the RDE measurements, the catalysts are ground with 73 wt% Vulcan carbon XC-72R (Cabot) so that the total Pt content of the Pt-SnO_x/VC catalysts is 1.9 wt%. Inks are made by stirring together a 1:6 mixture of a catalyst (1.9% Pt-SnO_x/VC or 10 wt% Pt/VC) and a Nafion® ionomer solution (5 wt% solids: Ion Power). A 6 µL drop of the ink is pipetted onto a polished 5-mm-diameter glassy-carbon RDE (Pine Instrument Company) and dried at 150 °C (9). The RDE is submerged in 0.1 M H_2SO_4 prepared from high purity H_2SO_4 (Optima, Fisher) and 18 MΩ•cm H_2O. The electrolyte is heated at 60 °C, and sparged with Ar and O_2 for deaeration and saturation, respectively. A Pt mesh is used as the auxiliary electrode and a charged Pd wire is used for reference to a normal hydrogen electrode (NHE). The speed of the RDE is controlled at 1000 rpm using a single element rotator (Pine Instrument Company). Voltammetric analysis is carried out at 10 mV/s using a potentiostat (PAR/EG&G Instruments model 263a).

Tafel plots are generated from the difference in the currents (I) of the RDEs under O_2 and Ar when swept from 1.3 and 0.2 V using Eq. [2], where 0.196 cm^2 is the electrode area (9). The limiting current (I_{Lim}) is obtained from the average current density at 0.1 ± 0.01 V. Eq. [3] is used to calculate the Tafel current (9).

$$I\,(\mathrm{mA/cm^2}) = 1000 \bullet (I_{O_2} - I_{Ar}) / 0.196\ \mathrm{cm^2} \qquad [2]$$

$$I_{tafel} = (I_{Lim} \bullet I) / (I_{Lim} - I) \qquad [3]$$

The Los Alamos National Laboratory protocol is used to make catalyst inks for evaluation in PEMFCs (1). The Pt-SnO_x catalyst is ground with 80 wt% VC. An ink made of 0.063 g of catalyst (Pt-SnO_x/VC or Pt/VC) and 0.5 g of Nafion® ionomer solution is stirred for 1 h and then 0.25 g of glycerol is added. After stirring for 30 min, two drops of as-received tetra-n-butylammonium hydroxide (TBAOH, 31% in methanol, Alfa) are added and the solution is stirred again for 1 h. Another 0.2 g of glycerol is added before stirring the solution overnight. The inks are applied to a 2.5 cm^2 carbon cloth (E-TEK) using a paintbrush. The painted cloths are oven dried at 150 °C. Catalyst loadings are calculated from the difference in the weight of the as-received carbon cloth and that of the dried, painted cloth.

To make the membrane electrode assembly (MEA) for the PEMFC, a Nafion 117 solid electrolyte is cleaned and protonated by boiling sequentially in 3% H_2O_2 (Fisher), 18 MΩ•cm H_2O, and 0.5 M H_2SO_4 solutions for 1 h each. The H^+-Nafion® 117 is sandwiched between the painted cathode and anode carbon cloths and pressed at 200 °C. The resulting MEA is boiled in 0.1 M H_2SO_4 for several hours. The MEA is tested in PEMFC hardware (ElectroChem Inc) with two graphite blocks having a serpentine flow pattern. H_2 and O_2 are humidified at room temperature by bubbling through water and then fed to the anode and cathode, respectively. Current is collected using a potentiostat, and the cell voltage is reported after 60 s under the target current.

RESULTS AND DISCUSSION

BET results on Pt-SnO_x show a surface area of 36 m^2/g, an average pore size of 3.8 nm and a pore volume of 0.016 cm^2/g. The data indicate that there are predominantly micropores rather than mesopores in the catalyst. Microporous walls are excellent proton conductors (5). We previously correlated the presence of micropores to increased ORR activity in the Pt-FeO_x compounds (7).

XRD analysis reveals that the Pt-SnO_x has a phase composition of SnO_2 and Pt; SnO_2 is present as the major phase. The material is partially crystalline with crystallites less than 100 nm and an amorphous portion.

Voltammetric results are shown in Fig. 1(a) and 1(b) for the 10% Pt/VC and 1.94 wt% Pt-SnO_x/VC RDEs, respectively. The RDEs are swept to negative potentials under Ar and O_2. A greater cathodic current is measured under the O_2 flow than under Ar because of the electrocatalytic reduction of oxygen on the electrodes, and the difference between O_2 and Ar curves (O_2 - Ar) reflects the total current of the ORR. The Pt-SnO_x/VC has a high ORR activity despite a low Pt content of 1.94% and behaves similarly to the 10 wt% Pt/VC catalyst when cycled under Ar and O_2. In comparison, the voltammetry of Pt-free SnO_x/VC has no electrocatalytic response to the O_2 (not shown). We surmise that the SnO_x phase improves the electrocatalytic properties of the Pt, though, because the Pt-SnO_x/VC electrocatalyst has higher activity than the Pt/VC standard despite having 5× less Pt (Fig. 1 (b)). The Tafel plots of the ORR for the catalysts reflect the same trends, as shown in Fig. 2.

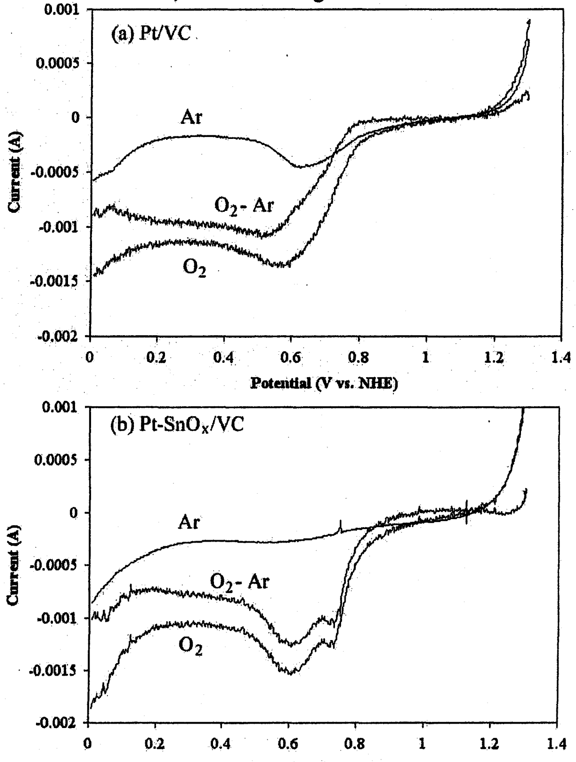

Figure 1. Voltammetric response of RDEs of (a) 10 wt% Pt/VC and (b) 1.94% Pt-SnO_x/VC. The ORR activity is derived from the difference of the O_2 and Ar sweeps (O_2-Ar) measured in 0.1 M H_2SO_4 at 1000 rpm, 60 °C, and 10 mV/s.

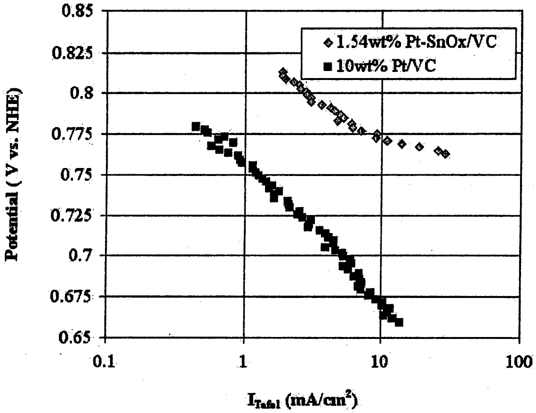

Figure 2. Tafel plots of the ORR on 1.94 wt% Pt-SnO$_x$/VC and 10 wt% Pt/VC as calculated from the voltammetry data in Fig. 1.

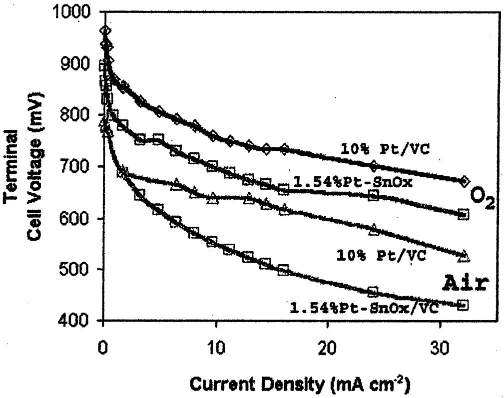

Figure 3. Polarization curves for PEMFCs having Pt-SnO$_x$/VC and Pt/VC cathode catalysts under H_2/O_2 and H_2/air at 25 °C and ambient pressure. The Pt loadings of the cathodes are 0.0109 mg Pt cm^2 for the Pt-SnO$_x$/VC and 0.26 mg Pt cm^2 for the Pt/VC PEMFCs. Both anodes are prepared from 10% Pt/VC and contain 0.29 mg Pt cm^{-2}.

Figure 3 compares the performance of the Pt-SnO_x/VC and Pt/VC catalysts in H_2/O_2 PEMFCs. The Pt loadings of the Pt-SnO_x/VC PEMFC are 0.0109 mg Pt cm^{-2} at the cathode and 0.29 mg Pt cm^{-2} at the anode. The Pt/VC standard PEMFC has 0.29 mg Pt cm^{-2} at both the cathode and anode. Note that the standard 10 wt% Pt/VC catalyst is used at the anode in both of the PEMFCs. Under our test conditions of H_2/O_2 at 25 °C and ambient pressure, the Pt-SnO_x/VC and Pt/VC PEMFCs have open circuit voltages of 0.927 and 0.951 V, respectively. At low current densities (<2 mA cm^{-2}), the performance of the fuel cells is nearly identical, even though the Pt loading at the Pt-SnO_x/VC PEMFC is 23× lower than that of the standard Pt/VC PEMFC. Under a current density of 20 mA cm^{-2}, the Pt-SnO_x catalyst has a higher overpotential than the standard Pt/VC PEMFC, as the former drops to 0.4 V while the latter to 0.6 V. The source of this overpotential is under investigation and is likely due to the room-temperature operation of these fuel cells and/or inadequate humidification. Improvements to the MEA fabrication and fuel cell operation conditions will likely be able to decrease this difference between the indications from the Tafel data and the PEMFC results.

Observations to date indicate that the Pt-SnO_x/VC materials are stable to corrosion. Voltammetry inks are reused months after being prepared with no change to their ORR activity, and the Pt-SnO_x/VC MEAs show no degradation of performance after removal from and then reassembly in a PEMFC.

CONCLUSIONS

The use of hydrous tin oxide as a support for Pt provides a means for lowering the Pt content of PEMFC cathodes. The ORR activity per weight % Pt is higher when the Pt is dispersed in hydrous tin oxide vs. in a standard 10 wt% Pt/VC catalyst. Future work will focus on improving the Pt-SnO_x catalysts by tuning the preparation of the metal oxides and the MEA fabrication procedures (e.g. heating conditions). Further testing of the electrocatalysts in a fuel cell test station operating at higher temperature and pressures will also give insight into the properties of these catalysts. Ultimately, using a metal-oxide-supported electrocatalyst with low Pt loadings will significantly reduce the cost of PEMFCs.

ACKNOWLEDGMENTS

The authors are grateful for financial support provided by the Department of Energy Office of Transportation Technologies (contract DE-A101-00EE50639) and the Office of Naval Research. We also thank Jason Stanley for preparing the SnO_x, and Dr. Francisco Uribe (LANL) for guidance on the preparation of the fuel cell inks. NPU is a visiting graduate student from the University of Texas-El Paso.

REFERENCES

1. M. S. Wilson, J. A. Valerio, and S. Gottesfeld, *Electrochim. Acta,* **40**, 355 (1998).
2. F. Jouen, G. Lindbergh, and G. Sundholm, *J. Electrochem. Soc.*, **149**, A437 (2002).
3. J. Ihonen, F. Jouen, G. Lindbergh, A. Lundblad, and G. Sundholm, *J. Electrochem. Soc.*, **149**, A448 (2002).
4. M. Eikerling and A. A. Kornshev, *J. Electroanal. Chem.*, **453**, 89 (1998).
5. P. Colomban, Ed., *Proton Conductors: Solids, Membranes and Gels – Materials and Devices*, Cambridge University Press, Cambridge (1992).
6. K. Swider Lyons, G. B. Cotton, J. A. Stanley, W. Dmowski, and T. Egami, "Low-platinum and platinum-free catalysts for oxygen reduction at proton-exchange membrane fuel cell cathodes," *2001 Progress Report for Fuel Cells for Transportation,* U.S. Department of Energy Office of Transportation Technologies, December 2001, 159-162.
7. K. Swider Lyons, G. B. Cotton, J. A. Stanley, W. Dmowski, and T. Egami, "Low-platinum catalysts for oxygen reduction at proton exchange membrane fuel cell cathodes," *2002 Progress Report for Fuel Cells for Transportation,* U.S. Department of Energy Office of Transportation Technologies, in press.
8. M. Watanabe, S. Venkatesa, and H. A. Laitinen, *J. Electrochem. Soc.*, **130**, 59 (1983).
9. S. Lj. Gojkovic, S. K. Zecevic, and R. F. Savinell, *J. Electrochem. Soc.*, **145**, 3713 (1998).

Proceedings of The Electrochemical Society, PV 2002-31, 74-88 (2002)
DOI: 10.1149/200231.0074PV © The Electrochemical Society

COMPARISON OF MODELING AND EXPERIMENTAL RESULTS OF MODIFIED Pt-BASED PEMFC CATHODE-CATALYSTS

Eini Puhakka[*], Ulla Koponen[#], Mikael Bergelin[#], Jari Keskinen[*], Unto Tapper [*],
Heikki Kumpulainen[*], Terttu Peltonen[*], Matti Valkiainen[*]
*VTT Technical Research Centre of Finland, VTT Processes, P.O.Box 1601,
FIN-02044 VTT, FINLAND
[#]Åbo Akademi Process Chemistry Group, Biskopsgatan 8,
FIN-20500 ÅBO, FINLAND

ABSTRACT

Pt-based binary and ternary alloy catalysts were investigated by modeling methods and experimentally. The lattice parameters of Pt, Pt_3Cr, Pt_3Co, Pt_3Ir, Pt_2CoCr, Pt_2CoIr, Pt_2Cr_2 and Pt_2Co_2 were determined by molecular modeling methods. According to the optimized structures, the most typical crystal faces were generated. In order to get a good description of sterical and electrostatic factors of material surfaces, reconstruction of surface atoms was taken into account. It was shown that the alloying of Pt with base metals affect surface charge densities, which enables steering of surface reactions into desired positions on the catalyst surface. Both commercial (E-TEK) and laboratory-made catalyst powders and inks based on Pt:Co/C and Pt:Co:Cr/C were characterized voltammetrically. The active Pt surface area increased after activating the catalyst. This can most likely be attributed to the dissolving of Co and Cr from the alloys. All laboratory-made catalysts were also characterized by XRD, TEM and STEM/EDS.

INTRODUCTION

In the PEM fuel cells the major potential loss takes place in the oxygen reduction on the cathode side. Recently, carbon-supported Pt has become the most frequently used catalyst on the cathode. The support material must have good electrical conductivity and have good corrosion resistance in the oxidizing conditions on the cathode. Essentially, the aim in the synthesis of carbon-supported Pt is to minimize the amount of Pt needed and to reach as high a specific surface area as possible. However, it has been shown in the case of phosphoric acid fuel cells that larger Pt particles are more active than smaller ones. The same might also be true with the PEM fuel cell, but in practice the topic is more complicated. Ralph and Hogarth (1) have also reported that the catalytic properties can be improved by alloying Pt with base metals. This can be due to differences in lattice parameters and surface phenomena. It is also possible that the surface area increases because of the etching of the base metal during cell operation. In the case of Pt alloy catalysts, it has been shown that the specific activities of Pt increase with decreasing surface area (2). In general, the preparation of supported catalysts includes two steps. First the metal precursor is dispersed on the surface of the support followed by drying, calcination and reduction (3). In the case of Pt catalysts, it is also possible to use hexachloroplatinate as the precursor (4). Completely different approaches have also been proposed by Denis et al. (5) who prepared Pt alloy catalysts by high-energy ball milling. A method has also been developed to produce nanoscale metal particles using hydrotriorganoborates as reducing agents (6,7). With this method, metal salts can be reduced using alkali hydrotriorganoborates in hydrocarbons at temperatures below 80°C. In this way, Pt can be alloyed with various metals by co-reduction of different metal salts.

The preparation and characterization of Pt alloy catalysts and the variation of alloy composition are time-consuming operations. Since the catalytic properties of materials depend on their lattice parameters and morphology, it is useful to utilize the modern molecular modeling methods in studies concerning crystal and surface structures. Thus, by modeling it is possible to avoid part of the enormous effort of preparing alloy catalysts. Earlier, molecular modeling methods have been used to study surface relaxations of Pt surfaces (8) and the driving force of relaxations on the (001) surfaces of transition metals (9). The surface reconstruction of stepped surfaces is indicated to be larger than that of basal surfaces (8). This can explain only small differences in heats of adsorption of simple gases as a function of Pt surface structures. In this work, a surface relaxation study is expanded for Pt alloy catalysts containing Cr, Co and Ir.

METHODS

Preparation and Characterization of Pt Alloy Catalysts

The catalysts were prepared by reduction of the $PtCl_2$ and $CoCl_2$ metal salts (6). Cr was obtained from $Cr(NO_3)_3 \cdot 9H_2O$. Hydrotriorganoborates were used in the process to facilitate the formation of nano-sized powders. The metal salts were dissolved in tetrahydrofurane (THF) after which the carbon carrier material (Vulcan XC72) was added to the solution. $LiB(C_2H_5)_3H$ (1 M in THF) was added slowly to the solution at 60°C. After a 16–20 h sedimentation, the solution was removed. The powder was consecutively washed with THF, ethanol, THF, and pentane. In the x-ray powder diffraction (XRD) measurements Mo-K_α radiation was used. The phases were identified with the JCPDS (Joint Committee on Powder Diffraction Standards) database. In addition, the prepared catalyst samples were characterized for particle morphology and elemental composition using transmission electron microscopy (TEM, Philips CM200 FEG/STEM) and scanning transmission electron microscopy (STEM) coupled with energy dispersive X-ray emission spectroscopy (EDS). Only the results concerning Pt:Co/C laboratory-made catalyst samples are shown and briefly discussed in this work.

Electrode Preparation

The catalyst inks were made as follows: the Pt/C catalyst was mixed for 4 hours with 5% Nafion solution (in methanol) in an ultrasonic bath. Tetrabutylammonium hydroxide (TBAOH) was then added to the mixture which was stirred continuously for several hours. The ink was then conditioned to proper consistency by adding H_2O and glycerol (10). A catalyst layer was prepared by coating a Nafion 117 membrane with the ink (*11*). The membrane was pre-treated by boiling for 1 h in 5% H_2O_2. After rinsing, the membrane was consecutively boiled for 1 h in 0.5 M H_2SO_4, H_2O and 0.5 M NaOH. The membrane was then rinsed and left to stand in water before spreading the catalytic layer. The ink-coated membrane was then dried and heat-treated. This procedure was then repeated with the other side of the membrane. Scanning electron microscopy photographs showed that a porous layer consisting of Pt/C particles was formed. Before the experiments the MEA was boiled in 0.5 M H_2SO_4.

Voltammetric Measurements

Catalyst powders and inks based on both commercial (E-TEK) and laboratory-made Pt:Co/C (1:1) and Pt:Co:Cr/C (2:1:1) were characterized by cyclic voltammetry. The catalyst alloy content in all powders was 20% of the total mass. A perforated box made of Au (1x1x0.5 cm) was used to contain the powders during the measurements. The amount of powder used in each experiment was in the range of 1.5–2.0 mg. After weighing the powders, the box was filled with Au thread to ensure electric contact, and the box was sealed with a perforated Au cap. An Au electrode, 3 mm in diameter, was used as a substrate for the inks. Approximately 1 μl of each ink was spin-coated onto the electrode. Before the experiment, the ink was dried in ambient temperature. Au was chosen as the substrate material for the catalysts since it hardly shows any activity towards hydrogen adsorption in the potential range of interest. This enables characterization of the catalysts with minimum substrate interference. All characterization measurements were carried out in 0.5 M H_2SO_4 (Merck, suprapur, Millipore MilliQ). Before the experiment the electrolyte was bubbled with Ar (99.998%) in order to remove any oxygen. All potentials were measured against a reversible hydrogen electrode. The currents measured for each catalyst powder are given with respect to the mass of alloy, whereas the currents measured for the inks are given with respect to the geometric area of the Au electrode.

Modeling Methods

Molecular modeling methods were used to investigate the crystal and surface structures of the Pt alloy catalysts. *Ab initio* quantum mechanics calculations were performed with the CASTEP (CAmbridge Serial Total Energy Package) code implemented into the Cerius^2 4.2, 4.2.1 and 4.6 versions (12). The exchange-correlation was described with generalized gradient approximation, GGA-PW91, during the geometry optimization. For each element, ultrasoft pseudopotentials were used. The kinetic cutoff energy for a plane wave expansion of the wave function was 280 eV. After the surface structures, with and without oxygen, and the geometry of a separate oxygen molecule were optimized, the adsorption energies were calculated from single-point energies of the components using GGA-RPBE exchange-correlation and kinetic cutoff energy 290 eV.

RESULTS AND DISCUSSION

Modeling

In the modeling work, the structural and electrostatic factors of different Pt alloy catalysts were compared. The investigated catalysts consisted of laboratory-made, commercial and new non-synthesized catalysts. The starting point for the calculations was the face-centred cubic crystal structure of Pt (12). After the unit cell of Pt was optimized, the unit cells of the Pt alloys were generated by replacing the Pt atoms by Cr, Co or Ir atoms with an atomic ratio of 3:1, 2:1:1 and 1:1. The modified unit cells were then optimized. The optimized unit cell parameters together with some experimental values are presented in Table I.

Table I. Optimized unit cell parameters for different Pt alloy catalysts.

	Exptl. (Å)		Calculated (Å)	
	a = b = c	A	B	C
Pt	3.924[a]	3.967	3.967	3.967
Pt_3Cr	3.883[b]	3.896	3.897	3.897
Pt_3Co	3.855[b]	3.884	3.884	3.884
Pt_3Ir		3.946	3.946	3.946
Pt_2CoCr		3.724	3.815	3.815
Pt_2CoIr		3.851	3.850	3.850
Pt_2Cr_2		3.893	3.762	3.762
Pt_2Co_2		3.635	3.837	3.837

[a] (12). [b] (2).

Comparison of the calculated lattice parameters to experimental values indicates that correspondence between the results is good. According to the calculated results, the modification of the Pt structure by Cr, Co or Ir with an atomic ratio of 3:1 affects under 0.1 Å on the lattice parameters, and the cubic structure is maintained. When the modification ratio is 2:1:1 or 1:1, the cubic structure is slightly disturbed. The only exception is Pt_2CoIr, which almost maintains its cubic structure because of the electronic structure of the Ir atom. After the crystal structures of the different catalyst materials were determined, the most typical crystal faces for the catalyst were generated. In order to get a good description of the sterical and electrostatic factors of the material surfaces, reconstruction of the surface atoms was taken into account. In Table II, the changes in the atomic layer spacing compared to the bulk structures are presented. Only those atomic layers that have a significant role in surface reactions are considered. The layer spacing is illustrated in Fig 1.

Table II. Surface relaxations of Pt alloy catalysts compared to their bulk structures.

Catalyst	Surface	Spacing X-Y [a]	d_{12} [b] (%)	d_{23} [b] (%)	d_{34} [b] (%)
Pt	(001)	Pt-Pt	-0.2	+0.1	+0.1
	(210)	Pt-Pt	-29.5	-0.8	+14.9
Pt_3Cr	(001)	Pt-Pt	-1.6	+0.8	+1.8
		Cr-Pt/Pt-Cr [c]	-7.3	+3.7	-1.2
Pt_3Co	(001)	Pt-Pt	+0.2	+0.1	+1.2
		Co-Pt/Pt-Co [c]	-3.7	+0.9	+0.8
Pt_2CoCr	(001)	Pt-Pt	+2.0	-2.3	-0.9
		Pt-Cr/Cr-Pt [d]	-12.6	+12.3	-2.1
		Co-Pt/Pt-Co [d]	-9.1	-1.9	-1.3
	(100)	Pt-Cr/Cr-Pt [c]	-10.8	+6.0	-0.7
		Pt-Co/Co-Pt [c]	-6.7	+1.9	-0.2
	(210)	Pt-Pt	-20.3	-21.5	+37.9
		Cr-Pt/Pt-Cr [d]	-22.2	-26.6	+43.0
		Pt-Co/Co-Pt [d]	-27.4	-14.5	+25.6
		Cr-Co/Co-Cr [d]	-29.4	-19.6	+30.7
Pt_2CoIr	(100)	Pt-Co/Co-Pt [c]	-3.4	+0.8	+0.9
		Pt-Ir/Ir-Pt [c]	-3.1	+0.5	+1.0
Pt_2Cr_2	(001)	Pt-Pt	+0.7	+0.1	-0.8
		Pt-Cr/Cr-Pt [d]	-12.2	+13.0	-5.2
		Cr-Pt/Pt-Cr [d]	-8.9	+4.0	-4.7
Pt_2Co_2	(001)	Pt-Pt	+0.1	-1.2	+1.1
		Pt-Co/Co-Pt [d]	-4.6	+3.5	+1.4
		Co-Pt/Pt-Co [d]	-6.5	-1.0	+0.9
	(100)	Pt-Co/Co-Pt	-4.4	+2.3	+1.6

[a] An *X* atom is on an upper layer and a *Y* atom is on a lower layer.

[b] Numbers in lower indices refer to spacing between layers d_{ij}, where an upper layer is *i* and a lower layer is *j*.

[c] Every second layer consists of two different atoms.

[d] All layers consist of two different elements.

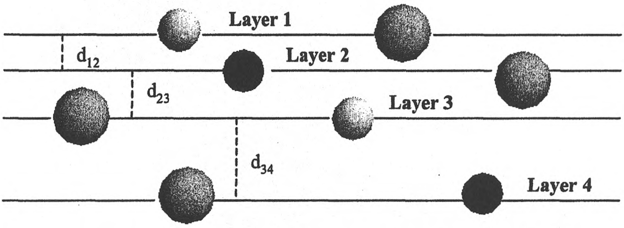

Fig. 1. Layer structure of Pt_2CoCr (210) surface. Big grey circles: Pt atoms. Small black circles: Co atoms. Small grey circles: Cr atoms.

The surface relaxations of Pt alloy catalysts depend on the type of surface and the composition of the alloy. On the basal (001) surfaces, the distances between the Pt atoms shift only slightly. The maximum change is a 2.3% contraction in the spacing between the second and third layer on the (001) surface of Pt_2CoCr. Comparison of the (001) surfaces of Pt_3Cr and Pt_3Co indicates that the relaxation of Cr-modified material is on average larger than that of Co-modified. The same observation applies to the case of Pt_2Cr_2 and Pt_2Co_2. The (100) surfaces are more stable than the (001) surfaces, because the top layer of the (100) surface consists of only Pt atoms. The relaxation of Pt_2CoIr can be compared to the relaxation of Pt_3Co, because the electrostatic properties of Ir are nearly the same as Pt. The most significant relaxation can be found on the stepped (210) surfaces. There is almost a 30% contraction in the spacing between the first and second layer. In pure Pt, the contraction in the spacing between the second and third layer is nearly zero, but in Pt_2CoCr, the contraction is still 14.4–26.6%. On the other hand, there is a 25.6–43.0% expansion in the spacing between the third and fourth layer. Because of the surface relaxation, the arrangement of Co and Cr atoms become more compact, and the surface area of Pt atoms increases as Fig. 2 depicts. In general, the surface relaxation is the most significant in the spacing between the first and second atomic layers.

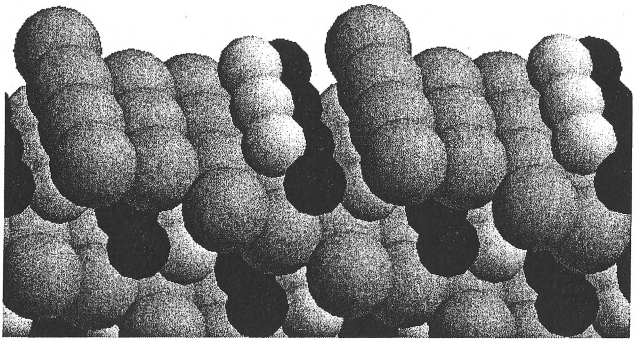

Fig. 2. The Pt_2CoCr (210) surface. Big grey circles: Pt atoms. Small black circles: Co atoms. Small grey circles: Cr atoms.

The electrostatic properties of the surfaces were considered by comparing the charge densities on different surfaces. In Fig. 3, some examples of typical charge density maps are presented. The results indicate that the charge density significantly depends on the composition of the surface atoms. On the (100) surface of Pt_2Co_2, the charge density varies from 0.2–2.4 electrons in Å^3, and the charge density surface spread rather equally over the Pt atoms. However, the charge density map is quite different, when the surface consists of atoms (Pt and Co) with different electronic structures. On the (001) surface of Pt_2Co_2, the high-charge density areas, 12.5 electrons in Å^3, are concentrated around the Co atoms. On the stepped (210) surface of Pt_2CoCr, the highest charge densities, 18.6 electrons in Å^3, are far apart. The benefit of these charge density maps is that they can be used to estimate the favourable adsorption sites for surface reactions. Further, the differences in the charge densities assist us in controlling the surface reactions into the desired direction.

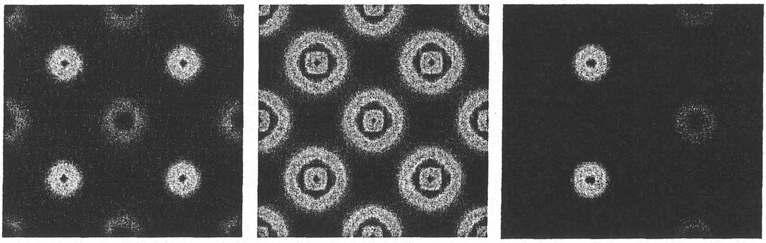

Fig. 3. Charge densities of Pt_2Co_2 (001) surface (left), Pt_2Co_2 (100) surface (middle) and Pt_2CoCr (210) surface (right). The charge density is higher in the light areas and lower in the dark areas.

In order to investigate the dissolving of Cr and Co atoms from the catalyst surfaces, the (001) surfaces of Pt_3Cr and Pt_3Co were modified by desorbing the Cr and Co atoms from the first atomic layer. After that, the surface structures were re-optimized (Table III), and the charge densities of the modified surfaces were determined. The results indicate that the desorption of Cr and Co atoms affect mostly the spacing of Pt atoms between the first and second atomic layer. Otherwise, the surface structures are rather stable. The charge densities of the Cr and Co desorbed surfaces vary from 0.1 to 2.6 electrons in Å^3. Because the surface charges are equally spread, the direction effect of the charge densities will be lost.

Table III. The effects of desorption of surface Cr and Co atoms on the spacing of Pt_3Cr and Pt_3Co (001) surfaces.

Catalyst	Surface	Spacing X-Y [a]	d_{12} [b] (%)	d_{23} [b] (%)	d_{34} [b] (%)
Pt_3Cr	Compact (001)	Pt-Pt	-1.6	+0.8	+1.8
		Cr-Pt/Pt-Cr [c]	-7.3	+3.7	-1.2
	Cr desorbed (001)	Pt-Pt	-6.3	-2.3	+1.3
		Cr-Pt/Pt-Cr [c]		-6.3	+5.4
Pt_3Co	Compact (001)	Pt-Pt	+0.2	+0.1	+1.2
		Co-Pt/Pt-Co [c]	-3.7	+0.9	+0.8
	Co desorbed (001)	Pt-Pt	-6.7	-1.9	+1.0
		Co-Pt/Pt-Co [c]		+2.4	+0.7

[a] An *X* atom is on an upper layer and a *Y* atom is on a lower layer.

[b] Numbers in lower indices refer to spacing between layers d_{ij}, where an upper layer is *i* and a lower layer is *j*.

[c] Every second layer consists of two different atoms.

Oxygen adsorption onto the (001) surfaces of Pt_2CoCr and Pt_2Co_2 was also investigated. The adsorption energy of oxygen is -127.6 kJ/mol on the Pt_2CoCr (001) surface and -160.6 kJ/mol on the Pt_2CoCr (001) surface. Therefore, oxygen binds weaker to the Pt_2CoCr surface than to the Pt_2Co_2 surface. On the other hand, the surface reactions can be deemed more favourable on the Pt_2CoCr surface, because the need of energy in order to break the surface bonds is also weaker than on the Pt_2Co_2 surface.

Characterization of the Processed Catalysts

The crystal/particle morphology and composition of the processed catalysts were characterized using transmission electron microscopy methods (TEM, STEM/EDS). As an example, in Fig. 4 results for Pt:Co/C heat-treated samples are shown. The Pt-Co particles were crystalline and according to STEM/EDS elemental point and high magnification (x1000k–x2000k) mapping analyses, the majority of the particles were composed of Pt and Co. In the non heat-treated sample shown in Fig. 4a the particle size is about 2–3 nm. The particle size increased in the heat-treated samples so that for the 300°C sample shown in Fig. 4b the particle size is about 4–6 nm whereas in the 700 °C sample in Fig. 4c the particle size is about 7–9 nm. The increase of crystal size is in accordance with the X-ray diffraction analysis (see below) which indicates clear peak narrowing with increasing temperature.

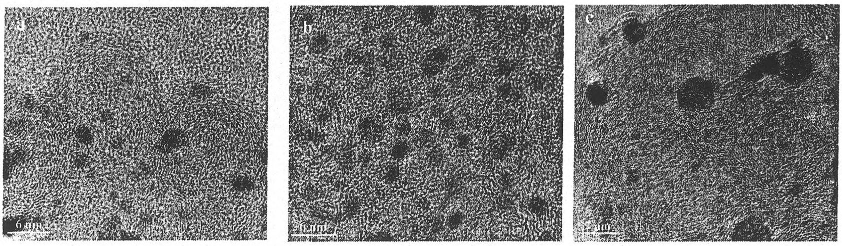

Fig. 4. STEM/EDS image of Pt:Co particles on carbon black support. The figures indicate typical Pt particle morphology and size in the heat-treated samples. a: room temperature, b: 300°C and c: 700°C). The scale bar is 6 nm except in c, 7 nm.

XRD was used to define the crystal structure and particle size of the synthesized catalysts. Fig. 5 shows an XRD pattern typical for a sample containing 20 wt.% Pt on carbon. The pattern was measured after synthesis without any heat-treatment. In this case the diffraction peaks characteristic for Pt can easily be identified. The wide peak, indicated with x, at about 12° is a contribution from the carbon support. From the Pt peak width the average Pt crystal size was determined to be between 4.5 and 5.5 nm using the Scherrer formula (13). Fig. 6 presents the XRD patterns for both the non heat-treated and heat-treated samples containing Pt:Co/C (1:1). The catalyst alloy content in the samples is 20 wt.%. The heat-treatment of the sample was performed in Ar atmosphere containing 4% H_2 and less than 2 ppm O_2.

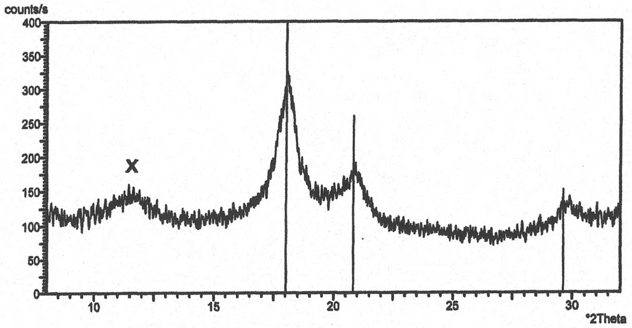

Fig. 5. Powder XRD pattern measured for Pt/C. Vertical lines: positions of Pt diffraction peaks. The height of the line tells the relative height of the corresponding peak according to the JCPDS database. x: carbon support (Vulcan XC72).

The pattern of the non-heat-treated sample, marked RT, shows very wide peaks indicating a very small crystal size. Probably, the Pt and Co atoms are situated quite randomly on carbon particles and an ordered crystal structure has not been formed. The same observations were also made for samples containing Pt:Co:Cr (2:1:1). Clear peaks were observed, however, after heat-treating the Pt:Co sample at 1100°C, which can be seen in Fig. 6. The average crystal size was determined as 8 nm. The positions of the Pt:Co diffraction peaks are indicated by dashed vertical lines in Fig. 6. As noted, these fit reasonably well to the pattern. In Fig. 6, the pattern obtained after heat-treatment at 300°C is also shown. Heat-treating the samples at 300 and 700°C did not result in patterns with clear Pt:Co peaks, but some ordering had happened during the heating. The pattern obtained at 300 °C is also very similar to the one measured after treating the sample at 700°C. The crystal size was estimated as about 3 nm in both cases.

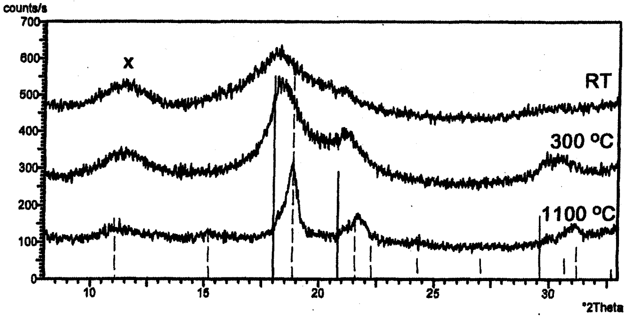

Fig. 6. Powder XRD pattern measured for 20wt.% Pt:Co/C. Solid vertical lines: peak positions for Pt. Dashed lines: peak positions for Pt:Co phase. x: carbon support (Vulcan XC72).

Voltammetric Characterization of Pt:Co and Pt:Co:Cr-Based Catalyst Powders

Cyclic voltammetry is a convenient and often used method for the study of surface processes. From the obtained voltammograms it is possible to estimate, for example, the active surface area, which enables the comparison of catalysts that are manufactured or pre-treated in different ways. Regarding alloy catalysts, cyclic voltammetry also gives information about the stability of the material, since, for instance oxidation and the removal of Co and Cr can be distinguished as an apparent increase of Pt surface area in the voltammograms. In cases where Co and Cr oxidation peaks can be distinguished, the change in shape and/or height of these oxidation peaks reflects changes in the material.

After placing the Au box into the electrochemical cell the electrode potential was cycled between 50 and 600 mV until a stable voltammogram was obtained. In Fig. 7 A the base voltammograms for both the commercial and laboratory-made Pt:Co catalyst powders are shown. In general the two voltammograms are quite similar. In both cases it is not possible to distinguish the two separate hydrogen peaks characteristic for polycrystalline (14) or kinked Pt in the potential region between 50 and 300 mV. It can also be seen that the commercially made catalyst possesses a higher hydrogen region charge than the laboratory-made one, assuming that the alloy-loading is the same in both cases. By integrating the currents between 50 and 400 mV it was possible to obtain the active surface areas for Pt in the catalysts. In the calculations it was assumed that 200 μC is consumed per square centimetre of surface Pt. The areas were determined as 480 and 175 cm^2 mg^{-1} Pt for the commercial and laboratory-made catalysts, respectively. A separate set of experiments was also performed where different amounts of Co were electrochemically deposited onto an Au electrode. This was done to verify that Co does not show any hydrogen adsorption in this potential interval, and the results clearly show that Co gives no contribution to the hydrogen region charge measured from the alloys.

The same characterization procedure was performed with the Pt:Co:Cr powders. A similar set of Cr deposition experiments on Au, as explained above, showed that Cr does not show any hydrogen adsorption between 50 and 400 mV either. The voltammograms obtained from the Pt:Co:Cr powders are shown in Fig. 7 B. Also in this case, it can be noted that the voltammograms for the commercial and laboratory-made powders resemble each other. However, the hydrogen region charges were of the same order of magnitude, determined as 335 and 270 cm^2 mg^{-1} Pt, respectively.

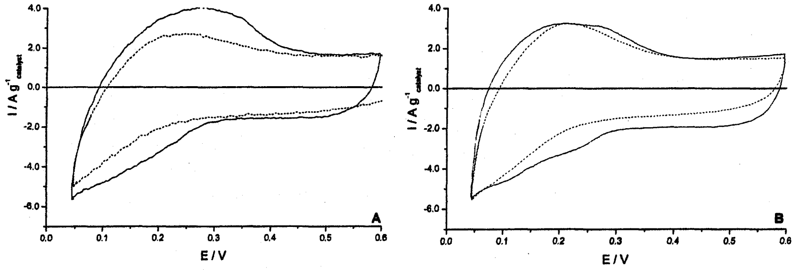

Fig. 7. Voltammograms for commercial (solid line) and laboratory-made (dotted line) catalyst powders in 0.5 H_2SO_4 at 10 mV s^{-1}. A) 20 wt.% Pt:Co (1:1) B) 20 wt.% Pt:Co:Cr (2:1:1).

In order to determine the stability of Co and Cr in the catalyst alloy, the electrode potential was swept between 50 and 1350 mV at 20 mV s^{-1} for 50 cycles. The end potential was chosen as 1350 mV to avoid getting any contribution from the oxidation of the Au substrate in the recorded voltammograms. The first (dotted line) and the fiftieth (solid line) cycles are depicted in Fig. 8 A and B for both the commercial and laboratory-made Pt:Co powders and in Fig. 8 C and D for the Pt:Co:Cr powders. As noted, the active surface area of Pt increases after activating the catalyst by the voltammetric cycling, from 480 and 175 to 760 and 555 cm^2 mg^{-1} Pt, respectively, for the Pt/Co catalysts, and from 335 and 270 to 1030 and 580 cm^2 mg^{-1} Pt, respectively, for the Pt/Co/Cr catalysts. This can be most likely attributed to the dissolving of Co and Cr from the alloys, thereby increasing the Pt surface coverage. During potential excursions up to 1350 mV Co may be less stable than Cr in the alloy, based on measurements involving the deposition and oxidation of Co and Cr adlayers on an Au electrode.

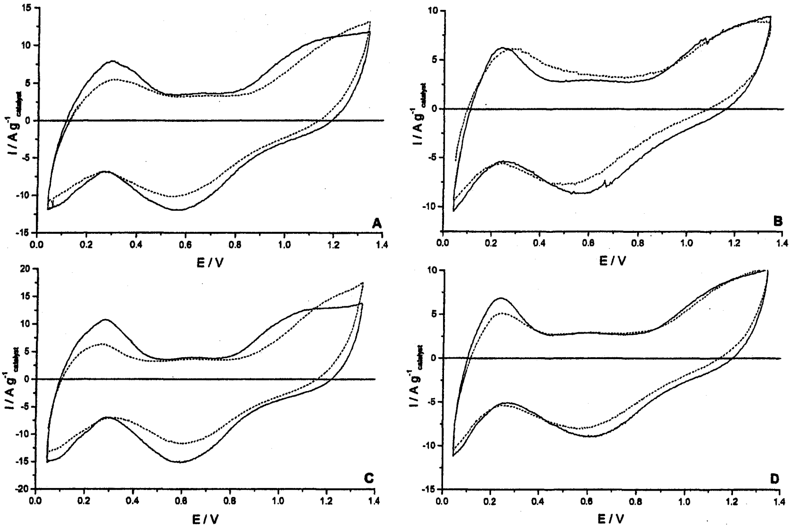

Fig. 8. 1st (dotted line) and 50th (solid line) activation sweep for catalyst powders in 0.5 M H_2SO_4 at 20 mV s^{-1}. A) 20 wt.% Pt:Co, 1:1 (E-TEK) B) 20 wt.% Pt:Co,1:1 (laboratory-made) C) 20 wt.% Pt:Co:Cr, 2:1:1 (E-TEK) D) 20 wt.% Pt:Co:Cr, 2:1:1 (laboratory-made).

Voltammetric Characterization of Pt:Co and Pt:Co:Cr-Based Catalyst Inks

Pt:Co and Pt:Co:Cr-based inks were laboratory-made from commercial (E-TEK) catalyst powders and spin-coated onto an Au electrode. After immersing the ink electrode into the electrochemical cell and obtaining a hanging meniscus configuration the electrode potential was swept between 50 and 600 mV until a stable voltammogram was obtained. These voltammograms (dotted lines) for both Pt:Co and Pt:Co:Cr inks are shown in Fig. 9. As can be noted, the inks show very little activity in the hydrogen region between 50 and 300 mV. This is most probably due to the complex ink matrix where surface processes are less well defined and different kinds of organic impurities may be present. The voltammograms indicated with solid lines in Fig. 9 are obtained after making potential excursions up to 1350 mV for 50 times. Here the hydrogen region charges of the catalysts have clearly increased. It should, however, be noted that this apparent increase in surface area is most likely due to both the removal of impurities and the dissolving of Co and Cr from the alloy, a feature also observed in the case of the catalyst powders.

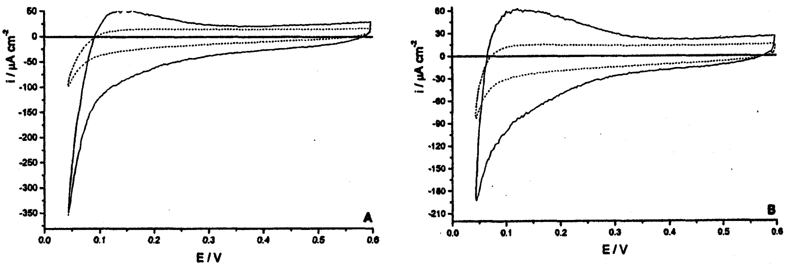

Fig. 9. Voltammograms for inks prepared from commercial (E-TEK) catalyst powders in 0.5 H_2SO_4 at 10 mV s^{-1}. Dotted line before and solid line after 50 activation cycles to 1350 mV. A) 20 wt.% Pt:Co (1:1) B) 20 wt.% Pt:Co:Cr (2:1:1).

The last step of the measurement chain is the measurement of current-voltage characteristics of MEAs in a single-cell test fixture and characterization of the overpotential in a half-cell.

4. CONCLUSIONS

It is reported that the properties of the Pt catalyst on the cathode side in PEM fuel cells can be improved by alloying Pt with base metals (1). According to the results presented in this study, alloying is a useful way to modify the charge density of a catalyst surface, which again depends on the atomary structure of the surface. E.g. the charge density of a Pt_2Co_2 (001) surface, which consists of Pt and Co atoms, is strongly different than that of a Pt_2Co_2 (100) surface where only Pt atoms are present. The differences in the charge densities assist in controlling the surface reactions into the desired directions. Because the charge densities can be determined by modeling methods, it is possible to estimate surface properties of the modified catalysts as a function of the composition even before their preparation. Pt:Co/C (1:1) and Pt:Co:Cr (2:1:1)/C alloy catalysts with 20 wt.% metal loading were synthesize and characterized by cyclic voltammetry, STEM/EDS and XRD. These characterizations were also carried out with corresponding commercial catalysts. By cyclic voltammetry it was possible to characterize both catalyst powders and inks and thus this method enabled the comparison of catalysts that were pre-treated and manufactured in different ways. It also provided a way to estimate the active surface area of the catalysts provided that (in case of alloys) the metal-composition was known. Additional information on stability of the material could also be obtained by cyclic voltammetric means. The base voltammetry of the commercial and laboratory-made catalyst alloys resembled each other, but the commercially made catalysts possessed, however, a higher hydrogen region charge than the laboratory-made ones. After 50 activation cycles up to 1350 mV, the active surface area of Pt significantly increased due to dissolving of Co and Cr from the alloys, thereby increasing the Pt surface coverage. STEM/EDS and XRD measurements were in accordance with each other. It was observed that the particle size of the Pt:Co and Pt:Co:Cr catalysts was bigger in the heat-treated samples. In the non-heat-treated samples the particle size was found to be 2–3 nm, whereas after heat-treatment the average particle size was 7–9 nm. As a whole, the work indicated that modeling, preparation of catalysts and voltammetric measurements form a complementary research chain.

ACKNOWLEDGEMENTS

This work was financially supported by Tekes, the National Technology Agency of Finland.

REFERENCES

1. T. Ralph and M. Hogarth, *Platinum Metals Rev.*, **46**, 3 (2002).
2. M-k. Min, J. Cho, K. Cho and H. Kim, *Electrochim. Acta*, **45**, 4211 (2000).
3. N. Yao, C. Pickney, S. Lin, C. Pak and G. Haller, *Microporous Mesoporous Mater.*, **44-45**, 377 (2001).
4. J. Buchanan, G. Hards and S. Cooper, GB2242203A (1990).
5. M. Denis, P. Gouérec, D. Guay, J. Dodelet, G. Lalande and Schultz R., *J. Appl. Electrochem.*, **30**,1243 (2000).
6. H. Bönnemann, W. Brijoux, R. Brinkmann, R. Fretzen, T. Joussen, R. Köppler, B. Korall, P. Neiteler and J. Richter, *J. Mol. Catal.*, **86**, 129 (1994).
7. R. Richards, R. Mörtel and H. Bönnemann, *Fuel Cells Bulletin*, **4**, 7 (2001).
8. W. T. Lee, L. Ford, P. Blowers, H. L. Nigg and R. I. Masel, *Surf. Sci.*, **416**, 141 (1998).
9. A. Filippetti and V. Fiorentini, *Comp. Mat. Sci.*, **20**, 423 (2001).
10. M. S. Wilson and S. J. Gottesfeld, *Electrochem. Soc.*, **139**, L28. (1992).
11. M. S. Wilson, *Membrane Catalyst Layer For Fuel Cells*. US Pat 5,211,984 (1993).
12. Accelrys Inc., *CASTEP Users Guide*, San Diego: Accelrys Inc., (2001).
13. B.D. Cullity, *Elements of x-ray diffraction*, 2nd ed. Addison-Wesley (1978).
14. S. Szabó and I. Bakos, *J. Electroanal. Chem.*, **230**, 233 (1987).

Proceedings of The Electrochemical Society, PV 2002-31, 89-98 (2002)
DOI: 10.1149/200231.0089PV © The Electrochemical Society

NON-NOBLE METAL CATALYSTS FOR PEM OXYGEN REDUCTION BASED ON SOL GEL DERIVED COBALT NIGROGEN COMPOUNDS

V. I. Birss. A. H. C. Sirk
University Of Calgary, Calgary, Alberta, Canada T2N 1N4

and

S. A. Campbell
Ballard Power Systems, Burnaby, British Columbia, Canada V5J 5J9

ABSTRACT

The majority of power loss in PEM fuel cells occurs at the cathode, due to the sluggish kinetics of the oxygen reduction reaction (ORR). Much higher loadings of Pt at the cathode, as compared to the anode, must be used to compensate for this, resulting in high costs. There have been numerous efforts to develop non-noble metal catalysts for the ORR, including Co-N_4 chelates, normally arising from porphyrin precursors and which have been shown to improve in activity with heat treatment. In this work, Co oxide sol-gel syntheses, known to yield nanoparticulate composite materials, have been modified by the incorporation of carbon and nitrogen in the form of ethylene diamine. These new catalysts have demonstrated very good ORR activity in acidic solutions after adsorption on carbon and subsequent heat treatment, with a maximum in performance and minimum in H_2O_2 generation at 700 °C. Catalyst activity was also found to increase with an increase in the concentration of the catalyst on the carbon powder and with increased loadings of the catalyst.

INTRODUCTION

Low temperature fuel cells provide an efficient and clean source of power. Through the oxidation of hydrogen or methanol at an anode and the reduction of oxygen at a cathode, with the electrodes separated by a proton exchange membrane (PEM), a current is generated. One of the limiting factors in fuel cell operation is the kinetics of the oxygen reduction reaction, which does not proceed at a reasonable rate until large overpotentials are reached. This results in a substantial power loss to the system. The best catalyst currently known is Pt, and even when employed in nanoparticulate form, it is still a very costly component of the fuel cell.

Therefore, numerous non-Pt catalysts have been investigated for their activity as an oxygen reduction (ORR) catalyst. Materials which have been examined in acidic media or in PEM fuel cells include Fe porphyrin (1), Co porphyrin (2, 3), ReRuS4, MoRuS (4), Mo_2RuS_5 (4), CrO_2 (5), Au (6), Ir porphyrins (7) Pt/Ru mixed pyrochlores (8), Pt macrocycles (9) and organo-Cu compounds (10). In terms of Fe and Co porphyrin based catalysts, it has been shown that it is not necessary to retain the porphyrin structure in order to observe catalytic behaviour. Indeed, heat treatment in an inert atmosphere was found to improve both the activity and stability of these catalysts (11). It has been suggested that the active site is a dimeric metal-C-N species (12). Also, active catalysts for the ORR in alkaline solutions are formed from amorphous sputter-coated Co-N-C (1, 13). Promising catalysts have also been formed by passing acetonitrile gas over V, Cr, Fe and Co metal salts at 1000° C, again suggesting that the active centre does not require an intact porphyrin structure (14).

Our recent work has focussed on the sol-gel (SG) synthesis of a wide range of compounds. This approach offers many advantages in the preparation of solid state electrode materials, including ease of formation of binary and ternary films, as well as the resulting high surface area (nanosized particles), with further modifications of the particle size and surface area possible by the adjustment of the drying temperature and time. Our prior work with SG-derived Ni and Co oxides (15) led us to the formation of amorphous Co-N-C ORR catalysts using the SG route. Good catalytic activity has been observed in acidic solutions, better than for comparable Co pthalocyanine (CoPC) prepared using identical procedures.

EXPERIMENTAL

Catalyst synthesis

The synthesis of the catalysts was carried out by the dropwise addition of 2 to 3 equivalents of ethylenediamine (en), diluted in ethanol and ethyl acetate, over 3 days to a refluxing stirred ethanol and ethyl acetate solution of the standard Co oxide sol (16). A white precipitate that initially formed was determined to be $HN_2C_2N_2HNO_3$ from its appearance, solubility and the likely chemical reactions taking place, and was filtered off. Water was added, as needed, to enhance the solubility of the purple precipitate which began to form after 3 hours. The reaction was followed by UV-Visible spectroscopy (UV-Vis) and cyclic voltammetry (CV), to determine the change in the bonding environment of Co. The final product of the synthesis was a red solution ($Co(en)_x$ sol) and several characterisation experiments were carried out on this material.

To absorb the $Co(en)_x$ sol onto carbon powder, it was refluxed with ethanol and C powder for 2-4 hours and then stirred overnight, followed by filtering and rinsing with ethanol. In the case of CoPc (Aldrich Chemicals), the solvent used was THF and sequential rinsings were carried out with hot and cold water. All powders were dried under vacuum overnight before testing. The initial and final solutions were examined by UV-Vis spectroscopy to determine the degree of adsorption of the $Co(en)_x$ sol catalyst onto carbon ($Co(en)_x/C$). To prepare higher concentrations of catalyst on the carbon powder, the carbon powder was saturated with the catalyst solution and then evaporated to a gel, which was stable on an electrode surface only after heat treatment.

Heat treatment involved subjecting the $Co(en)_x/C$ to a flow of nitrogen for at least 1 hour before transfer to a pre-heated tube furnace. The samples were heated at 500° to 900° for 2 hours and then allowed to cool under a flow of N_2. Whether heat treated ($Co(en)_x/C$-ht) or not ($Co(en)_x/C$), the catalyst powder was ground by mortar and pestle for at least 2 minutes before mixing with Nafion solution.

An 11% Nafion solution (1100EW) was diluted with acetonitrile or ethanol and mixed with the $Co(en)_x/C$-(ht) in the appropriate ratios. Just before application to the electrode surface, the suspension $Co(en)_x/C$-(ht)-Naf was sonicated for 10 minutes.

Electrochemical evaluation of ORR kinetics and mechanisms

A 5 or 7 mm diameter glassy carbon (GC) rotating disc electrode (RDE) or a Au /Pt or GC/Pt RRDE (5 mm disc for both) were used as the electrode substrate to determine the ORR activity of the catalysts. A measured volume (14 μL for a 7 mm disc) of the $Co(en)_x/C$-(ht)-Naf was applied by micropipette to the centre of the electrode disc to give a loading of 0.6 mg/cm^2 of dry catalyst powder. With a Co loading of 1.2 % Co/C, this gives a loading of 0.008 mg/cm^2 of Co. The electrode was then air-dried for approximately 5 minutes before drying for 1 minute using a heat gun.

The standard electrochemical conditions employed were 0.5 M H_2SO_4, purged with vigorously bubbling nitrogen or oxygen for at least sixty minutes and then with nitrogen or oxygen at a flow rate of 50 mL/min for 5 minutes. A three electrode electrochemical cell was used, containing a Pt black mesh counter electrode and a reversible hydrogen electrode reference electrode. CVs were collected first in nitrogen purged aqueous solution at 2 or 10 mV/s to obtain a baseline for comparison to the ORR data. The cell was then saturated with oxygen, as described above, and a CV was run at 2 or 10 mV/s at different rotation rates (0-2000 rpm) using a Pine analytical rotator (ASR2). Data collection was achieved using either Corrware (RDE) or PineChem (RRDE) software.

RESULTS AND DISCUSSION

$Co(en)_x$ sol synthesis

Fig. 1 shows the changes in the UV-Vis spectrum of the Co product formed as a function of the ratio of Co to en during the synthesis. The goal of this experiment was to ascertain that Co was indeed being complexed by the nitrogen of the ethylene diamine (en) and to establish whether oxygen continued to be in the Co bonding environment. A cobalt oxide sol-gel (O-Co-O-Co) and $Co(H_2O)_6^{2+}$ both have the same λ_{max} at 510-514 nm (515 nm (17). When the cobalt is complexed to nitrogen, as in pure $Co(en)_3^{3/2+}$, the λ_{max} shifts to 464-476 nm (Fig. 1). In the data of Fig. 1, it is seen that the molar absorptivity increases with increasing ligand ratio and that the λ_{max} shifts to lower wavelengths, indicating at least partial complexation of Co with en. The final product exhibits a λ_{max} at the same position as $Co(en)_3^{3+}$, but with a much broader peak and a shoulder near the Co-O peak. This suggests that both Co-N and Co-O bonds exist in the SG in solution, and it is assumed (but cannot be verified from these spectra) that each Co centre is complexed both to O and N.

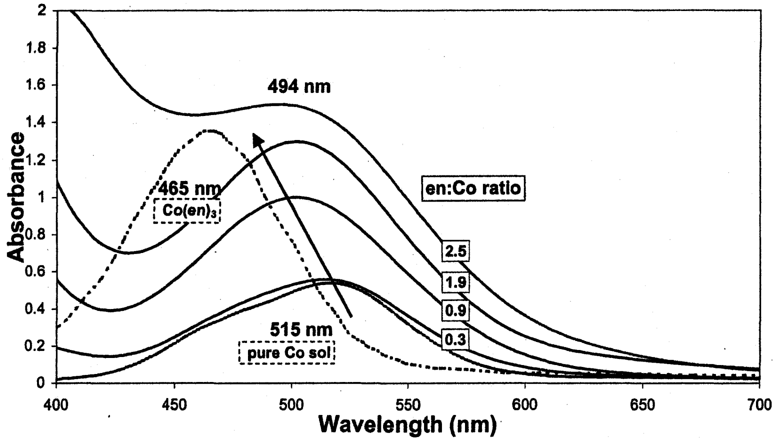

Figure 1: Evidence for Co-ethylene diamine complexation in Co oxide sol gel

Figure 2 shows the CV response of the non-carbon supported catalyst in alkaline solution. Also shown is the CV response of a pure Co oxide SG, formed using identical conditions to the catalyst (but without added en), revealing the known $Co^{2+/3+}$ oxide and $Co^{3+/4+}$ oxide redox transitions, typical of Co oxide dried at less than 200°C (15). In comparison, the $Co(en)_X$ sol reveals a different response, with significantly shifted potentials. This is evidence for the alteration of the Co centre in these catalysts vs. in Co oxide. Had the catalyst contained a mixture of Co oxide and Co-C-N, we would have expected to obtain the CV signatures of both Co oxide and the new material. The results in Fig. 1 and Fig. 2 therefore support the contention that all of the Co centres are in a mixed environment involving oxygen and nitrogen bonded to Co.

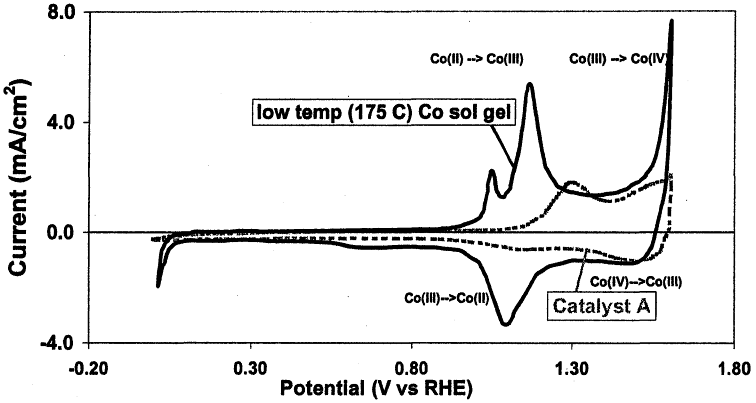

Figure 2: CV of pure Co sol and catalyst (Pt slide, scan rate 100 mV/s, 0.5 M NaOH)

ORR Activity of heat treated Co(en)$_x$/C and CoPC catalysts

The Co(en)$_x$/C catalysts initially exhibited quite low ORR activity. Consistent with the literature, the catalytic activity improved greatly upon heat treatment. Fig. 3 shows the improved activity after heat treatment at 650 °C for 2 hours under flowing N_2, demonstrating also that the Tafel slopes are lowered, consistent with a more active catalyst. Cobalt phthalocyanine (CoPC), prepared in parallel with our catalyst, also shows an improvement in ORR activity with heat treatment, as reported in the literature (2) for CoPC prepared using different processing steps. The exact mechanism by which heat treatment improves the activity of CoN_4 based catalysts is not known, but numerous suggestions have been made, including improvement in the dispersion of the catalyst, the formation of new bonds of the chelate to the carbon powder, the formation of a new type of Co species or carbon species (18), and the formation of dimeric CoN_4 sites (12).

The generation of H_2O_2 during the ORR was also examined for our SG-derived catalyst, in comparison with CoPC. The direct four-electron mechanism to water is the preferred reaction pathway, vs. the two-electron generation of H_2O_2, both because of the higher currents and voltages obtained, but also as corrosive H_2O_2 is not formed. Using the RRDE in oxygen-saturated 0.5 M sulphuric acid, it was found that 30% of the oxygen which reacted at the disc formed H_2O_2 when our catalyst was non-heat treated, compared to 50% for non-heat treated CoPC. After heat treatment at 650 °C, the value for the SG-formed Co(en)$_x$/C dropped to 20%, while the % H_2O_2 generated at CoPC did not change, consistent with previously reported results (2). These results demonstrate an additional advantage of the SG route for $Co(en)_x$ sol synthesis.

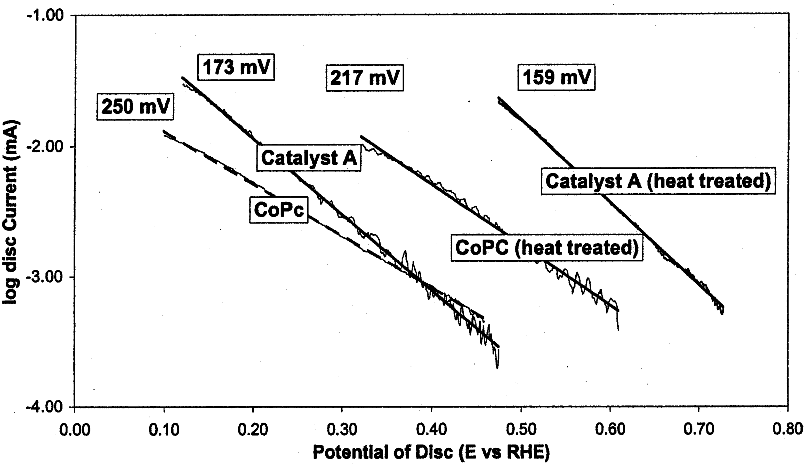

Figure 3: Effect of heat treatment on the ORR activity of CoPC compared to our catalyst.

To determine the optimum heat treatment temperature, for these catalysts, temperatures were varied from 500 to 900° C. Fig. 4 shows a plot of the potential at a selected current density of 2 mA/cm^2 as well as the % H_2O_2 generation as a function of

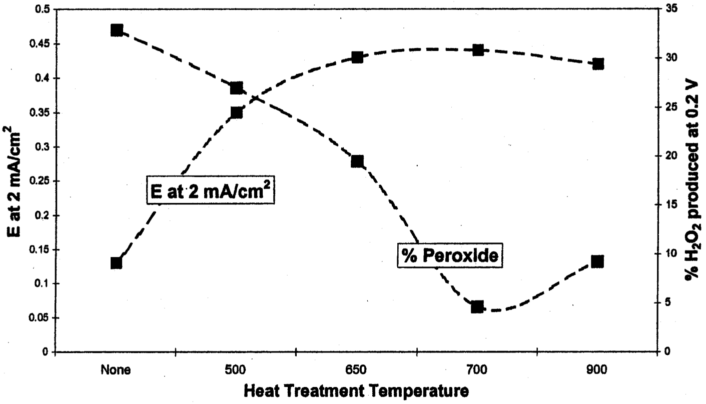

Figure 4: Optimisation of heat treatment temperature.

drying temperature, clearly revealing the benefits of temperatures over 700°C. Under these conditions, the ORR activity is the highest, while the amount of H_2O_2 formed is very small. An optimum heat treatment temperature of between 600° and 800° C has been generally reported (2, 12, 14) for CoPc, although a maximum at 600°C has also been reported (19).

In an effort to further increase catalyst performance towards the ORR, multiple layers of the Co(en)$_x$/C-ht-Naf were applied to the GC electrode to determine the effect of loading on the achievable reaction rate. The inset in Fig. 5 reveals the increasing amount of catalyst on the surface, based on the larger charging currents of the carbon support. Indeed, the ORR currents also increase and, in other experiments, it has been shown that up to 3 to 5 loadings of the catalyst can be applied, after which no further increases in the ORR activity are seen.

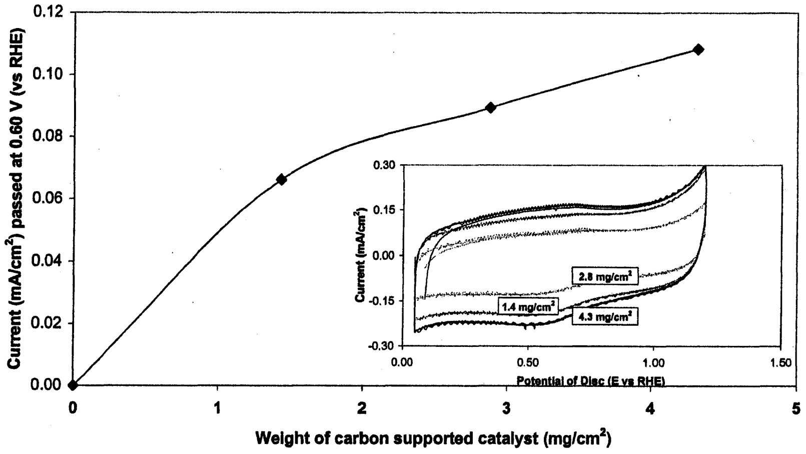

Figure 5: Increase in ORR activity with multiple loadings

Other experiments focussed on increasing the ORR activity by increasing the ratio of Co(en)$_x$ sol to the carbon support. Fig. 6 demonstrates the success of this approach up to a maximum loading of 20% by weight of the Co on carbon, after which the activity decreases again. This was observed with two separate batches of catalyst. The need for a relatively high amount of carbon points towards its involvement in generating the desired active sites. In our work, this is also clearly observed in other ways, e.g., as catalysts heated to 650 °C in the absence of carbon support yield only a very poor ORR activity of 10 to 20 %, relative to those that are pyrolized with carbon.

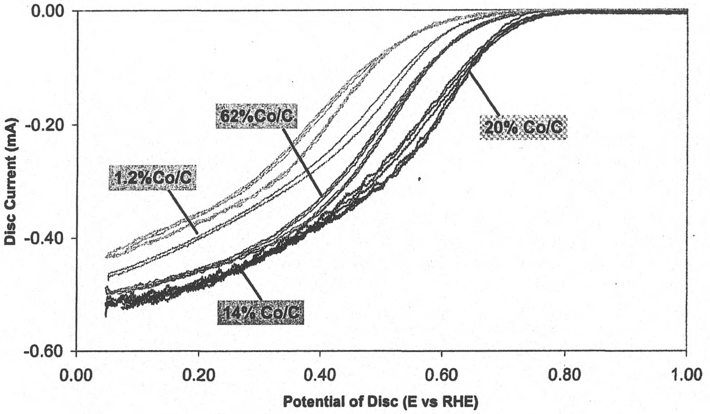

Figure 6: The effect of a higher concentration of Co on C powder

Fig. 7 demonstrates the improved performance of our SG-formed Co(en)$_x$/C-ht catalyst over approximately the last year of research.

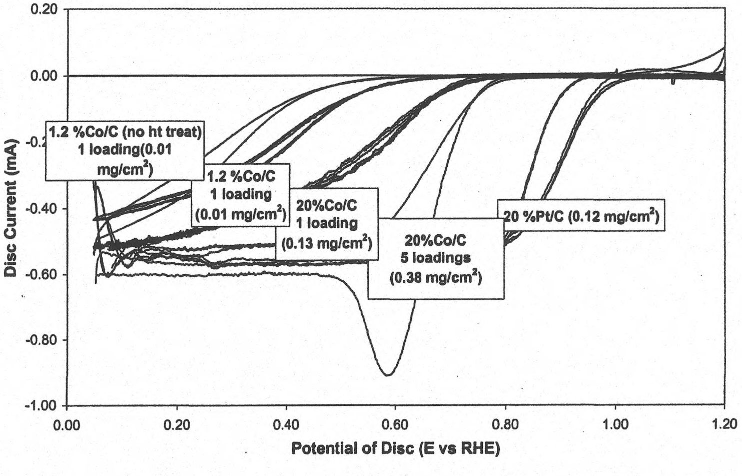

Figure 7: Improvements in catalytic activity with changing variables

The increase in activity shown from left to right in Fig. 7 was achieved by changing only one catalyst preparation variable at a time. Non-heat treated catalyst was relatively inactive, similar to other materials which we have prepared. Heat treatment was found to improve the activity significantly, while the method of initial drying of the catalyst after applying it to the electrode was also found to be very important. Initially, the catalyst was dried for 15 minutes at 175° C in air (in a furnace), but drying the catalyst for only one minute with a heat gun led to a notable activity increase. As described earlier (Fig. 6), increasing the catalyst loading led to a further substantial increase in activity, although a maximum was observed at 20% Co. Fig. 7 also shows that Pt (0.12 mg/cm^2) still gives ca. 100 times better performance than the Co(en)$_x$/C-ht, although at an approximately 800 times higher cost.

CONCLUSIONS

In this work, Co oxide sol-gel syntheses, known to yield nanoparticulate composite materials, have been modified by the addition of ethylene diamine in order to incorporate carbon and nitrogen into the Co environment. The successful achievement of this goal has been verified using UV-Visible spectrophotometry and cyclic voltammetric analysis in alkaline solutions. These new catalysts demonstrate very good oxygen reduction activity in acidic solution after adsorption on carbon and subsequent heat treatment. Based on the improved kinetics (both lowered Tafel slopes and higher exchange current densities), as well as the lower amount of H_2O_2 generated, the optimum heat treatment temperature was found to be 700 °C. By comparison, Co phthalocyanine catalysts, prepared identically, also showed an increase in activity with heat treatment, but less than that of Co(en)$_x$/C, and with no decrease in the amount H_2O_2 produced.

Catalyst activity was also found to increase with an increase in the concentration of the Co(en)$_x$ sol on carbon powder. However, this is limited to 20 wt % Co on carbon, after which the ORR activity decreased again. Increasing the quantity of catalyst impregnated carbon powder on the electrode surface also increased the activity, suggesting that the catalyst is a porous network. The beneficial effect of increasing the loading was limited to 3-5 layers (0.6 mg/cm^2 each), perhaps due to the blocking of active sites by the outer layers of catalyst.

ACKNOWLEDGEMENTS

The authors gratefully acknowledge financial support from the Natural Sciences and Engineering Council of Canada (NSERC) and Ballard Power Systems, to AHCS, in the form of an Industrial Post-graduate Scholarship. Thanks are also extended to NSERC for the support of this work in the form of equipment.

REFERENCES

---

1) C. Deng, M. Digman, *J. Electrochem. Soc.*, **145**, 10, 3513 (1998).
2) E. Claude, T Adduo, J. Latour, P. Aldebert. *J. Appl. electrochem.*, **28**, 1, 57 (1998).
3) P. Gouerec, M. Savy, J. Riga, *Electrochim. Acta*, **43**, 7, 743 (1998).
4) R. Reeve, P. Christensen, A. Hammett, *J. Electrochem. Soc.*, **145**, 10, 3463 (1998).
5) R. Manoharan, J. B. Goodenough, *Electrochim. Acta* , **40**, 3, 303 (1995).
6) J. Maruyama, M. Inaba, Z. Ogumi, *J. Electroanal. Chem.*, **458** 175 (1998).
7) A. Bouwkamp-Wijnoltz, W. Visscher and J. Van Veen, *Electrochim. Acta,* **39**, 11/12, 1641 (1994).
8) J. M. Zen, C. B. Wang, *J. Electrochem. Soc.,* **141**, 4, L51 (1994).
9) J. Bett, H. Kunz, J. Aldykiewicz Jr. J Fenton, W. Bailey and D. McGrath. *Electrochim. Acta*, **43**, 24, 3645 (1998).
10) V. Mahadevan, Z hou, A. Cole, *J. Am. Chem. Soc.,* **119**, 11996 (1997).
11) V.S. Bagotzky, M. R. Tarasevich, K.A. Radyushkina, O.A. Levina, and S.I.Andrusyova, *J. Power Sources*, **2**, 233 (1977/78).
12) T. Okada, M. Gokita, M. Yuasa, and I. Sekine, *J. Electrochem. Soc.,* **145**, 3 815 (1998).
13) C. Deng, M. Digman, *J. Electrochem. Soc.,* **145**, 10, 3507 (1998).
14) R. Cote, G. Lalande, G. Faubert, D. Guay, J. Dodelet and G Denes, *Journal of New Materials for Electrochemical Systems*, **1**, 7 (1998).
15) I. Serebrennikova and V.I. Birss, *J. Electrochem. Soc.*, **144**, 566 (1997).
16) F. Meaner and N. Lynam, Donnelly Corporation, *Electrochromic Coating and Method for Making Same*, US Patent # 4,959,247, Sept. 25, 1990.
17) A.B.P. Lever, *Inorganic Electronic Spectroscopy*, pg481 Amsterdam: Elsevier, (1984).
18) C. Deng, M. Digman, J. *Electrochem. Soc.*, **145**, 10, 3507 (1998) (and references therein).
19) G. Tamizhmani, J. Dodelet, D. Guay, Glalande and G. Capuano, *J. Electrochem. Soc.,* **141**, 1, 41 (1994).

Proceedings of The Electrochemical Society, PV 2002-31, 99-110 (2002)
DOI: 10.1149/200231.0099PV © The Electrochemical Society

ORR Kinetics of Pt based alloys using a RDE and a correlation with their Fuel Cell performance

Vivek Srinivasamurthi, R. Craig Urian and Sanjeev Mukerjee*
Department of Chemistry, Northeastern University, 360 Huntington Avenue, Boston, MA 02115-5000, USA

ABSTRACT

The effect of water on the electrocatalytic activity of Pt based transition metal alloy for oxygen reduction reaction was investigated using a rotating disk electrode (RDE). 1M and 6M Trifluromethane sulfonic acid (TFMSA) was used as the electrolyte to control the amount of water. The diffusion coefficient and solubility of oxygen in this electrolyte was measured using a micro disk electrode. The ORR activity of a polycrystalline Pt was compared with that of a 20wt.%Pt/C and a 20wt.%PtCo/C and the results indicate that although in 1M TFMSA PtCo/C shows enhanced ORR activity than the Pt plug and Pt/C in 6M TFMSA it shows lower or no change in the ORR activity. The polycrystalline Pt plug shows two tafel slopes of 59 and 112 mV/dec. in the low overpotential region (l.o.r) and the high overpotential region (h.o.r) respectively whereas Pt/C and PtCo/C shows only a single tafel slope of 120 and 140mV/dec respectively. This shows that the surface Pt is clean for a larger potential range which indicates that the surface poisoning due to Pt-OH formation is diminished and hence the enhanced ORR activity.

INTRODUCTION

Over potential loses at the cathode of a fuel cell for oxygen reduction reaction is one of the main sources of loses of power. ORR, because of its complex kinetics and the need for better electrocatalysts, continues to be in the focus. The rate determining step for ORR on an electrode surface is something that has been debated for years. There have been a few mechanisms that have been proposed so far. Yeager *et al.* [1, 2] have suggested three possible models including a dual site model for a four electron direct oxygen reduction and a single site pathway through a peroxide intermediate.

The effect of different electrolytes for ORR has been extensively investigated by [3-6]. The focus during that period was to investigate a better medium compared to phosphoric acid which has detrimental effects due to strong adsorption of the phosphate anion on Pt and reduces its ORR activity. TFMSA was used as an additive in phosphoric acid fuel cells to increase oxygen solubility and thereby increasing ORR kinetics. Extensive work done by Arvia *et al.* [7, 8] using TFMSA on Pt single crystals found that the ORR kinetics depended on the crystal structure of Pt.

Many Pt based transition metal alloys have been suggested for use as a cathode catalyst [9-14]. These Pt based alloys perform much better than Pt in a completely hydrated PEM fuel cell. Changes in short range atomic order, particle size, Pt d-band vacancy, pt skin effects and Pt-OH inhibition are some of the reasons attributed for the enhanced performance by these alloys [15-18]. Inhibition of the formation of Pt-OH at potentials above 800mV thereby leaving more number of Pt sites available for oxygen reduction reaction in these alloys is widely accepted by electrochemists. The Pt-OH formation has been proposed to be derived from the interaction of water with Pt and not from the reaction of O_2. A number of indirect evidence has been shown to this effect [19]. Watanabe *et al.* [20] have shown that O_2 adsorption increases with Pt 5d-band vacancy. Mukerjee *et* al. [9-13] used in-situ EXAFS to study various Pt transition metal alloys and have shown that the ORR activity decreases with increased Pt d-band vacancy. Increase in d-band vacancy in Pt makes it difficult to loose an electron for oxygen reduction. Hence PtCr which has the lowest d-band vacancy and minimal formation of Pt-OH does not impede the charge transfer process for oxygen reduction significantly and shows enhanced performance compared to other alloys. Another reason attributed to the formation of Pt-OH is the property of the alloying metal that may lie below the surface of the Pt skin but yet have surface accessibility which may have a higher affinity for water than Pt [22].

Whether these alloys perform the same way under higher temperature and low humidity conditions is unknown. The activity of water in TFMSA decreases with increase in concentration as a result of protonation of most of the water molecules by TFMSA[9]. As a result, the formation of Pt-OH is minimized. If the inhibition of Pt-OH is the reason why these alloys perform better then the ORR activity of pure Pt should improve with decreasing water content since its affinity for water is lower than the transition metals used as alloying metals. The investigation of different alloys in varying contents of water attempted in this work is aimed towards a better understanding of the role of the alloying metal.

EXPERIMENTAL

For the measurements described in this study we used a commercially available 20 wt.% Pt/C (E-TEK Inc.) and a 20 wt.% PtCo/C (Johnson-Mathey). Measurements were also made on a polycrystalline Pt disk obtained from Pine Instruments as a control experiment. All electrochemical measurements were made using an interchangeable ring-disk electrode setup from (Pine Instruments) connected to either an Autolab (Ecochemie Inc.) or Voltalab (Radiometer Analytical) potentiostat and at room temperature. The potentials were measured with respect to a reversible hydrogen electrode (RHE) made from the same solution as the electrolyte in the experiment.

Trifluoromethane sulfonic acid (TFMSA) was obtained from 3M Co. and doubly distilled under vacuum below 60° C and converted into its monohydrate. A detailed description of the distillation process is given in [23]. The monohydrate of TFMSA was then diluted further to form the required concentrations. The diffusion coefficient of oxygen and its solubility in these solutions were determined by a transient method using a Pt microelectrode.

Electrodes were prepared as follows. Suspensions of 1mg$_{catalyst}$ per ml in iso-propanol were obtained by ultrasonication for 30 min. 20 µl of 5wt.% Nafion® was added prior to mixing to act as a binder. Glassy carbon disk electrodes (0.283 cm^2) were used as the substrate for the supported catalysts and were polished to a mirror finish using 0.05µm alumina (Buehler). A 20 µl aliquot of the suspension was then loaded onto the glassy carbon to give a Pt loading of 14µg/cm^2 (geometric) and was allowed to dry before introducing it into the electrolyte.

After preparation, the electrodes were immersed in oxygen-free electrolyte solutions and cycled several times between 0 and 1.2 V at 100mV/sec and then cycled further at 5mV/sec. For oxygen reduction studies the electrode was immersed in oxygen saturated electrolyte and conditioned initially between 0.2 and 1.2 V at 1000 rotations per minute. For ORR experiments the electrode was scanned between 0.2 and 1.2 V at 25mV/sec for 10 cycles at each rotation and the last 3 scans at each rotation rate were used for data analysis. The rotation rates were limited between 400 rpm and 1600 rpm because of viscosity issues in high concentrations of TFMSA.

RESULTS AND DISCUSSION

The validity of the clean assembly of the rotating disk electrode was verified by the cyclic voltammetry recorded on the 20%Pt/C and 20%PtCo/C in nitrogen saturated 1M TFMSA (fig. 1). Comparison of the voltammetry also shows the difference in the formation of Pt-OH at 0.8V vs. RHE. The PtCo/C shows the formation of the hydroxide to a lesser extent thus consistent to the previous results. Fig. 2 shows the potential vs. current curves at different rotations (625, 900, 1225 rpm) for the Pt plug in 1M TFMSA and 6M TFMSA at room temperature. The diffusion limited currents in 6M TFMSA is lower than that in 1M TFMSA because of differences in diffusion coefficient and concentration of oxygen in these solutions. It can be seen from the plot that the rate at which the current drops in 6M TFMSA is slower than that in 1M TFMSA even though the limiting current density is higher. Comparison of the same for PtCo in 1M TFMSA and 6M TFMSA (fig. 3) shows the same trend but to a lesser extent, thus raising the doubt if Pt-transition metal alloy catalysts would perform much better than Pt under low water content. The diffusion coefficient of oxygen and its concentration in these solutions are given in table 1 along with the values found in literature for 1M TFMSA.

A koutecky-levich plot of I^{-1} vs. $\omega^{-1/2}$ (fig. 4 and 5) for Pt/C and PtCo/C in 6M TFMSA at various potentials yields straight lines with intercepts corresponding to the kinetic currents I_k showing that the reaction order for oxygen reduction does not change over these potential regions in high concentrated acid solutions. Since the amount of Nafion® in the catalyst alcohol suspension is only 20µl (which corresponds to a weight ratio of 1:200 Nafion® to Pt loading on the glassy carbon electrodes), it was decided to neglect its effect on the limiting currents. Fig. 6 shows a plot of current vs. potential of Pt/C and PtCo/C in 1M TFMSA at 1225 rpm. It is observed that PtCo shows a better performance than Pt plug and Pt/C. The calculated I_k at 0.9V is much higher for PtCo/C than Pt/C and the Pt plug (table 2). At 0.8V, PtCo continues to show better I_k than the Pt plug but is almost close to Pt/C. The anomalous behavior of high surface area Pt/C evident from the single Tafel slope of 120mV/dec in 1M TFMSA is not very well understood and provides a scope for further investigation. The comparison of Pt/C and PtCo/C in 6M TFMSA at 1225 rpm (fig. 7) shows that Pt/C is a better catalyst than PtCo/C. The kinetic current density of Pt/C at 0.8V (0.67mA/cm^2) is much higher than that of PtCo/C (0.458 mA/cm^2). However, the exchange current density of Pt/C and PtCo/C are very close (table 1). Mass corrected Tafel slope (fig. 8) of Pt plug in 1M TFMSA shows 59mV/dec and 112 mV/dec. at the low overpotential region (l.o.r) and high overpotential region (h.o.r) respectively. In 6M TFMSA, it shows a single Tafel slope of 110mV/dec consistent with a clean platinum surface. This shows that in 6M TFMSA, where the water content is low and hence its activity, Pt has a cleaner surface even in the low over potential region. This would mean that the surface poisoning due to the formation of a hydroxide species and adsorption of anions and other species on to the Pt surface is minimized. Since the anion adsorption effect due to TFMSA is insignificant the single Tafel slope would mean that the surface poisoning due to Pt-OH is minimized. Figures 9 and 10 show a single Tafel slope of ~140mV/dec for PtCo in both 1M and 6M TFMSA. Unlike Pt plug and Pt/C, the kinetic currents at 0.9V and 0.8V for PtCo/C do not show an enhancement in 6M TFMSA over that in 1M TFMSA. Table 2 summarizes the kinetic currents for the three electrocatalysts in 1M and 6M TFMSA at 0.9V and 0.8V and the respective Tafel slopes and exchange current density. Comparing the kinetics of Pt/C and PtCo/C in 6M TFMSA where the activity of water is low, Pt/C indicates a higher kinetic current than PtCo/C. This further confirms the explanation for Pt-OH formation based on water binding energy. Even though PtCo shows enhanced performance in the presence of excess of water, it fails to show any improvement under low water content.

CONCLUSIONS

1. Kinetic currents (i_k) values of Pt plug compared at1M and 6M TFMSA shows considerable improvement which reflects on the effect of water content on the kinetics for oxygen reduction reaction.
2. The same trend is seen in Pt/C although to a lesser extent. However the shift is much smaller in the case of PtCo/C which is consistent with the shift in the formation of Pt-OH.
3. Tafel slopes of Pt plug show a classic 60/120 mV/decade at the l.o.r and h.o.r in 1M TFMSA and a single slope of 120mV/decade in 6M TFMSA which is consistent with the shift in water activation. Whereas PtCo/C shows 140mV/decade in both 1M and 6M TFMSA.
4. The kinetic currents measured in a 1M TFMSA shows that PtCo/C is significantly better than Pt plug and to a lesser extent with Pt/C. 6M TFMSA data indicates that Pt/C is better than PtCo/C in terms of kinetic currents under low water activity conditions.

The data presented above illustrate the possibility of another step involved in the rate determining step for ORR involving Pt-transitional metal alloys. The interaction between water and the alloying metal has to be investigated in detail. If the reaction mechanism did not involve an interaction between water and Co then by alloying Pt, we are not increasing the activity for ORR. On the other hand, if there is an interaction between water and Co in the rate determining step, then it now becomes important to understand the behavior of different alloys at low water content as a function of the alloying metal property and to tie in the fundamental properties of the alloy metal surface to the true kinetics of ORR. The possibility of peroxides as an intermediate cannot be ruled out in these acid electrolytes and needs further investigation.

ACKNOWLEDGEMENTS

The authors gratefully acknowledge the financial support from E-Tek Inc. De Nora North America for financial support through a subcontract from the U. S. Department of Energy, Office of Transportation Technology. One of the authors (RCU) would like to thank the U. S. Department of Education for its support of the GANN Fellowship. The help rendered by Lei Zhang, Northeastern University, to determine the diffusion coefficient and concentration of oxygen is deeply appreciated. The authors would also like to thank Dr. M. A. Enayetullah, Protonex, for valuable advice and discussions towards the safe handling and distillation of TFMSA.

REFERENCES

1. E. Yeager, Electrochim. Acta, **29**(11), 1527 (1984)
2. E. Yeager, D. Scherson, and B. Simic-Glavaski, Proc. - Electrochem. Soc., **84-12**(Chem. Phys. Electrocatal.), 247 (1984)
3. E. Yeager, M. Razaq, D. Gervasio, A. Razaq, and D. Tryk, Journal of the Serbian Chemical Society, **57**(12), 819 (1992)
4. E. Yeager, M. Razaq, D. Gervasio, A. Razaq, and D. Tryk, Proceedings - Electrochemical Society, **92-11**(Proc. Workshop Struct. Eff. Electrocatal. Oxygen Electrochem., 1992), 440 (1992)
5. S.J. Clouser, J.C. Huang, and E. Yeager, Journal of Applied Electrochemistry, **23**(6), 597 (1993)
6. E. Yeager, M. Razaq, D. Gervasio, A. Razaq, and D. Tryk. 1993, Dep. Chem.,Case Western Reserve Univ.,Cleveland,OH,USA. FIELD URL:. p. 32.
7. C.F. Zinola, W.E. Triaca, and A.J. Arvia, J. Appl. Electrochem., **25**(8), 740 (1995)
8. C.F. Zinola, A.M.C. Luna, W.E. Triaca, and A.J. Arvia, J. Appl. Electrochem., **24**(2), 119 (1994)
9. R. Koetz, S. Clouser, S. Sarangapani, and E. Yeager, J. Electrochem. Soc., **131**(5), 1097 (1984)
10. S. Mukerjee, J. McBreen, and S. Srinivasan, Proc. - Electrochem. Soc., **95-26**(Oxygen Electrochemistry), 38 (1996)
11. S. Mukerjee and S. Srinivasan, J. Electroanal. Chem., **357**(1-2), 201 (1993)
12. S. Mukerjee, S. Srinivasan, and A.J. Appleby, Electrochim. Acta, **38**(12), 1661 (1993)
13. S. Mukerjee, S. Srinivasan, and M.P. Soriaga, J. Electrochem. Soc., **142**(5), 1409 (1995)
14. S. Mukerjee, S. Srinivasan, M.P. Soriaga, and J. McBreen, J. Phys. Chem., **99**(13), 4577 (1995)
15. R. Parsons and T. Vandernoot, J. Electroanal. Chem., **257**, 9 (1988)
16. V. Jalan and E.J. Taylor, J. Electrochem. Soc., **130**(11), 2299 (1983)
17. M.T. Paffett, J.G. Beery, and S. Gottesfeld, J. Electrochem. Soc., **135**(6), 1431 (1988)
18. K. Kinoshita, J. Electrochem. Soc., **137**, 845 (1990)
19. P. N. Ross et. al., J. Electrochem. Soc., **137**, 3368 (1990)
20. B.E. Conway and D.M. Novak, J. Electrochem. Soc., **128**(5), 956 (1981)
21. M. Watanabe, K. Tsurumi, T. Mizukami, T. Nakamura, and P. Stonehart, J. Electrochem. Soc., **141**, 2659 (1994)
22. A.B. Anderson, E. Grantscharova, and S. Seong, J. Electrochem. Soc., **143**(6), 2075 (1996)
23. M.A. Enayetullah, Ph.D. Thesis, Case Western Reserve University, Cleveland, OH, (1986)
24. K.L. Hsueh, E.R. Gonzalez, and S. Srinivasan, Electrochim. Acta, **28**(5), 691 (1983)

Electrolyte	C x 10^6 (mol/cm^3)	D x 10^6 (cm^2/s)	[Ref.] C x 10^6	[Ref.] D x 10^6
1M TFMSA	0.63	9.67	[24]1.6	[24]9.5
6M TFMSA	6.88	0.29	*	*

* Not available

Table 1. The concentration and diffusion coefficient of oxygen in 1M and 6M TFMSA at room temperature.

		i_K 0.9V mA/cm^2	i_K 0.8V mA/cm^2	i_0 mA/cm^2	Tafel slope mV/dec
Pt plug	1M	6.3 * 10^{-3}	0.076	0.056*10^{-6}	59/112
	6M	0.014	0.114	2.6*10^{-6}	110
Pt/C	1M	0.057	0.426	2.56	120**
	6M	0.122	0.67	3.65	123
PtCo/C	1M	0.106	0.413	3.39	140
	6M	0.101	0.458	3.35	142

Table 2. Kinetic data for Pt, 20wt.%Pt/C and 20wt.%PtCo/C in 1M and 6M TFMSA.

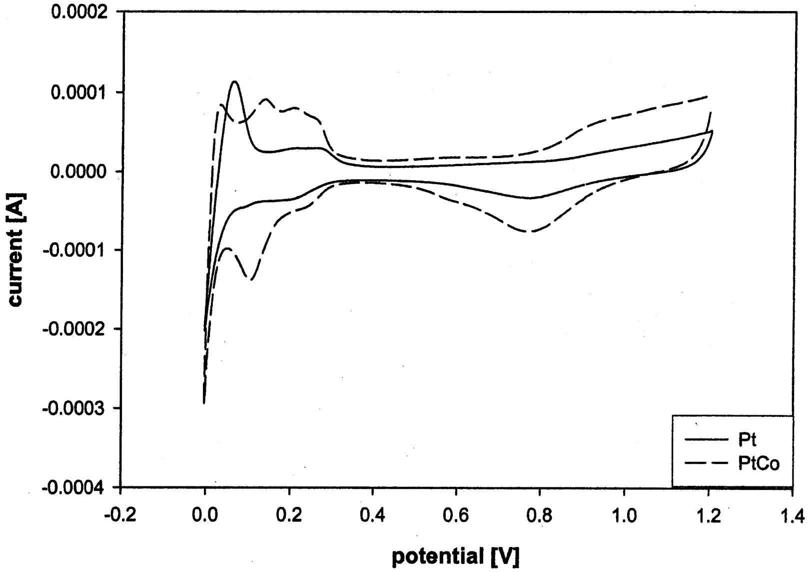

Fig. 1. Cyclic voltammetry of Pt and PtCo rotating disk electrodes in 1M TFMSA. Pt loading of 14μg/cm^2 ; Pt (——); PtCo (– –).

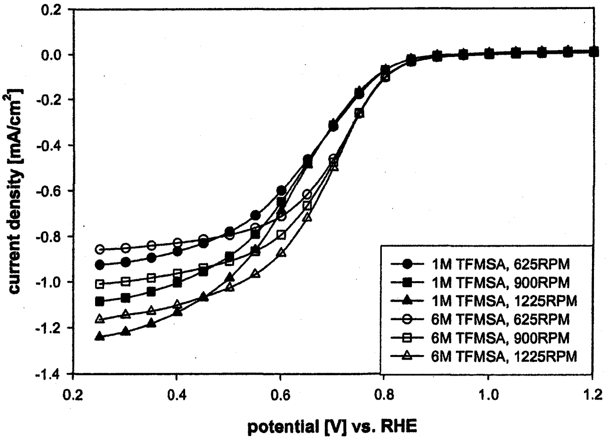

Fig 2. Disk currents obtained on Pt during ORR cathodic sweep using rotating disk electrodes in 1M and 6M TFMSA. Pt loading of 14µg/cm^2.

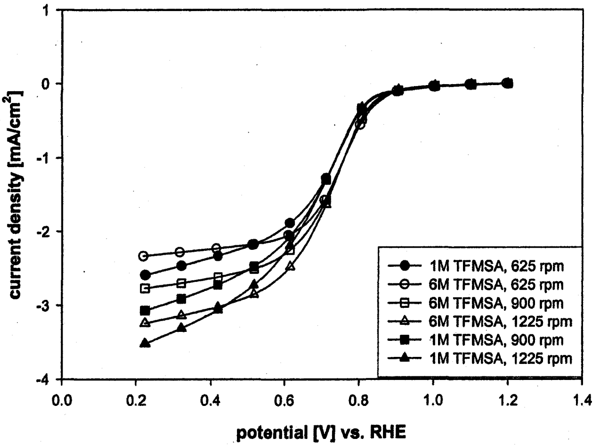

Fig 3. Disk currents obtained on PtCo during ORR cathodic sweep using rotating disk electrodes in 1M and 6M TFMSA. Pt loading of 14µg/cm^2.

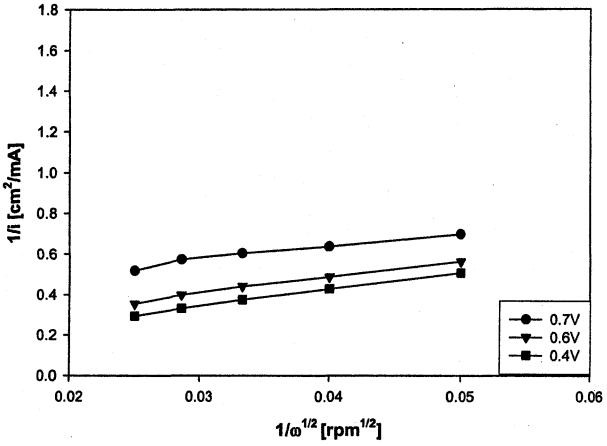

Fig. 4. Koutecky-Levich plots for the ORR on Pt/C at various potentials in 6MTFMSA. Current density normalized to the geometric area of the disk electrode.

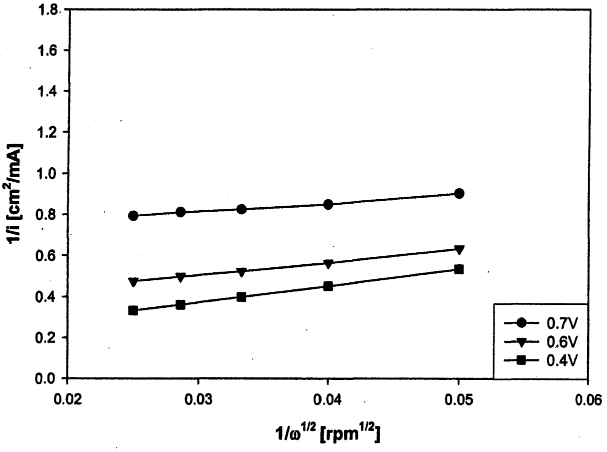

Fig. 5. Koutecky-Levich plots for the ORR on PtCo/C at various potentials in 6MTFMSA. Current density normalized to the geometric area of the disk electrode

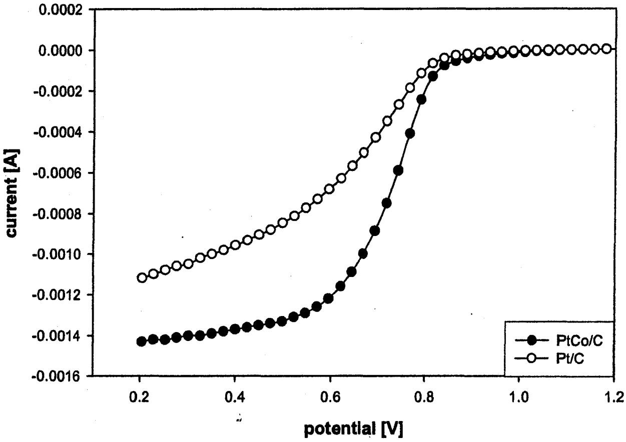

Fig. 6. Disk currents obtained on Pt/C and PtCo/C during ORR cathodic sweep using rotating disk electrodes in 1M TFMSA at 1225 rpm.

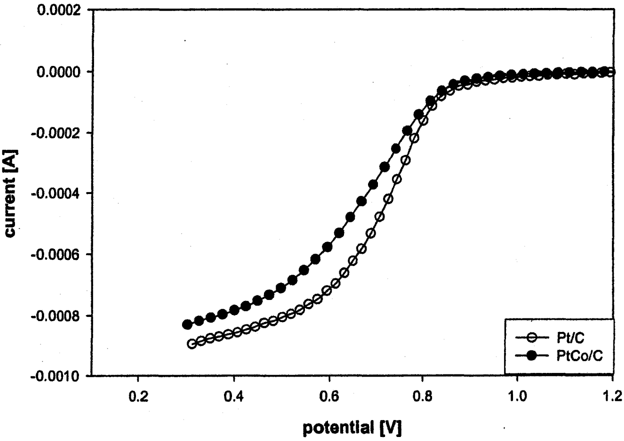

Fig. 7. Disk currents obtained on Pt/C and PtCo/C during ORR cathodic sweep using rotating disk electrodes in 6M TFMSA at 1225 rpm.

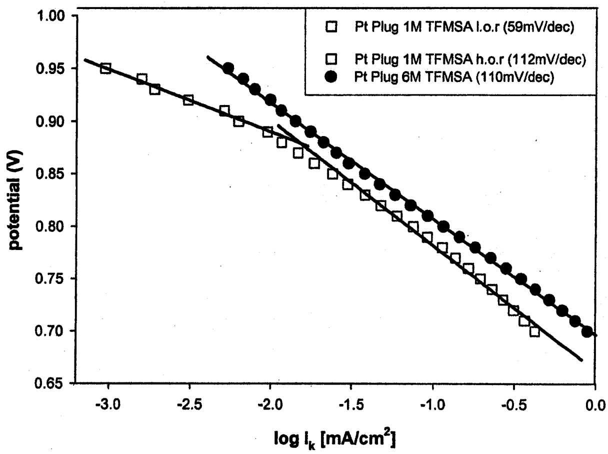

Fig. 8. Tafel plots for the ORR at room temperature, 1225 rpm on a smooth Pt in 1M and 6M TFMSA.

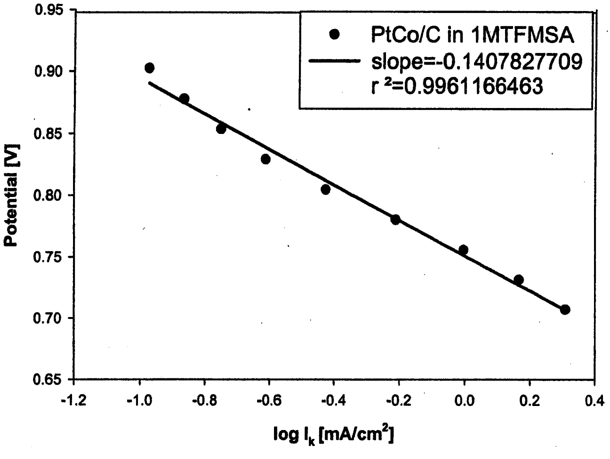

Fig. 9. Tafel plot for the ORR at room temperature, 1225 rpm on PtCo/C in 1M TFMSA.

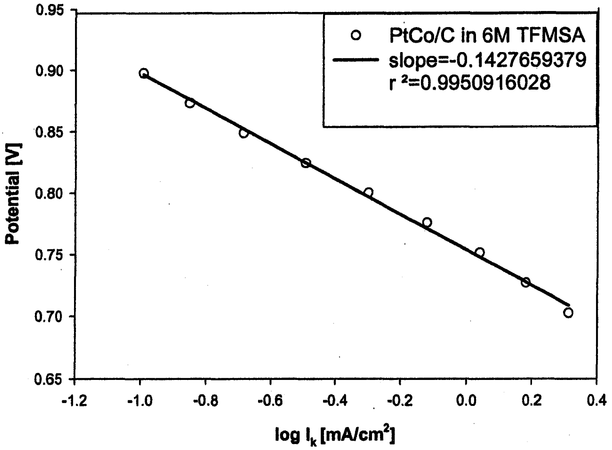

Fig. 10. Tafel plot for the ORR at room temperature, 1225 rpm on PtCo/C in 6M TFMSA.

Proceedings of The Electrochemical Society, PV 2002-31, 111-126 (2002)
DOI: 10.1149/200231.0111PV © The Electrochemical Society

Oxygen Reduction and Transport Characteristics at a Platinum /Sulfonated Poly ether Sulfone Membrane Interface

LEI ZHANG, CHENGSONG MA and SANJEEV MUKERJEE*

Department of Chemistry, Northeastern University
360 Huntington Avenue, Boston, MA 02115

ABSTRACT

Kinetic and mass transport properties were investigated for the oxygen reduction reaction in Nafion® 117 and a sulfonated poly (arylene ether sulfone) membrane (SPES-40) at 100% relative humidity (RH) as a function of pressure and temperature using a solid-state electrochemical cell. Kinetic parameters were obtained using slow-sweep voltammetry while mass transport parameters, the diffusion coefficient (*D*) and solubility (*C*), were obtained using chronoamperometry at a Pt/proton exchange membrane (PEM) interface. Oxygen reduction kinetics was found to be similar for both Nafion® 117 and SPES-40 membrane at the Pt microelectrode (100 μm) interface. The temperature dependence of O_2 permeation parameters showed similar trends for both the membranes while the pressure dependence of O_2 permeation parameters showed major differences. Despite lower equivalent weight and hence higher water content SPES-40 exhibited relatively lower values of *D* with Nafion® 117. The results are discussed in the context of their different microstructures.

INTRODUCTION

Proton exchange membrane fuel cells (PEMFC) are promising power sources for vehicular transportation, residential and consumer electronics[1]. The current state-of-the-art membrane material is based on perfluorinated sulfonic acid chemistry such as Nafion®. They have good mechanical strength, chemical stability and high proton conductivity[1] and achieve good performance when operating at 80-90°C and high relative humidity (>80% RH).[2-4] However, these membranes remain expensive and have several limiting factors such as low conductivity at low relative humidity,[5] high methanol permeability[6,7] and a low T_g (glass transition temperature) which restricts its application below 100°C. Transitioning to temperatures above 100°C provides for several attractive options including higher CO tolerance[8,9] and better water and heat management in fuel cell operations.

Alternative hydrated membranes to the perfluorinated sulfonic acid based systems possessing high proton conductivity at lower relative humidity and stability at elevated temperatures are currently the focus of a lot of research and development. In this search for elevated-temperature PEM, sulfonated poly (arylene ether sulfone) (SPES) family have recently been reported as promising candidate material.[10-14] Poly arylene ether sulfone (referred by Virginia Tech. group as PBPSH-XX) copolymers with high sulfonation levels (XX= 40-60, where XX represents the fraction of the sulfonated component in these copolymers), have shown proton conductivity in excess of 0.08 S/cm (at room temperature), which meets the requirement for high-performance PEMFC.[15]

Person to whom correspondence should be addressed.
Email: smukerje@lynx.neu.edu

These membranes however represent very different chemistry relative to the conventional perfluorinated sulfonic acid systems such as Nafion®. Their use as the ion conducting components in PEM fuel cells operating at elevated temperature not only requires excellent proton conduction at elevated temperatures, preferably at low relative humidity but also compatible reactant transport characteristics. For an electrochemical charge transfer to be successful only the dissolved reactant moieties are relevant, therefore efficient transport of reactant species such as oxygen within the electrolyte is crucial. This efficient reactant transport or permeation comprises of two important components, solubility (*C*), and diffusion coefficient (*D*). Together, they determine the crossover of gases across the membrane thus affecting the open circuit potential and more importantly, they determine the availability of the reactant at the electrocatalyst/electrolyte interface. This is most important, in determining the onset of mass transport limitations in a typical fuel cell performance.

This investigation aims to evaluate SPES-40 membrane as candidate electrolyte for PEMFC by investigating their oxygen permeation characteristics and interfacial kinetics at elevated temperatures and pressures. For this a solid-state microelectrode technique is employed, which is used to determine the kinetic and mass transport parameters (solubility and diffusivity) for O_2 reduction reaction at Pt microelectrode/membrane interface. Slow-sweep voltammetry and chronoamperometry measurements were conducted at various temperature and pressure conditions. The kinetic parameters, O_2 diffusion coefficient and solubility values obtained were compared with corresponding values for a Nafion® 117 membrane (control experiment).

EXPERIMENTAL

Membranes:

Two membranes were studied in this investigation. Poly (arylene ether sulfone) membrane with structure **A**, were prepared at Virginia Polytechnic and State University (Professor James McGrath's group). This polymer, referred to as PBPSH-40 (where 40 refers to the percentage of sulfonated component per repeat unit) by the Virginia Poly Tech. group, is referred to as **SPES-40** in this paper.

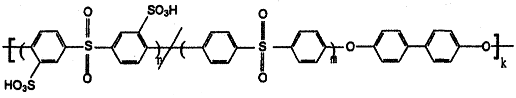

Structure A, Sulfonated poly (arylene ether sulfone)

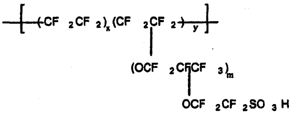

Nafion® 117

Nafion® 117 (Dupont) was bought from a commercial vendor (Aldrich chemicals). Chemical structure of this material is illustrated below.

Membranes were pretreated according to literature.[16] Measurements of water uptake followed typical methods reported earlier.[17]

Electrodes:

The working electrode was a 100µm diameter Pt microelectrode (Bio Analytical Systems, BAS, West Lafayette, IN). A solid-state dynamic hydrogen electrode (DHE) served as the reference electrode. The counter electrode was a 1.6 mm diameter Pt electrode (BAS) spot-welded to a 5mm × 5mm × 0.01 mm (thick) Pt foil.

Solid-state Electrochemical Cell Setup:

A new cell was designed to perform solid-state electrochemical experiments under controlled pressure, temperature and relative humidity. A schematic of the cell is given in Fig. 1. The apparatus consisted of three Teflon blocks. The bottom Teflon block housed a glass base with a built-in fritted glass filter (47mm diameter, Millipore), which had a porous and smooth flat surface to support the membrane of interest. The bottom end of the glass filter base was connected to the gas supply through a Swagelock® adapter. This Swagelock® adapter had arrangements for sealed thermocouple and humidity sensor attachments. This enabled measurement of inlet gas temperature and humidity immediately below the membrane electrode interface. The middle Teflon block had three through holes to fit in the working, counter and reference electrodes. This was used to provide conduit for the wires connecting these electrodes. The upper stainless steel block contained three flat-tip micrometer heads. By screwing forward its spindle, the micrometer head was capable of applying variable pressure to the electrode-membrane contact. Four screw rods and several nuts hold the three blocks tightly together. A thermocouple (Omega engineering, CT) was inserted into the cell from the bottom with its tip touching the membrane. Temperature control was achieved by using a temperature controller (Watlow, series-965). For these experiments, the cell was put into a pressure container that provided a constant temperature & pressure and also served as a Faraday cage. Gas was supplied using a special heating and humidity control unit. All results reported in this paper are at 100 % relative humidity. The relative humidity was independently measured using a humidity sensor (ELECTRONIK, series EE-30) at the bottom of the solid-state microelectrode assembly. The flow rate of the humidified gas entering the cell was set at about 600ml/min.

Electrochemical Techniques and Instrumentation

A computer controlled digital potentiostat/galvanostat (Autolab model, PGSTAT-30) was employed to conduct cyclic voltammetry, slow–sweep voltammetry and chronoamperometry experiments. All potentials stated here are relative to DHE.

Slow-sweep voltammograms between 1.2 and 0.3 V at 2 mV/s scan rate were recorded to determine the limiting current I_d. Electrode kinetic parameters were obtained using slow scan voltammograms. Chronoamperometry experiment was used to determine diffusion coefficient and solubility of oxygen. Details of the methodology and data analysis are discusses in detail elsewhere.[16,18-20]

Experimental procedure

After incorporation into the cell, the membrane was equilibrated with humidified gas at 30°C and 1atm for at least 12 hours. The temperature dependence studies of oxygen reduction and transport measurements were conducted at 100% relative humidity in a temperature range of 30-80°C and 3atm pressure. The pressure dependence studies of oxygen reduction and transport characteristics were conducted at 100% relative humidity in a pressure range of 1-4atm (abs) and 50°C. Series of electrochemical measurements for determining both interfacial kinetics and mass transport parameters were made at each condition after equilibration for at least 2 hrs at each specified condition. All experiments conducted for each of the membranes were repeated at least three times and the reproducibility monitored, these are reported as error bars in the data presented.

RESULTS AND DISCUSSION

Evaluation of the electrode kinetics of O_2 reduction at a Pt/PEM interface by Slow-scan Voltammograms:

a. Temperature dependence of the electrochemical reduction of O_2 at a Pt/PEM interface at 3atm pressure

Fig. 2 shows representative slow sweep voltammograms as a function of temperature in the range 30 to 80°C, at a Pt/SPES-40 interface under 3 atm O_2 pressure. As expected, the oxygen reduction waves are shifted away from the theoretical reversible potentials E_r because of the poor reaction kinetics. The limiting current associated with the reduction reaction displays an increasing trend with temperature. Plots of I_d versus temperature for the two membranes are shown in Fig. 3. Nafion® 117 exhibited significantly higher I_d over the whole temperature range as compared to SPES-40.

Previous investigations on Pt/Nafion 117 interface[16,18] have shown the existence of two regions in the mass transport corrected Tafel plots. The two sets of Tafel kinetic parameters at low and high current density regions correspond to the oxygen reduction reaction at oxide-covered and oxide-free surface of Pt. Tafel plots for Nafion® 117 (Fig.4 (a)) and SPES-40 (Fig. 4 (b)) show the two well-defined linear regions similar to those reported earlier.[18]

Table 1 lists the calculated kinetic parameters based on mass transport corrected Tafel equation. Comparison of the exchange current density for both the membranes in the low current density (*lcd*) and high current density (*hcd*) regions showed somewhat higher values at a Nafion®/Pt interface as compared to SPES-40. The Tafel slopes for all the membranes studied show small deviations from the "typical" number of –60 mv/decade[21] (*lcd*) and –120 mv/decade[22] (*hcd*). Further, the transfer coefficient α also exhibited small deviations from the characteristic value of 1 (*lcd*) and 0.5 (*hcd*). The activation energies of oxygen reduction reaction, E_a (kJ/mol), are also listed in Table 1. For all the membranes, the activation energies in *hcd* are slightly higher than in *lcd* as noted previously by Beattie *et. al.*[16]. In both the *lcd* and *hcd* region, the activation energies of SPES-40 and Nafion® 117 are close although SPES-40 shows a slightly lower value.

b. Pressure dependence of the electrochemical reduction of O_2 at a Pt/PEM interface

Fig. 5 shows the representative slow sweep voltammograms at Pt/SPES-40 interface as a function of pressure in the range 1-4 atm at 323K. The limiting current associated with the reduction reaction displays an increasing trend with pressure. Plots of I_d versus temperature for the two membranes are shown in Fig. 6. The plots as a function of pressure demonstrate nice linear relationships which is a consequence of Henry's law.[23] To determine the electrochemical reaction order (ρ), plots of log i_0 versus log P_{O_2} were used in both the low and high current density regions as illustrated in Fig. 7 (a), and (b). The slopes of which could be used to calculate ρ.[24] Table 2 showed that for Nafion® 117 and SPES-40, the values of ρ at both *lcd* and *hcd* regions are close to 1, which implies that the step $H_3O^+ + O_2 + e^- \rightarrow O_2H_{(ads)} + H_2O$ is the rate determining for the O_2 reduction reaction at Pt/PEM interface. The result for Nafion 117 is consistent with previous report.[16,20]

Table 3 lists the calculated kinetic parameters as a function of pressure at 323K. The result shows that the exchange current density for both the membranes in the low current density (*lcd*) and high current density (*hcd*) regions are roughly in the same order of magnitude.

According to above temperature and pressure dependence results, it could be concluded that under experimental conditions, SPES-40 and Nafion® 117 demonstrated approximately similar electrode kinetics for oxygen reduction reaction at the Pt/PEM interface.

Determination of Mass-transport Parameters by Chronoamperometric Method

a. Temperature dependence of the O_2 transport parameters at a Pt/PEM interface at 3 atm pressure

The mass transport results as a function of temperature in the range of 303-353°K under 3 atm pressure was given in Table 4. The principal features of this data can be summarized as following: (*i*) For all the membranes investigated, the diffusion coefficient *D* increases with temperature, the opposite trend is true for the solubility *C*, the overall permeability ($D\times C$), however shows an increasing trend with temperature. (*ii*) Over the temperature range studied, Nafion 117 has higher diffusion coefficients and solubility than SPES-40. (*iii*) The overall oxygen permeability for Nafion® 117 is much greater than SPES-40.

Increase of diffusion coefficient and decrease of solubility with temperature in Nafion® 117 membrane mirror earlier literature results.[16,19] However, we did not observe any sharp changes in the plots of log D and log C versus 1000/T (shown in Figure 8) as reported by Parthasarathy *et al.*,[19] and Beattie *et al.*[16]. Our Arrhenius plots for Nafion® 117 and SPES-40 membrane exhibit a linear response over the range of temperatures investigated (303-353K), which agrees well with our data of water uptake (Figure 9) by Nafion® 117 (data for Nafion® 117 is also corroborated by that of Hinatsu *et. al.*,[25]) and SPES-40. Therefore unique activation energy value for O_2 diffusion, E_d, and the enthalpy value of solubilization of O_2 in the membranes, ΔH_s, could to be determined (Table 5).

Our value of E_d and ΔH_s with Nafion® 117 is very close to those published earlier in the 303-323K range.[16,19] Comparison of the corresponding value for SPES-40 with Nafion® 117 shows a slightly higher value for E_d (27.55 kJ/mol for Nafion® 117, compared to 32.07 kJ/mol for SPES-40) and ΔH_s (-8.33 kJ/mol for Nafion® 117, compared to -15.06 kJ/mol for SPES-40). This higher activation energy can be explained on the basis of very different membrane morphology in SPES-40 as compared to Nafion® 117. The higher values of ΔH_s for SPES-40 as compared to Nafion® 117, indicates greater degree of spatial rearrangements during oxygen solubility in SPES-40. The exact mechanisms of these interactions however await a molecular modeling study.

It is well established that perfluorinated sulfonic acid membranes such as Nafion® 117 and other like membranes such as those from Asahi Chemicals (Aciplex® series) and Ballard (BAM® series) are phase-separated materials. It comprises of crystalline regions consisting of hydrophobic Teflon backbone and hydrophilic ionic domains made up of randomly attached pendant chains terminated with sulfonic acid groups. These are based on a wealth of earlier work such as those by Gierke *et. al.*,[26-28] which have established the formation of ionic clustering in these materials. The microstructure model, which has emerged, suggests the formation of inverted micelles with SO_3^- groups forming hydrated cluster embedded in fluorocarbon phase with diameters of 40 to 50 Å. As pointed out earlier,[29] the water content in the membrane is determined by a combination of three processes, (*i*) water sorption by the membrane, which is controlled by its ion exchange capacity (number of ionic groups per unit weight). (*ii*) Its electro-osmotic drag coefficient, which is a function of its proton conductivity and (*iii*) water diffusion caused by gradients in water activity. Recent AFM imaging studies,[15] using a tapping mode have shown the existence of roughly two phases in the SPES membranes. The ionic cluster phase, comprising of hydrophilic sulfonic acid groups contain most of the associated water and non-ionic matrix phase, which may be assigned to the relatively hydrophobic aromatic backbone. It has also been pointed out earlier[18,19,30] that water acts as a plasticizer in Nafion® and hence increase of the water content enables increase in the diffusion coefficient of oxygen. Opposite is true for the solubility,[18,19,30] where solubility of oxygen was determined by the fraction of the hydrophobic component in the membrane. Hence, shrinking of the hydrophobic phase leads to decrease in O_2 concentration, since O_2 tends to be more soluble in hydrophobic domains than in hydrophilic parts.[31]

The role of water content as determined by its equivalent weight (EW) has been demonstrated earlier using a comparison of sulfonated α, β, β-trifluorostyrene (BAM®, Ballard, Canada) membranes with Nafion® 117 as well as an investigation on perfluorinated sulfonic acid membranes (Nafion® series as well as Aciplex membranes). A comparison of BAM®-407 (EW=407) with Nafion®117 (EW=1100) showed the expected result of higher diffusion coefficient and lower solubility (approximately four times) for BAM®-407 relative to Nafion®117.[16] This was rationalized purely on the basis of water content in these membranes (87 w/o for BAM®-407 compared to 19 w/o for Nafion® 117 at 50°C).[16] This is also evident when comparing this effect for a particular membrane as a function of EW or water content. Prior results with BAM® (Ballard, Canada), DIAS® (DIAS Analytic, USA), Nafion® (Dupont, USA) and Aciplex® (Asahi chemicals, Japan),[17,30] show remarkable correlation with water content within each family of membranes.

As illustrated in Table 5, our previous oxygen permeation data comparing the SPES-40 and Nafion®117 membranes show relatively close values of diffusion coefficients at 1atm pressure condition. Moreover, results in this work demonstrate that under 3atm pressure, the SPES-40 membrane have even lower diffusion coefficient than Nafion® 117. This is in contrast to expectations based on ion exchange capacity (0.91 for Nafion® 117 vs. 1.72 for SPES-40) and the associated higher water uptake by SPES-40 (approximately double that of Nafion® 117). Hence despite higher water content, the O_2 diffusion in SPES-40 membrane ($D = 3.34 \times 10^{-6}$ cm^2/s) was lower than Nafion® 117 ($D = 5.51 \times 10^{-6}$ cm^2/s) under 3atm. Comparison of the percent volume of aqueous phase near room temperature (30°C, 1atm) shows that SPES-40 has approximately double the value than Nafion® 117 (Table 4). However, the variation of percent aqueous volume with temperature is greater for Nafion® 117 as compared to SPES-40 (approximately double as shown in Table 3). There is little correlation however between the results on water uptake and percent volume of aqueous phase with corresponding results on diffusion coefficient (D).

Although the wealth of prior results seems to indicate that water plays a central role in determining the O_2 permeation in proton exchange membranes, its exact mechanism remains unclear and deserves further investigation. It is evident in this comparison that SPES-40 membrane has a very different chemical structure as compared to Nafion®117. The hydrophobicity of the aromatic backbone of SPES-40 is not as strong as Nafion®'s perfluorinated backbone and the sulfonic acid functional group in SPES-40 is somewhat less acidic than in Nafion®. Therefore, one may expect a less pronounced hydrophilic/hydrophobic separation in SPES-40 as compared to Nafion® 117. Such behavior has been observed with the related sulfonated poly (ether-ether ketone) system using small angle X-ray scattering experiments.[32] As a result, one must use caution when comparing the mass transport characteristics of membranes with respect to difference in their water uptake alone. Difference in chemistry is also expected to play an important role.

Recent report based on results of AFM image analysis using tapping mode,[15] shows some striking findings concerning the morphologies of the ionic phases. For the SPES-40 membrane, the hydrophilic ionic domains are isolated and dispersed among the non-ionic matrix domains with an average of 25nm diameter.[15] In contrast, the image of Nafion® 117, are reported to have significantly smaller hydrophilic ionic domains (about 10 nm) which tend to form continuous channels in structure.[15] Assuming that O_2 diffusion is predominantly related to the water. The well-connected channels between ionic domains of Nafion® 117 may form three-dimensional water network, which seems a more favorable transport pathway for O_2. As for SPES-40, despite the larger size of hydrophilic clusters, the water filled channels may be narrower or more branched with greater number of dead-ends, O_2 therefore gets blocked to a larger extent within SPES-40 thus leading to relatively smaller increase in the diffusion coefficient despite higher water content in the membrane.

In terms of solubility, comparison of data for Nafion® 117 and SPES-40 shows a much better correlation with water content. As shown in Table 5, Nafion® 117 (EW=1100) has approximately 1.7 times higher solubility than SPES-40 at 50°C and 3atm, which agrees well with the approximately two fold lower water content of Nafion® 117. Comparison with previous results for BAM® (Ballard, Canada) membrane with EW=407 shows agreement with this trend. Even though reasonable correlation with water content is possible for SPES-40 membrane, in contrast to the corresponding characteristics with diffusion coefficient, the impact of their fundamental differences in chemistry cannot be ruled out.

b. Pressure dependence of the O_2 transport parameters at a Pt/PEM interface

The mass transport parameters as a function of pressure (1-4atm) at 323K were given in Table 6 and illustrated in Figures 10-12. Error bars in Figures 10-12 represent scatter of data from three separate experiments. Data in Table 6 represents the average of these values.

For Nafion®117 membrane, O_2 solubility increases with pressure as expected from Henry's law while diffusion coefficient is independent of pressure, which is well-agreed with previous report[16,19]. For SPES-40 membrane, however, the pressure dependence of D and C show different trends compared with Nafion® 117: diffusion coefficient of SPES-40 tends to increase as a function of pressure; its O_2 solubility on the other hand show only tiny improvements with pressure.

As proposed earlier in temperature dependence study of D and C, one possible way to explain the obvious difference in O_2 transport parameters as a function of pressure between the Nafion® 117 and SPES-40 membranes falls down on their microstructure. In our pressure dependence investigations, the temperature of the cell system was fixed as 323K; therefore the water content of the membranes should remain relatively constant during the overall pressure range. Since for the perfluorinated sulfonic acid type membrane whose O_2 diffusion process involving to a large extent with their hydrophilic ionic domains, it is reasonable to observe the diffusion coefficients of Nafion® 117 being independent of pressure. However in the case of SPES-40 membrane whose O_2 diffusion processes probably less influenced by the water content, its diffusion coefficient was found changing with pressure. The exact reason for this is not clear. But we could imagine that under pressurized conditions, some changes occurred within the microstructure of SPES-40 membrane. The rearrangements of the water-filled channels connecting the hydrophilic ionic clusters ended up with some conformations that appear more facilitate in the process of O_2 diffusion. The exact mechanism of these interactions awaits further experimental and molecular modeling study.

To evaluate the Henry's constant, we took average value of D from Table 6. For Nafion® 117, K_H was found to be 3.22×10^5 atm cm^3 mol^{-1}. Beattie *et al.*[16] have reported K_H for Nafion® 117 to be 3.48×10^5 atm cm^3 mol^{-1}, which is very close to our result. The calculated K_H for SPES-40 membrane was 7.5×10^5 atm cm^3 mol^{-1}. The higher K_H for O_2 in SPES-40 may be because of its lower O_2 solubility.

Finally, the O_2 permeability (product of D×C) is more dependent on C, so membrane with higher solubility of oxygen tends to also have higher permeability. From an overall perspective the SPES membranes has approximately three times lower O_2 permeability than Nafion® 117 (Table 4 and 6).

The lower solubility and permeability of oxygen in SPES-40, has very important implications for fabrication of practical membrane electrode assembly (MEA) using these materials. The choice of ionomer in the reaction layer of the electrode and its thickness will determine both the mass transport and activation overpotentials. Hence, a systematic evaluation of these oxygen permeability characteristics in these new class of membranes designed for elevated temperature operation is essential for designing improved PEM fuel cells.

CONCLUSIONS

Electrode kinetics and mass transport parameters were determined for Nafion® 117 and a sulfonated poly (arylene ether) sulfone membrane (SPES-40) at 3atm O_2 pressure in a temperature range of 303K to 353K and at 323K temperature in a pressure range of 1atm to 4atm(abs).

Like Nafion® 117, Tafel plots at a Pt/SPES-40 membrane interface displayed two slopes corresponding to oxide covered and free Pt surface (low and high current density regions). The electrode kinetics of the SPES-40 membrane was found to be in the same range as Nafion® 117.

The temperature dependence of O_2 transport parameters are found similar for the two membranes investigated: the O_2 diffusion coefficient D increases with temperature, while the solubility C decreases. The overall permeability $D \times C$ shows an increase as a function of temperature.

However our pressure dependence studies of O_2 transport parameters of the two membranes show some differences in the trends of D and C. For the Nafion®117 membrane, O_2 solubility increases with pressure while diffusion coefficient is independent of pressure. For the SPES-40 membrane, diffusion coefficient tends to increase as a function of pressure, but its O_2 solubility show tiny increase with pressure.

SPES-40 was found to have relatively lower diffusion coefficients than Nafion® 117 despite the higher water uptake by SPES-40 (approximately twice the IEC). Oxygen solubility for Nafion® 117 was however higher than SPES-40. These results were discussed in the context of water content and microstructure of the membranes. The conformations of water-filled channels connecting the hydrophilic ionic clusters appear to have important contributions in the process of O_2 diffusion. Chemistry of SPES membrane backbone appears to play a major role in determining the solubility of oxygen in these systems given its relatively lower hydrophobicity as compared to the perfluorinated backbone for Nafion®. From an overall perspective, the lower solubility of oxygen in the SPES membrane appears to effect the overall permeation of oxygen in this class of membranes.

ACKNOWLEDGEMENTS

The authors wish to acknowledge financial support from the Department of Energy, through a subcontract from Los Alamos National Laboratory. The authors would like to express their deep appreciation to Professor James McGrath at the Department of Chemistry, Virginia Polytechnic Institute and State University (Virginia Tech.) for providing SPES family of proton exchange membranes used in this work. The assistance of our group members in the design and set up of the electrochemical cell as well as the humidification control unit is deeply appreciated.

REFERENCE:

(1) Savadogo, O. *Journal of New Materials for Electrochemical Systems* **1998**, *1*, 47.

(2) Zawodzinski, T. A., Jr.; Springer, T. E.; Uribe, F.; Gottesfeld, S. *Solid State Ionics* **1993**, *60*, 199.

(3) Opekar, F.; Svozil, D. *J. Electroanal. Chem.* **1995**, *385*, 269.

(4) Sone, Y.; Ekdunge, P.; Simonsson, D. *J. Electrochem. Soc.* **1996**, *143*, 1254.

(5) Sumner, J. J.; Creager, S. E.; Ma, J. J. A.; DesMarteau, D. D. *Journal of the Electrochemical Society* **1998**, *145*, 107.

(6) Kauranen, P. S.; Skou, E. *Journal of Applied Electrochemistry* **1996**, *26*, 909.

(7) Jia, N.; Lefebvre, M. C.; Halfyard, J.; Qi, Z.; Pickup, P. G. *Electrochemical and Solid-State Letters* **2000**, *3*, 529.

(8) Kreuer, K. D. *Solid State Ionics* **1997**, *97*, 1.

(9) Malhotra, S.; Datta, R. *Journal of the Electrochemical Society* **1997**, *144*, L23.

(10) Nolte, R.; Ledjeff, K.; Bauer, M.; Muelhaupt, R. *BHR Group Conf. Ser. Publ.* **1993**, *3*, 381.

(11) Nolte, R.; Ledjeff, K.; Bauer, M.; Muelhaupt, R. *J. Membr. Sci.* **1993**, *83*, 211.

(12) Kim, Y. S.; Wang, F.; Hickner, M.; McGrath, J. E.; Zawodzinski, T. A. *Abstracts of Papers, 223rd ACS National Meeting, Orlando, FL, United States, April 7-11, 2002* **2002**, POLY.

(13) Brankovic, S. R.; Wang, J. X.; Adzic, R. R. *Electrochemical and Solid-State Letters* **2001**, *4*, A217.

(14) Hickner, M. A.; Wang, F.; Kim, Y. S.; Pivovar, B.; Zawodzinski, T. A.; McGrath, S. *Preprints of Symposia - American Chemical Society, Division of Fuel Chemistry* **2001**, *46*, 459.

(15) Wang, F.; Hickner, M.; Kim, Y. S.; Zawodzinski, T. A.; McGrath, J. E. *Journal of Membrane Science* **2002**, *197*, 231.

(16) Beattie, P. D.; Basura, V. I.; Holdcroft, S. *Journal of Electroanalytical Chemistry* **1999**, *468*, 180.

(17) Basura, V. I.; Chuy, C.; Beattie, P. D.; Holdcroft, S. *Journal of Electroanalytical Chemistry* **2001**, *501*, 77.

(18) Parthasarathy, A.; Martin, C. R.; Srinivasan, S. *J. Electrochem. Soc.* **1991**, *138*, 916.

(19) Parthasarathy, A.; Srinivasan, S.; Appleby, A. J. *J. Electrochem. Soc.* **1992**, *139*, 2530.

(20) Parthasarathy, A.; Srinivasan, S.; Appleby, A. J.; Martin, C. R. *J. Electrochem. Soc.* **1992**, *139*, 2856.

(21) Damjanovic, A.; Brusic, V. *Electrochim. Acta* **1967**, *12*, 615.

(22) Damjanovic, A.; Genshaw, M. A. *Electrochim. Acta* **1970**, *15*, 1281.

(23) Laidler, K. J.; Meiser, J. H.; Sanctuary, B. C. *Physical Chemistry*, 2002.

(24) Biegler, T.; Rand, D. A. J.; Woods, R. *Limiting oxygen coverage on platinized platinum; relevance to determination of real platinum area by hydrogen adsorption*, 1971; Vol. 29.

(25) Hinatsu, J. T.; Mizuhata, M.; Takenaka, H. *J. Electrochem. Soc.* **1994**, *141*, 1493.

(26) Gierke, T. D., Munn, G.E., Wilson, F.C.,. *J. Polymer Sci., Polymer Phys., Ed* **1981**, *19*, 1687.

(27) Hsu, W. Y., and Gierke, T. D.,. *Macromolecules* **1982**, *15*, 101.

(28) Hsu, W. Y., and Gierke, T. D.,. *J. Memb. Sci.*, **1983**, *13*, 307.

(29) Paddison, S. J.; Zawodzinski, T. A., Jr. *Solid State Ionics* **1998**, *113-115*, 333.

(30) Buechi, F. N.; Wakizoe, M.; Srinivasan, S. *J. Electrochem. Soc.* **1996**, *143*, 927.

(31) Lee, P. C.; Rodgers, M. A. J. *J. Phys. Chem.* **1984**, *88*, 4385.

(32) Kreuer, K. D. *Journal of Membrane Science* **2001**, *185*, 29.

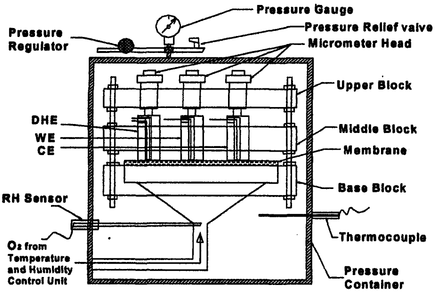

Figure 1. **Schematic of the solid-state electrochemical cell**

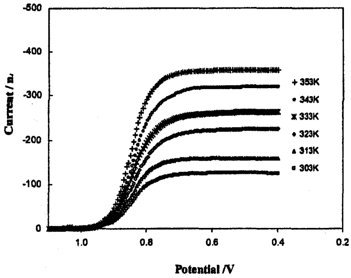

Figure 2. Representative plot showing a slow-sweep voltammogram for O_2 reduction at the Pt/SPES-40 interface under conditions of 100% RH, in the temperature range 303-353K, (303K (□), 313K (Δ), 323K (◊), 333K (*), 343K(O), 353K (+),). 3atm O_2 pressure (total); scan rate = 2mV/s.

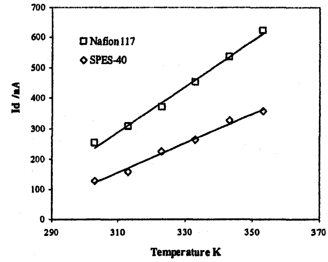

Figure 3. Plots of limiting current, I_d, versus temperature for Pt/PEM systems studied under conditions of 100% RH, as a function of temperature (303-353K), 3atm O_2 pressure (total). (Nafion® 117 (□), and SPES-40 (◊))

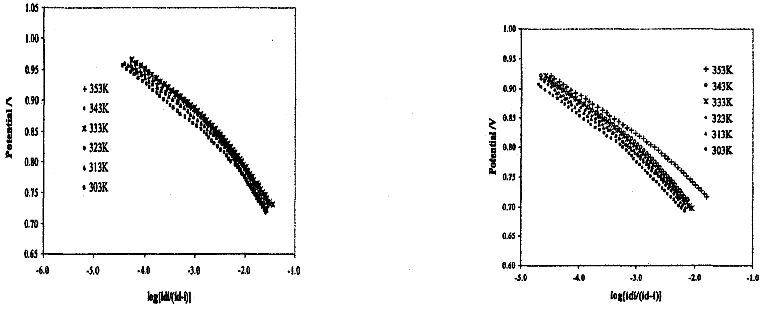

(a) Nafion® 117

(b) SPES-40

Figure 4. Plots of mass-transport corrected Tafel plots for (a) Nafion® 117, (b) SPES-40 membrane under conditions of 100% RH, as a function of temperature in the range 303-353K (303K (□), 313K (Δ), 323K (◊), 333K (*), 343K(0), 353K (+),). 3atm 0_2 pressure(total)

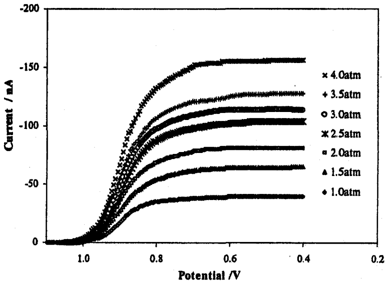

Figure 5. Representative plot showing a slow-sweep voltammogram for O_2 reduction at the Pt/SPES-40 interface under conditions of 100% RH, in the pressure range 1-4atm(total), (1atm (◊), 1.5atm(Δ), 2atm(□), 2.5atm (*), 3atm (O), 3.5atm (+), 4atm(×)), at 323K temperature, scan rate = 2mV/s.

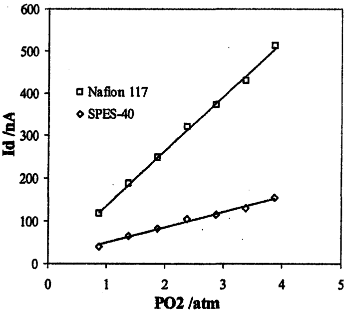

Figure 6. Plots of limiting current, I_d, versus temperature for Pt/PEM systems studied under conditions of 100% RH, in the pressure range 1-4atm(total), 323K temperature. (Nafion® 117 (□), and SPES-40 (◊))

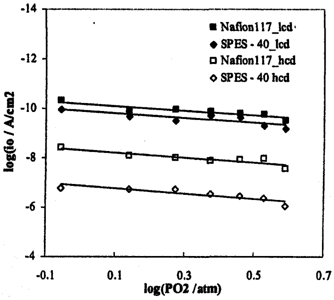

Figure 7. log i_0 versus log PO_2 for Nafion® 117 and SPES-40. (In *lcd*, Nafion® 117 (■), and SPES-40 (♦), in *hcd*, Nafion® 117 (□), and SPES-40 (◊),)

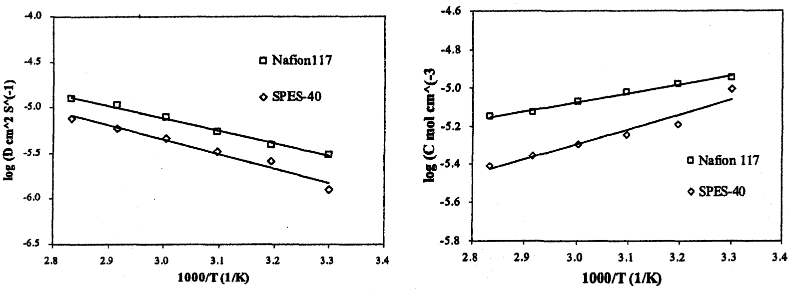

Figure 8. Arrhenius plots of (a) log *D* and (b) log *C* versus 1000/T for various PEM membranes studied under conditions of 100% RH, temperature range 303-353K, 3atm O_2 pressure (total). (Nafion® 117(□), SPES-40 (◊)). The values of *D* and *C* are average of three separate experimental data sets for each membrane system.

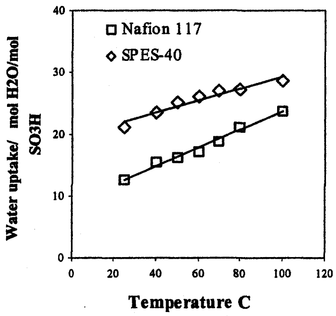

Figure 9. Water uptake (expressed as number of moles of water/SO_3^- group, λ) for various PEM membranes as a function of temperature. (Nafion® 117(□), SPES40 (◊)).

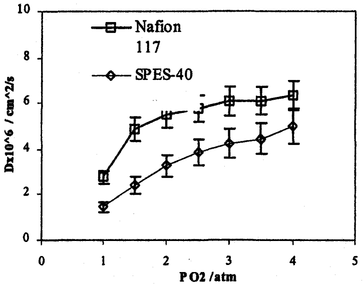

Figure 10. Pressure versus diffusion coefficient (*D*) of oxygen at Pt/PEM interface studied under conditions of 100% RH, temperature range 303-353K, 3atm O_2 pressure (total). (Nafion® 117(□), SPES-40 (◊)). The error bars represent the limits of the range of behavior for each PEM system based on a set of three separate experiments.

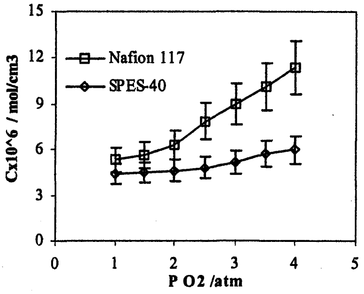

Figure 11. Pressure versus solubility of O_2 (*C*) at Pt/PEM interface studied under conditions of 100% RH, temperature range 303-353K, 3atm O_2 pressure. (Nafion® 117(□), SPES40 (◊)). The error bars represent the limits of the range of behavior for each PEM system based on a set of three separate experiments.

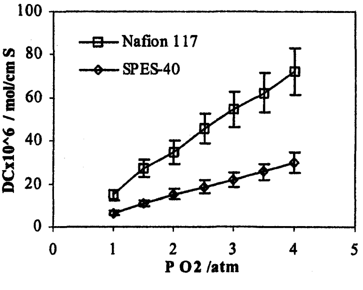

Figure 12. Pressure versus permeability of O_2 ($D \times C$) at Pt/PEM interface studied under conditions of 100% RH, temperature range 303-353K, 3atm O_2 pressure (total). (Nafion®117 (□), SPES40 (◊)). The error bars represent the limits of the range of behavior for each PEM system based on a set of three separate experiments.

Tables

Table 1. Electrode kinetic parameters for various PEM systems at the interface with a Pt micro-wire (100 μm) working electrode, studied as a function of temperature in the range 303-353K, under conditions of 100%RH, 3atm O_2 pressure.

Membrane	**T** K	**E_r** V (vs SHE)	**Slope** (*lcd*) mv/decade	**i_0** (*lcd*) A /cm^2	**α** (lcd)	**Ea** (*lcd*) kJ/mol	**Slope** (*hcd*) mv/decade	**i_0** (*hcd*) A/cm^2	**α** (hcd)	**Ea** (*hcd*) kJ/mol
Nafion® 117	303	1.303	-68.0	2.96E-14	0.88	31.65	-108.5	1.22E-11	0.55	36.01
	313	1.297	-66.9	4.19E-14	0.93		-114.6	2.73E-11	0.54	
	323	1.292	-70.4	1.47E-13	0.91		-108.6	2.21E-11	0.59	
	333	1.286	-69.2	1.54E-13	0.95		-109.9	3.17E-11	0.60	
	343	1.281	-70.5	2.22E-13	0.97		-124.2	8.10E-11	0.55	
	353	1.275	-67.1	1.22E-13	1.04		-123.3	1.02E-10	0.57	
SPES-40	303	1.303	-72.5	6.66E-15	0.83	34.31	-100.7	5.86E-13	0.60	43.07
	313	1.297	-71.2	8.25E-15	0.87		-97.6	6.44E-13	0.64	
	323	1.292	-72.4	1.41E-14	0.89		-104.4	1.49E-12	0.61	
	333	1.286	-74.3	3.22E-14	0.89		-105.6	2.50E-12	0.63	
	343	1.281	-70.0	2.43E-14	0.97		-108.3	4.41E-12	0.63	
	353	1.275	-67.9	2.06E-14	1.03		-101.7	4.92E-12	0.69	

Note: All current densities were calculated relative to the real area of the working electrode which obtained from an individual work(for Pt/Nafion®117, real A=7.45x10^{-4}. for Pt/SPES-40, real A= 7.41x10^{-4}). E_r at 3atm(totoal) and different temperatures was calculated according to Ref. [16]

Table 2. Electrochemical reaction orders for the oxygen reduction reaction at Pt/Nafion®117 and Pt/SPES-40 interfaces, calculated based on **Figure. 7**

Interface	ρ (*lcd*)	ρ (*hcd*)
Pt/ Nafion® 117	0.98	1.03
Pt/SPES-40	0.96	1.04

Table 3: Electrode kinetic parameters for various PEM systems at the interface with a Pt micro-wire (100 μm) working electrode, studied as a function of pressure in the range 1-4atm, under conditions of 100%RH, 323K.

Membrane	**Pressure**^{b} atm	**E_r**^{c} V (vs SHE)	**Slope** (*lcd*) mv/decade	**i_0**^{a} (*lcd*) A /cm^2	**α** (lcd)	**Slope** (*hcd*) mv/decade	**i_0**^{a} (*hcd*) A/cm^2	**α** (hcd)
Nafion® 117	0.88	1.283	-68.5	4.80E-15	0.99	-92.9	3.79E-13	0.69
	1.38	1.287	-67.6	1.40E-14	0.95	-95.0	7.62E-13	0.67
	1.88	1.289	-66.0	1.10E-14	0.97	-96.1	9.81E-13	0.67
	2.38	1.290	-66.5	1.33E-14	0.96	-97.7	1.26E-12	0.66
	2.88	1.292	-69.6	1.68E-14	0.92	-99.4	1.17E-12	0.64
	3.38	1.293	-69.1	1.80E-14	0.93	-96.8	1.10E-12	0.66
	3.88	1.294	-70.3	3.18E-14	0.91	-102.6	2.79E-12	0.62
SPES-40	0.88	1.283	-69.3	1.15E-14	0.92	-141.6	1.56E-11	0.45
	1.38	1.287	-70.7	2.13E-14	0.91	-142.2	1.78E-11	0.45
	1.88	1.289	-71.9	3.08E-14	0.89	-137.8	1.83E-11	0.47

	2.38	1.290	-69.5	2.03E-14	0.92	-142.1	2.77E-11	0.45
	2.88	1.292	-69.0	2.36E-14	0.93	-143.5	3.50E-11	0.45
	3.38	1.293	-67.3	4.93E-14	0.89	-146.5	4.27E-11	0.44
	3.88	1.294	-70.9	6.69E-14	0.87	-159.5	9.09E-11	0.40

a. All current densities were calculated relative to the real area of the working electrode which obtained from an individual work (for Pt/Nafion®117, real A=7.45x10^{-4}. for Pt/SPES-40, real A= 7.41x10^{-4}).

b. The values are the pressure of O_2, corrected for the saturation vapor pressure of water.

c. E_r at 1-4atm(totoal) and 323K was calculated according to Ref. [16], See reference[16]

Table 4: Comparison of mass transport properties for various PEM systems studied as a function of temperature in the range 303-353K, under conditions of 100% RH, 3atm O_2 pressure. The reported values are the average of three separate experiments for each PEM system. The calculated volume of aqueous phase is also given as a function of temperature.

T	Nafion® 117				SPES-40			
K	D × 10^6 cm^2/s	C × 10^6 mol/cm^3	DC × 10^{12} mol/cmS	Volume of aqueous phase* [%]	D × 10^6 cm^2/s	C × 10^6 mol/cm^3	DC × 10^{12} mol/cmS	Volume of aqueous phase* [%]
303	3.06	11.24	34.44	30. 6	1.24	9.84	12.22	58.9
313	3.88	10.51	40.82	35.5	2.55	6.41	16.38	61.6
323	5.51	9.42	51.88	37.3	3.34	5.69	19.04	63.2
333	7.81	8.52	66.51	38.1	4.56	5.10	23.25	63.8
343	10.67	7.47	79.75	40.6	5.87	4.40	25.82	64.6
353	12.51	7.08	88.55	43.5	7.72	3.90	30.07	65.2

*: Assuming a density of 2.2g/cm^3 for the membrane phase and 1 g/cm^3 for the aqueous phase, based on water up take values shown in Figure 9.

Table 5: Comparison of mass transport properties for various PEM systems studied as a function of pressure in the range 1-4atm, under conditions of 100% RH, 323K. The reported values are the average of three separate experiments for each PEM system. The calculated volume of aqueous phase is also given as a function of temperature.

	Nafion® 117		SPES-40	
IEC (meq/g)	0.91		1.72	
Water Content (wt %)	32		64	
O_2 Pressure (atm)	1^a	3	1^a	3
D x 10^6 cm^2/s (at 323K)	2.17	5.51	2.08	3.34
C x 10^6 mol/cm^3 (at 323K)	6.68	9.42	2.39	5.69
DCx 10^{12} mol/cm s (at 323K)	14.52	51.88	4.97	19.04
E_d kJ/mol	29.74^b	27.55	40.36^b	32.07
ΔH_s kJ/mol	-14.35^b	-8.33	-20.09^b	-15.06

a. Data under 1atm conditions come from previous experiments by the author.
b. Experimental condition: 100% RH, 303-343K, 1atm O_2 pressure

Table 6: Comparison of O_2 transport results under conditions of 100% RH, 323K, 1 and 3atm O_2 pressure for various PEM systems studied. The reported values are the average of three separate experiments for each PEM system. (1atm date comes from a submitted paper by the author)

		Nafion® 117			SPES-40		
T K	Pressure^a atm	D × 10^6 cm^2/s	C × 10^6 mol/cm^3	DC × 10^{12} mol/cm s	D × 10^6 cm^2/s	C× 10^6 mol/cm^3	DC × 10^{12} mol/cm s
323	0.88	2.77	5.32	14.75	1.43	4.38	6.25
323	1.38	4.87	5.62	27.34	2.41	4.52	10.89
323	1.88	5.48	6.35	34.81	3.27	4.63	15.11
323	2.38	5.78	7.86	45.40	3.88	4.82	18.70
323	2.88	6.08	8.98	54.64	4.26	5.12	21.84
323	3.38	6.10	10.16	62.03	4.44	5.76	25.57
323	3.88	6.34	11.38	72.07	5.00	5.99	29.91

a. The values are the pressure of O_2, corrected for the saturation vapor pressure of water. See reference[16]

Key words:
Sulfonated poly arylene ether sulfone; Diffusion coefficient; Solubility; Electrode kinetics; Oxygen permeability,

Proceedings of The Electrochemical Society, PV 2002-31, 127-138 (2002)
DOI: 10.1149/200231.0127PV © The Electrochemical Society

INFLUENCE OF AMMONIUM ON NAFION _ 117 MEMBRANES

Rune Halseid, Preben J.S.Vie, and Reidar Tunold
Norwegian University of Science and Technology
Department of Materials Technology
Sem Salands vei 6,NO .7491 Trondheim, Norway

ABSTRACT

The ion exchange equilibrium of ammonium between an aqueous phase and Nafion _ 117 were measured at 10.0,25.0,40.0,and 60.0 $_{o}$C by equilibrating the membrane in 0.1000 M chloride electrolytes of known cation composition. The water content in the membrane phase was found to decrease linearly with the cation fraction of ammonium in the membrane phase ($y_{NH^+_4}$) from ë$_{H_2O}$=21.2 (moles of water per mole sufonic acid groups) in proton form Nafion _ in pure water to ë$_{H_2O}$=13.2 in ammonium form Nafion _ in a 0.1 M chloride solution. The conductivity was measured by impedance in a two-electrode set- up using a stack of membranes. The conductivity was alşo found to decrease linearly with $y_{NH^+_4}$ from 97 mS/cm to 25 mS/cm at 25.0 $_{o}$C. The temperature dependence of the conductivity was measured, and the fitted activation energy in an Arrhenius-type equation was found to depend on membrane composition,E_a=10 .3+4 .2 ·$y_{NH^+_4}$ [kJ /mole].

INTRODUCTION

As resarch on low temperature Polymer Electrolyte Membrane Fuel Cells (PEMFC) has progressed, increasing focus has been put on how gaseous contaminants, and carbon monoxide in particular, influence the fuel cell performance, and how these effects may be alleviated. Less work has been published on other contaminants present in fuel and air streams, ammonia being one of these components. Ammonia may be formed in fuel reforming processes at levels up to 150 ppm (1)especially if the reforming involves homogeneous precombustion or the fuel itself contains nitrogen containing components (2).Ammonia may also be present as a trace component if ammonia is used as feedstock for hydrogen production by thermal splitting ((3)and references therein),or in ambient air as such. Earlier work by Szymanski et al. (4) on Phosphoric Acid Fuel Cells has shown that ammonia has an effect on fuel cell performance and cathode performance in particular.

Since ammonia is alkaline, it is expected that it will be readily absorbed by the acidic membranes used in PEM fuel cells forming ammonium in the membrane phase. An important factor determining the performance of PEM fuel cells, is the ionic conductivity. Ammonium reduces the conductivity of Nafion®[1] as pointed out by Uribe *et al.* (5). Reduced conductivity can be important both as a bulk effect increasing the Ohmic drop in the cell, as well as in the active layer(s) on either anode or cathode. Based on High Frequency Resistance (HFR) and other data collected from a fuel cell operating with 13 and 130 ppm ammonia in the fuel, Uribe *et al.* (5) concluded that the most important effect in the short term is reduced conductivity in the anode catalyst layer. When operating the fuel cell for longer times, bulk conductivity, as measured by HFR, was also affected.

The aim of this work is to quantify the ion exchange equilibrium between Nafion® 117 in an aqueous electrolyte containing different cation fractions of ammonium, $x_{\mathrm{NH}_4^+}$, and the corresponding membrane phase composition, $y_{\mathrm{NH}_4^+}$. The influence of composition and temperature on membrane conductivity, κ_{mem}, water content in the membrane, λ_{H_2O}, as well as swelling effects are studied. An aqueous phase is used since it is easier to control the membrane phase composition indirectly through an aqueous phase rather than through a vapor phase by addition of ammonia. It should be kept in mind that the parameters studied here (swelling, conductivity, and water content) may be differently influenced when Nafion® is in equilibrium with a vapor phase rather than a liquid electrolyte, and that other effects, such as catalyst poisoning, may also be important factors influencing PEM fuel cell performance.

EXPERIMENTAL

Preparation of membranes and solutions. Nafion® 117 membranes were purchased from IonPower Inc., and pretreated at 85 °C in purified water produced in a MilliPore Academic purifying system, thereafter in 5% aqueous H_2O_2(Merck *p.a.*), then again in purified water, then twice in 0.05 M H_2SO_4(Merck *p.a.*), and then finally four times in purified water (6). Membrane disks (20.35 mm ⌀) were then punched out for conductivity measurements, and these disks were again purified using the same procedure. Samples used for equilibrium measurements were cut in a rectangular shape (approximately 25 by 30 mm and 0.2 to 0.3 g dry) prior to membrane pretreatment. All samples were stored in purified water at least over night and until used in further experiments.

Equilibration of membrane samples. Standard solutions of known molality were prepared using HCl and NH_4Cl (Merck *p.a.*) and purified water. The required amounts of these solutions were weighed into measuring flasks to yield the desired cation compositions with a total chloride concentrations of 0.1000 M. All solutions were prepared in glassware calibrated with purified water. The membrane samples were equilibrated with the solutions of interest in water baths at the temperatures of interest (10, 25, 40 and 60 °C) within ± 0.1 °C. The equilibrating solutions were changed at least four times during a minimum of six days.

Water content. The weights of wet membranes were determined by quickly wiping off excess liquid with a lint-free paper, and then weighing the membrane

---

[1] **Nafion®** is a DuPont registered trademark for its brand of perfluorinated polymer products, made and sold only by E. I. du Pont de Nemours and Company.

samples. The samples were then held in the solution again for at least 30 seconds to re-equilibrate the membrane with water. This procedure was repeated until at least three readings identical to within 0.0005 g had been obtained. Zawodzinski *et al.* (7) found that rehydration of even completely dry membranes is rapid; in about 15 seconds the membrane is hydrated to 90% of it's equilibrium hydration level.

The membrane samples used for measurements at 25 °C were dried in their protonic form under vacuum at room temperature for 24 hours, and then transferred to a dessicator containing Merck SicaPent dessicant (P_2O_5). The membranes were not exposed to elevated temperatures during the drying process as that has been shown to affect the membrane properties (7, 8). After four to five days the membrane samples were weighed in a glove box (<5 ppm water vapor) and the dry weights determined. The dry weights of the membrane samples used at other temperatures were estimated from the wet weights at 25 °C assuming the same relative water content in these samples as in those that were dried.

Swelling properties. A slide caliper was used to measure the diameter of the samples used in conductivity measurements to determine changes in dimensions of the membranes due to swelling. Membrane thicknesses were measured using a micrometer screw. Dimensional measurements were only performed on membranes equilibrated at 25.0 °C since the sample dimensions had to be measured at room temperature (approximately 23 ± 2 °C).

Equilibrium isotherm measurements. The membranes were taken out of the equilibrating solutions, and weighed as described previously to determine the water content at a given temperature and external ammonium cation fraction. The samples were then transferred to flasks containing known volumes of 0.1 M pure hydrochloric acid to ion-exchange ammonium from the membranes. The membranes were kept in these solutions for seven to ten days at room temperature before the samples were transferred to a fresh hydrochloric acid solution for further ion-exchange. The concentrations of ammonium in the exchange solutions were determined by using an Ion Selective Electrode (NH4ISE25 from RadioMeter). The results were compared to analysis performed using Kjeldahl's method, and there was very good agreement between the two methods.

Conductivity measurements. The apparatus used to measure the conductivity is shown in Figure 1, and uses the same principle as used by Ottøy (9) and Halim *et al.* (10). The conductivity cell is made out of glass whereas the electrode pistons are made out of PTFE. The cell was thermostated from the same water bath as the membrane samples were kept in. The platinum electrodes were platinized prior to use, and stored short-circuited in 0.1 M HCl between measurements. In our experiments, four membranes were stacked between the two electrodes at the time, and loads added to ensure good contact. The cell was filled with the equilibrating electrolyte. The High Frequency Resistance (HFR) was measured using a Solartron 1287/1255B set-up (25 mV AC amplitude applied and the imaginary part of the impedance was zero at 2 to 6 kHz). The HFR as function of the number of membranes in the stack recorded. The coefficients of determination of the fitted straight lines, R^2, were larger than 0.9998 in all cases.

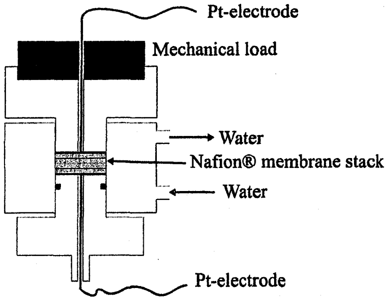

Figure 1: Conductivity cell used in this work. *Proportions shown are not actual.*.

The ohmic components in the membrane stack can be represented by the network of resistors shown in Figure 2. The total resistance, R_{tot}, is found from the slope of the HFR vs. number of membranes (the total resistance of all elements contained within the square brackets in Figure 2), and contains contributions from liquid layers between the membranes, R_{lay}, and resistance due to incomplete filling of the cross section in the conductivity cell, R_{gap}. Ottøy (9) showed by using electrolytes of different strengths that the liquid layer contribution, R_{lay}, is negligible. The conductivity of the membranes may also be affected by ingress of chloride into the membrane phase as discussed further later.

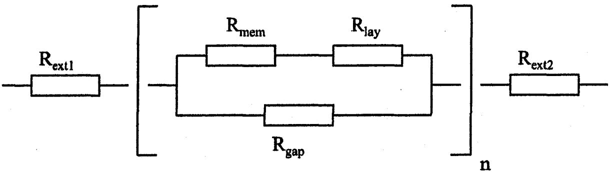

Figure 2: Equivalent circuit for the conductivity cell showing only the Ohmic components in the circuit for a stack of n membranes: membrane resistance, R_{mem}; contact resistances, R_{ext1} and R_{ext2}; contributions from liquid layers between the membranes, R_{lay}; and the parallel electrolyte resistance R_{gap} due to incomplete filling of the cross section in the conductivity cell.

Resistances in leads and the electrolyte film between electrodes and the membrane stack, R_{ext1} and R_{ext2}, do not affect the results since these are assumed to stay constant throughout the experiment, and thus does not influence the slope of the curve of HFR vs. number of membranes which is used in further calculations.

As shown later, the diameter of the membrane samples was found to depend on $y_{NH_4^+}$. The membranes were cut out from Nafion® in the protonic form, and hence contracted when exposed to ammonium containing external electrolytes. To correct for this we assume that the contraction is a linear function of $y_{NH_4^+}$, see Figure 5 for justification of this, and that the conductivity in the aqueous phase κ_{elec} is a linear function of the composition, *i. e.* $\kappa_{elec} = x_{H^+}\kappa^0_{HCl} + x_{NH_4^+}\kappa^0_{NH_4^+}$. The conductivity of pure 0.1000 M HCl and 0.1000 M NH_4Cl is 39.11 and 12.88 mS/cm respectively at 25 °C (11). The resistance due to the membrane, R_{mem} is then calculated from

$$1/R_{mem} = 1/R_{tot} - 1/R_{gap} = 1/R_{tot} - \kappa_{elec}\left(A_{tot} - A_{mem}\right)/l_{mem} \quad (1)$$

where A_{mem} is the actual area of the membrane, l_{mem} is the actual thickness of the membrane, and A_{tot} is the total cross sectional area of the conductivity cell.

Calculating the membrane conductivity κ_{mem} is then straightforward:

$$\kappa_{mem} = l_{mem}/(A_{mem}R_{mem}) \quad (2)$$

RESULTS AND DISCUSSION

Equilibrium between Nafion® and aqueous electrolytes

Membrane equivalent weight. The equivalent weight was found to be 1100 ± 40 g/mole SO_3^- based on addition of 20 ml aliquots 0.05 M sodium hydroxide to membrane samples that were in equilibrium with purified water and back titration with hydrochloric acid using Bromothymol Blue as indicator.

Based on analysis of Nafion® 117 membranes in equilibrium with 0.1000 M ammonium chloride, we found that the equivalent weight was 1056 ± 20 g/mole SO_3^-. A possible explanation of the observed difference is absorption of chloride into the membrane phase. Jones *et al.* (12) report that the content of chloride in Nafion® 117 in equilibrium with a 0.1 M NaCl solution is about $\lambda_{Cl^-} = 0.05$ (moles chloride per mole sulfonic acid group). The difference in the equivalent weights reported here corresponds to $\lambda_{Cl^-} = 0.04$.

The equivalent weight of 1100 g/mole SO_3^- is used in further calculations on water content since the reported λ_{H_2O} values are based on the number of sulfonic acid groups in the membrane. Equilibrium isotherms and membrane compositions are based on the total amount of ammonium in the membrane phase, *i. e.* including ammonium found as ammonium chloride in the membrane phase.

Equilibrium isotherms. Equilibrium isotherms at 10.0, 25.0, 40.0, and 60.0 °C were measured in Nafion® 117 in equilibrium with solutions with total chloride concentrations of 0.1000 M. Only the 25.0 °C isotherm is shown here in Figure 3.

Water content in Nafion®. The water content in Nafion® 117 was determined at room temperature (23 ± 2 °C), and was found to be $\lambda_{H_2O} = 21.2 \pm 0.4$ mole water per equivalent of sulfonic acid groups in the membrane two days after preparation. This is in good agreement with other results reported ($\lambda_{H_2O} = 21 - 23$ (7, 10, 13–15)).

If the membranes were left in water for additional time, the water content decreased from 21.2 ± 0.4 to 20.5 ± 0.4 as shown in Figure 4a. The water content

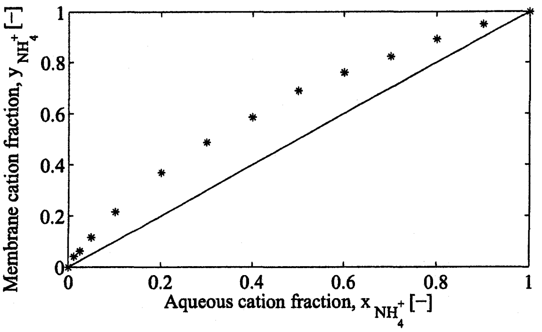

Figure 3: Ion exchange equilibrium between proton and ammonium at 25.0 ± 0.1 °C for Nafion® 117. The line $x_{NH_4^+} = y_{NH_4^+}$ is also shown.

of Nafion® was slightly dependent on the temperature, and was also lower when in equilibrium with 0.1000 M hydrochloric acid as compared to pure water, see Figure 4a. However, none of these observations are statistically significant at the 95% level.

The water content was found to vary significantly with the ammonium content of the membrane phase as shown in Figure 4b. We observed that the water content in pure ammonium form Nafion® is reduced to $\lambda_{H_2O} = 13.2$ at 25.0 °C. Xie and Okada (13) studied the water content in different alkaline and alkaline earth ionic forms of Nafion® in equilibrium with 0.03 M chloride solutions, and found that the water content of sodium form Nafion® 117 was $\lambda_{H_2O} = 16.5$ whereas the potassium form had a $\lambda_{H_2O} = 10.8$ at 25.0 °C.

Dimensions of Nafion® at various membrane composition. The diameters and thicknesses of membrane samples equilibrated at 25.0 ± 0.1 °C were measured at room temperature (23 ± 2 °C). The absolute values when in equilibrium with 0.1000 M HCl were 20.33 ± 0.05 mm and 207 ± 10 μm for diameter and thickness respectively. In Figure 5 the relative changes in diameter and thickness are shown as function of membrane composition. If we assume that 1) the total volume of Nafion® is the sum of the partial volumes of Nafion® and water, 2) the swelling is isotropic, and 3) that the density of both proton and ammonium form dry Nafion® is 2.05 g/cm³ (16), we estimate that the relative dimensions in ammonium form Nafion® should be 95.2% of those in proton form Nafion®. This is in good agreement with our findings for the diameter, see Figure 5a, but less good for the thickness. Morris and Sun (16) found that the thickness changed about two times more relatively to the diameter of Nafion® 117 when in equilibrium with different vapor pressures of water. Datasheets for Nafion® provided by Du Pont (17) states that the swelling is nearly equal in all directions. In our measurements the uncertainty for the determination of membrane thicknesses was much larger than for the diameter determinations, and even though the observed thicknesses change less than the diameter, this difference is not statistically significant.

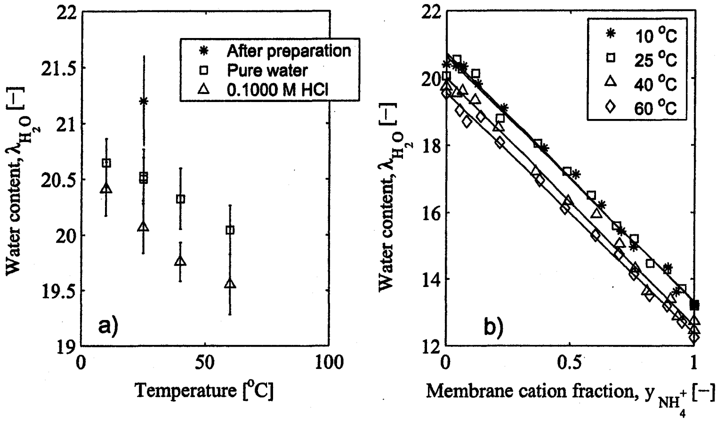

Figure 4: Water content in Nafion® 117 at a) different temperatures in pure water and 0.1000 M hydrochloric acid (error bars shown are only one standard deviation, data are averages of 4 to 8 observations) and b) at different ammonium contents in the membrane phase ($y_{NH_4^+}$). The regression lines for the different temperatures are also shown in b). The water content in Nafion® in 0.1000 M at 25.0 °C is estimated by regression to be λ_{H2O} = 20.6 ± 0.2.

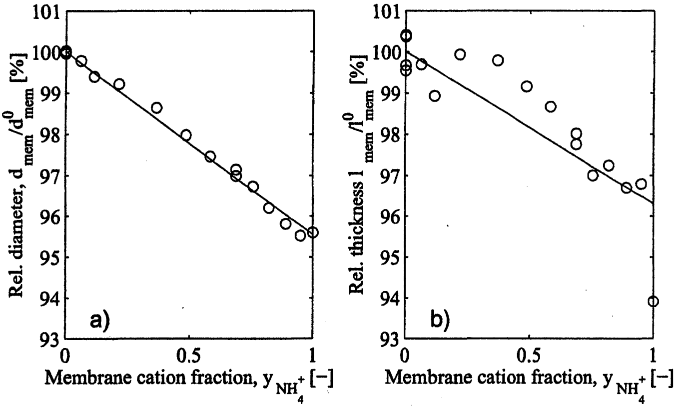

Figure 5: a) Relative diameter, and b) relative thickness of Nafion® 117 at 23 ± 2 °C. Also shown is the least square fits with the constraint that the lines shall go through (0,100). The fitted lines were a) 100 - (4.47±0.20)$y_{NH_4^+}$ and b) 100 - (3.69±1.10)$y_{NH_4^+}$. The measured diameter of proton form Nafion® was 20.33 ± 0.05 mm and the thickness 207 ± 10 μm.

Conductivity of Nafion® 117

The conductivity of Nafion® 117 in equilibrium with different electrolytes containing ammonium and protons was measured at 25.0 ± 0.1 °C. The results were corrected for the fact that the membrane diameter and thickness changed in different electrolytes (Equations 1 and 2). In pure proton and ammonium forms of Nafion® 117 the conductivities were found to be 97 mS/cm and 25 mS/cm respectively. The results are plotted in Figure 6 a) and b), and as seen from this figure, there is a linear relationship between membrane cation fraction of ammonium, $y_{NH_4^+}$, and conductivity, κ_{mem}. This is in accordance with the findings of Logette *et al.* (18), and indicates that the ionic mobilities of protons and ammonium are independent of membrane composition. This is somewhat surprising taking into account that the membrane is a rather concentrated solution. However, in situations involving di- and trivalent cations, the situation has been shown to be more complicated (14, 18–20).

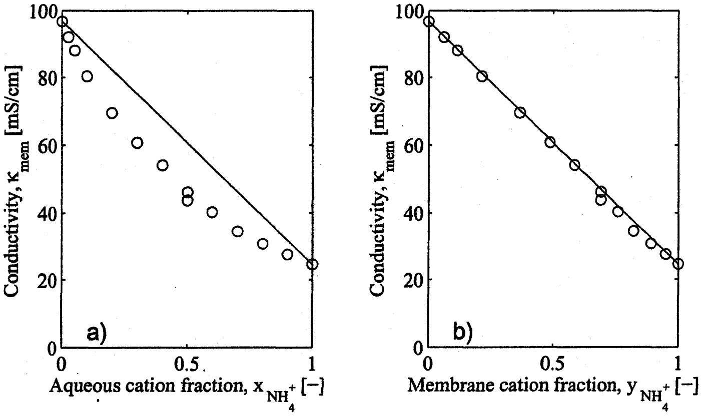

Figure 6: Conductivity at 25.0 ± 0.1 °C in Nafion® 117 plotted against a) ammonium content in the aqueous phase ($x_{NH_4^+}$), and b) ammonium content in the membrane phase ($y_{NH_4^+}$). The linear interpolation between the pure proton and the pure ammonium form Nafion® 117 conductivity is also shown in both plots.

The measured conductivity may be influenced by presence of chloride in the membrane phase. As discussed earlier, Jones *et al.* (12) report that the content of chloride in a 0.1 M NaCl solution in equilibrium with Nafion® 117 is about $\lambda_{Cl^-} = 0.05$. However, the mobility of the anions is probably low due to the structure of Nafion®, and there are indications that anions are transported in the hydrophobic regions of the membrane (21) which significantly reduces the mobility of the anions. However, the presence of chloride naturally also increases the amount of mobile cations in the membrane which increases the conductivity.

We used three different ensembles of membranes cut out of the same sheet of Nafion®. However, we measured differences in membrane conductivity between the different ensembles. The differences between the ensembles were within 2%. When the conductivity measurements at 25 °C and at different compositions were finished, the membranes were transferred back to their protonic form by ion exchange, and the conductivity measured again. It was noted that the conductivity in the pure protonic form had dropped by about 2% during the experiments. This was not recoverable even when the membranes were treated in hydrogen peroxide and dilute, hot sulfuric acid as described in the preparation procedures. We have not been able to identify the reason for this irreversible reduction of conductivity.

Comparison with available literature data. Using basically the same cell as in Figure 1, Ottøy (9) found the conductivity of proton form Nafion® 117 to be 93 mS/cm at 25 °C. Halim *et al.* (10) found the conductivity to be 90 mS/cm also using a membrane stack. Zawodzinski *et al.* (22), using in-plane conductivity measurements, found the conductivity to be 101 mS/cm. Datasheets from Du Pont (17) reports the conductivity to be 83 mS/cm. Okada *et al.* (13, 14, 20) reports the conductivity of proton form Nafion® 117 to be 160 to 200 mS/cm when measuring in a cell similar to the one described by Zawodzinski *et al.* (22). However, Okada *et al.* filled the voids of the cell with the equilibrating solution, hence, part of the current carried through the cell flowed through the aqueous electrolyte resulting in a higher observed conductivity. Logette *et al.* (18) found a conductivity of 62 mS/cm, but no detailed description of the conductivity cell employed was given in the paper.

Most data reported in literature are in good agreement with our findings (97 mS/cm). We see this both as a confirmation of the accuracy of the method and an indication that the conductivity in Nafion® is isotropic. In contrast, Gardner and Anantaraman (23, 24) found that the tangential component is three times larger than the normal component of the conductivity (85.6 vs 23.9 mS/cm). We have found no other literature data showing that the conductivity is anisotropic.

We found that ammonium reduces the conductivity by a factor of 3.8 (Table 1) to 3.9 (Figure 6) relative to pure H-form Nafion® 117 at 25.0 °C which is in good agreement with the findings of Uribe *et al.* (5) who found that the conductivity of Nafion® 1035 decreased from 133 to 32-33 mS/cm or by a factor of 4.0 to 4.2.

The ratio of conductivities, $\kappa^0_{HCl}/\kappa^0_{NH_4Cl}$, in 1.0 M aqueous electrolyte is about 3.10 (11). The higher relative conductivity in proton form Nafion® compared to an aqueous solution can possibly be explained by the fact that ammonium form Nafion® also contains less water thereby reducing the mobility of the ions within the membrane phase. It is well known that conductivity in Nafion® in equilibrium with water vapor depends strongly on water vapor activity and thus water content in the membrane (8, 16, 25). If we assume that the same correlation for conductivity as function of water content as used by Springer *et al.* (25) may be used in this case, we estimate that the conductivity ratio due to difference in water content should be 1.47. Multiplied with the relative conductivity ratio in 1.0 M aqueous solutions, a total conductivity ratio of 4.56 is estimated. This is slightly high suggesting that the effects of ionic form and water content on conductivity are not simply additive.

Temperature effect on conductivity. The conductivity of Nafion® 117 was also measured at various temperatures as summarized in Table 1. The same membranes were used as in previous measurements, and as noted above, the conductivities are slightly lower than the ones shown in Figure 6. From Table 1 we see that a linear relationship between membrane composition and conductivity still holds, and we are able to predict the conductivity at $x_{NH_4^+} = 0.5$ within 4%.

Table 1: Conductivity in Nafion® at different temperatures and ionic forms, equilibrium content of ammonium in membrane phase $y_{NH_4^+}$ at $x_{NH_4^+} = 0.5$, and estimated conductivity at κ_{mem}^{est} at $x_{NH_4^+} = 0.5$ assuming that a linear combination of conductivity in the two pure membrane forms is valid. Conductivities reported in this table are not corrected for R_{gap}, see Equations 1 and 2. Further, it is assumed that the dimensions of the membranes are the same at all temperatures as at 25 °C.

Temperature	κ_{mem} at			$y_{NH_4^+}$ at	κ_{mem}^{est}
	$x_{NH_4^+} = 0$	$x_{NH_4^+} = 0.5$	$x_{NH_4^+} = 1.0$	$x_{NH_4^+}$=0.5	$x_{NH_4^+} = 0.5$
[°C]	[mS/cm]	[mS/cm]	[mS/cm]	[-]	[mS/cm]
10	73	**35**	18	0.71	**34**
25	95	**47**	25	0.69	**47**
40	117	**61**	34	0.70	**59**
60	144	**79**	46	0.70	**76**

The temperature effect is also shown in Figure 7. The data for each composition of Nafion® 117 were fitted to an Arrhenius type equation:

$$\ln\left(\frac{\kappa_{mem}(T)}{\kappa_{mem}(T_0)}\right) = k_1\left(\frac{1}{T_0} - \frac{1}{T}\right) \tag{3}$$

The datum temperature, T_0, was taken to be 298.15 K. The parameter k_1, often denoted activation energy, $E_a = R \cdot k_1$, was found to vary with membrane composition as shown in the insert graph in Figure 7 and we used a linear relation to describe k_1, $k_1 = 1238 + 502 \cdot y_{NH_4^+}$[K] or $E_a = 10.3 + 4.2 \cdot y_{NH_4^+}$[kJ/mole]. The calculated temperature variation using this model is also shown in Figure 7. The deviation between experimentally measured conductivities and those calculated using the model given in Equation 3 is within ±5%.

The parameter k_1 for pure proton form Nafion® 117 based on regression results for proton form Nafion® only (*i. e.* not using the linear model for k_1) is 1256 K or an E_a equivalent to 10.4 kJ/mole, in even better agreement with the findings of Springer *et al.* (25) who found k_1 to be 1268 K. Halim *et al.* (10) found k_1 to be 1024 K. Sone *et al.* (8) found a more complex relation between temperature and conductivity when measuring on samples in the vapor phase. Below 45 °C they did not measure any temperature dependence, whereas above 45 °C they found the activation energy to be less than 2 kJ/mole equivalent to a k_1 of 240 K.

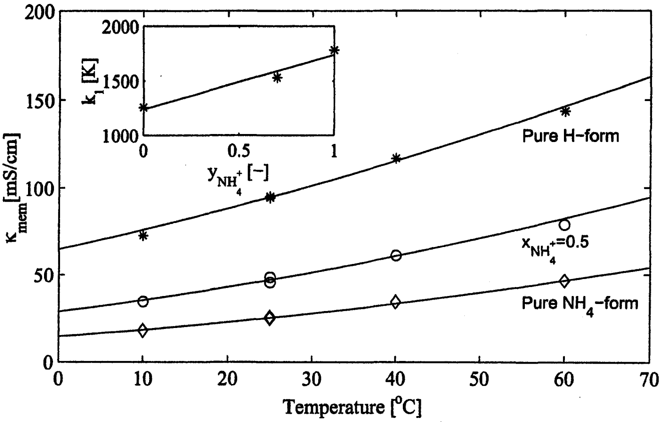

Figure 7: Conductivity of Nafion® 117 at different temperatures and membrane compositions. The parameter $k_1 = 1238 + 502 \cdot y_{NH_4^+}$[K] in Equation 3 is also shown as an insert as function of membrane composition.

CONCLUSIONS

The ion exchange equilibrium of ammonium between an aqueous phase and Nafion® 117 were measured at 10.0, 25.0, 40.0, and 60.0 °C. The water content in the membrane phase was found to decrease linearly with the cation fraction of ammonium in the membrane phase ($y_{NH_4^+}$) from $\lambda_{H_2O} = 21.2 \pm 0.4$ in proton form Nafion® in pure water to $\lambda_{H_2O} = 13.2$ in pure ammonium form Nafion® in a 0.1 M chloride solution. The conductivity was also found to decrease linearly with $y_{NH_4^+}$ from 97 mS/cm to 25 mS/cm at 25.0 °C. The relative conductivity ratio of proton form Nafion® compared to ammonium form Nafion® is higher than the relative conductivity ratio of pure aqueous 1.0 M HCl and 1.0 M NH_4Cl (a factor of 3.8 – 3.9 vs. 3.10). This difference may be explained by the additional effect of lower water content in the membrane phase when in the ammonium form resulting in a lower conductivity. The temperature dependence of the conductivity was measured, and the fitted activation energy was found to depend on membrane composition, $E_a = 10.3 + 4.2 \cdot y_{NH_4^+}$[kJ/mole].

ACKNOWLEDGEMENT

We gratefully acknowledge Norsk Hydro ASA and the Research Council of Norway for support of this work.

REFERENCES

1. Arthur D. Little Inc., Cost Analysis of Fuel Cell System for Transportation – Baseline System Cost Estimate `http://www.ott.doe.gov/pdfs/baseline_cost_model.pdf`, 2000.
2. R. Borup, M. Inbody, J. Tafoya, T. Semelsberger, and L. Perry, Durability Studies: Gasoline /Reformate Durability `http://www.eren.doe.gov/hydrogen/pdfs/nn0123ba.pdf`, 2002.
3. A. S. Chellappa, C. M. Fischer, and W. J. Thomson, *Appl. Catal. A-Gen.*, **227**, 231 (2002).
4. S. T. Szymanski, G. A. Gruver, M. Katz, and K. H. R., *J. Electrochem. Soc.*, **127**(7), 1440 (1980).
5. F. A. Uribe, T. A. Zawodzinski, Jr., and S. Gottesfeld, *J. Electrochem. Soc.*, **149**(3), A293 (2002).
6. E. Rasten *Electrocatalysis in Water Electrolysis with Solid Polymer Electrolyte* PhD thesis, Norwegian University of Science and Technology, (2001).
7. T. A. Zawodzinski, Jr., C. Derouin, S. Radzinski, R. J. Sherman, V. T. Smith, T. E. Springer, and S. Gottesfeld, *J. Electrochem. Soc.*, **140**(4), 1041 (1993).
8. Y. Sone, P. Ekdunge, and D. Simonsson, *J. Electrochem. Soc.*, **143**(4), 1254 (1996).
9. M. Ottøy *Mass and Heat Transfer in Ion-Exchange Membranes – Applicable to Solid Polymer Fuel Cells* PhD thesis, Norwegian University of Science and Technology, (1996).
10. J. Halim, F. N. Büchi, O. Haas, M. Stamm, and G. G. Scherer, *Electrochim. Acta*, **39**(8-9), 1303 (1994).
11. G. H. Aylward and T. J. V. Findlay, *SI Chemical Data*, John Wiley & Sons, 2 ed., 1974.
12. L. Jones, P. N. Pintauro, and H. Tang, *J. Membrane Sci.*, **162**(1-2), 135 (1999).
13. G. Xie and T. Okada, *Denki Kagaku*, **64**(6), 718 (1996).
14. T. Okada, Y. Ayato, M. Yuasa, and I. Sekine, *J. Phys. Chem. B*, **103**(17), 3315 (1999).
15. C. M. Gates and J. Newman, *AICHE J.*, **46**(10), 2076 (2000).
16. D. R. Morris and X. D. Sun, *J. Appl. Polym. Sci.*, **50**(8), 1445 (1993).
17. E. I. du Pont de Nemours and Company, Product information: Nafion® Membranes NE-112, NE-1135, N-115, N-117 `http://www.dupont.com/fuelcells/pdf/nae101.pdf`, 2000.
18. S. Logette, C. Eysseric, A. Pourcelly, and C. Gavach, *J. Membrane Sci.*, **144**(1-2), 259 (1998).
19. G. Pourcelly, P. Sistat, A. Chapotot, C. Gavach, and V. Nikonenko, *J. Membrane Sci.*, **110**(1), 69 (1996).
20. T. Okada, N. Nakamura, M. Yuasa, and I. Sekine, *J. Electrochem. Soc.*, **144**(8), 2744 (1997).
21. M. Rankothge, J. Hook, L. vanGorkom, and G. Moran, *Macromolecules*, **30**(15), 4357 (1997).
22. T. A. Zawodzinski, Jr., M. Neeman, L. O. Sillerud, and S. Gottesfeld, *J. Phys. Chem.*, **95**(15), 6040 (1991).
23. C. L. Gardner and A. V. Anantaraman, *J. Electroanal. Chem.*, **395**(1-2), 67 (1995).
24. C. L. Gardner and A. V. Anantaraman, *J. Electroanal. Chem.*, **449**(1-2), 209 (1998).
25. T. E. Springer, T. A. Zawodzinski, and S. Gottesfeld, *J. Electrochem. Soc.*, **138**(8), 2334 (1991).

Proceedings of The Electrochemical Society, PV 2002-31, 139-148 (2002)
DOI: 10.1149/200231.0139PV © The Electrochemical Society

THE EFFECT OF RELATIVELY HIGH AMMONIA CONCENTRATIONS IN REFORMATE ON PEMFC PERFORMANCE

Herie J. Soto, W-k. Lee and J. W. Van Zee
Fuel Cell Research Laboratory
Department of Chemical Engineering
University of South Carolina, Columbia, SC 29208

Mahesh Murthy
W. L. Gore & Associates, Inc.
201 Airport Road, Elkton, MD 21922-1488

ABSTRACT

Data are reported for Gore's advanced PRIMEA® Membrane Electrode Assembly (Series 5621) with reformate at 101 kPa and at 70°C. The steady state polarizations curves for different NH_3 concentrations (i.e., 80 and 200 ppm NH_3) in neat reformate (40% H_2, 17% CO_2, and 43% N_2) were measured and compared with a polarization curve for 500 ppm NH_3 in neat H_2. The polarization losses from neat hydrogen and neat reformate are discussed. The results show that cell performance was decreased when ammonia was introduced in the reformate (for example, the current density dropped from 825 to 200 mA/cm^2 at 0.6 V). A cyclic transient test for 80 ppm NH_3 was performed to determine rates of poisoning and recovery.

INTRODUCTION

As the PEMFC industry approaches commercialization, fuel cell stack and systems suppliers are performing field testing and are consequently being confronted with operating their systems in more demanding environments than those utilized in well controlled laboratory testing. Thus, it is imperative that studies be conducted relating to the effect of contaminants in the fuel on the fuel cell performance. In the use of PEMFC, reforming methanol, natural gas, gasoline, or other types of hydrocarbon fuels can produce a hydrogen rich gas[1] (30~40% H_2). This hydrogen rich gas may contain traces of impurities such as the well-known carbon monoxide, hydrogen sulfide and ammonia. These poisons or impurities affect the performance of PEMFC.

The literature contains a number of references reporting the effect of impurities on the performance of perfluorosulfonic acid membranes in chloralkali electrolyzers. Some work has been carried out on the effect of impurities such as ammonia. Uribe *et al.*[2] reported that traces of NH_3 in neat H_2 degrade the PEMFC performance. They showed that the performance could be fully recovered by neat H_2 after short times of NH_3 exposure (1 to 3 hours). However, the longer times NH_3 exposure decreased the cell performance to levels that can not be recovered even several days of neat H_2 operation.

Recently, we studied the response of Gore's advanced PRIMEA® Series 56 Membrane Electrode Assemblies (MEAs) exposed to levels up to 1,000 ppm NH_3 in neat hydrogen for a PEMFC[3]. These data provide a baseline to compare data obtained on simulated reformate mixtures of hydrogen, carbon dioxide, and nitrogen containing various levels of NH_3. In this study, we added ammonia in the neat reformate as an anode gaseous impurity. Though data on fuel cell performance utilizing hydrogen/NH_3 and reformate mixtures is separately available, a detailed analysis of the individual components in the reformate mixtures and their effect on cell performance is lacking. In an effort to begin this analysis, the study reported here will show the effects of NH_3 in reformate on the cell performance and compare these effects with hydrogen/NH_3 mixture data.

EXPERIMENTAL

The experiment focused on the performance of PEM fuel cells in the presence of NH_3 in reformate at the anode side. At the beginning, polarization performances were measured for neat hydrogen (100 % H_2) and a "standard" neat reformate (RMS) consisting of, 40 % H_2, 17 % CO_2, and 43 % N_2. After obtaining polarization curves with neat hydrogen and neat reformate, polarizations for reformate containing NH_3 were measured. In the experiments, two different levels of NH_3 in the reformate were examined to study the interaction of ammonia with diluted H_2. The concentration of NH_3 was 80 ppm in the reformate and 200 ppm in the neat H_2 fuel. Thus if we operate at the same dew point or partial pressure of water vapor, the ratio of ammonia to hydrogen will be constant. Polarization curves were obtained by randomly setting the cell voltage from 0.45 V to open circuit voltage and measuring the resulting steady state currents. The randomization gave reproducible results and accounted for any hysteresis in the reported current densities. While recording the polarization curve, the flow rates were adjusted to maintain the desired stoichiometry as discussed below. Also, cyclic voltammetry (CV) studies were performed for the different NH_3 concentrations. A scan rate of 5 mV/s was used and the voltage range between 50 mV and 800 mV was used. During these CVs, nitrogen gas was added at a flowrate of 200 cm^3/min on the anode, while in the cathode, hydrogen was used at a flowrate of 200 cm^3/min.

After establishing steady state behavior, the transient experiment was conducted for 80 ppm NH_3 at a fixed current density of 600 mA cm^{-2}. These transient conditions corresponded to repetitive introductions of NH_3 concentration (10 hrs) followed by periods with reformate (10 hrs) for 3 cycles. The objective of this experiment was to determine the relative rates of poisoning and recovery for NH_3 in reformate. The procedures used to obtain the rates of poisoning and recovery are discussed in detail by Murthy *et al.*[4]

The MEAs used in the experiment were PRIMEA® MEA Series 5621 (W.L Gore & Associates, Inc., Elkton, MD), consisting of GORE-SELECT® membranes (35 μm nominal membrane thickness) and catalyst loadings 0.45 mg/cm^2 Pt-Ru alloy on the anode and 0.6 mg/cm^2 Pt on the cathode. The active area of the membrane was 25 cm^2 and the triple-serpentine flow fields consisted of 30 equally spaced channels of height 0.1 cm and width 0.08 cm. The gas diffusion media (GDM) used in the experiment were CARBEL™ CL GDM (16 mils = 0.406×10^{-3} m) for both the anode and the cathode sides of the MEA. A compressible material (silicone coated fiberglass) with a measured thickness of 0.254×10^{-3} m (10 mils) was used as a gasket. Another thin gasket (1.2 mils = 0.305×10^{-5} m), referred to as the sub-gasket, was placed between the MEA and the gas diffusion media for maintaining the right compression inside the fuel cell and also ensures a robust alignment of the GDM on the active area during cell assembly. This sub-gasket reduced the active area from the nominal 25 cm^2 of flow field to 22 cm^2 of active MEA. Eight bolts were lubricated and threaded into tapped holes on one of the end plates, and the cell was compressed by applying a torque of 5.65 J/bolt (50 in-lb_f /bolt).

All experiments were performed using test stations with a reformate unit made by Scribner Associates. This reformate unit controls the mixture of the gases by adjusting mass flow controllers. These mass flow controllers were calibrated with a bubble flow meter. Ultra High Purity (UHP) hydrogen (99.999 %), premixed high purity NH_3/H_2, bottled air (industrial grade), high purity N_2 (99.998 %), and instrument grade carbon dioxide (99.99 %) were used. Note that this CO_2 contains traces of CO less than 5 ppm. The stoichiometry corresponded to flow rates that were 1.2 times greater than that required (by the measured current) for hydrogen (*i.e.*, 20 % excess hydrogen) and 2.0 times greater than that required for air (*i.e.*, 100 % excess air). In the experiment, dry NH_3 was added through mass flow controller at the anode inlet (i.e., NH_3 was injected between the humidity bottle and the fuel cell). The gas temperature and its humidity were controlled by sparging the gases through water in a humidity tank. The temperature of the cell was fixed at 70 °C for all of the experiments. Also, the pressures of the anode and the cathode sides were both 101 kPa (0 psig). The temperatures of humidification bottles were set at 85 °C for the anode and 75 °C for the cathode streams and these temperatures correspond to measured dew points of 80 °C and 70 °C for the anode and cathode respectively[5, 6]. Multiple MEAs were used for different levels of NH_3 in reformate. The MEAs typically were operated continuously for 250 to 350 hours, and therefore, the data reported here can be considered beginning-of-life data.

RESULTS AND DISCUSSION

Figure 1 shows the polarization curves for neat hydrogen and neat reformate. The cell performance was decreased when the neat reformate was introduced (i.e., the current density dropped from 1.05 to 0.825 A/cm^2 at 0.6 V). This performance difference between neat H_2 and neat reformate is associated with dilution of hydrogen in the anode stream as reported by Murthy *et.al.*[7]. It is noted that the composition of the neat reformate was 40 % H_2 and 17 % CO_2 balanced with N_2. The effects of NH_3 in the reformate are also shown in this figure for two levels of concentration: 80 ppm NH_3 and 200 ppm NH_3. The cell performance decreased as the NH_3 concentration in the reformate increased. Also shown in Fig.1, cell performance for 200 ppm and 500 ppm NH_3 in neat hydrogen was compared with the performance of 80 ppm and 200 ppm NH_3 in reformate. Note that the ratios of NH_3 to H_2 for the 200 ppm and 500 ppm NH_3/H_2 mixtures are the same as the 200 ppm NH_3 in reformate (i.e. the ratio of 500 ppm NH_3 with 100 % H_2 is same as the ratio of 200 ppm NH_3 with 40 % H_2). The result shows that the performances of 500 ppm NH_3 in neat H_2 and 200 ppm NH_3 in reformate are comparable and that at these high concentrations of ammonia, substantial poisoning of the surface controls the polarization. At lower concentrations, such as with the 80 ppm NH_3 in RMS, the concentration of ammonia appears not to be sufficient to cover all of the sites and the performance in reformate is better than with 200 ppm in H_2 at higher current densities. The difference in exposure time is not thought to be a reason for the better performance by 80 ppm in RMS at current densities greater than 0.4 A/cm^2 but additional experiments with the same exposure or dosage are being performed to verify this conclusion.

Figure 2 shows the anode overpotential for the various NH_3 concentrations in reformate and in neat H_2. The anode overpotential was obtained from the data shown in Fig. 1. These overpotentials are calculated from the difference between the cell potential with neat hydrogen and the cell potential with different NH_3 concentrations at the same current density. This calculation removes the cathode overpotential and the IR losses from the data if we assume that both of these losses are a function of current density only. Again the lower coverage at 80 ppm NH_3 in RMS is shown at current densities greater than 0.3 A/cm^2. Additional experiments at lower concentrations should be performed to determine if there is a lack of interaction between H_2 and NH_3 adsorption. This lack of competitive adsorption may simplify the understanding of the poisoning mechanism.

Figure 3 shows an example of the transient performance at a constant current density 600 mA/cm^2 for 200 ppm NH_3 in reformate. It shows how the cell voltage changes when 200 ppm NH_3 was added for 19.5 hours followed by a neat reformate for 20 hours. The cell voltage substantially decreased (from 0.64 V to 0.34 V) when the 200 ppm NH_3 was added at the anode side. The polarization curve was measured with 200 ppm NH_3 after introducing 200 ppm NH_3 for 9.0 hours (i.e., the V-I curve for 6.5 hours shown by the label on Fig. 3). After finishing the polarization measurement, the cell voltage was measured in the presence of 200 ppm NH_3 at 600 mA/cm^2 for four more hours. Then the neat reformate was introduced for 20 hours. The cell voltage was almost recovered by 20 hours of neat reformate. Thus the poisoning/recovery rates are slow but the decrease in the number of active sites appears to be reversible in neat reformate. Also, Figure 3 shows that the membrane resistance (obtained by a current interrupt technique) was increased when the cell voltage was decreased. However, this resistance (i.e., $5x10^{-3}$ Ω during NH_3 exposure) does not account for the 0.3 V of loss. This accounts only for 0.066 V loss. The fact that the resistance cannot account for all of the voltage loss may indicate the presence of adsorption on the catalysts as well as a reversible complexation reaction of the ammonia with the ionomer in the electrode. The current interrupt measurement typically does not include ionic resistance changes in the electrode. The gradual increase in resistance may be related to the part of the poisoning mechanism related to the complexation with the ionomer in the membrane. Clearly more studies are required for a better and more complete explanation. Figure 4 shows the polarization curve with 200 ppm NH_3 after 9 hours of exposure. The cell performance was completely recovered, compared to the baseline of neat reformate, by 20 hours of neat reformate after 19.5 hours exposure of 200 ppm NH_3.

Figure 5 shows the cyclic transient test with 80 ppm NH_3 in reformate. The cell performance decreased from 0.65 V to 0.45 V for the first cycle as the 80 ppm of NH_3 were introduced. After exposing the fuel cell to neat reformate for 10 hours the performance increased to 0.63 V. For the second and third cycle the recovery is almost constant, reaching a performance of 0.60 V. Poisoning rates were measured for each cycle and, these rates were 0.23 mV/min for the first cycle, 0.20 mV/min for the second cycle, and 0.24 mV/min for the third cycle. Recovery rates were also measured, these rates were 0.64 mV/min for the first cycle and 0.46 mV/min for the second cycle. Table

1 shows a comparison of these rates for 80 ppm NH_3 in reformate and 200 ppm NH_3 in H_2. The rates of poisoning decreased when the ammonia is in reformate but at the same time the recovery step is almost four times slower in reformate.

Figure 6 shows the CV performed after exposing the anode to 200 ppm NH_3 in reformate for 19.5 hrs. The resulting peak from 0.28 V to 0.5 V is a CO peak. This CO is resulting due to the reverse water gas shift reaction as discussed by de Bruijin *et al.*[8] That is, one would expect an equilibrium reaction to occur on the Pt sites of the anode:

$$CO_2 + H_2 = CO + H_2O \qquad [1]$$

Electrochemically the reactions are:

$$\text{anode: } CO + H_2O = CO_2 + 2H^+ + 2e^- \qquad [2]$$

$$\text{cathode: } 2H^+ + 2e^- = H_2 \qquad [3]$$

For reaction [1], $\Delta H^\circ_{343\ K} = 41.16$ KJ/mol, $\Delta S^\circ_{343\ K} = 42.03$ J/mol, and $\Delta G^\circ_{343\ K} = 26.7$ kJ/mol. The equilibrium potential of electrochemical reaction [2] is $E^\circ = -138$ mV vs. SHE. Using thermodynamic data for the involved species, the equilibrium concentration of CO was calculated. This was calculated for inlet and outlet conditions assuming saturation of water vapor at 343 K. For our case, these equilibrium concentrations were 19.2 ppm CO for inlet and 3.5 ppm CO for the outlet. To prove that the peak was CO, a voltammogram was measured after the anode was exposed to 500 ppm NH_3 in neat H_2 shown in Figure 7. No peak was observed, leading one to conclude that the peak in Fig. 6 is a CO oxidation peak. Another voltammogram was recorded after exposing the anode with reformate free of NH_3 for just five minutes and the same peak as in Fig. 6 was observed. This tells us that the CO in the anode is due to the reverse water gas shift reaction. Future work will study the interaction of CO and NH_3.

CONCLUSION

In our preliminary experiments, the polarization curves for various levels of NH_3 concentration in reformate and in hydrogen were measured. The results show that at high concentrations of NH_3 (i.e., 500 ppm NH_3 in H_2 and 200 ppm NH_3 in reformate), substantial poisoning of the surface controls the polarization and at lower concentrations (i.e., 80 ppm NH_3 in reformate) ammonia does not cover all the reaction sites. Note that the data reported here cannot differentiate between NH_3 adsorption on Pt or the ionomer. This difference should be determined in future experiments. Poisoning and recovery rates are much slower in reformate than in hydrogen but the decrease in the number of active sites appears to be reversible in reformate. It appears that NH_3 and CO is both at the surface and there are some interactions between them.

ACKNOWLEDGMENTS

The authors gratefully acknowledge that W.L. Gore & Associates, Inc., supported this work.

REFERENCES

1. S.G. Chalk, J.M. Miller, and F.W. Wagner, *J. Power Sources*, 86, 45 (2000).
2. F.A. Uribe, S. Gottesfed, T.A. Zawodzinski, *J.Electrochem. Soc*, 149 (3), A293-A296 (2002).
3. H.J. Soto, W-k. Lee, J.W. Van Zee, and M. Murthy, submitted *Electrochemical and Solid-State Letters*, August 2002.
4. M. Murthy, M. Esayian, A. Hobson, S. MacKenzie, W-k. Lee and J.W. Van Zee, *J. of the Electrochemical Society,* 148 (10), A1147 (2001).
5. W-k. Lee, Ph.D. dissertation, Department of Chemical Engineering, University of South Carolina, Columbia, SC, 29208 (2000).
6. W-k. Lee and J.W. Van Zee, S. Shimpalee, S. Dutta, ASME IMECE Conference Proceedings, HTD-Vol. 364-1, 359, Nashville, TN, Nov. 1999.
7. M. Murthy, W-k. Lee, and J.W. Van Zee, *AIChE Spring National Meeting*, Paper T9 #83i, New Orleans, LA, March 10 – 14, 2002.
8. A.F. de Bruijin, D.C. Papageorgopoulos, G.J.M. Janssen, *J. Power Sources,* 110, 117 (2002).

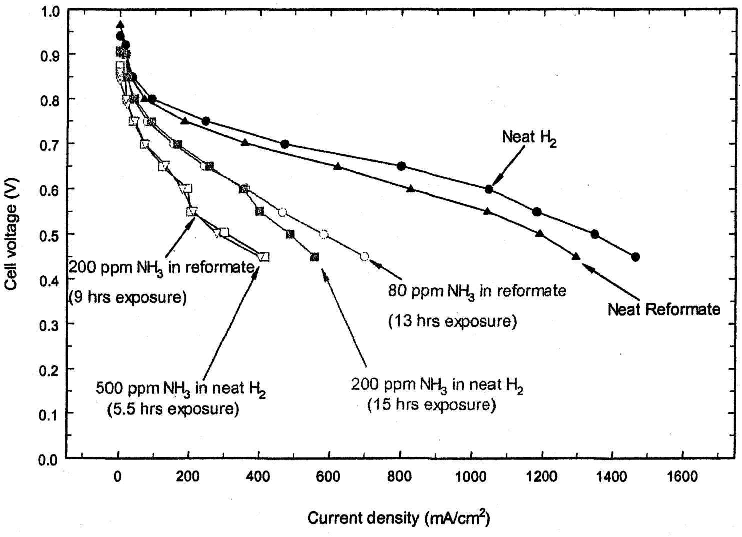

Figure 1. Performance comparisons for 80 and 200 ppm NH_3 in reformate; and 200 and 500 ppm NH_3 in H_2 (T_{cell} = 70 °C, T(A/C) = 85/75 °C, P(A/C)= 101/101 kPa).

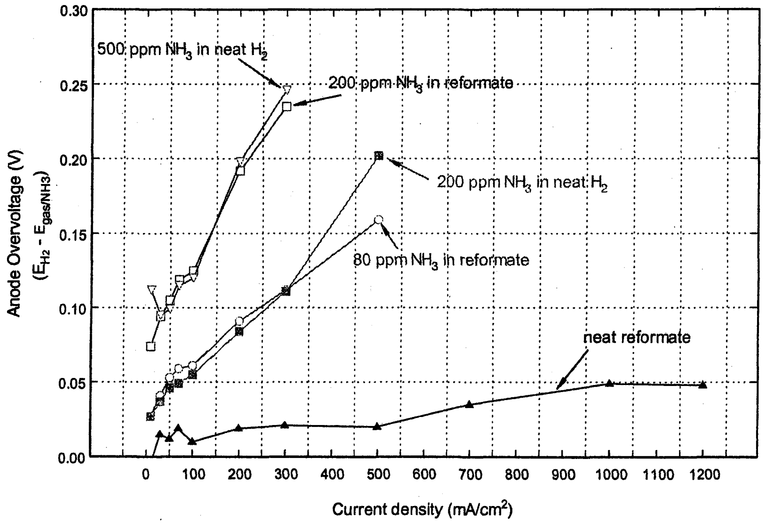

Figure 2. Comparison of anode overpotential for 80 and 200 ppm NH_3 in reformate; and 200 and 500 ppm NH_3 in H_2 (T_{cell} = 70 °C, T(A/C) = 85/75 °C, P(A/C)= 101/101 kPa).

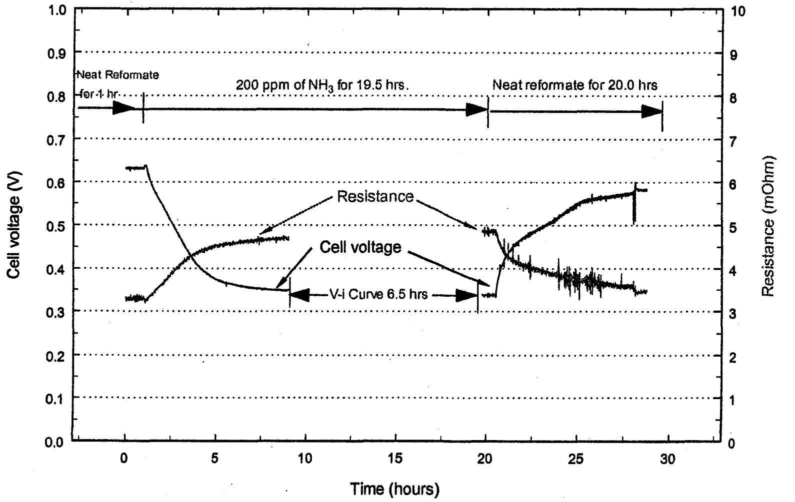

Figure 3. Transient performance for 200 ppm NH_3 in neat reformate at 600mA/cm^2 (T_{cell} = 70°C, T(A/C) = 85/75 °C, P(A/C)= 101/101 kPa).

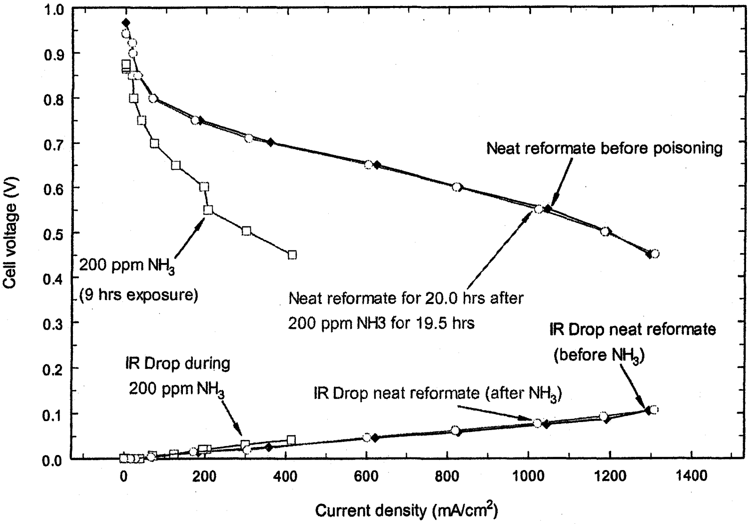

Figure 4. Effects on the cell performance with 200 ppm NH_3 in reformate (T_{cell} = 70°C, T(A/C) = 85/75 °C, P(A/C)= 101/101 kPa).

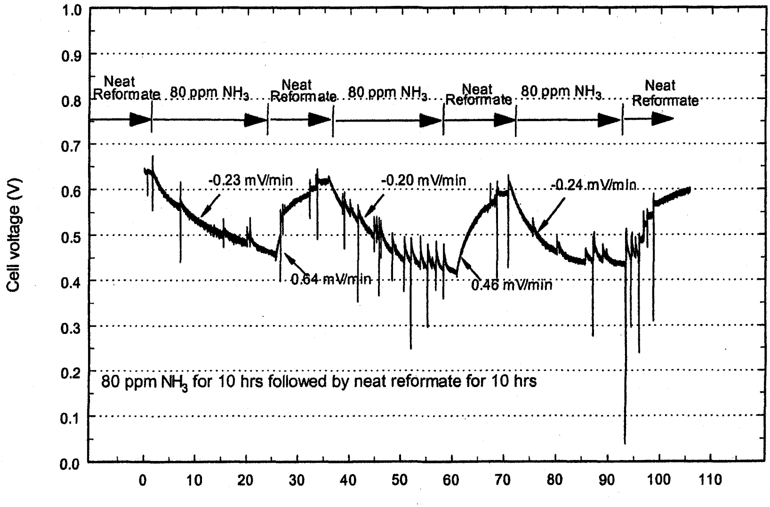

Figure 5. Cyclic transient performance of 80 ppm NH_3 in reformate at 600 mA/cm^2 (T_{cell} = 70 °C, T(A/C) = 85/75 °C, P(A/C)= 101/101 kPa).

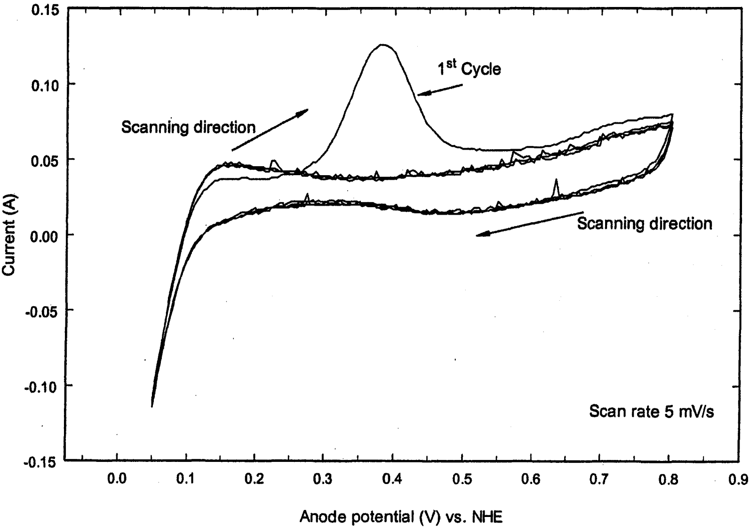

Figure 6. Cyclic voltammogram with 200 ppm NH_3 in reformate to show the CO oxidation (T_{cell} = 70 °C, T(A/C) = 85/75 °C, P(A/C)= 101/101 kPa).

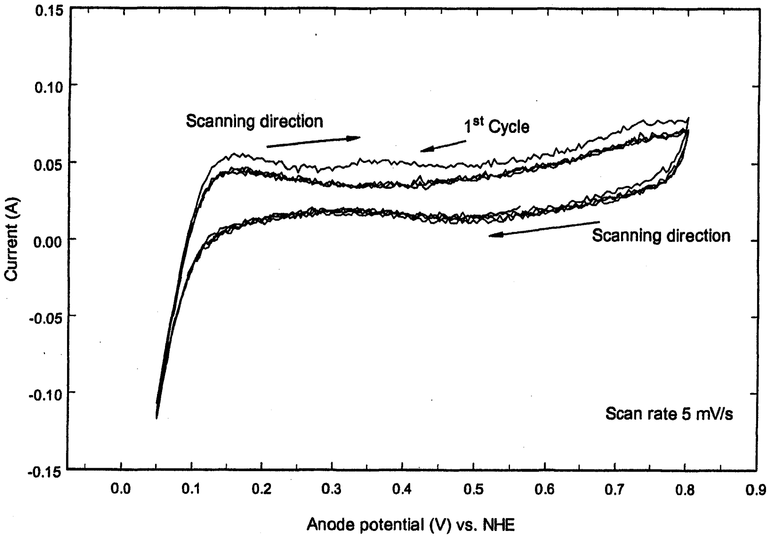

Figure 7. Cyclic voltammogram with 500 ppm NH_3 in neat H_2 (T_{cell} = 70°C, T(A/C) = 85/75 °C, P(A/C) = 101/101 kPa).

NH_3 concentration	Poisoning rate (mV/min)	Recovery rate (mV/min)
200 ppm NH_3 in H_2	-0.96*	2.12*
80 ppm NH_3 in reformate	-0.22	0.55

Table 1. Comparisons of the poisoning and recovery rates for NH_3 in neat H_2 and in reformate.

* Quoted from paper T9 #76d in *AIChE Spring National Meeting*, New Orleans, LA, March 10 – 14, 2002.

Proceedings of The Electrochemical Society, PV 2002-31, 149-158 (2002)
DOI: 10.1149/200231.0149PV © The Electrochemical Society

RATES OF ADSORPTION, DESORPTION, AND OXIDATION OF CO ON PEM ELECTRODES

Balasubramanian Lakshmanan, and John W. Weidner
Center for Electrochemical Engineering
Department of Chemical Engineering
University of South Carolina
Columbia, SC 29208

Abstract

The rates of CO adsorption, desorption, and oxidation on proton exchange membrane fuel cells (PEMFC) electrodes are determined. Desorption was controlled by the parallel desorption of CO from linear bridge bonded sites and rearrangement between them. The kinetic rate constant for rearrangement from linear to bridge bonding is 3 to 4 orders of magnitude higher than either of the two desorption rate constants. Adsorption was significantly influenced by convection of the gas along the flow channel and diffusion of CO into the catalyst layer. Oxidation of preadsorbed layer of CO followed a dual path mechanism as well. However, rearrangement between the two types of bonding was negligible since the time duration of CO oxidation was 2 to 3 orders of magnitude smaller than the desorption time. Hence oxidation rates were determined by the sum of two exponential terms corresponding to linear and bridge bonded CO molecules.

Introduction

Proton exchange membrane fuel cells (PEMFC) operating on pure hydrogen show very good polarization characteristics over a wide range of load and temperature conditions. However, the use of reformate gas (a mixture of nitrogen (40 –50%), hydrogen (35 – 45%), CO_2 (10 –20%), CO, water vapor and traces of other gases) causes a drop in Fuel Cell performance due to CO poisoning.

Study of CO poisoning of platinum and other alloy electrodes are usually carried out in aqueous electrolyte on a pre-adsorbed monolayer of CO.[1,2]. However, these techniques have their own limitations in estimating the rates of CO adsorption, desorption, and oxidation on composite electrodes. In this study, we conduct experiments on a conventional fuel cell membranes electrode assembly (MEA) to estimate the rates of CO adsorption, desorption and oxidation under different temperature conditions.

Experimental

Flow Cell

Catalyzed membranes were prepared using a procedure similar to the steps described in patent # 5211984 [1]. The active area of the electrodes was 50 cm^2, the anode side had a catalyst loading of 0.45 mg/cm^2 of 1:1 atomic ratio Pt-Ru catalyst or 0.5 mg/cm^2 of Pt, while the cathode was made of 0.5 mg/cm^2 of Pt. The membrane was catalyzed by hot pressing at 140 °C under 1000 psig pressure for 2 minutes against Teflon® decals sprayed with catalyst ink. The catalyzed membrane was then bonded to carbon cloth gas diffusion layers (GDL) at 140 °C under 500 psig pressure for 2 minutes to form a membrane electrode assembly (MEA). The MEA was assembled into a fuel cell with single channel serpentine flow field plates bought from Fuel Cell Technologies. The cathode side had H_2 flowing at 0.05 standard liters per minute (SLM). The cathode side was used as the counter and reference electrode (i.e., dynamic hydrogen electrode DHE) such that all the potentials reported here are referred to the H_2 cathode. The anode side had a flow of N_2, or CO/N_2 (476 ppm). All the gases were obtained from Air Products and the concentrations certified by the manufacturer. All the pure gases used were certified ultra high purity (UHP).

Cyclic voltammetry

For electrochemical characterization of the MEA, N_2 was first flowed at 0.10 SLM through the anode side, and the cell was left at open circuit. The N_2 flow was switched to a flow of 476 ppm CO in N_2 with a total flow rate of 0.10 SLM for a specified period of time (referred as exposure time) after which N_2 flow was restored. The cell was held at a constant potential of 50 mV for 15 seconds, which was followed by a cyclic voltammetry (CV) for three cycles, at a scan rate of 20 mV/s from 50 to 1150 mV and back to 50 mV. Experiments were conducted using a M263A potentiostat/galvanostat and ECHEM software made by EG&G. The area under the CO oxidation peak relative to the background current was used to calculate the amount of CO oxidized, which is reported as the amount of CO adsorbed. The experiment was repeated for various durations of CO/H_2 exposure. Between each experiment, the electrode was polarized at 0.9 V for 2 minutes to oxidize any remaining pre adsorbed CO on the catalyst layer.

Desorption

For determining the rate of desorption of CO from a Pt MEA, the electrode was saturated with CO by exposing it to 476 ppm CO for 300 s after which N_2 flow was restored. A cyclic voltammetry was conducted after a specified period of time (referred as desorption time) as per the procedure discussed above. The experiment was repeated for various durations of CO desorption at different temperatures.

Oxidation

For determining the rate of oxidation of CO on a Pt MEA, the electrode was saturated with CO by exposing it to 476 ppm CO for 300 s after which N_2 flow was restored. The electrode was polarized to a specific potential, (referred as oxidation potential) for a specific duration of time (referred as oxidation time), followed immediately by a cyclic voltammetry as per the procedure discussed above. The experiment was repeated for various durations of CO oxidation at different oxidation potentials and temperatures.

Model development

Reactions

Adsorption, desorption, and oxidation of CO occur through the following reactions

$$CO + Pt \underset{k_{-1}}{\overset{k_1}{\rightleftarrows}} Pt\text{-}CO \qquad [1]$$

$$k_2 \uparrow\downarrow k_{-2} \qquad [2]$$

$$2Pt + CO \underset{k_{-3}}{\overset{k_3}{\rightleftarrows}}$$

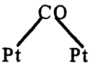

[3]

$$Pt\text{-}CO + H_2O \xrightarrow{k_4} CO_2 + 2\,H^+ + 2e^- + Pt \qquad [4]$$

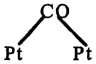

$$+ H_2O \xrightarrow{k_5} CO_2 + 2\,H^+ + 2e^- + 2Pt \qquad [5]$$

Reaction [1] corresponds to the adsorption of CO onto the Pt catalyst (i.e., CO poisoning) through linear bonding. Reaction [2] corresponds to rearrangement of rearrangement of CO between linear and bridge type bonding and reaction [3] corresponds to the CO adsorption through bridge bonding. Reactions [4] and [5] correspond to the electrochemical oxidation of linear and bridge bonded CO molecules, respectively.

Desorption

During desorption since the gas phase CO concentration is zero, the material balance for pre adsorbed CO layer during desorption time can be given as

$$\rho\frac{\partial\theta^l_{CO}}{\partial t} = -k_{-1}\theta^l_{CO} - k_2\theta^l_{CO}(1-\theta^l_{CO}-\theta^b_{CO}) + k_{-2}\theta^b_{CO} \qquad [6]$$

$$\rho\frac{\partial\theta^b_{CO}}{\partial t} = k_2\theta^l_{CO}(1-\theta^l_{CO}-\theta^b_{CO}) - k_{-2}\theta^b_{CO} - k_{-3}\theta^b_{CO} \qquad [7]$$

where ρ, is the molar density of catalyst sites in the electrode. Equation [6] and [7] represents the site balance for linear (θ^l_{CO}) and bridge (θ^b_{CO}) bonded platinum sites, respectively. Equations [6] and [7] were solved simultaneously with k_{-1}, k_2, k_{22}, and k_{-3} as parameters using the principles of parameter estimation described by Constantinides *et al*[4] along with confidence interval analysis. The total CO coverage is calculated by using equation [8]

$$\theta_{CO} = \theta^l_{CO} + \frac{\theta^b_{CO}}{2} \qquad [8]$$

Adsorption

Adsorption of CO in the platinum catalyst is limited by both diffusion of CO into the catalyst layer and convection along the flow channel. Figure 1, shows a schematic of the flow channel and the catalyst region. The material for CO in the flow channel is given by equation [9]

$$\frac{\partial C_{CO}}{\partial t} = -u\frac{\partial C_{CO}}{\partial z} - \frac{a}{area}\frac{N_x}{d} \qquad [9]$$

where C_{CO} and u refer to the concentration of CO and velocity of the gas in the flow channel, respectively, a refers to the equivalent area of the catalyst layer based on roughness and N_x is the flux of CO into the catalyst layer evaluated at the channel – catalyst layer interface.

The material balances for CO both in dissolved phase and adsorbed phase (catalyst sites) are given by equations [10] and [11]

$$\frac{\partial C_{CO}}{\partial t} = D_{CO}\frac{\partial^2 C_{CO}}{\partial x^2} - k_1 C_{CO}(1-\theta^l_{CO}) - k_{-1}\theta^l_{CO} + k_3 C_{CO}(1-\theta^b_{CO})^2 - k_{-3}\theta^b_{CO} \qquad [10]$$

$$\rho\frac{\partial \theta_{CO}}{\partial t} = k_1 C_{CO}(1-\theta^l_{CO}) - k_{-1}\theta^l_{CO} + k_3 C_{CO}(1-\theta^b_{CO})^2 - k_{-3}\theta^b_{CO} \qquad [11]$$

In equation [10], D_{CO} is the diffusion coefficient of CO in Nafion® ionomer in the catalyst layer. Equations [9], [10], and [11] were solved using Femlab in a pseudo 2-dimensional domain.

Oxidation

The material balances for linear and bridge bonded pt sites during electrochemical oxidation are given by equations [12] and [13], respectively. Once again the total coverage is calculated using equation [8].

$$\frac{\partial \theta^l_{CO}}{\partial t} = -k_4\theta^l_{CO} - k_2\theta^l_{CO}(1-\theta^l_{CO}-\theta^b_{CO}) + k_{-2}\theta^b_{CO} \qquad [12]$$

$$\frac{\partial \theta^b_{CO}}{\partial t} = k_5\theta^b_{CO} + k_2\theta^l_{CO}(1-\theta^l_{CO}-\theta^b_{CO}) - k_{-2}\theta^b_{CO} \qquad [13]$$

However, rearrangement between the two types of bonding was negligible since the time duration of CO oxidation was 2 to 3 orders of magnitude smaller than the desorption time. Hence oxidation rates were determined could be predicted by the sum of two exponential terms corresponding to linear and bridge bonded CO molecules

Results and Discussion

Figure 2 shows the data from the first cycle of CV's obtained from the CO adsorption experiments for different durations of CO bleed. The area under the CO peak is used to calculate the surface coverage of CO. CO oxidation shows two overlapping peaks. These peaks were deconvoluted using a bimodal Gaussian distribution and the areas under each peak were determined independently. For example, the CV after 300 s of CO exposure normalized for the back current is shown in Figure 3. The area under the first peak corresponds to 52 percent of the total area under the experimental curve. This fraction was assumed to be the initial fraction of bridge bonded CO sites after 300 s of CO exposure and used in the analysis of CO desorption and oxidation.

Figure 4 shows the cyclic voltammetry on a Pt electrode at 50 °C under 0.10 SLM flow of N_2 after different durations of CO desorption from a saturated electrode. The area under the curve gives the amount of CO remaining in the Pt electrode after desorption time. The surface coverage as a function of desorption time was used to determine the rate of CO desorption. CO desorption cannot be predicted by a simple exponential decay of surface coverage. Hence the mechanism involving parallel desorption from linear and bridge bonded sites along with rearrangement of both species is needed for better prediction.

Figure 5 shows the surface coverage as a function of desorption time the symbols and the dotted line correspond to the experimental data and model prediction, respectively. The initial coverage of bridge bonded sites was determined to be 57 % by deconvoluting the peaks from a cyclic voltammetry conducted after 300 seconds CO exposure. The surface coverage of linear and bridge bonded sites as a function of time predicted by the model is shown as an inset. The coverage of linear sites decreases throughout desorption time. However, the coverage of bridge bonded sites increases initially, attains a peak, and starts to decrease. The initial increase in surface coverage of bridge bonded sites is due to the rearrangement of linear bonded CO through reaction [2].

Figure 6 shows the surface coverage as a function of exposure time the symbols and the dotted line corresponds to the experimental data and model prediction, respectively. The pseudo two dimensional model was used to predict the experimental data. The model predictions show that the adsorption is significantly influenced by the convection along the flow channel and the diffusion of CO into the catalyst layer.

Figure 7 shows some of the cyclic voltammograms conducted on a Pt electrode after different durations of CO oxidation at 650mV under 0.10 SLM of N_2 at room temperature. Prior to oxidation the electrode was saturated with CO by 300 s exposure to 476 ppm CO in N_2. The symbols correspond to different duration of CO oxidation. The peak at the lower potentials (600 – 750 mV) CO and it oxidizes faster than the peak at higher potentials (750 – 850 mV) corresponding to bridge bonded and linear bonded CO sites, respectively. It should be noted that no CO was remaining on the electrode surface after 300 seconds of oxidation.

Figure 8 shows the surface coverage of CO as a function of oxidation time on a Pt electrode at room temperature. The symbols and the dotted line correspond to experimental data and model prediction, respectively. The experimental data is the area under the CV after different durations of CO oxidation shown in figure 7. The rate of CO oxidation was determined by the sum of two exponential corresponding to the linear and bridge bonded CO sites. The dependence of the oxidation rate constants is shown in figure 9. The experimental data is the summary of rate constants determined using the exponential fits at various potentials. At 25 °C the pre exponential for CO oxidation on bridge bonded sites is nearly 3 orders of magnitude higher than the linear bonded sites. However, the exponential factor for the oxidation of both bridge bonded and linear CO molecules are nearly equal at 0.025 decades/mV corresponding to a Tafel slope of 40 mV/decade.

Conclusions

Experiments were conducted to study the rate of CO adsorption, desorption, and oxidation in PEM electrodes. Mathematical models were developed to analyze the experimental results. Table I summaries the rate constants for various reactions.

Table 1: Summary of determined parameters

Kinetic Constant	Value (Units)	Kinetic Constant	Value
k_1	1300 /s	k_3	
k_{-1}	2.1×10^{-6} mol/s	k_{-3}	9.0×10^{-9} mol/s
k_2	2.0×10^{-3} mol/s	k_4 (V)	$6.8 \times 10^{-11} e^{(0.0287V)}$
k_{-2}	3.6×10^{-5} mol/s	k_5 (V)	$1.2 \times 10^{-8} e^{(0.0253V)}$

Desorption was controlled by the parallel desorption of CO from linear bridge bonded sites and rearrangement between them. The kinetic rate constant for rearrangement from linear to bridge bonding is 3 to 4 orders of magnitude higher than either of the two desorption rate constants. Adsorption was significantly influenced by convection of the gas along the flow channel and diffusion of CO into the catalyst layer. Oxidation of preadsorbed layer of CO followed a dual path mechanism as well. However, rearrangement between the two types of bonding was negligible since the time duration of CO oxidation was 2 to 3 orders of magnitude smaller than the desorption time. Hence oxidation rates were determined by the sum of two exponential terms corresponding to linear and bridge bonded CO molecules.

References

1. H A. Gasteiger, N. Markovic, P N. Ross, and E J. Cairns. J. Phys Chem, 98, 617, (1994)
2. R. J. Bellows and E. Marcuchi-Soos, in Proton Conducting Membrane Fuel Cells II, S. Gottesfield and T. F. Fuller, Editors, PV 98-27, p.218, The Electrochemical Society Proceedings Series, Pennington, NJ (1998).
3. M. S. Wilson. United States Patent #5211984. May 18, 1993
4. A. Constantinides, and N. Mostoufi, Numerical Methods for Chemical Engineers with MATLAB Applications, p.522, Prentice Hall PTR, New Jersey (1999).

Acknowledgement

The authors acknowledge the support from the National Reconnaissance Office for *Hybrid Advanced Power Sources* under grant # NRO-00-C-1034.

Figures

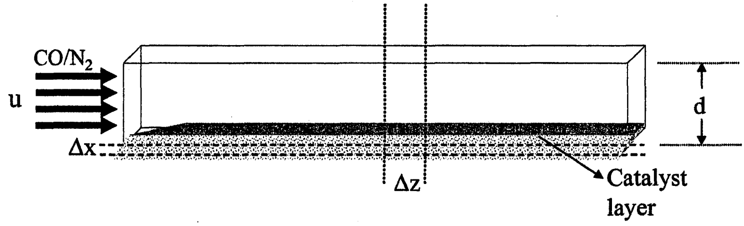

Figure 1: Schematic of the flow channel and the catalyst layer in a fuel cell. The channel and the catalyst layer are not drawn to scale.

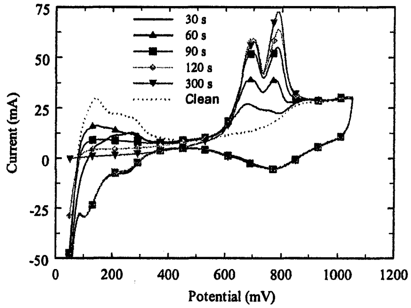

Figure 2: Cyclic voltammetry on a Pt composite electrode at room temperature under atmospheric N_2 flow after various exposure times to CO. The total flow rate was 0.1 SLM. The symbols correspond to time duration indicated by the legend.

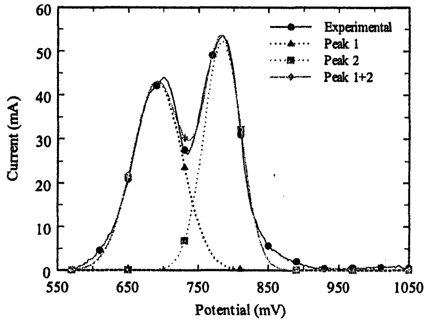

Figure 3: The CV on electrode conducted after an exposure time of 300 s normalized for the background current is shown (●). The deconvoluted peaks using a bimodal Gaussian distribution along with the sum of the two peaks are also shown. The symbols ▲, ■, and ♦ show peaks 1, 2 and sum of 1and 2, respectively. The experimental data is the CV after 300s exposure time shown in figure 2.

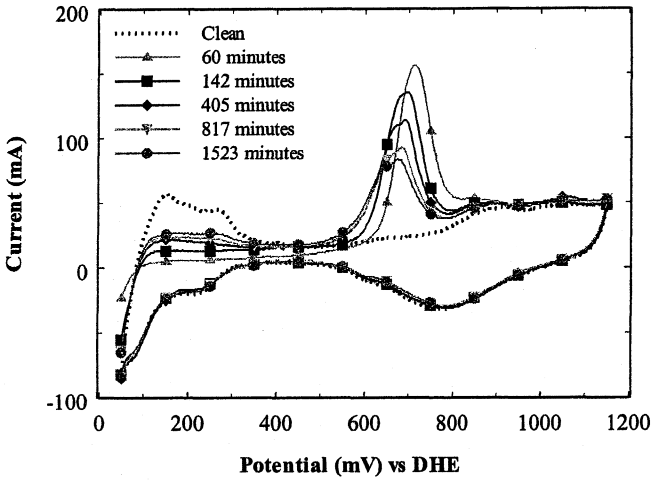

Figure 4: Cyclic voltammetry on a Pt composite electrode at 50 °C under atmospheric N_2 flow following saturated coverage. The total flow rate on the anode side was 0.1 SLM. The symbols correspond to different duration of CO desorption indicated by the legend.

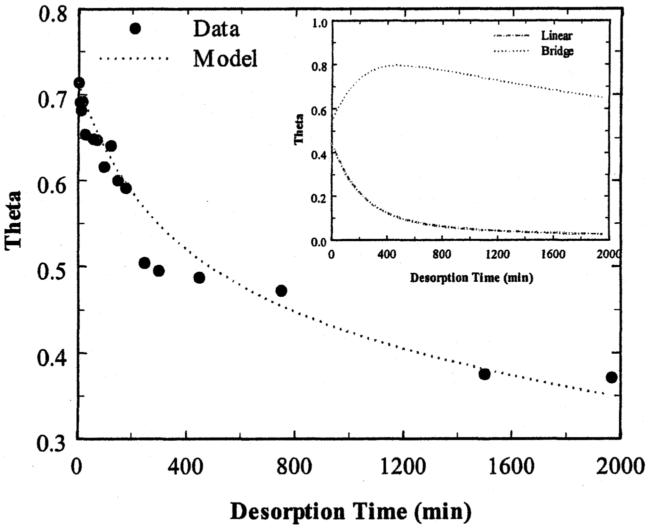

Figure 5: Surface coverage of CO as a function of time on a Pt electrode at 50 °C. The symbols and the dotted line correspond to experimental data and model prediction, respectively. The predicted surface coverage of bridge and linear bonded sites is shown on the inset.

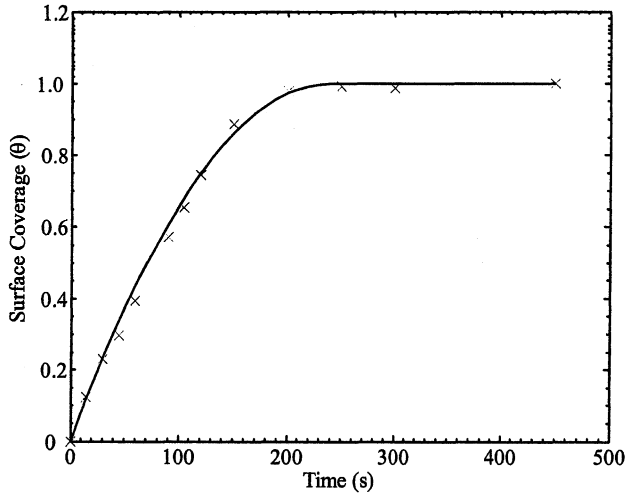

Figure 6: Surface coverage as a function of time during adsorption of CO. The symbols and the line correspond to the experimental data and model prediction, respectively. The experimental data is the summary of the results shown in figure 2.

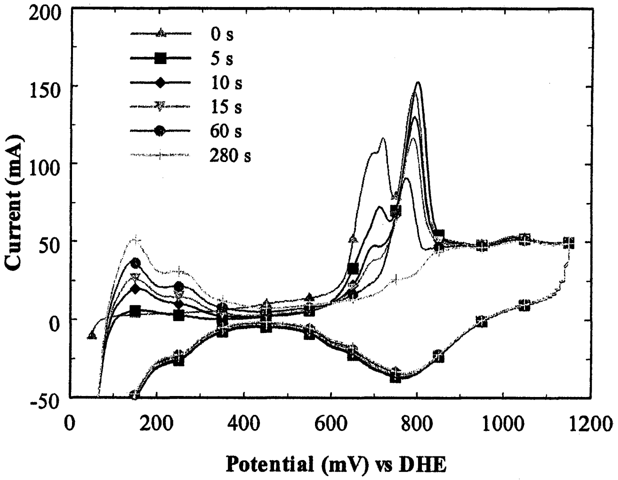

Figure 7: Cyclic voltammetry on a Pt composite electrode at room temperature under atmospheric N_2 flow after various duration of CO oxidation. The total flow rate was 0.1 SLM, Co exposure time was 300 s and a potential of 650 mV was used during the oxidation step. The symbols correspond to time duration indicated by the legend.

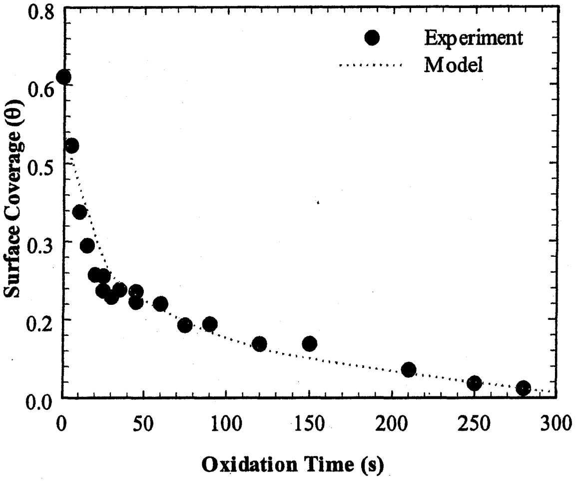

Figure 8: Surface coverage of CO as a function of oxidation time on a Pt electrode at room temperature after CO oxidation at 650 mV. The symbols and the dotted line correspond to experimental data and model prediction, respectively. The data is the summary of the area under the cyclic voltammograms shown in figure 7.

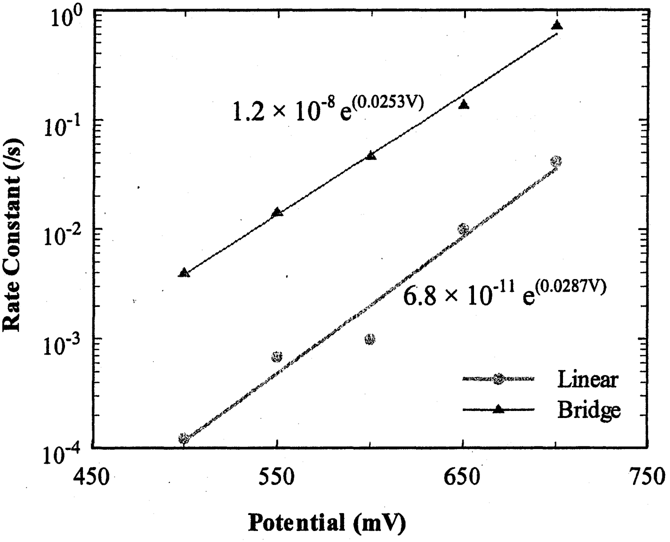

Figure 9: Rate constants as a function of the applied potential. The ▲ and ● symbols correspond to bridge and linear bonded CO sites. The experimental data is the summary of rate constants determined using the exponential fits at various potentials.

Proceedings of The Electrochemical Society, PV 2002-31, 159-173 (2002)
DOI: 10.1149/200231.0159PV © The Electrochemical Society

MAXIMIZATION OF CO TOLERANCE OF PEMFC SYSTEMS USING RECONFIGURED ANODES

Peter A. Adcock, Susan Pacheco, Eric Brosha, Thomas A. Zawodzinski[1], and Francisco A. Uribe

Electronic and Electrochemical Materials and Devices Group
MST-11, MS D429
Los Alamos National Laboratory
Los Alamos, NM 87545

ABSTRACT

The reconfigured anode (RCA) system is a small modification to the backing cloth placed on the anode side of each MEA in a PEM fuel cell stack. A catalyst layer is placed on the gas feed side of the cloth, to catalyze oxidation of CO utilizing the oxygen introduced in a small air-bleed. The purpose is to achieve a high CO-tolerance at a temperature below 100 °C. The development and status of this technology are described. Investigation of catalyst systems based on inexpensive transition metal oxides continues.

INTRODUCTION

Practical PEM fuel cells for automotive and large stationary applications are expected to operate on reformate, obtained by reforming gasoline, diesel, natural gas, or methanol fuels. A very troublesome impurity in reformate is residual carbon monoxide, CO, which poisons the platinum catalyst surface (1). CO is still at a significant level even if water-gas shift and preferential oxidation reactors are included. In the on-board reformate production option, complex processing to remove CO would have a high capital cost and weight penalty. It would be desirable to be able to eliminate one or both of the conventional preferential oxidation and water gas shift reactors. However, even 50-100 ppm CO is normally enough to shut down operation of a polymer electrolyte fuel cell. Hence, reasonable CO-tolerance requires special measures at the cell operational stage, such as an anode air-bleed. For instance, in previous work at Los Alamos National Laboratory, a minimal air-bleed was added to the fuel stream to catalyze chemical oxidation of CO. Originally, this reaction was catalyzed by the platinum anode catalyst itself (2).

---

[1] Present Address: Case Western Reserve University, 10900 Euclid Avenue, Cleveland, OH 44106

It was later found more effective for the anode gas to make contact with a CO oxidation catalyst before reaching the anode active layer (1). This led to the development, in our laboratory, of the reconfigured anode (RCA) system (1), to improve performance of low temperature (< 100 °C) Nafion®-based MEAs on reformate fuel. The reconfigured anode operates in conjuction with an air-bleed, added to the fuel stream. In essence, this method is designed to perform a preferential oxidation as the gas is distributed to the fuel cells. Depending on the catalyst, there may be a contribution from the water gas shift pathway, also.

The RCA system is shown schematically in Figure 1. A thin layer of a catalyst, based on an inexpensive transition metal oxide, is immobilized on the side of the gas distribution cloth adjacent to the flow field plate. Oxidation of CO by the oxygen from the air-bleed is catalyzed by the additional layer of chemical catalyst, before the anode gas reaches the electrochemically active layer.

Similar approaches have also been suggested by Ballard (3), and workers at ZSW Ulm (4), but their respective devices used precious metal catalysts or nickel foam structures. Gas filtration through hydrogen-selective membranes has been suggested, but requires much development to bring to practice. In other variants of CO oxidation, other workers have suggested the "ruthenium filter" (5), or the addition of pure oxygen (4,6) or hydrogen peroxide (7) instead of air. Alternative means suggested for achieving high CO tolerance are operation with pulsed current (8), the use of an alloy catalyst with very high intrinsic tolerance to CO (9), and the use of a high temperature membrane, such as acid doped polybenzimidazole (PBI) (10).

OVERVIEW OF EXPERIMENTS

General Experimental Details

All fuel cell tests were carried out at 80 °C, at an anode stoichiometry of 1.5, with anode and cathode backpressures of 30 psig. The anode and cathode feed gases respectively were humidified at 105 °C and 80 °C. MEAs were fabricated by the decal method of pressing thin electrocatalyst layers onto Nafion® 112. Synthetic reformate consisted of 40% H_2, 35% N_2 and 25% CO_2. RCA catalyst loadings (dry ink) were typically 1.0-1.5 mg cm^{-2}, but a higher loading of 3.5 mg cm^{-2} was used for cobalt-exchanged cryptomelane. Test conditions were always allowed to settle for at least 0.5 h before measuring a polarization curve over about 0.5-1 h.

Initial Experiments (5 cm^2 Cells)

A number of commercially available transition metal oxides, as well as tungsten carbide and the pure metals: Zr, Sn, Mo, W, and Cu, were combined with carbon black to produce inks for painting anode gas diffusion layers. Additional copper-based catalysts were also tested. For instance, CuO (ac) was prepared by thermal decomposition of the acetate salt onto carbon black. The ink preparation procedure was as follows: The active material (metal or oxide) was mixed with Carbon Black (Vulcan XC-72), a Teflon suspension, glycerol, and isopropanol. This mixture produced an ink that could be brush painted onto the carbon cloth.

The cloths with reconfigured anode layers were tested in 5 cm^2 single MEA fuel cells. The cells were operated for periods of about 1 hour on hydrogen (or synthetic reformate) mixes containing CO (typically 100 ppm) with and without air-bleeds of 2-6%, then allowed to recover on neat hydrogen. Cell polarization curves were obtained under each condition, after the cell had stabilized.

Experiments in 50 cm^2 Cells

It was desired to investigate more fully, oxides of Co and Fe supported on carbon black, prepared by thermal decomposition of the acetate salt of the respective metal. These are denoted CoO_x (ac) and FeO_x (ac). A cryptomelane, KMn_8O_{16}, (porous manganese dioxide with residual negative charge) "doped" by exchange with cobalt in place of some of the usual balancing K^+ ions, was also tested. This catalyst has been reported in the literature (11) as a stable catalyst, selective for CO oxidation in preference to hydrogen. These catalysts were tested with Nafion® – based MEAs with platinum/carbon anode and cathode. The iron oxide catalysts were also tested with "state of the art" alloy anodes (Pt-Ru at standard and reduced loadings) and cathodes (Pt_3Cr). Pt-Ru provides increased intrinsic tolerance to CO (5,8,9).

These RCA layers and MEAs were tested in single cell tests (50 cm^2 geometric active area) which were carried out on hydrogen and synthetic reformate with up to 500 ppm CO, using air-bleeds of 6% or less. The test cells were compared to cells otherwise identical but without the RCA modification of the anode gas distribution cloth. Sometimes these baseline tests were run simultaneously with a particular test cell.

One definition of full tolerance is: voltage losses no greater than 5% at any attainable cell current, in the presence of CO relative to its absence. For this definition to be applicable to the reconfigured anode, we should be investigating conditions for which the cell voltage drops significantly in response to CO, even with airbleed, in the absence of a reconfigured anode catalyst layer.

For the tests on 5 cm^2 cells, CO-tolerance was evaluated from the net effect of CO and air-bleed on the cell voltage at 0.6 A cm^{-2} for a cell operating on hydrogen fuel. For the tests on 50 cm^2 cells, CO-tolerance was evaluated from the net effect of CO and air-bleed on the cell voltage at 0.5 A cm^{-2}, for a cell operating on either hydrogen or simulated reformate fuel.

RESULTS

Performance on Hydrogen

Figure 2 compares results for the tests on 100 ppm CO in hydrogen performed in 5 cm^2 cells. At both 4% and 6% air, La_2O_3, Cr_2O_3 and WC had negative impacts. Zr and MnO_2 were positive at 6% but negative at 4%. Consistent, positive effects, but less than full tolerance were seen with Sn and Mo. Full tolerance with 6% air was obtained for W and for CoO_x. Full tolerance at both 4% and 6% air-bleed was observed for TbO_x, CuO, CuO (ac), Fe_2O_3, and CuO/ZnO.

Figure 3 shows the effect of various levels of air-bleed on a 50 cm^2 cell operated with CO in hydrogen, in the absence of an RCA layer, for a platinum catalyzed MEA. For 100 ppm CO, Figure 4 compares the performance of several different RCA layers using air-bleed. The CoO_x (ac) RCA catalyst showed marginally increased CO tolerance with 4% (or 6%) air-bleed. The FeO_x (ac) RCA catalyst showed complete tolerance at 2% (and 4%) air-bleed and appeared particularly promising in this test. Comparable results were obtained using an MEA with a low loading of Pt-Ru anode electrocatalyst.

A cell with the FeO_x (ac) RCA catalyst and Pt electrocatalyst layers (0.2 mg Pt cm^{-2}) was tested with hydrogen containing levels of up to 500 ppm CO. In short term tests, full tolerance was observed for the conditions 100 ppm CO + 2% air-bleed, 200 ppm CO + 4-6% air-bleed, 300 ppm CO + 4-6% air-bleed, and 500 ppm + 6% air-bleed (Figure 5). This is a preliminary demonstration of full tolerance to 500 ppm CO in hydrogen.

With a Pt-Ru anode (0.2 mg Pt cm^{-2}) and a Pt_3Cr cathode, in a cell with the FeO_x (ac) RCA catalyst, the anode was much less susceptible to poisoning by a given CO concentration, as is already known from the literature (9). In the present experiments, full tolerance to 100 ppm CO in hydrogen could be achieved with a 1% air-bleed and no RCA catalyst. Therefore, under these conditions, it was not possible to determine whether there is an improvement by adding RCA catalyst with air-bleed.

Recently, additional tests have been carried out in cells with a Pt-Ru anode at a reduced loading (0.1 mg Pt/cm^2) and a Pt_3Cr cathode. In hydrogen containing 500 ppm CO, the combination of 6% air-bleed with FeO_x (ac) RCA catalyst gave full tolerance. Under these conditions, full tolerance was not achieved in the absence of an RCA catalyst layer.

Performance with Synthetic Reformate

Some experiments were carried out on the 5 cm^2 cells. Results are presented in Figure 6. From this, it was concluded that the Fe_2O_3 catalyst allowed full tolerance to 100 ppm CO in reformate, using 4-6% airbleed. An air-bleed of only 2% gave poor results.

Figure 7 shows data for a stream containing 100 ppm CO through a 50 cm^2 cell with a platinum catalyzed MEA and no catalyst on the backing layer. Figure 8 shows the effects of a combination of 100 ppm CO and various levels of air-bleed on similar cells incorporating each of several catalysts in the backing layer. Similar trends are seen, to those in Figure 4.

In Figure 7, curve D shows data for no catalyst on the backing layer, with a higher CO level (250 ppm). Figure 9 shows the net effect of this level of CO and air-bleed for each catalyst. For MEAs with a Pt-Ru electrocatalyst at low loading, FeO_x (ac) and CoO_x (ac) had similar activity. The results for platinum-catalyzed MEAs are somewhat different from those in Figure 4 for hydrogen, in the presence of the FeO_x (ac) or CoO_x (ac) RCA catalysts. They indicate that CoO_x (ac) becomes the better RCA catalyst on reformate. Even 250 ppm CO was tolerated fully, with a 6% air-bleed in two cases with Pt electrocatalytic layers: using CoO_x, and using cobalt-exchanged cryptomelane mixed with a carbon ink. However, this data is of a preliminary nature, since few experiments were completed in this region of operation. For the latter catalyst, which contained K^+, there appears to be an ageing effect. The initial, good results, shown in Figure 9, could not be repeated with the same batch of catalyst.

For a Pt-Ru anode (0.2 mg Pt cm^{-2}), 100 ppm CO was tolerated fully, with a 4% air-bleed and no RCA layer. Even 250 or 500 ppm CO was tolerated fully with a 6% air-bleed and no RCA layer. Under these conditions, marginal benefits were obtained at high air-bleeds with an RCA layer. Additional tests have been carried out in cells with a Pt-Ru anode at a reduced loading (0.1 mg Pt cm^{-2}) and a Pt_3Cr cathode (0.4 mg Pt cm^{-2}). In reformate containing 250 ppm CO, 6% air-bleed gave full tolerance with either FeO_x (ac) or CoO_x (ac) RCA catalyst.

The contrast between Pt-Ru anodes (0.1 mg Pt cm^{-2}) and Pt anodes (0.2 mg cm^{-2}) is illustrated in Figure 10. Even for the former type of anode, full tolerance has not been achieved at 500 ppm CO. The best result to date is that of curve E in Figure 10. With no RCA catalyst, full tolerance was only achieved at the 100 ppm CO level, using 6% air-bleed.

Stability of RCA Chemical Catalysts

Various catalysts have been characterized by TGA, XRD, XRF, and EDAX. Detailed results are to be presented elsewhere (12). In brief, the CoO_x (ac) RCA catalyst consists of mainly Co_2O_3. The FeO_x (ac) RCA catalyst contains both Fe_3O_4 and Fe_2O_3. The cryptomelane crystal structure was verified by XRD. Exchanging cobalt produced slight line broadening, which may be due to reduced grain size or increased lattice strain.

Preliminary endurance experiments (3 days) were run at 0.60 V on combinations of hydrogen, CO and air-bleed, which had displayed complete tolerance over about 1 hour. Two cells with the FeO_x (ac) RCA catalyst were operated under these conditions. One had Pt electrocatalytic layers (both 0.2 mg Pt /cm^2) and the other had Pt-alloy electrocatalytic layers (Pt-Ru at 0.2 mg Pt /cm^2 for the anode and Pt_3Cr at 0.4 mg Pt /cm^2 for the cathode). A slow decay in performance was seen, with an average of 25% loss after 3 days with 100 ppm CO + 4% airbleed. The cell with alloy electrocatalytic layers was slightly less affected than the Pt-catalyzed cell.

Additional, ex-situ work is being carried out using a facility for measuring catalyst activity and/or catalyst mass changes, while monitoring gas streams by gas chromatography (GC). The purpose is to test catalyst activity by purely chemical mechanisms at temperatures around 80 °C, where Nafion®-based MEAs operate. These methods will also be used to evaluate potential new catalyst formulations.

DISCUSSION

From the trends in Figure 2, we suggest that the metals (or most probably their oxides) that promote the oxidation of CO more effectively are those with two stable, low oxidation states (+4 or lower). Examples of these are: Cu, Fe, Co, and Sn. This hypothesis is consistent with the poor performance of Zr and La_2O_3; Zr and La have only one stable oxidation state (+4 and +3 respectively). Cr and Mn on the other hand, may be found in much higher oxidation states (+6 and +7 respectively) as chromates and permanganates. Borderline are Mo and W, which show moderate performance and have stable oxidation states from +2 to +6. Sn (+2 and +4) was not as effective as the metals with two lower oxidation states (+3 or lower). Indeed other non-precious metals, with two stable, low oxidation states, such as Eu, Ti, Tl, Ni, or Pb, could be tested for CO tolerance.

The answers to the questions, which anode is best and which re-configured anode layer is best, could depend strongly on the fuel stream, the CO level, and the amount of air-bleed allowable. (a) For hydrogen and a low air-bleed (2%), FeO_x (ac) gave the best RCA performance, and for 100 ppm CO, the Pt anode was actually superior to Pt-Ru. (b) If an air-bleed is to be used, a suitable RCA layer will be about as effective as using a Pt-Ru (0.2 mg Pt cm^{-2}) catalyst in the anode layer of the MEA. It will also be much cheaper. (c) For reformate using a 6% air-bleed, there appear to be several RCA catalyst options for 100 or even 250 ppm CO. In this case the use of Pt-Ru (0.2 mg Pt cm^{-2}) is in competition with adding an RCA layer to a cell with a Pt electrocatalyst. So far, the very best result obtained for the latter situation was with the partially cobalt-exchanged cryptomelane. However CoO_x (ac) also gave acceptable results, more repeatably. Above 100 ppm CO in reformate, results with the iron oxide catalyst were poor, except when a Pt-Ru electrocatalyst was used. (d) At 500 ppm CO in reformate, Pt-Ru anodes (0.2 mg Pt cm^{-2}) continued to give good results with 6% air-bleed, even without an RCA layer. In contrast, this fuel feed rapidly disabled cells with Pt anodes, even at 6% air-bleed. In this regard, the combination of high CO and reformate seems to be more detrimental than CO and hydrogen.

We aimed to find conditions under which 500 ppm CO in reformate could be tolerated. Tests have confirmed that a 4-6% air-bleed without RCA layer allows operation of Pt-Ru anodes under these conditions, at least on the timescale of an hour. Further tests in progress, using anodes with reduced loadings of Pt-Ru, are designed to get a better ranking of the promise of various RCA catalysts for cells with Pt anode electrocatalysts. It is hoped that the best catalyst we can develop for these conditions will eventually achieve full tolerance to 500 ppm CO in reformate when a Pt anode is used.

Using a reconfigured anode and a Pt electrocatalyst, at least 250 ppm CO in reformate can be tolerated for a timescale of 1-2 hours under steady state conditions. Therefore, this system can certainly deal with transient CO levels of this order during continuous operation at generally lower CO. This makes it attractive for applications on reformate fuel with some other CO clean-up process which may not operate at its rated CO output all of the time, epecially during start-up or changes in load. Such a cell system will be cheaper than cells with high levels of platinum and another precious metal as the electrocatalyst.

For future commercial exploitation in fuel cell stacks, the advantages of the reconfigured anode technique for maximization of CO tolerance include the following. It works with the proven MEA material Nafion® at temperatures as low as 80 °C. It avoids or minimizes the use of relatively expensive catalyst materials such as ruthenium, which have been suggested for other CO removal systems, and as a major component of the anode catalyst. Finally, it does not significantly increase the dimensions or mass of a fuel cell stack, but may help to minimize bulky purification stages following reforming.

There is a definite concern about the long-term stability of iron oxides and cryptomelanes under fuel cell conditions. The studies to date, prove the principle of the reconfigured anode. However, further study is required to find catalysts, which will maximize lifetime as well as initial performance. Although FeO_x (ac) has shown the best performance on hydrogen, when synthetic reformate is fed to the cell, CoO_x (ac) appears superior over the full range of anode electrocatalysts and CO levels.

A possible explanation for the marked interactions with an air-bleed, on changing the anode from Pt to Pt-Ru (0.2 mg Pt cm^{-2}), may lie in the fact that Pt-Ru favors the surface water gas shift reaction over its reverse (6). Further evidence for suppression of the reverse water gas shift is found in the literature (13, 14). In reformate, the combination of high initial CO_2 and H_2 (or surface adsorbed H) concentrations could ensure that no net CO_2 would be formed from CO by the water gas shift reaction reaction. In this feed stream, the reaction with oxygen would be the dominant pathway for CO removal. This would hold for either a Pt-Ru or a Pt electrocatalyst. In hydrogen, the water gas shift reaction on Pt-Ru could provide a faster pathway for CO conversion to CO_2, in the absence of CO_2 initially. However, in this case, oxygen additions and reaction over the RCA catalyst may produce enough CO_2 to suppress the water gas shift reaction on the Pt-Ru, leading to an apparent, negative overall effect of air-bleed. These effects would not occur for a Pt electrocatalyst.

The reasons for the improvement in behavior of the CoO_x (ac) RCA catalyst, on going from hydrogen to reformate, and the degradation of the performance of FeO_x (ac), with a Pt anode, are not clear. Again, interactions between the water gas shift reaction and the chemical oxidation reaction may be involved. It is also possible that, with CoO_x (ac), peroxo intermediates may interfere with oxygen utilization in hydrogen, but be decomposed back to oxygen by the high CO_2 level in reformate. Alternatively, catalytic activity may be a function of potential, altered by the RCA layer being in contact with the anode via the electronically conducting carbon cloth. These phenomena will be probed to the extent possible, by ex-situ and in-situ tests with GC analysis.

Future work on the reconfigured anode scheme will concentrate on catalyst optimization, endurance experiments with reformate containing 500 ppm CO, investigation of dispersion of catalysts on mesoporous support materials, and stack studies.

CONCLUSIONS

The reconfigured anode system is a means of increasing the CO tolerance of platinum catalyzed Nafion® MEAs to a level similar to that achieved with alloyed electrocatalysts, e.g. Pt-Ru, at 80 °C. This system can deal with transient CO levels of at least 250 ppm during continuous operation at generally lower CO. Such a cell system will be cheaper than cells containing high levels of platinum and another precious metal as the electrocatalyst. Unlike some other systems, it will not add significant volume or mass to a PEM fuel cell stack.

The use of reconfigured anodes could be attractive for applications on reformate fuel with some other CO clean-up process which may not operate at its rated CO output all of the time, epecially during start-up or changes in load.

A further application may be to allow operation on a relatively high CO containing reformate stream, by combining the RCA layer with an anode of high intrinsic tolerance to CO (such as Pt-Ru at 0.1 mg Pt cm^{-2}) and/or a high temperature membrane, since the tolerance of Pt to CO increases markedly with temperature.

ACKNOWLEDGEMENTS

We gratefully acknowledge funding from the US DOE Office of Hydrogen, Fuel Cells, and Infrastructure Technologies. We also thank Fernando Garzon for discussions, advice, and assistance with catalyst characterization, and Tommy Rockward and Judith Valerio for assistance in the the fuel cell laboratory.

REFERENCES

1. F.A. Uribe and T.A. Zawodzinski, Abstract 806, The Electrochemical Society Meeting Abstracts, Vol. 2002-1, Philadelphia, PA (May 2002).
2. S. Gottesfeld and J. Pafford, *J. Electrochem. Soc.*, **135**, 2651 (1988).
3. D.P. Wilkinson, H.H. Voss, J. Dudley, G.J. Lamont and V. Basura, US 5 482 680, (Jan. 9, 1996).
4. B. Rohland and V. Plzak, *J. Power Sources*, **84**, 183 (1999).
5. A.T. Haug, R.E. White, J.W. Weidner and W. Huang, Abstract 336, The Electrochemical Society Meeting Abstracts, Vol. 2001-2, San Francisco CA (September 2001).

6. M.S. Wilson, T.E. Springer, T.A. Zawodzinski and S. Gottesfeld, *Proc. 28th Intersociety Energy Conversion Engineering Conf.*, American Chemical Society (Washington DC) Vol. 1, Atlanta GA (1993), p. 1203.

7. D.P. J. Barz, A. Frey and V.M. Schmidt, Abstract 338, The Electrochemical Society Meeting Abstracts, Vol. 2001-2, San Francisco CA (September 2001).

8. L.P.L. Carrette, K.A. Friedrich, M.Huber and U. Stimming, *Phys. Chem. Chem. Phys.*, **3**, 320 (2001).

9. H. Massong, H. Wang, G. Samjeské, and H. Baltruschat, *Electrochim. Acta*, **46**, 701 (2000).

10. Y. Ma, A. Schechter, J.S. Wainwright and R.F. Savinell, Abstract 55, The Electrochemical Society Meeting Abstracts, Vol. 2001-2, San Francisco CA (September 2001).

11. G.G. Xia, Y.G. Yin, W.S. Willis, J.Y. Wang and S.L. Suib, *J. Catal.*, **185**, 91 (1999).

12. P.A. Adcock, E. Brosha, F. Garzon and F.A. Uribe, Paper FF1.4 for presentation at the Materials Research Society Meeting, Boston, MA (December 2002).

13. F.A. de Bruijn, D.C. Papageorgopoulos, E.F. Sitters and G.J.M. Janssen, *J. Power Sources*, **110**, 117 (2002).

14. S. Gottesfeld and T.A. Zawodzinski, in *Advances in Electrochemical Science and Engineering*, Vol. 5, R.C. Alkire and D.M. Kolb, Editors, Wiley VCH, Weinheim, Germany (1997), p. 195.

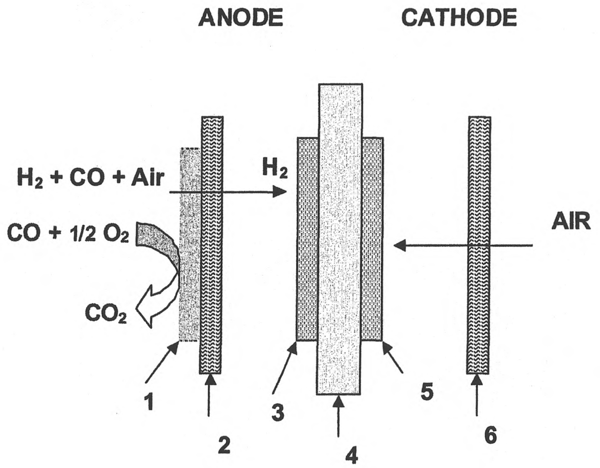

Figure 1. RCA schematics and functionality. 1) Non-precious-metal-based chemical catalyst layer; 2) anode gas distribution carbon cloth; 3) Pt-based anode electrocatalyst layer; 4) ionomer membrane; 5) Pt-based cathode electrocatalyst layer; 6) cathode gas distribution carbon cloth.

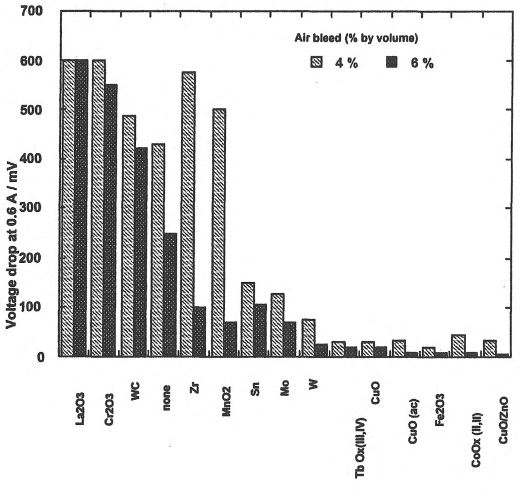

Figure 2. Comparison of substances tested as RCA catalysts with base performance without RCA layer. Voltage loss for 100 ppm CO + air-bleed measured at 0.6 A cm^{-2} and referred to neat hydrogen (5 cm^2 cell with 0.2 mg Pt cm^{-2} anode and cathode electrocatalyst layers).

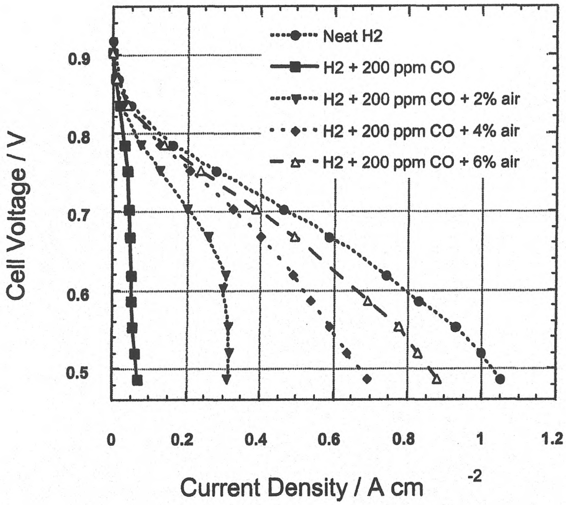

Figure 3. Performance of cell with no RCA layer on hydrogen, in response to air-bleed. (50 cm^2 cell with 0.2 mg Pt cm^{-2} anode and cathode electrocatalyst layers).

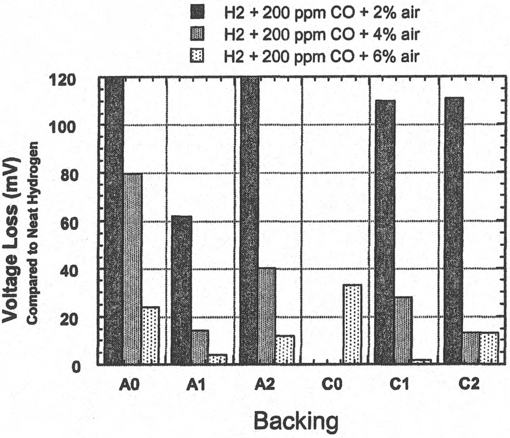

Figure 4. Comparison of three RCA catalysts with base performance as shown in Figure 3. Voltage loss measured at 0.5 A cm^{-2} and referred to neat hydrogen. A0 = no RCA layer; A1 = FeO_x (ac); A2 = CoO_x (ac); A3 = Co-exchanged KMn_8O_{16}. A Series = Pt anode electrocatalyst (0.2 mg cm^{-2}); C Series = Pt-Ru at 0.1 mg Pt cm^{-2}.

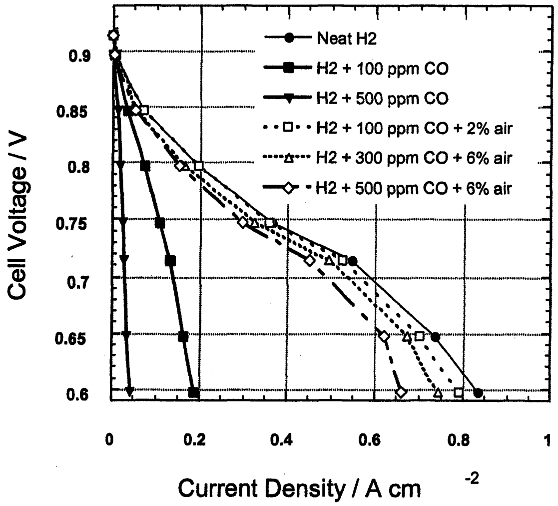

Figure 5. Effect of air-bleed with up to 500 ppm CO in a hydrogen feed on the performance of FeO_x (ac) catalyst (A1) in RCA layer in cell with 0.2 mg Pt cm^{-2} anode and cathode electrocatalyst layers.

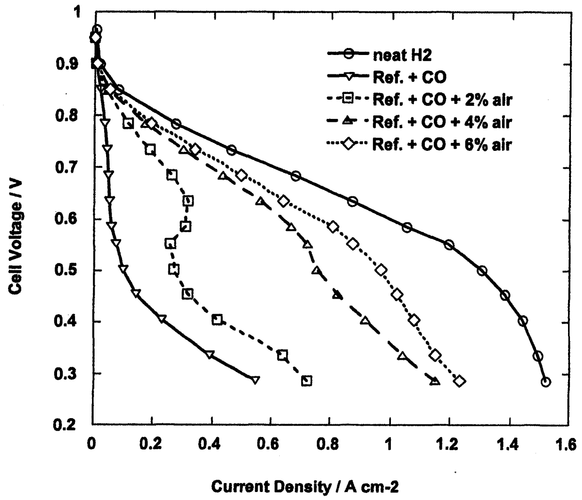

Figure 6. Performance of Fe_2O_3 catalyst with synthetic reformate containing 100 ppm CO, and various levels of air-bleed (5 cm^2 cell with 0.2 mg Pt cm^{-2} anode and cathode electrocatalyst layers).

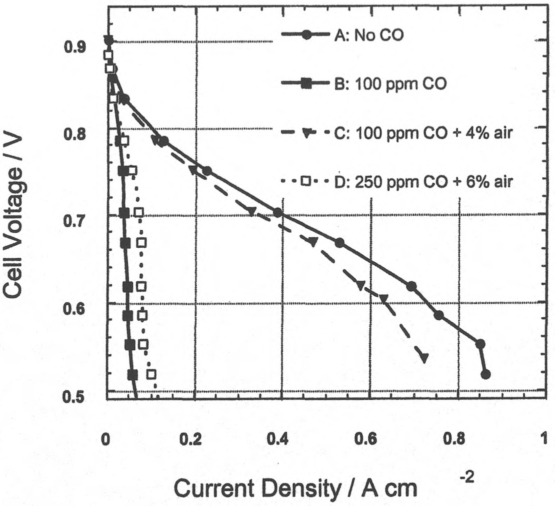

Figure 7. Performance of cell with no RCA layer on synthetic reformate under various conditions of CO level and air-bleed (50 cm^2 cell with 0.2 mg Pt cm^{-2} anode and cathode electrocatalyst layers).

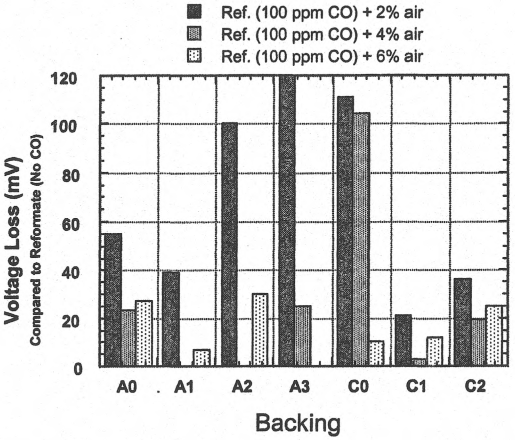

Figure 8. Comparison of three RCA catalysts with base performance at 100 ppm CO. Voltage loss measured at 0.5 A cm^{-2} and referred to synthetic reformate with no CO. A0 = no RCA layer; A1 = FeO_x (ac); A2 = CoO_x (ac); A3 = Co-exchanged KMn_8O_{16}. A Series = Pt anode electrocatalyst (0.2 mg cm^{-2}); C Series = Pt-Ru at 0.1 mg Pt cm^{-2}.

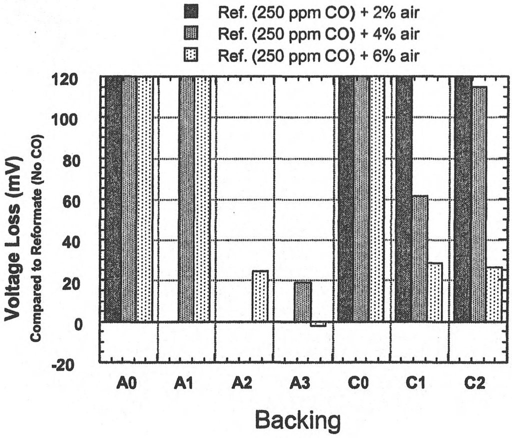

Figure 9. Comparison of three RCA catalysts with base performance at 250 ppm CO. Voltage loss measured at 0.5 A cm^{-2} and referred to synthetic reformate with no CO. A0 = no RCA layer; A1 = FeO_x (ac); A2 = CoO_x (ac); A3 = Co-exchanged KMn_8O_{16}. A Series = Pt anode electrocatalyst (0.2 mg cm^{-2}); C Series = Pt-Ru at 0.1 mg Pt cm^{-2}.

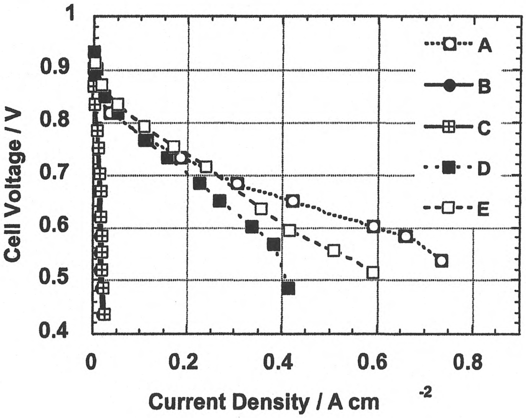

Figure 10. Effects of anode type and FeO_x (ac) reconfigured anode layer on tolerance to 500 ppm CO in synthetic reformate, using a 6% air-bleed. Measured in 50 cm^2 cells. Curve A: Pt Anode (0.2 mg cm^{-2}), RCA layer, no CO or air-bleed; Curve B: As in A, but with 500 ppm CO; Curve C: As in B, but with 6% air-bleed; Curve D: Pt-Ru anode (0.1 mg Pt cm^{-2}), no RCA layer, 500 ppm CO, 6% air-bleed; Curve E: As in D, but with RCA layer.

Proceedings of The Electrochemical Society, PV 2002-31, 174-182 (2002)
DOI: 10.1149/200231.0174PV © The Electrochemical Society

POROUS FLOW PLATE WITH INTERDIGITATED FLOW FIELDS FOR PEM FUEL CELLS

Jung S. Yi, Jonathan Puhalski, and Constance King
UTC Fuel Cells
195 Governor's Highway
South Windsor, CT 06074

ABSTRACT

Enhanced water removal capability in the gas diffusion layer of a PEM fuel cell with the interdigitated flow field is demonstrated. This results in water accumulation in the gas flow channels. A porous flow plate with an interdigitated flow field is proposed to enhance mass transport in the gas diffusion layer and to eliminate excess liquid water along the gas flow path. Benefits of this flow plate configuration are discussed, including demonstration of performance and stability improvements.

INTRODUCTION

The proton exchange membrane (PEM) fuel cell is gaining great attention for terrestrial application for power generation. Because of the requirements for gas humidification and for operation below the boiling point of water, one of the main issues for the PEM fuel cell is water management. In the under-humidified region in the cell, water needs to be supplied from the flow stream, through the gas diffusion layer to the membrane to maintain high membrane conductivity. In the water vapor saturated region, excess liquid water needs to be removed from the catalyst layer first through the gas diffusion layer and then along the reactant stream. To achieve proper water management, water handling capability in each component of the PEM fuel cell is critical. In addition, a complete consideration of the water transport interactions among the fuel cell components is also an important design aspect for high power-density PEM fuel cells.

For better water management and uniform gas distribution, the interdigitated flow field (IDFF) design has been considered. The IDFF, first introduced by Amakawa and Uozumi (1) for phosphoric acid fuel cells, allows the reactant stream to flow through the gas diffusion media, which improves the gas transport rate. This concept has since been reinvented and adopted by many to the PEM fuel cell (2-5). The interdigitated, dead-ended, gas flow channels of the IDFF design force the convective gas flows through the gas diffusion layers (GDL). This convective flow improves the reactant transport rates through the GDL not only by faster transport mechanism, but, more importantly, by flushing the liquid water out from the GDL to the gas flow channels of the PEM fuel cell. The more effectively utilized GDL area under the ribs of the flow channels provides a more even distribution of the reactant stream across the active area, unlike parallel flow fields (PFF). Since the pressure drop across the cell can be controlled by the permeability of the GDL, the machining tolerance required for the channel dimension can be relaxed, which may be significant for low cost development.

The effect of the IDFF compared to the parallel flow field and the serpentine flow field has been demonstrated experimentally for a relatively small-sized single cell and showed superior performance, especially at higher current densities (6, 7). Theoretical comparisons with the parallel flow field have also supported this improved performance (8, 9). Additionally, the gas transport behavior through the GDL has been theoretically investigated to understand the transport characteristics of gases through the GDL with various complexities (8-11). In the analysis by Kazim et al., (8) and Yi and Nguyen (10), the simulated gas flow pattern through the GDL estimated an electrochemical performance associated with the enhanced gas transport rates. In addition to the gas transport effects, the liquid water transport behavior in the GDL is included in He's model (11), demonstrating the liquid water removal capability of the IDFF. However, these theoretical analyses consider only the region through the GDL without incorporating the consequent effect of excess liquid water flow along the channels. The three dimensional model of Um and Wang (9) includes the gas flow along the channel in addition to the IDFF flow through the GDL, but does not consider the presence of liquid water in the stream. A comprehensive experimental and/or theoretical analysis of the IDFF design which includes the liquid water transport behavior not only in the GDL but in the complete flow path has not yet been reported.

In this communication, an interdigitated flow field design is experimentally evaluated in a fuel cell of practical size for stationary and transportation applications. Channel flooding for this flow field design has been identified as a critical issue. To address the channel flooding issue, an advanced gas distributor design, combined with a porous flow plate to actively remove liquid water within the cell, has been introduced, and the effectiveness of the proposed design has been demonstrated with an IDFF design.

EXPERIMENTAL

The experiments were carried out in 400cm^2 (active area) single cells using a Gore 5561 MEA, which is sandwiched between the anode and cathode gas diffusion layers. Porous carbon papers are used for the GDL. For the anode flow plate, a hydrophilic, porous, graphitized plate with parallel flow fields was used for all testing (12). This plate acts to distribute the reactant gas as well as to humidify the anode, if needed. Parallel or interdigitated flow fields were used for the cathode side. Also, both porous and solid graphitized carbon plates were used to investigate the effect of liquid water in the cathode flow plates. When porous plates were used, a intra-cell water-exchange coolant system was used (13, 14). A description of this system is presented later.

The cells were tested at ambient gas exit pressure and 65 °C cell temperature. Pure hydrogen and air was used for the anode and cathode respectively. Dry reactants were fed into the system unless specified. During each performance measurement, a 10-minute hold was applied to reach a stabilized performance before taking the measurement. The gas flow rate was determined from the fixed gas utilization applied for the measurement. A utilization of 80% was applied to the anode side for this analysis, and the oxygen utilization was specified for each test. Often, a gas-purge step was added between testing to flush water out from the cell. During the purge, 2 liter/min of dry nitrogen flowed through the gas flow channels for 20-30 minutes. Other operating conditions are specified with the figures.

RESULTS AND DISCUSSION

IDFF with Solid Flow Plate

Figure 1 shows the performance of a PEM fuel cell using an interdigitated flow field on the cathode side and solid flow plates (Solid IDFF). Initially, performance is relatively high, however, a significant performance decay is observed over time. With the IDFF, a significant amount of liquid water is purged through the GDL into the gas flow channels. This water accumulates in the flow channels, especially at the dead-ended corners of the interdigitated flow channels, lowering the cell performance over time as is shown in the series of performance calibration curves. Performance can be recovered with a high velocity gas purge, as we would expect. Supporting information for channel flooding is that an even lower performance is observed with the 100% humidified air inlet case, even in the first calibration after the purge, as is also shown in Figure 1. The pressure drop across the gas flow channel is shown in Figure 2. The increasing pressure-drops observed after the first calibration are indicative of water accumulation in the gas flow path as well. Higher pressure-drops are observed with a humidified air stream due to the additional water accumulation condensing from the humidified inlet air.

Similar problems are also indirectly indicated in the literature. In Wilkinson et al.'s patent (3), significant performance differences were reported when two different sizes of cells were tested with IDFF on solid graphite plates, especially at higher current densities. The degree of water accumulation in the dead-ended section of an IDFF increases with the increased cell size. With a larger cell or stack, there is more freedom to take a lower pressure-drop path, avoiding flow through the flooded region of the cathode stream until the minimum pressure becomes higher than the pressure required to blow the flooded water out from the cell. When water accumulation starts in the flow channels, it reduces the use of the active area, lowering cell performance. Another indication is the non-overlapping IDFF design proposed by Wynne et al. (15). The typical interdigitated design employs a plurality of flow channels branching off from a main flow channel. In contrast, Wynne's IDFF design employs non-overlapping flow channels each extending from a reactant stream port reducing gas exchange among the flow channels. They claim that their design results in a more uniform fluid flow distribution, reducing channel water retention, and decreasing the channel pressure-drop. This suggests liquid water flooding in the flow channels when the IDFF design is used with a solid flow plate. Therefore, to fully utilize the effectiveness of the IDFF in reducing mass transport resistance in the GDL, the liquid water handling capability in the flow field layer also needs to be improved. This water management problem in the channel layer is more significant for the larger size cells or stacks.

IDFF with Porous Flow Plate

A porous flow plate is used as a water management method to both remove and provide water along the gas stream (13, 14). This system utilizes a liquid-water-filled, porous, water transport plate (WTP). Thus the WTP is gas impermeable, similar to a solid flow plate, preventing gas ingestion into the coolant streams while allowing water exchange. In this system, the reactant gas streams are maintained at a higher pressure than the pressure in the coolant stream, with a predetermined pressure difference between the gas and coolant flow fields. This pressure difference causes excess liquid water in contact with the WTP to be wicked into the WTP and moved to the coolant passage network at a local level, eliminating issues associated with liquid water accumulation along the channel. In addition to the liquid water removal capability, the water in the WTP pores spontaneously vaporizes from the coolant channels when the reactant stream is dry. Therefore, water balance in every location of the cell is spontaneously achieved with intra-cell water removal or reactant humidification as needed.

Since water accumulation in the flow channels is a critical issue for practical-sized, IDFF fuel cells, a combination of the IDFF concept with the porous WTP can be a solution to truly utilize all the benefits of the IDFF concept discussed by many (16). Figure 3 shows the performance comparison of the porous IDFF design versus the porous PFF and the solid IDFF designs. Compared to the solid IDFF design, the porous PFF showed a better and more stable performance at lower than 1 A/cm^2, where the water generation rate is relatively small. A better liquid water distribution over the gas flow plate occurs because the amount of water supplied to the flow channel is relatively smaller than the IDFF. However, a rapid decrease in performance is reported due to improper water management in the GDL and/or electrode caused by the slower reactant-transport rate and poor water removal capability of the GDL. The porous IDFF showed a superior performance to the porous PFF because of better reactant transport and water removal capability in the GDL. The improvement in performance is more significant at higher current densities because of the increase in water generation rates at higher current densities. Much better performance is reported than with the solid IDFF, even at the lower current densities. This is the result of the better reactant distribution over the flow field obtained by removing liquid water through the pores of the flow plate to the circulating water coolant loop.

Lower pressure drops across the air flow-channels, linearly dependent on current densities, are shown in Figure 4, indicating effective liquid water removal in the gas flow channel by the porous flow plates. The porous IDFF design showed a higher pressure-drop than the porous PFF because of the added flow path through the GDL layer. However, the pressure drop with the IDFF is still significantly low in terms of the parasitic power required to blow the air for the configuration tested in this study. The pressure drop through the GDL can be manipulated by controlling the properties of GDL. For a smaller pore size, the pressure drop increases, improving the liquid water removing capability through the GDL and lessening the significance of the dimensional tolerance of the gas flow field. However, higher parasitic power is required because of the loss of energy through the GDL.

The effect of oxygen utilization (gas stoichiometry) on cell performance is shown in Figure 5. For the solid IDFF, a rapid increase in performance occurs with lower oxygen utilization, i.e. higher velocity, approaching the porous IDFF performance. This is because of the better liquid water removal capability that is provided by the increased velocity through the gas flow plate. Better oxygen utilization behavior is also observed with the porous PFF and even more so by the porous IDFF design. When the IDFF design is combined with porous flow plates, the better gas distribution and water removal characteristics of the IDFF can be fully utilized, demonstrating a superior oxygen utilization response. It allows the cell to operate well at high utilizations, which is preferable for high efficiency and system water balance for a high-power-density fuel cell system (14).

CONCLUSIONS

Performance of the IDFF design has been experimentally measured and compared using different flow plate designs to understand the water transport behavior within the cell. The following conclusions have been drawn from this analysis.

(1) An interdigitated flow field with solid flow plates causes liquid water accumulation within the plate in the cathode side resulting in rapid performance decrease over time.
(2) The intra-cell water-exchange system, using porous bipolar plates, effectively removes liquid water from the gas flow channels for both the parallel flow field design and the interdigitated flow field design, providing a relatively higher performance than a solid flow plate.
(3) The effective water removal capability of porous flow plates provides a significantly lower pressure drop across the cathode flow field, potentially reducing parasitic power for the cathode gas delivery system.
(4) With the porous flow plate configuration, the interdigitated flow field showed superior performance because of an enhanced reactant transport rate. Due to a faster mass transport mechanism as well as the improved water removal capability in the GDL, the cell can operate at higher oxygen utilization, which increases the system efficiency.
(5) With the porous flow plate configuration, a higher pressure-drop is observed for the IDFF compared to the PFF because of the added flow path through the GDL.

REFERENCES

1. K. Amakawa and N. Uozumi, *US Patent* 4,615,955 (1986).
2. K. Ledjeff, A. Heinzel, F. Mahlendorf, and V. Peinecke, *Dechema Monographien*, **128**, 103 (1993).
3. D. P. Wilkinson, H. H. Voss, and K. B. Prater, *WO Patent* 94/11912 (1994).
4. T. V. Nguyen, *J. Electrochem. Soc.*, **143**, L103 (1996).
5. M. S. Wilson, *US Patent* 5,641,586 (1997).
6. D. L. Wood, J. S. Yi and T. V. Nguyen, *Electrochimica Acta*, **43** (1998).
7. A. S. Arico, P. Creti, V. Baglio, E. Modica and V. Antonucci, *J. of Power Sources*, **91**, 202 (2000).
8. A. Kazim, H. T. Liu, and P. Forges, *J. Applied Electrochemistry*, **20**, 1409 (1999).

9. S. Um and C. Y. Wang, *Proceedings of the ASME Fuel Cell Division*, 5 (2000).
10. J. S. Yi and T. V. Nguyen, *J. Electrochem. Soc.*, **145**, 4 (1999).
11. W. He, J. S. Yi, and T. V. Nguyen, *AIChE J.* **46**, 2053 (2000).
12. J. A. Bett, D. J. Wheeler, and C. Bushnell, *US Patent* 5,840,414 (1998).
13. C. Reiser, *US Patent* 5,700,595 (1997).
14. J. S. Yi, D. J. Yang, and C. King, *Fuel Cell Technology: AIChE Conference Proceeding*, 475 (2002).
15. R. K. Wynne, J. K. Neutzler, F. Barbir, V. Gurau and W. E. Pierce, *US Patent* 6,207,312 (2001).
16. J. S. Yi and J. Puhalski, *US Patent Application* US2001/0004501 A1 (2001).

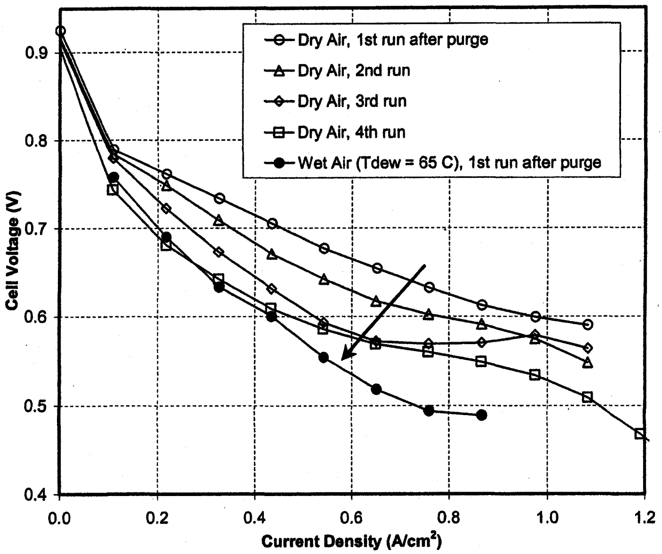

Figure 1. Performance of interdigitated flow field with solid cathode plate for various run times. H_2/Air, ambient pressure, UO_2 = 40%, T = 65 °C.

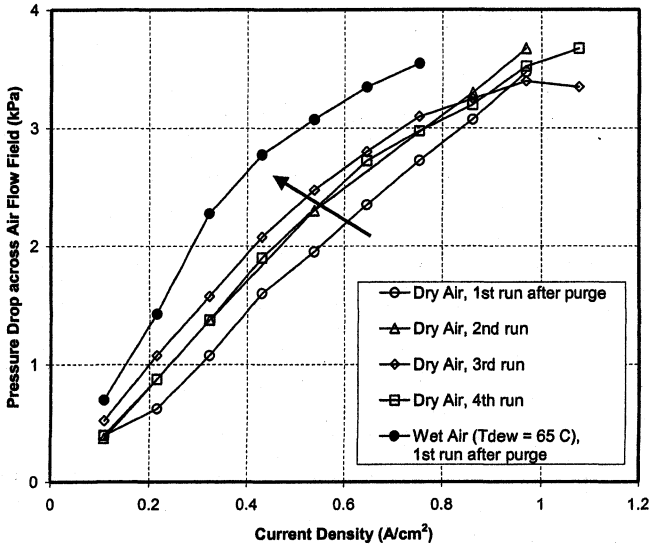

Figure 2. Comparison of the pressure drop across the interdigitated solid cathode plate. H_2/Air, ambient pressure, UO_2 = 40%, T = 65 °C.

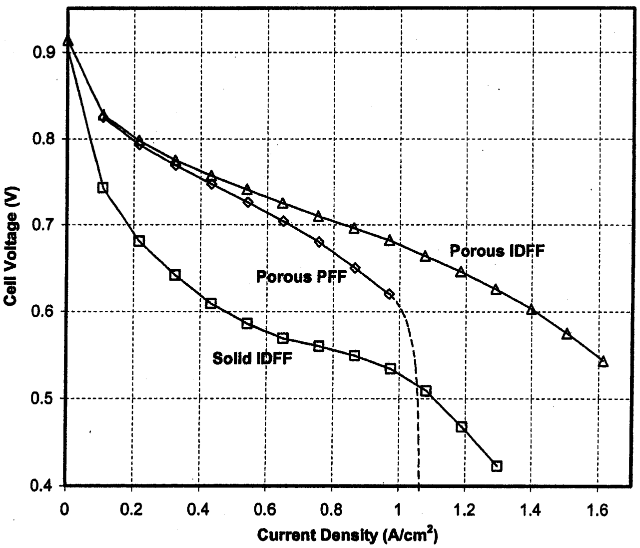

Figure 3. Comparison of the performances of PEM fuel cells with various flow plate designs. H_2/Air, ambient pressure, UO_2 = 40%, T= 65 °C, dry air.

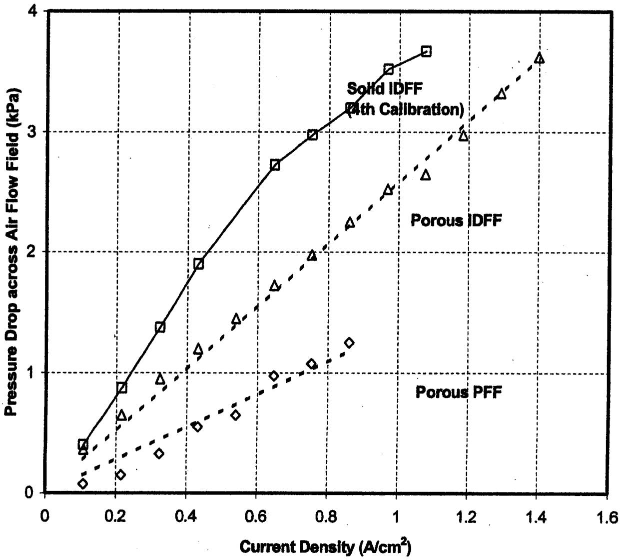

Figure 4. Comparison of the pressure drop across the air flow field for various flow plate designs. H_2/Air, ambient pressure, UO_2 = 40%, T=65 °C, dry air.

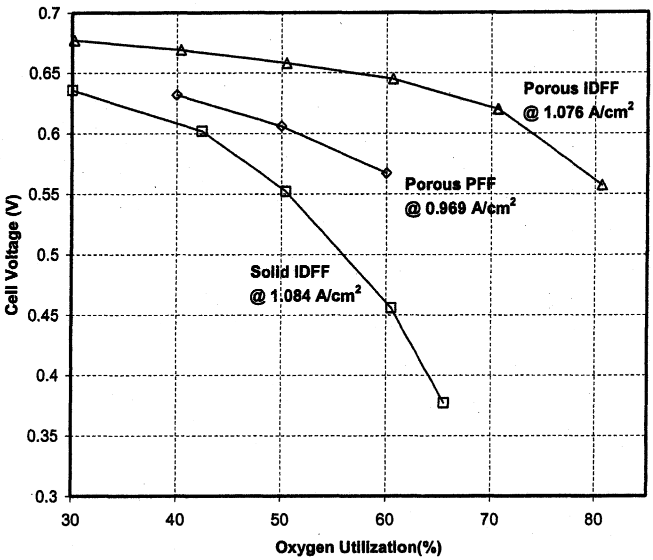

Figure 5. Comparison of oxygen utilization response for various flow plate designs, H_2/Air, ambient pressure, T = 65°C, dry air.

Proceedings of The Electrochemical Society, PV 2002-31, 183-197 (2002)
DOI: 10.1149/200231.0183PV © The Electrochemical Society

IN SITU WATER DISTRIBUTION MEASUREMENTS IN AN OPERATING POLYMER ELECTROLYTE FUEL CELL

M. M. Mench[1,2], Q. L. Dong, and C. Y. Wang[1]
Electrochemical Engine Center, and
Department of Mechanical and Nuclear Engineering
The Pennsylvania State University
University Park, PA 16802

ABSTRACT

The water balance between the flow channels, gas diffusion layer, and electrolyte membrane is a critical phenomenon affecting polymer electrolyte fuel cell (PEFC) performance. This paper presents data on the *in situ* water distribution within the gas channel of an operating PEFC. Following careful calibration and instrumentation, a gas chromatograph (GC) was interfaced directly to the fuel cell at various locations along the serpentine anode and cathode flow paths of a specially designed fuel cell. The 50 cm^2 active area instrumented fuel cell also permits simultaneous current distribution measurements via the segmented collector plate approach. The on-line GC method allows discrete measurements of the water vapor content of the flow about every two minutes. Water distribution data are shown at several inlet relative humidities and cell operating voltages. For the thin electrolyte membranes used (51 μm), there is little functional dependence of anode gas channel water distribution on current output. For thin membranes, this indicates that there is little gradient in the water activity between anode and cathode, for the conditions tested (i < 1 A/cm^2).

INTRODUCTION

The hydrogen polymer electrolyte fuel cell (PEFC) has tremendous promise as a future power system due to its low pollution, high efficiency, and stealth. Many studies, too numerous to completely list, have examined various aspects of PEFC performance as a function of operating conditions (1-9). Gottesfeld wrote an excellent review of PEFC

---

[1] Electrochemical Society Active Member
[2] Author to whom correspondence should be addressed: e-mail mmm124@psu.edu; Phone: (814) 865-0060; Fax: (814) 863-4848

components and operation, and the reader is referred to it for additional information on PEFC fundamentals (10). In addition to experimental characterization, much research has been focused on first-principles based modeling of the PEFC system (11-21). However, advances in modeling of the PEFC have thus far outpaced the ability to experimentally verify the predicted performance. In particular, scant experimental data are presently available regarding current density and species distributions. As indicated by Wang (22), it is this type of detailed validation that will permit an ultimate understanding of the physicochemical phenomena in the PEFC as well as development of useful computer-aided tools for design and development.

Determination of the mass distribution is critical to understanding water management and reactant distribution effects. In particular, it is desirable to understand the water vapor distribution within the gas channels of the flowfield. Many authors have conducted detailed studies or deduced models that describe the water transport through fuel cell components including the electrolyte and porous gas diffusion layers (23-30). In order to integrate these models and validate their accuracy, it is desired to determine the *in situ* mole fraction distribution of water vapor, at various locations within the gas channel flow path. A few authors have completed detailed studies of the water balance in an operating cell by collection of the fuel cell effluent, and condensation of the gas-phase water vapor (31-34). While useful, these studies do not provide data on the water distribution throughout the cell, which could vary widely depending on operating conditions, current distribution, and local non-isotropic transport parameters. In order to delineate the effects of current distribution on water distribution, it is also desirable to couple water and current distribution measurements to provide detailed information on non-uniform transport and generation effects. The instrumented cell used in this study allows for simultaneous measurement of current and mass distribution.

As has been discussed by Mench and Wang (35,36), several authors have developed different methodologies for current density distribution (37-41). The instrumented cell utilized in this work utilizes gold plated, segmented current collector similar to that described by Mench and Wang (35,36). The reader is referred to these papers for more detail on this methodology for current distribution measurements using a non-segmented MEA. This paper is concerned solely with mass distribution measurement technique.

EXPERIMENTAL

Instrumented Cell Design

Specific details and geometry of the instrumented cell and segmented flowfield are given in Finckh (42). The flowfield of the anode and cathode is a single-pass serpentine flowfield. Figure 1 is a schematic diagram detailing the relevant dimensions of the fuel cell. The dimension of the flow channel was chosen to be 2.16 mm wide, 3.18 mm in depth and had an average pass length of approximately 71 mm. With a total of 22 serpentine passes, the total path length is 1577 mm. Teflon® gaskets were press fit over the protruding gold-plated rib landings to form a flush surface with the polycarbonate slab. Two additional sealing gaskets surrounded both gas diffusion layers (GDL) of the MEA to compensate for GDL thickness. Gold plating, and use of an optimized compression torque for the cell of 35 in-lbs minimized electrical contact resistance between rib landings and the GDL. Pressure indicating film (Pressurex® by Sensor Products, Inc.) was used to determine the *in-situ* pressure distribution of the landings onto the MEA, as a function of compression torque. The assembly was checked to ensure a homogeneous pressure distribution from all landings onto the gas diffusion layer, thus ensuring a uniform contact resistance distribution between the gold-plated landings and GDL. The entire fuel cell assembly was leak proof tested to 0.3 MPa under water.

A schematic of the test and control system is shown in Fig. 2. Ultra-high purity (>99.999%) hydrogen and standard compressed air were supplied from compressed gas-cylinders. A steam-injection humidifier system (Lynntech Inc.) was used to provide the desired humidification to anode and cathode flows through control of the precise amount of water vapor added to the gas streams. Between humidifier and fuel cell, electric heating tapes were wrapped around the pipes to eliminate any condensation. Directly upstream of the inlet to the fuel cell, a gas sampling port was installed to measure the input humidity to the fuel cell by an Agilent 3000 MicroGC. This port was in addition to those along the fuel cell anode and cathode flow paths and provided accurate measurement and control of the humidification entering the cell.

The fuel cell system, including all lines leading to the fuel cell, were heated to the desired temperature, which was maintained with several Omega Engineering, Inc. model 8500 PID controllers. The cell and input lines maintained a steady temperature after suitable time to eliminate thermal transients. This start-up time was determined to be about ninety minutes by system check-out tests using thermocouples affixed to the GDL under non-flowing conditions.

To control and measure accurate current/voltage polarization curves, the fuel cell was connected to a multi-channel potentiostat/galvanostat (Arbin Instruments). For current density measurements, a gold-plated, electrically segmented current collector is used in direct contact with the unaltered GDL on the anode and cathode. In this segmented current collector technique, the potentiostat system maintains a constant voltage and the current sensors measure amperage emerging from each segmented current collector location, without the need for shunt resistors.

The membrane electrode assemblies (MEA) used for testing consisted of Nafion™ 112 as the polymeric membrane, sandwiched between the catalyst and ELAT™ (E-Tek, inc.) carbon cloth diffusion layers. All MEAs used had a carbon-supported catalyst loading of 0.5 mg Pt/cm^2 on both anode and cathode. Other general operating conditions are given in Table 1.

For mass distribution measurements, eight species extraction ports are located within the 1st (4.3% *of the fractional distance along the single serpentine path from the channel inlet*), 4th (17.4%), 7th (30.4%), 10th (43.5%), 13th (56.5%), 16th (69.6%), 19th (82.6%) and 22nd (95.7%) reactant channel passes. The extraction takes place along the back wall of the polycarbonate plate, at the farthest distance from the MEA to reduce water droplet blockage and false readings. The fittings on the backing plates used for species extraction were Teflon™ to eliminate corrosion.

RESULTS AND DISCUSSION

Micro GC Calibration and Measurement

In order to accurately measure the hydrogen, oxygen, nitrogen, and water species present in the fuel cell, an Agilent 3000 MicroGC (GC) was utilized. Two GC columns were used for gas species separation, a Plot-U column, and a molecular sieve (Molsieve) column with backflush module for prevention of excess water damage. This type of GC is capable of performing a single measurement about every two minutes. The column temperature was set to 120°C to avoid water condensation, and carrier gases of UHP helium, a 7.5% H_2 balance helium, or argon were used. The GC was interfaced to the fuel cell through a 0.318 cm (0.125 in.) stainless steel, heated tube connected to the sample ports of the cell. The sample line temperature was monitored and kept well above 100°C. Since reduced pressure flow can hold a greater mole fraction of water than pressurized flow, there is no condensation resulting from the pressure drop from the fuel cell channel to the GC inlet. The flow is directed toward the GC inlet and a bypass valve that allows continuous flow of atmospheric pressure sample gas. Sample availability at atmospheric pressure eliminates any error associated with varying sample inlet pressure, which can greatly affect results. The bypass flow was measured continuously with a mass flow meter to ensure that the extracted sample was a small fraction of the total fuel cell reactant flow. Typical values of bypass were 2-3% of the total flow, and this value never exceeded 5% during measurement. The possible disruption of performance by sample gathering on various channels was examined and determined to be minimal. Figure 3 shows continuous performance measurements between 0.4, 0.6, and 0.8 V at many locations along the anode path. During this continuous measurement, the sample extraction line was removed and replaced at several different locations, and many samples were taken. It is clear from this figure that no significant performance change results from withdrawal of such a small fraction of total flow from the channel. In addition, the reproducibility of the current distribution results over long time scales and through voltage cycling is demonstrated with Figure 3.

Depending on the pressure of the fuel cell, the delivery time for species to go from the fuel cell to the GC varied from seconds to minutes, based on calculations of interior tube volume and known flow rate. All GC measurements were given adequate time to ensure ample tube purge had occurred, and several measurements were taken to ensure accurate measurement.

In typical GC measurement applications, water vapor is condensed from the flow before entering the GC device. This is to prevent damage or degradation to the columns and detector elements. Indeed, if liquid water reaches the inlet of the GC or condenses inside the detector, system failure will likely occur. However, all temperatures of the columns, inlets, and sample tubes are kept well above 100°C to prevent this. Because of the high amounts of water present and resultant accelerated deactivation of the separation columns, a backflush module was installed to block vapor flow into the molsieve column, and frequent GC column cleaning was conducted. Provided that all flow is maintained well above the dew point, very accurate and repeatable measurement of water content up to 90% mole fraction can be achieved.

Sample calibration: Calibration is required before every set of test runs to maintain accuracy of measurement. Calibration is accomplished with a gas-bubbler humidifier at low flow rate and controlled temperature as a standard to ensure a known exit humidity of the calibration gas mixture. Pressure is monitored at the humidifier exit to correct for any losses in the sample line. To complete calibration, a single point calibration is made at a low temperature of around 50°C, to correlate the measured response area to the thermodynamically known water vapor mole fraction. Then, the temperature of the humidifier is increased and the calibration correlation is not altered, but the output is checked against the theoretical value to ensure accuracy. The results are very consistent. The measured mole fraction is typically within ±2% of the theoretical value, up to very high values of water mole fraction up to 95°C. Calibration curves taken for fully humidified hydrogen and fully humidified air flow are shown in Figs. 4 and 5. The data shown represent an average of five measurements, and it can be seen that the expected accuracy is around ± 2%. Note the close agreement between the measured values of water fraction compared to the thermodynamically expected values, which change very steeply with temperature in the range of fuel cell operation. This calibration also indicates that the humidifier is near 100% humidification efficiency. Due to the steepness of the theoretical water vapor mole fraction curve, if the humidifier were significantly less than 100% efficient, the measured calibration curve would not follow the rapidly changing slope of the theoretical curve.

Anode inlet humidity variation: Figure 6 shows the measured water mole fraction at various locations within the anode flow channel for three fuel cell voltages. The current distribution associated with these measurements is shown in Fig. 3. The fuel cell exit pressure was ambient, with 100% humidification at 80°C on the air cathode, and either 100% or 0% RH at 65°C on the anode. Each data point shown represents an average of at least five data points. There was very little scatter in the data. This series of tests were designed to illustrate the following:

1) The uptake of water into the gas channel from dry inlet conditions in the anode.
2) The effect of current density (and thus changing electro-osmotic drag of water through the PEFC) on anode gas channel humidity ratio.

It can be seen from Fig. 6, that for both cases of different inlet humidity ratio, the water uptake follows an exponential approach to an asymptotic value that is greater than the thermodynamically allowed maximum at 80°C. One explanation for increased water content is that the cell temperature could be slightly higher than the prescribed 80°C. It should be noted that the inlet gas temperature to the anode was 90°C. In addition, the thermal contact resistance between the control thermocouple and the polycarbonate backing plate was demonstrated to be responsible for a one-degree difference between measured and true polycarbonate temperature. A one-degree temperature difference would account for a 5% change in the maximum theoretical mole fraction, within the limits of measurement. Another explanation for the increased water mole fraction beyond thermodynamic limit at 80°C is the possibility of entrained mist flow. It is difficult to gauge the latter, as experimental correlations do not publicly exist for the specific geometry of the fuel cell flowfield.

It can also be seen from Figure 6, that in most cases, the measured anode channel water content was not affected to a great degree by the voltage (and hence current) draw. In most cases, the highest current output (lowest cell voltage) condition resulted in the lowest measured anode channel water vapor content, although not to any significant degree. This strongly indicates that the electro-osmotic drag of water from the anode to the cathode is nearly evenly balanced by back diffusion. This is expected for very thin membranes, such as the 51 μm Nafion PEFC used for testing. This near balance of drag and diffusion of water with thin membranes has been observed experimentally by water condensation and collection techniques as well (32).

CONCLUSIONS

Gas chromatography has been used to measure the *in situ* flow channel water vapor distribution of an operating, specially instrumented fuel cell flow field. Additionally, the fuel cell used permits simultaneous current density distribution measurements. This technique can be used to directly map water distribution in the anode and cathode of an operating fuel cell with a time resolution of approximately two minutes, and a spatial resolution limited only by the closeness of sample extraction ports located in the reactant gas channels. Along with other diagnostic techniques such as current distribution mapping, this species mapping technique provides an important tool to understand water management and reactant distribution in PEFC. The anode channel water distribution was not greatly influenced by the current density. For the thin (51 μm) membranes used, the electro-osmotic drag of water from the anode to the cathode is nearly evenly balanced by back diffusion.

ACKNOWLEDGEMENTS

Financial support of CD-Adapco Japan is gratefully acknowledged. Additionally, Chao-Yang Wang acknowledges partial support of DOE and Conoco under cooperative agreement No. DEFC26-01NT41098. The authors would also like to acknowledge the contributions of Oliver Finckh and Qunlong Dong in the design of the fuel cell and calibration of the test stand components.

REFERENCES

1. A. Parthasarathy, S. Srinivasan, and A. J. Appleby, and C. Martin, *J. Electrochem. Soc.*, **139**, 2530 (1992).
2. A. Parthasarathy, S. Srinivasan, A. J. Appleby, and C. Martin, *J. Electrochem. Soc.*, **139,** 2856 (1992).
3. Y. W. Rho, O. A. Velev, S. Srinivasan, and Y. T. Kho, *J. Electrochem. Soc.*, **141**, 3838 (1994).
4. J. C. Amphlett, R. M. Baumert, R. F. Mann, B. A. Peppley, P. R. Roberge, and T. J. Harris, *J. Electrochem. Soc.*, **142**, 9 (1995).

5. R. Mosdale, and S. Srinivasan, *Electrochim. Acta*, **40**, 413 (1995).
6. H. –F. Oetjen, V. M. Schmidt, U. Stimming, and F. Trila, *J. Electrochem. Soc.*, **143**, 3838 (1996).
7. F. N. Büchi, and D. Srinivasan, *J. Electrochem. Soc.*, **144**, 2767 (1997).
8. F. A. Uribe, S. Gottesfeld, and T. A. Zawodzinski, *J. Electrochem. Soc.*, **149**, A293 (2002).
9. E. A. Ticianelli, C. R. Derouin, and S. Srinivasan, *J. Electroanal. Chem.*, **251**, 275 (1988).
10. S. Gottesfeld, in Advances in Electrochemical Science and Engineering, C. Tobias, Editor, **Vol. 5**, Wiley and Sons, New York (1997).
11. T. E. Springer, T. A. Zawodinski, and S. Gottesfeld, *J. Electrochem. Soc.*, **138**, 2334 (1991).
12. D. M. Bernardi and M. W. Verbrugge, *AIChE J.*, **37**, 1151 (1991).
13. D. M. Bernardi, and M. W. Verbrugge, *J. Electrochem. Soc.*, **139**, 2477 (1992).
14. T. E. Springer, M. S. Wilson, and S. Gottesfeld, *J. Electrochem. Soc.*, **140**, 3513 (1993).
15. T. V. Nguyen and R. E. White, *J. Electrochem. Soc.*, **140**, 2178 (1993).
16. C.Y. Wang and W.B. Gu, *J. Electrochem. Soc.*, **145**, 3407 (1998).
17. V. Gurau, H. Liu, and S. Kakac, *AIChE J.*, **44**, 2410 (1998).
18. J. S. Yi and T. V. Nguyen, *J. Electrochem. Soc.*, **146**, 38 (1999).
19. S. Um, C. Y. Wang and K. S. Chen, *J. Electrochem. Soc.*, **147**, 4485 (2000).
20. Z. H. Wang, C. Y. Wang and K. S. Chen, *J. Power Sources*, **94**, 40 (2001).
21. C. Y. Wang, S. Um, H. Meng, U. Pasaogullari, and Y. Wang, "Computational fuel cell dynamics (CFCD) models," *in 2002 Fuel Cell Seminar*, Nov. (2002).
22. C. Y. Wang, "Two-phase flow and transport in PEM fuel cells," *in Handbook of Fuel Cells*, John Wiley and Sons, (2002).
23. D. M. Bernardi, *J. Electrochem. Soc.*, **137**, 3344 (1990).
24. T. E. Springer, T. A. Zawodzinski, and S. Gottesfeld, *J. Electrochem. Soc.*, **138**, 2334 (1991).
25. D. M. Bernardi and M. W. Verbrugge, *J. Electrochem. Soc.*, **139**, 2477 (1992).
26. T. F. Fuller and J. Newman, *J. Electrochem. Soc.*, **140**, 1218 (1993).
27. M. Eikerling, Y. I. Kharkats, A. A. Kornyshev, and Y. M. Volfkovich, *J. Electrochem. Soc.*, **145**, 2684 (1999).
28. J. S. Yi and T. V. Nguyen, *J. Electrochem. Soc.*, **146**, 38 (1999).
29. I-M. Hsing, and P. Futerko, *Chem. Eng. Sci.*, **55**, 4209 (2000).
30. Z.H. Wang, C. Y. Wang and K. S. Chen, *J. Power Sources*, **94**, 40 (2001).
31. X. Ren and S. Gottesfeld, *J. Electrochem. Soc.*, **148**, A87 (2001).
32. G. J. Janssen, *J. Electrochem. Soc.*, **148**, A1313 (2001).
33. G. J. Janssen, M.L. Overvelde, *J. Power Sources*, **101**, 117 (2001).
34. W.K. Lee, J. W. Van Zee, S. Shimpalee, and S. Dutta, *Proceedings of ASME Heat Transfer Division*, **1**, 339 (1999).
35. M. Mench, and C.Y. Wang, *J. Electrochem. Soc.*, **150**, A79 (2003).
36. M. Mench, C. Y. Wang, and M. Ishikawa, *Proceedings of the 202nd Meeting of the ECS*, ECS-S1-0814 (2002).
37. C. Wieser, A. Helmbold, and E. Gülzow, *J. of Appl. Electrochem.*, **30**, 803 (2000).
38. J. Stumper, S. Campell, D. Wilkinson, M. Johnson, and M. Davis, *Electrochim. Acta*, **43**, 3773 (1998).
39. S. Cleghorn, C. Derouin, M. Wilson, and S. Gottesfeld, *J. of Appl. Electrochem.*, **28**, 663 (1998).

40. M. Noponen, T. Mennola, M. Mikkola, T. Hottinen, and P. Lund, *J. Power Sources*, **106**, 304 (2002).
41. D. Brett, S. Atkins, N. Brandon, V. Vesovic, N. Vasileiadis, and A. Kucernak, *Electrochem. Comm.* 3, 628 (2001).
42. O. H. Finckh, "Dilution effects and current distribution on hydrogen proton exchange membrane fuel cells," MS Thesis, *The Pennsylvania State University*, May 2002.

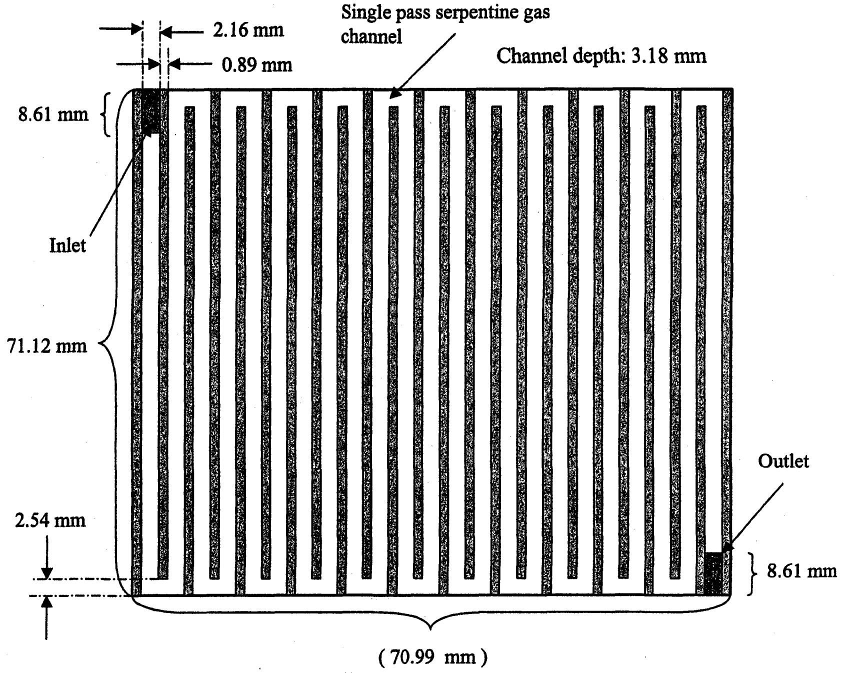

Figure 1. Schematic diagram of the 50 cm^2 instrumented test cell showing relevant dimensions.

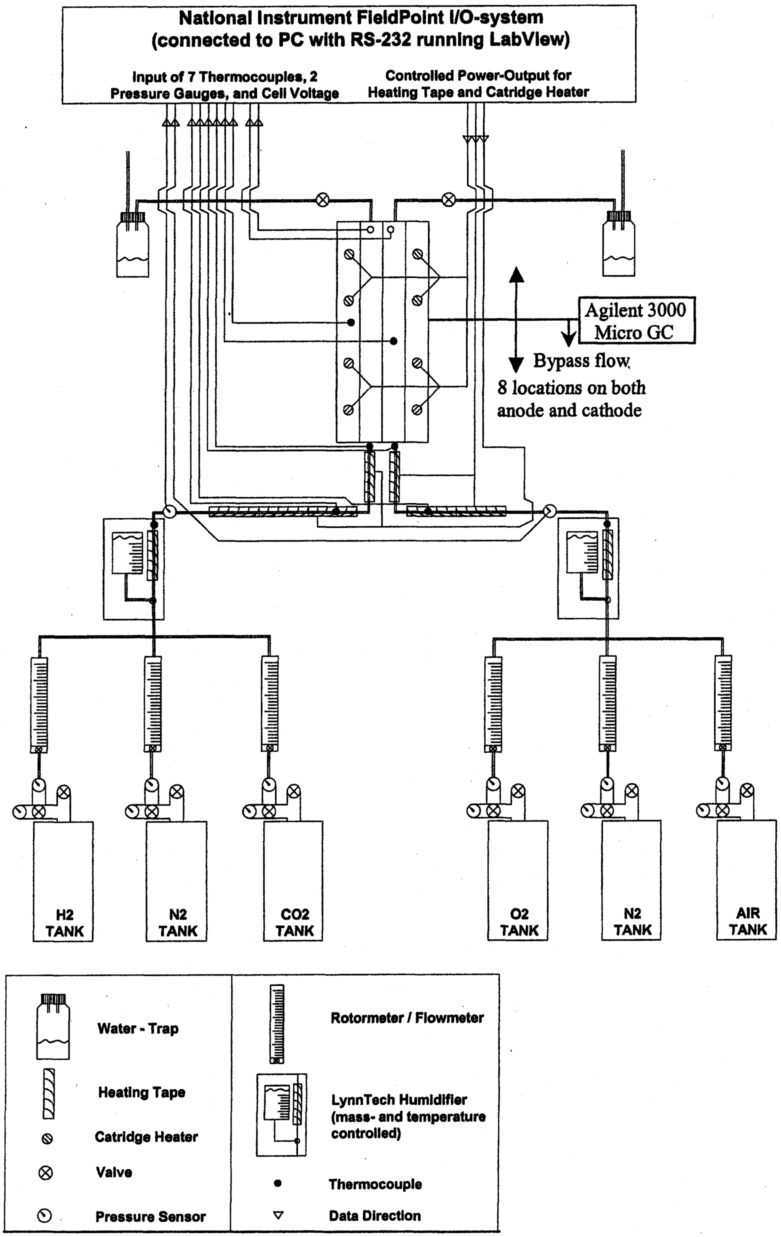

Figure 2. Schematic of the experimental test stand and control system.

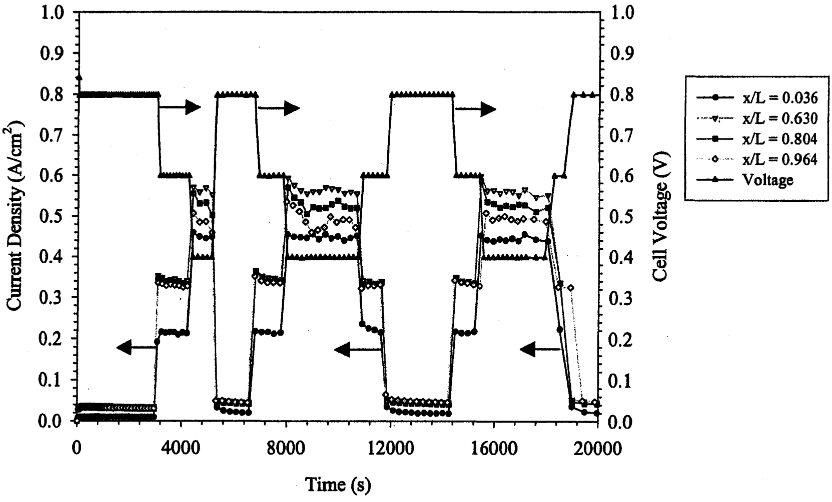

Figure 3. Time varying performance at 0.4, 0.6, and 0.8 V while mass distribution measurements were taken, indicating little effect of measurement on cell performance.

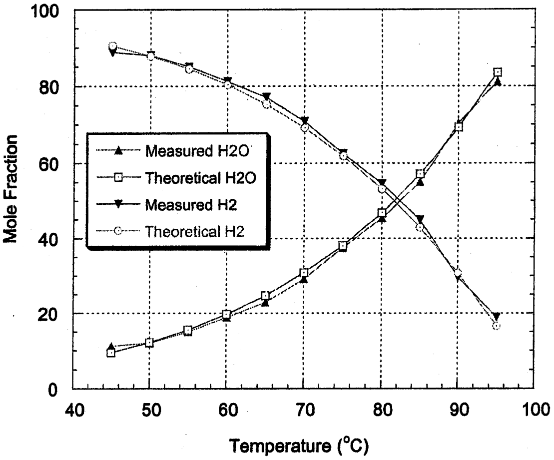

Figure 4. Comparison between measured and theoretical water vapor and hydrogen concentrations measured with GC with baseline value at 50 °C. The humidifier bottle was at 1.1 atm pressure.

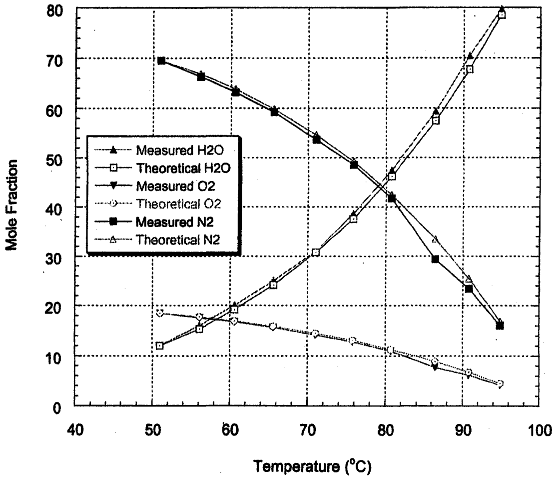

Figure 5. Comparison between measured and theoretical water vapor, nitrogen and oxygen concentrations measured with GC with baseline value at 50 °C. The humidifier bottle was at 1.1 atm pressure.

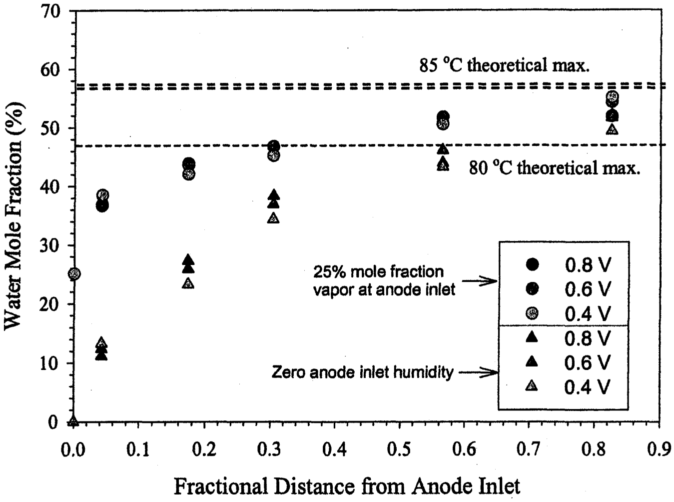

Figure 6. Measured water distribution as a function of fractional distance from anode inlet for partially, and non-humidified anode conditions. Test conditions: exit pressure A/C = 1 atm, 100% RH @ 80°C air cathode, 100% or 0% RH @ 65°C neat H_2 anode ξ_c = 2.5 @ 0.7 A/cm2 ξ_a = 1.0 @ 0.7 A/cm^2

Table 1. Baseline operating conditions.

Parameter	Value	Units
Electrolyte	Nafion 112	NA
Gas diffusion layer	ELAT® (De Nora North America) anode and cathode	NA
Catalyst loading (carbon supported)	0.5	mg/cm^2
Cell temperature	80	°C
Anode inlet temperature	90	°C
Cathode inlet temperature	80	°C
Anode and cathode pressure	0.1	MPa
Cathode humidification	100% at 80°C	NA
Anode gas	Ultra high purity H_2 (>99.999 %)	NA
Cathode gas	Commercial air (79% N_2, 21% O_2)	NA

Proceedings of The Electrochemical Society, PV 2002-31, 198-211 (2002)
DOI: 10.1149/200231.0198PV © The Electrochemical Society

INVESTIGATION OF GAS DIFFUSION MEDIA USING CFD MODELING

Uwe Beuscher and Greg Rusch
W. L. Gore & Associates, Inc.
201 Airport Road, Elkton, MD 21922-1488

Sirivatch Shimpalee and John W. Van Zee
Department of Chemical Engineering
University of South Carolina, Columbia, SC 29208

ABSTRACT

The performance of a gas diffusion layer comprised of a macro porous and micro porous layer has been studied both experimentally and by numerical simulation. Experimental data at different humidification conditions has been compared to full cell, three dimensional computational fluid dynamics calculations to validate the physical model of the cell. Local distributions of current density, membrane conductivity, temperature, and gas composition are discussed in detail. Model calculations with and without the micro porous layer show that this layer has a small effect on the overall performance. However, the local distributions show significant differences.

INTRODUCTION

The main purpose of Gas Diffusion Media (GDM) in a Polymer Electrolyte Membrane Fuel Cell (PEMFC) is to distribute the reactants along the active surface of the electrodes. In addition, the GDM has to ensure proper transport of product water, electrons, and heat of the reaction. Porous carbon materials are most often used to accomplish this complex task. A micro porous layer or diffusion layer (1,2) is sometimes added between the main macro porous GDM layer and the Membrane Electrode Assembly (MEA) as illustrated in Fig. 1. The purpose of this micro layer is to aid in the distribution of the reacting gas flows to the MEA surface, mechanical compatibility between the layers, the contact resistance, local current density distribution, and water management. The micro layer is usually comprised of carbon for electrical conductivity and PTFE for hydrophobicity. The objective of this study is to understand the role of the micro porous layer as well as the interactions with the macro layer and the flow field configuration.

Computational Fluid Dynamics (CFD) is gaining more interest as a tool to understand fuel cell performance (3-6). The model calculations provide insight into the fuel cell on a local level and describe distributions of current density, temperature, reacting gases, and water (vapor and liquid). Thus, modeling will help in gaining an understanding of the physics inside the PEMFC, aid in data analysis, and identify limiting parameters. A previously published model (6-8) has been used to estimate the performance of a PEMFC using a layered GDM structure. In this study, experimental performance data are compared to numerical results to validate the CFD model and to study the local distributions. Furthermore, the effect of the micro porous layer is studied by comparison of numerical results to calculations without the micro layer.

EXPERIMENTAL

Experimental data was obtained with 40% hydrogen in nitrogen on the anode and air on the cathode using a 5620 PRIMEA® membrane electrode assembly from W.L. Gore & Associates, Inc. (Elkton, MD). It was assembled in a 25 cm^2 test cell (Fuel Cell Technologies, Inc., Albuquerque, NM) using SGL hydrophobized macro gas diffusion media (SGL Carbon AG, Meitingen, Germany) and CARBEL^{TM} MP micro gas diffusion media (W.L. Gore & Associates, Inc.). The average compression in the cell was about 150 psi. The cell contained a triple serpentine flow pattern and was operated in the co-flow configuration. All tests were performed with a standard gas delivery unit (Globe Tech, Inc., Bryan, TX) with a Scribner 890b electronic load with PC control (Scribner Associates, Inc., Southern Pines, NC). All mass flow controllers and sparger bottles were calibrated for flow rate and dew point, respectively. All polarization curve data was collected using automated test protocols (Fuel Cell^{TM} software by Scribner Associates, Inc.) by holding 10 minutes at each set point and averaging the last minute of collected data. The operating conditions were 65°C cell temperature with 0 psig back pressure and an anode and cathode stoichiometry of 1.2 and 2.0, respectively. The gas humidification was varied during the experiments for a comparison of model calculations and experimental data over a range of operating conditions. Four conditions were tested: fully humidified gas streams (condition #1: 65°C/65°C dew point on anode and cathode, respectively), highly oversaturated streams (condition #2: 85°C/85°C), dry anode (condition #3: dry/65°C), and dry cathode (condition #4: 65°C/dry).

NUMERICAL

The numerical work is based on a steady state, multi-phase phenomena, and three-dimensional mass transfer model including heat transfer aspects of a full-cell PEMFC. The typical single cell PEMFC used for testing is a sandwich of two graphite flow channel blocks laced with channels with designed flow-field pattern, separated by GDM and a MEA. The MEA consists of a membrane and two electrodes that have dispersed platinum catalysts. The flow channel geometries used in this work is shown in Fig. 2. It has triple pass channel with 10 serpentine fashions. The flow channel has dimension of 0.09 (height) x 0.07 (width) cm^2 cross-section flow area in each channel with the length of 5.00 cm. Each diffusion layer (macro and micro) has dimensions of 0.033 (height) x 5.00 (width) x 5.00 (length) cm^3. Therefore, the active area of the MEA is 25 cm^2. A total of 68 x 272 x 41 cells (elements) were used in the flow channels and gas diffusion layers to model the fuel cell. The MEA is placed in between anode and cathode diffusion layers, which are containing macro and micro structures.

Model equations

The equations used in this work (conservation of mass, Navier-Stokes equations, species transport equations, energy equation, and water phase change model, with the source terms) were developed in previous studies (7,8). In addition, the water phase change model is extended in this work to include a liquid water film presented on the membrane surface for both anode and cathode (9). When the local activity of water exceeds unity, liquid water is present in the control volume and a liquid water film forms. The thickness of this liquid film depends on the rate of condensation/evaporation and the production of water by electrochemical reaction. The solubility of H_2 and O_2 is included in this model using Henry's Law to account for the diffusion of reacting gases to the MEA surface through the liquid water film. Thus, the local current is decreased as water condenses. Further, the overpotential equation shown in references (7,8) has been modified by simplifying the general form of the Butler-Volmer Equation to include the effect of concentration for both anode and cathode as shown in Eq. [1]:

$$\eta(x,y) = \frac{RT}{4F}\ln\left(\frac{P_{O2,in}}{P_{O2}(x,y)}\right) - \frac{RT}{2F}\ln\left(\frac{P_{H2}(x,y)}{P_{H2,in}}\right) + \frac{RT}{0.84F}\ln\left(\frac{i(x,y)\,P_{O2,in}}{i_{0,O2}\,P_{O2}(x,y)}\right) + \frac{RT}{2F}\left(\frac{i(x,y)\,P_{H2,in}}{i_{0,H2}\,P_{H2}(x,y)}\right) \qquad [1]$$

A control volume technique based on a commercial flow solver, FLUENT (version 4.56), is used to solve the coupled governing equations. This software requires specification of the source terms for species transport equations, two-phase equations for water, and heat generation equations created by electrical losses as shown in references (7,8). The new subroutines with the inclusion of the solubility effect were written to calculate the electrochemical overpotential and permeability for this simulation. Also, FLUENT requires a subroutine to account for the flux of protons and water across the membrane. The operating conditions and parameters used in the numerical model are shown in Table 1. All material properties were determined from ex-situ observations, except the exchange current density for the hydrogen oxidation reaction, $i_{0,H2}$, which was adjusted to obtain a better fit to the experimental data at condition #1. The results will be presented in the form of distributions of current density, membrane conductivity, temperature, liquid water fraction, and alpha. The net water transfer coefficient per proton, alpha, is a measure of the water management in the cell. A positive value indicates that electro-osmotic drag dominates over back diffusion and a net transport of water from anode to cathode. A negative value for alpha shows a net transport from cathode to anode. A well-balanced fuel cell will result in an alpha value close to zero.

RESULTS AND DISCUSSION

Figure 3 shows four polarization curves taken from experimental data compared to numerical results. The four data points at a cell potential of 0.65 V were chosen to compare to the model calculations. The numerical results agree very well with experimental data for all cases. Both experiment and numerical calculations show that condition #1 (65°C anode dew point and 65°C cathode dew point) gives the highest performance with a current density of 644 mA/cm^2, and condition #4 (65°C anode dew point and dry cathode) gives the lowest performance with a current density of 298 mA/cm^2. Further, condition #2 (85°C anode dew point and 85°C cathode dew point) gives lower performance (569 mA/cm^2) than condition #1 due the water flooding. Finally, condition #3 (dry anode and 65°C cathode dew point) provides a current density of 462 mA/cm^2 at 0.65 V.

Condition #1: 65° C dew point on anode and 65° C dew point on cathode

Figures 4 a-d presents the local current density, membrane conductivity, temperature, and alpha distributions on the membrane surface for condition #1 (65/65°C dew point). Fig. 4a shows the current density distribution with an average of 644 mA/cm^2 at 0.650 V. The distribution is very non-uniform with the highest current density of ~800 mA/cm^2 from the entrance region toward the outlet with the lowest value of ~400 mA/cm^2. This is caused by the concentration reduction of the reacting gases, even though the membrane conductivity increases from inlet toward outlet as shown in Fig. 4b. The membrane conductivity increases from inlet to outlet due to an increase in water activity. Even though the gases enter the fuel cell fully humidified, the activity inside the cell is less than unity due to the increased temperature of up to 72° C caused by the heat of reaction. Further, in the region of the channel bends, the current density is slightly lower at inner channel of the triple serpentine compared to the outer channel. This is because at the inner bend, the velocity magnitude is lower than the outer bend. Therefore, the heat transfer coefficient of the inner bend is lower than at the outer bend. Thus, the temperature of the inner bend is higher than the outer area as shown in Fig. 4c and this creates the lower membrane conductivity at the inner bend that outer bend shown in Fig. 4b. The distribution of alpha as shown in Fig. 4d, the net water transfer coefficient, is very uniform and has an average value close to zero indicating a good balance of water transport between anode and cathode.

Condition #2: 85° C dew point on anode and 85° C dew point on cathode

Figures 5 a-d present the local current density, membrane conductivity, temperature, and liquid water distributions on the membrane surface for condition #2 (85/85°C dew point). Fig. 5a shows the current density distribution with an average of 569 mA/cm^2 at 0.660 V. The current distribution shows more non-uniformity than the distribution of 65/65°C dew point. The highest value is ~900 mA/cm^2 at the entrance region and the lowest value is ~200 mA/cm^2 at the exit region. This is because the higher inlet humidity applied in this condition leads to a well-hydrated membrane even in the entrance region. Fig. 5b shows that the membrane conductivity is very uniform with the high value. This is because the inlet humidity condition of both anode and cathode are higher than the actual cell temperature. The cell temperature is high in the inlet region (>75° C) as Fig. 5c shows caused by the high current density and water condensation. However, the temperature drops towards the outlet, which results in the accumulation of liquid water resulting in flooding. Fig. 5d shows that the liquid water fraction increases above 10% especially in the bends of the channels. This will significantly affect the concentration of oxygen at the MEA by the liquid water film resistance.

Condition #3: dry anode and 65° C dew point on cathode

Figures 6 a-d present the local current density, membrane conductivity, temperature, and alpha distributions on the membrane surface for condition #3 (dry/65°C dew point). Fig. 6a shows the current density distribution with an average 462 mA/cm^2 at 0.645 V. This condition results in the opposite distribution compared with Figs. 4a and 5a. The lowest current density is shown at the entrance region with the value of ~200 mA/cm^2 and the current density increases toward the exit region with the value of ~520 mA/cm^2. This is because the dry anode inlet results in low membrane hydration at the entrance region, giving the lowest local performance. Further down the cell, water from the cathode humidity and electrochemical reaction is transported across the membrane by back diffusion to hydrate the MEA. This results in increasing membrane conductivity from inlet toward outlet as shown in Fig. 6b. The temperature distribution illustrated in Fig. 6c is very uniform with the minimum value of 68°C at the entrance region and the maximum of 72° C at the exit region. The distribution of alpha in Fig. 6d shows a large negative value in the inlet region, indicating a strong water back transport from cathode to anode. Towards the outlet of the cell alpha approaches zero, which shows a balance between electro osmotic drag and back diffusion.

Condition #4: 65C dew point on anode and dry cathode

Figures 7 a-d present the local current density, membrane conductivity, temperature, and alpha distributions on the membrane surface for condition #4 (65°C/dry dew point). Fig. 7a shows the current density distribution with an average of 298 mA/cm^2 at 0.660 V. The distribution is similar to Figs. 4a and 5a, but the value is much lower. The current density shows the highest value at the inlet region with a value of ~450 mA/cm^2. The current density decreases toward the outlet with the lowest value of ~250 mA/cm^2. The performance is dominated by the low membrane conductivity illustrated in Fig. 7b, which gives a similar distribution as the current density contour. The low membrane conductivity is due to the reduction of anode water activity by electro-osmotic drag from anode to cathode. The distribution of alpha shown in Fig. 7d indicates that alpha is always positive, which indicates that the electro-osmotic drag dominates over back diffusion even though the current density is low. There is little water back diffusion because of dry gas on the cathode. The temperature distribution shown in Fig. 7c is very uniform with an average value of 70°C.

Influence of micro layer

Simulations were performed without the micro diffusion layer for conditions #1 and #3 to study the influence of the micro layer on the behavior of the fuel cell. Fig. 8 shows current density and membrane conductivity distributions for condition #1 (65° C dew point on anode and 65° C dew point on cathode). Comparison of Fig. 8a with Fig. 4a, which is the current density distribution including the micro layer reveals that the configuration including the micro layer gives slightly higher performance than the case of no micro layer (see Fig. 8a) by 18 mV at similar averaged current density. Furthermore, the distribution without the micro layer shows more non-uniformity than the case including the micro layer with a higher current density at the entrance region and lower value at the exit region. This could be because the micro layer aids in the distribution of the reacting gas flows to the MEA surface. The membrane conductivity including the micro layer (Fig. 4b) shows higher values throughout, but particularly in the exit region compared to the case without the micro layer (Fig. 8b). It appears that the micro layer has a beneficial effect on local water management at this condition.

Fig. 9 shows current density and membrane conductivity distributions for condition #3 (dry anode and 65° C dew point on cathode). The current density distribution without the micro layer shown in Fig. 9a increases from inlet to about ⅔ of electrode width and then it decreases toward outlet. Fig. 6a shows that the current density including the micro layer has a more uniform distribution and is continuously increasing from inlet to outlet. Again, the performance including the micro GDM layer is slightly higher by about 15 mV. Interestingly, Fig. 9b shows that the membrane conductivity without the micro layer shows higher values throughout, but particularly in the exit region compared to the case including the micro layer (Fig. 6b). The reason for this behavior is the low current density in the exit region, which results in increased water transport towards the anode and subsequent membrane humidification.

In summary, the micro diffusion layer appears to have a beneficial effect. Even though the overall performance of the fuel cell is very similar, the local distributions may be very different depending on the operating condition.

CONCLUSIONS

Full-cell numerical calculations of PEM fuel cell performance agree very well with experimental data. The cell potentials at four different operating conditions with vastly different humidification conditions are predicted to be within 2% of the experimentally determined value. The simulation provides valuable insight into the local distribution of current density, membrane conductivity, temperature, and transport rates. Comparison of these distributions explains the performance under the different operating conditions. Super-saturation of the incoming gas streams results in a very high current density at the inlet, but also to the formation of liquid water (flooding), which lowers the performance due to the increased film resistance for diffusion. Dry gas streams on either anode or cathode cause a low membrane conductivity and low performance. The two cases show opposite current density distributions and reveal details of the water management inside the cell.

Simulations without the micro porous gas diffusion layer show slightly better performance when the micro layer is present. The local distributions, however, can be very different, and it appears that the micro layer assures more uniform local distributions.

REFERENCES

1. L.R. Jordan A.K. Shukla, T. Behrsing, N.R. Avery, B.C. Muddle, and M. Forsyth, *J. Power Sources*, **86**, 250 (2000)
2. E. Antolini, R.R. Passos, ans E.A. Ticianelli, *J. Power Sources*, **109**, 477 (2002)
3. D. Baker, B. Steidle, M. Schoenweiss, J. Roth, S. Fell, M. Mathias, and Mark Murphy, *AIChE Spring National Meeting*, New Orleans, LA, paper 86f (2002)

4. J.V. Cole and S. Mazumder, *201st Meeting of the ECS*, Philadelphia, PA, paper 1134 (2002)
5. A. Kumar and R.G. Reddy, *201st Meeting of the ECS*, Philadelphia, PA, paper 1139 (2002)
6. S. Shimpalee, J. Glandt, S. Greenway, W.K. Lee and J.W. Van Zee, *201st Meeting of the ECS*, Philadelphia, PA, paper 1135 (2002)
7. S. Shimpalee, S. Dutta, and J.W. Van Zee, *Proc. ASME IMECE,* HTD **366-1,** 1 (2000)
8. S. Shimpalee, and S. Dutta, *Numerical Heat Transfer – Part A*, **38**, 111-128 (2000)
9. W-k. Lee, S. Shimpalee, and J. W. Van Zee, *J. of Electrochem Soc.*, accepted (2002)

Table 1: Inlet conditions for 4 data points.

		Condition # 1 (I_{avg} = 644 mA/cm^2)	Condition # 2 (I_{avg} = 569 mA/cm^2)	Condition # 3 (I_{avg} = 462 mA/cm^2)	Condition # 4 (I_{avg} = 298 mA/cm^2)
Anode channel inlet	Velocity (m/s) per channel	7.552	18.363	2.383	3.494
	Mole fraction of H_2	0.30	0.17	0.40	0.30
	Mole fraction of water vapor	0.25	0.57	0.0	0.25
	Mole fraction of N_2	0.45	0.26	0.60	0.45
	I_{oH2} (mA/cm^2)	60,000	60,000	60,000	60,000
	Temperature (K)	338	338	338	338
Cathode channel inlet	Velocity (m/s) per channel	11.99	29.15	8.60	2.44
	Mole fraction of O_2	0.152	0.086	0.152	0.20
	Mole fraction of N_2	0.608	0.344	0.608	0.80
	Mole fraction of water vapor	0.24	0.57	0.24	0.0
	I_{oO2} (mA/cm^2)	60	60	60	60
	Temperature (K)	338	338	338	338
	Condensation rate (1/s)	1.0	1.0	1.0	1.0
Operating conditions	Membrane thickness (μm) + catalyzed layers (μm)	50.0	50.0	50.0	50.0
	Graphite collector conductivity (W/m-K)	5.7	5.7	5.7	5.7
	MEA conductivity (W/m-K)	0.143	0.143	0.143	0.143
	Operating pressure (Psig)	0	0	0	0

PRIMEA, GORE & designs are trademarks of W. L. Gore & Associates, Inc.

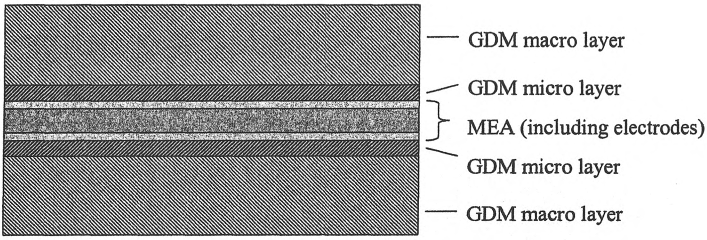

Fig. 1: . Schematic representation of GDM layers and the MEA.

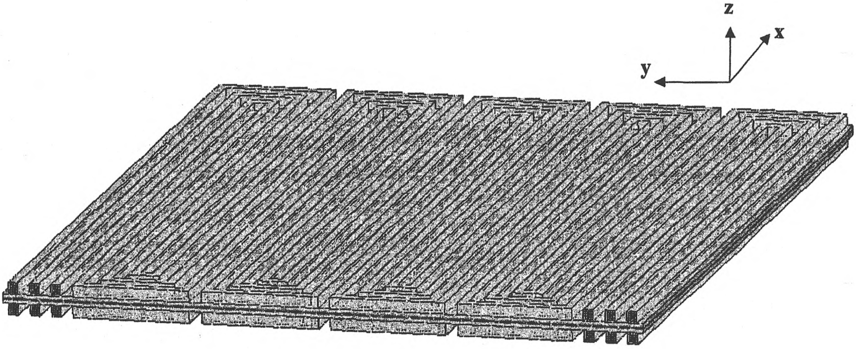

Fig. 2: The geometrical model of the 25-cm^2 triple serpentine flowfield.

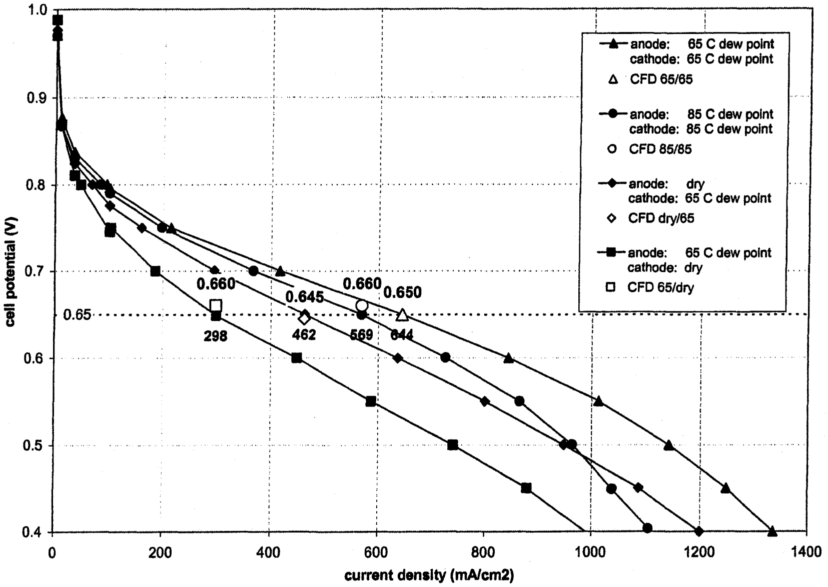

Fig. 3: Polarization curves of four operating conditions compared to four calculated points.

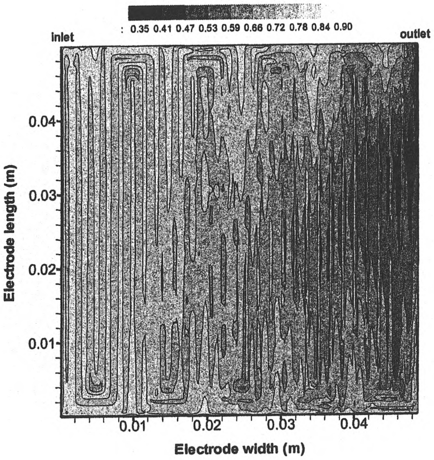

Fig. 4a: Current density distribution, $I_{avg} = 644$ mA/cm^2.

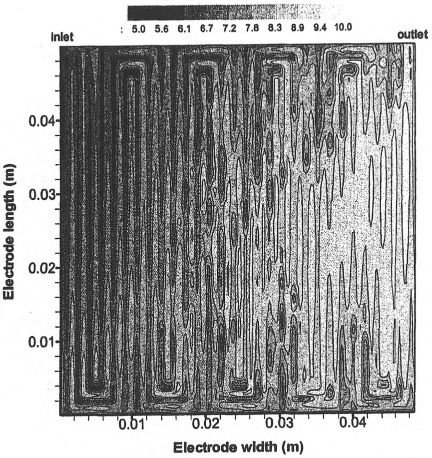

Fig. 4b: Membrane conductivity distribution, $\sigma_{avg} = 7.5$ S/m.

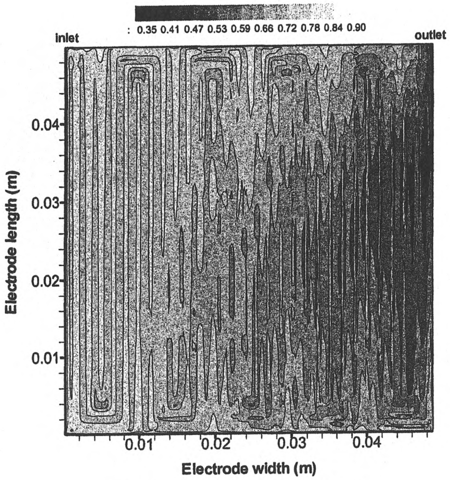

Fig. 4c: Temperature distribution, $T_{avg} = 342.2$ K

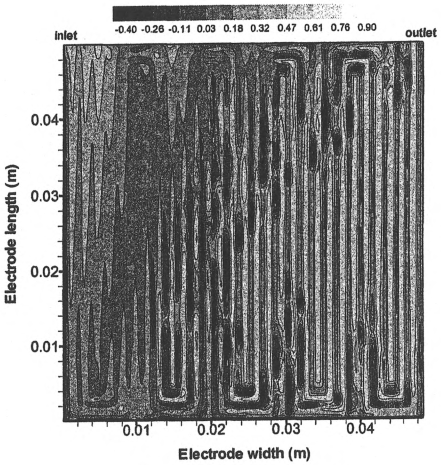

Fig. 4d: alpha distribution, $alpha_{avg} = 0.129$

Fig. 4: Local distributions on MEA surface at 0.650 V for condition #1: 65°C anode and 65°C cathode dew point

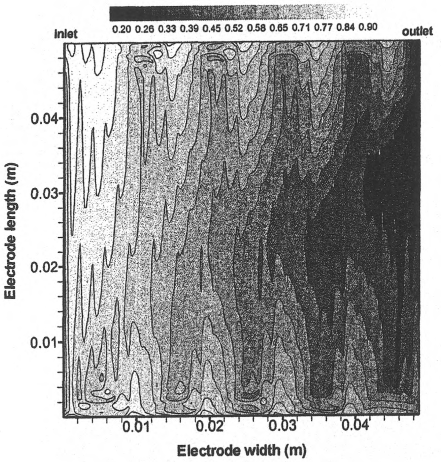

Fig. 5a: Current density distribution, $I_{avg} = 0.569$ A/cm^2.

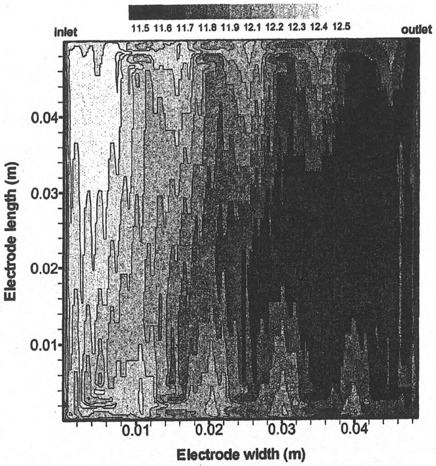

Fig. 5b: Membrane conductivity distribution, $\sigma_{avg} = 12.0$ S/m.

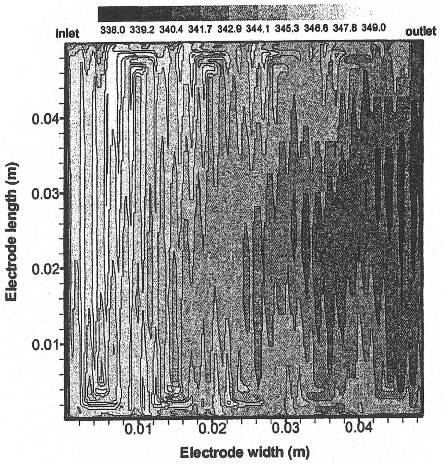

Fig. 5c: Temperature distribution, $T_{avg} = 344$ K

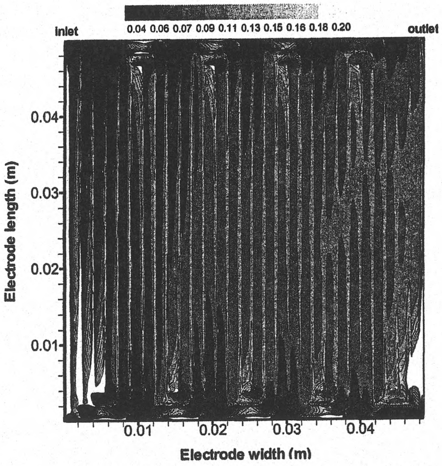

Fig. 5d: liquid water mass fraction at cathode, average = 0.07

Fig. 5: Local distributions on MEA surface at 0.660 V for condition #2: 85°C anode and 85°C cathode dew point

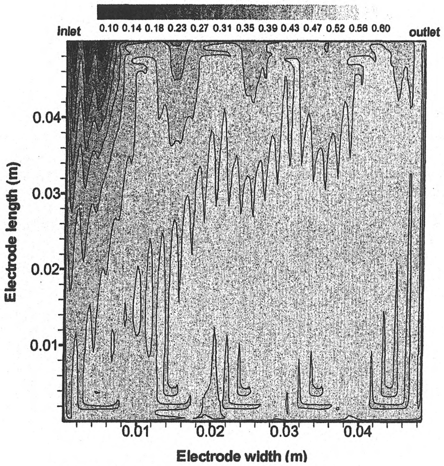

Fig. 6a: Current density distribution,
$I_{avg} = 0.462$ A/cm^2.

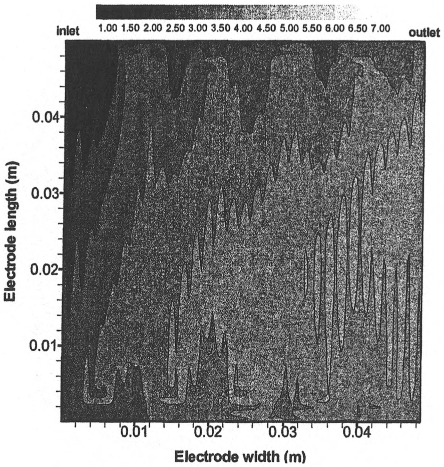

Fig. 6b: Membrane conductivity distribution,
$\sigma_{avg} = 2.66$ S/m.

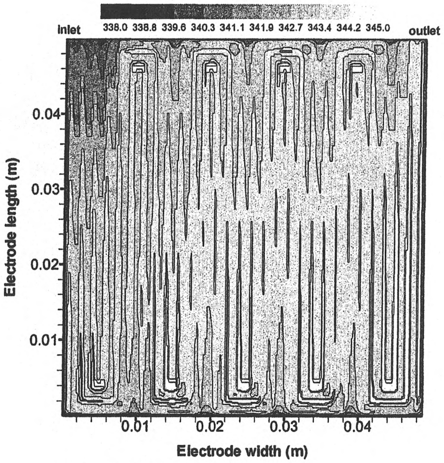

Fig. 6c: Temperature distribution,
$T_{avg} = 342.2$ K

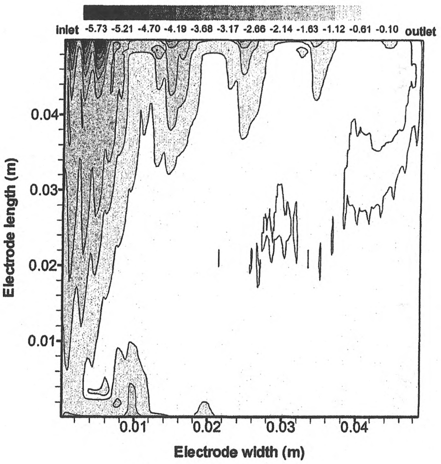

Fig. 6d: alpha distribution,
$alpha_{avg} = -0.70$

Fig. 6: Local distributions on MEA surface at 0.645 V for condition #3:
dry anode and 65°C cathode dew point

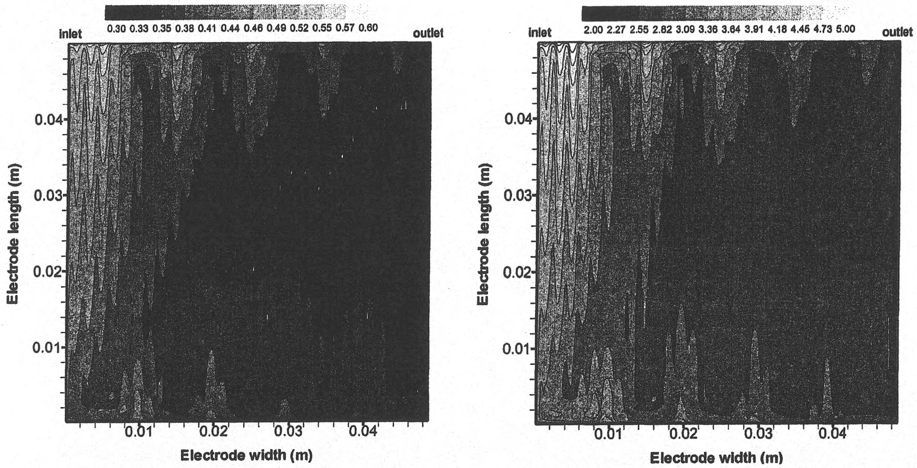

Fig. 7a: Current density distribution, $I_{avg} = 0.298\ A/cm^2$.

Fig. 7b: Membrane conductivity distribution, $\sigma_{avg} = 2.6$ S/m.

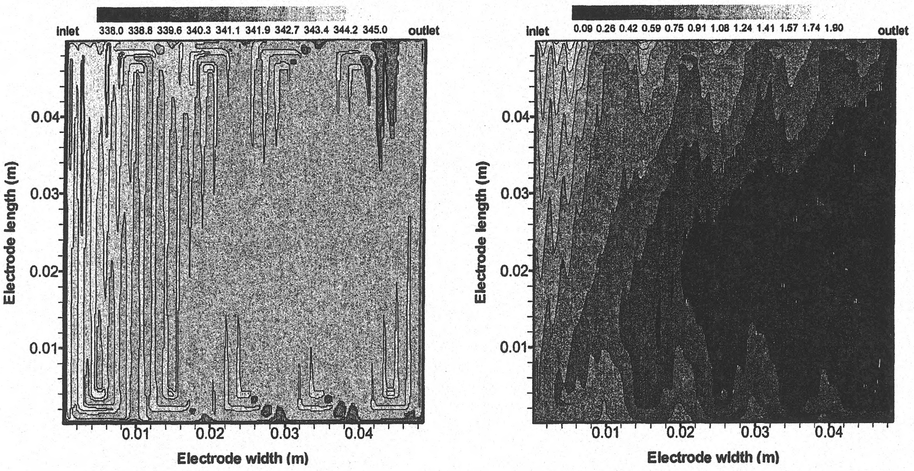

Fig. 7c: Temperature distribution, $T_{avg} = 342.2$ K

Fig. 7d: alpha distribution, $alpha_{avg} = 0.54$

Fig. 7: Local distributions on MEA surface at 0.660 V for condition #4: 65°C anode dew point and dry cathode

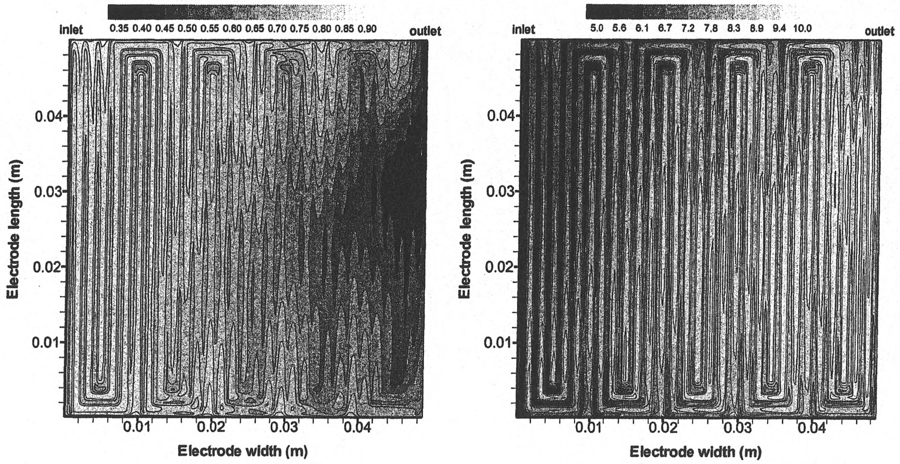

Fig. 8a: current density distribution, $I_{avg} = 0.644$ A/cm^2.

Fig. 8b: Membrane conductivity distribution, $\sigma_{avg} = 7.25$ S/m.

Fig. 8: Local current density (A/cm^2) and membrane conductivity distribution at 0.632 V for condition 65/65°C dew point without micro layer.

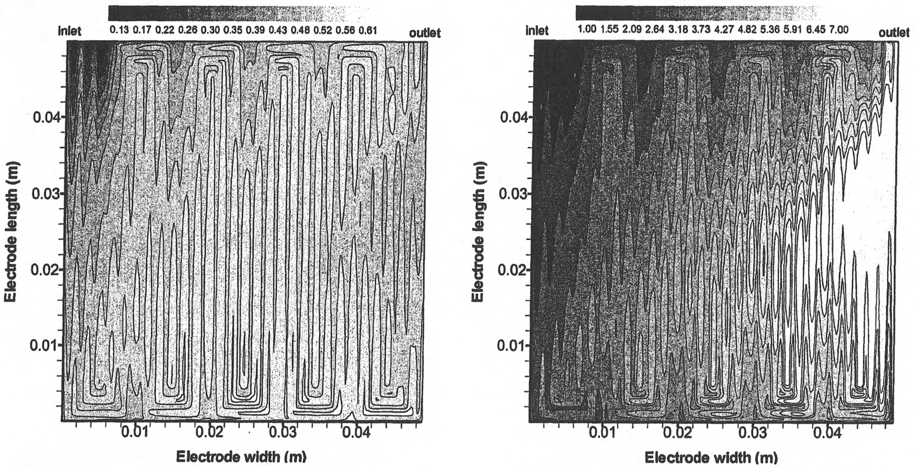

Fig. 9a: current density distribution, $I_{avg} = 0.462$ A/cm^2.

Fig. 9b: Membrane conductivity distribution, $\sigma_{avg} = 3.75$ S/m.

Fig. 9: Local current density (A/cm^2) and membrane conductivity distribution at 0.630 V for condition dry/65°C dew point w/out micro layer.

Proceedings of The Electrochemical Society, PV 2002-31, 212-219 (2002)
DOI: 10.1149/200231.0212PV © The Electrochemical Society

SPATIAL DISTRIBUTION OF THE CO TRANSIENT RESPONSE OF A PEFC

Guido Bender and Thomas A. Zawodzinski [1]
Electronic and Electrochemical Materials and Devices Group
MST-11, MS D429
Los Alamos National Laboratory
Los Alamos, NM 87545
[1] Present Address: Case Western Reserve University, 10900 Euclid Avenue,
Cleveland,OH 44106

ABSTRACT

We report on the investigation of the current distribution of a PEFC under the influence of CO impurities in the hydrogen feed stream by application of the segmented cell system. Stepping the CO partial pressure of the anode feed stream from 0 to 100 ppm CO the current response of the cell was recorded for different stoichiometric flows. A poisoning time delay occurs along the flow path due to the anode flow rate. Also anode and cathode processes, e.g. CO turnover and oxygen mass transport limitation contribute to the time response of the cell.

INTRODUCTION

Practical PEM fuel cells based on perfluorinated ionomer membranes (e.g. Nafion) are likely to use reformed carbon based fuels as the primary source for the anode feed. Besides hydrogen, the reformate may contain trace amounts of carbon monoxide (CO, from a few to several hundred ppm) which would be detrimental to the cell performance. CO strongly adsorbs on the Pt catalyst surface, causing a decrease of the available active Pt surface area for H_2 electro-oxidation resulting in unacceptable losses in electrical current.

The overall current density obtained in a polymer electrolyte fuel cell (PEFC) is an average of widely varying local currents. Gradients of humidification, water generated at the cathode, hydrogen and oxygen partial pressures, and other factors impart a spatial dependence to current generation.

Similarly, time-dependent gradients of CO partial pressure influence the performance of a PEFC. To understand CO poisoning processes in a reformer operated fuel cell system in more detail and to design strategies for improving the overall CO tolerance, information on the current distribution of the fuel cell during CO transients is beneficial. Application of the sophisticated segmented cell approach, recently further developed at Los Alamos, reveals this information. The segmented cell system is capable of measuring current changes of ten individual segments in response to CO injected into the cell and moving downstream. It allows measurement of cell voltage and current of each segment as well as of the total cell with high resolution time. Thus, it can provide localized information about the rate of CO poisoning and the rate of CO recovery along the anode flow channel.

Here, we present a study with the segmented cell that examines the influence of CO on cell performance. Results will be shown for spatially resolved poisoning processes arising from different CO partial pressures and flow rates. Also, the discovery of trace amounts of CO oxidation to CO_2 will be discussed along with the influence of cathode processes onto the anode poisoning process.

EXPERIMENTAL

Measurement Setup

The most recent segmented cell hardware consists of a one-piece cathode and a segmented anode. The cathode has an active area of 104 cm2 with the same outer dimensions as the segmented anode hardware. The anode is composed of 10 separate segments, each with an area of 7.71 cm2 leading to a total active area of 77.1 cm2. Segmentation of the anode catalyst layer, the anode gas diffusion backing, and the current collector was implemented to enable current and CO coverage distribution measurements. Individual current collector plates for the segments allow low contact resistance per segment and result in high measurement accuracy. The flow field is a six fold serpentine feeding the fuel to the segments in consecutive order.

Sample Preparation

Membrane Electrode Assemblies (MEAs) of the segmented cell system were prepared in a two-step process for improving homogeneity of the catalyst layers and durability of the MEAs. Using a machine driven doctor blade spreader the cathode catalyst layer was coated onto a Kapton decal medium, hot pressed, proton exchanged and dried as reported previously [1], [2]. The resulting half-cell was completed by spraying the anode catalyst onto the membrane using an automated spray system build in-house. Thus, geometric integrity of the cell and proper alignment within the setup was ensured.

Typical standard catalyst loadings of the MEAs were approximately 0.3 mg Pt/cm^2 on the cathode and 0.2 mg Pt/cm^2 on the anode with an average loading deviation of smaller than 3%. Both electrodes consisted of supported platinum catalyst (20 % Pt/C ETEK).

Prior to operation, the anode catalyst layer was activated using cyclic voltammetry. For this purpose N_2 was injected into the anode and H_2 into the cathode. The anode was used as the working electrode and the cathode as the reference and counter electrode. CV cycling was performed in the potential range from 0.1 – 1.4 V.

Reference and test measurements assured proper operation of the MEA before any transient measurements were executed.

Operating Conditions

Unless mentioned, the cell was operated under the following conditions, which we entitle as standard conditions. The humidifier temperature for the anode and the cathode were 105 °C and 80 °C respectively. The gas humidification levels were below 100% saturation, especially at high gas flow rates as a result of limited residence time in the humidifier liquid [3]. The temperature of the cell was 80 °C. Operating back pressure for both the anode and the cathode was 30 psig. Gas flows were controlled by electronic mass flow controllers (MKS, RS 485), calibrated with a digital flow meter (Fisher Scientific, Model 650) adjusted for the atmospheric pressure and the temperature in the laboratory. The gases flowed in parallel fashion from cell inlets to cell outlets through six channel serpentine flow fields.

The anode was operated on hydrogen at a fixed stoichiometric gas flow of 1.1, 1.5 or 2.0, calculated for a total cell current of 60 A at a cell voltage of 0.6 V. The cathode was typically operated with a fixed air flow of 4000 sccm, corresponding to a cathodic stoichiometric flow of around 4.

Measurements & Setup

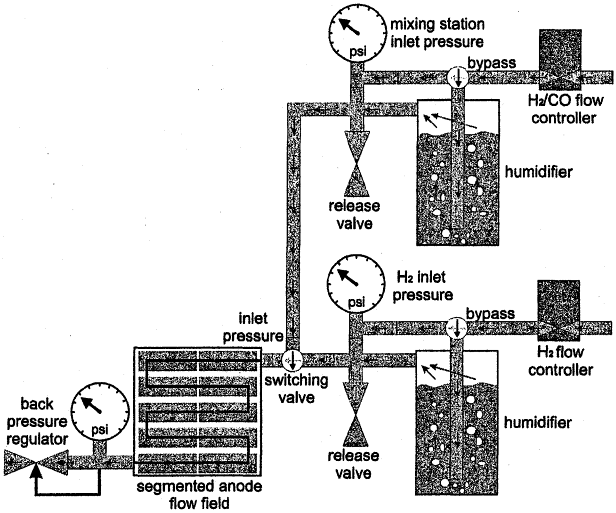

Figure 1: Schematic of CO transient measurements setup for fixed CO partial pressures.

Figure 1 shows a schematic of the transient measurement setup. The inlet consisted of two individual gas feeds, one for the pure hydrogen gas, the other for hydrogen contaminated with CO (H_2/CO). The system included computer controlled mass flow controllers, temperature controlled gas humidifiers, inlet pressure gauges, and pressure release valves.

At the beginning of each measurement, the cell was operated with humidified pure hydrogen for 1 minute. In the meantime, the H_2/CO line was first purged, and then pressurized to the hydrogen inlet pressure. Poisoning of the cell was initiated by switching the gas source from the H_2 line to the H_2/CO line. The release valves helped to avoid over-pressurization of the inlet lines and allowed to switch back to pure hydrogen in the same manner, for testing cell recovery with neat H_2. Substitution of the three-way valve with a T-intersection and a two-way valve, allowed mixing of the two source gases and thus injection of variable concentrations of CO.

The current response of the cell was measured with a Hall sensor setup built in-house, along with three data acquisition cards, and a PC. In house written LabVIEW programs controlled and recorded up to 18 data points per second. Cell voltage, total cell current, single segment voltages and single segment currents were recorded, resulting in twenty-two parallel high speed input channels.

Additionally, four-way valves allowed experiments involving counter-flow of reagents and using gas chromatography.

RESULTS & DISCUSSION

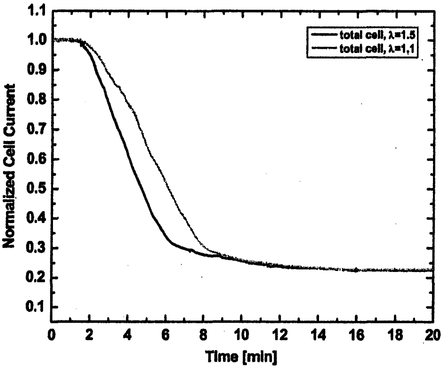

Figure 2: Transient response of a 80 cm^2 PEFC to an increase in CO partial pressure from 0-100 ppm CO at 1 minute operation time. Increasing gas flow rates result in faster degradation of the cell performance. Steady state currents remain constant at both flow rates.

Figure 2 shows the transient response of the normalized total cell current of the segmented cell for stoichiometric hydrogen flows of 1.1 and 1.5, hereafter referred to as 1.1 or 1.5 stoich. Cell currents and segment currents operating on pure hydrogen were measured and averaged during the first minute of operation. Subsequently, the measured currents were divided by this value, generating a normalized current value. At 1 minute operation time the anode was exposed to 100 ppm CO which causes the cell current to drop, due to CO poisoning. Steady state conditions were reached after saturation of the catalyst layer with CO. As in previous studies by Bauman et. al. [4], the saturation time of a platinum electrode was dependent on the anode inlet flux and the CO mole fraction, while the current at steady state conditions was only dependent on the CO mole fraction. Both these effects are visible in the measurement of the total cell transients shown in

Figure 2. With 1.1 stoich, the saturation time was about 10 minutes and with 1.5 stoich about 7 minutes. In both cases the cell eventually reached the same steady state current of about 23% of the initial cell currents. The higher flow rate resulted in a faster decay of cell performance, but the same steady state current.

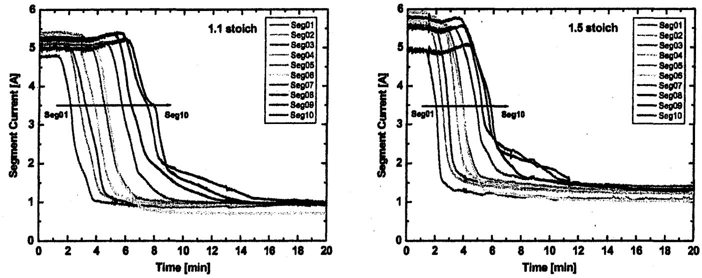

Figure 3: Single segment current distribution for stoichiometric flows of 1.1, and 1.5. The poisoning of the cell is strongly dependent on the position of the segment at a given flow.

Figure 3 shows the distribution of single segment currents of the measurements shown in Figure 2. A strong spatial dependence of the poisoning process occurs for both flow rates. In both cases the poisoning patterns are identical. Current at Seg01, the segment located closest to the inlet, dropped first. Current drops in all of the other segments followed in consecutive order downstream.

The CO injected into the fuel stream gradually poisoned the segments while moving downstream. CO saturation time of each segment dependented on catalyst loading, CO mole fraction, anode flow, and position in the cell. A decrease in anode flow from 1.5 stoich to 1.1 stoich lengthened the time an individual segment is saturated with CO, due to an increased residence time at the individual segments. Consequently, the poisoning delay time between the segments increased. The time for the last segments to become saturated with CO under the given operating conditions, was 12 minutes for 1.5 stoich and 16 minutes for 1.1 stoich respectively.

At the beginning of the poisoning process, downstream segments, e.g. Seg08, Seg09, Seg10, showed a small increase in performance. This effect was stronger at lower anode flow rates. CO adsorption at the cell inlet decreased hydrogen and oxygen utilization causing the concentrations closer to the cell outlet to increase. Also, less water was transported through the MEA at the upstream segments and, due to the smaller currents, less water was produced at the cathode. Consequently, oxygen transport to the reaction sites of the cathode was facilitated. To determine which electrode had a stronger effect on the results, further investigations were carried out in that matter and are described below.

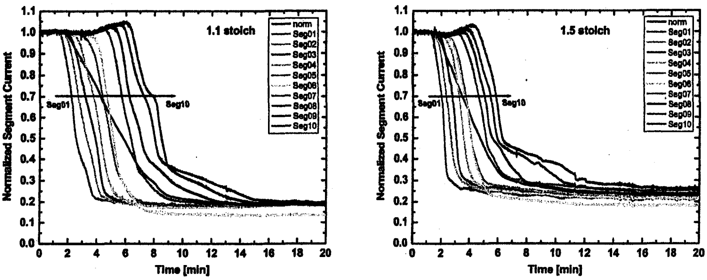

Figure 4: Current distribution of the normalized transient response for stoichiometric flows of 1.1 and 1.5.

The data of the CO transient measurement in normalized form is shown in Figure 4. The features discussed above are more apparent in this format. The poisoning time delay is clearly visible, as well as the small performance increase of the segments near the outlet.

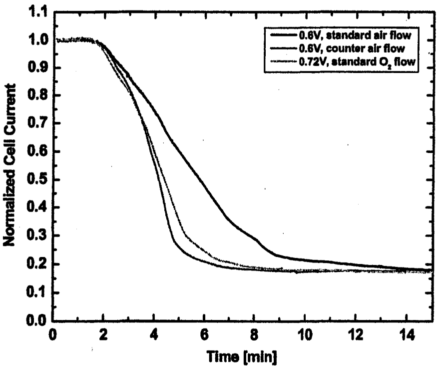

Figure 5: Transient response of PEFC operated at standard air flow, counter air flow and standard oxygen. The cell was operating at a fixed flow of 1.1 stoich before poisoning with 100 ppm CO. Cell voltage varies from 0.6 V for both air flows, to 0.72 V for oxygen operation, to keep the generation of water identical for all measurements.

Figure 5 shows transient measurements of the total cell operating with standard air flow, with counter air flow, and with standard oxygen flow. The cell was operated at the same total cell current before poisoning with 100 ppm CO. Cell operation with O_2 was carried out at 0.72 V, in order to have the same initial current as during operation with air. This adjusted the initial amount of water generated at the cathode to be identical in all of the experiments.

Both variations of the cathode flow with respect to the standard flow, e.g. changing to air counter flow or changing to oxygen flow, show the same effect on the transient measurement of the cell. The cell responds to cell poisoning substantially faster than operating at standard conditions. In both cases steady state conditions are reached at about 8 minutes operation time, compared to about 10-15 minutes of the standard cathode operation mode. This result is very surprising, since the anode flow conditions, including the CO partial pressure were identical.

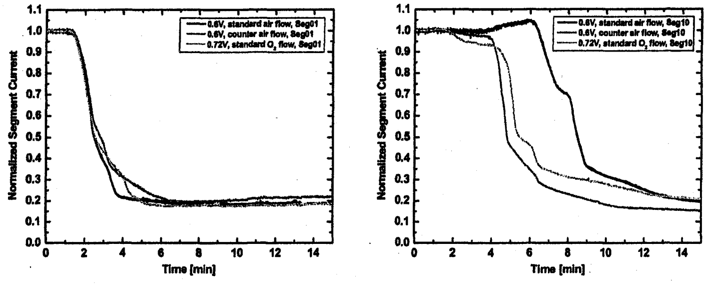

Figure 6: A comparison of the transient response from Seg01 and Seg10 operated at standard air flow, counter air flow, and standard oxygen flow. The poisoning process of Seg01 is identical, proofing identical prepoisoning conditions of the cell. Poisoning varies with oxygen access within the cell. Presence of liquid water and oxygen supply and demand of the cathode influence the poisoning process of the fuel cell.

Figure 6 shows the transient response of Seg01 and Seg10 for the three cases introduced in Figure 5. The transient response of Seg01 is fairly identical. The measurements show identical segment current drops. They reach the same steady state currents of about 20% after 6 minutes operation time. This indicates identical poisoning conditions, identical flow rates, and identical CO partial pressures.

At the cell outlet, the transient response of Seg10 varies for the three measurements. The poisoning process for the standard case is significantly delayed and slower. Instead of observing a starting decay of the cell current at 4 minutes, as in the air counter flow or oxygen case, the segment current increases instead. It starts dropping at about 6 minutes operation time, a poisoning delay of about 2 minutes. Furthermore, the rate of current decay is significantly slower.

How can the cathode flow have a possible influence on anode poisoning processes? Although the cell voltage is kept constant during the measurements, different current densities occur at the various segments due to mass transport limitations and fuel/oxidant concentrations. Consequently different anode and cathode potentials adjust throughout the cell. Since anode and cathode potential is linked together through the electrochemical system, potential changes on one electrode influence the potential situation on the other electrode. The poisoning process is dominated by the potential situation at the anode, but influence of the cathode potential is inevitable. For example increasing oxygen partial pressure will increase the cathode potential, i.e. will decrease the cathode overpotential. Hence, the anode overpotential increases together with the current density of the cell. The increase of the anode potential counteracts CO poisoning and slows the poisoning process. Thus changing the oxygen concentration at the cathode indirectly influences the CO poisoning at the anode.

CONCLUSIONS

We have employed a segmented fuel cell system to investigate CO poisoning processes in a PEFC. Spatial dependence of CO poisoning occurs along the anode feed stream of the cell. During the CO adsorption process, spatial operation conditions within the cell are changing. These occurring processes have an influence on spatial and total cell poisoning delays. Also cathode operation conditions contribute to the poisoning response of the cell, offering new strategies for CO tolerance improvements.

Current research efforts include enhancing our understanding of the interaction between anode and cathode processes with and without CO in the hydrogen feed stream. Furthermore, modeling of the observed effects should help to develop strategies to improve CO tolerance in fuel cell systems.

ACKNOWLEDGEMENTS

We gratefully acknowledge the US DOE Office of Advanced Automotive Technology for support of this work.

REFERENCES

[1] G.Bender, T.A. Zawodzinski, and A.P. Saab, '*Fabrication of High Performance PEFC Membrane Electrode Assemblies Using a Machine Spreader*', to be published

[2] M. S. Wilson, J. A. Valerio, S. Gottesfeld, Electrochimica Acta **40**, 355-363, (1995)

[3] S. Cleghorn, C.R. Derouin, M.S. Wilson, S. Gottesfeld, Journal of Applied Electrochemistry **2**, 663-672, (1998)

[4] J.W. Bauman, T.A. Zawodzinski, Jr., S. Gottesfeld, in *Proton Conducting Membrane Fuel Cells II/1998,* S.Gottesfeld and T.F. Fuller, Editors, PV 98-27, p.136, The Electrochemical Proceedings Series, Pennington, NJ (1999).

Proceedings of The Electrochemical Society, PV 2002-31, 220-247 (2002)
DOI: 10.1149/200231.0220PV © The Electrochemical Society

TRANSIENT AND STEADY STATE CURRENT DENSITY DISTRIBUTION MEASUREMENTS IN A POLYMER ELECTROLYTE FUEL CELL

M. M. Mench[1,2], **C. Y. Wang**[1]
Electrochemical Engine Center, and
Department of Mechanical and Nuclear Engineering
The Pennsylvania State University
University Park, PA 16802

and

Masatoshi Ishikawa
CD-adapco Japan Ltd.
Yokohama, Japan

ABSTRACT

There has been much recent interest and development in methods to accurately measure the current distribution in an operating polymer electrolyte fuel cell. This paper presents results from a novel technique that uses a segmented flow field with standard, non-altered membrane electrode assemblies and gas diffusion layers. Multiple current measurements are taken simultaneously with a multi-channel potentiostat, providing high-precision temporal and spatial distribution data. Current distribution data are shown over a wide variety of test conditions with significant variations across the fuel cell. In addition, the effects of cathode flooding and pore filling with time are investigated, and it is shown that the time scale for liquid accumulation in gas diffusion layer pores is much greater than that of any electrochemical process or gas-phase species transport. In order to facilitate state-of-the-art polymer electrolyte fuel cell (PEFC) model validation, an idealized single-pass serpentine flow field was used, and the exact geometry is presented.

INTRODUCTION

---

[1] Electrochemical Society Active Member

[2] Author to whom correspondence should be addressed: e-mail mmml24@psu.edu; Phone: (814) 865-0060; Fax: (814) 863-4848

The hydrogen polymer electrolyte fuel cell (PEFC) has tremendous promise as a future power system due to its low pollution, high efficiency, and stealth. Many studies, too numerous to completely list, have examined various aspects of PEFC performance as a function of operating conditions (1-10). Gottesfeld wrote an excellent review of PEFC components and operation, and the reader is referred to it for additional information on PEFC fundamentals (11). In addition to experimental characterization, much research has been focused on first-principles based modeling of the PEFC system (12-23). However, advances in modeling of the PEFC have thus far outpaced the ability to experimentally verify the predicted performance. In particular, scant experimental data are presently available regarding current density and species distributions. As indicated by Wang (24), it is this type of detailed validation that will permit an ultimate understanding of the physicochemical phenomena in PEFCs as well as development of useful computer-aided tools for design and development.

Determination of the current distribution is critical to understanding key phenomena including water management, CO poisoning, and reactant distribution effects. Weiser et al. described a novel technique utilizing a magnetic loop array embedded in the current collector plate to measure two-dimensional current distribution of a hydrogen PEFC (25). The authors showed that cell compression can drastically affect the local current density. Stumper et al. demonstrated three methods for the determination of current distribution of a hydrogen PEFC (26). First, the partial membrane electrode assembly (MEA) technique involves either masking different areas or partially catalyzing segments of the MEA to determine local current distribution. Secondly, the subcell technique involves electrically isolating individual locations of catalyzed anode and opposing cathode from the main cell in order to measure the performance of the desired location. In the passive current mapping technique, an array of shunt resistors are located normal to an unmodified MEA surface, between the flowfield and a buss plate. Voltage sensors passively determine the potential drop across each resistor and, through Ohm's law, current distribution though the flow plate is determined. Cleghorn et al. implemented another technique to utilize a printed circuit board for current distribution measurements using a segmented current collector, anode catalyst, and anode gas diffusion layer (27).

While each of the described methods for determination of current distribution has advantages, it is desirable to utilize a non-segmented MEA in order to preserve true fuel cell operation characteristics and avoid highly individualized specialty membranes. MEA segmentation is also undesirable because it does not simulate performance in a true fuel cell environment.

In addition to use of conventional MEAs and good spatial resolution, the ability to determine transient effects from sudden changes in operating conditions is desired. The non-segmented passive current mapping technique approach of Stumper et al. allows transient measurement and has good spatial resolution, but requires a vast array of embedded and highly precise shunt resistors (26). The magnetic loop method of Weiser et al. also allows transient measurements with unaltered MEAs and flowfields, but is more difficult to implement than the other methods and cannot be applied to stacks (25). Recently, Mench and Wang have demonstrated an improved technique for accurate current distribution measurements on direct methanol fuel cells that is applied to hydrogen PEFCs in this work (28). Independently, Noponen et al. (29) and Brett et al., (30) have developed and demonstrated a similar technique as well.

EXPERIMENTAL

Instrumented Cell Design

In order to construct an electrically segregated flowfield, forty-eight, 0.81 mm thick stainless steel current collecting ribs were gold-plated and embedded into an insulating polycarbonate slab with 0.89 mm wide gaps, as described by Finckh (31). The ribs were arranged to produce a single-pass serpentine flowfield. Each rib was affixed to a gold-plated wire that extended through the polycarbonate for current collection. Figure 1 is a schematic diagram detailing the relevant dimensions of the fuel cell flow field. The diameter of the current-conducting wires that interface the gold-plated ribs with the data acquisition source was 0.81 mm. The dimension of the flow channel was chosen to be 2.16 mm wide wide, 3.18 mm in depth and had an average pass length of approximately 71 mm. With a total of 22 serpentine passes, the total path length was 1577 mm.

Teflon® gaskets were press fit over the protruding gold-plated rib landings to form a flush surface with the polycarbonate slab. Two additional sealing gaskets surrounded both gas diffusion layers (GDL) of the MEA to compensate for GDL thickness. Gold plating and use of an optimized compression torque for the cell of 35 in-lbs minimized electrical contact resistance between rib landings and the GDL. Pressure indicating film (Pressurex® by Sensor Products, Inc.) was used to determine the *in-situ* pressure distribution of the landings onto the MEA, as a function of compression torque. The assembly was checked to ensure a homogeneous pressure distribution from all landings onto the gas diffusion layer, thus ensuring an even contact resistance distribution between the gold-plated landings and GDL. The entire fuel cell assembly was leak proof tested to 0.3 MPa under water.

A schematic of the test and control system is shown in Fig. 2. Ultra-high purity (>99.999%) hydrogen and standard compressed air were supplied from compressed gas-cylinders. A steam-injection humidifier system (Lynntech Inc.) was used to provide desired humidification to anode and cathode flows through control of the precise amount of water vapor added to the gas streams. Between humidifier and fuel cell, electric heating tapes were wrapped around the pipes to eliminate any condensation. Directly upstream of the inlet to the fuel cell, a gas sampling port was installed to directly measure the input humidity to the fuel cell by an Agilent 3000 MicroGC with PlotU column. This provided accurate measurement and control of the humidification entering the cell, as described by Mench et al. (32).

The fuel cell system, including all lines leading to the fuel cell, were heated to the desired temperature, which was maintained with several Omega Engineering, Inc. model 8500 PID controllers. The cell and input lines maintained a steady temperature after suitable time to eliminate thermal transients. This start-up time was determined to be about 90 minutes by system check-out tests using thermocouples affixed to the GDL under non-flowing conditions.

To control and measure accurate current/voltage polarization curves, the fuel cell was connected to a multi-channel potentiostat/galvanostat (Arbin Instruments). The active current density mapping method used in this paper is fundamentally similar, and essentially a modification of the passive current density mapping technique of Stumper et al. (26). However, an electrically segmented flowfield/current collector replaces the separate array of shunt resistors normal to the MEA. The segmented flowfield is in direct contact with the unaltered GDL on the anode and cathode. This technique eliminates the challenge to reduce current spreading due to high in-plane conductivity of the flowfield plates. Instead, a gold-plated, electrically segmented current collector is used, and repeatable current density data can be obtained. In this active current density mapping technique, the potentiostat system maintains a constant voltage and the current sensors measure amperage emerging from each segmented current collector location, without the need for shunt resistors.

It is important to note that this technique measures the true current density distribution of an operating cell, as it flows from the gas diffusion layer, not as it emerges from the catalyst layer. Although current spreading through the gas diffusion layer occurs, this is similar to the real operating system. Artificially segmenting the MEA disrupts the true current distribution reaching the current collectors and is therefore inappropriate for these measurements or model validation.

Calculation of Active Area Segments

To calculate the current density of a set of current collecting landings, the active area directly under the landings, and half of the adjacent gas channels, were taken. The reported measurement location along the cathode flow path is the center of this total area in the flow path. Area under current collection landings is counted toward current density calculations. It is important to note that the current density data are represented at a discrete distance along the flow path, when it actually is gathered from a distributed region. In order to represent this area as a discrete location, the distances have been weighted in order to take into account adjacent channels and more accurately represent the mean location of current collection. This discretization gave very consistent results.

The membrane electrode assemblies (MEA) used for testing consisted of Nafion™ 112 as the polymeric membrane, sandwiched between the catalyst and ELAT™ carbon cloth diffusion layers. All MEAs used had a catalyst loading of 0.5 mg Pt/cm^2 on both anode and cathode. Other general operating conditions are given in Table 1. It is important to note that due to the particular nature of the distributed current measurements, variation of the flow to achieve a constant stoichiometry is not possible. Therefore, the stoichiometry is set at a given current density and the flow rate was held constant for individual tests.

RESULTS AND DISCUSSION

Homogeneous Distribution

It is expected that at relatively high mass flow rates with full humidification and low pressures, a nearly uniform distribution of current would result. An experiment was designed to observe this condition. The distributed polarization curve for this experiment is shown in Fig. 3. There is some indication of flooding, as can be seen from the characteristic 'comma' shaped (26,28) local polarization curves for the channels closest to the cathode exit location. The two channels near the end of the cathode path, at $x/L =$ 0.891 and 0.964 (corresponding to 89 and 96% along the length of the single serpentine cathode path), roll over into comma shapes at low cell voltage, while the overall bulk cell output increases. The current density versus fractional location along the cathode flow path at several cell voltages is given in Fig. 4. From Fig. 4, a nearly homogeneous current distribution can be seen, except at very low cell voltage (0.4V) corresponding to high current output and near depletion of hydrogen in the anode.

The Effect of Cathode Stoichiometry

In PEFCs, the performance is extremely sensitive to cathode stoichiometry, due to relatively sluggish oxygen reduction kinetics and mass transport. In order to isolate the effects of stoichiometry from accumulated flooding, a rapid-scan polarization curve was taken to prevent sufficient time for flooding to occur and affect measured performance. *The results of the rapid-scan are therefore appropriate for model validation in the absence of two-phase effects.* For the rapid-scan, the applied voltage was varied at a rate of 5 to 10 mV/s in increments of 50 mV from OCV. This provided very reproducible data with generally higher performance than steady state values, in which thirty minutes to an hour elapse between voltage variations at low cell voltage to allow time for flooding accumulation to reach steady state.

A high anode stoichiometry of 2.5 at 0.75 A/cm^2 was used for this series of tests, so that no appreciable mass transport limitation on the anode exists. Cell humidification was 100% at 90°C and 80°C on the anode and cathode, respectively. Cell temperature was maintained at 80°C and cell inlet pressure was maintained at 1.5 atm. Cathode stoichiometry was varied from 1.5 to 3.0 at 0.75 A/cm^2. It is important to recall that the stoichiometry is set at a given current density. That is, flow rate was held constant during these tests.

Low cathode stoichiometry of 1.5 @ 0.75 A/cm^2. Figures 5 and 6 are plots of the distributed polarization curves and current density versus fractional location along the cathode flow path for the case of low cathode stoichiometry. From Fig. 5, it can be seen that severe mass transport limitations exist at low cell voltage. The comma shaped curves resemble the characteristic shape of flooded distributions from Mench and Wang (28). As discussed, the polarization curves were taken with a high enough voltage scan rate to avoid significant flooding accumulation. Therefore, the performance limitation can be attributed to mass transport losses at the cathode, and the comma shaped curve is a characteristic feature of a fuel cell operating in a mass-limiting condition, whether from flooding or low stoichiometry. The distribution of performance along the cathode channel shown in Fig. 6 is in agreement with this conclusion, as performance decreases monotonically with distance along the cathode channel for high current densities. For low values of current density, a nearly homogeneous distribution is observed, corresponding to the abundant supply of oxygen for these low power conditions.

As discussed, the data on Figs. 5 and 6 were taken with a rapid-scan technique. Figures 7 and 8 are a distributed polarization curve and a performance variation versus location plot, deduced from data taken allowing adequate time to achieve steady state. That is, these figures show the steady state values for the performance at identical conditions of Fig. 5, except about an hour elapsed between each cell voltage increment below 0.6 V. It can be seen that the steady state curves all suffer reduced performance compared to the corresponding results taken with the rapid-scan, especially for lower cell voltage corresponding to larger current density (and hence cathodic water production). This reduced performance is attributable to the pore blockage effect of liquid accumulation in the GDL resulting from cathode flooding at high current densities.

Increased cathode stoichiometry of 2.0 @ 0.75 A/cm^2. As the cathode stoichiometry and flowrate of air is increased, it is expected that the severe performance limitations observed in Fig. 5 would be somewhat diminished. This is observed, as can be seen in Figs. 9-12, which are polarization and current density distribution plots for a cathode stoichiometry of 2.0 at 0.75 A/cm^2 for both rapid-scan and steady-state measurements. Although the performance is improved compared to the case of 1.5 cathode stoichiometry, significant mass transport limitations still exist at high current densities. In comparison of Fig. 5 to Fig. 9, the bulk fuel cell performance is increased, and the location and severity of the decrease in output has been pushed farther downstream the cathode flow channel. The point at which the distributed polarization curve rolls over into a mass-limited comma shape has been pushed from ~40% downstream to ~60% downstream. Once again, the steady state curves all suffer reduced performance compared to the corresponding results taken with the rapid-scan, especially at lower cell voltages corresponding to larger mean current density.

Increased cathode stoichiometry of 2.5 @ 0.75 A/cm^2. Figures 13 and 14 are a rapid-scan distributed polarization plot and a current density versus location plot for a cathode stoichiometry of 2.5 @ 0.75 A/cm^2. This condition is expected to exhibit decreased mass transport limitation on the cathode, compared to lower cathode stoichiometry. From Fig. 13 it is seen that the distributed polarization curves are more uniform, indicating a more homogeneous overall distribution compared to lower stoichiometry conditions. Also, the bulk fuel cell performance is increased, and the location and severity of the decrease in output due to mass transport has been pushed farther downstream the cathode flow channel. The location at which the distributed polarization curve rolls over into a comma shape has been pushed from ~60% for the ξ_c=2.0 case to ~80% downstream for this case. Even at this high cathode stoichiometry, there is still some portion of the fuel cell that is not performing to full potential due to cathode reactant deficiency.

Increased cathode stoichiometry of 3.0 @ 0.75 A/cm^2. Figures 15 and 16 show a rapid-scan distributed polarization curve and a current density versus location curve for a cathode stoichiometry of 3.0 @ 0.75 A/cm^2. From Fig. 15 it is seen that the distributed polarization curves are much closer together, indicating a more homogeneous overall distribution compared to lower stoichiometry cases. There does not appear to be any location within the cathode that suffers severe performance loss due to oxidizer mass limitation at any current density tested. Each increase in cathode stoichiometry of 0.5 at 0.75 A/cm^2 pushed the location of performance rollover downstream 20%, beginning with a roll-over location of ~40% at ξ_c=1.5. This is not a universal result, and is a function of cell design and total performance at a given voltage.

Discussion on flooding and definition of steady state

It is appropriate to discuss the definition of steady-state used. This is because in a vast majority of PEFC publications, the definition is ambiguous. Much of the published work reports polarization data based on rapid-scan polarization curves, similar to those presented in this work where noted. While these data are highly useful for separation of the effects of flooding from stoichiometry mass transport limitations or humidity variation, it does not necessarily represent the true steady-state that would be achieved if the given cell condition was held indefinitely.

Where flooding occurs, the location of flooding will show a gradual decrease in performance corresponding to the gradual accumulation of liquid water. This process can take minutes to hours, depending on the initial condition of the MEA. Figure 17 shows flooding degradation for a sudden cell voltage perturbation from 0.55 to 0.50 V. Immediately following perturbation, the current density generally adjusts to a high value corresponding to the increased overpotential to drive the electrochemical reactions. The performance then degrades to a steady-state value. More interestingly, it is seen that the local current densities near the cathode inlet (i.e. x/L = 0.036 and x/L=0.109) jump to high values and remain there due to the absence of pore flooding. In the middle section of the fuel cell (i.e. x/L = 0.370 and x/L=0.543), the local current densities undergo substantial decay after the initial jump in performance due to liquid accumulation in pores and more moist air coming from the upstream. Near the cathode exit, the local current densities do not respond to the initial voltage perturbation much, due to depleted reactant, and then experience a similar decay due to flooding.

It has been observed that, depending on the initial state, there can be multiple steady states, depending on the history of operation. This is a result of the relatively long time scales of GDL pore filling and recovery compared to electrochemical and gas transport processes. As an example, once flooding has been allowed to fully saturate the gas diffusion layer, a sudden decrease in cell voltage will not induce much change in output. However, the same voltage perturbation occurring from a non-flooded initial condition will induce a sharp initial change, flowed by a gradual flooding process to nearly the same final 'fully flooded' state. Therefore, transient flooding data are highly dependent on initial conditions. A thorough treatment of these transient flooding effects is beyond the scope of this paper.

CONCLUSIONS

A robust current mapping technique based on segmented flow field and a multi-channel potentiostat, previously implemented on a direct methanol fuel cell, was successfully used with H_2 PEFCs. Along with other diagnostic techniques such as water distribution mapping (32), this current mapping technique provides an important tool to understand water management and reactant distribution in PEFCs. While simple to implement and convenient to measure, this technique has been demonstrated to provide spatial and temporal current distribution data with high-resolution. Specifically:

- Benchmark current and species distribution data have been obtained using a specially designed single-pass serpentine fuel cell. These data are particularly valuable for computational fuel cell dynamics (CFCD) model validation.
- Data were presented that systematically show the effect of cathode flow rate. The location within the cathode flow channel of mass-limited performance was shown to be a function of cathode stoichiometry.
- The time scale of cathode flooding was shown to be quite slow relative to other transport and electrochemical phenomena. Transient current density results demonstrate a slow flooding process that does not reach a steady state for several minutes of operation. Recovery is similarly slow.

ACKNOWLEDGEMENTS

Financial support of CD-Adapco Japan is gratefully acknowledged. Additionally, Chao-Yang Wang acknowledges partial support of DOE and Conoco under cooperative agreement No. DEFC26-01NT41098. The authors would also like to acknowledge the contributions of Oliver Finckh and Qunlong Dong in the design of the fuel cell and calibration of the test stand components.

REFERENCES

1. D. M. Bernardi, *J. Electrochem. Soc.*, **137**, 3344 (1990).
2. A. Parthasarathy, S. Srinivasan, A. J. Appleby, and C. Martin, *J. Electrochem. Soc.*, **139**, 2856 (1992).
3. A. Parthasarathy, S. Srinivasan, and A. J. Appleby, and C. Martin, *J. Electrochem. Soc.*, **139**, 2530 (1992).
4. Y. W. Rho, O. A. Velev, S. Srinivasan, and Y. T. Kho, *J. Electrochem. Soc.*, **141**, 3838 (1994).
5. J. C. Amphlett, R. M. Baumert, R. F. Mann, B. A. Peppley, P. R. Roberge, and T. J. Harris, *J. Electrochem. Soc.*, **142**, 9 (1995).
6. R. Mosdale, and S. Srinivasan, *Electrochim. Acta*, **40**, 413 (1995).
7. H. –F. Oetjen, V. M. Schmidt, U. Stimming, and F. Trila, *J. Electrochem. Soc.*, **143**, 3838 (1996).
8. F. N. Büchi, and D. Srinivasan, *J. Electrochem. Soc.*, **144**, 2767 (1997).
9. F. A. Uribe, S. Gottesfeld, and T. A. Zawodzinski, *J. Electrochem. Soc.*, **149**, A293 (2002).
10. E. A. Ticianelli, C. R. Derouin, and S. Srinivasan, *J. Electroanal. Chem.*, **251**, 275, (1988).
11. S. Gottesfeld, in Advances in Electrochemical Science and Engineering, C. Tobias, Editor, **Vol. 5**, Wiley and Sons, New York (1997).
12. T. E. Springer, T. A. Zawodinski, and S. Gottesfeld, *J. Electrochem. Soc.*, **138**, 2334 (1991).
13. D. M. Bernardi and M. W. Verbrugge, *AIChE J.*, **37**, 1151 (1991).
14. D. M. Bernardi, and M. W. Verbrugge, *J. Electrochem. Soc.*, **139**, 2477 (1992).
15. T. E. Springer, M. S. Wilson, and S. Gottesfeld, *J. Electrochem. Soc.*, **140**, 3513 (1993).
16. T. F. Fuller and J. Newman, *J. Electrochem. Soc.*, **140**, 1218 (1993).
17. T. V. Nguyen and R. E. White, *J. Electrochem. Soc.*, **140**, 2178 (1993).
18. C.Y. Wang and W.B. Gu, *J. Electrochem. Soc.*, **145**, (1998).
19. V. Gurau, H. Liu, and S. Kakac, *AIChE J.*, **44**, 2410 (1998).
20. J. S. Yi and T. V. Nguyen, *J. Electrochem. Soc.*, **146**, 38 (1999).
21. S. Um, C. Y. Wang and K. S. Chen, *J. Electrochem. Soc.*, **147**, 4485 (2000).
22. Z. H. Wang, C. Y. Wang and K. S. Chen, *J. Power Sources*, **94**, 40 (2001).
23. C. Y. Wang, S. Um, H. Meng, U. Pasaogullari, and Y. Wang, "Computational fuel cell dynamics (CFCD) models," *in 2002 Fuel Cell Seminar*, Nov. (2002).
24. C. Y. Wang, "Two-phase flow and transport in PEM fuel cells," *in Handbook of Fuel Cells*, John Wiley and Sons, (2002).
25. C. Wieser, A. Helmbold, and E. Gülzow, *J. of Appl. Electrochem.*, **30**, 803 (2000).
26. J. Stumper, S. Campell, D. Wilkinson, M. Johnson, and M. Davis, *Electrochim. Acta*, **43**, 3773 (1998).
27. S. Cleghorn, C. Derouin, M. Wilson, and S. Gottesfeld, *J. of Appl. Electrochem.*, **28**, 663 (1998).

REFERENCES

28. M. Mench, and C.Y. Wang, *J. Electrochem. Soc.*, **150,** A79 (2003).
29. M. Noponen, T. Mennola, M. Mikkola, T. Hottinen, and P. Lund, *J. Power Sources*, **106**, 304 (2002).
30. D. Brett, S. Atkins, N. Brandon, V. Vesovic, N. Vasileiadis, and A. Kucernak, *Electrochem. Comm.* **3**, 628 (2001).
31. O. H. Finckh, "Dilution effects and current distribution on hydrogen proton exchange membrane fuel cells," MS Thesis, *The Pennsylvania State University*, May 2002.
32. M. M. Mench, Q. L. Dong and C. Y. Wang, "*In Situ* water distribution measurements in an operating polymer electrolyte fuel cell", *Proceedings of the 202nd meeting of the Electrochemical Society*: Proton Conducting Membrane Fuel Cells III, J.W. Van Zee, M. Murthy, T.F. Fuller and S. Gottesfeld, Eds. (2003).

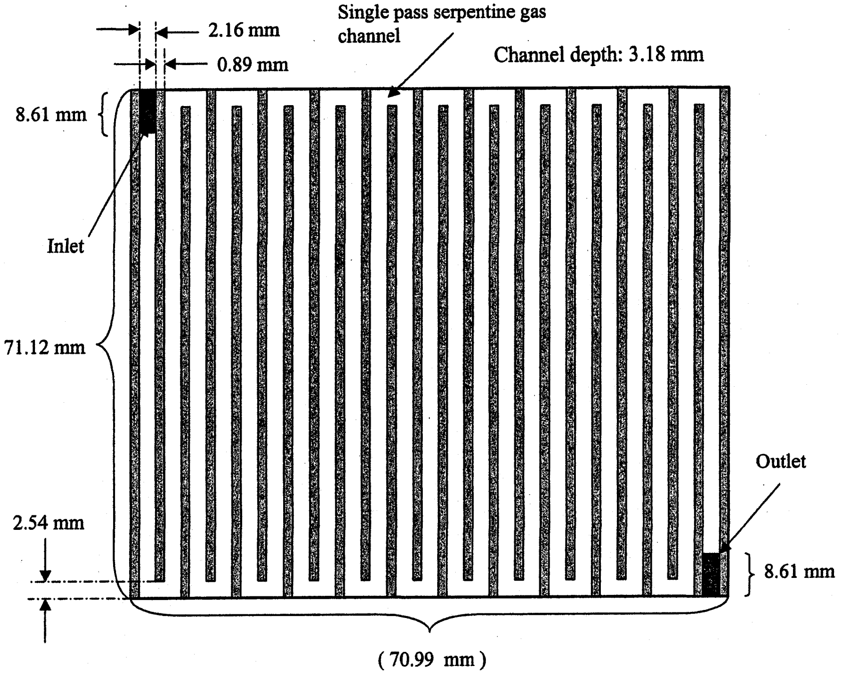

Figure 1. Schematic diagram of the 50 cm^2 instrumented test cell showing relevant dimensions.

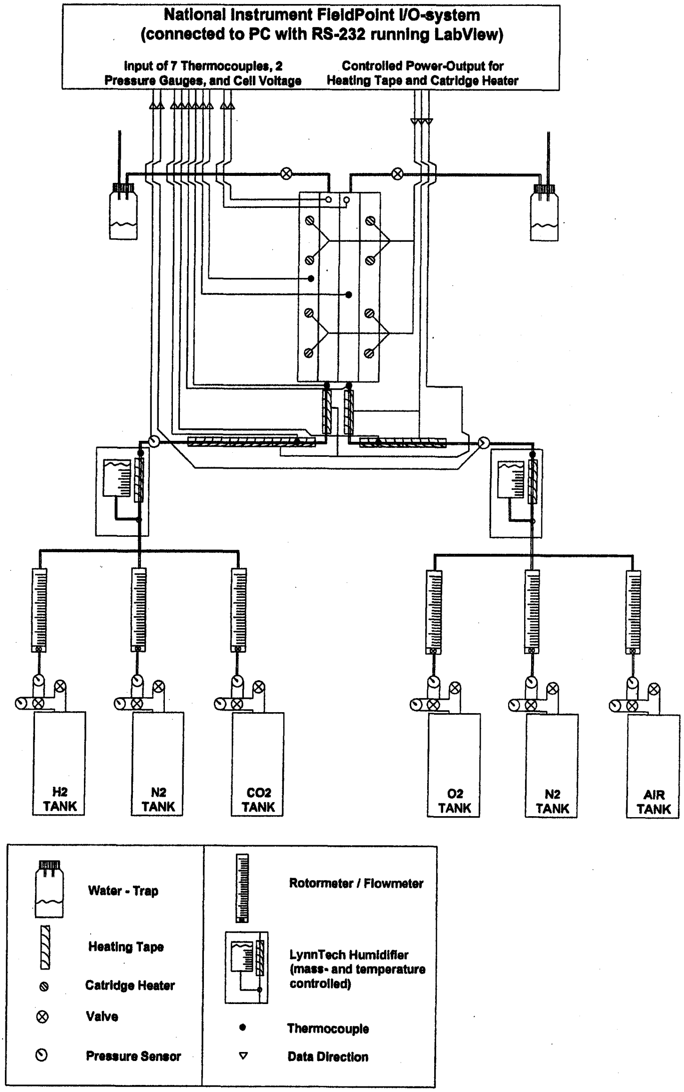

Figure 2. Schematic of the experimental test stand and control system.

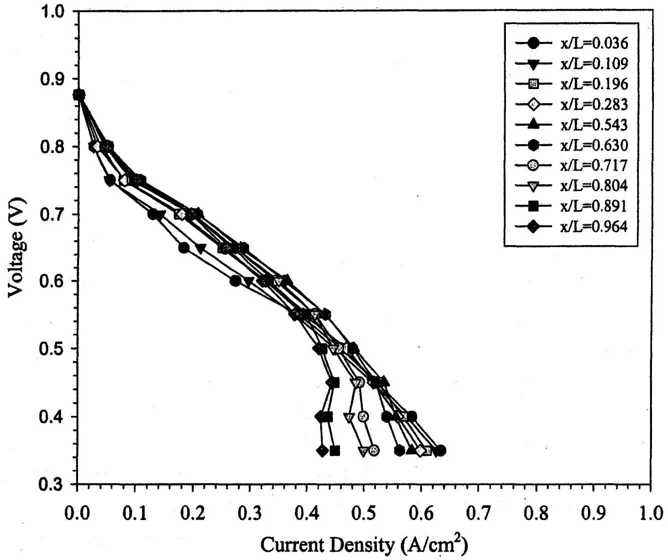

Figure 3. Steady-state distributed polarization curve for a low pressure, fully humidified, high flow rate condition. Cell temperature: 80°C, anode inlet humidity: 100% RH @ 90°C, cathode inlet humidity: 100% RH @ 80°C, ξ_a: 1.0 @ 0.7 A/cm^2, ξ_c: 2.5 @ 0.7 A/cm^2, anode and cathode exit pressure: 1 atm.

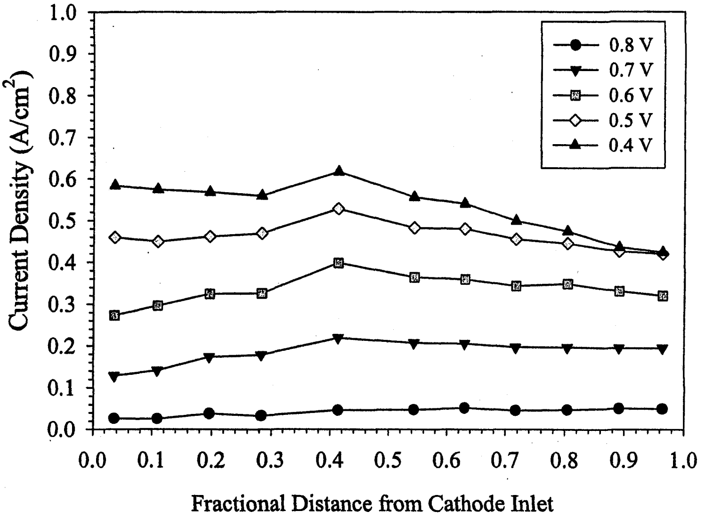

Figure 4. Performance versus fractional location along the cathode path for a fully humidified, high flow rate conditions. Cell temperature: 80°C, anode inlet humidity: 100% RH @ 90°C, cathode inlet humidity: 100% RH @ 80°C, ξ_a: 1.0 @ 0.7 A/cm^2, ξ_c: 2.5 @ 0.7 A/cm^2, anode and cathode exit pressure: 1 atm.

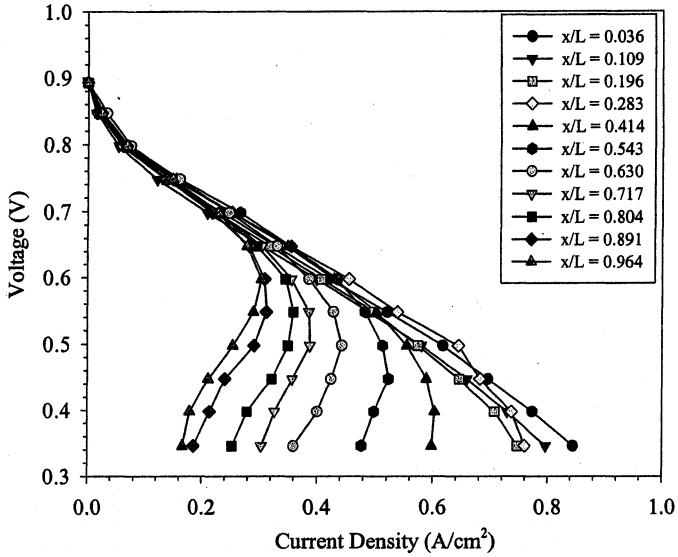

Figure 5. Distributed rapid-scan polarization curve for low cathode stoichiometry of 1.5 @ 0.75 A/cm^2, showing mass transport limited performance. Cell temperature: 80°C, anode inlet humidity: 100% RH @ 90°C, cathode inlet humidity: 100% RH @ 80°C, ξ_a: 2.5 @ 0.75 A/cm^2, anode and cathode exit pressure: 1.5 atm.

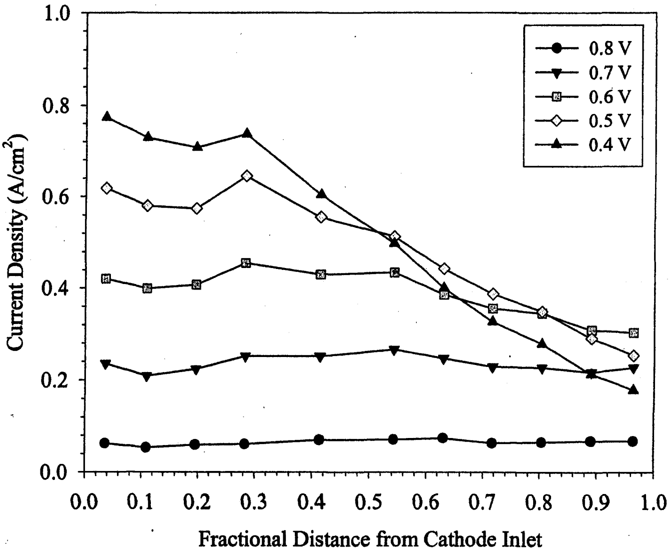

Figure 6. Rapid-scan performance versus fractional location for low cathode stoichiometry of 1.5 @ 0.75 A/cm^2, showing mass transport limited performance at high current density. Cell temperature: 80°C, anode inlet humidity: 100% RH @ 90°C, cathode inlet humidity: 100% RH @ 80°C, ξ_a: 2.5 @ 0.75 A/cm^2, anode and cathode exit pressure: 1.5 atm.

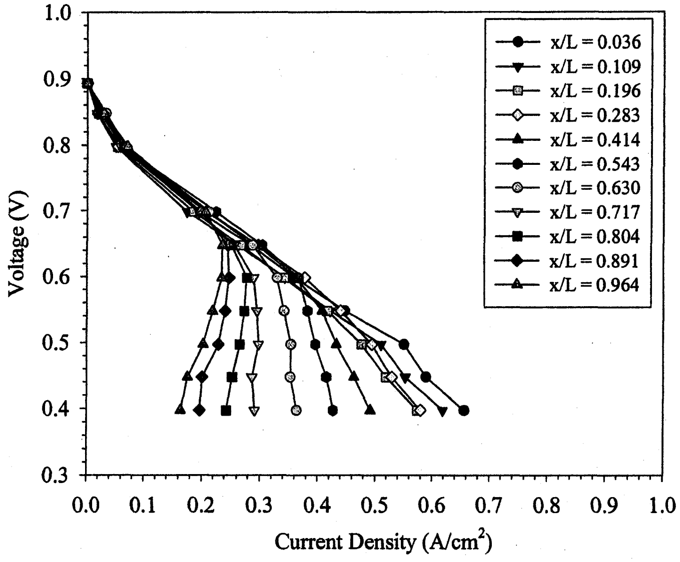

Figure 7. Distributed steady state polarization curve for low cathode stoichiometry of 1.5 @ 0.75 A/cm^2, showing mass transport limited performance. Cell temperature: 80°C, anode inlet humidity: 100% RH @ 90°C, cathode inlet humidity: 100% RH @ 80°C, ξ_a: 2.5 @ 0.75 A/cm^2, anode and cathode exit pressure: 1.5 atm.

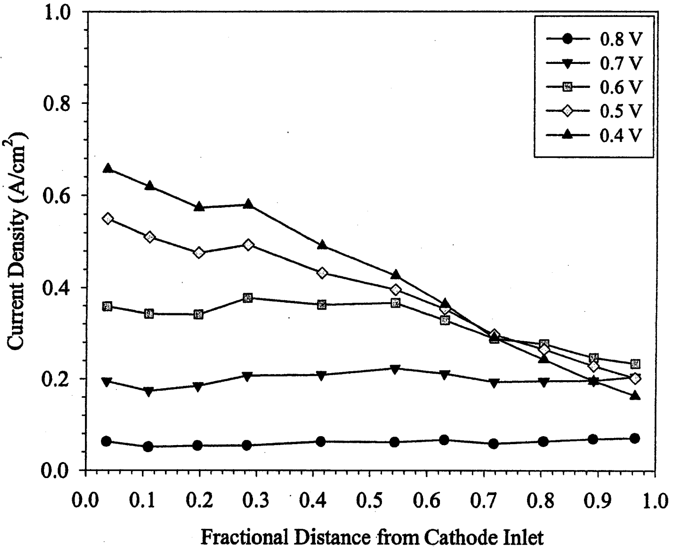

Figure 8. Steady-state performance versus fractional location for low cathode stoichiometry of 1.5 @ 0.75 A/cm^2, showing mass transport limited performance at high current density. Cell temperature: 80°C, anode inlet humidity: 100% RH @ 90°C, cathode inlet humidity: 100% RH @ 80°C, ξ_a: 2.5 @ 0.75 A/cm^2, anode and cathode exit pressure: 1.5 atm.

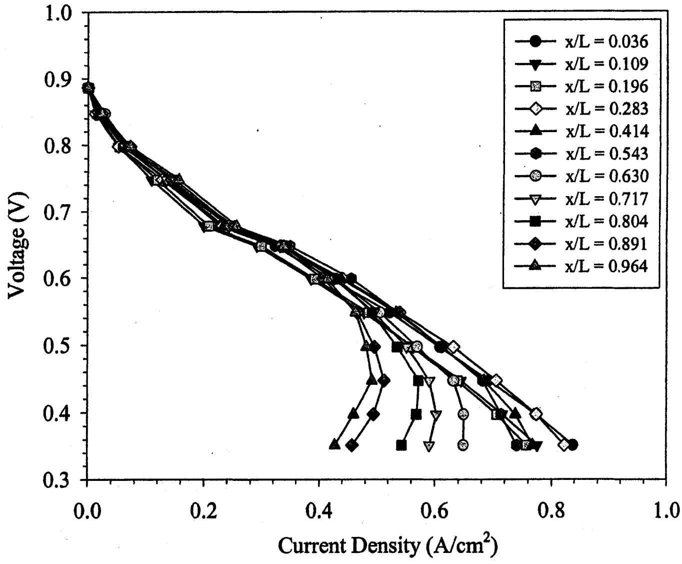

Figure 9. Rapid-scan distributed polarization curve at a cathode stoichiometry of 2.0 @ 0.75 A/cm^2, showing reduced mass transport limited performance. Cell temperature: 80°C, anode inlet humidity: 100% RH @ 90°C, cathode inlet humidity: 100% RH @ 80°C, ξ_a: 2.5 @ 0.75 A/cm^2, anode and cathode exit pressure: 1.5 atm.

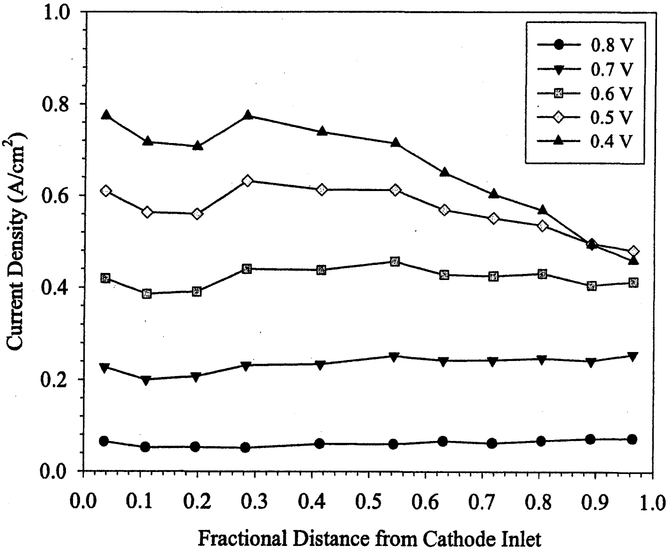

Figure 10. Rapid-scan performance versus fractional location at a cathode stoichiometry of 2.0 @ 0.75 A/cm^2, showing mass transport limited performance at high current density. Cell temperature: 80°C, anode inlet humidity: 100% RH @ 90°C, cathode inlet humidity: 100% RH @ 80°C, ξ_a: 2.5 @ 0.75 A/cm^2, anode and cathode exit pressure: 1.5 atm.

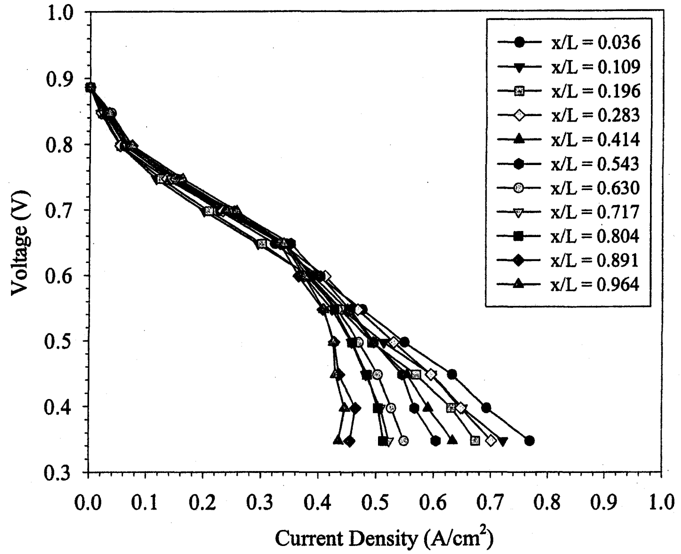

Figure 11. Distributed steady state polarization curve at a cathode stoichiometry of 2.0 @ 0.75 A/cm^2, showing mass transport limited performance. Cell temperature: 80°C, anode inlet humidity: 100% RH @ 90°C, cathode inlet humidity: 100% RH @ 80°C, ξ_a: 2.5 @ 0.75 A/cm^2, anode and cathode exit pressure: 1.5 atm.

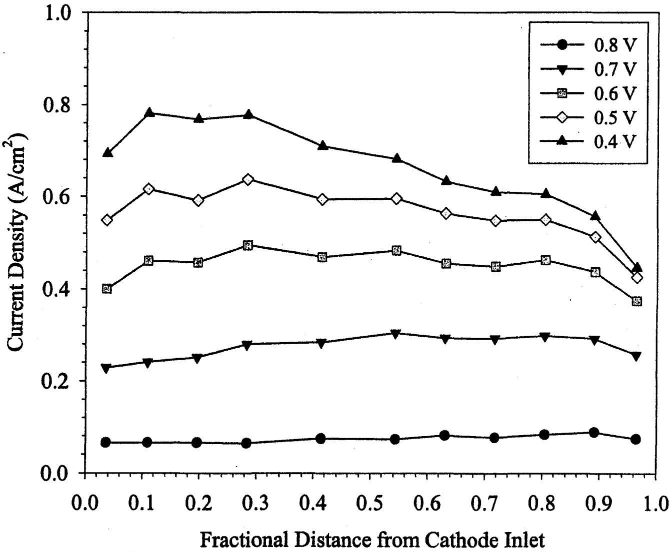

Figure 12. Steady-state performance versus fractional location at a cathode stoichiometry of 2.0 @ 0.75 A/cm^2, showing mass transport limited performance at high current density. Cell temperature: 80°C, anode inlet humidity: 100% RH @ 90°C, cathode inlet humidity: 100% RH @ 80°C, ξ_a: 2.5 @ 0.75 A/cm^2, anode and cathode exit pressure: 1.5 atm.

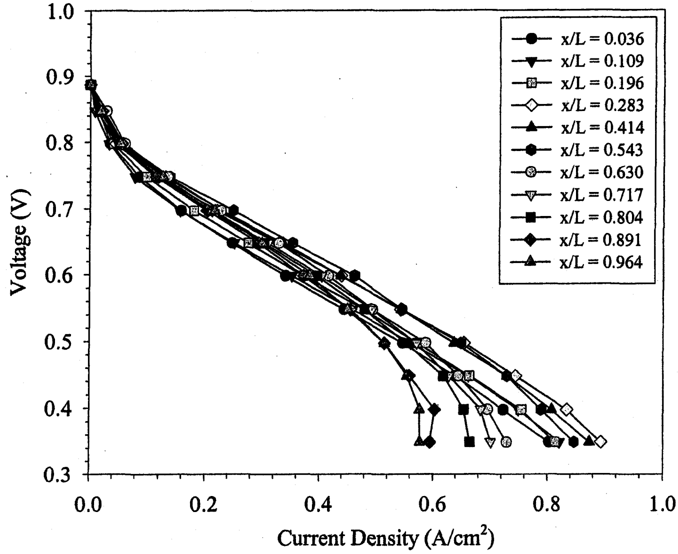

Figure 13. Distributed rapid-scan polarization curve for a cathode stoichiometry of 2.5 @ 0.75 A/cm^2. Cell temperature: 80°C, anode inlet humidity: 100% RH @ 90°C, cathode inlet humidity: 100% RH @ 80°C, ξ_a: 2.5 @ 0.75 A/cm^2, anode and cathode exit pressure: 1.5 atm.

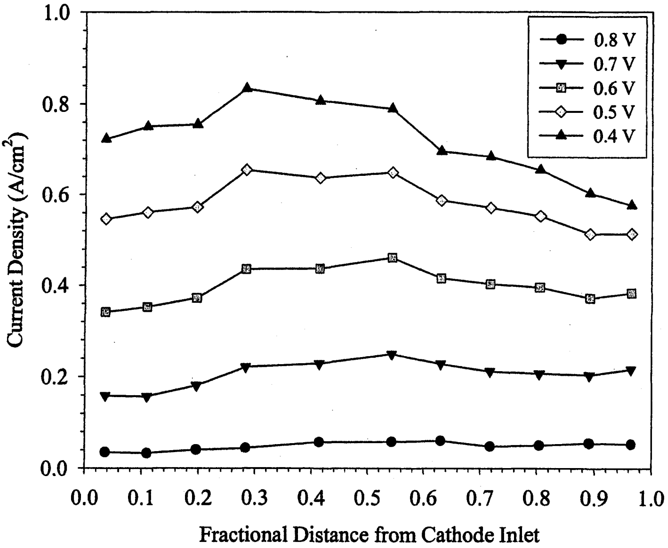

Figure 14. Rapid-scan performance versus fractional location for a cathode stoichiometry of 2.5 @ 0.75 A/cm^2. Cell temperature: 80°C, anode inlet humidity: 100% RH @ 90°C, cathode inlet humidity: 100% RH @ 80°C, ξ_a: 2.5 @ 0.75 A/cm^2, anode and cathode exit pressure: 1.5 atm.

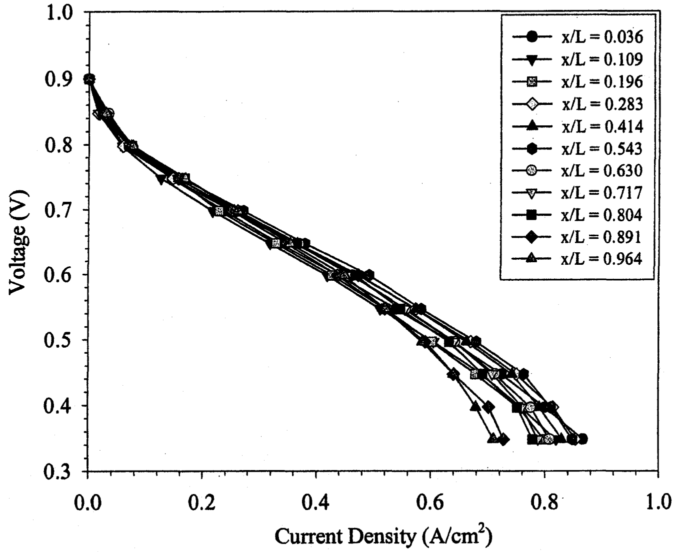

Figure 15. Distributed rapid-scan polarization curve for a cathode stoichiometry of 3.0 @ 0.75 A/cm^2. Cell temperature: 80°C, anode inlet humidity: 100% RH @ 90°C, cathode inlet humidity: 100% RH @ 80°C, ξ_a: 2.5 @ 0.75 A/cm^2, anode and cathode exit pressure: 1.5 atm.

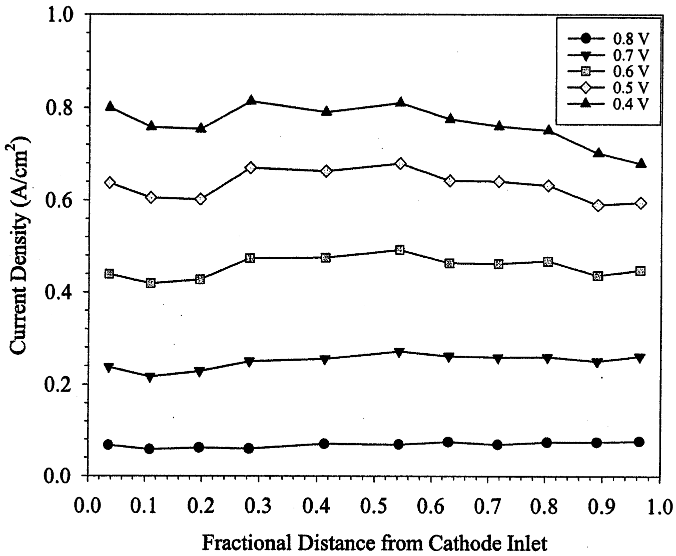

Figure 16. Rapid-scan performance versus fractional location for a cathode stoichiometry of 3.0 @ 0.75 A/cm^2. Cell temperature: 80°C, anode inlet humidity: 100% RH @ 90°C, cathode inlet humidity: 100% RH @ 80°C, ξ_a: 2.5 @ 0.75 A/cm^2, anode and cathode exit pressure: 1.5 atm.

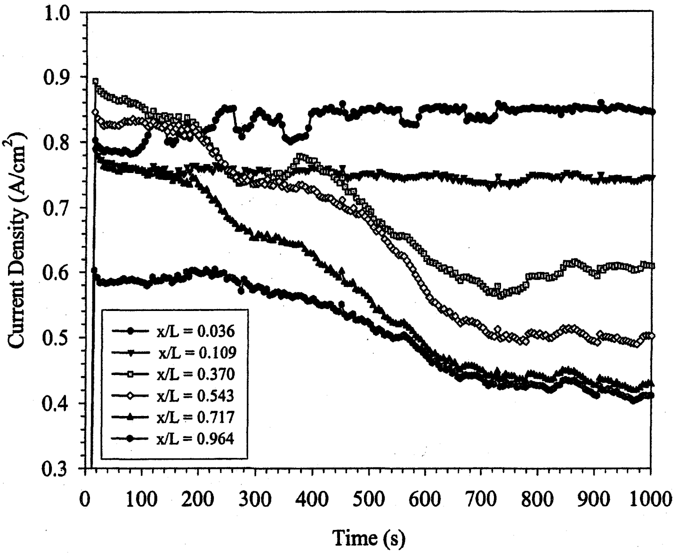

Figure 17. Distributed performance data after perturbation from $V_{cell} = 0.55$ V to $V_{cell} = 0.5$ V. Slow flooding accumulation is seen to degrade performance over nearly 20 minutes. Transient performance Cell temperature: 80°C, anode inlet humidity: 100% RH @ 90°C, cathode inlet humidity: 100% RH @ 80°C, ξ_a: 1.5 @ 1.0 A/cm^2, ξ_c: 2.5 @ 1.0 A/cm^2, anode and cathode exit pressure: 2 atm.

Table 1. Baseline operating conditions.

Parameter	Value	Units
Electrolyte	Nafion 112	NA
Gas diffusion layer	ELAT® (De Nora North America) anode and cathode	NA
Catalyst loading (carbon supported)	0.5	mg/cm^2
Cell temperature	80	°C
Anode inlet temperature	90	°C
Cathode inlet temperature	80	°C
Anode and cathode pressure	0.1-0.2	MPa
Anode humidification	100% at 90°C	NA
Cathode humidification	100% at 80°C	NA
Anode gas	Ultra high purity H_2 (>99.999 %)	NA
Cathode gas	Commercial air (79% N_2, 21% O_2)	NA

Proceedings of The Electrochemical Society, PV 2002-31, 248-256 (2002)
DOI: 10.1149/200231.0248PV © The Electrochemical Society

MEASUREMENT OF THE DISTRIBUTIONS OF LOCAL CURRENT DENSITY AND LOCAL IONIC RESISTANCE OF PEFCS

Y. Morimoto, T. Suzuki and H. Yamada

Toyota Central R&D Laboratories, Inc.
Nagakute, Aichi 480-1192, Japan
Email: morimoto@mosk.tytlabs.co.jp

ABSTRACT

An experimental apparatus for a PEFC was constructed with which the local ionic resistance distribution can be measured as well as the local reaction current distribution, using segmented current collectors and an AC resistance meter. The apparatus presented a clear view on the current distribution and its causes: hydration and dehydration of the membrane and the oxygen consumption along the gas streams. The effects of flow direction, gas stoichiometry and humidification were examined.

INTRODUCTION

In a standard fuel cell experiment, the primary interest is focused on its voltage-current relationship because it indicates the overall performance of the cell. To analyze the properties of the cell in detail, however, this relationship is not relevant because the current density is not uniform in most cases. One of the main causes of this nonuniformity is that the reactant gases flown on the electrode are consumed gradually along the way. In addition, water, the reaction product, is accumulated and affects the conductivity of the membrane and the gas diffusion. To obtain local information of a cell, several attempts have been made recently. Gottesfeld *et al.* applied a printed circuit board on segmented current-collectors and two load boxes and obtained the current of each segment by introducing the current from a targeted segment to one load box while the rest of the current was introduced to the other load box [1]. Stumper *et al.* used graphite blocks as shunt resistors contacting with the back of a flow-field/current-collector [2]. Wieser *et al.* applied a Hall sensor to obtain the local current density [3]. In either case, although the current density distributions were successfully obtained, the causes of the distributions were still only speculated and more detailed local information has been craved.

In this study, we introduce a simple but effective method to determine the local ionic resistance as well as the local current density. Ionic resistance of a whole fuel cell is usually measured by the current interruption method or the AC impedance method and IR correction is carried out to expose other overpotentials: reaction and concentration overpotentials. This approach, however, can be misleading because the local resistance also can be nonuniform and the local current density distribution does not necessarily correspond with the local resistance distribution. Therefore, determining the local ionic resistance along with the local current density is an essential first step for the performance analysis of a cell.

EXPERIMENTAL

Principle of Measurement

Using a segmented flow-field/current-collector, it is relatively simple to obtain the local current flowing into each segment by directly measuring the current using a cramp type current meter or using a shunt resistor and a DC voltmeter. Figure 2 shows the schematic diagram of the system using the latter. The DC voltage drop in the shunt resistor is measured with a DC voltmeter. Using the Ohm's law, the DC current, $I_d{}^i$, flown to the segment *i*, is determined by:

$$I_d{}^i = \frac{V_d{}^i}{R_s} \qquad [1]$$

where $V_d{}^i$ is the measured DC voltage drop in the shunt resistor; and R_s is the resistance of the shunt resistors.

To obtain a local resistance, an AC impedance technique is necessary. In this system, an AC voltage of 1 kHz is applied between the cathode and the anode. The AC current, $I_a{}^i$, flown to the segment *i*, is also determined by:

$$I_a{}^i = \frac{V_a{}^i}{R_s} \qquad [2]$$

where $V_a{}^i$ is the measured AC voltage drop in the shunt resistor. Assuming this segmental AC current is inversely proportional to the local cell resistance of the area that the segment is facing, the local cell resistance, R_i, for the segment *i*, is determined by:

$$R_i = \frac{V_a{}^t}{I_a{}^i} = R_s \frac{V_a{}^t}{V_a{}^i} \qquad [3]$$

where $V_a{}^t$ is the applied AC voltage between the cathode and anode. In this calculation, R_s is assumed to be small enough comparing to the cell resistance, R_i. Even if the diffusion layer, a carbon cloth, is not segmented, the in-plane resistance of the carbon cloth is usually large enough if R_s is selected properly.

If an AC voltmeter and a DC voltmeter or an AC current meter and a DC current meter, are available for each one of the segments, continuous measurement can be carried out. Otherwise, a switch box is necessary to select the shunt resistor to be measured one by one and some interval is needed to finish a set of measurement.

A further simpler instrumentation, which we employed, can be used. Instead of using an AC power supply and an AC voltmeter separately, an AC resistance meter is applicable, which applies a preset AC current between the two current-terminals, measures the AC voltage between the two voltage-terminals and displays the calculated result, *i.e.* the measured AC voltage drop / the preset AC current, as the measured resistance. In this application, the two current-terminals were connected with the cathode and the anode. The two voltage- terminals were also connected with the cathode and the anode firstly to measure the resistance of the whole cell area. The AC terminal voltage can be obtained by:

$$V_a{}^t = I_a{}^t R^t \qquad [4]$$

where $I_a{}^t$ is the AC current preset in the AC resistance meter; and R^t is the measured resistance. Then the two voltage-terminals of the AC resistance meter were switched to the both ends of each shunt resistor one after another. The AC voltage drop in each shunt resistor is determined by:

$$V_a{}^i = I_a{}^t R_s{}^i \qquad [5]$$

where $R_s{}^i$ is the reading of the AC resistance meter. Using Eqs. [4] and [5], Eq. [3] becomes:

$$R_i = R_s \frac{R^t}{R_s{}^i} \qquad [6]$$

Experimentation

An MEA having an active area of 13 cm^2 was used. The anode flow-field/current-collector was segmented to electrically separated 10 small segments according to its flow pattern (Fig.2). The MEA was prepared using techniques similar to those used by Wilson and Gottesfeld [4]. The catalysts were house-made carbon-supported platinum and the loadings are 0.4 mgPt/cm^2 for the both electrodes. An ETEK diffusion layer was used for the both sides.

An AC resistance meter (Hioki 3560), a switch box and a DC voltmeter were controlled and monitored with a PC for automatic control and data acquisition. A DC power supply was used for the FC operation and controlled under the galvanostatic mode. The gas flow rates for the both electrodes were automatically adjusted to corresponding values to the current density using mass flow controllers such that a predetermined gas stoichiometry be maintained even when the current density was varied.

Firstly the cell was operated under the condition that fully humidified oxygen and fully humidified hydrogen were introduced to the cell at 80°C at much higher flow-rates than necessary. The local current density and the local ionic resistance were obtained and the nearly uniform distributions were confirmed. Then the cathode gas was switched to air and the humidification and the gas stoichiometry for the both sides were changed to more realistic conditions. Besides, two types of gas flow direction: co-flow and counter flow, were employed.

RESULTS AND DISCUSSION

Flow Direction

Figures 3 and 4 respectively show the IV & IR characteristics and the current-density and ionic-conductivity distributions when the cell was operated under the non-humidified condition with an air and hydrogen stoichiometry of 1.25 changing the directions of the gas flows: counterflow and co-flow. In the case of co-flow, the ionic conductivity at the gas inlet area (cell 10-7) was too low (high resistance) to allow a meaningful current density in this area. Nevertheless, in the mid area (cell 6-4), the conductivity increased because of produced water, resulting in a large current density. In the gas outlet area (cell 3-1), although the conductivities were high, the current density decreased because of the oxygen depletion effect. On the contrary, in case of counterflow, the conductivities were rather homogeneous. In this case, a dry gas introduced into the area where the other gas humidifies the membrane with produced water [5] and, therefore, no area is excessively dried. As a result, the current density seemed to depend only on the oxygen concentration, which was decreased in the air outlet area.

Gas Stoichiometry

Gas stoichiometry for the both electrodes was varied from 1.25 to 3.0. The IV and IR characteristics and the current and ionic conductivity distributions are shown in Figs. 5 and 6 respectively. At a high gas stoichiometry of 3.0, although the ionic conductivity is low throughout the membrane due to the dehydration, the current density is relatively uniform and high. On the contrary, at a low gas stoichiometry of 1.25, in spite of the uniform and higher conductivity, the current density is drastically decreased from the inlet to the outlet of the air.

Gas Humidification

The gas stoichiometry was fixed to 1.25 and the gas humidification was varied. The results are shown in Figs. 7 and 8. The conductivity was low near the air inlet for low humidification conditions because of membrane dehydration and the current density distribution reflected this conductivity distribution.

CONCLUSION

The ionic resistance distribution was successfully measured as well as the current density distribution with the system described in this paper. Under realistic operation conditions: *i.e.* low humidification and low gas stoichiometry, the current density was heavily nonuniform and this nonuniform current density was attributed quantitatively to the membrane dehydration effect and the O_2 concentration effect. As shown in these results, this system can be used as a very powerful tool to reveal the real situation inside the cell and can give us various hints to improve the performance of PEFCs.

REFERENCES

[1] J. Stumper, S. A. Campbell, D. P. Wilkinson, M. C. Johnson and M. Davis, Electrochim. Acta **43**, 3773(1998)
[2] S .J. C. Cleghorn, C. R. Derouin, M. S. Wilson and S. Gottesfeld, J. Appl. Electrochem. **28**, 663(1998)
[3] Ch. Wieser, A. Helmbold and E. Gülzow, J. Appl. Electrochem. **30**, 803(2000)
[4] M. S. Wilson and S. Gottesfeld, J. Electrochem. Soc., **139** L28(1992)
[5] F. N. Büchi and S. Srinivasan, J. Electrochem. Soc. **144**, 2767(1997)

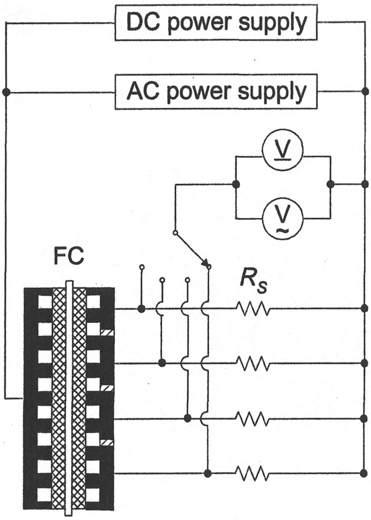

Fig. 1 Circuit diagram of the measuring system.

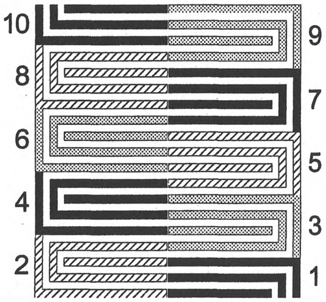

Fig. 2 Schematic image of the segmented current collector. Segmented Cell numbers are shown in the figure. The total active area is 13 cm^2.

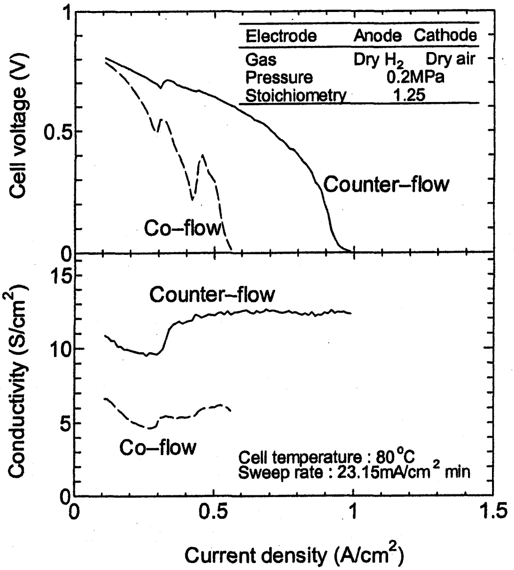

Fig. 3 Comparison between co-flow and counter-flow: IV characteristic and overall ionic conductivity. Cell temperature was 80C. Air and hydrogen were not humidified. Air and hydrogen stoichiometries were 1.25.

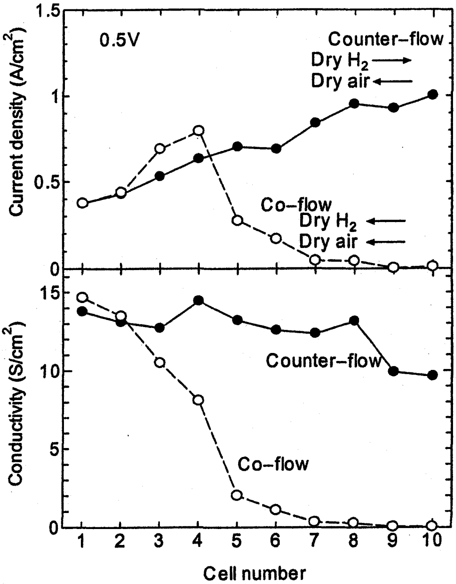

Fig. 4 Distributions of current density and ionic conductivity at 0.5V. The same condition with Fig.3. Ionic conductivity is employed instead of ionic resistance because the resistance could be too large to confine the graph with an appropriate y-axis range.

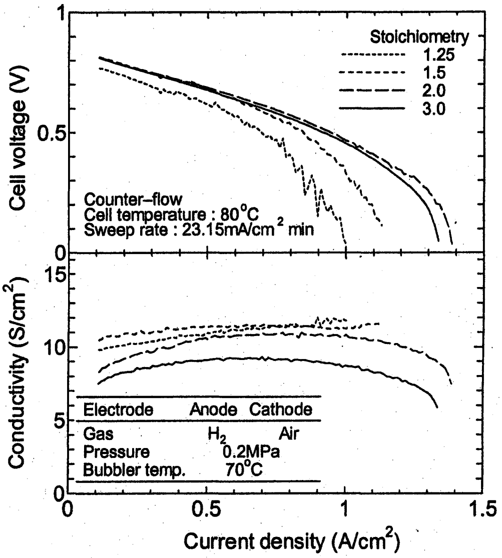

Fig. 5 Stoichiometry dependence of the cell performance. Stoichiometries for the anode and the cathode were equal.

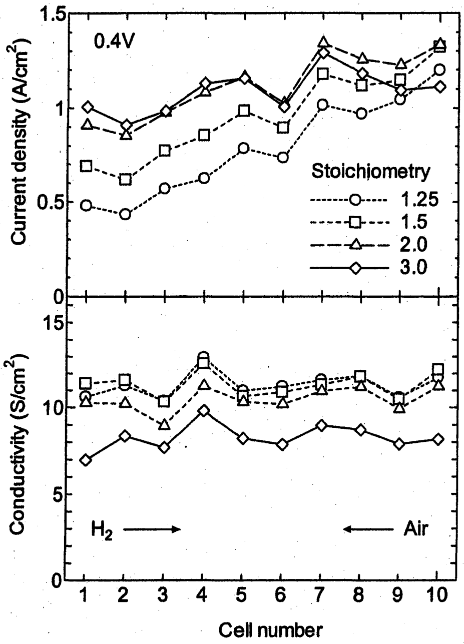

Fig. 6 Stoichiometry dependence of the distributions of current density and ionic

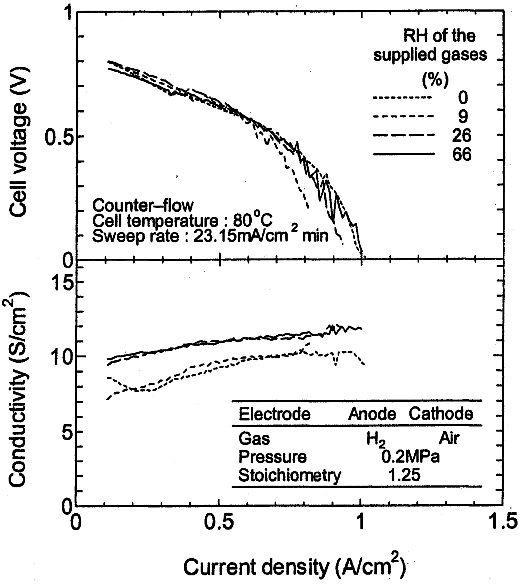

Fig. 7 Relative humidity (RH) dependence of the cell performance.

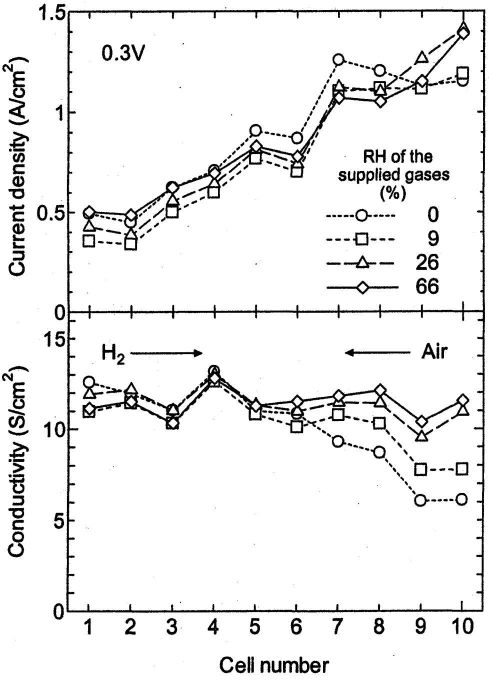

Fig. 8 Relative humidity dependence of the distribution at 0.3V.

Proceedings of The Electrochemical Society, PV 2002-31, 257-269 (2002)
DOI: 10.1149/200231.0257PV © The Electrochemical Society

PROBING ELECTRODE STRUCTURE USING ELECTROCHEMICAL IMPEDANCE SPECTROSCOPY

Mahesh Murthy
Gore Fuel Cell Technologies
W. L Gore & Associates, Inc.
201 Airport Road, Elkton, MD 21922

ABSTRACT

In this work, we extend the technique described by Lefebvre *et al.* to perform impedance measurements in N_2/N_2 using Membrane Electrode Assemblies (MEAs) containing symmetrical electrodes at different relative humidities. The average ionic resistance of the individual catalyst layer can therefore be estimated from one half of the total average ionic resistance. The trends in the ionic resistance with RH can be extrapolated to obtain the value at 100% RH. The value at 100% RH is useful for benchmarking different electrode structures and compositions in terms of maximum possible ionic conductivity and for comparisons with fuel cell data obtained under stationary conditions wherein the RH is typically 100%. This paper discusses the details of the methodology adopted and provides examples wherein the use of impedance measurements allow us to gain valuable insight related to the composition and structure of these electrodes. For certain types of electrodes, or electrodes operating under sub-saturated conditions typical for automotive conditions, lower proton conductivity should have a significant negative effect on fuel cell performance.

INTRODUCTION

The use of Electrochemical Impedance Spectroscopy (EIS), otherwise known as AC impedance, as a diagnostic tool in PEM fuel cell research is well discussed in the literature (1-6). For example, this tool has been extensively used to measure proton conduction in membranes (1) at high frequencies, to measure cathode polarization in the presence of air and O_2 (2), and to determine anode polarization in the presence of CO (3-5). Notable among these, and probably the earliest published, is the work by Springer *et al.* (2) on the use of this tool to resolve kinetic, ohmic and mass transport control observed in a PEM fuel cell. The experimentally measured spectra are also modeled using first principles to estimate useful kinetic and diffusion parameters. In Figure 7 of Ref. 2, the authors describe the presence of a 45° angle of approach of the measured impedance to the real axis at high frequencies. This response was described as a measure of catalyst layer proton resistance. However, in some cases the proton resistance of the electrode cannot be accurately experimentally determined because the impedance response becomes dominated by the faradaic processes occurring at the electrode.

More recently Lefebvre *et al.* (7) described the usefulness of performing impedance measurements in H_2/N_2 rather than in H_2/Air. Measurements using N_2 allows for the elimination of any faradaic processes due to oxygen reduction reaction on the cathode. However, during measurements at OCV, a low frequency arc can be observed due to oxidation of hydrogen molecule on the N_2 side resulting from the finite cross-over of H_2 that exists in membranes from the H_2 on the anode side. The authors in Ref. 7 report experimental measurements performed at 0.95 V vs. NHE. We believe that at this cathode potential formation of Pt-O or other forms of oxide species on Pt may impact the low frequency end of the impedance spectra.

In this paper we modify the technique described by Lefebvre *et al.* to describe impedance measurements in N_2/N_2 using Membrane Electrode Assemblies (MEAs) with symmetrical electrodes. We describe the methodology wherein these measurements are performed at well-controlled relative humidities. There are two distinct advantages to this technique relative to the ones described by others (2,7) in the past. Firstly, the data reported in this paper clearly shows the strong effect of RH on this measurement and the need for superior RH control and measurement within the cell. Similar measurements in a fuel cell would be difficult due to the inability to control the RH locally within the electrode during fuel cell operation, especially if measurements are desired at sub-saturated conditions. It is quite well known that under sub-saturated inlet feed conditions, the local RH may increase significantly along the gas flow channel as water produced at the cathode is used to humidify the gas stream. Also, it is well known that within a fuel cell the local RH is governed by the rate of the reaction which is exothermic during O_2 reduction, the water fluxes across the membrane governed both by electro-osmotic drag and back diffusion. Therefore, measurements of ionic resistance during fuel cell operation would be difficult, especially without well controlled and uniform RH conditions. Secondly, measurements in N_2/N_2 eliminates the faradaic effects associated with H_2 oxidation on the cathode due to cross-over from the anode during measurements performed at OCV in H_2/N_2.

Figure 1 shows a simple schematic of the electrode describing the three phases necessary for the electrochemical reaction. Apart from porosity and electronic conductivity within the carbon layer of the catalyst, it is of prime importance to optimize the ionic pathways within the electrode and assure the presence of a strong ionic interface between the electrode and the proton conducting membrane. During AC impedance investigations, this type of physical structure is usually modeled using a transmission line RC network of resistors and capacitors (7). The transmission line under blocking conditions, (*i.e.*, when no faradaic reactions take place) can be simplified to consist of two parallel rails of resistors with capacitors across them as shown below in Figure 2. This type of electrode structure was initially reported by Wilson *et al.* whereby the ionomer is used as a binder to form thin film catalyst layers (8). These thin film catalyst layers can either be directly applied onto the membrane or can be hot pressed to the membrane surface using a decal process to form the MEA.

Since the electrical conductivity of the carbon layer within the electrode is very good, the electronic resistive rail is very low in magnitude and can be neglected from the transmission line network. Use of N_2 allows for eliminating the need for charge transfer resistance (since the charge transfer resistance has infinite impedance due to blocking conditions) in parallel with the individual double layer capacitors. The RC circuit can be electrically resolved using Kirchoff's law to estimate the total impedance.

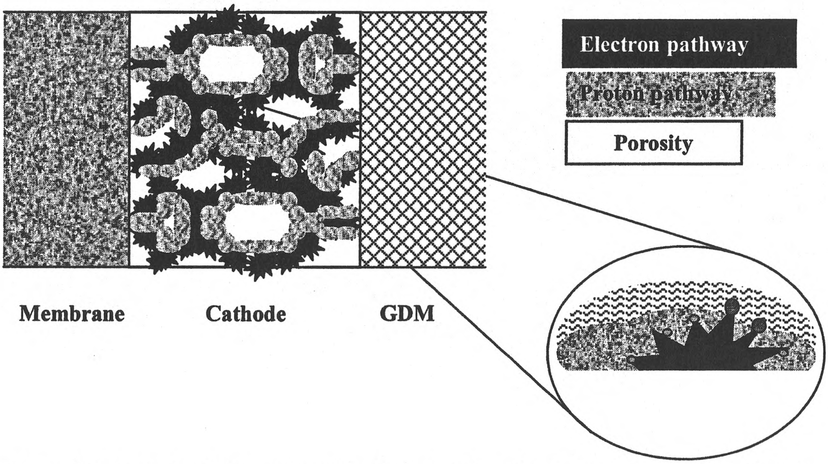

Figure 1. Schematic of the membrane-cathode interface describing the presence and need for proton pathways in the electrode.

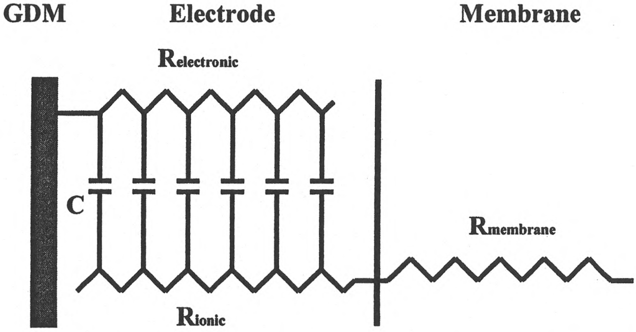

Figure 2. RC transmission line equivalent circuit used to model physical structure of PEM fuel cell electrode as the one shown in Figure 1.

Figure 3 shows the simulated impedance spectra based on the equivalent circuit shown in Figure 2 for 1000 R-C elements. The spectra in Nyquist form has two interesting characteristics. At frequencies higher than the critical frequency, ω_c, the impedance has a 45° slope which is characteristic of proton transport in the catalyst layer. At frequencies lower than ω_c, the spectrum becomes nearly vertical and gradually becomes dominated by the capacitance of the electrode. The intercept at the X-axis of the asymptote of the data at frequencies lower that ω_c equals $R_i/3$. In typical experimental measurements, the intercept at ω_c is considered to be equal to $R_i/3$ as shown in Figure 3 as the data at lower frequencies most likely suffers from artifacts as was explained earlier.

An analytical expression derived from first principles can also be derived from the physical model of the electrode shown in Figure 1 (9). The solution is obtained by solving the three governing phenomena in an electrode- O_2 transport governed by Stefan-Maxwell equation for multi-component diffusion, ohm's law for proton migration, and Butler-Volmer kinetic expression for reaction rate to estimate the overall impedance due to a sinusoidal voltage perturbation. This analytical expression can be further simplified under 'Blocking' boundary condition, i.e., when no faradaic reaction occurs to obtain an expression for the total impedance. When $\omega >> \omega c$, the total impedance can be simplified to result in the following expression:

$$Z \sim \sqrt{\frac{R_p}{C\omega}} \quad [1]$$

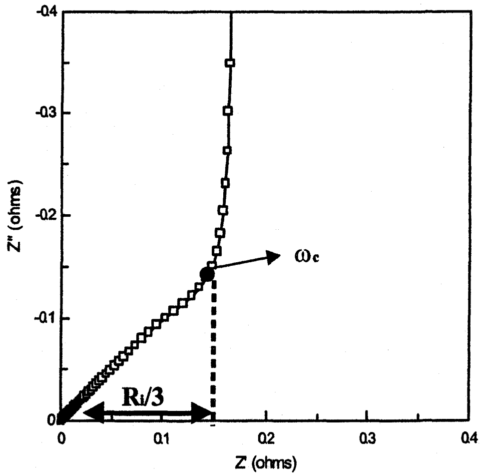

Figure 3. Simulated impedance spectra for 1000 R-C elements with a total resistance of 0.5 ohms and a total capacitance of 1 F (also shown in Ref. (7)).

EXPERIMENTAL

Figure 4 shows the details of the experimental set-up that was used to perform impedance measurements. The flow of N_2 gas is split into two fractions. One part is bubbled through the humidifier using a sparger type humidification scheme. The temperature of the humidifier is set 5 degrees higher than the cell temperature to account of slight inefficiencies in the humidification apparatus. The other fraction at ambient condition is mixed with the humidified stream to obtain a certain relative humidity of the gas stream. For example, if it is necessary to obtain an RH of 0.3, then the total flow of N_2 is split wherein 30% of the total is sparged through the humidifier and 70% is dry, and finally the two streams are allowed to mix before entering the cell. Further, the actual RH of the combined stream is measured within the cell using calibrated humidity probes

(Vaisala, Woburn, MA, Readout No- HM138, Probe No- HMP37E, Sensor No. Humicap 16663 HM). Both anode and cathode sides have similar designs to allow for well controlled RH of the N_2 stream.

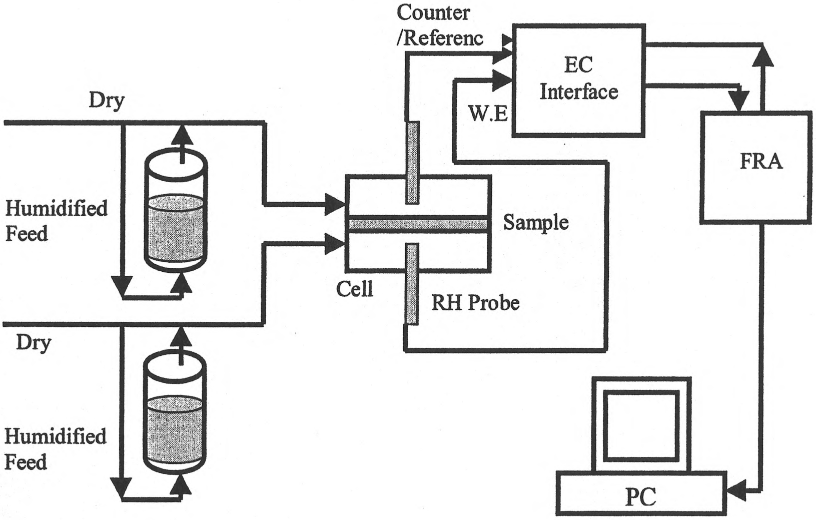

Figure 4. Schematic of experimental set-up with RH control and impedance measurements.

Figure 5 shows a close-up of the cell assembly and the location of the MEA. As Figure 5 describes, the MEA (1.27 cm^2 in active area) is clamped using gaskets and gas diffusion media in between the top and bottom cell chamber of the cell assembly. Both halves of the cell assembly have a straight channel for gas flow and can be heated independently using cartridge heaters. The current collectors are porous Stainless Steel (SS) which is sputtered with a thin layer of Pt. The pressure at the active area of the MEA is controlled by the current collector at the bottom. That is, the top current collector is fixed while the bottom can be moved towards the top using pressurized air. The cell is connected to an Impedance Analyzer (Solartron Model No. 1280B) and the impedance measurements are performed using a personal computer with Zplot/Zview® software (Scribner Associates, Southern Pines, NC). During a typical measurement, the frequency is scanned from 15 kHz to 0.01 Hz with an AC perturbation of 10 mV and the total impedance is resolved into real and imaginary parts. Typically, measurements are performed with an MEA after 10 to 15 minutes of initial equilibration time. Since impedance measurements are relatively short and equilibration times are within 5 to 10 minutes at a given RH, each sample can be tested within a relatively short time. Measurements are also performed without the MEA at higher frequencies to estimate the total electrical resistance of the experimental set-up including contact resistances not associated with the MEA. A proprietary software, "MTS", developed by Scribner Associates, Inc. allowed for automatic control of the RH with simultaneous impedance measurements at each RH using the PC controlled interface. All data collected at a specified RH was analyzed using Zview® software.

It is worthwhile to reiterate the usefulness of a smaller active area during these measurements. Measurements using small active area allows for better resolution to estimate $R_i/3$ while minimizing inductive effects and other resistances within the experimental set-up (*eg.* lead resistance, contact resistance, etc.). Due to blocking conditions, the higher impedance can be measured easily in N_2/N_2 as a higher voltage perturbation can be imposed without concerns about faradaic effects. Therefore, a larger voltage perturbation results in a stronger signal in terms of the current response for a given value of the measured impedance.

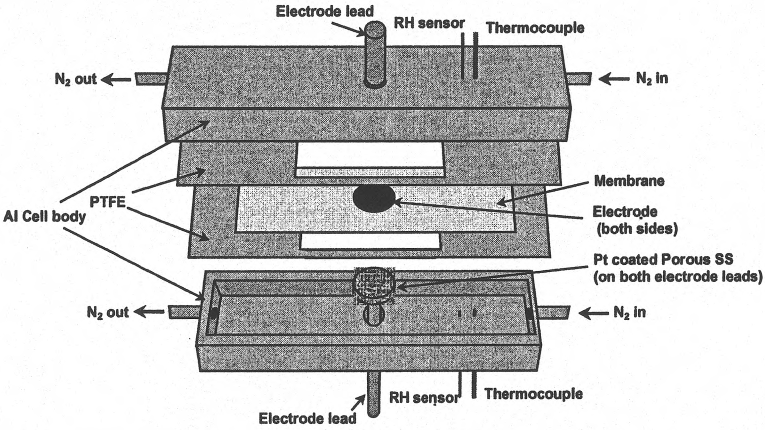

Figure 5. Design of cell assembly used for impedance measurements

RESULTS AND DISCUSSION

Figures 6a and 6b show typical impedance spectra (both in Nyquist and Bode forms) obtained at 60°C cell temperature at three different relative humidities. The 45° feature is associated with proton conduction along a transmission line (assuming electrical resistance of the carbon layer being extremely low and negligible). The average ionic resistance is a strong function of RH as can be observed from the impedance spectra. Typical measurements are performed at four relative humidities and the average ionic resistance estimated as explained earlier. The phase angle versus frequency plot exhibits two constant phase regions at 45 degrees and 90 degrees. Since symmetrical electrodes are used for these measurements, the average ionic resistance of the individual electrodes can be calculated by using one half of the measured value (since these resistances are in series).

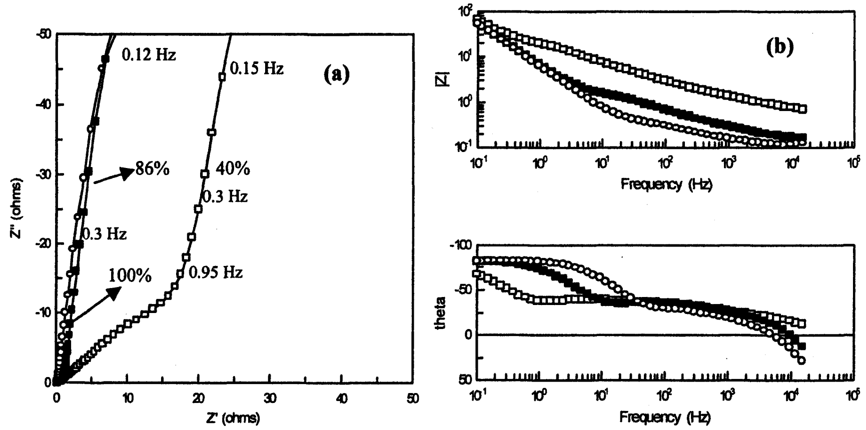

Figure 6 (a). Nyquist plots for a typical catalyst layer as a function of RH and (b). Bode plot representation of the data in Fig. 6a. Notice the dramatic reduction in average ionic resistance as the RH is increased from 40% (open squares) to 86% (open circles), and finally to 100% (closed squares).

The measured average ionic resistance can be plotted as a function of RH on a log-log plot as shown in Figure 7. The ionic resistance data is then fitted using a power law equation (which is linear on a log-log plot) to estimate the average ionic resistance at 100% RH. The value at 100% RH can be used to compare with fuel cell data obtained under typical stationary operating conditions. The value at much lower RHs and the exponent term in the power law equation is useful for comparison with fuel cell data operating under typical automotive conditions. The pre-exponent in the power law represents the value at 100% RH, and the exponent value is a measure of the sensitivity of the ionic resistance to RH. The ionic resistance values can also be used to estimate the ionic conductivity of the electrode as a function of RH. In case of Figure 7, an electrode thickness of 20 μm is assumed to calculate an average ionic conductivity of 2.6 mS/cm at 100% RH.

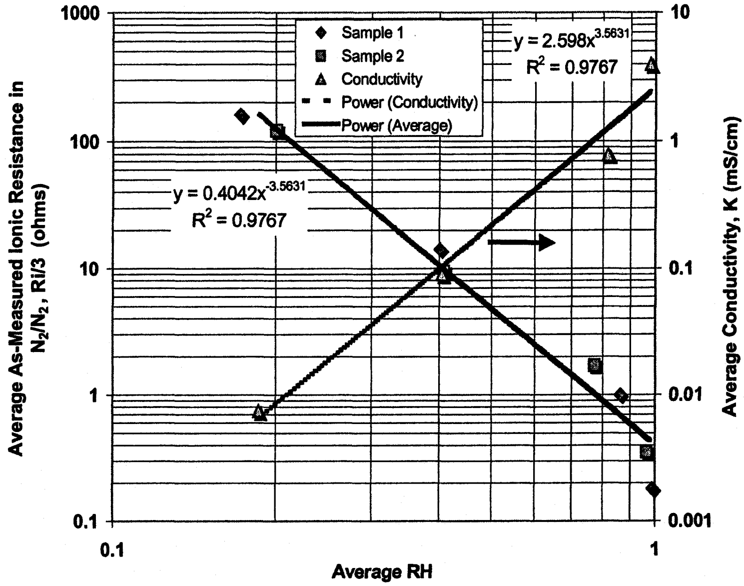

RH.

Since a detailed description of the experimental set-up and methodology has been provided above, two examples are described below to illustrate the usefulness of this technique to probe electrode composition and structure.

Example I:

Example I illustrates that changes in the composition of the electrode in terms of the amount of ion conducting polymer can significantly impact the average ionic resistance. Therefore, direct measurements of electrode composition can be supplemented by impedance measurements. Two electrodes were prepared with 0.38 and 0.56 mg cm^{-2} of ion conducting polymer with commercially available 40 wt.% Pt on carbon. Comparison of impedance data is made at 30% and 65% RH. It is clear from Figures 8a and 8b that the higher the amount of ion conducting polymer, the lower the ionic resistance. For example, in Figure 8a, an increase in ionomer content by a factor of 1.5X results in a decrease in average ionic resistance by a factor of 11X at approximately 30% RH, and by a factor of 7X at 65% RH. Therefore, small changes in ionomer content should have a significant effect on the measured ionic resistance especially under sub-saturated conditions.

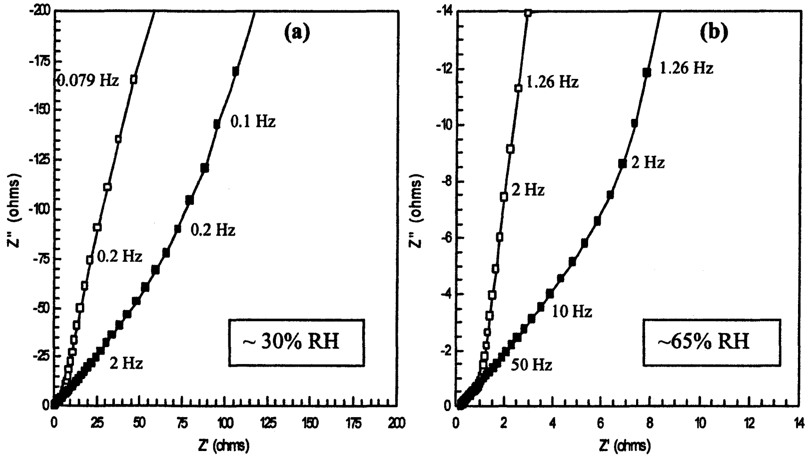

Figure 8(a). Comparison of impedance spectra measured in N_2/N_2 for two electrodes with 0.38 mg cm^{-2} (filled squares) and 0.56 mg cm^{-2} (open squares) of ion conducting polymer in the catalyst layer at ~30% RH and 8(b). similar comparison at ~65% RH.

The effect of different amounts of ionomer in the electrode on fuel cell performance is well discussed in the literature (10,11). The amount of ionomer in the electrode impacts the electrochemical area, therefore, the Pt utilization, the porosity of the electrode, and therefore, mass transfer characteristics, and finally the protonic pathways within the electrode. The authors in Refs. 10 and 11 report an optimum amount of ion conducting polymer in the electrode for peak fuel cell performance. The data in Figure 8 indicates that increasing the ionomer content certainly shows a definite reduction in the ionic resistance measurements, and we envision the lower ionic resistance should translate to higher fuel cell performance for cases wherein proton transport is the key limitation. For very high ionomer content, the electrode is probably limited by porosity loss, and therefore, mass transport limitations. Also, under extreme cases, loss in electronic conductivity may occur. Under these conditions, ionic resistance should not be expected to impact fuel cell response.

Example II.

Example II is described below to illustrate the differences in impedance signature due to differences in electrode structure. In this case, two electrodes were prepared, each using different ionomer contents along the thickness of the electrode. In one case, the ionomer content was varied from a lower value at the electrode-GDM interface to a higher value at the electrode-membrane interface (Structure A). In the second case, the ionomer content was in an opposite direction to the one described above (Structure B). Therefore, based on the prototypes created, we would anticipate creating an ionomer gradient in both electrodes with these gradients being in opposite directions for Structure A versus Structure B. The average amount of ion conducting polymer, was however, kept constant, *i.e.*, approximately 0.59 mg cm^{-2} in both cases. This type of approach to create gradients in ion conducting polymer (PFSA) along the electrode thickness was previously reported by Vanderborgh *et al.* (12).

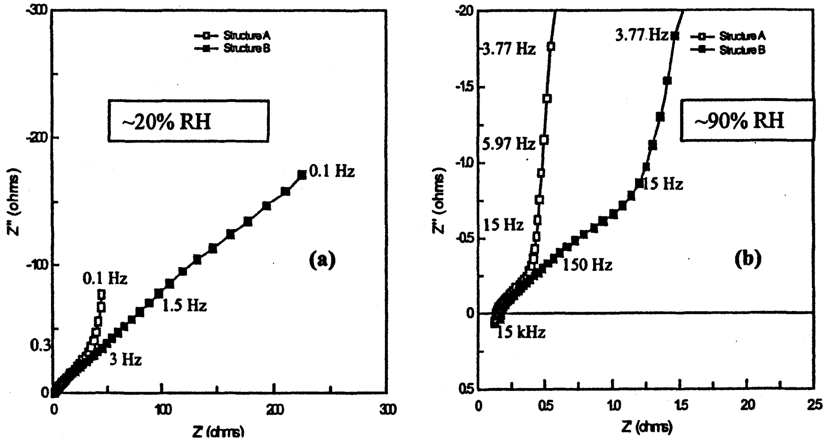

Figures 9a. Effect of electrode structure on impedance response in N_2/N_2 at ~20% RH and (b). RH of ~90% RH. Both electrodes have approximately 0.59 mg cm^{-2} of ion conducting polymer.

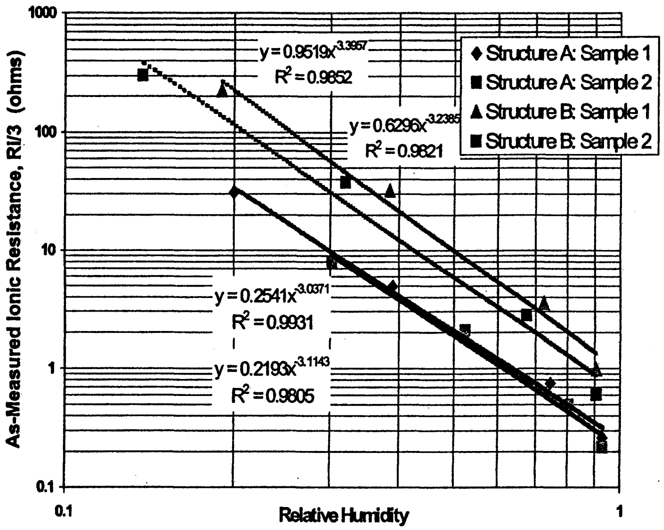

Figure 10. Effect of RH on the measured ionic resistance for Structure A and Structure B electrodes.

Figure 9 compares the impedance response at 20% RH and 90% RH for both these types of electrodes. It is clearly seen that the electrode with Structure A has lower proton resistance at both the RH conditions. It is especially interesting to note that the decrease in ionic resistance is especially significant at ~20% RH for Structure A electrodes. For instance, the average ionic resistance for electrode with Structure A is 58.77 ohm-cm^2, while that for Structure B is 425.27 ohm-cm^2. Therefore, the improvement is 7X for Structure A at 20% RH. At ~90% RH, Structure A has an average ionic resistance of 0.49 ohm-cm^2, while that for the Structure B electrode is 1.86 ohm-cm^2. That is, the improvement at ~90% RH is 3.8X observed in Structure A electrodes. Figure 10 below shows the as-measured values of the average ionic resistance with RH for two samples each of Structure A and Structure B.

CONCLUSIONS

A detailed description of a technique for performing impedance measurements in N_2/N_2 is provided. These measurements allow for determining the average ionic resistance of electro-catalyst layers in a Membrane Electrode Assembly (MEA) as a function of relative humidity. Key advantages of performing these measurements were discussed which are:

a. Elimination of any faradaic reaction by switching to N_2 on the cathode side as also discussed by Lefebvre *et al.*
b. Using N_2 on the anode to eliminate low frequency arc observed due to H_2 cross-over from the anode to cathode side and other faradaic effects associated with H adsorption/desorption and Pt-O formation.
c. Use of symmetrical electrodes to estimate the average ionic resistance by calculating one-half of the measured value.
d. Use well controlled RH and small active areas to maximize signal to noise.
e. Measurements at four different RH were performed to estimate the value at 100% RH, as well as lower RHs and the sensitivity factor.

Two examples were discussed to illustrate the usefulness of this technique to distinguish between compositional changes and structural changes in the electrode layer. Also, for electrodes with extremely low protonic conductivity, the fuel cell performance should be extremely sensitive to this value and the proton conductivity can be used as a suitable measure to predict to fuel cell performance and its sensitivity to RH changes.

ACKNOWLEDGMENTS

The author would like to firstly thank Daniel Frydrych of Gore Fuel Cell Technologies and Prof. Peter Pickup from Memorial University in Newfoundland for fruitful discussions, useful suggestions and guidance to accomplish this work. Also, the following associates on the Gore Fuel Cell Technologies team deserve special mention for help with the experimental set-up, generation of key prototype samples, and for performing impedance measurements: Wen Liu, Mark Edmundson, Lynn Greene, Debi Moore, Dave Everson, and Joseph Moore. Finally, the technical and editorial suggestions provided by Will Johnson and Uwe Beuscher are also greatly appreciated.

REFERENCES

(1) Cahan, B.D., Wainright, J.S., *J. Electrochem. Soc.*, Vol. 140, No. 12, pp. L185 (1993).

(2) Springer, T.E., Zawodzinski, T. A., Wilson, M. S., and Gottesfeld, S., *J. Electrochem. Soc.*, Vol. 143, No. 2, pp 587 (1996).

(3) Cuireanu, M., Wang, M., and Qi, Z., *J. Phys. Chem.*, Vol. 103, Issue 44, pp 9645 (1999).

(4) Ciureanu, M., Wang, H., *J. New Materials for Electrochemical Systems*, 3, pp. 107 (2000).

(5) Kim, J-D., Park, Y., Kobayashi, K., Nagai, M., and Kunimatsu, M., *Solid State Ionics*, 140, pp. 313 (2001).

(6) Wang, X., Hsing, I.M., Leng, Y.J., Yue, P-L, *Electrochimica Acta*, 46, pp. 4397 (2001).

(7) Lefebvre, M.C., Martin, R.B., and Pickup, P.G., *Electrochem. and Solid-State Letters*, 2(6), pp. 259 (1999).

(8) Wilson, M.S., and Gottesfeld, S., *J. Applied Electrochemistry*, 22, pp. 1 (1992).

(9) Eikerling, M., Kornyshev, A.A., *J. Electroanalytical Chem.*, 453, pp. 89 (1998).

(10) Lee, S.J., Mukerjee, S., McBreen, J., Rho, Y.W., Kho, Y.T., and Lee, T.H., *Electrochimica Acta*, 43, 24, pp. 3693 (1998).

(11) Passalacqua, E., Lufrano, F., Squadrito, G., Patti, A., and Giorgi, L., *Electrochimica Acta*, 46, pp. 799 (2001).

(12) Vanderborgh, N.E., Huff, J.R., Leddy, J., *U.S Patent No. 4,804,592*, Feb. 14 (1989).

Proceedings of The Electrochemical Society, PV 2002-31, 270-286 (2002)
DOI: 10.1149/200231.0270PV © The Electrochemical Society

CHARACTERIZATION OF GAS DIFFUSION LAYERS FOR PEMFC

Williams, M. V., Begg, E., Bonville, L.J., Kunz, H.R., Fenton, J.M.

Department of Chemical Engineering, University of Connecticut, Storrs, CT 06269

In proton-exchange membrane fuel cells, gas diffusion layers serve as current collectors that allow ready access of fuel and oxidant to the anode and the cathode catalyst surfaces, respectively. There is no electrochemical reaction in the gas diffusion layer, therefore the main polarization associated with it is due to mass transport limitation. Critical properties of in-house and commercial gas diffusion layers have been characterized and compared in this work in order to determine factors limiting the mass transport in the cathode gas diffusion layer. These properties are electrical conductivity, fraction of hydrophobic pores, gas permeability (Gurley number), pore size distribution, morphology, and the limiting current. Polarization curves for air and neat oxygen were collected to determine the limiting current at three operating temperatures, 80°C, 100°C, and 120°C, at atmospheric pressure. Linear empirical relationships for Gurley number versus limiting current were found at each of the three temperatures. Characterization of different gas diffusion layers through porosimetry provides a pore size distribution for each gas diffusion layer. Finally, an explanation of the correlation between Gurley number and limiting current tested is proposed, which relies on the pore size distribution of the gas diffusion layer associated with the data points.

INTRODUCTION

Proton exchange membrane fuel cells (PEMFC) require that the anode and cathode catalyst layers have electrical contact with current collectors that allow ready access of fuel and oxidant to the anode and the cathode catalyst surfaces, respectively. These current collectors are called gas diffusion layers (GDL) and are critical components in achieving high performance in PEMFC. The requirements of an ideal gas diffusion layer are several, including diffusing the gas reactants effectively to the catalyst layers, having high electrical conductivity, having a surface that enhances good electrical contact, and having proper hydrophobicity for each application. It is desirable for fuel cells to operate at a relatively high current density for the highest power output, while remaining compact and light. The higher the operating current density of fuel cells, the higher flux of gas needed. This implies that the ideal gas diffusion layer be able to effectively diffuse reactant gases to the catalyst surfaces at high demand. Limiting current of a cathode is an extrapolated current density at zero voltage. This current represents the maximum current density that can be obtained from a cell as the oxygen concentration at the cathode catalyst layer goes to zero. A gas diffusion layer that yields a high limiting current is strongly needed. Thorough characterization of gas diffusion layers is necessary for determining factors limiting the mass transport limitation at high current density.

EXPERIMENTAL

There are several commercial gas diffusion layers available for PEMFC operation. Several were selected for comparison in this work including E-TEK_EFCG carbon paper (E-TEK Inc.), SGL_10BB carbon paper (SGL Carbon Group), E-TEK_V.2.11 carbon cloth, E-TEK_V.2.20 carbon cloth, and E-TEK_V.3.1 carbon cloth. Each GDL consists of two layers: a layer of macro-porous substrate, and a partially hydrophobic micro-porous layer on top of the macro-porous substrate. The micro-porous layer is in contact with the catalyst layer while the macro-porous substrate is in contact with the gas feed. Two different kinds of bare macro-porous substrates, TGPH-120 carbon paper (Toray Corporation, Japan) and SGL_10BA carbon paper (SGL Carbon Group), were also characterized for comparison. In-house gas diffusion layers were prepared using TGPH-120 carbon paper as the macro-porous substrate. The hydrophobic micro-porous layer of in-house gas diffusion layers was applied to the macro-porous substrate using a silk-screen technique [1]. The micro-porous layer of an in-house GDL consists of Vulcan XC-72R and 14wt% polytetrafluoroethylene (PTFE) with the total loading of 1.5 mg/cm^2. In-house gas diffusion layers were sintered at 343°C for 30 minutes. All gas diffusion layers were characterized and compared both quantitatively and qualitatively as described below.

Single Cell Polarization Measurement

In preparing a membrane electrode assembly (MEA), cathode and anode catalyst ink were sprayed directly onto each side of an in-house membrane. The catalyzed membrane was then sandwiched between two gas diffusion layers to create a 5-cm^2 MEA for a single cell polarization measurement. Membrane thickness is 1 ± 0.1 mils. Cathode catalyst is 40 wt% Pt/C (Alfa Aesar), while the anode catalyst is 40 wt% Pt-Ru/C with 1:1 atomic ratio (E-TEK Inc.). Nafion® loading in the catalyst ink is 25 wt% for both cathode and anode. Cathode and anode loading of precious metals is 0.45 ± 0.05 mg/cm^2 each. Membrane electrode assemblies comprised of similar catalyzed membranes but different gas diffusion layers were tested at three different operating temperatures and atmospheric pressure. The three operating temperature conditions are as follow. The first condition is for a cell temperature of 80°C, with an anode humidifier temperature of 80°C and a cathode humidifier temperature of 73°C. The corresponding inlet relative humidity for this condition is 100% for the anode and 75% for the cathode. The second condition is for a cell temperature of 100°C, with an anode humidifier temperature of 90°C and a cathode humidifier temperature of 90°C. The corresponding inlet relative humidity for this condition is 70% for both the anode and the cathode. The third condition is for a cell temperature of 120°C, with an anode humidifier temperature of 90°C and a cathode humidifier temperature of 90°C. The corresponding inlet relative humidity for this condition is 35% for both the anode and the cathode. The utilization is defined as the amount of a substance oxidized or reduced at an electrode at any specific current density according to Faraday's law divided by the feed amount of the substance in the inlet stream. All cells were tested at constant utilization with 33% utilization on the anode, and 25% utilization on the cathode.

Electrical Conductivity

In-plane electrical conductivity of all GDL substrate materials was measured. The method used was a four-point resistivity measurement in compliance with the ASTMC611 standard. Strips of substrate, 0.2 cm x 14 cm, were used in the measurement. Resistance was measured using a QuadTech model 1750 LCR Digibridge with Kelvin clip leads and then converted to resistivity with the test specimen geometry information.

Hydrophobicity

The micro-porous layer of each gas diffusion layer has some degree of hydrophobicity from added hydrophobic dispersion agent. The most widely used hydrophobic dispersion agent is polytetrafluoroethylene. Hydrophobicity is needed to provide a gas passage in the presence of liquid water. Hydrophobic fluorocarbon surfaces (with chains of $-CF_2-$) have the critical surface tension of 18 dyne/cm at 20°C [2]. Liquids with open-chain aliphatic hydrocarbons have low liquid surface tension, in the range of 27-31 dynes/cm at 20°C. Therefore the hydrophobic pores in gas diffusion layers can be filled when in contact with these liquids. Water fills only hydrophillic pores. Decane fills both hydrophillic and hydrophobic pores. The steady state porosity and fraction of hydrophobic and hydrophillic pores can be determined by filling substrate specimens with a hydrophobic acting liquid, decane, and a hydrophillic acting liquid, water, and then weighing them [3,4].

Gas Permeability

Permeability of gas flow through a gas diffusion layer was characterized using a parameter called the Gurley number, which is defined as the volume flow rate of nitrogen at a fixed pressure difference through a fixed area of sample. The measurement of Gurley number indicates the resistance to gas flow [5], reported here in (L/min)/(cm-water x cm^2). A Gurley device, shown schematically in Fig.1, was used to measure pressure drop and volumetric flow rate. The pressure drop was measured by a differential pressure gauge in units of centimeters of water.

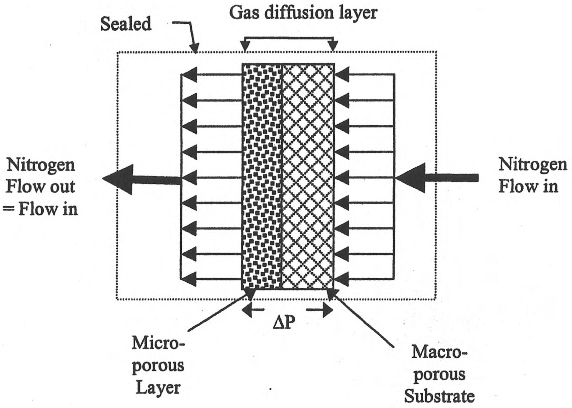

Fig. 1 Gurley measurement device; Gurley number = Flow/(ΔP x Area of sample)

Pore Size Distribution

Information on internal structure of a gas diffusion layer was obtained using a mercury pore size analyzer, which measures the amount of mercury penetrated into pores of a porous media as a function of the applied pressure. The pressure required to penetrate mercury into a particular pore is a function of the pore diameter. Pore size distributions of all gas diffusion layers and bare macro-porous substrates were collected using a Quantachrome PoreMaster®33, for any porous media with a pore size range of 3 nm – 300 microns.

Morphology

The morphology of the micro-porous surface of a GDL, which is normally in contact with the catalyst layer, was examined using an AMRAY 1810 Scanning Electron Microscope.

RESULTS AND DISCUSSION

All membrane electrode assemblies were assembled using a similar catalyzed membrane, but with different gas diffusion layers for each one. The polarization curves were collected at the three operating temperatures of 80°C, 100°C and 120°C, using both air and neat oxygen as cathode gases. Figs. 2a-2c show polarization curves for air of six different cells each with different gas diffusion layers at the three temperatures. Figs. 2d-2f show the same membrane electrode assemblies with neat oxygen. The data shown is

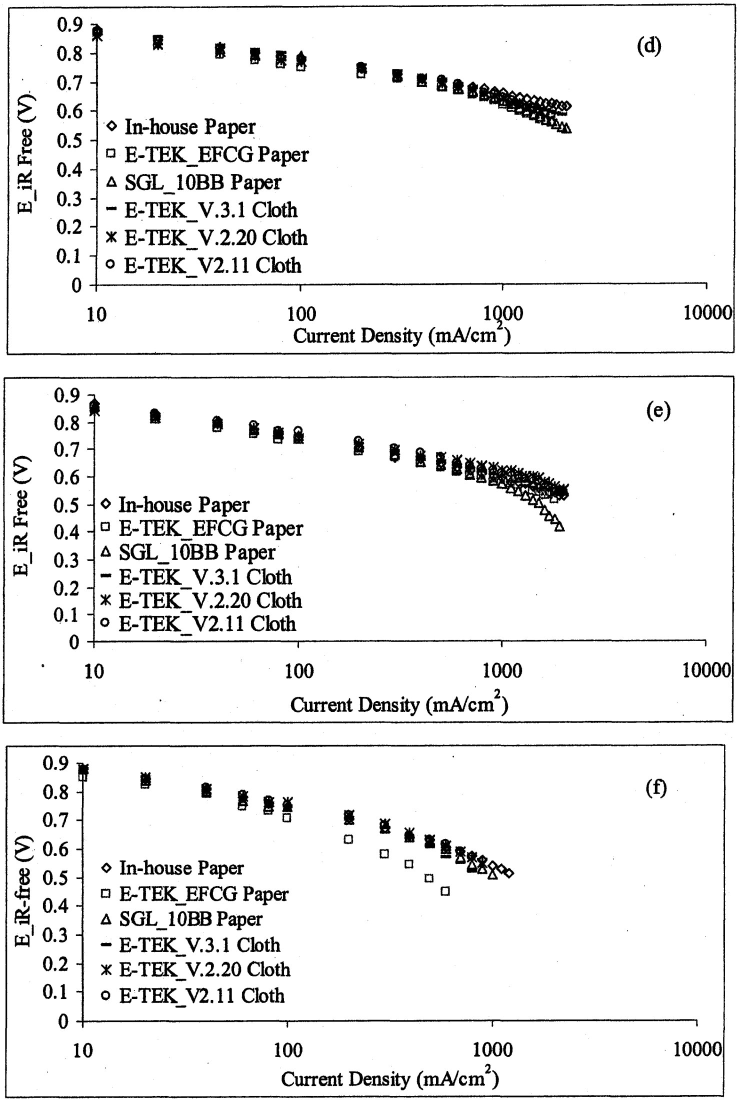

Fig. 2 (Cont.) Polarization curves of iR-free data for (a) Air, 80°C, (b) Air, 100°C, (c) Air, 120°C, (d) O_2, 80°C, (e) O_2, 100°C, and (f) O_2, 120°C

the cell voltage after correcting for the cell total resistance (iR-free). Cell resistance was measured using the current-interrupt method.

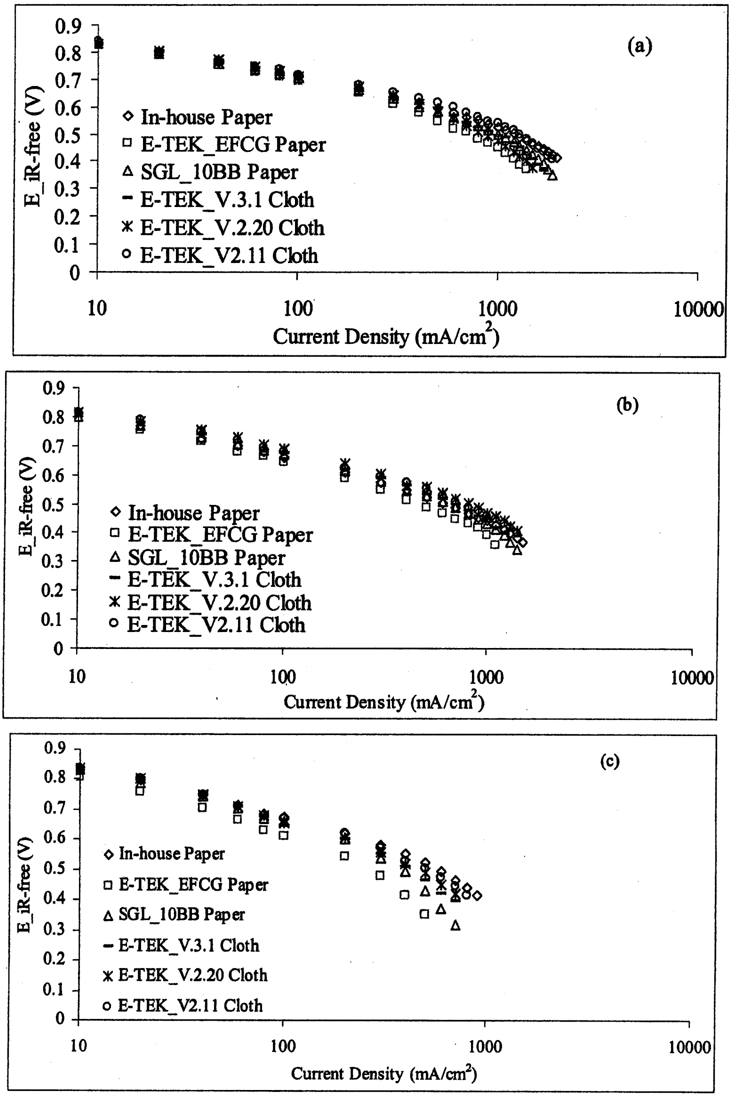

Fig. 2 Polarization curves of iR-free data for (a) Air, 80°C, (b) Air, 100°C, (c) Air, 120°C, (d) O_2, 80°C, (e) O_2, 100°C, and (f) O_2, 120°C

In determining the limiting current (I_{lim}), which is representative of the mass transport limitation on the cathode of a PEMFC, both air and oxygen polarization curves are analyzed together. The three steps for determining limiting currents are as follow. First, the cell total resistive loss obtained from the current-interrupt method is added to the cell voltage at each current density to yield iR-free voltage (E_iR-free). The resistance obtained from this method includes the membrane ionic resistance and all contact resistances, but does not include the ionic resistance in the cathode catalyst layer ($R_{cathode}$). Second, the ionic resistance in the cathode catalyst layer is determined by comparing the iR-free voltage of the oxygen and air polarization curves. Current ratio is defined as the ratio of current obtained from neat oxygen to that obtained from air at the same cell voltage. The ratio of the average oxygen mole fraction, which is the log-mean average of inlet and exit, of air and neat oxygen cathode gas at the three operating temperatures equals to 5.3. If the current ratio of neat oxygen and air obtained from iR-free voltage is anything less than 5.3, it is an indication of an ionic resistive loss in the cathode catalyst layer. This is because current is first order to oxygen mole fraction according to the Butler-Volmer equation and Fick's first law in the activation control and mass transport control regions of the polarization curve, respectively. Any polarization loss that makes the current ratio not first order to oxygen mole fraction, especially at high current densities, comes from ionic resistance. The membrane ionic resistive loss was already corrected by the current-interrupt method in the first step. Therefore, the only loss left to cause a lower current ratio is the ionic resistive loss in the cathode catalyst layer. Using an iterative procedure, the value of $R_{cathode}$ is obtained. The value of $R_{cathode}$ will make the plot of [E_iR-free + $iR_{cathode}$] of both neat oxygen and air yield a current ratio of as close to 5.3 as possible. After correcting for the ionic resistance of the cathode catalyst layer, the current is now first order to oxygen mole fraction for the whole range of current density. The third step, which is the determination of limiting current, can then be implemented. The theoretical basis of the limiting current correction is based on the Butler-Volmer equation and Fick's first law at the limiting current condition of zero concentration of oxygen at the cathode catalyst layer. When the limiting current correction is applied, the plot of [E_iR-free + $iR_{cathode}$] vs. log [$I/(1-I/I_{lim})$] yields a straight line. The straight line is the polarization curve corrected for all ionic resistive and mass transport losses, therefore the Tafel region is extended to the whole range of current density. From an iteration procedure, the value of I_{lim} is found. The value of I_{lim} will make the plot of [E_iR-free + $iR_{cathode}$] vs. log [$I/(1-I/I_{lim})$] become a straight line for the MEA at that test condition. Since both ionic resistance of the membrane and that of the cathode catalyst layer were corrected before determining the limiting current, the I_{lim} obtained represents the mass transport limitation associated with each gas diffusion layer.

Fig. 3 demonstrates the three steps for determining limiting current. Fig. 3a is the cell voltage of air without any correction. Figs. 3b and 3c are the cell voltage of air and neat oxygen, respectively, corrected for the cell total resistance obtained from the current-interrupt method according to the first step. Figs. 3d and 3e are the cell voltage of air and neat oxygen, respectively, corrected further for the ionic resistance of the cathode catalyst layer by an iteration procedure according to the second step. Fig. 3f is the plot of [E_iR-free + $iR_{cathode}$] vs. log [$I/(1-I/I_{lim})$] of air, on the same log-scale with the other curves, representing the air polarization curve corrected further for the mass transport loss by another iteration procedure according to the third step. A straight line extending the Tafel region to high current density is then obtained after correcting for all ionic resistive and mass transport losses.

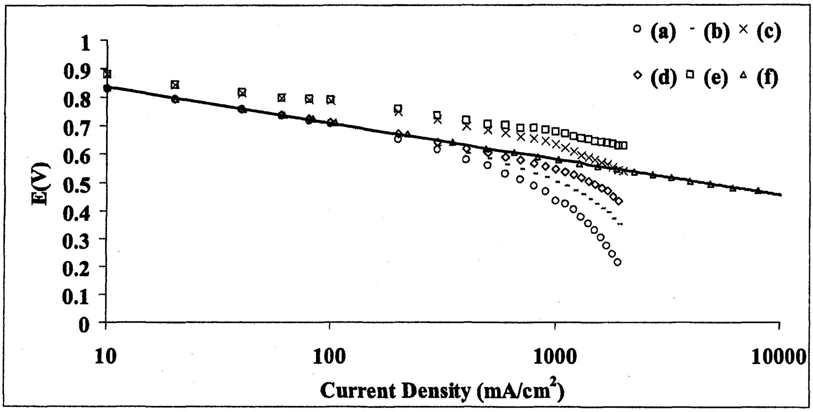

Fig. 3 Demonstration of the limiting current determination
(a) E_cell of air, (b) E_iR-free of air, (c) E_iR-free of O_2,
(d) E_iR-free + $iR_{cathode}$ of air, (e) E_iR-free + $iR_{cathode}$ of O_2,
and (f) Plot of E_iR-free + $iR_{cathode}$ of air vs. $\log[I/(1-I/I_{lim})]$

The $R_{cathode}$ is nearly negligible at 80°C operating temperature due to its near-saturated condition. As the operating temperature goes up, the relative humidity goes down for one atmospheric absolute operating pressure, which leads to higher ionic resistive loss in the cathode catalyst layer. The $R_{cathode}$ is between 0.020 and 0.035 Ohm-cm^2 at 100°C operating temperature and between 0.075 and 0.100 Ohm-cm^2 at 120°C operating temperature for all cells. The limiting currents of all gas diffusion layers at the three operating temperatures are reported in Table 1. The liming current varies from 1720 to 2400 mA/cm^2 for 80°C operating temperature, 1420 to 2070 mA/cm^2 for 100°C operating temperature, and 630 to 1540 mA/cm^2 for 120°C operating temperature, due to different diffusion characteristics of each GDL. In order to understand the difference between the different gas diffusion layers, the important parameters explained earlier were examined and compared.

Table 1 Comparisons of limiting current, in-plane resistivity and fraction of hydrophobic pores of all examined gas diffusion layers and bare macro-porous substrates

Substrates	Limiting Current			In-plane resistivity	Fraction Hydrophobic Pores
	80 °C	100 °C	120 °C		
	mA/cm^2			Ohm-cm	[-]
In-house Paper	2400	2070	1540	0.0043	0.81
E-TEK EFCG Paper	1720	1420	630	0.0081	0.96
SGL 10BB Paper	2160	1840	860	0.0200	0.99
E-TEK V.3.1 Cloth	1890	1530	830	0.0156	0.97
E-TEK V.2.20 Cloth	1760	1800	1200	0.0153	0.98
E-TEK V.2.11 Cloth	2130	1820	1450	0.0154	1.00
TGPH-120, Bare Paper	N/A	N/A	N/A	0.0048	0.85
SGL10BA, Bare Paper	N/A	N/A	N/A	0.0208	0.98

In-plane electrical conductivity and fraction of hydrophobic pores are also shown in Table 1. Using the laboratory fabricated hardware and standard measurement techniques, the measured value of in-plane conductivity of TGPH-120 bare carbon paper, 0.0048 ohm-cm, is very close to the value reported on its specification sheet of 0.005 ohm-cm. Among all gas diffusion layers, the in-house and E-TEK_EFCG gas diffusion layers have the lowest electrical resistivity of 0.0043 and 0.0081 ohm-cm respectively. Both of these gas diffusion layers have TGPH-120 bare carbon paper as their macro-porous layer. The lower resistivity of the in-house GDL than that of the TGPH-120 bare carbon paper shows that the added micro-porous layer reduce the overall electrical resistivity of the gas diffusion layer, possibly from two reasons. One reason is that the micro-porous layer of the in-house GDL has a relatively low loading of PTFE, therefore the thin carbon/PTFE layer has high electrical conductivity. The other reason is that the micro-porous layer penetrates some distance into the macro-porous substrate. The penetration of this conductive micro-porous layer into the substrate helps fill gaps in macro-pores therefore increases the conductivity of the macro-porous layer. SGL_10BB GDL has the highest electrical resistivity of 0.0200 Ohm-cm. This is due to the high resistivity of SGL_10BA bare carbon paper used as the macro-porous layer. Gas diffusion layers with lower electrical resistivity will serve more effectively as current collector and thus reduce the total cell resistance.

It was reported that the PTFE content in anode gas diffusion layers affects the fraction of hydrophobic pores, which could be correlated with the obtained current density in direct methanol fuel cells [4]. Hydrophobicity is needed in PEMFC to provide gas passage for the reactant gases in operating conditions where there is a presence of liquid water. Fraction of hydrophobic pores might be expected to correlate with the limiting current at the 80°C operating condition where there is a possibility of liquid water presence. However, according to the results reported in Table 1, there is no significant difference in this parameter from one commercial gas diffusion layer to another. All examined commercial gas diffusion layers have higher than 95% hydrophobic pores. This is the result of strongly hydrophobic surfaces of all commercial gas diffusion layers. In the case of strongly hydrophobic surfaces, our method does not allow the estimate of the hydrophilic pores imbedded in the body of a GDL. The fraction of hydrophobic pores thus does not appear to be applicable in comparing different commercial gas diffusion layers. However, in the case where the surface hydrophobicity is known to be similar to that in the body of a GDL, such as in the in-house GDL, this method of determining fraction of hydrophobic pores could be useful in the optimization of gas diffuison layer properties.

The bulk porosity of each gas diffusion layer was determined using two different methods. One method is mercury porosimetry, which gives the maximum intruded pore volume. The other method is weighing the sample before and after immersing in decane which as the ability to fill all pores. The overall porosity is reported in Table 2. A good agreement between the two methods is obtained for all substrates. The fourth column of Table 2 reports the percent difference between the porosity of the two methods, which was calculated from [(Porosity from Weighing) – (Porosity from Porosimetry)]/(Porosity from Porosimetry) x 100. The difference between two methods is less than 5%. Bulk porosity of a gas diffusion layer is defined as its total pore volume divided by the summation of its total pore volume and its solid volume. Bulk porosity might be expected to affect the effective diffusion coefficient of porous media from $D_{eff} = \varepsilon/\tau \times D$, where ε is the porosity and τ is the tortuosity [6]. The maximum 83.3% porosity of SGL-10BB paper and the minimum 69.9% porosity of E-TEK_V3.1 cloth are only 13% apart from each other. It appears that the bulk porosity difference in this range does not have a significant impact on the limiting current. This is an indication that there are other factors more important than the bulk porosity affecting and controlling the limiting mechanism of oxygen mass transport.

Table 2 Comparisons of porosity and Gurley numbers of all examined gas diffusion layers and bare macro-porous substrates

Substrates	Porosity From Porosimetry	Porosity From Weighing	%Δ of Porosity	Gurley Number
	%	%	%	(L/min)/(cm-water x cm^2)
In-house Paper	74.4	72.7	-2.3	0.159
E-TEK_EFCG Paper	75.8	73.8	-2.6	0.005
SGL_10BB Paper	83.1	83.3	0.2	0.046
E-TEK_V.3.1 Cloth	69.9	73.3	4.9	0.018
E-TEK_V.2.20 Cloth	77.1	78.2	1.4	0.040
E-TEK_V.2.11 Cloth	75.1	77.5	3.2	0.079
TGPH-120, Bare Paper	75.6	75.9	0.4	0.788
SGL_10BA, Bare Paper	87.7	87.5	-0.2	2.660

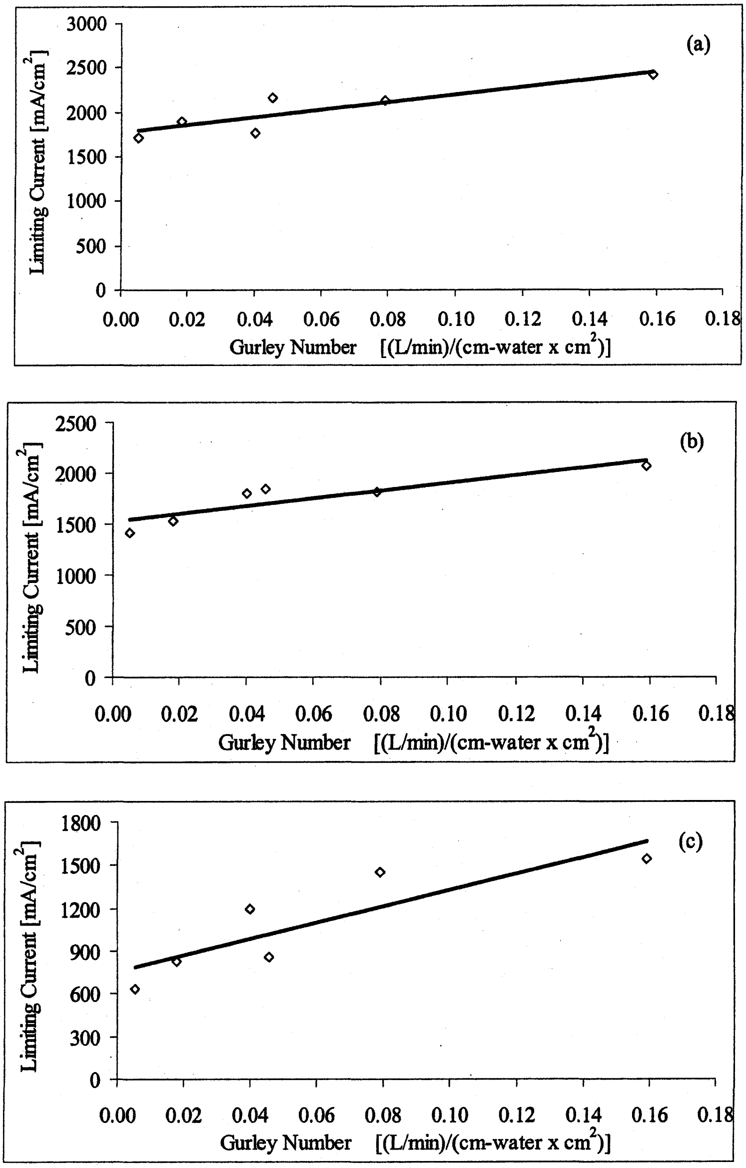

Fig. 4 Plots of limiting currents versus Gurley numbers at (a) 80°C, (b) 100°C, and (c) 120°C

Even though the Gurley number is a measure of resistance due to viscous flow, while the diffusion layer performance is dependent on the resistance due to flow driven by diffusion, it is expected to correlate with gas diffusion layer performance in a PEMFC. Fig. 4 shows plots of limiting currents associated with all examined gas diffusion layers versus their corresponding Gurley numbers, for the three operating temperatures. Gurley number is an indicative parameter of the resistance to gas flow. From the definition of the Gurley number, the higher the value, the less resistance to gas flow. The Gurley number appears to have a correlation with the limiting current at all three temperatures. In order to understand this result, it is necessarily to look at the pore size distribution of each of the gas diffusion layers whose data is presented in Fig. 4. The cumulative pore volume and the pore size distribution or dV/dD, shown in Fig. 5 and Fig. 6, are the values normalized to the same area of a gas diffusion layer, 10.15 cm^2. The pore size distribution of a GDL has an effect on its diffusion properties. At the operating condition of 80°C, the cathode exit relative humidity is between 84%, in the case when none of the water from the anode is available at the cathode, and 105% when all of the water from the anode is available at the cathode. When the pore size of any hydrophilic pores gets smaller than a critical pore diameter, water condensation will occur before the vapor pressure reaches saturation pressure at a given temperature. Therefore, small pores will be filled with liquid water even when the relative humidity is less than 100%. The pressure at which the condensation occurs depends on the pore diameter according to the Kelvin equation [7]. At 80°C operation, with water surface tension of 68 dye/cm, for pore radius smaller than 0.05 μm, water condensation occurs at a relative humidity of 98%. A plot of the percent pore volume of pores with the diameter of 0.1 μm or smaller versus Gurley number is shown in Fig. 7. The data plotted here is from the porosimetry data of all examined gas diffusion layers, and of several extra in-house gas diffusion layers manufactured for different Gurley numbers ranging from 0.14 to 0.22 (L/min)/(cm-water x cm^2). The higher the Gurley number, the smaller the fraction of pore volume associated with the range possibly affected by the capillary condensation, and the higher ability to avoid the mass transport limitation due to water flooding effects at near-saturated operating conditions.

For gas diffusion in small pores, the mean free path determines whether the collision between gas molecules and the wall is important or not. At standard temperature and pressure, the mean free path of nitrogen is 67.6 nm, while that of oxygen is 73.6 nm, therefore the mean free path of air is approximately 70 nm. Bulk diffusion in pores dominates when the pore diameter is bigger than one hundred times the mean free path or 7 μm. The Knudsen diffusion in pores dominates when the pore diameter is smaller than a tenth of the mean free path or 0.007 μm. Any pore diameter between these two limits will have the effects of both the Knudsen diffusion and the bulk diffusion combined [6]. The effective diffusion coefficient in bulk diffusion regime is as high as three orders of magnitude higher than that in the Knudsen regime. A plot of the percent pore volume of pores with the diameter of 7 μm or bigger versus Gurley number is shown in Fig. 8. This shows that higher Gurley number is related to larger pores. The larger pores are beneficial because they aid bulk diffusion and convection, which enhance mass transport through the substrate.

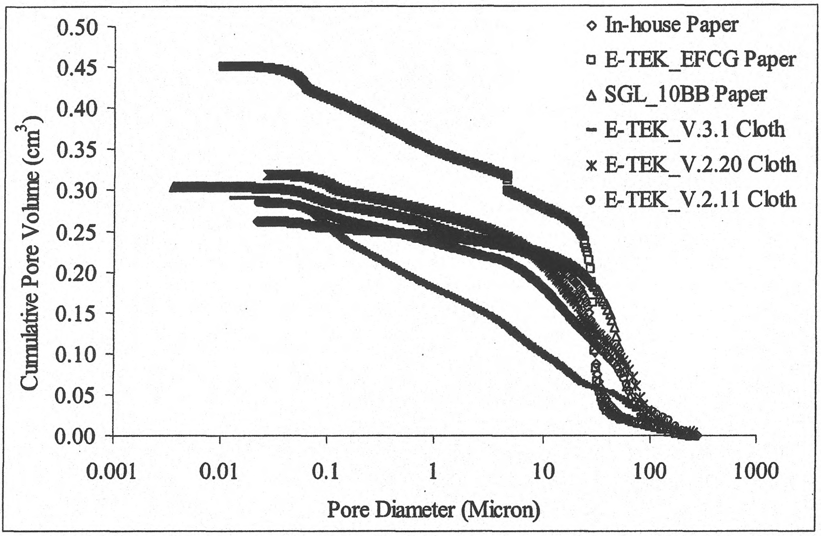

Fig. 5 Cumulative pore volume of different gas diffusion layers, normalized to the same area of 10.15 cm^2

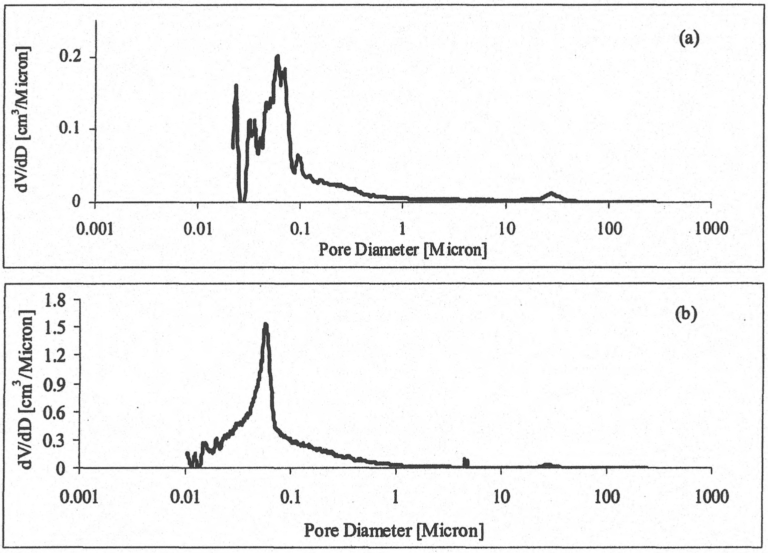

Fig. 6 Pore size distribution of different gas diffusion layers:
(a) In-house Paper, (b) E-TEK_EFCG Paper, (c) SGL_10BB Paper,
(d) E-TEK_V.3.1 Cloth, (e) E-TEK_V.2.20 Cloth, and (f) E-TEK_V.2.11 Cloth

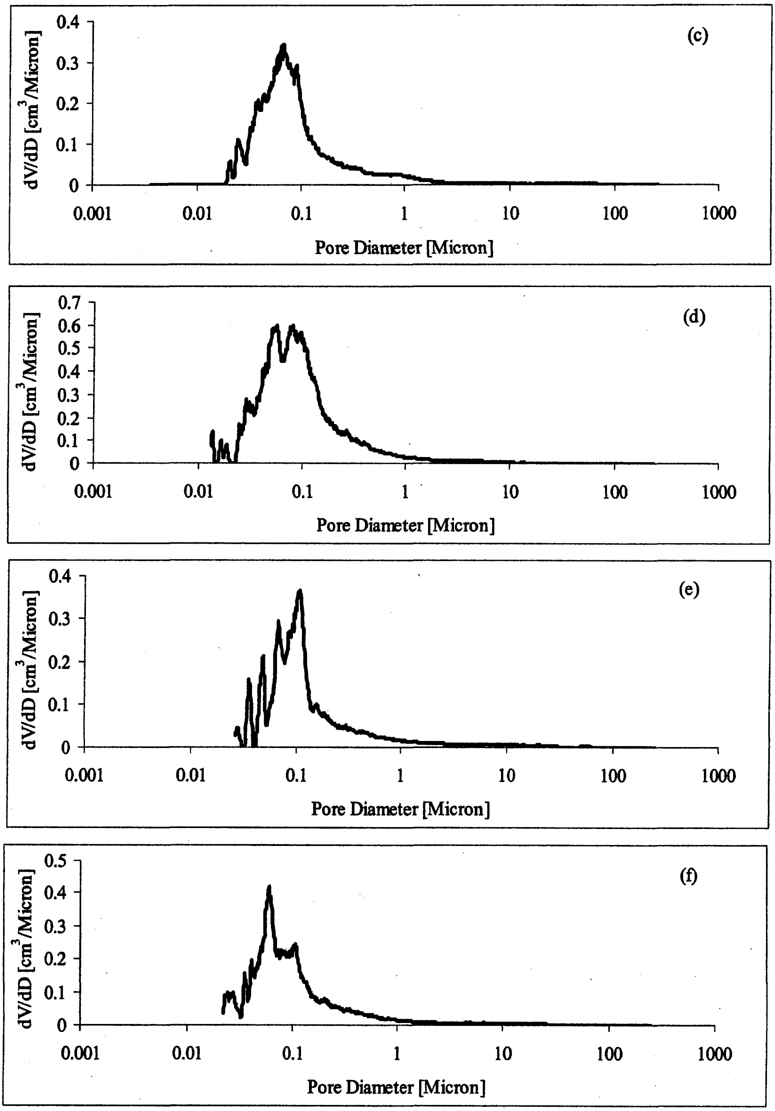

<u>Fig. 6</u> (Cont.) Pore size distribution of different gas diffusion layers:
(a) In-house Paper, (b) E-TEK_EFCG Paper, (c) SGL_10BB Paper,
(d) E-TEK_V.3.1 Cloth, (e) E-TEK_V.2.20 Cloth, and (f) E-TEK_V.2.11 Cloth

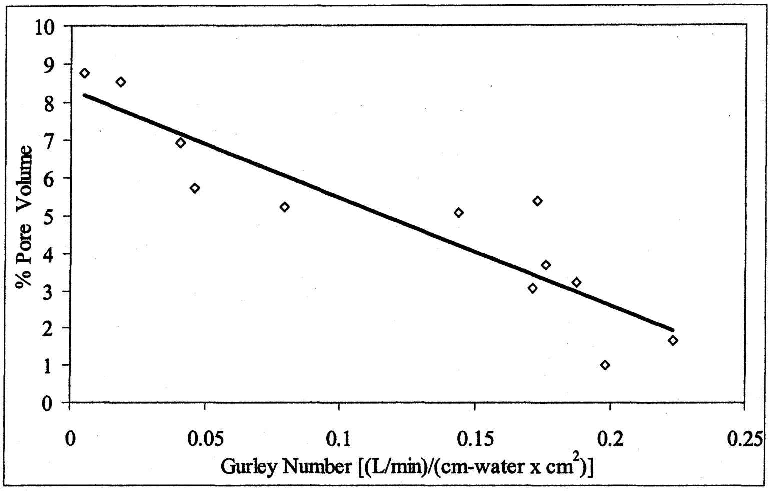

Fig. 7 Percentage pore volume of pores with the diameter of 0.1 μm or smaller

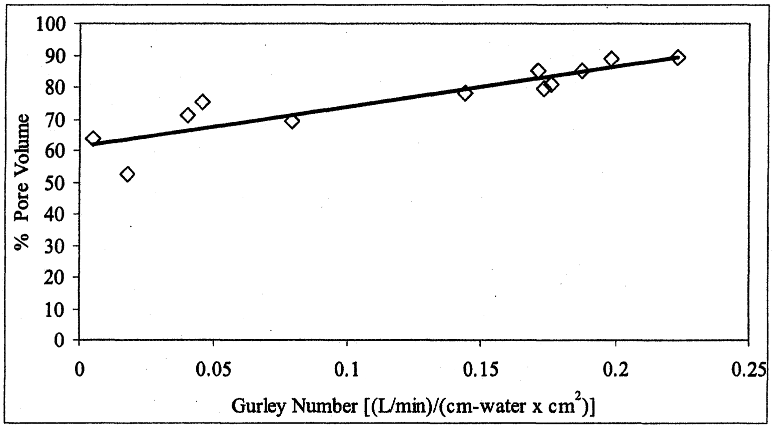

Fig. 8 Percentage pore volume of pores with the diameter of 7 μm or bigger

The surface morphology of all gas diffusion layers is shown in Fig. 9 as scanning electron micrographs at 450X magnification. The in-house gas diffuison layer appears to have large pores on the micro-porous surface while none of the commercial gas diffuison layers has this feature. This could be the reason for the higher Gurley number of the in-house GDL compared to the commercial ones. The surface roughness might affect the contact resistance between a gas diffusion layer and a catalyst layer. However, the total cell resistance of different cells with different gas diffusion layers does not reflect significant differences in contact losses. The detailed examination of the correlation between contact resistance and the surface roughness will be examined in the future.

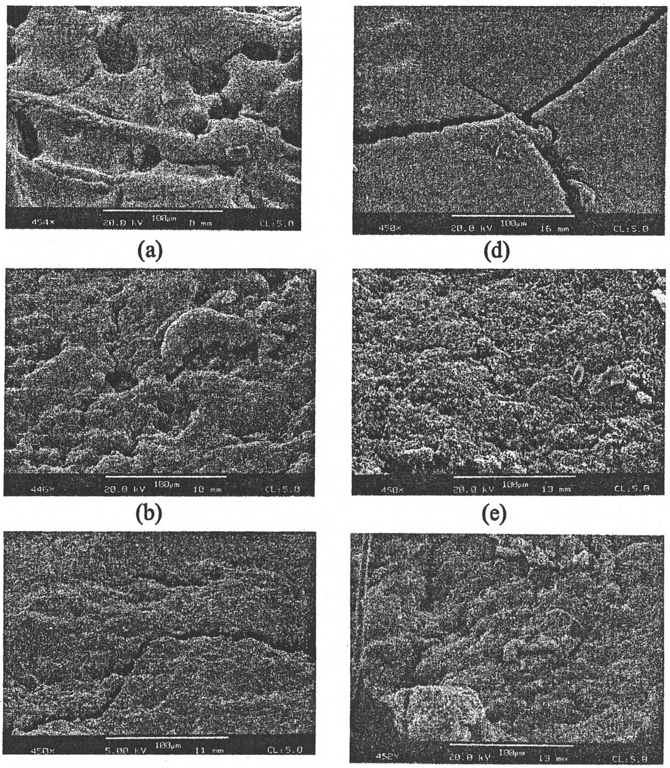
(a) (d)
(b) (e)
(c) (f)

Fig. 9 SEM pictures at 450X magnification for (a) In-house Paper, (b) E-TEK_EFCG Paper, (c) SGL_10BB Paper, (d) E-TEK_V.3.1 Cloth, (e) E-TEK_V.2.20 Cloth, and (f) E-TEK_V.2.11 Cloth

CONCLUSION

Thorough characterization of different gas diffusion layers has been done to determine factors limiting the mass transport in the GDL. The limiting current, the electrical conductivity, the fraction of hydrophobic pores, the gas permeability, the pore size distribution, and the morphology of five different commercial gas diffusion layers are compared with one prepared in-house. The electrical conductivity of each GDL is strongly dependent on that of its macro-porous substrate. The in-house GDL shows the highest electrical conductivity compared to all other commercial ones. The fraction of hydrophobic pores and the overall porosity have no direct correlation with the limiting current, while the Gurley number shows a correlation at the three operating temperatures, 80°C, 100°C, and 120°C. Characterization of gas diffusion layers through porosimetry reveals the internal structure of gas diffusion layer, which provides a means for understanding of this correlation. A gas diffusion layer with a higher Gurley number shows a smaller fraction of pore volume associated with the range affected by the capillary condensation, therefore it has a higher ability to avoid the mass transport limitation due to water flooding effects at near-saturated operating conditions. A higher Gurley number is also related to larger pores. Larger pores are beneficial in gas phase mass transport because they aid bulk diffusion and convection through the substrate. The in-house GDL has the highest Gurley number compared to all commercial ones. Its surface morphology shows big pores, which could be the reason of its high Gurley number.

ACKNOWLEDGEMENT

We would like to acknowledge Arturo Marin (under the Research Experience for Undergraduates Program at the University of Connecticut) for his help in the conductivity measurement, and Dave Wood at the SGL Carbon Group for SGL substrates.

REFERENCES

1. M. Vatanatham, Y.Song, L. Bonville, H.R. Kunz, J. Fenton, A. Smirnova, X.Wang, *Electrochemical Society Extended Abstract 02-1*, **Abstract#29** (2002).
2. W. A. Zisman, Contact Angle, *Wettability, and Adhesion, Advances in Chemistry Series, No. 43*, p. 13, American Chemical Society, Washington (1964).
3. Y. M. Vol'fkovich, E.I. Shkol'nikov, Institute of Electrochemistry, *Academy of Sciences of the USSA, Moscow. Translated from Elektrokhimaya*, **15**, 8 (1979).
4. H. Dohle, H. Schmitz, T. Bewer, J. Mergel, D. Stolten, *J. Power Sources*, **106**, 313 (2002).
5. B. Mueller, T. Zawodzinski, J. Bauman, F. Uribe and S. Gottesfeld, PV 98-27, p.1, The Electrochemical Society Proceedings Series, Pennington, NJ (1998).
6. R.H. Perry, D. W. Green, *Perry's Chemical Engineers' Handbook*, 7th Edition, p. 5-55, McGraw Hill (1997).
7. R. Defay, I. Prigogine, A. Bellemans, *Surface Tension and dsorption*, p. 220, Wiley, New York (1966).

Proceedings of The Electrochemical Society, PV 2002-31, 287-297 (2002)
DOI: 10.1149/200231.0287PV © The Electrochemical Society

THE DILUTION EFFECT OF REFORMATE COMPONENTS ON PEMFC PERFORMANCE

Tao Gu, W-k. Lee, and J. W. Van Zee
Department of Chemical Engineering
University of South Carolina
Columbia, SC 29208

M. Murthy
W.L. Gore & Associates, Inc.
201 Airport Rd., Elkton, MD 21922

ABSTRACT

This paper shows how the performance of a PEMFC with a Pt/Ru anode changes when nitrogen and carbon dioxide are present in the fuel. The data with N_2/H_2 mixtures show deviations of 10-30 mV from Nernst behavior at currents above 0.3 A/cm^2. Similar deviations were observed with CO_2/H_2 mixtures and differences between the anode polarization with the two types of mixtures was within the experimental error of the load cell (i.e., ± 5 mV). However, closer inspection of the anode with Cyclic Voltammetry (CV) after exposure to these mixtures indicates that the CO_2/H_2 mixtures produced some CO from the reverse water gas shift reaction. The CO stripping area showed dependence on the inlet composition of the anode gas and the coverage of anode was found to be in the order of 10^{-7} mol/cm^2. Equilibrium calculations at different temperatures and pressures show that the equilibrium CO concentration can reach between 10-100 ppm.

INTRODUCTION

Proton Exchange Membrane Fuel Cells (PEMFCs) operating on neat H_2 show good performance over a wide range of load and temperature conditions. In a "hydrogen challenged economy" PEMFCs may use reformate gas which contains 35~40% H_2, 40~50% N_2, 10~20% CO_2, and with trace amounts of CO (1). While much attention has been given to the poisoning effect of the trace amount of CO in the reformate gas (see for example, (2,3) for typical membrane electrode assemblies (MEAs) and (4) for high performance MEAs) there is not much literature that seeks to understand if N_2 and CO_2 are inert and how their presence affects performance. In a previous study we showed that the cell performance was affected by the neat reformate components, namely N_2 and CO_2 (5), but the effect of composition was not discussed. Bellows *et al.* (6) and Bruijin *et al.* (7) discussed the effect of CO_2 and studied the reverse water gas shift reaction in H_2SO_4 solution using cyclic voltammetry.

Here we studied the dilution effect of nitrogen and carbon dioxide separately and we analyze the loss in the cell performance. We also discussed the equilibrium of the reverse water gas shift reaction when carbon dioxide is present in the anode gas stream. Cyclic voltammetry was used to study the conditions that affect the rate and formation of CO inside a PEM fuel cell and.

EXPERIMENTAL

The data reported here were obtained with PRIMEA® MEAs Series 5621 and 5561, comprised of GORE-SELECT® membranes and Pt/Ru alloy on the anode. The active electrode area was 20 cm^2 and a serpentine triple channel flow-field (with a channel width and rib width of 0.08 cm each and a channel depth of 0.1 cm) was used on both the anode and cathode sides. The anode and cathode flows in the channel were co-current. The gas diffusion media (GDM) used in the experiment was CARBEL™ CL (thickness 0.41 mm). Compressible gaskets of an appropriate thickness were employed so that the internal pressure on the gas diffusion media was approximately 150 psi. Fuel cells were controlled by either a Model 890B test station made by Scribner Associates, Inc. or a Model DTS test station from Fuel Cell Technologies, Inc. For the nitrogen dilution experiments, ultra high purity hydrogen (99.999%), and bottled premixed hydrogen and nitrogen ($80\%H_2/20\%N_2$, $60\%H_2/40\%N_2$, $40\%H_2/60\%N_2$, $20\% H_2/80\%N_2$) were used as the fuels. For the carbon dioxide dilution experiments, carbon dioxide (research grade) and hydrogen (ultra high purity) were mixed with Tylan FC-260 series mass flow controllers to obtain CO_2/H_2 mixture (i.e., 20 % CO_2/80 % H_2 and 60 % CO_2/40 % H_2). The stoichiometries were 1.2 and 2.0 for anode and cathode, respectively (i.e., the hydrogen flow rates were 20 % greater and the air flowrates were 100 % greater than that required for the average current). The minimum flowrates for hydrogen and air were 50 standard cm^3/min (sccm) and thus at very low currents, the stoichiometries exceeded 1.2/2.0.

The MEAs typically were used continuously for 250 to 350 hours, and therefore, the data reported here can be considered as Beginning-Of-Life (BOL) data. All of the fuel cells were held at a constant voltage of 0.6 V for 70 hours before the polarization data were obtained. The cell temperature was held at 70°C and pressures of both anode and cathode sides at 101 kPa. The humidification temperatures were held at 85/75 °C for anode and cathode side and these correspond to approximate dew points of 80 °C and 70 °C for the anode and cathode respectively. The cell polarization curves were obtained with both constant voltage and constant current methods. Trial experiments showed that these two methods do not give significant difference, which is less than 5 mV at the same current density.

CV experiments were performed with an EG&G 263A potentiostat after the fuel cell had been subjected to normal break-in of the MEA and/or after typical polarization experiments. To perform these CV experiments, the cell was disconnected from the test station load and connected to the potentiostat so that the anode current collector was connected with the working lead of the potentiostat and cathode current collector was connected with both the reference and counter leads. At the beginning, nitrogen (300 sccm) was introduced on both anode and cathode sides to purge out the residual gas inside the fuel cell. Then, H_2 (100 sccm) and N_2 (100 sccm) was introduced at the cathode and anode side, respectively to obtain a base line CV curve. This flowrate was kept constant through the whole cyclic voltammetry experiments.. After obtaining a base line in neat nitrogen, the anode was exposed to pure CO_2 or a CO_2/H_2 mixture at 100 sccm for a fixed period of time, and then the anode was purged with N_2 for 5 minutes. The voltamegram was measured for various exposure times (i.e., dosage) of the CO_2/H_2 mixture. The exposure times were 1.5, 2, 3, 5, and 10 minutes. The scanning rate was 10 mV/s and scanning range was between 0.085 V and 0.700 V.

RESULTS AND DISCUSSION

Fig. 1 shows the cell polarization curves for dilutions of neat H_2 with N_2. The voltage loss increases with the increase of the current density and the N_2 concentration in the anode stream. Fig. 2 shows the voltage difference between neat H_2 and H_2/N_2 mixtures corresponding to Figure 1. The precision of the voltage measurements is ± 3 mV and thus the decreases in the voltage difference are within experimental error. When the N_2 concentration is within 60%, the voltage loss increases by about 10 mV as the nitrogen concentration in the mixture gas increases by 20 %. But, when current densities is higher than 0.6 A/cm^2, the voltage loss of 80% N_2 increases much faster than that of lower N_2 concentrations, which shows that mass transfer starts control the losses. Mass transfer polarization is negligible for neat H_2 within practical range of current density. However when there is N_2 in the anode gas, the mass transfer process across the GDM and the porous electrode obeys the Stephen-Maxwell equations and a larger partial pressure gradient is needed to keep the same flux of H_2.

Fig. 3 shows the calculated thermodynamic voltage loss due to an inert (N_2) gas dilution effect. Since H_2 is consumed along the channel, it's partial pressure decreases from the inlet to the outlet for a H_2 and N_2 mixture. The calculation was based on 3 different H_2 consumption conditions. The bottom line corresponds to the inlet condition, namely zero consumption of H_2. The top one corresponds to the outlet condition and the middle one corresponds to one half consumption of the hydrogen (anode stoic is 1.2). The measured data points were taken from Fig. 2. The comparison between the measured points and the calculated lines show that at zero current density the voltage loss agree accurately with calculation (for zero H_2 consumption). The data points correspond to 300 mA/cm^2 ~ 1000 mA/cm^2 and 20% ~ 60% N_2 concentration distribute near the thermodynamic calculation under the outlet condition. That means within that range, thermodynamics controls most part of the voltage loss. But, when current density gets high (>700 ma/cm^2) and N_2 concentration gets high (>60%) also, the voltage loss is more than 3 times of the thermodynamic calculation.

When H_2/CO_2 mixtures were studied, the CO_2 in the anode gas can also have the same dilution effect like N_2. Fig. 4 shows the comparison between the effect of CO_2 and that of N_2 to the cell polarization curves for a different MEA than in Fig. 1. The voltage loss caused by CO_2 appears to be about 3~5 mV larger than that caused N_2 but theses differences approach the precision of our measurement. This difference, while small and not so noticeable on the Pt/Ru alloys, may be a result of reverse water gas shift reaction:

$$CO_2 + H_2 = CO + H_2O \qquad [1]$$

Based on the thermodynamic data of the involved species (Table 1), the enthalpy and entropy change for reaction [1] are, $\Delta H° = 41.16$ KJ/mol and $\Delta S° = 42.03$ J/mol.

Assuming that ΔH° and ΔS° do not change from a standard state (298 K) to the operating temperature of 343 K in a PEMFC, the concentration of CO reaction [1] can be calculated.

Figs. 5 and 6 show the result of equilibrium calculation for the CO produced by the reverse water gas shift reaction. In the calculations of Figs. 5 and 6, we assumed saturation condition of water vapor but we plot the mole fraction in terms of a dry gas. Fig. 5 is based on the inlet conditions (i.e., no consumption of H_2). It shows that the CO concentrations have a bell shape relation with the change of the mole fraction of CO_2 in the anode gas. That is because, according to reaction [1], the concentration of CO depends on the product of the partial pressures of CO_2 and H_2. Fig. 5 also shows that the CO concentration is higher at a lower temperature. When the temperature decreases from 80°C to 70°C, the CO concentration increases by about 20 ppm. It also shows that the total pressure has a big effect on the equilibrium. At 70°C, when the total pressure increases from 101 kPa to 303 kPa, the CO concentration increases from 35 ppm to 172 ppm. Fig. 6 shows the calculation under the outlet conditions of a PEM fuel cell, in which the anode inlet stoic is assumed to be 1.2. Fig. 6 differs from Fig. 5 only for a shift of the position of the peaks of the equilibrium CO concentrations.

Figs. 7 – 9 show direct proofs that the reverse water gas shift reaction does occur in a PEM fuel cell. They show peaks at about 390 mV vs. cathode (neat H_2 reference and counter electrode), which are believed to be CO oxidation peaks due to

$$CO + H_2O \rightarrow CO_2 + 2H^+ + 2e^- \qquad [2]$$

Integration of the peaks gives CO coverage in the order of 10^{-7} mol/cm^2 (Note that the impurity of CO in the anode gas of less than 0.1 ppm does not affect the CO stripping area). In Fig. 7, the anode was exposed to pure CO_2 (100 sccm). For Fig. 8 and Fig. 9, the anode was exposed to (80 sccm) CO_2 + (20 sccm) H_2 and (10 sccm) CO_2 + (90 sccm) H_2, respectively. The peak areas show a dependence on the ratio of CO_2/H_2. Fig. 10 shows a baseline of CV with N_2 on the anode side and H_2 on the cathode side. Fig. 11 shows the peak areas of CO oxidation of a series of CV experiments for various CO_2 concentrations in the anode inlet stream. In this figure, the highest peak area is observed at 80 % CO_2. When the CO_2 mole fraction approaches to zero, the peak area decreases to zero because the reverse water gas shift reaction does not occur without CO_2. However, when the CO_2 mole fraction approaches to 1, the CO peak was observed (i.e. not approaches to zero). Note that calculated CO concentration from thermodynamics (shown in Fig. 5) is zero at 100 % CO_2. The difference between Fig. 5 and Fig. 11 at 100 % CO_2 might be explained by the H_2 crossover from cathode side to anode side. We observed that the open circuit potential was 85 mV when H_2 and N_2 were introduced on the cathode and anode side, respectively. According to the Nernst equation, 85 mV corresponds to 2.4×10^{-3} atm of H_2 partial pressure on anode side (at temperature:70 °C and H_2 partial pressure on the cathode: 0.7 atm). Fig. 12 shows the CO oxidation peak area as a function of CO_2 exposure time. It shows that the formation of CO is very fast (i.e., CO was formed on the surface within 3 minutes).

CONCLUSIONS

Thermodynamic loss can explain about one half of the decrease of cell performance due to nitrogen dilution effect. The remaining part comes from both mass transfer and kinetic losses. At high current (> 1 A/cm^2), mass transfer starts to show control. Thermodynamics tells that the reverse water gas shift reaction can occur in PEM fuel cells and produce significant amount of CO. Under normal operating conditions (70°C, 101 kPa, water vapor saturated) equilibrium CO concentration can reach 35 ppm for CO2 and H2 mixture. But, you may not see big effect on the cell polarization curves for high CO tolerant MEAs. However, cyclic voltammetry experiments showed direct proof that CO was produced inside a PEM fuel cell. The ratio of CO_2/H_2 affects the amount of CO produced. The time it takes is in the order of minutes for the electrode coverage of CO produced by the reverse water gas shift reaction to approach its steady state value.

ACKNOWLEDGEMENTS

The authors acknowledge the support of W.L Gore & Associates, Inc., for this work.

REFERENCES

1. S.G. Chalk, J.M. Miller, and F.W. Wagner, *J. Power Sources,* 86, 45 (2000).
2. C. Yang, P. Costamagna, S. Srinivasan, J. Benziger, and A.B. Bocarsly, *J. Power Sources,* 103, 1 (2000).
3. M. T. M. Koper, J. J. Lukkien, A. P. J. Jansen, and R. A. van Santen, *J. Phys. Chem. B*, 103, 5522 (1999)
4. M. Murthy, M. Esayian, A. Hobson, S. MacKenzie, W-k. Lee, and J.W. Van Zee, *J. of the Electrochemical Society,* 148 (10), A1147 (2001).
5. M. Murthy, W-k. Lee, and J. Van Zee, *AIChE Presentation No.* 83i, 352, (Spring 2002),
   New Orleans.
6. R.J. Bellows, E.P. Marucchi-Soos, and D. Terence Buckley, *Ind. Eng. Chem. Res.,* 35, 123 (1996).
7. F.A. de Bruijn, D.C. Papageorgopoulos, E.F. Sitters, and G.J.M. Janssen, *J. Power Sources,* 110, 117 (2002).

Table 1: Thermodynamic data relevant to the reverse water gas shift reaction.

Species	CO_2	H_2	CO	H_2O
$\Delta_f H°_{gas}$ /KJ/mol	-393.52	0	-110.53	-241.83
$S°_{gas,1\ bar}$ /J/mol	213.79	130.68	197.66	188.84

Quoted from NIST web chemistry book.

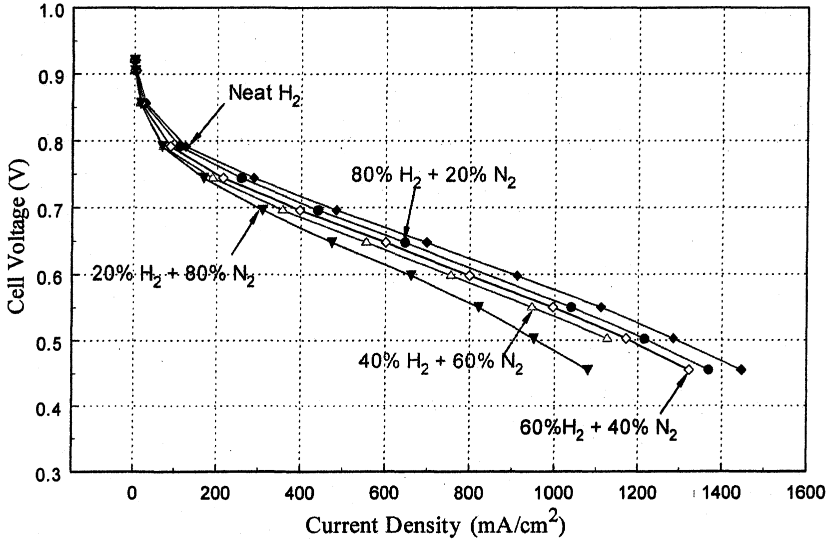

Figure 1. Effects of N2 dilution on the cell performance (MEA Series 5621)
(T_{cell} = 70 °C, T_D(A/C) = 80/70 °C, P(A/C) = 101/101 kPa, Stoic.(A/C) = 1.2/2.0)

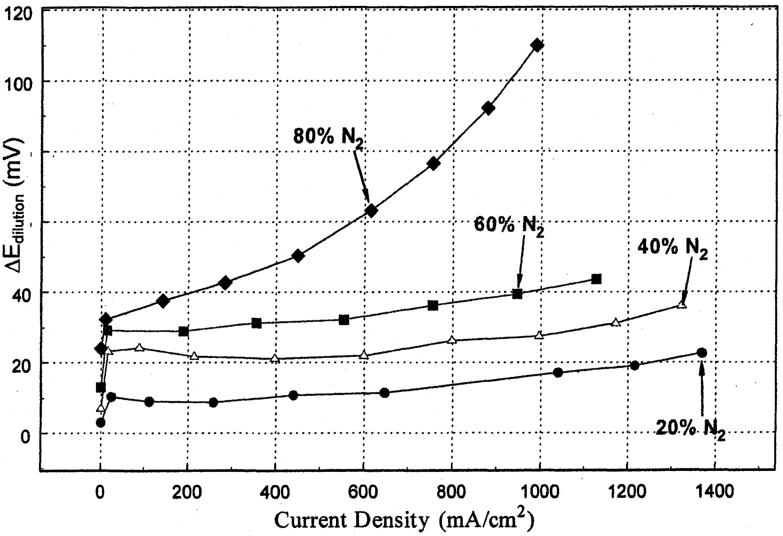

Figure 2. Voltage loss due to nitrogen dilution (MEA Series 5621)
(T_{cell} = 70 °C, T_D(A/C) = 80/70 °C, P(A/C) = 101/101 kPa, Stoic.(A/C) = 1.2/2.0)

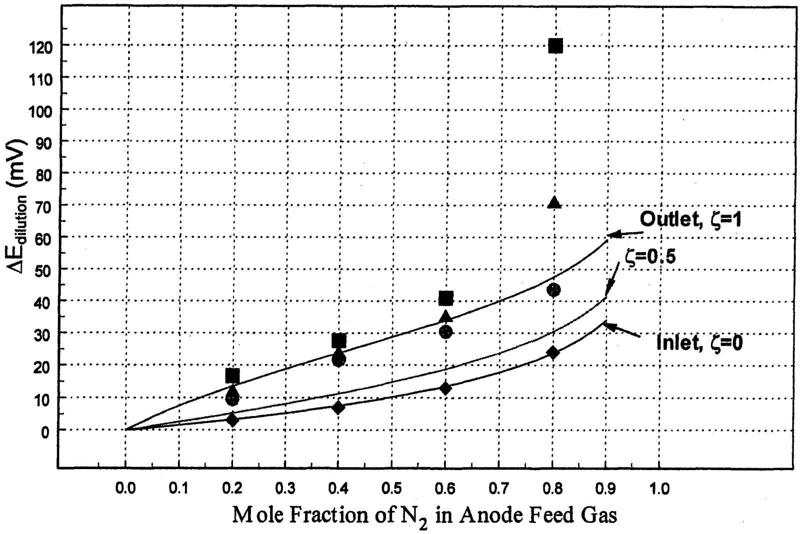

Figure 3. Comparison of measured and calculated voltage loss due to N_2 dilution (♦ = 0 mA/cm^2, ● = 300 mA/cm^2, ▲ = 700 mA/cm^2, ■ = 1100 mA/cm^2)

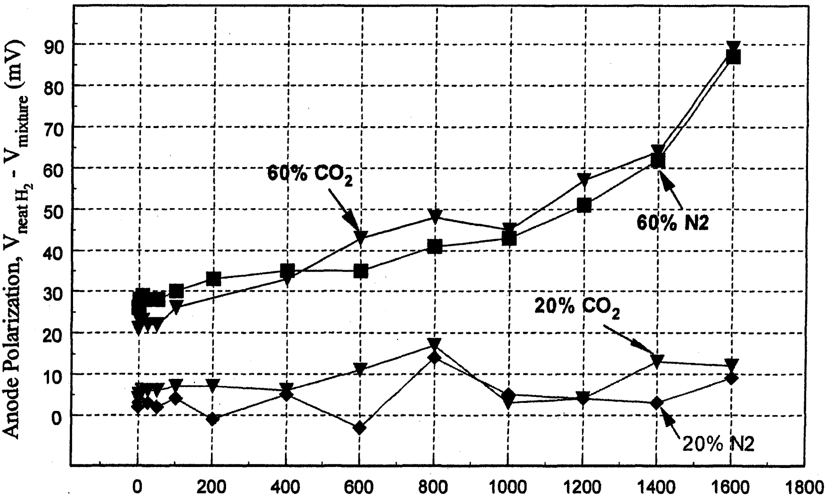

Figure 4. Voltage loss due to CO_2 and N_2 dilution (MEA Series 5561) (T_{cell} = 70 °C, T_D(A/C) = 80/70 °C, P(A/C) = 101/101 kPa, Stoic.(A/C) = 1.2/2.0)

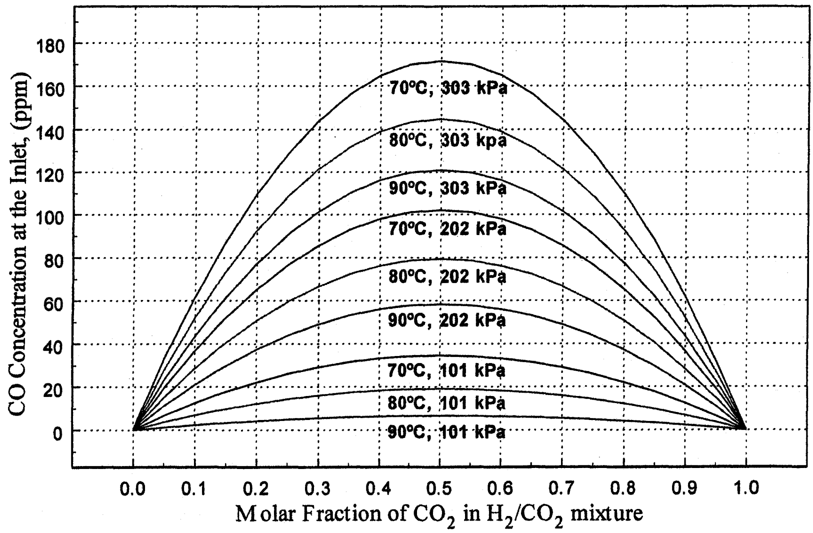

Figure 5. Equilibrium concentration of CO in water gas shift reaction as a function of inlet gas stream conditions

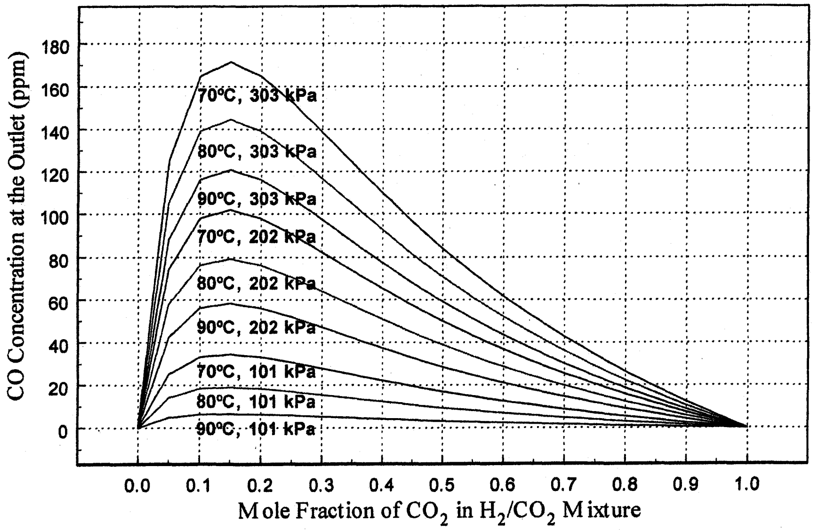

Figure 6. Equilibrium concentration of CO in water gas shift reaction as a function of outlet gas stream conditions

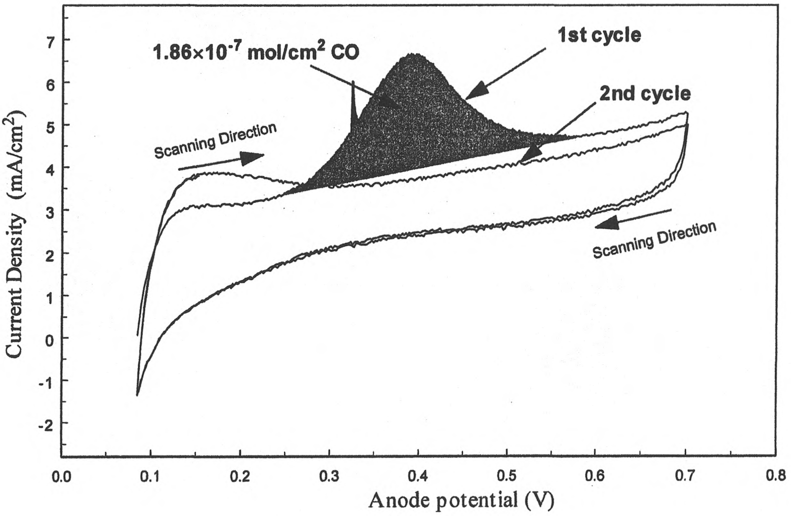

Figure 7. Cyclic voltammogram to show CO oxidation for 5 min. exposure of CO_2 (T_{cell} = 70 °C, T_D(A/C) = 80/70 °C, P(A/C) = 101/101 kPa, Scanning rate = 10 mV/s)

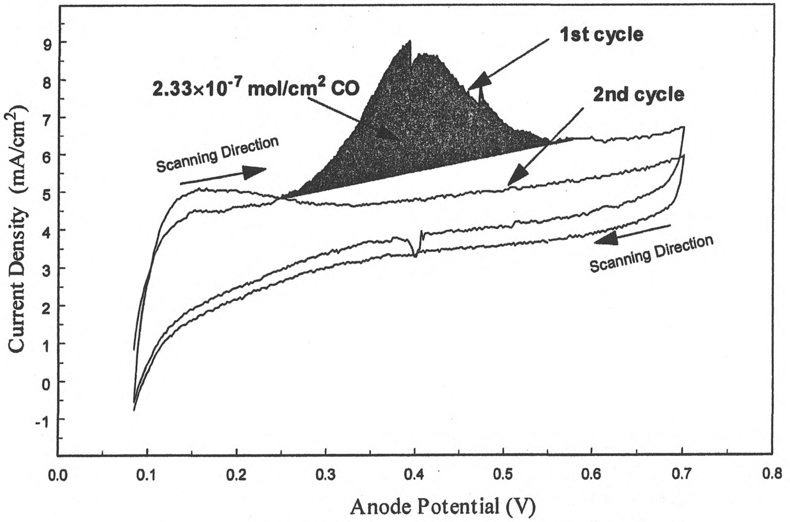

Figure 8. Cyclic voltammogram to show CO oxidation for 5 min. exposure of 80 % CO_2/20 % H_2 mixture (T_{cell} = 70 °C, T_D(A/C) = 80/70 °C, P(A/C) = 101/101 kPa, Scanning rate = 10 mV/s)

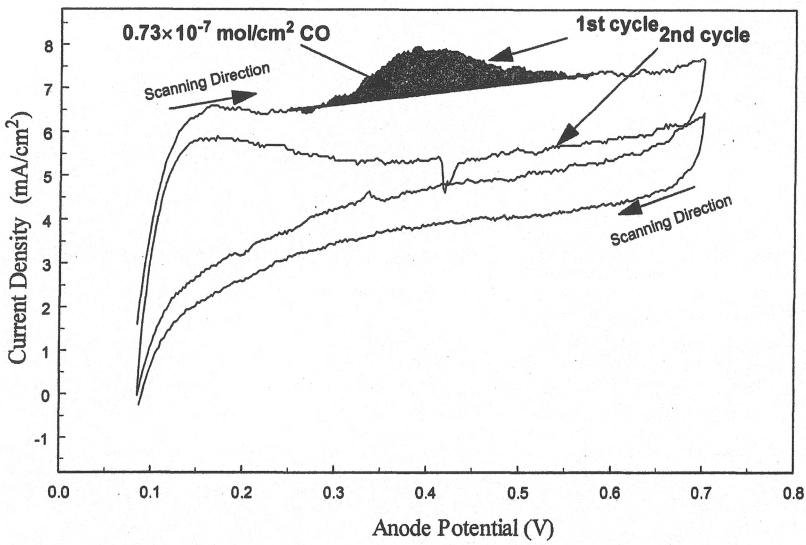

Figure 9. Cyclic voltammogram to show CO oxidation for 5 min. exposure of 10 % CO_2/ 90 % H_2 mixture (T_{cell} = 70 °C, T_D(A/C) = 80/70 °C, P(A/C) = 101/101 kPa, Scanning rate = 10 mV/s)

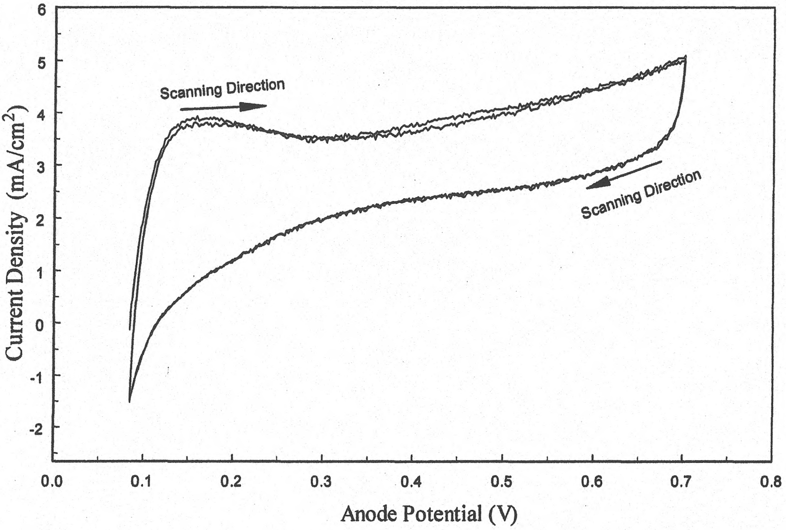

Figure 10. Base line of cyclic voltammogram (anode: N_2, cathode: H_2) (T_{cell} = 70 °C, T_D(A/C) = 80/70 °C, P(A/C) = 101/101 kPa, Scanning rate = 10 mV/s)

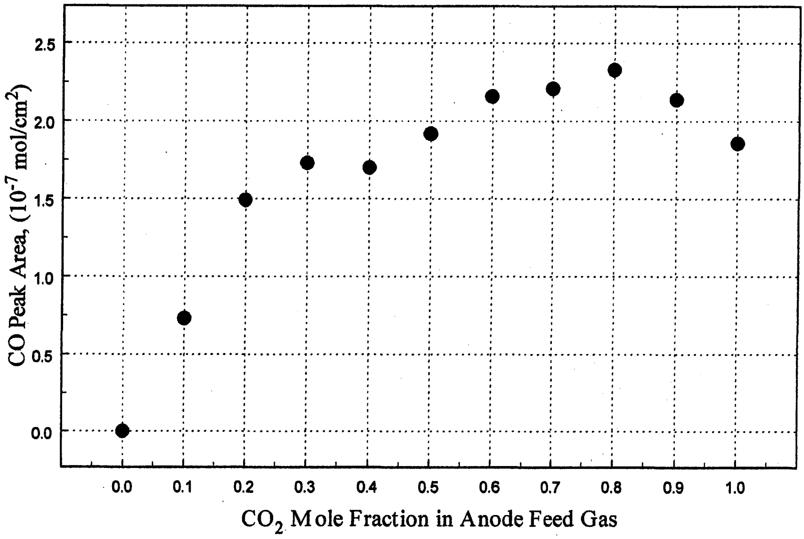

Figure 11. CO oxidized during cyclic voltammetry as a function of CO_2 concentration in the inlet gas stream.

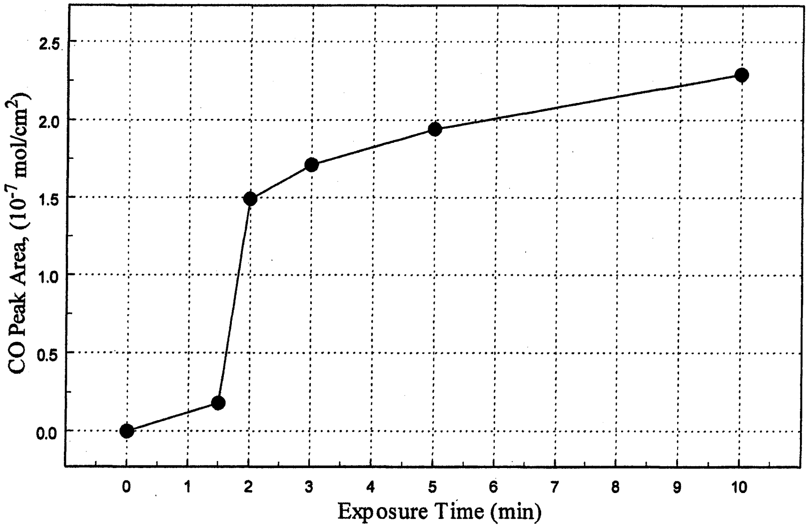

Figure 12. CO oxidation as a function of exposure time of CO_2

Proceedings of The Electrochemical Society, PV 2002-31, 298-314 (2002)
DOI: 10.1149/200231.0298PV © The Electrochemical Society

ELECTROLYTE RESISTANCE MEASUREMENT IN THE CATALYST LAYER OF POLYMER ELECTROLYTE FUEL CELLS USING ELECTROCHEMICAL IMPEDANCE SPECTROSCOPY

Rohit Makharia, Mark F. Mathias, Daniel R. Baker, John Iaculli, Michael W. Murphy

General Motors – Fuel Cell Activities
GM Global R&D, Honeoye Falls, NY, USA

ABSTRACT

In this paper, Electrochemical Impedance Spectroscopy is used to resolve various sources of polarization loss in a pure hydrogen-fueled polymer electrolyte fuel cell (PEFC). Experimental impedance data are fitted to a fuel cell model in which the catalyst layer physics are accurately represented by a transmission line model. Extracted parameters include cell ohmic resistance and catalyst layer electrolyte resistance and double layer capacitance. For a given MEA construction, similar results are obtained for two operating methods, in-situ (H_2/O_2) and ex-situ (H_2/N_2), and for two cell active areas, 5 and 50 cm^2. The measured electrolyte resistance increases with decreasing ionomer concentration in the electrode, as expected. We also observed that the real impedance measured at 1 kHz, often interpreted as the ohmic resistance in the cell, can include significant contributions from the electrolyte in the catalyst layer. Our results show that the catalyst layer electrolyte resistance can be a significant source of PEFC efficiency loss, and it is therefore important to accurately characterize it using methods such as those described here.

INTRODUCTION

Due to extensive research in recent years on low-temperature hydrogen-fueled polymer electrolyte fuel cells (PEFCs), membrane electrode assembly (MEA) performance has significantly improved. However, continued advancement in MEA technology is needed to further decrease cost and to improve fuel cell efficiency. It is therefore critical to identify and measure sources of efficiency loss so that research can be properly focussed on decreasing the most significant losses. Such assessments show that MEA performance is limited mainly by oxygen reduction reaction (ORR) kinetics followed by transport losses due to proton conduction in the cathode catalyst layer and/or oxygen transport to the cathode catalyst (1).

This work concentrates on using Electrochemical Impedance Spectroscopy (EIS) to measure the electrolyte resistance (i.e. resistance to proton migration) within PEFC catalyst layers. Such measurements are helpful in optimizing the electrode structure (ionomer/carbon ratio, drying process, hot-press process), quantifying the degradation of ionomer in the electrodes with time, and understanding the effect of operating conditions on MEA performance. EIS has been used in PEFC-related research to study ORR kinetics (2,3) and to characterize transport losses (4,5,6,7).

In this paper, we will discuss two experimental methods to characterize the electrode, one we call "in-situ" (H_2/O_2-pure hydrogen as fuel, pure oxygen as oxidant, constant DC current) and another we call "ex-situ" (H_2/N_2-pure hydrogen on anode, pure nitrogen on cathode, zero DC current). The effect of ionomer concentration on electrolyte resistance is shown using the in-situ method on 5 cm^2 active area MEAs. The application of the in-situ method is also applied to the larger 50 cm^2 active area cell, a size that is popular among MEA and PEFC developers. The 45° region impedance response, representing the electrolyte resistance in the catalyst layer, is clearly visible in both 5 and 50 cm^2 active area MEAs. Various parameters such as inductance (L), ohmic resistance (R_{ohmic}), double layer capacitance (C), and electrolyte resistance (R), are extracted by fitting experimental data to an equivalent circuit, where the catalyst layer physics can be accurately represented by a transmission line model. The rationale for using this transmission line model for the PEFC catalyst layer is also presented. Results from the in-situ method are confirmed using the ex-situ method.

EXPERIMENTAL

MEA Preparation and Cell Assembly

Catalyst-coated membranes (CCMs) with both 5 and 50 cm^2 active areas were prepared using carbon-supported Pt catalyst (47 wt% Pt/Vulcan XC72, Tanaka, Japan) and ionomer solution (5% wt Nafion® in organic solvents, 1100 equivalent weight (EW), DuPont, USA). The electrodes were coated on Teflon® decals and transferred onto extruded Nafion® 112 (50 μm thickness, DuPont) via hot-press. The Pt loading was maintained at 0.4 mg_{Pt}/cm^2 for both anode and cathode for all CCMs. The Nafion/Carbon (N/C) weight ratio was maintained at nominally 0.8 or 0.4 for all electrodes. The N/C ratio values are approximate because some of the Nafion can be lost during processing; nevertheless we have experimentally determined that the error is less than 10%. The electrodes were 13 ± 1 μm thick with a porosity (void volume) of approximately 68% and 75% for 0.8 and 0.4 N/C ratio MEAs, respectively. Nafion occupied approximately 15% of the electrode volume for 0.8 N/C ratio MEA and 7% for 0.4 N/C ratio MEA. Porosities and volume fractions are calculated using the measured electrode thickness and the bulk density of the ionomer (2 g cm^{-3}), carbon-support (2 g cm^{-3}) and platinum (21.5 g cm^{-3}).

The gas diffuison media (DM) used in the MEAs was carbon-fiber-paper-based substrates (Toray Inc., Japan). Both anode and cathode DMs were teflonated and processed using a proprietary surface treatment. Serpentine flow-fields (POCO) with channels machined into graphite blocks were used. Multiple-path channels (2 and 3 parallel channels for anode and cathode, respectively) were used for 50 cm^2 cells, whereas single-path channels (anode and cathode) were used for 5 cm^2 cells. The flow-field (FF) channel width was approximately 0.5 mm with a channel/land width ratio of 1.3/1. Single cells (50 and 5 cm^2) were assembled using appropriate MEA, DM, gasket, and flow-field by applying a compressive load of approximately 1500 kPa$_{abs}$ to the active area.

Fuel Cell Testing

Fuel cell test stations from Fuel Cell Technology (Los Alamos, NM) were used to test DC performance of 5 and 50 cm^2 cells. Pure hydrogen was used as fuel; pure oxygen was used on the cathode for in-situ experiments. For ex-situ experiments, pure hydrogen was used on the electrode that served as counter and reference, and nitrogen was used on the electrode under study. All gases used were of 99.99% purity. High gas stoichiometry of 50 to 150 was used for both anode and cathode gases to achieve uniform reactant and current distribution. Calibrated water-bubblers (humidifiers) were used to obtain reactant humidification. Cell ohmic resistance (the sum of proton-conduction resistance in the membrane and various electronic contact and bulk resistances) was determined from the real part of the impedance (Z') using alternating current (AC) perturbation at a frequency of 1 kHz. For each data point, the cell voltage was stabilized over 15 minutes and averaged over the last 10-15 minutes.

Impedance data were collected using Zahner IM6e Potentiostat. The potentiostat has a current range of 0 - 1 A and frequency range of 1 MHz- 0.01 mHz. Significant attention was given to reduce the effect of inductance on the alternating sinusoidal response of the system. We succeeded in reducing the inductance of the system by three orders of magnitude by choosing the appropriate type, length and arrangement of sense leads. Low-capacitance shielded leads were connected to the cell by drilling holes into the flow-fields and subsequently sealing them. For in-situ (H_2/O_2) testing, impedance data were collected after stabilizing the cell at DC conditions for 10-15 minutes. In the case of ex-situ experiments (H_2/N_2), the cathode side was purged with nitrogen gas until a stable voltage was achieved before collecting the impedance data. An alternating sinusoidal peak-to-peak perturbation of 100 mA and 1 mV were superimposed on direct current/voltage for galvanostatic and potentiostatic operation, respectively. The software displays alternating output signal during the experiment to identify noisy responses due to external noises and/or due to non-linearities in the system. All the experiments discussed and mentioned in this paper were free of such noisy response.

FUEL CELL EQUIVALENT CIRCUIT REPRESENTATION

Figure 1 shows the equivalent circuit of the fuel cell operating under hydrogen and oxygen. The circuit is divided into three main sections i.e. membrane, catalyst layer (CL), and hardware. The upper rail of the circuit carries current due to proton conduction (H^+) and the lower rail carries current due to electron conduction (e^-). $R_{membrane}$ represents the resistance to proton conduction in the membrane. A transmission line model represents the catalyst layer. R_p (total, R), R_{CT} (total, R_k) and C_{dl} (total, C) represent distributed electrolyte resistance in the catalyst layer, distributed charge transfer resistance, and double layer capacitance, respectively. The electronic resistance in the catalyst layer was assumed to be negligible. $R_{bulk+contact}$ includes the electronic bulk resistance (FF, DM, cable) and contact resistance (FF/DM, DM/CL) in the system. We will represent the total ohmic resistance ($R_{membrane} + R_{bulk+contact}$) as R_{ohmic}. Under AC operation, L represents the inductance of the system, presumably due mostly to the cables.

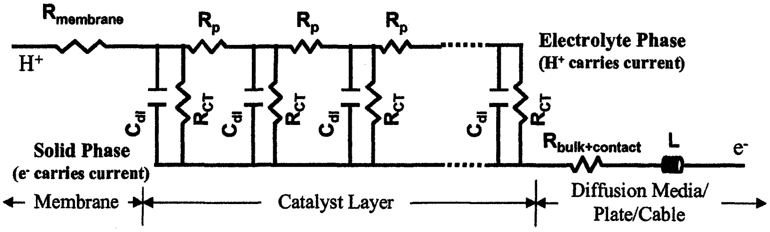

Figure1: Equivalent circuit of a fuel cell under in-situ (H_2/O_2) operation represented by a transmission line model for the porous electrode.

Eikerling and Kornyshev (4) have constructed impedance models for PEM fuel cells and derived analytical solutions for a number of special cases. The authors also point out that there are two different ways to approach the modeling: (a) using a system of differential equations to describe the physics and electrochemistry, or (b) using a finite transmission line of resistors and capacitors, as shown in Fig.1. In section 3 of their paper, they write, "The transmission line equivalent circuit has a continuous limit $m \rightarrow \infty$, in which the equations of the discrete model resemble the equations of the continuous model." Here m is the number of fundamental cells used in the transmission line model. Indeed the transmission line model can be thought of as a finite-difference approximation to the corresponding differential equations. In what follows, we give a set of differential equations that reduces to a special case of the equations considered in Eikerling and Kornyshev, and we restate the impedance they derive from these equations (equation 14 of their paper) in our notation.

We start out with the Ohm's law applied to the electrolyte in the catalyst layer

$$\frac{\partial \eta}{\partial y} = \rho\, i \qquad [1]$$

where η is the overpotential (solid minus electrolyte), ρ is electrolyte resistivity in ohm-cm, and i is current density in A/cm^2 in the electrolyte. The coordinate y gives the position within the catalyst layer, with $y=\delta$ at the interface to the membrane and $y=0$ at the interface to the diffusion medium. When no electrochemical reaction takes place, the charge transfer resistance is infinite (R_{CT} resistors in Fig. 1 are removed, becoming open circuit). The conservation of charge equation is

$$\frac{\partial i}{\partial y} = C_D \frac{\partial \eta}{\partial t} \qquad [2]$$

where C_D is the local double layer capacitance in F/cm^3 and t is the time. We now use a dimensionless coordinate $Y=y/\delta$, and write

$$\frac{\partial}{\partial y} = \frac{1}{\delta}\frac{\partial}{\partial Y} \qquad [3]$$

We will use a prime sign (') to denote $\partial/\partial Y$. Then we define a sheet resistance $R=\delta\rho$ in ohm-cm^2 and a sheet capacitance $C=\delta C_D$ in F/cm^2 and arrive at

$$\eta' = R\, i \qquad [4]$$

$$i' = C \frac{\partial \eta}{\partial t} \qquad [5]$$

For a small perturbation, $\eta = \eta_0 + \tilde{\eta}\exp(j\omega t)$, where ω is frequency, and we combine Eqs. [4] and [5] to get

$$\tilde{\eta}'' = j\omega RC\, \tilde{\eta} \qquad [6]$$

with boundary conditions $\tilde{\eta}'(0) = 0$ (at the interface of catalyst layer and DM) and $\tilde{\eta}(1) = 1$ (at the interface of catalyst layer and membrane). The solution is

$$\tilde{\eta}(Y) = \frac{\cosh[\sqrt{j\omega RC}\,Y]}{\cosh[\sqrt{j\omega RC}]} \qquad [7]$$

The resulting impedance due to the catalyst layer is

$$Z(\omega) = R\tilde{\eta}(0)/\tilde{\eta}'(0) = \frac{R\coth[\sqrt{j\omega RC}]}{\sqrt{j\omega RC}} \qquad [8]$$

In the limit of high frequency ω, the Nyquist plot for this impedance takes on a 45° angle to the real axis and approaches

$$\underset{\text{as } \omega\to\infty}{Z} \approx \sqrt{\frac{R}{j\omega C}} \qquad [9]$$

At low frequencies, the catalyst layer impedance approaches the vertical line

$$\underset{\text{as } \omega\to 0}{Z} \approx \frac{R}{3} + \frac{1}{j\omega C} \qquad [10]$$

Referring back to Fig. 1, for a transmission line circuit model with n repeating units,

$$R = nR_p \text{ and } C = nC_{dl}, \qquad [11]$$

Following Eikerling and Kornyshev, one can also introduce an electrochemical reaction with a kinetic resistance. For the case of linear kinetics, the corresponding transmission line model is shown in Fig 1, and the analytical solutions for impedance are given in equation 14 of their paper. Eq. [2] becomes

$$\frac{\partial i}{\partial y} = K_1 + K\eta + C_D \frac{\partial \eta}{\partial t} \qquad [12]$$

where $K_1 + K\eta$ is the kinetic expression for the local faradaic current in A/cm^3. The charge-transfer resistors shown in the equivalent circuit of Fig. 1 are given as

$$R_{ct} = \frac{n}{\delta K} \qquad [13]$$

The impedance is then given as

$$Z(\omega) = \sqrt{R_p Z_{ct}} \coth\left(n\sqrt{\frac{R_p}{Z_{ct}}} \right) \qquad [14]$$

with

$$Z_{ct} = \frac{R_{ct}}{1 + j\omega R_{ct} C_{dl}} \qquad [15]$$

For the case of nonlinear kinetics, the analogue to Eq. [12] is difficult to solve analytically. Furthermore, in such cases the charge-transfer resistance R_{CT} is no longer constant, and the use of a transmission line model becomes difficult. Thus these models will become inaccurate at high overpotentials, when the variations of η in the catalyst layer are so large that the faradaic current cannot be approximated using linear kinetics. If the fit values in the transmission line model satisfy the criterion

$$n^2 \frac{R_p}{R_{ct}} << 1 \qquad [16]$$

then the assumption that R_{CT} remains close to constant in the catalyst layer will be accurate.

EXPECTED VALUES OF R_{ohmic}, R, and C

Ohmic Resistances (R_{ohmic})

At high frequencies, the capacitors in the equivalent circuit of Fig. 1 behave as shorts and the AC response is solely due to the pure resistances of the system (including any catalyst layer electronic resistance). Table 1 shows the resistances of various components of ohmic resistance, R_{ohmic}, measured using ex-situ experiments (8). It was estimated that the total ohmic resistance should be approximately 59 mΩ-cm^2.

Table I: Estimated Components of Ohmic Resistance (R_{ohmic})

Components of Ohmic Resistance (R_{ohmic})	**Resistance (mΩ-cm^2)**
Membrane Resistance (50 μm thick) (Nafion conductivity = 0.13 S/cm @ 100% RH, 80°C) (9)	38.4
Two FF/DM Contact Resistances	13.0
Two DM/CL Contact Resistances	3.4
Two Bulk DM Electronic Resistances	2.8
Two CL Electronic Resistances	1.2
Total	**58.8**

Catalyst Layer Electrolyte Resistance (R)

Expected values for the catalyst layer electrolyte resistance can be bracketed using the following theoretically calculations relying on the ionomer conductivity and volume fraction in the catalyst layer

$$R_{min} = \frac{1}{\sigma_i} \cdot \frac{\delta}{\varepsilon_i / \tau(=1)} = 67 \mathrm{m}\Omega - \mathrm{cm}^2 \qquad [17]$$

$$R_{max} = \frac{1}{\sigma_i} \cdot \frac{\delta}{\varepsilon_i^{1.5}} = 159 \mathrm{m}\Omega - \mathrm{cm}^2 \qquad [18]$$

where,

σ_i - ionomer conductivity @ 100% RH, 80°C (0.13 S/cm)
δ – catalyst layer thickness (13 μm)
ε_i - volume fraction of ionomer in the catalyst layer (0.15 for 0.8/1 N/C)
τ - tortuosity of the electrode

Equation 17 assumes the tortuosity of the path of proton travel in the catalyst layer to be equal to unity and thus gives a low-end estimate of R. Equation 18 considers the effect of tortuosity and provides an upper-end estimate of R (10).

Double Layer Capacitance

The double layer capacitance for the electrode under study was calculated from double layer charging current obtained from a cyclic voltammogram (CV) (H_2/N_2) in the 0.3 to 0.5 V range. We assumed the total real surface area (cm^2_{real}) of platinum and carbon to be 250 m^2/g. The double layer capacitance was found to be approximately 20 $\mu F/cm^2_{real}$.

IN-SITU (H_2/O_2) TESTING

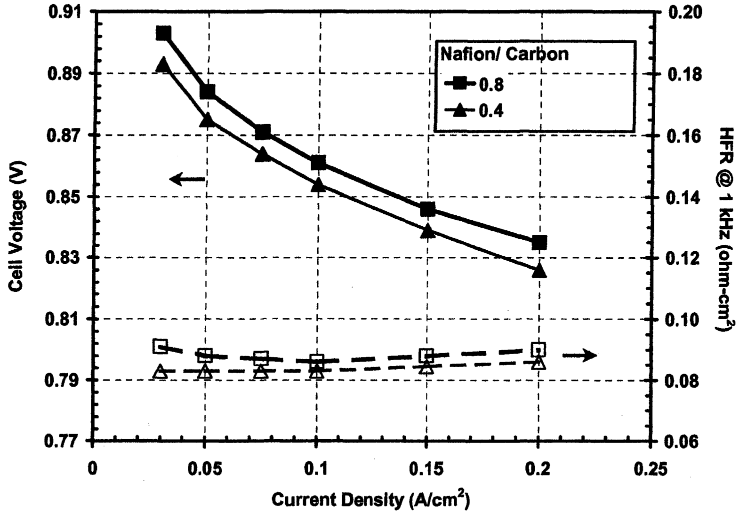

Figure 2: Effect of Nafion loading on cell voltage for H_2/O_2 operation at constant H_2/O_2 flow rate of 250 sccm (36 stoic at 0.2 A/cm^2) and 500 sccm (143 stoic at 0.2 A/cm^2), respectively, at constant current density. Nafion 112 CCMs (5 cm^2) with anode/cathode loading of 0.4/0.4 mg_{Pt}/cm^2 and N/C weight ratio of approximately 0.8 and 0.4; cell temperature of 80°C, reactant dewpoints of 86°C, and reactant pressure of 270 kPa_{abs}. Voltages were averaged between 10 and 15 minute holding time at each current density.

DC and AC response for 5 cm^2 MEAs

Effect of ionomer loading: Figure 2 shows polarization curves for MEAs with 0.8 and 0.4 N/C ratios under H_2/O_2 operation in 5 cm^2 active area fuel cell hardware at 80°C. The flow rates of the reactants were maintained at high stoichiometric ratios to ensure uniform distribution of gases. The reactants are over-saturated to ensure that the system is fully humidified. The MEA with 0.4 N/C ratio performs lower by 7-10 mV than 0.8 N/C ratio MEA. The 1 kHz resistance of the cells was very similar, 0.8 N/C exhibiting 50 mΩ-cm^2 higher values than the 0.4 case.

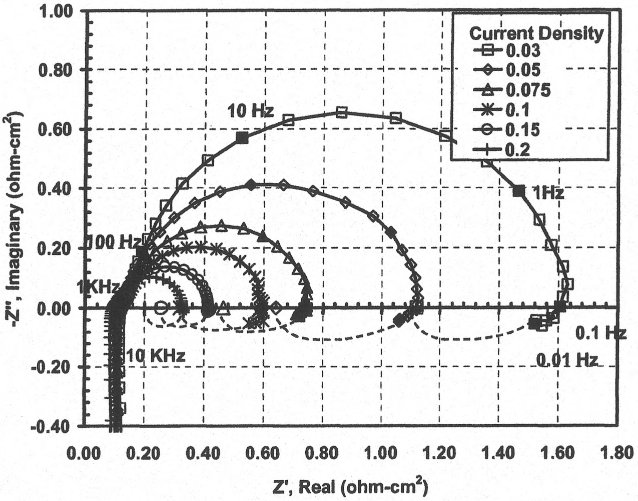

Figure 3: Complex-plane impedance plots for H_2/O_2 operation at constant current density (A/cm^2) for conditions described in Figure 2. Nafion 112 CCM (5 cm^2) with anode/cathode loading of 0.4/0.4 mg$_{Pt}$/cm^2 and N/C weight ratio of approximately 0.8; frequency range of 100 kHz – 0.01 Hz; peak-to-peak perturbation of ± 0.02 A/cm^2.

AC impedance spectroscopy was carried out on MEAs with low and high N/C ratio at current densities shown in Figure 1 after the cell was stabilized for 15 minutes at DC current. Figure 3 shows the AC response of a 0.8 N/C ratio MEA for different current densities on a Nyquist plot representation. Typical features of the plot includes pure inductance at very high frequencies, a shift of the real impedance from the origin due to ohmic resistance, a 45° region representing the electrolyte resistance in the catalyst layer, typical RC response due to kinetics and an inductive behavior at low frequency. At steady state, the low frequency intercept on real impedance axis must equal the slope of the DC polarization curve at the corresponding current density. Symbols in Figure 3 are actual experimental data points whereas the dashed lines are drawn to represent the inductive loop to meet the real impedance axis based on the slopes calculated from the

DC polarization curve of Figure 2. Antoine et al. related the low frequency inductive loop to the relaxation of intermediate species in an electrochemical-chemical-electrochemical (ECE) ORR mechanism (2).

Parameters were extracted from each impedance curve at various current densities by fitting the experimental data to the equivalent circuit shown in Figure 1 using ZView software (Scribner Associates Inc.). For data fitting purposes, one hundred rungs were used in the transmission line model of the catalyst layer, and further increasing the number of rungs did not change the results. Figure 4 shows the AC response for 0.8 and 0.4 N/C ratio MEAs after subtracting the inductance and the ohmic resistance from the data. The subtraction of these components helps reveal the 45° region representing the electrolyte resistance as shown in the inset. The dotted circle in the inset represents the approximate region where the response transitions from the 45° region to the RC circle. It is clear that for 0.4 N/C ratio MEA, the 45° response extends to higher impedance suggesting a higher electrolyte resistance in the catalyst layer.

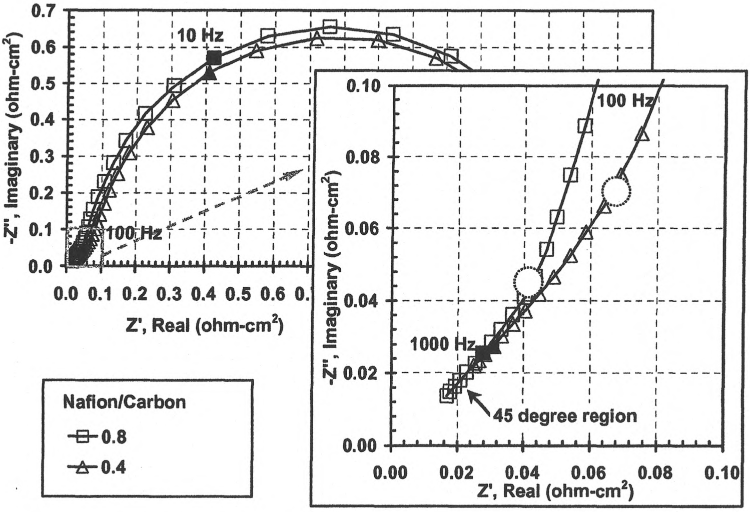

Figure 4: Complex-plane impedance plots for H_2/O_2 operation at constant current density for MEAs with N/C weight ratio of 0.8 and 0.4, respectively. The data are corrected for pure resistance and inductance calculated from model. Nafion 112 CCM (5 cm^2) with anode/cathode loading of 0.4/0.4 mg$_{Pt}$/cm^2; test conditions as described in Figure 2; frequency range of 100 kHz – 0.01 Hz; peak-to-peak perturbation of ± 0.02 A/cm^2.

The parameters extracted from the experimental data for MEAs with 0.8 and 0.4 N/C ratios are tabulated in Table II. The inductance in the system was of the order of μH when testing the 5 cm^2 cell. The ohmic resistance extracted using the AC impedance model for both MEAs matches closely the value estimated from ex-situ experiments (Table I). It is noteworthy that for both MEAs the ohmic resistance calculated from the model is about 25-32 mΩ-cm^2 lower than that measured at 1 kHz. This suggests that at 1 kHz, the ohmic resistance estimate includes some contribution from the catalyst layer electrolyte resistance. We will elaborate on this topic later in the paper. The electrolyte resistance for the 0.8 N/C ratio electrode is 105 mΩ-cm^2 and falls within the 67-159 mΩ-cm^2 bracket discussed above. The electrolyte resistance increases by approximately a factor of two for 0.4 N/C ratio MEA to 235 mΩ-cm^2. The double layer capacitance is about 20 μF/cm^2_{real} as predicted. Similar double layer capacitance for both MEAs suggest that for both cases all of the Pt is electrochemically accessible. We next consider if the performance loss of the lower N/C ratio MEA (Figure 2) can be explained by the increase in the cathode catalyst layer electrolyte resistance.

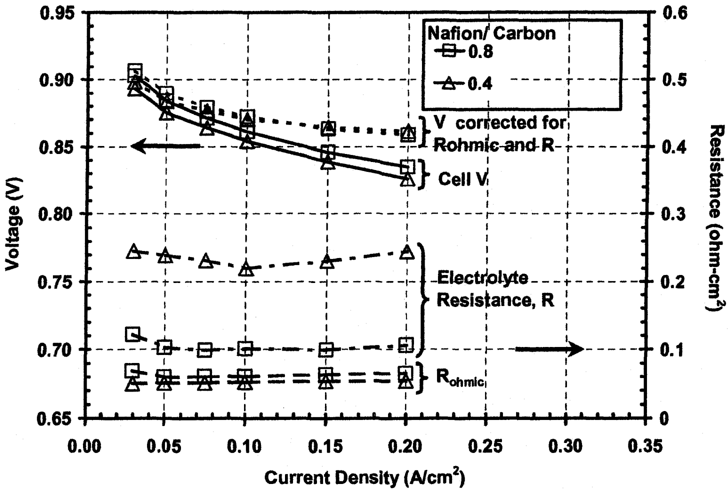

Figure 5: Cell voltages of MEAs with 0.8 and 0.4 N/C ratio corrected for ohmic and catalyst layer electrolyte resistance calculated from the model to obtain resistance corrected voltages.

Figure 5 shows the voltages obtained by correcting the cell voltage for ohmic and catalyst layer electrolyte determined by the impedance data. This was done using

$$V_{resistance free} = V_{cell} + i \cdot (R_{ohmic} + \frac{R}{2}) \qquad [19]$$

The catalyst layer electrolyte resistance correction is only half the resistance of the full layer because on average the protons travel through half the thickness of the catalyst layer before reacting. The resistance-corrected voltages for the two MEAs are very similar, thus confirming that the performance loss for lower N/C ratio case can be explained by its larger catalyst layer electrolyte resistance.

Frequency-Dependence of Ohmic Resistance (R_{ohmic}) Measurement: As stated earlier, the resistance measured at 1 kHz is higher than the more accurate estimate of R_{ohmic} value calculated from the fitting a model to data over a frequency range. The same can be seen in the Figure 4 inset; after correcting AC impedance data for R_{ohmic} calculated from the model, the resistance (Z') at 1 kHz is about 25-30 mΩ-cm^2 (the contribution to R_{ohmic} from catalyst layer electrolyte resistance at that frequency). Figure 6 shows the real impedance (Z') response for different the N/C ratio MEAs with respect to frequency. The error in high frequency resistance (HFR) measurement for N/C=0.8 (difference between experimental and model) is decreased to 7 mΩ-cm^2 at 10 kHz as compared to measurements made at 1 kHz where the error is 18 mΩ-cm^2. We also note that the error in the ohmic resistance estimate using the real impedance values increases with increase in catalyst layer electrolyte resistance (at 1 kHz, 18 mΩ-cm^2 error for N/C=0.8 and 33 mΩ-cm^2 error for N/C=0.4).

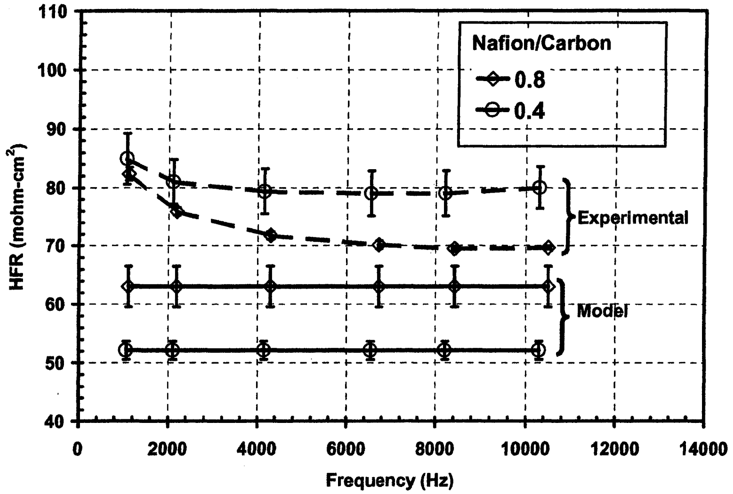

Figure 6: Estimate of ohmic resistances with respect to frequency. The experimental values are the real impedance at the given frequency, and the model values are estimates of R_{ohmic} from fitting impedance data. The error bars represent deviation of resistance from the mean measured at different current densities, for both model and experimental results.

MEA / Method	Current Density (A cm^{2}) / Voltage (V)	Inductance (H)	Ohmic Resistance, Rohmic (ohm-cm^{2})	Electrolyte Resistance, R (ohm-cm^{2})	Double Layer Capacitance,C (μF cm^{-2} $_{Real}$)*	Charge Transfer Resistance,Rk (ohm-cm^{2})	HFR @ 1KHz (ohm-cm^{2})	R/Rk**
0.8 Nafion/Carbon 5 cm2 active area In-situ (H2/O2)	0.030	1.32E-06	0.0687	0.122	19.67	1.215	0.091	0.100
	0.050	1.32E-06	0.0596	0.103	20.00	0.783	0.088	0.132
	0.075	1.32E-06	0.0604	0.099	19.19	0.538	0.087	0.184
	0.100	1.34E-06	0.0608	0.101	19.03	0.406	0.086	0.249
	0.150	1.31E-06	0.0634	0.100	18.90	0.272	0.088	0.366
	0.200	1.32E-06	0.0654	0.106	18.70	0.204	0.090	0.523
	Average	**1.32E-06**	**0.0631**	**0.105**	**19.25**	—	**0.088**	
	Standard Deviation	**7.9E-09**	**0.0035**	**0.008**	**0.49**	—	**0.002**	
0.4 Nafion/Carbon 5 cm2 active area In-situ (H2/O2)	0.030	1.10E-06	0.0502	0.246	21.57	1.241	0.083	0.198
	0.050	1.10E-06	0.0513	0.239	21.30	0.772	0.083	0.310
	0.075	1.11E-06	0.0512	0.232	21.32	0.503	0.083	0.461
	0.100	1.10E-06	0.0523	0.220	21.10	0.367	0.083	0.600
	0.150	1.08E-06	0.0537	0.231	21.39	0.254	0.084	0.909
	0.200	1.09E-06	0.0542	0.245	22.41	0.183	0.086	1.340
	Average	**1.10E-06**	**0.0521**	**0.235**	**21.52**	—	**0.084**	
	Standard Deviation	**1.1E-08**	**0.0015**	**0.010**	**0.46**	—	**0.001**	
0.8 Nafion/Carbon 50 cm2 active area In-situ (H2/O2)	0.005	5.42E-09	0.0558	0.110	21.72	0.511	0.074	0.215
	0.010	5.57E-09	0.0561	0.108	20.90	0.511	0.074	0.212
	0.015	5.94E-09	0.0573	0.114	21.52	0.545	0.077	0.210
	0.020	6.08E-09	0.0626	0.129	19.88	0.488	0.084	0.265
	Average	**5.75E-09**	**0.0579**	**0.115**	**21.00**	—	**0.077**	
	Standard Deviation	**3.1E-10**	**0.0032**	**0.010**	**0.83**	—	**0.005**	
0.8 Nafion/Carbon 50 cm2 active area Ex-situ (H2/N2)	0.500	6.28E-09	0.0561	0.091	23.83	-----	0.074	-----

*Double layer capacitance is calculated for real carbon and platinum surface area. The total surface area of the catalyst is assumed to by 250 m^{2} gm^{-1}.

** The model shown in Figure 1 closely represents the real electrode behavior if $R/R_k<1$

DC and AC response for 50 cm^2 MEAs

One would ideally like to apply impedance diagnostics to stack-size MEAs to extend their impact beyond materials development studies to fuel cell characterization.in real-world hardware. The impedance of an MEA (and thus the signal-to-noise ratio) is inversely proportional to the active area. For this reason, it becomes more difficult to obtain an AC response with a clear 45° region as the active area is increased. To confirm independence of the results on the active area, we tested nominally identical MEAs in 5 and 50 cm^2 hardware. Figure 7 shows the DC response of 5 and 50 cm^2 MEAs operating under H_2/O_2 at 60°C, 270 kPa$_{abs}$, with gases flowing at a high stoichiometric rate with over-saturated inlet streams. The DC performance is not affected by hardware scale-up from 5 to 50 cm^2 as the voltages match closely throughout the current density range once the cell voltages are corrected for ohmic losses.

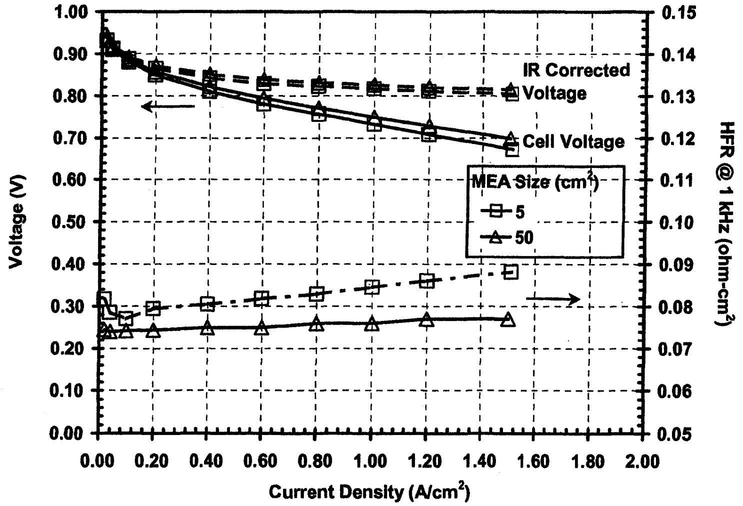

Figure 7: MEA performance comparison in 5 cm^2 vs. 50 cm^2 hardware for H_2/O_2 operation at constant H_2/O_2 stoic of 50/50 throughout the current density range. Nafion 112 CCM (5 cm^2) with anode/cathode loading of 0.4/0.4 mg$_{Pt}$/cm^2 and N/C weight ratio of approximately 0.8; cell temperature of 60°C, reactant dewpoints of 70°C (160% RH$_{inlet}$), and reactant pressure of 270 kPa$_{abs}$. Voltages were averaged between 10 and 15 minute holding time at each current density.

Figure 8 shows the AC response of 50 cm^2 active area MEA with N/C ratio of 0.8. While transitioning from 5 to 50 cm^2 active area MEA, we realized that to get a good set of data with a clear 45° region, it is extremely important to reduce the inductance of the system. As shown in Figure 8, reduction of inductance by three orders of magnitude revealed the 45° region on 50 cm^2 active area. The results obtained by fitting the data to the equivalent circuit of Figure 1 are tabulated in Table II. The results on 50 cm^2 active area compare well to those of 5 cm^2.

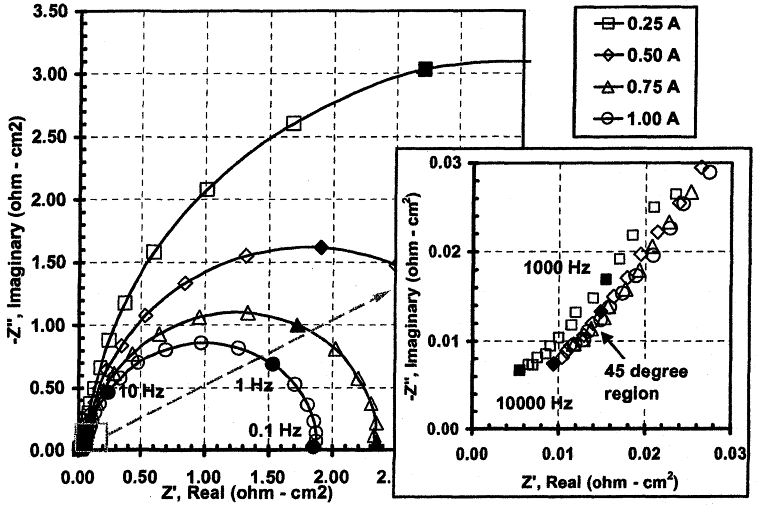

Figure 8: Complex-plane impedance plots for H_2/O_2 operation at constant H_2/O_2 stoic of 50/50 throughout the range of the current density. Data are corrected for inductance and ohmic resistance calculated from the model. Nafion 112 CCM (50 cm^2) with anode/cathode loading of 0.4/0.4 $mg_{Pt}/$ cm^2 and N/C weight ratio of approximately 0.8; cell temperature of 60°C, reactant dewpoints of 70°C (160% RH_{inlet}) and reactant pressure of 270 kPa_{abs}. Voltages were averaged between 10 and 15 minute holding time at each current density; frequency range of 100 kHz – 0.1 Hz; peak-to-peak perturbation of ± 0.002 A/cm^2.

EX-SITU (H_2/N_2) TESTING

Ex-situ testing (zero DC current) is useful for MEA diagnostics like measurement of catalyst utilization and hydrogen cross-over current. The setup is referred to as the driven-cell mode where hydrogen flows over one electrode (counter and working) and nitrogen flows on the electrode under study (the cathode in this work). Pickup et al. have applied AC impedance techniques to fuel cells operating in this driven-cell mode, estimating the electrolyte distribution and its resistance in the catalyst layer (6). We have studied the AC response of a fuel cell operating under the driven-cell mode on both 5 and 50 cm^2 hardware. For such operation, the equivalent circuit of Figure 1 reduces to that shown in Figure 9. As described earlier by Equation 10, under AC operation the response of the system is purely capacitive represented by a straight vertical line at low frequencies where the real-axis intercept equals R/3.

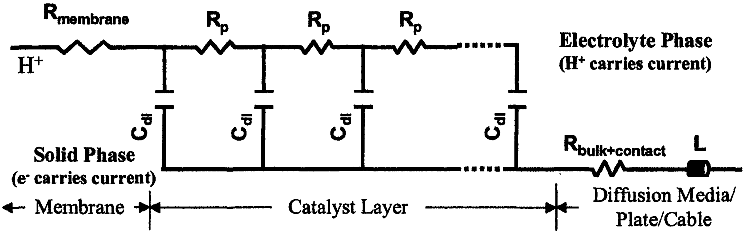

Figure 9: Equivalent circuit of a fuel cell under ex-situ (H_2/N_2) operation represented by a transmission line model for the porous electrode.

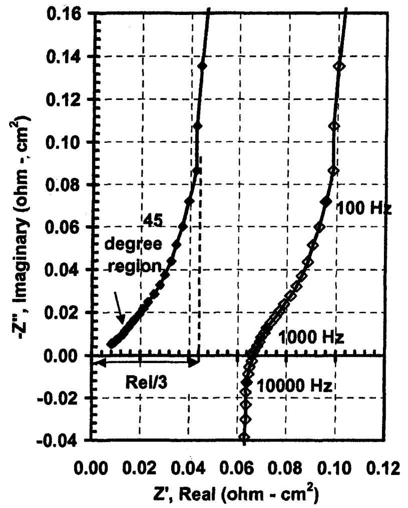

Figure 10: Complex-plane impedance plots for H_2/N_2 operation at 0.5 V for constant H_2/N_2 flow of 500/ 500 sccm. Nafion 112 CCM (50 cm^2) with anode/cathode loading of 0.4/0.4 mg_{Pt}/cm^2 and N/C weight ratio of approximately 0.8; cell temperature of 60°C, reactant dew points of 70°C (160% RH_{inlet}) and reactant pressure of 270 kPa_{abs}; frequency range of 100 kHz – 10 Hz; peak-to-peak perturbation of ± 0.002 V. Solid symbols represent the data corrected for system inductance and ohmic resistance.

AC Response for 50 cm^2 MEAs

Figure 10 shows the AC response of a fuel cell operated in the driven-cell mode for a 50 cm^2 MEA with a N/C ratio of 0.8. At 0.5 V, the DC response is purely dominated by double layer capacitance charging. The AC response consists of inductance at very high frequency, a shift of the real impedance from the origin due to ohmic resistance in the cell, a 45° region representing the electrolyte resistance and purely capacitive response at low frequencies. The parameters extracted by fitting the experimental data to the equivalent circuit in Figure 9 are tabulated in Table II. The results compare well with those calculated using in-situ AC testing on both 5 and 50 cm^2 cells.

SUMMARY

We have demonstrated that AC impedance is a powerful tool to resolve voltage losses due to ohmic resistance in the cell and electrolyte resistance in the catalyst layer. The method has been implemented for both in-situ and ex-situ operation on 5 and 50 cm^2 active area cells. The results show that the electrolyte resistance in the catalyst layer is significant and increases with decreasing ionomer concentration in the catalyst layer. Also, it is evident that ohmic resistance measured using AC impedance at 1 kHz includes some contribution from the electrolyte resistance in the catalyst layer. The error in ohmic resistance estimate increases with increasing electrolyte resistance.

REFERENCES

1. H. Gasteiger, W. Gu, R. Makharia, M. F. Mathias, B. Sompalli in 'Handbook of Fuel Cells – Fundamentals, Technology and Applications', W. Vielstich, H. Gasteiger and A. Lamm (Eds), John Wiley & Sons (2003)
2. O. Antoine, Y. Bultel, R. Durand, *J. Electroanalytical Chemistry*, **499**, 85 (2001)
3. A. Parthasarathy, B. Dave, S. Srinivasan, J. Appleby, *J. Electrochem. Soc.*, **139**, 1634 (1992)
4. M. Eikerling, A.A. Kornyshev, *J. Electroanalytical Chemistry,* **475**, 107 (1999)
5. A. Parthasarathy, B. Dave, S. Srinivasan, J. Appleby, *J. Electrochem. Soc.*, **139**, 1634 (1992)
6. M. Lefebvre, R.B. Martin, P.G. Pickup, *Electrochemical and Solid State Letters,* **2**, 259 (1999)
7. T.E. Springer, T.A. Zawodzinski, M.S. Wilson, S. Gottesfeld, *J. Electrochem Soc.*, **143**, 587 (1996)
8. W. Gu, unpublished results (GM Global R&D, Fuel Cell Activities, Honeoye Falls, NY, USA)
9. G. Alberti, M. Casciola, L. Massinelli, and B. Bauer, *J. Membrane Science*, **185**, 73 (2001).
10. C. Boyer, S. Gamburzev, O. Velev, S. Srinivasan, A. J. Appelby, Electrochimica Acta, **43**, 3703 (1998)

Proceedings of The Electrochemical Society, PV 2002-31, 315-323 (2002)
DOI: 10.1149/200231.0315PV © The Electrochemical Society

ELECTROCATALYTIC LAYER MICROSTRUCTURE-RESISTANCE RELATIONSHIP

V. Stanic

Teledyne Energy System Inc.
West Palm Beach, Florida 33407, USA

ABSTRACT

The effect of electrocatalytic layer microstructures of various conventional membrane electrode assemblies (MEAs) on their bulk resistance has been investigated. Materials characterization was carried out by optical microscopy and *ac* impedance spectroscopy. A base line for the microstructure – resistance relationship was established with three MEAs obtained from manufacturer A. These MEAs had the same compositions of cathodes and different compositions of anodes. The results of Type A cathode analyses show that the size of cracks in the electroctalytic layers is the major cause for the linear resistance to increase from 274 to 643 Ω/cm. The linear resistance of Type A anodes increased from 204 to 527 Ω/cm. This increase was attributed to the different catalysts and Nafion® polymer loadings in Type A anodes. The resistance increase in anode A3 was correlated to the Nafion® loading increase and not to the microstructure change. This conclusion was confirmed by a study done using carbon coatings that contained various Nafion® loadings. The study showed that when the Nafion® content was less than 20%wt and more than 30%wt, the resistance of the carbon coatings increased. For the case of Nafion® content between 20 and 30%wt, the carbon coatings had the lowest resistances. The characterization results of two additional MEAs prepared by manufacturers B and C were compared to A. Type B MEA had an irregular electrocatalyst microstructure and high electrocatalyst resistance (560 Ω/cm). Type C MEA, which had the most uniform microstructure, had resistances of 94 and 106 Ω/cm for cathode and anode, respectively.

INTRODUCTION

Membrane electrode assemblies (MEAs) used in polymer electrolyte membrane (PEM) fuel cells consist of polymer electrolyte membranes and electrocatalytic layers. The major components of the electrocatalytic layers are a metal catalyst supported on carbon powder and the same proton conductive polymer electrolyte used for the membrane. The catalyst commonly used in PEM fuel cells for oxygen reduction and hydrogen oxidation is Pt. The Pt-Ru alloy catalyst has been successfully used for hydrogen oxidation in the presence of carbon monoxide.

The MEA preparation involves several steps such as ink preparation from a catalyst and the polymer, ink deposition on a substrate, and drying and hot pressing of the deposited layer onto the polymer electrolyte membrane. The microstructure of the prepared elctrocatalytic layers depends on the catalyst particle size, the catalyst / polymer weight ratio, the coating technique, the drying rate, the processing temperature as well as many other processing parameters.

The approach used in this paper for the quantitative microstructure characterization is analogous to the methodology used for metals and semiconductors. It is well known that perfect monocrystals and amorphous materials have the lowest resistances due to lack of imperfections and grain boundaries [2]. It is similarly expected that MEAs with small grains surrounded with wide cracks have higher resistance than the MEAs with uniform crack free microstructure.

In this paper the total ohmic resistance of a single electrocatalytic layer of an MEA is correlated to the microstructure of the layer. The first objective was to determine how the size of fluctuations in the electrocatalyst features, such as grains and cracks, affects the linear resistance in electrocatalytic layers with the same compositions. Since several of the MEAs studied differed in both the microstructure and the Nafion® polymer content, the second objective of this work was to study the linear resistance dependence on the Nafion® content in order to differentiate the effects of these two parameters on the resistance. For this purpose carbon coated membranes were prepared in-house. Materials characterization was carried out by optical microscopy and *ac* impedance spectroscopy.

EXPERIMENTAL

MEAs studied

MEAs obtained from three different manufacturers A, B, and C were used to study the influence of electrocatlayst layer microstructure on bulk resistance. Three MEAs received from manufacturer A were used to establish a base line for the electrocatalyst microstructure – bulk resistance relationship since the MEAs had known compositions. These MEAs had different compositions of the anode layers and the same compositions of the cathode layers. Since the MEAs were in the developmental stage, in addition to the known catalyst loading, the relative changes in polymer content and the changes in the catalyst loading were revealed by manufacturer A. Type A1 MEA had 2.5 times higher catalyst loading than Types A2 and A3, while Type A3 MEA had 2 times higher content of Nafion® than Types A1 and A2.

Two additional MEAs provided by manufacturers B and C were also used for microstructure-resistance study. Type B MEA had identical electrocatalyst on both anode and cathode sides, while Type C MEA had different electrocatalyst compositions on anode and cathode. All the MEAs were tested as received without any additional treatment.

Carbon coating preparation

The carbon coating of the Nafion® 117 membrane was done using a carbon-Nafion® ink. The ink was prepared from Vulcan XR 7RC carbon powder and 5% Nafion® solution. The methods used for the ink and the coating preparations are described earlier by Wilson et al.[1]. All carbon coatings prepared contained the same loading of carbon powder (1.25 mg/cm^2). However, the loading of Nafion® varied, and it was 10, 20, 30, 40, 45, and 50%wt. The carbon coating was made only on one side of the Nafion® 117 membrane. The areas coated were 16 cm^2. Two samples of each composition were prepared.

Optical microscopy characterization

The microstructures of the MEAs received from manufacturers A, B, and C and in-house prepared carbon coated membranes were observed by an Olympus BX 60 optical microscope at magnifications from 50 to 200. The size of MEAs examined was 150 cm^2. Two samples of each MEA type were tested. Each sample was randomly examined first and then five micrographs were taken from each layer. The micrographs were used for the quantitative characterization of the electrocatalyst microstructure that consisted of the measuring and calculating the average grain diameter, the linear grain density and the maximum crack width.

The optical microscope was also used for measurements of the electrocatalyst and carbon coating layer thicknesses. The technique applied was based on the image focusing at different layer depths. For this purpose the cracks in the layers were used. The image was first focused on the surface of the layer and then it was focused on the membrane at the bottom of the layer. The difference in the positions of the fine focus adjustment knob between previous and later focusing was correlated to the layer thickness since one increment on the fine focus knob represents 1 μm.

Linear resistance measurements

The bulk resistance of the layers was measured using a two electrode *ac* impedance method. The resistance was measured in the frequency range from 1 to 20 kHz using the Solartron 1280 B and z-plot software version 2.1. The measurements were performed under controlled temperature (23 ± 2)°C and relative humidity (47 ± 3)% conditions.

Two gold pins (area 7.8x10^{-3} cm^2) attached to a plastic handle were used as electrodes. The pins were placed 1 cm apart. The resistance was measured laterally along the electocatalyst surface. During each measurement, a constant pressure was applied to the electrodes. The resistance was measured in the same areas where the micrographs were taken. The spots tested on the anode and the cathode sides of each sample did not overlap in order to avoid the effect of any physical changes in the layers caused by the electrode compression. The layer's bulk resistance was obtained at the intersection of the impedance response curve (Cole-Cole plot) with the impedance real axis. The resistance measured represents the total ohmic resistance that includes the electrical resistance of metal conductors used, and the electronic and ionic resistances of electrocatalyst.

The method reproducibility was checked by repeating the measurements at the same spot five times in both current directions (forward and reverse) between the pins. For the calculation of the results presented, the average of these measurements was taken. The standard deviation was <5%.

RESULTS AND DISCUSSION

Microstructure

The results of microstructure characterization for Type A MEAs are summarized in Table 1. The values presented are the averages of measurements taken per each electrocatalyst.

Table 1: Catalyst grain sizes, crack widths, and the linear grain densities for various MEAs.

MEA Type	CATHODE			ANODE		
	Grain diameter (µm)	Maximum crack size (µm)	Number of grains/cm	Grain diameter (µm)	Maximum crack size (µm)	Number of grains/cm
A1	115	24	87	247	< 4	40
A2	185	48	54	67	< 4	150
A3	164	112	61	67	8	150

Type A1 anode has a 2.5 higher catalyst loading than type A2 and A3 anodes and different microstructure than the other two anodes. It has grains with diameter 247 µm that are 3.7 times larger than the grains in A2 and A3 anodes. Due to larger grains, the linear density is lower than in A2 and A3 anodes (40 grains/cm vs 150 grains/cm). Cracks in anode A1 are < 4 µm wide and do not penetrate to the membrane surface. It appears that the A1 anode was deposited as a catalyst multi layer. Even though the crack size of anode A2 is also < 4µm, they propagate from the surface of the layer to the surface of the membrane. Cracks in A3 are wider than in anodes A1 and A2 (8 µm) and they run from the top of the layer to the membrane surface. The thickness of anode A1 is 34 µm and it is ~ 2 times thicker than anodes A2 and A3 which have an average thickness of ~16 μm. Therefore, it is apparent that the microstructure of type A anodes varied with the composition. Increased catalyst loading in anode A1 resulted in thicker layer with larger grains than in the other two anodes. However, the increased polymer loading increased the crack size in A3 anode.

Although the cathode catalyst layers in Type A MEAs have the same composition, their microstructures differ visually (Fig. 1 and 2) and quantitatively (Table 1). From Fig. 1 and 2, it is obvious that cathode A1 has smaller grains (115 μm) with large pores (~16 μm), than cathode A3. Cathode A1 micrograph shows that the grains are tightly packed and the cracks are narrow (< 8 μm). There are some short and localized enlargements of the crack width from ~ 8 to 24 μm (Fig. 1) that reveal the membrane surface. On the other hand, cathodes A2 and A3 have much larger grains 185 and 164 μm, respectively, with wider cracks (Table1). In cathode A3 the cracks are 112 μm wide and in some areas completely surround the grains (Fig. 2).

The differences in the microstructures of Type A1 cathode and Types A2 and A3 cathodes, indicate that the preparation process of cathode A1 is different than of cathodes A2 and A3. Some of the possible reasons are that the ink of this electrocatalyst might be deposited in more than one layer or it may be made using different solvents. The appearance of cathodes A2 and A3 indicate that their preparation process is basically the same, with slight differences in their quantitative characteristics (grain size and crack width). Dissimilarity in the microstructures of cathodes A2 and A3 is most likely the consequence of the variations in the layer deposition parameters such as drying temperature or drying rate. All Type A cathodes have thickness ~ 16 μm.

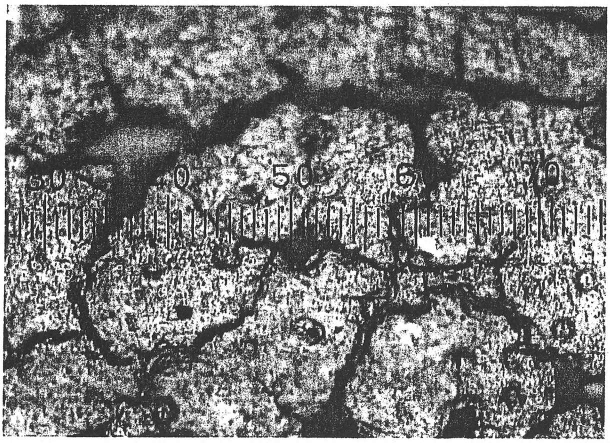

Figure 1: Type A1 MEA cathode catalyst has linear resistance 274 Ω/cm. Dark lines in the micrograph are the cracks in the electrocatalytic layer. Scale: 1 increment is 8 μm.

Type B MEA has the same composition of anode and cathode layers and therefore their microstructures are identical. The layers have very non uniformly cracked structure with a maximum crack width of 140 μm. However, Type C MEA has cathode and anode with different compositions. The microstructures of both the cathode and the anode electrocatalysts are very uniform with cracks localized in small areas (diameter <160 μm).

The carbon coatings with 20 and 30%wt of Nafion® polymer have crack free microstructures. However, the samples that contain 10 and 40-50%wt of the polymer have uniform centers and cracks around the edges of the layer. The average thickness of the carbon coatings is 16 μm. Since the Nafion® loading did not change the microstructure or thickness of the carbon coatings significantly, the resistance change measured can be attributed solely to the Nafion® content.

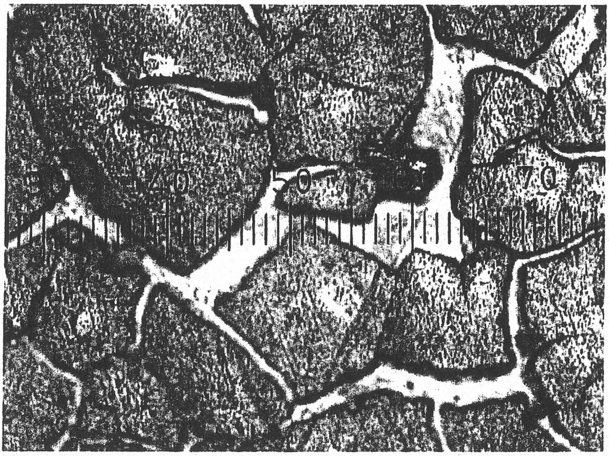

Figure 2: Type A3 MEA cathode catalyst with linear resistance 643 Ω/cm. The white areas in this micrograph are the cracks widely open in the elctrocatalyst that expose the Nafion® membrane. Scale: 1 increment is 16 μm.

<u>Linear resistance</u>

The linear resistance results obtained for all MEAs tested are presented in Table 2. For Type A MEAs, the results show that the cathode layers have higher resistance than the anode layers. This result is opposite to the one expected, if the grain size and the grain linear density are considered. Usually for other conductors (metals and semiconductors), the resistance increases if the size of grains decreases as the result of increased grain surface boundary. Another result that is also opposite to the metal and semiconductor behavior is the linear resistance of cathode A1. The resistance of cathode A1 is lower than cathodes A2 and A3 although it has the smallest grains and the largest grain linear density. Among all microstructure properties measured, only crack width has the same change trend as the cathode resistance.

Table 2: Linear resistance of electrocatalysts measured for different MEAs.

MEA TYPE	CATHODE LINEAR RESISTANCE (Ω/cm)	ANODE LINEAR RESISTANCE (Ω/cm)
A1	274	204
A2	413	388
A3	643	527
B	560	503
C	94	106

Cathode A1 apparently has the tightest cracks (Table 1) while cathode A3 has the widest. Therefore, the crack size is the major factor that affects the linear resistance in electrocatalysts with the same composition.

The linear resistance of anodes also increases form A1 to A3. It follows from the data in Table 1 that the crack size in this case is not a major parameter that can be correlated with the linear resistance variations. As previously described, the anode compositions and thicknesses are different. The higher catalyst loading of anode A1 creates a thicker layer with larger grains than in anodes A2 and A3. These two changes apparently caused the lowest resistance in anode A1. Furthermore, anode A3 has different Nafion® content than the other two and the highest linear resistance. If differences in linear resistance between anodes A1 and A2 and anodes A2 and A3 are compared, it is concluded that linear resistance is affected more with the thickness change (from A1 to A2) than with the Nafion® loading increase (from A2 to A3). The reason why the thickness affects the linear resistance is most likely due to the multilayer structure of anode A1 that stops the cracks from propagating through the entire electrocatalyst layer to the surface of a membrane. In this multiplayer structure, the catalyst grains have continuous electronic and ionic contacts in 3D.

The effect of the Nafion® content on the linear resistance of electrocatalyst was measured on carbon coated Nafion® membranes. The dependence of linear resistance on Nafion® content for the thin films studied is shown in Fig. 3. It is apparent that there is an optimum polymer concentration range for which the carbon coatings have the lowest linear resistance. For the carbon loading used (1.25 mg/cm^2) this optimum dry polymer concentration range is 20-30%wt. This result is in agreement with data previously reported by Lee et al. [3] on the effect of Nafion® loading on the total ohmic resistance of a PEM fuel cell. Therefore, Nafion® loading in electrocatalyst layers is an important factor that determines its linear resistance.

Type B MEA had the same electrocatalyst on the anode and the cathode sides. Their microstructure was non uniformly cracked. The high linear resistance can be attributed to the large cracks that exist in the layers. The difference in the linear resistances measured between these two layers can be a consequence of the membrane electrode assembly procedure.

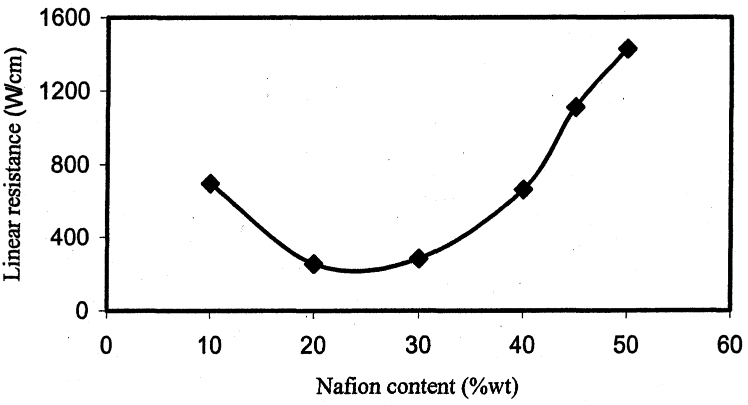

Figure 3: Linear resistance vs. Nafion® content of the carbon coated layers deposited on a Nafion ® 117 membrane.

Type C MEA has the least linear resistance than the other two types. Although the electrocatalyst layers have different compositions, their microstructures are very similar. They have scarcely distributed cracks localized on 160 μm areas. It appears that crack free microstructure is a dominant factor that determines the low resistance of this type of MEA since the compositions and the catalyst loadings of these two layers are different.

CONCLUSIONS

The electrocatalytic layer microstructures of various MEAs were correlated to their linear resistance. The microstructure features such as grain size, linear grain density and crack width were measured and used as quantitative parameters for the microstructure characterization. The trends of their changes (increase or decrease) were compared to the trend of the electrocatalyst linear resistance. For the electrocatalysts with the same compositions, the crack width size has a major effect on the resistance. Thus, an increase in crack width of 24 μm to 112 μm caused resistance to increase from 274 Ω/cm to 643

Ω/cm. In addition to the crack size influence, the dry Nafion® loading in the electrocatalyst layer has a predominant effect on the resistance even though there are slight changes in the crack width. Therefore, the crack size and the Nafion® content are two major factors that affect the resistance of the electrocatalystic layers in MEAs for PEM fuel cells. Crack free electrocatalyst with the optimum Nafion® will have the least possible resistance for the composition used.

REFERENCES

1. M.S. Wilson and S. Gottesfeld, Journal of Applied Electrochemistry, **22**, 1 (1992).
2. D. R. Askeland, *The Sience and Engineering of Materials*, p. 633, Chapman and Hall, New York, 1990.
3. S.J. Lee, S. Mukerjee, J. McBreen, Y. W. Rho, Y. T. Kho, and T.H. Lee, Electrochemical Acta, **43**, 3693 (1998).

Keywords: MEA characterization, MEA microstructure, electrocatalyst resistance.

Proceedings of The Electrochemical Society, PV 2002-31, 324-335 (2002)
DOI: 10.1149/200231.0324PV © The Electrochemical Society

OXYGEN TRANSPORT IN COMPOSITE BIOCATHODES

Scott Calabrese Barton
Columbia University, New York, NY 10027
scb2001@columbia.edu

Presented at
The Third International Symposium on Proton Conducting Membrane Fuel Cells
202 nd Meeting of the Electrochemical Society
Salt Lake City, UT, October 2002.

ABSTRACT

A numerical simulation of an enzyme-catalyzed oxygen cathode is presented and applied to the analysis of transport limitations in such electrodes, with the goal of optimization for maximum electrode current density. Based on macrohomogeneous and thin-film theories, and accounting for Michaelis-Menten enzyme kinetics, the one-dimensional model predicts a maximum current density of 7.8 mA/cm ^{2} for a 300 µm thick electrode relying on diffusion of dissolved oxygen. However, by introducing gas-phase diffusive transport, or alternatively a convective, flow-through design, current densities near 100 mA/cm ^{2} may be achieved. Such current densities would move biocatalytic oxygen electrodes closer to practical implementation in low-temperature fuel cells such as direct methanol fuel cells.

INTRODUCTION

The field of biocatalytic fuel cells is currently emerging in response to growing demand for electrical power devices that can operate under conditions where conventional fuel cell and battery technologies fail. Key characteristics of redox enzymes such as selectivity and room temperature activity may be exploited in, for example, physiologically implantable fuel cells and direct methanol fuel cells. The limitations of current biofuel cells for conventional applications are low achievable current density and low stability. Substantial efforts are required to study and develop materials, electrode structures, and devices that fully harness enzyme activity within a stable environment. The focus of this work is the issue of achievable current density. Recent efforts have led to improvements in the operating current density and potential of an oxygen cathode using a novel electrocatalyst made of 10 µm diameter hydrophilic carbon fibers coated with a crosslinked electrostatic adduct of laccase from *Coriolus hirsutus* (a polyanion above pH 4) and an electron-conducting redox polymer (a polycation) (1,2). The redox polymer electrically connects the laccase reaction centers to the carbon fibers, and when chemically crosslinked forms a hydrogel. With this approach, mass-transfer limited oxygen reduction current densities near 6 mA/cm^2 at 0.6 V (SHE) were obtained in pH 5 citrate buffer at room temperature up to 37°C.

The reaction scheme for catalytic electroreduction of O_2 to water is shown in Figure 1: The copper-containing reaction centers of laccase are oxidized by O_2. These centers, having a redox potential of +0.82 V based on open-circuit potential measurements, oxidize Os^{2+} centers of the electron and ion-conducting redox polymer to Os^{3+}, and the redox polymer is reduced at a potential negative of its +0.78 V redox potential. Although the performance of these enzyme electrodes is at least an order of magnitude higher than values reported for other biofuel cells, and is sufficient for microwatt-scale implantable applications, it falls orders of magnitude short of power densities required by conventional fuel cell electrodes, typically 0.25 to 1 W/cm^2 (3-6).

For biocatalysts to replace precious metals in low power fuel cell applications, current densities an order of magnitude higher than the ~ 5 mA/cm^2 achievable today are required. In this work, we have used a one-dimensional, porous electrode model to estimate the performance improvements obtainable by the following modifications to the biocathode described above:

1. Optimizing the morphology of porous conducting structures in which biocatalysts are immobilized. Key parameters are porosity, thickness, and fiber diameter.
2. Improving transport of oxygen via gas diffusion or convective, flow through designs. The additional key parameter here is gas-phase porosity, or fraction of the electrode structure open to convective flow.

MODEL

Several assumptions have been made here to simplify the analysis. Migration effects due to the presence of electrical potential gradients are neglected. Additionally, mass transfer resistance external to the electrode is ignored, and the enzyme kinetics are treated with a "ping-pong" type Michaelis-Menton model (7,8). Geometric parameters such as the active area of the carbon structure and the effective thickness of the hydrogel film deposited on that structure are obtained from simple geometric arguments. The model is developed from a macrohomogeneous viewpoint and treats the gas diffusion and flow-through systems using the well-known film diffusion approach (9,10).

Enzyme Kinetics

The overall reaction described in Fig. 1 can be expressed in three steps: Reduction of oxygen by the enzyme; regeneration of the enzyme by the mediator; and electron transfer between the mediator and an electrode:

$$O_2 + 4H^+ + E_{red} \xrightarrow{k'_S} 2H_2O + E_{ox} \qquad [1]$$

$$4M_{red} + E_{ox} \xrightarrow{k'_M} 4M_{ox} + E_{red} \qquad [2]$$

$$M_{ox} \xleftrightarrow{k} M_{red} + ne^- \qquad [3]$$

where E_{red} and E_{ox} are the reduced and oxidized form of the enzyme, and M_{red} and M_{ox} are the reduced and oxidized form of the electron mediator; k'_S, k'_M and k are rate constants. The effect of pH on enzyme kinetics is complex and dependent on the mediator involved. Reaction rate dependence on the proton (H^+) will therefore not be considered here. Reactions 1 and 2 can be described by Michaelis-Menten kinetics by expanding the rate coefficients k'_S and k'_M to:

$$k'_S = \frac{k_S}{K_S + [S]}; \quad k'_M = \frac{k_M}{K_M + [M_{red}]} \qquad [4]$$

where [S] is the concentration of the substrate oxygen, and K_S and K_M are Michaelis constants for the substrate and reduced form of the mediator, M_{red}, respectively. With this substitution, the steady-state rate expression is

$$R = -\frac{\partial[S]}{\partial t} = \frac{k_{cat}[E]}{1 + \frac{K'_M}{[M_{red}]} + \frac{K'_S}{[S]}} \qquad [5]$$

where k_{cat} is the effective rate constant and K'_M, and K'_S are effective Michaelis constants for the "ping-pong" kinetics and are defined as

$$k_{cat} = \frac{k_M k_S}{k_M + k_S}; \quad K'_S = K_S \frac{k_{cat}}{k_S}; \quad K'_M = K_M \frac{k_{cat}}{k_M} \qquad [6]$$

Unsupported electrode

The core of the model considers a one-dimensional, unsupported hydrogel film immobilized on a conducting surface, as shown in Fig. 2 except without carbon fibers. Conservation of mass, accounting for diffusion and reaction within polymer film, again assuming steady state, gives two differential equations:

$$D_M \frac{\partial^2[M_{red}]}{\partial x^2} = s_M R; \quad D_S \frac{\partial^2[S]}{\partial x^2} = s_s R \qquad [7]$$

where D_M and D_S are diffusion coefficients and s_M and s_S are stoichiometric coefficients for the mediator and substrate, respectively, x defines the local position within the film, and R is defined by the rate expression, Eq. 5.

Boundary conditions at the solution side of the film are bulk concentration of substrate and zero mediator flux, or

$$\text{At } x = L: \; [S] = [S]_\infty, \; d[M]/dx = 0 \qquad [8]$$

On the electrode side of the film, the substrate concentration gradient is zero, corresponding to zero diffusive flux. The mediator concentration is controlled by the applied potential, and for fast electron transfer kinetics can be treated with a Nernstian expression:

$$\text{At } x = 0: \; d[S]/dx = 0, \; [M_{red}] = [M]\left[1 + \exp\frac{-nF(E - E^o)}{RT}\right] \qquad [9]$$

where E is the electrode potential and E^o is the redox potential of the mediator couple.

Upon solution for the substrate concentration [S] as a function of position within the electrode film, electrode current density can be calculated from the substrate concentration gradient on the solution side of the film, by the expression:

$$i = \frac{n}{s_S} F D_S [\mathrm{S}]_\infty \left. \frac{d[\mathrm{S}]}{dx} \right|_{x=L} \qquad [10]$$

Supported electrode

In the case of the composite electrode, where the hydrogel is assumed to be supported by carbon fibers, the hydrogel is treated as a film on the fibers, the thickness of which, l_f, is related to the average fiber spacing. The total fiber area per unit electrode volume, a, is estimated from the fiber diameter and the void fraction. The expressions used to calculate the effective hydrogel film thickness and fiber area per unit volume were:

$$a = 4\,(1-\varepsilon)\,/\,d_f; \quad l_f = \varepsilon\,/\,a \qquad [11]$$

A modified version of the unsupported model given above can then be used to calculate an effective reaction rate, j_{in}, (consumption of substrate per unit area) for a given effective film thickness l_f, as a function of substrate concentration. In this approach, the local substrate concentration is treated as the bulk concentration $[\mathrm{S}]_\infty$ in the context of the unsupported model. The reaction rate j_{in} is related to the current obtained by Eq. 10 by

$$j_{in} = \frac{-s_S}{nF} i \qquad [12]$$

Using a macrohomogeneous model of the composite electrode, a single mass balance for the substrate concentration is therefore required (9):

$$\varepsilon D_S \frac{d^2[\mathrm{S}]}{dx^2} = a j_{in}([\mathrm{S}]) \qquad [13]$$

with boundary conditions

$$\text{At } x = 0\text{: } d[\mathrm{S}]/dx = 0. \text{ At } x = \mathrm{L},\ [\mathrm{S}]=[\mathrm{S}]_\infty \qquad [14]$$

Electrode current density can be calculated using Eq. 10, substituting εD_S for the diffusion coefficient D_S.

Gas diffusion electrode

The gas diffusion electrode case is treated by dedicating an a volume fraction in the electrode, ε_g, to which gas-phase diffusion of substrate. The presence of the gas phase reduces the volume fraction occupied by the film, used in Eq. 11, to ε - ε_g. Additionally, the gas-phase diffusion coefficient, $D_{S,g}$, must be introduced to Eq. 13, as well as a partition coefficient, $k_{p,S}$ to account for the concentration drop across the gas-liquid interface. Eq. 13 then becomes

$$\varepsilon_g D_{S,g} \frac{d^2[\mathrm{S}]}{dx^2} = a j_{in}(k_{p,S}[\mathrm{S}]) \qquad [15]$$

Flow-through electrode

The flow-through electrode is treated by replacing gas diffusion with liquid convection in Eq. 15. The gas-phase porosity now becomes the open, non-hydrogel, liquid-filled volume fraction. Eq. 15 then becomes

$$\varepsilon_g D_S \frac{d^2[\mathrm{S}]}{dx^2} - v\frac{d[\mathrm{S}]}{dx} = a j_{in}([\mathrm{S}]) \qquad [16]$$

Here, the current-collecting electrode is itself assumed to be porous, such that the flow velocity is parallel to the electrode thickness. Pressure drop can be calculated for a given flow velocity, v, using Darcy's law (11)

$$\frac{\Delta P}{l} = -\frac{\mu}{K} v \qquad [17]$$

where the permeability term K is a function of fiber diameter and volume fraction, and can be estimated according to a pseudo-Carman-Kozeny relation:

$$K = \frac{d_f^{\,2} \varepsilon_g^{\,3}}{K'_{CK}(1-\varepsilon_g)^2} \qquad [18]$$

The coefficient K'_{CK} was estimated from data supplied for Toray carbon papers.

Parameter values and numerical solution.

Values and sources of fixed parameters are given in Table 1. Numerical solution of equations 7 (unsupported electrode), 13 (supported electrode), 15 (gas diffusion electrode) and 16 (flow-through electrode), cast in nondimensional form with appropriate boundary conditions, were obtained using the finite difference method and a linear, coupled differential equation solver (9). In all supported-electrode cases, the unsupported case was solved for the given film thickness (l_f, Eq. 11) as a function of substrate concentration. These results were expressed as $j_{in}([\mathrm{S}])$ to be used as input to Eqs. 13, 15 and 16.

RESULTS

Unsupported electrode

Calculated results for the unsupported case are shown in Fig. 3 in comparison to experimental data, acquired using a rotating disk electrode (2). These results were fit to experiment in order to extract the kinetic parameters k_{cat} and K_s; resulting values are given in Table 1. Concentration profiles through the electrode are shown in Fig. 4a. Due to the extremely low value of the mediated electron diffusion coefficient (D_M), nonzero concentrations of the oxidized mediator exist only in a very small portion of the electrode near the carbon surface ($x/L = 0$). Therefore, utilization and current density are limited by electron diffusion.

Carbon supported electrode

Calculated results for the supported electrode using diffusion of dissolved oxygen are also shown in Fig. 3 compared to experimental results (2). A poor match with experiment is obtained in two respects. First, the maximum current density, i_{max}, is of by 40% (3.6 compared to 6.1 mA/cm^2). This discrepancy is most likely due to the presence of convection in the experimental electrode. The electrode structure is thick (L = 300 µm) compared to the Levich mass transfer boundary layer (~4 µm at 4000 rpm). This fact, combined with large void fraction of the supporting carbon paper, point to the possibility of significant convective transport within the electrode structure. Current density enhancement due to convective transport of substrate can be harnessed in a flow-through electrode, as discussed below. Second, the activation potential is too high by more than 100 mV. This error could be due to the assumption of fast kinetics at the carbon surface (Eq. 9), migration effects, or errors in estimates of the Michaelis constant for the mediator. These possibilities are currently under investigation. In any case, the key polarization value in this study is maximum current density, i_{max}, therefore errors in potential were ignored.

Calculated polarization of the optimized supported electrode is also shown in Fig. 3. Optimization was achieved by decreased electrode thickness, L, and fiber diameter, d_f, and by increasing porosity, ε (refer to Table 2). Maximum current density, i_{max}, increases only by a factor of two, but utilization is increased substantially using the thinner electrode, as shown in Fig. 5, where substrate concentration and reaction rates of the baseline and optimized cases are profiled. Even in the optimized case, however, low substrate concentrations lead to near-zero local reaction rates far from the electrolyte interface, and therefore control overall current density.

Gas diffusion electrode

Calculated results for the gas diffusion electrode predict that devotion of just 20% of the available void volume to gas transport leads to dramatically increased current density. Electrode utilization is increased to near unity in an electrode of identical thickness to the baseline supported electrode, as shown in Fig. 5. In Fig. 6, i_{max} is shown to become independent of electrode thickness above L = 30 µm for the dissolved O_2 case, but the gas diffusion electrode favors thicknesses approaching 500 µm. In saturated oxygen gas, the model predicts current densities exceeding 100 mA/cm^2 for thick electrodes. In air, ,current densities above 30 mA/cm^2 are expected with slightly different geometry (Table 2).

Flow-through electrode

Convective flow-through electrodes provide the opportunity to achieve, in the dissolved-substrate electrode, current densities approaching those predicted for the gas diffusion electrode. In Fig. 7a are presented predictions of maximum current density for

O_2-saturated and air saturated liquid substrate, as functions of bulk flow velocity, v. Velocity approaching 1 cm/s is required to achieve current density comparable to the gas diffusion electrode, but velocities near 0.1 cm/s lead to five-fold improvement in current density. Fig 7b gives estimated pressure drops associated with convection through the porous electrode, along with relative parasitic losses for both air-saturated and O_2-saturated liquids. According to this estimate, parasitic losses do not exceed 5% in the velocity range shown, even for the saturated air case.

CONCLUSIONS

A simple numerical simulation has enabled visualization and analysis of mass transfer limitations in composite oxygen biocathodes. The simulation predicts current densities approaching 100 mA/cm^2 for pure O_2-breathing enzyme electrodes, and 30 mA/cm^2 for air breathing electrodes. Additionally, flow-through electrodes are predicted to provide similarly favorable performance in systems where oxygen is available in dissolute form.

Technical hurdles remain to be overcome in order to realize practical enzymatic gas diffusion electrodes, such as chemical-mechanical stability and the need to provide ionic conductivity in the gas diffusion electrode. It is envisioned, however, that such electrodes as described here would provide an attractive replacement for noble metal-catalyzed cathodes in low-temperature, low power density fuel cells such as direct methanol fuel cells.

REFERENCES

1. S. Calabrese Barton, H.-H. Kim, G. Binyamin, Y. Zhang, A. Heller, *J. Am. Chem. Soc.*, **123**, 5802-5803 (2001).
2. S. Calabrese Barton, H.-H. Kim, G. Binyamin, Y. Zhang, A. Heller, *J. Phys. Chem. B*, **105**, 11917-11921 (2001).
3. E. Katz, I. Willner, A. B. Kotlyar, *J. Electroanal. Chem.*, **479**, 64-68 (1999).
4. J. R. Rao, G. Richter, F. Von Sturm, E. Weidlich, M. Wenzel, *Bio-Med. Eng.*, **9**, 98-103 (1974).
5. A. T. Yahiro, S. M. Lee, D. O. Kimble, *Biochim. Biophys. Acta*, **88**, 375-383 (1964).
6. S. Gottesfeld, T. A. Zawodzinski, *Adv. Electrochem. Sci. Eng.*, **5**, 195-301 (1997).
7. K. Kano, T. Ikeda, *Analytical Sciences*, **16**, 1013-1021 (2000).
8. P. N. Bartlett, K. F. E. Pratt, *J. Electroanal. Chem.*, **397**, 53-60 (1995).
9. J. S. Newman, *Electrochemical Systems, Second Ed.*(1991).
10. J. Giner, C. Hunter, *J. Electrochem. Soc.*, **116**, 1124-1130 (1969).
11. D. A. Nield, A. Bejan, *Convection in Porous Media*; Springer-Verlag, New York (1992).
12. R. Battino, *Oxygen and Ozone*; 1st ed.; Pergamon, New York (1981).
13. J. Jordan, E. Ackerman, R. L. Berger, *J. Am. Chem. Soc.*, **78**, 2979-2983 (1956).
14. T. R. Marrero, E. A. Mason, *J. Phys. Chem. Ref. Data*, **1**, 3-118 (1972).
15. A. Aoki, A. Heller, *J. Phys. Chem.*, **97**, 11014-11019 (1993).
16. O. V. Koroljova-Skorobogat'ko, E. V. Stepanova, V. P. Gavrilova, O. V. Morozova, N. V. Lubimova, A. N. Dzchafarova, A. I. Jaropolov, A. Makower, *Biotechnology and Applied Biochemistry*, **28**, 47-54 (1998).

Table 1. Fixed Parameter Values

Parameter	**Value**	**Source**
$[S]_\infty$ (mM)	1 (aq) 8 (air) 40 (O_2)	(12)
$k_{p,O2}$	0.025	From (12)
[M]	131 mM	Measured
[E]	1.9 mM	Measured
D_{O2} (cm^2/s)	3×10^{-5} (*aq*) 1×10^{-3} (*gas*)	(13,14)
D_M	1×10^{-8} cm^2/s	(15)
k_{cat}	50 /s	Fit to experiment
K_S	500 μM	Fit to experiment
K_M	500 μM	(16) (typ.)
E_o	0.77 V re: SHE	(1)
K'_{CK}	$1.2\times10e^{-4}$ cm^2	From Toray data

Table 2. Experimental and Optimized Parameter Values

Parameter	*Unsupported (experiment)*	*Supported (experiment)*	*Supported (Optimum)*	*Gas Diffusion (Optimum, O_2)*	*Gas Diffusion (Optimum, air)*
L (μm)	50	300	30^b	450^b	470^b
d_f (μm)	—	10	1.0^a	1.0^a	1.0^a
ε	—	0.78	0.9	0.92	0.95
ε_g	—	—	—	0.18	0.29
i_{max} (mA/cm^2)	1.1	6.1	7.8	116	34

[a] Chosen as realistic minimum; [b] Beyond this value, $i \geq 0.95\ i_{max}$.

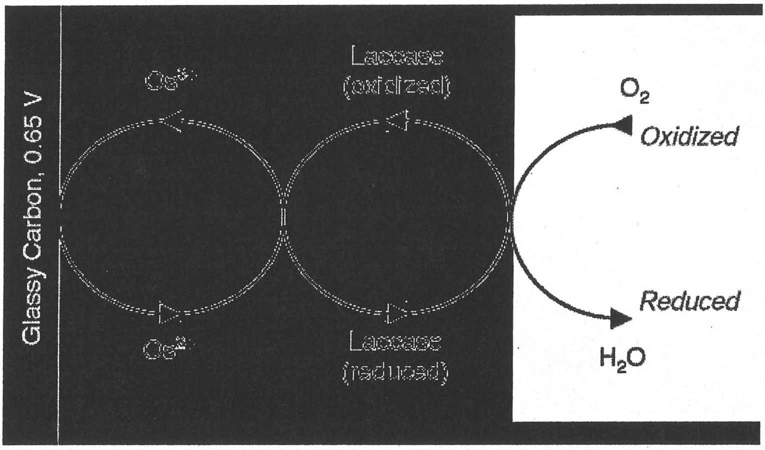

Figure 1. Reaction schematic for oxygen-reducing laccase cathode.

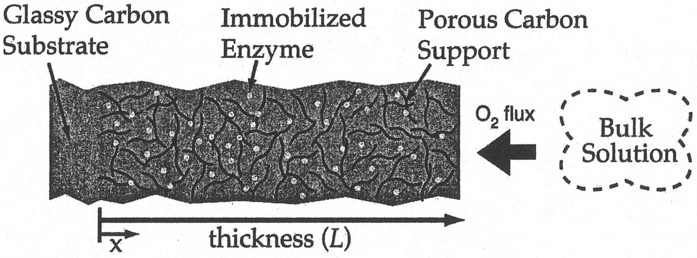

Figure 2. One-dimensional model diagram for supported laccase cathode.

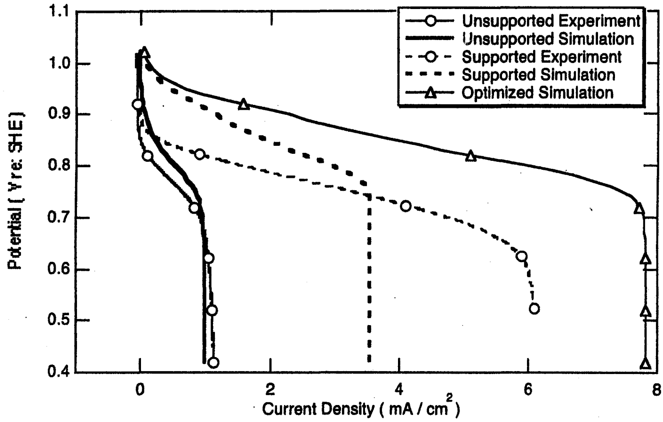

Figure 3. Potential-dependence of the O_2 electroreduction current density, comparing simulation results with experiment. Conditions: 1 mV/s sweep rate at 1 atm O_2 pressure, 0.2 M citrate buffer, pH 5, 37°C. Current densities were based on the projected area of a 4-mm carbon cloth disk (0.13 cm^2) Electrode geometry as in Table 2.

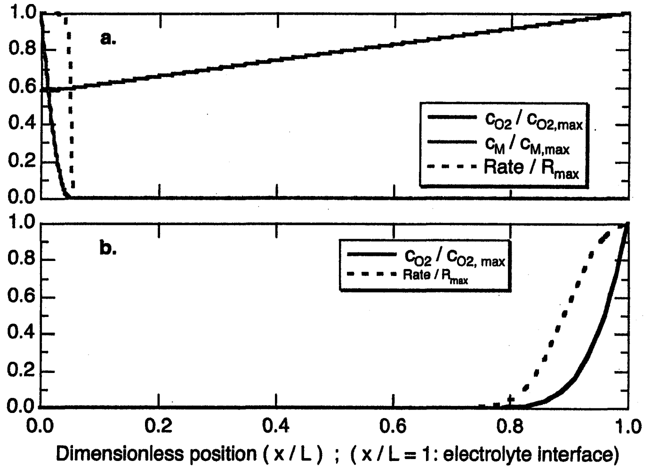

Figure 4. Calculated concentration and rate profiles in baseline **(a)** unsupported electrode and **(b)** carbon-fiber supported electrode. Conditions as in Fig. 2, at 0.6 V re: SHE. In the unsupported electrode, utilization is strongly limited by electron transport via the redox mediator, in the supported electrode oxygen transport limits utilization.

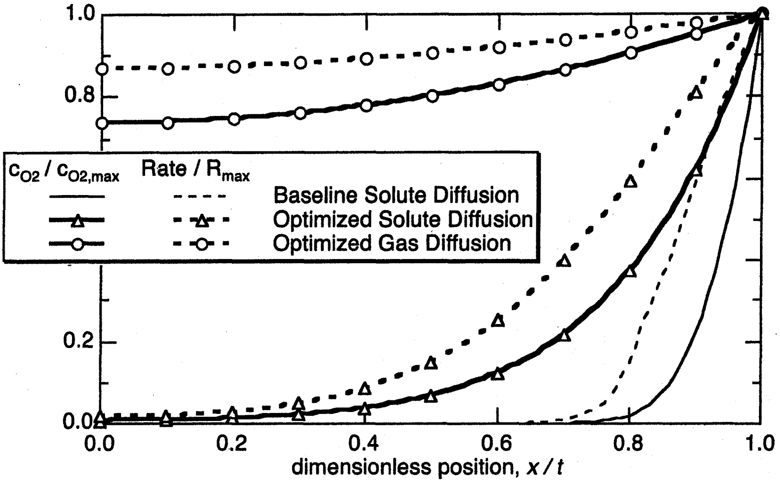

Figure 5. Calculated concentration and rate profiles in optimized, carbon-fiber supported electrode. Conditions as in Fig. 2, (L = 300 μm for gas diffusion case) at 0.6 V re: SHE. Changes to electrode morphology and enhanced oxygen transport via gas phase improves utilization, and therefore current density (see Fig. 6.)

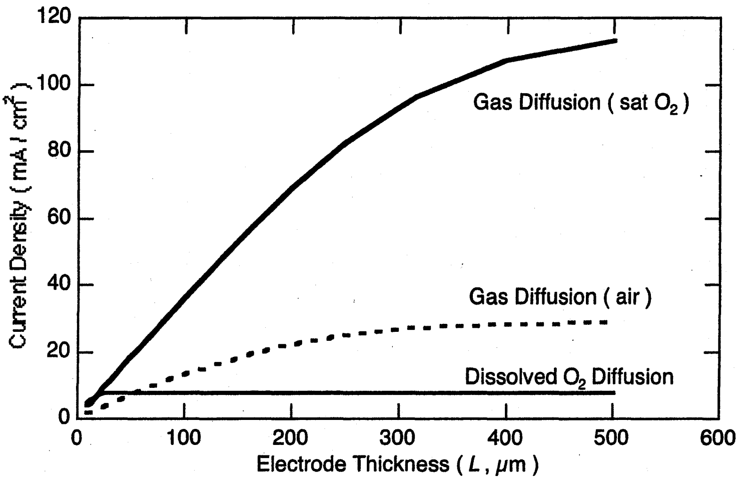

Figure 6. Effect of electrode thickness. Conditions as in Fig. 2, at 0.6 V re: SHE. Limited dissolved oxygen diffusion favors thin electrodes. Gas diffusion favors thick electrodes.

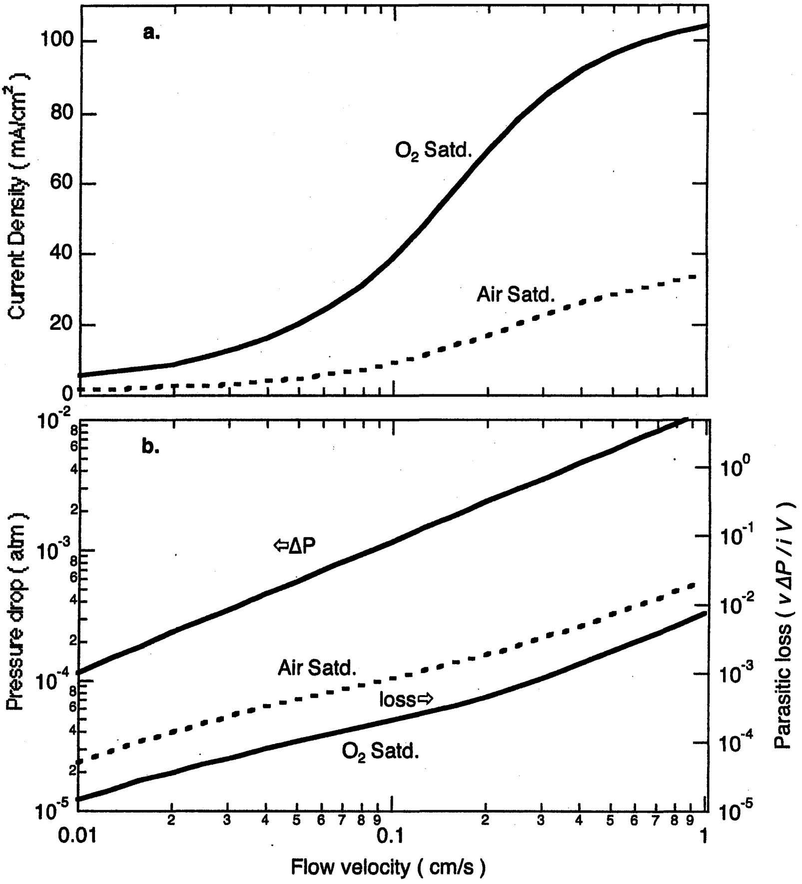

Figure 7. Effect of flow-through convection. **(a)** Maximum current density; **(b)** Predicted pressure drop and parasitic loss. Parameters as in O_2 gas diffusion electrode case (Table 2), 300 µm electrode thickness. Velocities near 0.4 cm/s are required to approach GDE current densities.

Proceedings of The Electrochemical Society, PV 2002-31, 336-348 (2002)
DOI: 10.1149/200231.0336PV © The Electrochemical Society

LOCALISED ELECTROCHEMICAL IMPEDANCE MEASUREMENTS ON A SINGLE CHANNEL OF A SOLID POLYMER FUEL CELL

Daniel J. L. Brett*, Steve Atkins*, Nigel P. Brandon**, Velisa Vesovic***, Nikos Vasileiadis**, and Anthony Kucernak*†

*Department of Chemistry, Imperial College, London SW7 2AZ, UK
**Department of Chemical Engineering, Imperial College, London SW7 2BY, UK
***Department of Earth Science and Engineering, Imperial College, London SW7 2BP, UK

ABSTRACT

A novel method of acquiring localised electrochemical impedance measurements (LEIS) in a solid polymer fuel cell (SPFC) is presented. Measurements were made at a constant reactant flow rate at a potential of 0.8 V and 0.6 V, each representing a different regime of operation as determined by localised dc measurements. The fuel cell on which the measurements were performed is a highly idealised one composed of a single linear flow channel. A distribution of impedance characteristics is seen along the channel with evidence of mass transport effects that are not evident from localised dc measurements. Localised membrane conductivity measurements did not show any variation along the channel at either of the potentials studied, as is expected from the fully humidified mode that the fuel cell was operated in. Simulation of reactant distribution has been achieved by using the known current distribution as an input into a simple flow model.

INTRODUCTION

The progress of Solid Polymer Fuel Cells (SPFC) from a promising alternative energy device to a commercially successful product depends on the solution of certain problems. These problems include lowering capital cost and increasing the fuel cell's efficiency. The best way to address these challenges is to gain a comprehensive understanding of how fuel cells function. The most direct way to achieve this understanding is by making detailed measurements of the parameters that affect fuel cell performance. This insight provides a means of determining which alterations to a fuel cell's design and operating conditions are most beneficial. As well as this empirical approach, data obtained will

---

† Ph: +44 20 75945831, Fax: +44 20 75945804, a.kucernak@ic.ac.uk

allow more sophisticated mathematical models to be constructed that realise a predictive pathway to system design. The purpose of our work is to ascertain how a SPFC is functioning by making these internal measurements. Presented here is the first report of localised impedance measurement in a fuel cell.

Various efforts to map the current distribution within both electrolysis cells (1) and inside SPFCs have been reported (2,3,4,5). Recently we have published results on a new approach which provides unparalleled time and distance resolution (6,7). Results show that there can be a dramatic variation in the current density at different parts of a fuel cell depending on the operating conditions. This spatial variation is influenced by factors such as reactant composition and humidity; operating temperature and pressure; pore flooding; hardware issues such as bipolar plate design and manufacturing inconsistencies; edge effects; moisture content of the membrane; orientation of the fuel cell and the load requirements. In addition, these factors are not all discrete variables since a complex interplay can exist between each of them. This makes it difficult to accurately control the conditions within the fuel cell that result in optimal performance. This emphasises the need to make internal measurements in real time.

One of the most insightful ways that fuel cells can be analysed is by making Electrochemical Impedance Spectroscopy (EIS) measurements. This technique has been applied to all varieties of fuel cells (8), as well as studies aimed specifically at the SPFC (9,10,11,12,13,14,15). This alternating current technique complements direct current measurements by providing a new dimension of information. Impedance measurements furnish values of membrane resistance, kinetic and mass transport information as well as giving an insight into the overall mechanism of operation. Since these factors are expected to change depending on the load, it is important that these measurements can be made at different operation potentials. One limitation to the application of EIS to larger fuel cells is that the bandwidth of most commercial loads operating at large current densities is not large enough to encompass the high frequency (ca. 10 kHz) features.

Localised impedance measurements will aid system design and performance optimisation but will also address a problem associated with using EIS with fuel cells. A fundamental limitation of conventional EIS when applied to fuel cells is that the measurement is performed on the entire cell i.e. the fuel cell is treated as a two-terminal device and a bulk measurement is made. This is only reasonable if the fuel cell is being operated under a mode in which local conditions are invariant within the fuel cell i.e. that there is an even distribution of reactant and current generation. In reality, such a mode of operation will rarely be encountered. One way in which this leads to inaccurate interpretation of EIS results is in the choice of the equivalent circuit with which the data is analysed. Various equivalent circuits have been proposed to mimic SPFC operation ranging from simple 4 component circuits to more complicated transmission line representations (16). The problem when choosing an equivalent circuit is that it must suit the bulk EIS result; when in actual fact different parts of the fuel cell may be fit to the equivalent circuit with very different parameters or may require a different equivalent circuit altogether. Thus knowledge of the way in which impedance characteristics vary should in itself lead to improved generic equivalent circuit design.

In this paper we describe localised impedance measurements in a simplified SPFC comprising of one linear channel. Such a simplified geometry allows significant information to be determined whilst still providing a system that can be modelled (17). Our measurement system divides the current generated between many separate loads, thus allowing access to the whole range of applicable frequencies. This study looks at the cathode side of the fuel cell since most operating limitations are associated with delivery and reaction of oxygen, especially when using air as oxidant.

EXPERIMENTAL

The fuel cell system used was the same as that described in a previous paper (6). In essence the anode is supplied with hydrogen gas (100% relative humidity) via a cross-flow configuration that is machined into a graphite plate. Air is supplied to the cathode (dry) via a single channel that is 110 mm long, 2 mm wide and 1 mm deep. This channel is machined out of a printed circuit board that has 10 segmented current collectors running adjacent and along the channel. The current flows from each contact is and routed through its own individual electronic load circuit. The carbon diffusion layer adjacent to each contact is driven to the same potential with dynamic compensation for all electronic iR losses (i.e. in cables and at the MEA/contact interface). The system does not require a segmented MEA, as each contact drives local region of the MEA to the same potential and thus there is no lateral flow of current due to potential gradients. The MEA used was composed of a Nafion 112 membrane with 0.6 mg cm^{-2} PtRu on the anode and 0.6 mg cm^{-2} Pt on the cathode, and was supplied by Johnson Matthey. The catalysed area of the MEA was 120 mm × 15 mm, although a significant part of the catalysed area away from the channel is not utilised on the cathode to produce current, as the only way that reactant can get to those regions is by lateral diffusion through the gas diffusion backing material.

The distinction between this and our previous work – in which DC current distribution was measured along the channel - is that all loads apply a potential on which is superimposed a small ac modulation from an impedance analyser (Solartron 1260). Measuring the local modulated current and potential at each load provides the impedance spectrum for that local region of the fuel cell. Figure 1 shows a simplified diagram of the system configuration.

In order to make measurements with non-segmented MEAs it is necessary to operate the fuel cell in constant cell potential mode – otherwise differences in cell potential at the gas diffuser would result in lateral current flow. Thus it is not possible to run the system at precise stoichiometries, and instead these must be determined after the experiment. In this paper the stoichiometry on the anode is approximately 10-20, and on the cathode in the range 1.1-2. Thus operation of the fuel cell is always governed by the cathode.

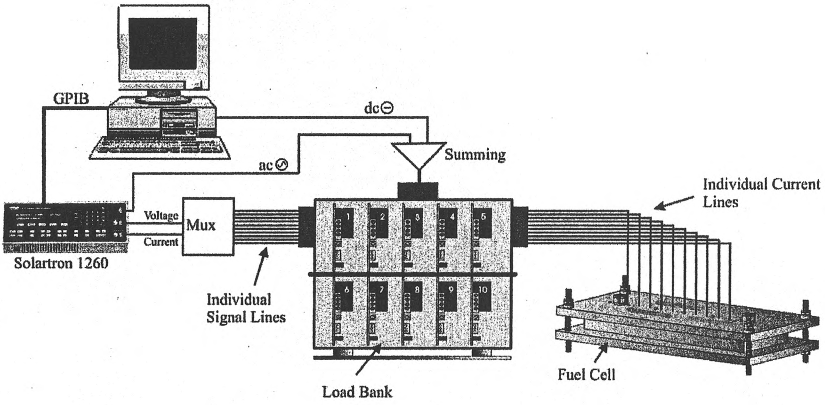

Figure 1: Diagram of experimental set-up for making localised impedance measurements.

Localised impedance measurements can be made with this system since every contact is associated with its own load. This allows an ac signal to modulate all of the loads and the current measurement to be made on each load individually. This process ensures that there is no lateral current flow between contacts at different potentials, since each load is modulated in unison.

The modulation frequency ranged from 10 kHz to 0.1 Hz at an amplitude of 10 mV rms (as recommended by Parthasarathy et al. (9)). An air-flow rate of 20 $cm^3 min^{-1}$ and a hydrogen flow rate of 40 $cm^3 min^{-1}$ were used. The exhaust end of both the anode and cathode was at atmospheric pressure. The fuel cell temperature was under PID control and set to 30 ± 0.5°C. The large stoichiometric excess of hydrogen was used to minimise loses on the anode side and to ensure that the membrane was well hydrated. One hundred frequency points were collected (20 / decade) and an entire frequency scan took 450 seconds. All measurements were made with the system under steady-state conditions and the current profile along the channel did not change over the time required to collect all 10 spectra.

RESULTS AND DISCUSSION

DC and EIS measurements were made at 0.8 V and 0.6 V. Figure 2(a) shows the current distribution along the length of the cathode flow channel at each potential. These two potentials represent two different operation regimes for this particular reactant flow rate. At 0.8 V the current is relatively evenly distributed along the channel (a standard deviation of only 42 mA cm^{-2} – i.e., 15% of the average current of 0.28 A cm^{-2}), whereas at 0.6 V after an initial plateau there is a significant loss of current density along the channel. This behaviour has been described before (6,7) and is attributed to a starvation effect, whereby the oxygen content of the air is depleted as the flow moves down the channel. This effect is confirmed by plots of oxygen utilisation as a function of position along the channel, also displayed in Figure 2(a). Operation at the higher potential means that the air flow rate has the capacity to satisfy the entire length of the channel, and at the end of the channel about half the oxygen in the air has been consumed. In comparison, at the lower potential the larger current at the start of the channel leaves the downstream channel depleted of reactant, and about 90% of the oxygen is utilised in the gas when it reaches the end of the channel.

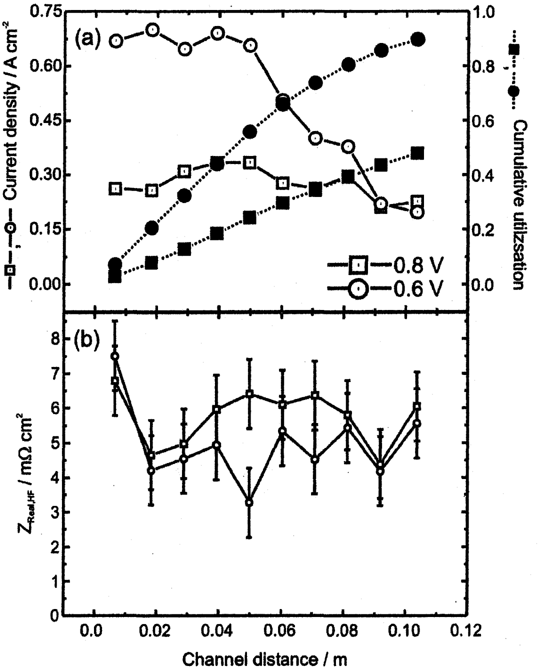

Figure 2: Plot as a function of position down the channel the current density and cumulative utilisation, (a); and the high frequency real resistance, (b), (extracted from the results in Fig. 3) at cell potentials of 0.8 V and 0.6 V. Conditions described in the experimental section.

Figure 3a and 3b show the complex plane plots at different positions along the channel for operation at 0.8 V and 0.6 V respectively. It is immediately clear that the EIS response contains much more information than the dc measurements. In this paper we only make qualitative assessments of the Impedance data and concentrate on the lower frequency features.

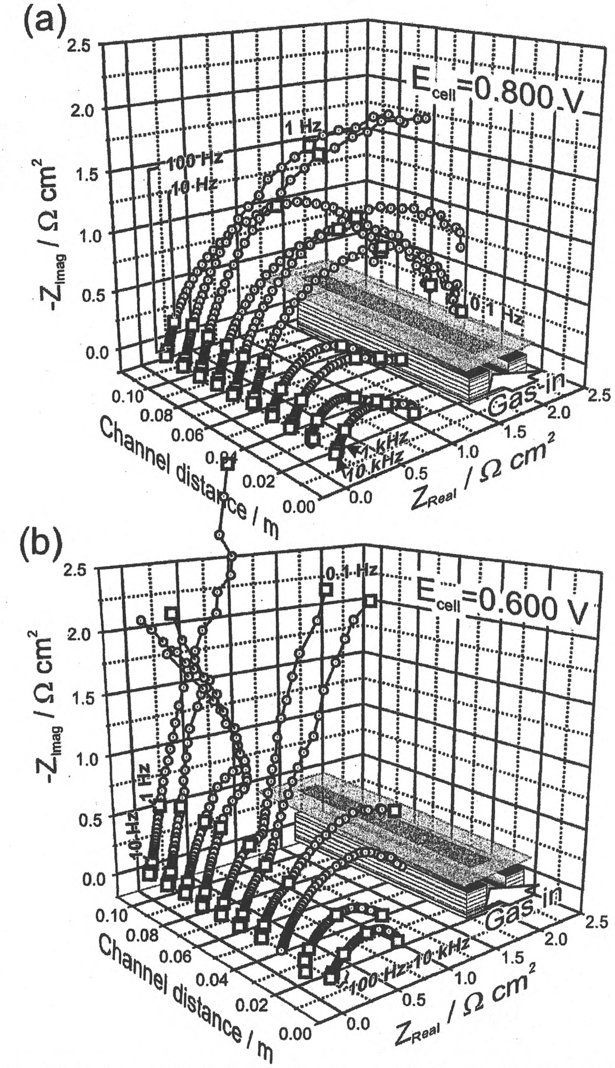

Figure 3: Complex plane EIS plots as a function of distance along the channel at cell potentials of 0.8 V, (a); and 0.6 V, (b). Conditions as for Fig. 2. Square points represent decadic frequencies (0.1, 1, 10, 100, 1000, and 10,000 Hz).

At 0.8 V, Figure 3a, a clear trend is observed as the arc radius increases with distance along the channel. The dc response shows no sign of a decrease in current density along the channel so the reaction is not being limited by reactant consumption. However, reactant is being consumed along the channel so there will be a depletion of oxygen in the channel and diffuser. This increase in the arc radius at low frequencies has been attributed to oxygen diffusion limitation in the diffuser of the electrode (10,11,15). It has been proposed that this limitation is due to the impediment of oxygen diffusion through nitrogen in the pores of the diffuser. Evidence to support this comes from the fact that no low frequency arc is observed for operation with pure oxygen and the arc radius is seen to increase when the thickness of the backing layer is increased (18,19).

The same work also shows that the characteristic frequency of the low frequency arc (corresponding to the maximum imaginary component of the semicircle) is a measure of the thickness and tortuosity of the backing layer. The characteristic frequency for all of the arcs in the 0.8 V case share a similar frequency (1.3 ± 0.7 Hz). This consistency is indicative of a diffuser with an even thickness and tortuosity distribution. The EIS profile for the contact at the exit end of the channel does not follow the trend; we believe that these smaller arcs are due to edge effects, or due to the open-ended operation.

The EIS plot at 0.6 V shows a different trend as a function of position down the channel. The first four contacts exhibit the same opening of the arc as seen at 0.8 V, but the subsequent plots show a distinct direction change away from the closing of the semicircle. The deviation initially approximates to a vertical profile before bending back, with the later contacts showing a transfer of the impedance into the negative real resistance quadrant. Higher flow rates in the channel (i.e. greater flux of reactants) delay this transition (results not shown). This means that a situation exists in which an increase in reactant consumption, with a corresponding current increase, at one point in the fuel cell (brought about by a decrease in cell voltage) can cause a decrease in current at another point of the fuel cell. We have already shown how reactant starvation in a channel can result in a decrease in local current when the cell voltage decreases, leading to negative polarisation plot gradients (6). The impedance feature seen here, where the plot curves backward into the negative real resistance quadrant, is a manifestation of operation under conditions of reactant starvation.

The transformation of the impedance plot into a negative resistance loop can be understood by considering the individual dc polarisation plots for each contact. Figure 4(a) shows a dc polarisation plot at a point 0.07 m from the start of the channel. The polarisation plot shows an initial increase in current with decreasing cell potential, this reaches a maximum at about a cell potential of 0.4 V after which the current decreases. The slope of the VI plot changes sign, and in the limit of very low frequencies the differential resistance thus also changes sign. The reason for this change in slope is that as the cell potential is decreased the cumulative utilisation of reactants at a given point along the channel increases. When the reaction occurring on the electrode is entirely under diffusion control, the decrease in partial pressure of the oxygen in the channel results in a decrease of local current density. This aspect of the VI response has been reported previously (6).

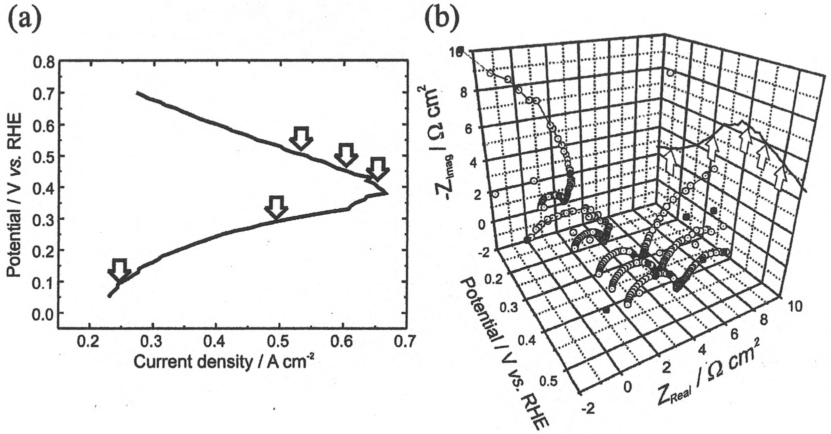

Figure 4: Polarisation plot, (a), and EIS response, (b), at 5 different potentials at a point 0.07 m along the channel. Same conditions as for Fig. 3 except channel width was 3 mm and the fuel cell temperature was 25°C.

Thus we would expect that the EIS response at cell potentials above 0.4 V to appear normal, and for the low frequency response at potentials below 0.4 V to appear in the negative real quadrant. EIS plots at a point 0.07 m from the start of the channel as a function of cell potential are shown in Fig. 4(b). Because of the use of a wider channel (3 mm vs. the 1 mm wide channel used in Fig. 3), two arcs are seen in the EIS plots, resulting from the larger iR drop in the gas diffusion medium. For the potentials at which the VI curve has not folded back on itself, the EIS responses appear normal. For cell potentials below this value, the EIS responses at low frequency fall in the negative real impedance quadrant.

The impedance measurements taken at various polarisations show how operation in the regime after the maximum current point results in formation of a negative resistance loop. The impedance response at this potential contains high frequency information related to membrane conductivity and reaction kinetics but the low frequency range picks up the starvation effect and is manifest by the negative resistance loop which starts to form at ca. 0.5 Hz. This value is characteristic of reactant flow rate in the channel (5 cm s^{-1} average gas flow rate).

If we now compare the localised EIS measurements with the total averaged response of the entire cell, the potentially misleading nature of a bulk EIS measurement can be appreciated. Figure 5 compares the localised response at 0.8 V and 0.6 V for the local measurements at the start and end of the channel, along with the average response of the entire cell.

Taking the 0.8 V case first, Fig. 5(a), we can see that the combined response is of the same general shape as that at the start and end of the channel. So in this case the global response is an accurate indicator of the local response, although any precise numerical parameters determined from the analysis of the arc cannot be totally relied upon. However, the response at 0.6 V, Fig. 5(b), shows that there is a significant difference between the response at the start, the end and the average response. The EIS response at low frequency taken at the start of the channel exhibits no sign of reactant limitation; the response at the end shows that reactant starvation is occurring due to upstream consumption of reactant and the global response is that of an overall mass transport limitation i.e. the response is purely capacitive. In this case, a conventional global EIS measurement would be misleading if it were assumed that the fuel cell was reacting homogeneously.

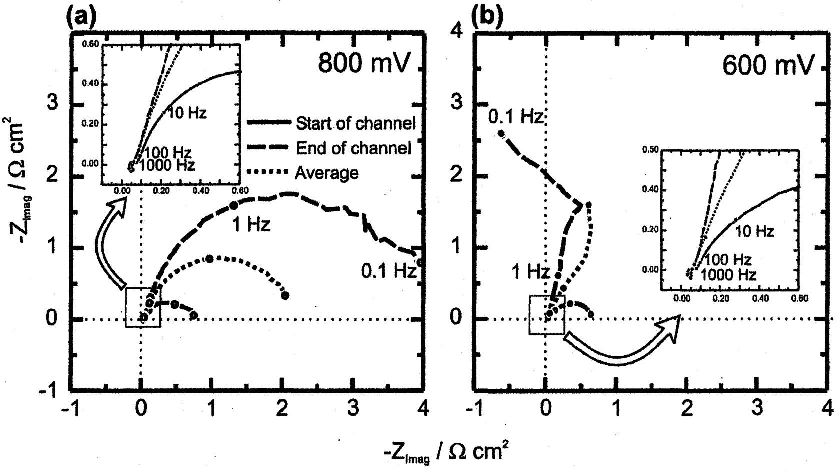

Figure 5: Comparison of the EIS response at 0.8 V, (a), and 0.6 V, (b) at the start, the end and for the global average of the channel. Conditions as for Fig. 3.

Membrane Conductivity Profiles

Localised impedance measurements also allow membrane conductivity maps to be generated from the real impedance measured at high frequency (11). Figure 2(b) shows the membrane resistance distribution along the channel for the two set potentials. It can be seen that there is little variation in membrane resistance along the length of the channel or between the two set potentials. This result suggests that under the operating conditions used, external factors such as the drying effect of the reactant flow do not affect the membrane, or at most affect the membrane in a uniform manner along the channel.

The average resistance at 0.8 V is slightly higher than in the 0.6 V case although this difference is probably within experimental error. It has been reported that variation in the membrane resistance with current density, reactant humidification level and temperature is not significant for thin electrolyte layers. Since the solid electrolyte used in the MEA is Nafion® 112, no notable variation along the channel or between each operating potential is expected. However, more extreme conditions, such as operation at higher temperature or low stoichiometry and without external humidification are expected to show such effects. We are currently examining these operation regimes.

These results are another demonstration of the need to fully understand how the fuel cell operates in order to determine the optimal settings of operating parameters. It also shows how conventional impedance measurements on the bulk fuel cell would not be representative of how the system is actually performing, especially under low stoichiometry conditions.

Visualisation of Reactant Distribution in the Channel

Knowledge of the channel current distribution and utilisation of a simple flow model allows for the visualisation of reactant concentration distribution along the length of the channel and gas diffuser. The model is set-up with two separate regions, the flow channel and the gas diffuser. A continuity boundary condition is set between these two regions and the catalyst layer is assumed to be infinitely thin and therefore stated as a boundary. In the solution domain we solve the Nernst-Plank equation:

$$-D_{O_2}\cdot\left(\frac{\partial^2 c_{O_2}}{\partial x^2}+\frac{\partial^2 c_{O_2}}{\partial y^2}\right)+\mathbf{u}\cdot\left(\frac{\partial c_{O_2}}{\partial x}+\frac{\partial c_{O_2}}{\partial y}\right)=R_i \qquad [1]$$

Where D_{O_2} is the diffusion coefficient, $\mathbf{u}$ is the velocity vector, and R_i is the reaction rate, which in our case is zero, as we treat the reaction layer as a boundary. The independent variables x and y refer to the direction along and across the channel respectively.

The gas velocity in the channel was set as for the experiment, but convection in the diffuser is not considered since diffusion is the dominant mode of transfer. The effective diffusion coefficient in the diffuser was corrected to account for the, porosity of the medium according to the equation (ε is the porosity, and in our case is equal to 0.75):

$$D_{O_2}^{eff}=D_{O_2}\cdot\varepsilon^{1.5} \qquad [2]$$

To overcome the scaling problem rising from the significant difference between the length of the channel and the width, the equation had to be rewritten in a dimensionless form with the introduction of new dimensionless independent variables. The boundary at the edge of the diffuser towards the membrane was segmented into ten individual regions to conform to the experimental setup. The current, and therefore reactant flux, at each contact was input as recorded in the experiment. The oxygen concentration at the channel input was set to have a partial pressure of 0.21, with the exit concentration unspecified.

Since the finite element method was employed, there was no need to specify internal boundary conditions, all the other boundary conditions apart from the catalyst layer were set to:

$$\left(\frac{\partial c_{O_2}}{\partial x}+\frac{\partial c_{O_2}}{\partial y}\right)=0 \qquad [3]$$

The equations for this system were solved using FEMLAB© for the two different operating conditions and the results are shown in Figure 6. The model shows how the higher overpotential (0.6 V case) results in greater utilization of reactant and subsequently more rapid decrease in the concentration of oxygen along the channel compared to the 0.8 V case. In the 0.6 V case it can be seen that there is significant depletion of reactant in the diffuser towards the end of the channel, whereas in the 0.8 V case the amount in the diffuser is ample enough to satisfy the current requirement along the length of the channel.

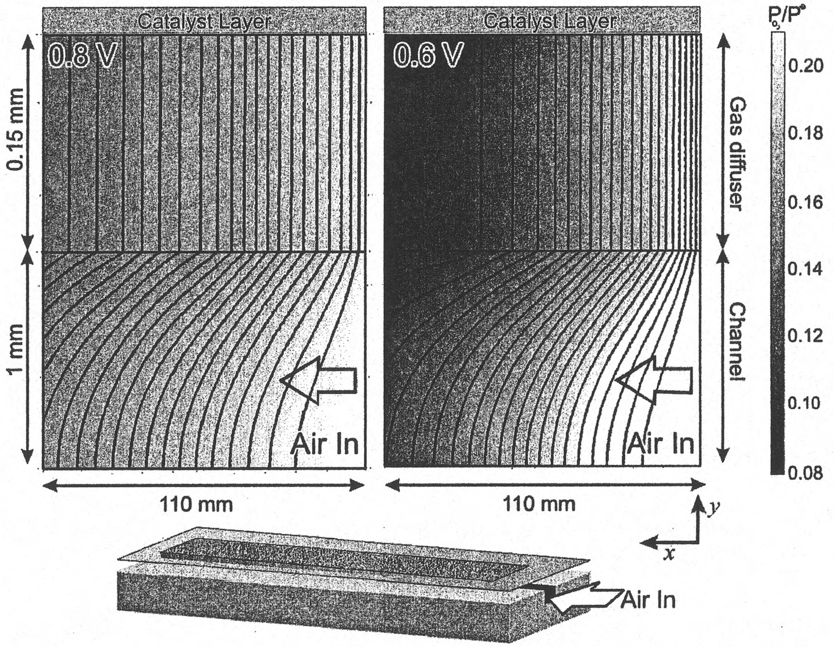

Figure 6: Visualisation of reactant concentration in the cell operating at 0.8 V and 0.6 V. The air enters from the right hand side.

This model, along with the data that our system generates combines to provide a useful visualization tool that can show how the reactant profile varies in the diffuser and into the depth of the channel. Such information may be useful in the interpretation of impedance results where mass transport limitation is a major feature of the response.

CONCLUSION

Localised electrochemical impedance measurements in an SPFC over a frequency range 0f 0.1 Hz to 10 kHz has been demonstrated for the first time. The technique illustrates how reactant starvation occurs along the flow channel and shows that dc measurements alone are not enough to properly characterise the operation of a fuel cell. These results also show that care should be taken when performing bulk EIS measurements, since there may be significant variations in the performance of the fuel cell that will not be appreciated unless localised measurements are performed. This system is ideal for monitoring fuel cell performance and is a valuable tool for system design. The impedance results emphasise the complex nature of making ac measurements on fuel cells.

Measured dc current distribution has been used as input to a simple flow model to provide a means of reactant distribution visualisation in the channel. Such information may be useful in the interpretation of impedance results where mass transport limitation is a major feature of the response. Future work will involve fitting results to equivalent circuits to obtain quantitative parameters; developing more sophisticated equivalent circuits and performing measurements on different flow field geometries and operating conditions.

ACKNOWLEGEMENTS

We wish to thank Johnson Matthey for providing MEAs. Simon Turner for help with fuel cell construction. This project has been funded by the United Kingdom EPSRC under Grant GR/M 73552.

REFERENCES

1 C. J Brown, D Pletcher, F. C. Walsh, J. K. Hammond and D. Robinson, *J. Applied Electrochem.* **22,** 613 (1992).

2 J. Stumper, S. A. Campbell, D. P. Wilkinson, M. C. Johnson and M. Davis, *Electrochimica Acta,* **43,** 3773 (1998).

3 S. J. C. Cleghorn, C. R. Derouin, M. S. Wilson, S. Gottesfeld, *J. Appl. Electrochem.*, **28,** 663 (1998).

4 Ch. Wieser, A. Helmbold And E. Gülzow, *J. Appl. Electrochem.*, **30,** 803 (2000).

5 M. Noponen, T. Mennola, M. Mikkola, T. Hottinen and P. Lund, *J. Power Sources,* **106** , 304 (2002).

6 D. J. L. Brett, S. Atkins, N. P. Brandon, V. Vesovic, N. Vasileiadis and A. R. Kucernak, *Electrochem. Comm.,* **3,** 628 (2001).

7 D. J. L. Brett, S. Atkins, N. P. Brandon, V. Vesovic, N. Vasileiadis and A. R. Kucernak, Proc. 1st European PEFC Conference 297 (2001).

8 J. R. Selman and Y. P. Lin, *Electrochim. Acta,* **38,** 2063 (1993).

9 A. Parthasarathy, B. Dave, S. Srinivasan, A. J. Appleby and C. R. Martin, *J. Electrochem. Soc.,* **139,** 1634 (1992).

10 V. A. Paganin, C. L. F. Olivaira, E. A. Ticianelli, T. E. Springer and E. R. Gonzalez, **43,** 3761 (1998).

11 T. E. Springer, T. A. Zawodzinski, M. S. Wilson and S. Gottesfeld, *J. Electrochem. Soc.,* **143,** 587 (1996).

12 J. –P. Diard, B. Le Gorrec, C. Montella, C. Poinsignon and G. Vitter, *J. Power Sources*, **74,** 244 (1998).

13 N. Wagner, Schnurnberger, B. Müller and M. Lang, *Electrochim. Acta*, **43,** 3785 (1998).

14 J. M. Song, S. Y. Cha and W. M. Lee, *J. Power Sources*, **94,** 78 (2001).

15 J. T. Mueller and P. M. Urban, *J. Power Sources,* **75,** 139 (1998).

16 M. Eikering and A. A. Kornyshev, *J. Electroanal. Chem.,* **475,** 107 (1999).

17 N. Vasileiadis , D. J. L. Brett, S. Atkins, N. P. Brandon, V. Vesovic, and A. R. Kucernak, *In preparation.*

18 T. E. Springer, T. A. Zawodzinski, M. S. Wilson and S. Gottesfeld, *Electrochemical Society Proceedings*, **95-23,** 137 (1995).

19 M. S. Wilson, T. E. Springer, J. R. Davey and S. Gottesfeld, *Electrochemical Society Proceedings*, **95-23,** 115 (1995).

Proceedings of The Electrochemical Society, PV 2002-31, 349-360 (2002)
DOI: 10.1149/200231.0349PV © The Electrochemical Society

PREDICTION OF TRANSIENT RESPONSE FOR A 25-CM^2 PEM FUEL CELL

S. H. Kim, S. Shimpalee, and J.W. Van Zee
Department of Chemical Engineering, University of South Carolina,
Columbia, South Carolina, 29208

ABSTRACT

The response of Gore's advanced PRIMEA® 5510 Membrane Electrode Assemblies (MEAs) during a change in the electrical load during operation with fixed flow rates of hydrogen and air, anode and cathode, respectively, the cell voltage of between 0.5 V and 0.7 V has been studied in a laboratory proton exchange membrane fuel cell (PEMFC)[3]. Using a 25cm^2 cell, with a 20cm^2 reaction area, due to sub-gasket, some cases were studied at the operating condition of dew point temperature of anode, that of cathode, and, cell temperature, 80°C, 70°C, and 70°C, respectively.

The cell voltage differences, 0.1V, 0.2V, and 0.3V, for the transient may show different magnitude of overshoot and undershoot behavior. They are compared as dimensionless current densities. Also, the flow channel effects on time dependant performance are presented in this work.

INTRODUCTION

A Proton exchange membrane fuel cell (PEMFC) is a strong candidate that may replace the internal combustion engine. Reduction of local emissions and improved fuel efficiency of passenger cars has for many years been the driving force for new power train technologies. Various experimental studies about PEM fuel cell have been achieved, such as, water management [7-9], Clamp-torque effect[10], fuel cell stack[11], micro fuel cell[12], and CO poisoning effect[13]. Also some numerical predictions about PEM fuel cell were presented[2-3, 5-6, and 18-20]. Transient operation of PEM fuel cells during stationary and automotive applications may expose the MEA to various degrees of stoichiometry and cell capacitance. This transient operation may be a result of a sudden demand as appliance starts or as a vehicle is accelerated or decelerated. Further these transients may be of sufficient magnitude and speed that gas flow rates cannot be adjusted by feedback control or that the capacitors in the system cannot accommodate the demand. Thus, the fuel cell by default or design may need to act as a capacitor during the power demand surge. Some full-scale three-dimensional solution to the transient response of fuel cell were presented by Shimpalee, et. al.[32].

In this study, the transient cell performance of a PEMFC with 25-cm^2 with 20-cm^2 of reaction area as shown in Figure 1 is investigated with various cell voltage differences, 0.3 V, 0.2 V, and 0.1V. Because the current densities corresponding to various cell voltages are different from each other, it is very difficult to compare them directly. So we introduced the dimensionless current densities.

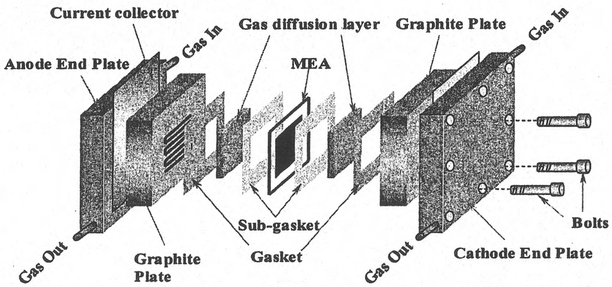

Figure 1. The picture shows schematics of fuel cell assemble of 25-cm^2 PEMFC. There are sub-gaskets between MEA and gas diffusion media so that the active area is reduced to 20-cm^2. Anode side and cathode side flow channels are symmetric.

EXPERIMENTAL PROCEDURE

Figure 2 shows the schematic diagram of transient experimental setup. A two channel digital oscilloscope (TDS 210, Tektronix Inc.) was hired to record both the current response and the voltage forcing function simultaneously. It recorded both current and cell voltage 2500 points in 50 seconds. When the voltage reached at some set voltage, triggering point, the signals were recorded in the oscilloscope from 10 seconds before the triggering point to 40 seconds after the triggering point, total was 50 seconds. The channel 1 of the oscilloscope collects the current and the channel 2 collects cell voltage. The "hall effect current sensor" converts the current into voltage signal, so that the oscilloscope can collect the current. All of the data reported here were obtained with PRIMEA® Series 5510 MEA (W.L. Gore & Associates). Between diffusion layers and MEA, there are sub-gaskets for both anode and cathode sides. Therefore the reaction area of MEA is reduced from 25-cm^2 to 20-cm^2. The gas diffusion media (GDM) used for both anode and cathode were CARBEL™ CL. The anode and cathode humidification dew point temperatures were 80 and 70 °C, respectively. The cell was operated at the temperature of 70 °C and the backpressure of 101.3 kPa. The cell voltage change rates are shown in Table 1. Also, the flow rates for each condition are listed in Table 2. We focused on the transient conditions for two cases, from normal to starved condition and from starved to normal condition.

Before changing the cell voltage, we waited 30 minutes to ensure a steady state value of the current and membrane humidity at the constant voltage. We performed the experiment twice for reproducibility.

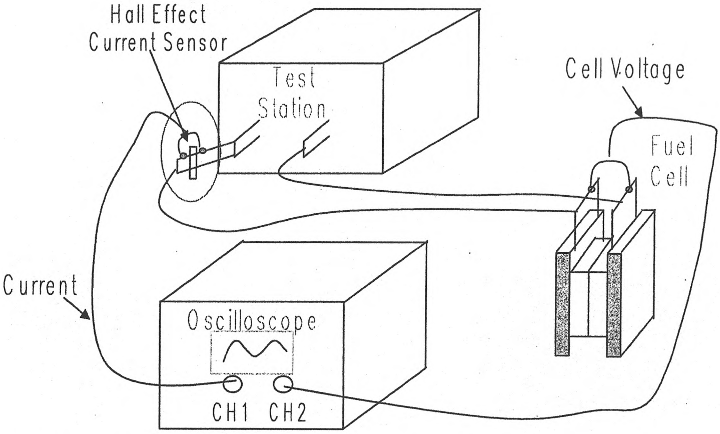

Figure 2. Schematic diagram of oscilloscope and fuel cell for experimental setup. This shows that how the two-channel oscilloscope measures and collects the current and cell voltage.

Table 1: Cell Voltage Change Rates for each voltage ranges for various cases.

0.1 V Changes	0.5 V – 0.6 V	0.17 V/s
	0.6 V – 0.5 V	0.14 V/s
	0.6 V – 0.7 V	0.17 V/s
	0.7 V – 0.6 V	0.14 V/s
	0.7 V – 0.8 V	0.17 V/s
	0.8 V – 0.7 V	0.14 V/s
0.2 V Changes	0.5 V – 0.7 V	0.25 V/s
	0.7 V – 0.5 V	0.25 V/s
	0.6 V – 0.8 V	0.25 V/s
	0.8 V – 0.6 V	0.25 V/s
0.3 V Changes	0.5 V – 0.8 V	0.38 V/s
	0.8 V – 0.5 V	0.38 V/s

Table 2. Flow rates for each cell voltage stoic.

Cell Voltage (V)	0.5 V	0.6 V	0. 7 V	0.8 V
Flow Rate (cm^3/s)	277/1594	172/717	78/326	50/69

RESULTS AND DISCUSSION

Figure 4 shows the comparison of dimensionless current densities for different flow field when the cell voltages are changed from 0.5 V to 0.7 V. The fuel supply condition is changed with cell voltage change, from normal, 20 and 100 excess for anode and cathode, respectively, to starved condition. Note that the transient current result of triple channel is taken from our previous work[3]. The current densities shown in this figure are dimensionless as presented below. The current density is divided by the steady state value when $t > 0$. The results of this figure reveal that the magnitude of overshoot for the single channel is little bit higher than that of triple channel. The significant different between single and triple channel is that the triple channel gave "undershoot" behavior after overshoot behavior but the single path did not. The linear velocity of each flow channel is faster than that of triple path's, so that the outlet hydrogen flow does not flow back.

Figure 5 shows the reverse case of Figure 3. The flow rate is the same as Figure 3. The cell voltage is changed from 0.5 V to 0.7 V. The fuel condition is from starved to normal condition. The dimensionless current density is expressed according to the steady state current density of at 0.7 V. The dimensionless current density is expressed similarly as figure 3. The steady state current density is at 0.7 V. As explained about the undershoot behavior in our previous work[3], the hydrogen was consumed before reaching the end of the flow channel so that not all the reaction area was utilized. The outlet flow of hydrogen out of the fuel cell was zero flow. Then sudden cell voltage drop reduced the reaction rate with the unutilized reaction area, the moment of undershoot. Then the continuous hydrogen flow fills up the unused reaction are. The current density recovery in the figure shows it. The single path flow channel yields a little bit bigger magnitude of undershoot than that of triple channel. From the figure the valley of single channel is wider than that of triple path. Because the flow rate in triple channel is more uniform than that of single, the triple channel shows faster cell performance recovery.

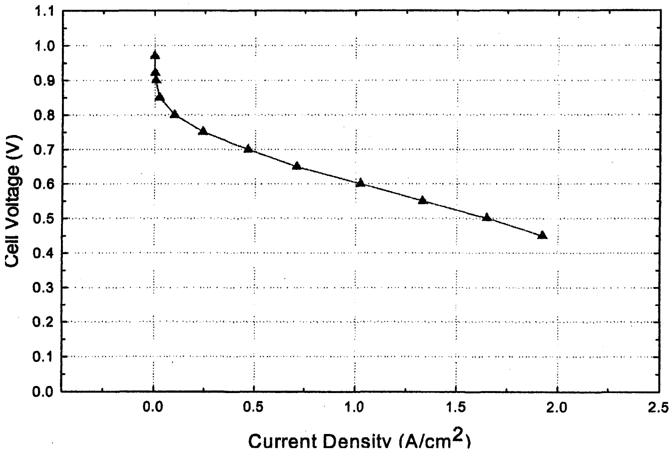

Figure3. The steady state value of current density, V-I curve. The stoichiometry is 1.2 and 2.0 for anode and cathode, respectively.

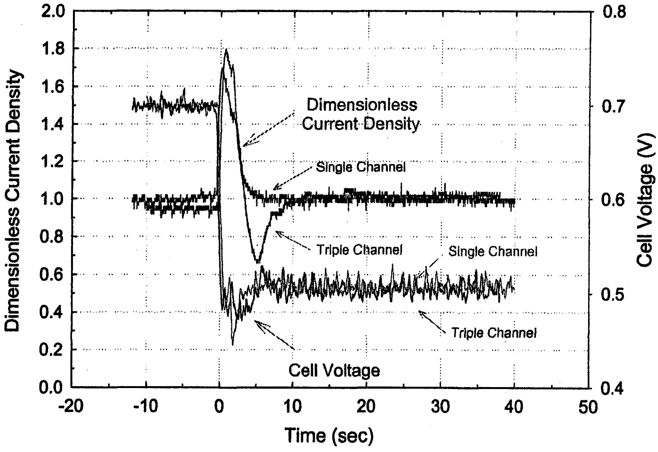

Figure 4. Comparison of Current densities for different types of channel structures with cell voltage change from 0.7 V to 0.5 V. The voltage change rates are same, 0.7 V/sec.

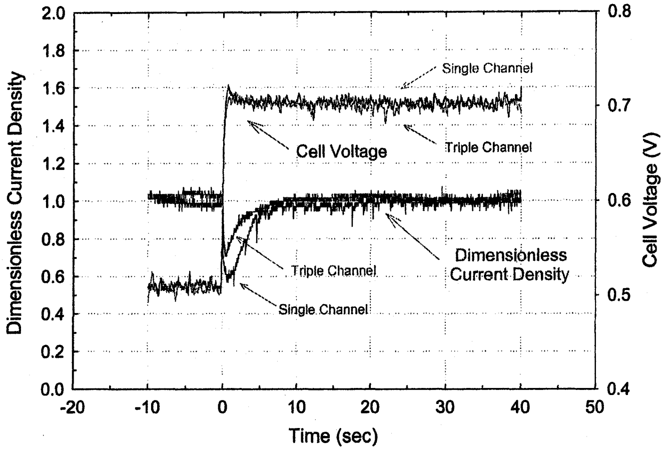

Figure 5. Comparison of Current densities for different types of channel structures with cell voltage change from 0.5 V to 0.7 V. The current densities are displayed with the form of dimensionless current densities.

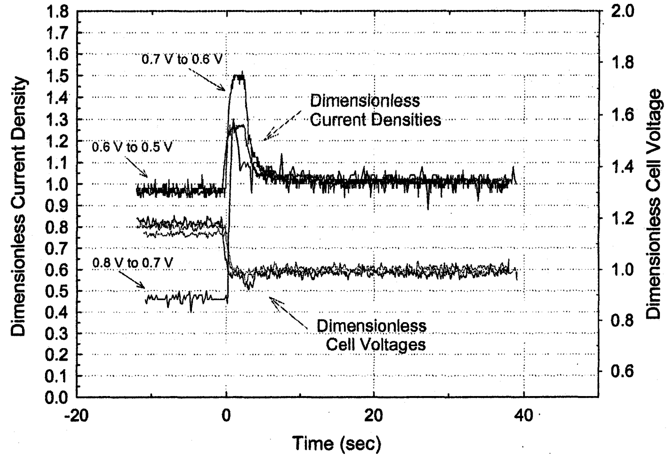

Figure 6. Comparison of current density responses with 0.1 V of cell voltage drop. The cell voltage change ranges are from 0.8 V to 0.7 V, from 0.7 V to 0.6 V, and 0.6 V to 0.5 V.

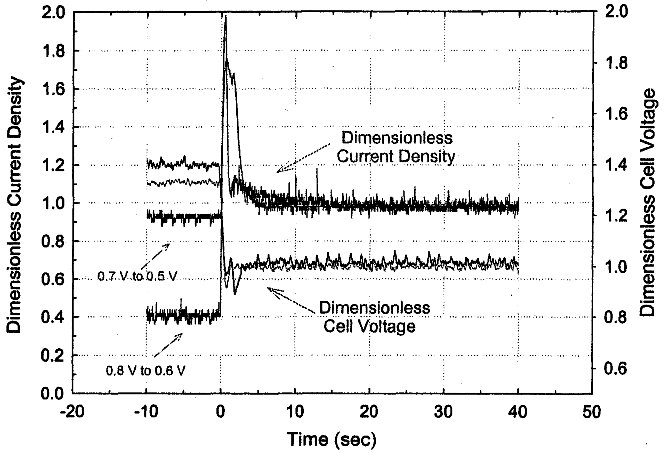

Figure 7. Comparison of Current density response with 0.2 V of cell voltage drop. The cell voltage change ranges are from 0.7 V to 0.5 V and 0.8 V to 0.6 V.

Figure 6 shows the comparison of different cell voltage ranges of 0.1 V drop. There are three cell voltage ranges, they are, 0.8 V to 0.7 V, 0.7 V to 0.6 V, and 0.6 V to 0.5 V. The current densities as well as cell voltages are presented as dimensionless form. When cell voltage is reducing from 0.7 V to 0.6 V, the magnitude of overshoot is larger than that of the change from 0.6 V to 0.5 V. The current difference of the voltage the range of 0.7 V to 0.6 V is higher than that of 0.6 to 0.5 V. Due to mass flow controller's accuracy the anode side flow rate at the cell voltage of 0.8 V was 50 sccm. It is higher than the stoichiometry of 0.8 V, which should be 17 sccm. The stoichiometry changes are from normal, 1.2/2.0, to starved condition.

Figure 7 shows the comparison of different cell voltage ranges of 0.2 V down. The cell voltage change ranges are 0.8 V to 0.6 V, and 0.7 V to 0.5 V. The overshoot amplitude of 0.8 V to 0.6 V is higher than that of 0.7 V to 0.5 V. Like the case of figure 6 the steady state value difference is the higher at the change of 0.8 V to 0.7 V. The magnitude of overshoot is the biggest when the cell voltage change is 0.3 V (from figure 5 to 7).

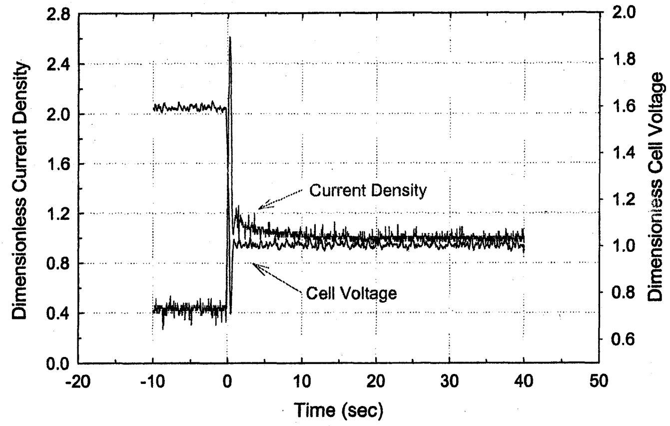

Figure 8. Current density response with 0.3 V of cell voltage drop. The cell voltage was changed from 0.8 V to 0.5 V.

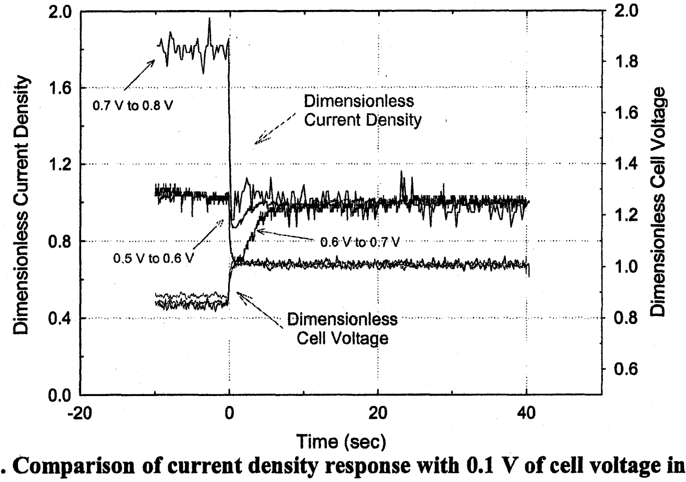

Figure 9. Comparison of current density response with 0.1 V of cell voltage increase. The cell voltage change ranges are from 0.7 V to 0.8 V, from 0.6 V to 0.7 V, and 0.5 V to 0.6 V.

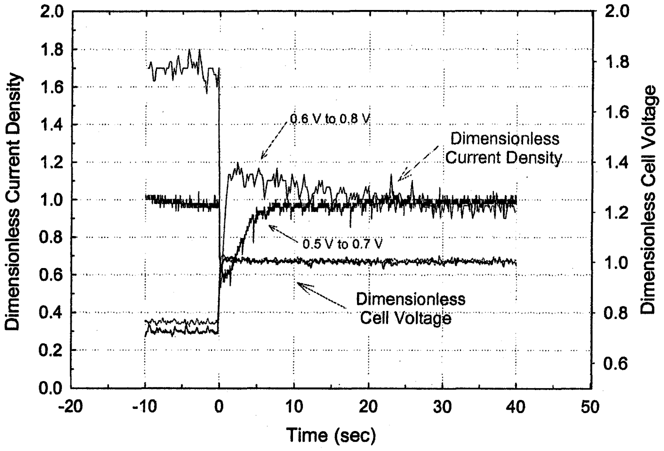

Figure 10. Comparison of Current density response with 0.2 V of cell voltage jump up. The cell voltage change ranges are from 0.5 V to 0.7 V and 0.6 V to 0.8 V.

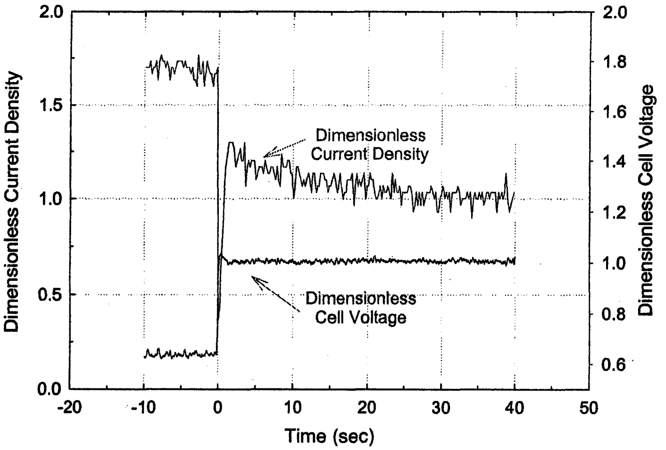

Figure 11. Current density response with 0.3 V of cell voltage increase. The cell voltage was changed from 0.5 V to 0.8 V.

Figure 8 presents the transient behavior of 0.3 V of cell voltage drop. The cell voltage is reduced from 0.8 V to 0.5 V. The flow rate was 50 and 69 sccm for anode and cathode, respectively.

Figure 9 shows the comparison of undershoot behavior at the change of 0.1 V cell voltage increase. The ranges are Like figure 6, 0.7 V to 0.8 V, 0.6 V to 0.7, and 0.5 V to 0.6 V, the magnitude of undershoot is the bigger when the cell voltage change from 0.6 V to 0.7 V.

Figure 10 shows the comparison of 0.2 V of cell voltage increase. Like previous pictures the undershoot behavior is significant at the cell voltage change from 0.6 V to 0.8 V.

Figure 11 shows the comparison of 0.3 V of cell voltage increase. Note that, seen from figure 9 to 11, the higher cell voltage difference, the bigger amplitude of undershoot behavior.

Conclusions

An experiment about transient of PEM fuel cell was studied at fixed flow rates of fuels. There were two conditions, from starved to normal and from normal to starved conditions. The cell voltage was changed various ranges as explained above. The overshoot/undershoot behavior is significant when the steady state current density difference is smaller. We observed that the higher cell voltage difference, the bigger magnitude of overshoot and undershoot value.

As our previous work[3] the overshoot/undershoot behavior is caused by paucity of hydrogen gas. The single path channel did not show the "vacuum effect" when the fuel condition is changed from normal to starved condition. It happen when the cell voltage is increased. It is because the linear velocity in single channel is more uniform and faster than that in triple channel, so that the driving force at the outlet of cell is not strong enough to flow back.

ACKNOWLEDGEMENT

Financial support by the South Carolina State University/University Transportation Center (Grant no. 2000-013), Department of Energy-EPSCoR (Grant no. DE-FG02-91ER75666), and Office of Naval Research, ONR (Grant no. N00014-98-1-0554) is gratefully acknowledged. The authors gratefully acknowledge that W. L. Gore & Associates, Inc supplied the MEAs used in this work.

REFERENCES

1. S-h. Kim, W-k. Lee, S. Shimpalee, and J. W. Van Zee. *Presented in of 201st meeting of the Electrochemical Society*, Philadelphia, PA. May 12-17, **2002**.

2. S. Shimpalee, S. Dutta, and J. W. Van Zee,, *Numerical Heat Transfer*, Part A, **2000**, 38, 111-128.
3. S. Shimpalee, W-K. Lee, H. Naseri-Neshat, and J. W. Van Zee, *Proceedings of ASME IMECE*, Orlando, FL., **2000**, 1, 1.
4. S. H. Kim, and J. W. Van Zee, submitted to *J. Power Source,* **2002**.
5. S. Shimpalee, W-K. Lee, H. Naseri-Neshat, and J. W. Van Zee, submitted to *J. Fuel Cells,* **2001**.
6. S. Dutta, S. Shimpalee, and J. W. Van Zee, *Intl. J. of Heat and Mass Transfer*, **2001**, 44/11, 2029-2042.
7. W-k. Lee and J.W. Van Zee, S. Shimpalee, S. Dutta, *Proceedings of the ASME IMECE*, Vol. 5, Nashville, TN, November, 1999, 454.
8. T. F Fuller, and J. Newman, *J. Electrochemical Soc.*, 140, 1993, 1218-1225
9. T. V. Nguyen, and R. E. White, *J. Electrochemical Soc.*, 140, 1993, 2178-2186.
10. W-k. Lee, C. Ho, J.W. Van Zee, and M. Murthy, *J. of Power Sources.*, 84, 1999, 45.
11. R. Jiang, D.Chu, *J. of Power Sources.*, 93, 2001, 25-31.
12. J.P. Meyers, H.L. Maynard, *J. of Power Sources.*, 109, 2002, 76-88.
13. Mahesh Murthy, Manuel Esayian, Alex Hobson, Steve MacKenzie, Woo-kum Lee, and J. W. Van Zee, *J. Electrochem. Soc.*, 148, 2001, A1141.
14. M.L. Ng, C.-L. Lin, and Y.-T. Cheng, *J. of Power Sources.*, 74, 1998, 159-168.
15. J. Hamelin, K. Agbossou, A. Laperriere, F. Laurencelle, and T.K. Bose, *Int, J. Hydrogen Energy.*, 26, 2001, 625-629.
16. J.C. Amphlett, R.F. Mann, B.A. Peppley, P.R. Roberge, and A. Rodrigues, *J. of Power Sources.* 61, 1996, 183-188.
17. 11. B. Emonts, J. Bogild Hansen, H. Schmidt, T. Grube, B. Hohlein, R. Peters, and A. Tschauder, *J. of Power Sources.*, 86, 2000, 228-236.
18. S. Shimpalee, H. Naseri-Neshat, W-k. Lee and J.W. Van Zee, *J. Electrochem. Soc.*,2002, submitted for publication.
19. S. Shimpalee, W. K. Lee, and J.W. Van Zee, *presented at the 2002 meeting of the Electrochem. Soc.*, Philadelphia, PA, May, 2002, paper#1136.
20. S. Um, C.-Y. Wang, and K. S. Chen, *J. Electrochemical Soc.*, 147, 2000, 4485-4493.
21. J.C. Amphlett, R.F. Mann, B.A. Peppley, P.R. Roberge, and A. Rodrigues, *J. of Power Sources.*, 61, 1996, 183-188.
22. M. De Francesco, E. Arato, *J. of Power Sources.*, 108, 2002, 41-52.
23. W. He, Q. Chen, *J. of Power Sources.*, 73, 1998, 182-192.
24. S. Shimpalee, S. Dutta, W-k. Lee and J.W. Van Zee, *Proceedings of the ASME IMECE*, Vol. 5, Nashville, TN, November, 1999, 464.
25. C. Haynes, *J. of Power Sources.*, 109, 2002, 365-376.
26. P. Argyropolous, K. Scott, and W.M. Taama, *J. of Power Sources.*, 87, 2000, 153-161.
27. E. Achenbach, *J. of Power Sources.*, 57, 1995, 105-109.
28. P. Argyropolous, K. Scott, and W.M. Taama, *Electrochim. Acta.*, 45, 2000, 1983-1998.
29. K. Sundmacher, T. Schultz, S. Zhou, K. Scott, M. Ginkel, and E.D. Gilles, Chem. *Eng. Science.*, 56, 2001, 333-341.
30. A. Simoglou, P. Argyropolous, E.B. Martin, K. Scott, A.J. Morris, and W.M. Taama, *Chem. Eng. Science.*, 56, 2001, 6761-6772.
31. D. Thirumalai, R.E. White, *J. Electrochemical Soc.*, 144, 1997, 1717-1723.

32. S. Shimpalee, S. Dutta, and J. W. Van Zee, *Proceedings of ASME IMECE*, Orlando, FL., **2000**, 1, 1.

Proceedings of The Electrochemical Society, PV 2002-31, 361-372 (2002)
DOI: 10.1149/200231.0361PV © The Electrochemical Society

Physical Model of Transport in Polymer-Electrolyte Membranes

Adam Weber and John Newman

Department of Chemical Engineering,
University of California, Berkeley, CA 94720-1462

In this paper, a physical model is developed that is semi-phenomenological and takes into account Schroeder's paradox. The model is based on the wealth of knowledge contained in the literature regarding polymer-electrolyte membranes. Along with the structural changes of the membrane due to water content, two different transport mechanisms are presented and discussed. These mechanisms and the structural changes represent the complete physical model of the membrane. The model is shown to agree qualitatively with different membranes and different membrane forms, and is applicable to modeling perfluorinated sulfonic acid (PFSA) and similar membranes. It is also the first physically based comprehensive model of membrane transport that includes the description of Schroeder's paradox.

INTRODUCTION

Polymer-electrolyte membrane (PEM) fuel cells have emerged as one of the eminent technologies of the 21st century. What makes PEM fuel cells unique among other fuel cells is that their electrolyte is an ionomer that conducts protons. Over the last couple of decades, PEM fuel cell research and improvements have reached an all time fervor (1)(2). Along with their attractiveness as efficient and clean energy producers, they may provide the energy structure of not only cars but also residential applications.

A critical problem and design issue of PEM fuel cells is water management (3). Due to the low operating temperatures, liquid water is produced. This can lead to the problem that too much water will cause flooding of the cathode region and not allow the reactant gases to reach the electrocatalyst. On the other hand, the membrane's transport properties are highly water dependent, and thus too little water will cause the anode side of the membrane to dry out and lose its conductivity. A correct water balance must be maintained in order to guarantee an optimal and sometimes even a functional performance, as well as control heat generation. Since the membrane is a key component in the water balance, it is desirable to understand and model the processes that occur in it, where there is room for new understanding and improvement. It should be noted that these processes include not only transport phenomena, but also observations like Schroeder's paradox: the uptake of water by the membrane from a liquid reservoir and a saturated vapor reservoir differ under the same conditions (4).

Although there have been various membranes used, none is more researched or seen as the standard than the Nafion family by E. I. du Pont de Nemours and Company. Like the other membranes used, the general structure of Nafion is a copolymer between polytetrafluoroethylene and polysulfonyl fluoride vinyl ether. These perfluorinated ionomer membranes exhibit many interesting properties such as a high conductivity, prodigious water uptake, and high anion exclusion, to name a few. Nafion will be the base membrane studied in this paper. The model developed and presented in this paper describes the transport in the membrane from a physical standpoint. This model goes beyond those presently in the literature by striking a balance between its robustness and scope; it is still essentially a macroscopic model. Throughout the paper and at the end, the model is compared to qualitative experimental observations from the literature for both Nafion and other membranes.

Background

In terms of modeling, polymer-electrolyte membranes have been modeled within two extremes, the macroscopic and the microscopic. In terms of microscopic models, there have been many models based on statistical mechanics (5), molecular dynamics (6), and macroscopic phenomena applied to the microscopic structure of the membrane (7)(8). These models provide the fundamental understanding of processes like diffusion and conduction in the membranes on a microscopic scale. They allow for the evaluation of how small perturbations like nonhomogeneity of pores and electric fields affect transport, as well as incorporation of small-scale effects. While these models yield valuable information about what goes on inside the membrane, some of which we will use, in general they are usually too complex to use in an overall fuel-cell model.

On the other side of the scale are the macroscopic models. These often are more empirical and focus only on describing the transport and relevant parameters of the membrane. There have been many of them proposed over the last decade, and they can be sorted into two main categories, those that assume the membrane is a single phase, and those that assume it is two phases. The former usually leads to a diffusion type model (9)(10)(11), and the later to a hydraulic type one (12)(13). Both types of models can be made to agree with experimental data, but neither describes the full range of data nor all of the observed effects, like Schroeder's paradox. It should also be noted that almost all of the microscopic models treat the membrane as a pseudo two-phase system.

One of the earliest and most recognized models is that by Bernardi and Vebrugge (12). That model treated the membrane as a two-phase system similar to a porous medium, where there were separate gas and liquid channels, and the porosity remained constant. Eikerling and coworkers (13) advanced this bundle-of-pores model to include effects of saturation, pore-size distribution, and hydrophobicity. The problems with these models are that they assume that the membrane is composed of two different pore pathways, one for gas and one for liquid. This does not necessarily make physical sense. For example, in the case of a porous medium that has pores filled with vapor, oxygen should have a pathway to diffuse through with a larger flux than that observed (14). The models just increase the tortuosity of the pore pathway, but this does not necessarily agree with the complete physical picture of the membrane. Furthermore, in the case of a low-saturated membrane, there is no continuous liquid pathway across the medium, and the membrane matrix interacts significantly with the water. Thus, concentration and not hydraulic pressure seems to be the more appropriate driving force; a one-phase model should be used.

On the other side of the modeling debate, Fuller (10) and Springer *et al.* (9) were the first to popularize the idea of the membrane as a single homogenous phase. They treat it like a solvent, and use experimental data to describe the diffusion-like transport mechanism through the polymer. This type of membrane modeling has also found a strong support base, and has been modified by Meyers (15) and Okada *et al.* (16) in order to account for additional effects. A very interesting adaptation of the single-phase model is that done recently by Janssen (11) and earlier by Thampan and coworkers (17), in which transport through the membrane is described using only gradients in chemical potential, avoiding the complication of trying to separate out diffusive and pressure-driven flow components. The single-phase models do have some limitations including the inability to predict completely the correct water profiles and transport. For example, they fail to predict the observed sharp drying boundary on the anodic side of the membrane (18). Furthermore, when the membrane is saturated, it does not make sense to have only a diffusion-type flow since the concentration of water in the membrane is uniform; there is no concentration gradient. Thus, a two-phase or hydraulic model should be used in this case.

Both types of macroscopic models mentioned above have both advantages and limitations. They describe part of the transport that is occurring, and this is why they are both still popular, but the correct model is some kind of superposition between them, as has been briefly mentioned before (19). The physical model that we develop in this paper combines the two types of models and is the first to pursue this combination in a consistent manner. The need for a combination model is also apparent in that the above models do not describe or present a physical picture of Schroeder's paradox, whereas the combination model naturally describes it. As a side note, most of the models use a discontinuity in uptake when going from a vapor contact to a liquid contact or neglect the paradox altogether.

In this paper, we describe a membrane model that can be used easily in a complete fuel-cell model. Thus, it is robust enough to describe the membrane properties and transport under various operating conditions (liquid and vapor boundaries, constrained, swollen, temperature, *etc.*), but it is not too complex and unwieldy. In a specific sense, it is phenomenological, but we make a serious attempt at using all relevant data and observations, and imparting a physical significance to everything. Also, our model, like the ones above, is one-dimensional (1-D). It should be noted that there have been 2-D and 3-D models for the membrane proposed, and that these higher-dimension models are more often of the two-phase type (20)(21). Even with these higher dimension models, the membrane itself can usually be taken as a 1-D structure, and the higher dimensions are needed only to describe the complete transport in a fuel cell (*e.g.*, depletion of reactants down the flow channel). In this paper, we describe the physical model of what is occurring in the membrane including the introduction of membrane structure and relevant phenomena, and qualitatively correlate it with observed phenomena.

PHYSICAL MODEL OF MEMBRANE STRUCTURE

The physical model of the polymer-electrolyte membrane that we use is relatively simple. It is based on experimental evidence and is in-line with modern thoughts of transport within the membrane. As alluded to above, transport in the membrane occurs by two separate mechanisms. The first is a diffusion type mechanism in which the membrane is treated as a single phase, and the second is a hydraulic mechanism in which the membrane is treated as a two-phase system. The first mode corresponds to a membrane in contact with water vapor, and the second to a membrane in contact with liquid water. By modeling the membrane in this fashion, Schroeder's paradox and other phenomena can be described.

The key to the model is how the structure of the membrane changes with water content. The structure of the hydrated membrane is affected by many factors including pretreatment procedures, operating temperature, water content, length of side-chains, and equivalent weight to name a few. However, there are still some global changes and structural elements common to all of the perfluorosulfonated ionomers as a function of water content.

The general structure of the membrane as a function of water content has been the source of many studies including rheological (22), swelling (23)(24), infrared (25), porosimetry (26), and especially X-ray (27)(28)(29) and microscopy studies (30)(31)(32). For the most part, all of these have shown that a hydrated membrane contains two phases, an ionic phase which water is associated with, and a matrix or nonionic phase. The ionic phase is associated with the hydrated sulfonic acid groups, and the matrix phase with the polymer backbone. Thus, in our model, there are two separate regions, one is hydrophilic (ionic phase) and the other is hydrophobic (matrix phase). The actual form of the phases depends on the water content, as discussed below.

There are many different forms into which the two phases can separate. The consensus is that at lower hydration levels, those that correspond to a membrane equilibrated with vapor, the actual structure is that of an inverted micelle. This is known as the cluster-network model first proposed by Hsu and Gierke (33). In this model, the water is contained in a spherical domain of about a 4 nm diameter into which the polymer side-chains infiltrate. The reason for this structure is that it is an energetically favored state of the membrane (34). As the membrane initially takes on water, the sulfonic acid groups are hydrated and dissociate, creating charged groups that participate in coulombic repulsions. These interactions are opposed by the work required to deform the polymer matrix. Hence, there is a balance between the surface or electrostatic energy and the elastic or deformation energy (33)(35). The clusters are connected by short pathways of around 1 nm in diameter, as calculated experimentally (36), and were determined by Hsu and Gierke to be transient connections with a stability on the order of ambient thermal fluctuations. The cluster-network model has also been verified by microscopy studies.

The other popular model for vapor-equilibrated membrane structure is that of Yeager and Steck (37). They proposed the existence of three regions in the membrane: the matrix, the ionic cluster, and an interfacial zone. They further supposed that the ionic clusters are nonspherical. While the structure of the ionic clusters has been seen and calculated to be roughly spherical, there has been evidence of the interfacial zone. For example, transition electron microscopy of stained membranes shows that there is a region surrounding the ionic clusters containing a lower concentration of sulfonic acid sites along with some of the polymer backbone (31).

We treat the Hsu and Gierke model as an idealization of the Yeager and Steck model, where the channels are the interfacial regions. However, the concentration of the sulfonic acid sites is not high enough to make the channel entirely hydrophilic, and thus it is slightly hydrophobic. The reasoning is that the deformation caused by forming the clusters makes the channels hydrophobic in the middle, and with increasing sulfonic acid sites as the cluster is approached. For the whole channel though, the average surface is hydrophobic. As a final piece of evidence, the channels are attributed with causing co-ion exclusion, and thus must have some sulfonic acid groups in them, perhaps at their periphery (38). In all, for a vapor-equilibrated membrane, the structure is that of ionic clusters in the shape of inverted micelles that are hydrophilic and filled with water. These clusters are connected by channels that are continuously forming and deforming at ambient conditions and contain sulfonic acid sites at their periphery, making them more hydrophilic than the matrix, but still hydrophobic overall.

As the water content increases, the membrane clusters swell and reorganize themselves, trying to minimize the total energy of the system, aided by the fact that water plasticizes the membrane (22)(33). This reorganization is started by the presence of liquid water at the boundary of the membrane. The way in which water stabilizes the channels is unknown, but is undoubtedly due to the polar nature of water and the presence of a fluorocarbon-rich skin on the surface of Nafion (23)(32). This skin is repelled from the surface, causing the surface and the nearby channels to become more hydrophilic (39). Water then enters the channels and somehow helps to stabilize them and continue the process across the membrane. The reorganization results in an agglomeration of clusters such that they appear by X-ray analysis to be larger but the distance between sulfonic sites is about the same (27). Hence, the liquid water helps to stabilize and lower the hydrophobicity of the channels (although they are still hydrophobic overall) and the clusters are coming together and making the channels larger. In essence, this reorganization forms a porous structure. In fact, this is what has been seen in swollen membranes by the microscopy studies. The pore-size distribution shows an average pore size of about 2 nm, which agrees with the average size between a swollen channel and shrunken cluster.

In summary, Figure 1 shows the way our model describes the structural changes of the membrane with water content, where λ is the number of waters per sulfonic acid site. In the first step, the dry membrane absorbs water in order to solvate the acid groups, which form inverse micelles in the polymer matrix. With more water uptake, these clusters grow and form interconnections with each other. These connections are transitory and have hydrophobicities comparable to the matrix. This structure corresponds to a membrane that is in contact with saturated water vapor. If there is liquid water at the boundary of the membrane, structural reorganization occurs due to the fluorocarbon-rich skin of the ionomer and the liquid water infiltrating the channels, causing the channels to stabilize, and the various clusters to agglomerate along the channels; thus forming a pore-like structure. In this structure, the channels are still hydrophobic on average, but only slightly since the agglomeration causes a higher concentration and farther penetration of sulfonic acid sites into the channel. Since now the channels are filled with liquid, the uptake of the membrane has increased. Obviously, our model is somewhat of an idealization, but it is strongly based on and agrees with the physical evidence.

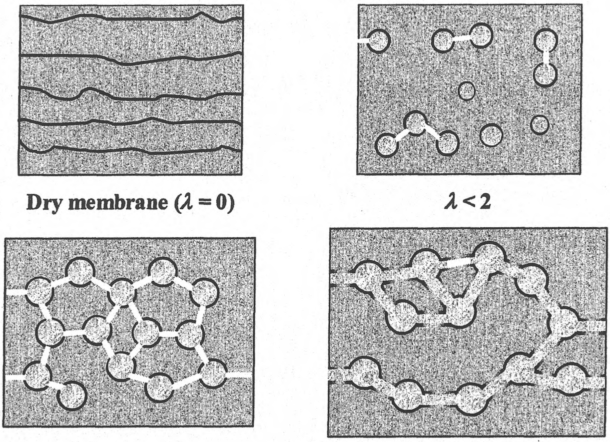
Dry membrane ($\lambda = 0$)

$\lambda < 2$

$\lambda = 14$

$\lambda \sim 22$

Figure 1 – Evolution of membrane structure as a function of water content, λ (the number of waters per sulfonic acid site). The gray area is the fluorocarbon matrix, the white the fluctuating channels, the black the polymer side-chains, and the light gray the liquid water.

The values of λ for the saturated vapor and liquid-equilibrated membranes are taken from studies of Schroeder's paradox (15)(40). The behavior described above does not depend on whether the membrane is going from vapor to liquid or liquid to vapor. In the former, liquid water is present and infiltrates the channels, and in the latter, the liquid water is pushed out because the channels are hydrophobic and there is not any liquid water in contact with the membrane. Of course, the liquid water in the membrane will have some pressure at the very edge of the membrane due to capillary forces and the gas pressure at the boundary, but the capillary pressure will be zero and thus the water will move out due to the hydrophobicity of the channels. Furthermore, the reemergence of the fluorocarbon-rich skin may aid in this process. It is noted that the structural rearrangements, like the fluorocarbon skin and the fact that the water has to go through clusters and other channels, make the overall process relative slow, which is verified in the observed length of time it takes to reach equilibrium (41).

The above idea is not entirely novel and has been mentioned off-hand as one of a few possible explanations for Schroeder's paradox (42), but it has never been incorporated into a model. There is also experimental evidence to back this explanation. First, as λ goes from 14 to 22, the water is seen as becoming more bulk-like by various analysis and experimental data including freezing-point studies (5)(25)(43). These results indicate that a separate liquid phase if forming that is not like the bound water or cluster water formed in the case of the vapor-equilibrated membrane. Also, the electroosmotic coefficient sharply increases with a membrane in contact with liquid (44) and approaches the value for a hydrated proton in pure water (45); the permeation coefficient of oxygen in the membrane increases greatly and approaches the value of oxygen in pure water (46); and the conductivity increases (16). All of these results suggest that there is now a continuous channel of liquid water where before there was not. One last piece of evidence for the channel structure is that while the vapor-phase uptake is temperature dependent due to the change in interaction energies, the liquid-phase uptake is not since it is the same as filling an inert porous medium (41). These observations are in exact agreement with our concept of what is occurring between a vapor-equilibrated and liquid-equilibrated membrane. With the defined physical structure of the membrane, we have been able to explain Schroeder's paradox, and now can develop a transport mechanism that follows from these ideas.

TRANSPORT MECHANISMS

By the above physical model, there are two different types of transport occurring, depending on whether the membrane is in contact with liquid or vapor water. Thus, we should divide the model into two separate transport modes, the vapor and the liquid. The two different modes of transport are considered independent of each other except for properties that affect the entire membrane/water system as a whole, like density and pressure. A continuous transition is assumed between the two modes based on the water content of the membrane. Finally, based on various experimental data, all species transported through the membrane, including water, protons, and gases move by way of the clusters and channels and not through the fluorocarbon matrix (33)(37). Thus, we treat the fluorocarbon matrix as inert. All that it does is to add mechanical strength, raise the weight of the polymer, and make the channels hydrophobic.

Transport in a vapor-equilibrated membrane

For a membrane that is in contact with water vapor only, there is a percolation threshold value for the water content before it is conductive. There is liquid water in the clusters (the water condenses due to the hydrophilicity of the clusters), but none in the channels, except for the bound water hydrating the few sulfonic acid sites present. The channels are always fluctuating, but the clusters are close enough together to form conductive channels. Due to the nature of the fluctuating channels and the interfacial region, it is best to treat the membrane as a homogenous single-phase system. In this sense, the water vapor does not penetrate into the channels, but dissolves by an equilibrium mechanism into the membrane. Thus, the vapor-equilibrated membrane transport mechanism is similar to the single-phase transport models mentioned previously.

The conductivity and other properties in the single-phase model can be explained based on the percolation concept. Thus, they increase as more channels are formed and the pathways become less tortuous due to the addition of water into the system. The electroosmotic coefficient, or the number of water molecules carried by a proton, is dependent on the type of complexes that water forms with a proton, and in the absence of a contiguous liquid pore network, the only complex that can form and be transported is a hydronium ion. Thus, the conductivity and the electroosmotic flow are due to a hydronium ion that hops from acid site to acid site through the clusters and across the channels. Finally, the nonelectroosmotic water movement is caused by a gradient in the water chemical potential. The above lays the foundation for the transport mode of the single-phase system when the membrane is in contact with a vapor boundary, and is shown pictorially in Figure 2.

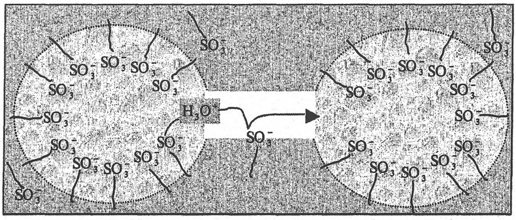

Figure 2 – Vapor-equilibrated membrane transport and structure.

Transport in a liquid-equilibrated membrane

In this mechanism, the structure of the membrane can be interpreted to be more akin with a noninteracting porous medium rather than the interacting description given above. This is because only the channels connecting the clusters are being filled with liquid water, if the liquid pressure is enough to overcome the hydrophobicity of the pore. If it is not, then the liquid phase cannot penetrate further into the porous medium. The transport in this two-phase system is very similar to that modeled by Bernardi and Verbrugge (12) and Eikerling and coworkers (13) and is summarized in Figure 3.

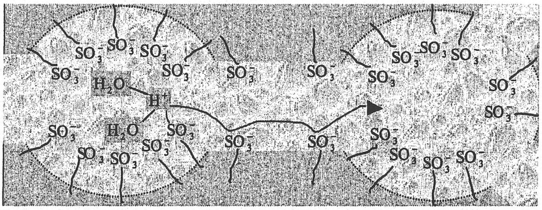

Figure 3 – Liquid-equilibrated membrane structure and transport.

When filled with liquid water, the channels are able to make a continuous water pathway from cluster to cluster and membrane side to side. Thus, the nonelectroosmotic movement of water is caused by a liquid pressure gradient. The conductivity is explained by the Grotthuss mechanism and proton hopping or diffusion through the membrane, where once again the conductivity will increase with water content since more water means more filled channels and better and shorter conduction pathways, up to a point. The electroosmotic flow is described by the vehicle mechanism and proton hydration effects, including the formation of the Zundel, $H_5O_2^+$, and Eigen, $H_9O_4^+$, ions (47). Thus, unlike in the previous transport mechanism, the electroosmotic coefficient will be larger than one, and something more like 2.5 since it is slightly less than that in pure water because of the small pore sizes (48).

QUALITATIVE COMPARISONS OF THE MODEL WITH OBSERVATIONS

As mentioned previously, most of these membranes are based on the Nafion copolymer idea and as such are polyfluorosulfonic acid membranes. In this section, we briefly examine some of the observed behavior and effects, and see whether the physical model can qualitatively predict them. We first examine the family of Nafion membranes and then look at some other membranes.

The pretreatment conditions can have a large impact on the structure of the membrane. In order to make the ionomer active, it must be heated in the appropriate cationic solution. Next, the ionomer is usually dried, and the drying temperature can lead to drying out of the sulfonic groups, which leads to the destruction of the clusters. After this destruction, heating in an aqueous environment above the glass-transition temperature must be applied to allow sufficient reorientation of the polymer chains. This is why water uptake decreases with drying temperature, since there are not as many clusters that can accept water (49). The physical model predicts this behavior since there are not as many clusters and pores.

The equivalent weight of an ionomer is very similar to a molecular weight. The higher the equivalent weight, the more ionomer is needed for the same acid behavior, and the higher the content of the perfluorinated polymer matrix. For high equivalent weight Nafions, the clusters should be farther apart and smaller since it is harder to deform the polymer. Thus, the transport properties will not be as good, and the percolation threshold for conductivity is expected to be higher. These effects have been seen in comparing Nafion 1200 with Nafion 1100 (33). Furthermore, it has been shown that as the equivalent weight increases, the electroosmotic coefficient is higher, the diffusion coefficient is poorer, and the conductivity is lower, because water is now complexing with the fluorocarbon chains and ether oxygens in the clusters as well as the pores for a water-saturated membrane (25). The physical model explains this since the channels are longer and will have more interaction with the matrix, thus making them more hydrophobic and yielding lower water uptakes and worse properties. It should be noted that as the equivalent weight decreases past 1000 g/equiv, Nafion becomes soluble in water because there is not enough hydrophobic matrix to keep it in a gel-like state (50).

In addition to equivalent weight and structure, the ionic form of Nafion also leads to different behavior. The conductivity of the acid or H-form of Nafion is highest, and that is due to the enhancement by the Grotthuss mechanism for proton transport, as explained by our physical model (48). With the other cations, the smaller the cation, the higher its hydration level and thus the higher the water content of the membrane. The physical model explains this observation because the smaller cations can form larger clusters since their ionic radius is smaller and their preferential hydration level is higher (51). This is especially the case with cesium ions, since the uptake is almost nothing since the ions are too big and block the channels. The effect of cation functionality is also seen with hydrophilic versus hydrophobic cations. In that case, the hydrophilic cations give a higher water content, which agrees with the model since the clusters are filled with water and will be larger. Finally, the smaller cations have larger electroosmotic drag coefficients because the water is more bulk-like, meaning that larger water complexes can form. The reason for the bulk-like water is that the clusters and channels are larger and the water in the middle of the clusters is shielded by the water solvating the sulfonic acid sites (7).

Besides Nafion, other membranes have been considered. These membranes include the sulfonated polyetherketones (PEEK) membranes, the Aciplex and Flemion membranes, and the Dow company series of membranes. The PEEK membranes have a structure that has narrower channels and a less-connected network of clusters (42). This structure results in a higher dependence of the various transport properties on water content due to percolation ideas. In addition, it results in lower drag coefficients since larger water-proton complexes are inhibited from forming. These analyses are in accordance with the referenced data and our physical model. The Aciplex and Flemion membranes have a bilayer structure comprised of carboxylic type on the cathode side and sulfonic type on the anode side (52). This type of arrangement gives them lower gas permeation and lower resistance because they are thinner and have a higher ion-exchange capacity, meaning that physically the clusters are closer together and form a more hydrophilic and interlinking continuous network. This analysis is also verified by their higher water uptake (49). Finally, the Dow membranes are perhaps the most researched after those of Nafion. Their structure is very similar to Nafion, except that they have a much shorter side-chain (40)(53)(54). Due to the short side-chain, it is expected that the elastic deformation energy is higher and thus the formed clusters will be smaller. These smaller clusters allow for a slightly higher water content than for Nafion since there is a larger volume of interconnecting channels, but the water uptake when in contact with the vapor-phase should be slightly lower than that of Nafion for membranes with the same number and type of sulfonic acid sites. This water uptake description also means that diffusion coefficients and conductivities will be roughly the same for the vapor-equilibrated membrane, but will be higher than those in Nafion for the liquid-equilibrated membrane. In addition, gas diffusion can be described by the higher levels of interconnectivity between the clusters and thus a shorter overall diffusional path. All of the above is verified experimentally.

CONCLUSIONS

We have presented a physical picture of the membrane, which agrees with the observed data. In this model, the dry membrane forms a cluster-network model composed of ionic clusters and connected by fluctuating hydrophobic channels. This is true up to water contents equal to the equilibrium water content of the membrane when exposed to saturated water vapor. Due to the structure of the membrane, it is best to treat the membrane as a single-phase system even though there is a liquid water phase contained inside of the clusters. The transport is thus described by a gradient in water chemical potential and a hopping mechanism of hydronium ions. When the membrane is exposed to liquid water at a high enough pressure, water can infiltrate the channels between the clusters, thus forming a second phase. The liquid water also causes the clusters to rearrange into a more pore-like network. Hence, the transport is treated as a two-phase system or that in a porous medium. The flow of liquid water is described now by a pressure gradient, conductivity by the Grotthuss and diffusion mechanisms, and electroosmotic flow by the vehicle mechanism and proton hydration in the pores. When the membrane is neither completely in the liquid- or vapor-transport mode, the mode is assumed to be a superposition of the two with water being able to evaporate and condense between the two modes. Work is now on-going to make a mathematical transport model based on the above physical model.

ACKNOWLEDGEMENTS

This research has been supported by UTC Fuel Cells, LLC, and by an EPA STAR graduate fellowship (91601301-0).

REFERENCES

1. P. Costamagna and S. Srinivasan, *J. Power Sources*, **102**, 242 (2001).
2. M. L. Perry and T. F. Fuller, *J. Electrochem. Soc.*, **149**, S59 (2002).
3. EG&G Services, Parsons Inc., and Science Applications International Corporation, *Fuel Cell Handbook (Fifth Edition)*, U.S. Department of Energy, West Virginia (2000).
4. P. Schroeder, *Z. Phys. Chem.*, **45**, 57, 1903.
5. S. J. Paddison, R. Paul, and T. A. Zawodzinski, Jr., *J. Chem. Phys.*, **115**, 7753 (2001).
6. X.-D. Din and E. E. Michaelides, *AIChE Journal*, **44**, 35 (1998).
7. B. R. Breslau and I. F. Miller, *Ind. Eng. Chem. Fundam.*, **10**, 554 (1971).
8. Y. Yang and P. N. Pintauro, *AIChE J.*, **46**, 1177 (2000).
9. T. E. Springer, T. A. Zawodzinski, and S. Gottesfeld, *J. Electrochem. Soc.*, **138**, 2334 (1991).
10. T. F. Fuller, *Solid-Polymer-Electrolyte Fuel Cells*, Ph.D. Dissertation, University of California – Berkeley (1992).
11. G. J. M. Janssen, *J. Electrochem. Soc.*, **148**, A1313 (2001).
12. D. M. Bernardi and M. W. Verbrugge, *J. Electrochem. Soc.*, **139**, 2477 (1992).
13. M. Eikerling, Yu. I. Kharkats, A. A. Kornyshev, and Yu M. Volfkovich, *J. Electrochem. Soc.,* **145**, 2684 (1998).
14. Z. Ogumi, Z. Takehara, and S. Yoshizawa, *J. Electrochem. Soc.*, **131**, 769 (1984).
15. J. P. Meyers, *Simulation and Analysis of the Direct Methanol Fuel Cell*, Ph.D. Dissertation, University of California – Berkeley (1998).
16. T. Okada, G. Xie, and M. Meeg, *Electrochimica Acta*, **43**, 2141 (1998).
17. T. Thampan, S. Malhotra, H. Tang, and R. Datta, *J. Electrochem. Soc.*, **147**, 3242 (2000).
18. F. N. Buchi and G. G. Scherer, *J. Electrochem. Soc.*, **148**, A183 (2001).
19. K. D. Kreuer, *Solid State Ionics*, **97**, 1 (1997).

20. S. Dutta, S. Shimpalee, and J. W. Van Zee, *J. Appl. Electrochem.*, **30**, 135, 2000.
21. P. Futerko and I-M. Hsing, *Electrochimica Acta*, **45**, 1741 (2000).
22. S. C. Yeo and A. Eisenberg, *J. Appl. Poly. Sci.*, **21**, 875 (1977).
23. G. Gebel, P. Aldebert, and M. Pineri, *Polymer*, **34**, 333 (1993).
24. R. S. Yeo, *Polymer*, **21**, 432 (1980).
25. M. Falk, *Can. J. Chem.*, **58**, 1495 (1980).
26. J. Divisek, M. Eikerling, V. Mazin, H. Schmitz, U. Stimming, and Yu M. Volfkovich, *J. Electrochem. Soc.*, **145**, 2677 (1998).
27. J. A. Elliott, S. Hanna, A. M. S. Elliott, and G. E. Cooley, *Macromolecules*, **33**, 4161 (2000).
28. G. Gebel, *Polymer*, **41**, 5829 (2000).
29. H.-G. Haubold, T. Vad, H. Jungbluth, and P. Hiller, *Electrochimica Acta*, **46**, 1559 (2001).
30. P. J. James, T. J. McMaster, J. M. Newton, M. J. Miles, *Polymer*, **41**, 4223 (2000).
31. T. Xue, J. S. Trent, and K. Osseo-Asare, *J. Memb. Sci.*, **45**, 261 (1989).
32. R. S. McLean, M. Doyle, and B. B. Sauer, *Macromolecules*, **33**, 6541 (2000).
33. W. Y. Hsu and T. D. Gierke, *J. Memb. Sci.*, **13**, 307 (1983).
34. A. Eisenberg, *Macromolecules*, **3**, 147 (1970).
35. K. A. Mauritz and C. E. Rogers, *Macromolecules*, **18**, 483 (1985).
36. G. Xie and T. Okada, *J. Chem. Soc., Faraday Trans.*, **92**, 663 (1996).
37. H. L. Yeager and A. Steck, *J. Electrochem. Soc.*, **128**, 1880 (1981).
38. S. W. Capeci, P. N. Pintauro, and D. N. Bennion, *J. Electrochem. Soc.*, **136**, 2876 (1989).
39. T. A. Zawodzinski, Jr., S. Gottesfeld, S. Shoichet, and T. J. McCarthy, *J. Appl. Electrochem.*, **23**, 86 (1993).
40. T. A. Zawodzinski, Jr., T. E. Springer, J. Davey, R. Jestel, C. Lopez, J. Valerio, and S. Gottesfeld, *J. Electrochem. Soc.*, **140**, 1981 (1993).
41. T. A. Zawodzinski, Jr., C. Derouin, S. Radzinski, R. J. Sherman, V. T. Smith, T. E. Springer, and S. Gottesfeld, *J. Electrochem. Soc.*, **140**, 1041 (1993).
42. K. D. Kreuer, *J. Memb. Sci.*, **185**, 29 (2001).
43. M. Cappadonia, J. W. Erning, and U. Stimming, *J. Electroanal. Chem.*, **376**, 189 (1994).
44. T. A. Zawodzinski, J. Davey, J. Valerio, and S. Gottesfeld, *Electrochimica Acta*, **40**, 297 (1995).
45. N. Agmon, *Chem. Phys. Lett.*, **244**, 456 (1995).
46. T. Sakai, H. Takenaka, and E. Torikai, *J. Electrochem. Soc.*, **133**, 88 (1986).
47. K. D. Kreuer, *Solid State Ionics*, **136-137**, 149 (2000).
48. M. Eikerling, A. A. Kornyshev, A. M. Kuznetsov, J. Ulstrup, and S. Walbran, *J. Phys. Chem. B*, **105**, 3646 (2001).
49. J. T. Hinatsu, M. Mizuhata, and H. Takenaka, *J. Electrochem. Soc.*, **141**, 1493 (1994).
50. D. I. Ostrovskii, A. M. Brodin, and L. M. Torell, *Solid State Ionics*, **85**, 323 (1996).
51. A.G. Guzman-Garcia, P. N. Pintauro, M. W. Verbrugge, and R. F. Hill, *AIChE J.*, **36**, 1061 (1990).
52. N. Yoshida, T. Ishisaki, A. Watakabe, and M. Yoshitake, *Electrochimica Acta*, **43**, 3749 (1998).
53. E. E. Boakye and H. L. Yeager, *J. Memb. Sci.*, **69**, 155 (1992).
54. Y.-M. Tsou, M. C. Kimble, and R. E. White, *J. Electrochem. Soc.*, **139**, 1913, (1992).

Proceedings of The Electrochemical Society, PV 2002-31, 373-387 (2002)
DOI: 10.1149/200231.0373PV © The Electrochemical Society

SIMPLE MATHEMATICAL MODEL FOR WATER DIFFUSION IN NAFION® MEMBRANES

Jean St-Pierre
Ballard Power Systems
9000 Glenlyon Parkway, Burnaby, BC, Canada, V5J 5J9

ABSTRACT

A simple mathematical model for water diffusion in Nafion® membranes was derived assuming that membrane properties are independent of membrane water content (water diffusion coefficient, membrane thickness), an equilibrium exists at the interface between channel and membrane, and the relationship between membrane water content and channel water concentration is linear. General analytical expressions were obtained as well as approximations. Comparison with experimental data showed good agreement with an error generally smaller than 20 %. Membrane properties derived from curve fitting the model general relative humidity equation to experimental data do not agree with independently obtained values. As a result, model calibration is required for predictive purposes.

INTRODUCTION

Polymer electrolyte fuel cell (PEFC) models are necessary to predict cell performance for a range of operating conditions and cell designs as well as to optimize performance resulting in reduced development costs and time. Water management plays a significant role in many models due to its potentially large effect on ohmic and mass transport overpotentials depending on cell arrangement, operating conditions and membrane/electrode assembly design (MEA). For example, the ohmic overpotential was observed to vary by 50 mV at 0.54 A/cm^2 by changing the flow configuration (1-2). Furthermore, the mass transport overpotential was also observed to vary by as much as 100 mV at 1.08 A/cm^2 by changing the temperature difference between the inlet and outlet coolant temperature (1).

However, simplicity, is usually not an objective of many modeling activities (3-21). Consequently, many secondary effects are often included such as convective water flow through the membrane (Darcy flow), water activity coefficients, membrane swelling, and, dependency of membrane properties on water content (diffusion coefficient, etc). Model simplicity is desirable for a number of reasons including reduced model development time, reduced computational time, readily available dependencies for analytical models (for example, easier curve fitting to experimental data) and ability to more easily tackle larger problems (stack containing several tens of similar MEAs, each described by a simple model). Furthermore, a model accuracy such as < 20 % error is sufficient in many cases (rough design, etc).

This communication discusses the first necessary building block to derive a simple water management model for PEFCs. Water transport in Nafion® membranes is controlled by two mechanisms: diffusion and electro-osmotic drag. A water diffusion model in Nafion® membranes is presented and is compared to previously published data.

MODEL

Figure 1 shows that water diffusion takes place between two compartments separated by a Nafion® membrane or an MEA based on a Nafion® membrane (in this case, the rate determining step is assumed to be water diffusion in the membrane and not in the gas diffusion layer). Water circulates in one compartment whereas gas circulates in the second compartment. The main assumptions include:

- steady state
- water diffusion occurs perpendicularly to the membrane surface (membrane thickness is much smaller than the channel length)
- constant pressure along the channels
- constant concentration in the gas stream at any given location along the channel (plug flow behavior)
- constant temperature
- ideal gas behavior
- negligible gas diffusion through the membrane
- negligible pressure drop across the membrane (no permeation through the membrane)
- membrane properties are independent of water content (diffusion coefficient, membrane thickness)
- equilibrium between channel and membrane interface
- linear relationship between membrane water content and channel water concentration (analogous to Henry's law)

A mass balance on the control volume defined in Figure 1 leads to:

$$\frac{dN_w(y)}{dy} = bN_w(z) \qquad [1]$$

The water molar flow rate can be expressed as a function of the other components in the gas stream (ideal gas):

$$N_w(y) = \frac{N_g RH(y) p_s}{p - RH(y) p_s} \qquad [2]$$

Combination of equations 1 and 2 leads to:

$$\frac{N_g p_s p}{\left(p - p_s RH(y)\right)^2} \frac{dRH(y)}{dy} = bN_w(z) \qquad [3]$$

Equation 3 requires a definition of $N_w(z)$ which is obtained by making use of the steady state assumption:

$$\frac{dN_w(z)}{dz} = 0 \qquad [4]$$

which leads to:

$$N_w(z) = N_{w,z} \qquad [5]$$

The water flux through the membrane is determined by using Fick's law and making use of the membrane properties independence (diffusion coefficient, thickness) on water content:

$$N_{w,z} = D\frac{dc_w(z)}{dz} \qquad [6]$$

which leads to:

$$N_{w,z} = \frac{D(c_w(\delta) - c_w(0))}{\delta} \qquad [7]$$

The water concentration on both sides of the membrane is defined in terms of the saturation water pressure an using a simplified relationship between channel water concentration and membrane water content (Henry's law analog):

$$c_w(\delta) = kp_s, c_w(0) = kp_s RH(y) \qquad [8]$$

With equation 8, equation 7 is rewritten as:

$$N_{w,z} = \frac{Dkp_s(1 - RH(y))}{\delta} \qquad [9]$$

Insertion of equation 9 into equation 3 leads to the differential equation describing the change in relative humidity along the gas filled channel:

$$\frac{dRH(y)}{(1 - RH(y))(p - p_s RH(y))^2} = \frac{bDkdy}{N_g p\delta} \qquad [10]$$

In practice, the volumetric gas flow rate under standard conditions is commonly used instead of the molar flow rate:

$$N_g = \frac{p_r \dot{V}_{g,s}}{RT_r} \qquad [11]$$

The initial condition (the inlet gas may or may not be dry) is written as:

$$RH(0) = RH_0 \tag{12}$$

With equations 11 and 12, the solution of equation 10 is found by integration. The implicit relationship between the gas flow rate and the local relative humidity is:

$$\dot{V}_{g,s} = \frac{\dfrac{DkbRT_r y}{\delta p p_r}}{\left(\dfrac{1}{p-p_s}\right)\left(\dfrac{1}{p-p_s RH_0} - \dfrac{1}{p-p_s RH(y)}\right) + \dfrac{\ln\left[\dfrac{(1-RH_0)(p-p_s RH(y))}{(1-RH(y))(p-p_s RH_0)}\right]}{(p-p_s)^2}} \tag{13}$$

A similar relationship is derived using the molar flow rate instead of the relative humidity. For this case, equation 2 is rewritten as:

$$RH(y) = \frac{N_w(y)p}{p_s(N_g + N_w(y))} \tag{14}$$

Substitution of equation 14 in equation 9 and combination with equation 1 leads to an equation 10 equivalent:

$$\frac{p_s(N_g + N_w(y))}{N_g p_s - N_w(y)(p-p_s)} dN_w(y) = \frac{Dkbp_s dy}{\delta} \tag{15}$$

In this case, the initial condition (the inlet gas may or may not be dry) is written as:

$$N_w(0) = N_{w,0} \tag{16}$$

With equation 16, the solution of equation 15 is found by integration. The implicit relationship between the gas flow rate and the local water flux is:

$$\frac{Dkbp_s l}{\delta} = \frac{p_s(N_{w,0} - N_w(y))}{p-p_s} + \left(\frac{pp_s N_g}{(p-p_s)^2}\right)\ln\left[\frac{p_s N_g - N_{w,0}(p-p_s)}{p_s N_g - N_w(y)(p-p_s)}\right] \tag{17}$$

Equation 17 is a function of the gas flow rate if equation 11 is substituted. There are two limiting cases, which simplify the previous derivations. In the first case, it is assumed that the gas flow rate is so large that the inlet gas relative humidity is maintained along the entire flow field length (RH(y) ≅ RH₀). Under this condition, equation 9 becomes:

$$N_{w,z} = \frac{Dkp_s(1-RH_0)}{\delta} \tag{18}$$

Combination of equation 18 with equation 3 leads to the differential equation:

$$\frac{N_g p_s p}{\left(p - p_s RH(y)\right)^2} \frac{dRH(y)}{dy} = \frac{Dkbp_s\left(1 - RH_0\right)}{\delta} \qquad [19]$$

which leads with equation 11 to the explicit solution:

$$RH(y) = \frac{p}{p_s} - \frac{1}{p_s\left(\dfrac{1}{p - p_s RH_0} + \dfrac{Dkbp_s RT_r y\left(1 - RH_0\right)}{\delta p p_r \dot{V}_{g,s}}\right)} \qquad [20]$$

If equation 1 is used in combination with equation 18, the differential equation is:

$$\frac{dN_w(y)}{dy} = \frac{Dkbp_s\left(1 - RH_0\right)}{\delta} \qquad [21]$$

which has, with equation 11 and equation 14 for y = 0, the following explicit solution:

$$N_w(y) = N_{w,0} + \frac{Dkbp_s y}{\delta}\left(1 - \frac{N_{w,0} p}{p_s\left(N_{w,0} + \dfrac{p_r \dot{V}_{g,s}}{RT_r}\right)}\right) \qquad [22]$$

In the second case, it is assumed that the water flux through the membrane is much smaller than the gas flow rate ($N_w(y) << N_g$). With this condition equation 2 reduces to:

$$N_w(y) = \frac{p_s N_g RH(y)}{p} \qquad [23]$$

Combination of equation 23 with equation 1 and 9 leads to the differential equation:

$$\frac{p_s N_g}{p} \frac{dRH(y)}{dy} = \frac{Dkbp_s\left(1 - RH(y)\right)}{\delta} \qquad [24]$$

which in turn leads with equation 11 to the explicit solution:

$$RH(y) = 1 - \left(1 - RH_0\right)\exp\left(-\frac{DkbpRT_r y}{\delta p_r \dot{V}_{g,s}}\right) \qquad [25]$$

If equation 1 is used in combination with equation 23, the differential equation is:

$$\frac{dN_w(y)}{dy} = \frac{Dkbp_s}{\delta}\left(1 - \frac{pN_w(y)}{p_s N_g}\right) \qquad [26]$$

which has, with equation 11, the following explicit solution:

$$N_w(y) = \frac{p_s N_g}{p}\left(1 - \exp\left(-\frac{DkbpRT_r y}{\delta p_r \dot{V}_{g,s}}\right)\right) + N_{w,0}\exp\left(-\frac{DkbpRT_r y}{\delta p_r \dot{V}_{g,s}}\right) \qquad [27]$$

The accuracy of the different limiting equations is compared to the general case equations in figures 2 and 3. Figure 2 illustrates the three relative humidity equations (13, 20 and 25) for $y = l$. Clearly, both approximations match the general case at high gas flow rates where both approximations are expected to be accurate ($RH(y) = RH_0$, $N_w(y) << N_g$). All equations also have the correct limiting behavior ($RH(l) = 0$). At low gas flow rates equation 25 is more accurate than equation 20. Equations 13 and 25 also have the correct limiting behavior ($RH(l) = 1$). Figure 3 illustrates the three water flux equations (17, 22 and 27) for $y = 1$. Equation 22 is only valid at very large gas flow rates (uniform concentration gradient at every point along the membrane surface). Equation 27 matches well the general case equation 17 especially at low gas flow rates (both equations have the correct limiting behavior, $N_w(0) = 0$). However, at large gas flow rates, the error is significant. This is due to the different limiting values obtained from equations 17 and 27 at large gas flow rates.

On the basis of the comparisons made in figures 2 and 3, it can be argued that all relative humidity equations are preferable to fit experimental data at large gas flow rates whereas only two water flux equations are preferable at low gas flow rates (equations 17 and 27).

EXPERIMENTAL

Water diffusion rates through Nafion® membranes have previously been published (22-24). Data from Motupally *et al* (22) and Sridhar *et al* (24) are used to validate the model. Motupally *et al* data were obtained using an MEA based on a Nafion® N115 membrane (E-TEK carbon cloth, catalyst layers applied to the membrane, 50 cm^2 active area). Dry N_2 was used and circulated in a single channel (0.36 cm effective width, 136 cm long). Data from Sridhar *et al* were obtained using Nafion® membranes (N112, N115), dry H_2, 3.77 bara and various active areas (100 and 300 cm^2). It should be noted that not all data from Sridhar *et al* were used for model validation. For N115 membranes, the water flow rate shows a maximum instead of reaching a constant value. This may likely be attributed to heat transfer issues (gas residence time is either too short thus leading to a cooler gas flow than desired or gas flow is sufficient at large flow rates to cool the cell). For N112 membranes and a 300 cm^2 active area, the water flow rate does not reach a constant value at large gas flow rates. Full range model validation is therefore not possible. Only data related to N112 and a 100 cm^2 active area were used for model validation.

Equation 13 was used to curve fit experimental relative humidity data using SigmaPlot 5.0 (Marquardt-Levenberg method). Equation 13 only has one parameter pertaining mostly to membrane and cell characteristics ($a = DkblRT_r/\delta p_r$). Other terms are either known (operating conditions p, p_s and RH_0) or are measured ($RH(l)$). Equation 13 is preferred since an explicit relationship is required to perform the curve fitting procedure (equation 17 does not have an obvious explicit form). However, equation 13 presents a singularity at a relative humidity of 1 (the logarithmic term in the denominator) and consequently the relative humidity data ≥ 1 cannot be used for curve fitting. With the determined a values, equation 17 was generally used to generate model curves for the corresponding water flux data. Since equation 17 is implicit, MathCAD 7.0 was used to find water flux values for a range of gas flow rates (secant method). It should be noted that the MathCAD algorithm did not provide a solution at low gas flow rates and further work is required to find an alternate approach.

RESULTS AND DISCUSSION

Figure 4 shows that the simple relative humidity model correlates well with Motupally *et al* data (22) with a maximum difference between measured and predicted values of approximately 15 % at low gas flow rates. Figure 5 also shows good agreement between measured and predicted water flux values with a maximum difference of approximately 15 % at large gas flow rates. In this case, equation 27 was used to generate a model curve for high pressure data (for the reason given in the experimental section). The measured a value is 2.15 l/min bar. This value translates to a Dk/δ value of 3.20 x 10^{-3} mol/s cm^2 bar with bl = 50 cm^2 (R, T_r and p_r are known constants).

Motupally *et al* (22) also developed a simplified model to describe water diffusion in Nafion® membranes. There are two main differences between the model proposed by Motupally *et al* (22) and the model developed in this paper. The effect of water content on the water diffusion coefficient was taken into account. Also, the equilibrium relationship between water concentration in the gas stream and the membrane is not linear. With these assumptions, a single analytical equation describing the water flux was not proposed but model accuracy is claimed to be < 5 %. The relatively small error difference between both models indicates that water diffusion within Nafion® can satisfactorily be treated by ignoring or simplifying the effect of membrane water content on some membrane properties.

Figure 6 shows that the simple relative humidity model also correlates well with Sridhar *et al* data (24) with a maximum difference between measured and predicted values of < 20 % at low gas flow rates. Figure 7 also shows good agreement between measured and predicted water flux values with a maximum difference of < 25 % at intermediate gas flow rates. The measured a values are respectively 6.716 and 4.537 l/min bar at respectively 50 and 60 °C. These values translate to Dk/δ values of 5.00 x 10^{-3} and 3.37 x 10^{-3} mol/s cm^2 bar at respectively 50 and 60 °C with bl = 100 cm^2.

Table I compares experimental Dk/δ values with those derived from other sources. The value of k in equation 8 is obtained by first computing the maximum membrane water concentration. Membrane water content data are available for Nafion® (25-28) and were recently rationalized by Futerko and Hsing (29). Membrane water content is dependent on the water state outside the polymer (vapor or liquid). The maximum membrane water content $\bar{\lambda}$ is assumed to be an average computed using the minimum (water vapor, 100 % relative humidity) and maximum membrane water content (liquid water, membrane in normal form) as modeled by Futerko and Hsing (29). The membrane water concentration on a dry polymer basis is defined as (5, 12):

$$c_w = \frac{\lambda \rho}{M} \qquad [28]$$

The membrane density is determined by using West and Fuller's expression (11), which depends on membrane water content. As a result, membrane expansion is also taken into account:

$$\rho = \frac{1.98 + 0.0324\lambda}{1 + 0.0648\lambda} \qquad [29]$$

Insertion of equations 28 and 29 with $\lambda = \bar{\lambda}$ into equation 8 leads to an expression for k:

$$k = \frac{\bar{\lambda}}{p_s M}\left(\frac{1.98 + 0.0324\bar{\lambda}}{1 + 0.0648\bar{\lambda}}\right) \qquad [30]$$

Values for the water diffusion coefficient in Nafion® are available (3-4, 11-12). Motupally *et al* (22) have determined that the following expressions are the most accurate:

$$D = 0.0031\lambda(\exp(0.28\lambda) - 1)\exp\left(\frac{-2436}{T}\right) \text{ (for } 0 < \lambda \leq 3) \qquad [31]$$

$$D = 0.000417(1 + 161\exp(-\lambda))\exp\left(\frac{-2436}{T}\right) \text{ (for } 3 \leq \lambda < 17) \qquad [32]$$

However, equation 32 yields water diffusion coefficient values, which are inconsistent with Motupally *et al* (22) simulations (see their equation 12 and figure 2). For this reason, West and Fuller's expression is used instead (11):

$$D = 0.0025\lambda\exp\left(\frac{-2436}{T}\right) \qquad [33]$$

Since the membrane water content is a function of position in the present model and that the water diffusion coefficient is also expected to vary with position, an average value is computed using equation 33, replacing λ by $\bar{\lambda}$ ($\lambda_{\min} = 0$ due to the dry inlet gas):

$$D = \frac{\exp\left(\frac{-2436}{T}\right)}{\lambda_{\max}}\left(\int_0^{\lambda_{\max}} 0.0025\bar{\lambda}\, d\bar{\lambda}\right) \qquad [34]$$

The dry membrane thickness was used as a first approximation since its actual value is dependent on water content and consequently on position. The resulting values of D, k based on equations 30 and 34 as well as δ appear in table I and are used to compute the estimated value of Dk/δ. It is clear that there is a difference between measured and predicted Dk/δ values ranging from a factor of 16 to 54. The reason for such a discrepancy is not readily obvious but could include the averaging procedure for the water diffusion coefficient, which could underestimate its value.

CONCLUSION

A simple model for water diffusion within Nafion® membranes was derived which leads to analytical expressions for both gas stream relative humidity and water flux. Agreement between general analytical expressions and experimental data is within 20 % for a range of gas flow rates and pressures. Other effects need to be investigated to confirm the model's adequacy such as temperature, inlet gas relative humidity and contact area size. However, the model cannot be used for predictive purposes without calibration since a discrepancy still exist between independently measured membrane properties and those resulting from model equation fit to experimental data.

NOMENCLATURE

a	Parameter (l/min bar)
b	Gas compartment channel width (cm)
c_w	Membrane water concentration (mol/cm^3)
D	Membrane water diffusion coefficient (cm^2/s)
k	Proportionality constant between channel water concentration and membrane surface water concentration (mol/cm^3 bar)
l	Gas compartment channel length (cm)
M	Membrane molecular weight (g/mol)
N_g	Molar gas flow rate (mol/min)
N_w	Molar water flow rate in the gas compartment channel (mol/s cm^2)
$N_{w,z}$	Molar water flow rate through the membrane (mol/s cm^2)
$N_{w,0}$	Inlet molar water flow rate in the gas compartment channel (mol/s cm^2)
p	Pressure (bar)
p_r	Reference pressure (1 bara)
p_s	Water vapor saturation pressure (bar)
R	Gas constant (0.08315 J/mol K)
RH	Relative humidity in the gas compartment channel
RH_0	Inlet relative humidity in the gas compartment channel
T	Temperature (K)
T_r	Reference temperature (273 K)
$\dot{V}_{g,s}$	Volumetric gas flow rate at standard conditions (l/min)
y	Coordinate along the gas compartment channel (cm)
z	Coordinate along the membrane thickness (cm)
δ	Membrane thickness (cm)

λ	Membrane water content (mol water/mol sulfonate site)
$\bar{\lambda}$	Average membrane water content (mol water/mol sulfonate site)
λ_{max}	Maximum membrane water content (mol water/mol sulfonate site)
λ_{min}	Minimum membrane water content (mol water/mol sulfonate site)
ρ	Membrane density (g/cm^3)

REFERENCES

1. J. St-Pierre, D. P. Wilkinson, H. Voss, R. Pow, in *Proceedings of the Second International Symposium on New Materials for Fuel Cell and Modern Battery Systems II*, O. Savadogo and P. Roberge Editors, p. 318, École Polytechnique, Montréal (1997).
2. J. St-Pierre, D. P. Wilkinson, S. Knights, M. L. Bos, *J. New Mat. Electrochem. Systems*, **3**, 99 (2000).
3. T. E. Springer, T. A. Zawodzinski, S. Gottesfeld, *J. Electrochem. Soc.*, **138**, 2334 (1991).
4. H. P. L. H. van Bussel, F. G. H. Koene, R. K. A. M. Mallant, *J. Power Sources*, **71**, 218 (1998).
5. S. Dutta, S. Shimpalee, J. W. van Zee, *J. Appl. Electrochem.*, **30**, 135 (2000).
6. D. R. Sena, E. A. Ticianelli, V. A. Paganin, E. R. Gonzalez, *J. Electroanal. Chem.*, **477**, 164 (1999).
7. P. Futerko, I-Ming Hsing, *Electrochim. Acta*, **45**, 1741 (2000).
8. T. Okada, G. Xie, Y. Tanabe, *J. Electroanal. Chem.*, **413**, 49 (1996).
9. T. Okada, G. Xie, M. Meeg, *Electrochim. Acta*, **43**, 2141 (1998).
10. M. Eikerling, Y. I. Kharkats, A. A. Kornyshev, Y. M. Volfkovich, *J. Electrochem. Soc.*, **145**, 2684 (1998).
11. A. C. West, T. F. Fuller, *J. Appl. Electrochem.*, **26**, 557 (1996).
12. T. V. Nguyen, R. E. White, *J. Electrochem. Soc.*, **140**, 2178 (1993).
13. T. F. Fuller, J. Newman, *J. Electrochem. Soc.*, **140**, 1218 (1993).
14. J. S. Yi, T. V. Nguyen, *J. Electrochem. Soc.*, **145**, 1149 (1998).
15. G. Maggio, V. Recupero, L. Pino, *J. Power Sources*, **101**, 275 (2001).
16. G. Murgia, L. Pisani, M. Valentini, B. D'Aguanno, *J. Electrochem. Soc.*, **149**, A31 (2002).
17. D. Natarajan, T. V. Nguyen, *J. Electrochem. Soc.*, **148**, A1324 (2001).
18. S. Dutta, S. Shimpalee, J. W. Van Zee, *Int. J. Heat Mass Transfer*, **44**, 2029 (2001).
19. J.-T. Wang, R. F. Savinell, *Electrochim. Acta*, **37**, 2737 (1992).
20. D. M. Bernardi, M. W. Verbrugge, *AIChE J.*, **37**, 1151 (1991).
21. A. Rowe, X. Li, *J. Power Sources*, **102**, 82 (2001).
22. S. Motupally, A. J. Becker, J. W. Weidner, *J. Electrochem. Soc.*, **147**, 3171 (2000).
23. K. H. Choi, D. J. Park, Y. W. Rho, Y. T. Kho, T. H. Lee, *J. Power Sources*, **74**, 146 (1998).
24. P. Sridhar, R. Perumal, N. Rajalakshmi, M. Raja, K. S. Dhathathreyan, *J. Power Sources*, **101**, 72 (2001).
25. J. T. Hinatsu, M. Mizuhata, H. Takenaka, *J. Electrochem. Soc.*, **141**, 1493 (1994).
26. M. Laporta, M. Pegoraro, L. Zanderighi, *Phys. Chem. Chem. Phys.*, **1**, 4619 (1999).
27. K. Broka, P. Ekdunge, *J. Appl. Electrochem.*, **27**, 117 (1997).
28. T. A. Zawodzinski, C. Derouin, S. Radzinski, R. J. Sherman, V. T. Smith, T. E. Springer, S. Gottesfeld, *J. Electrochem. Soc.*, **140**, 1041 (1993).

29. P. Futerko, I-Ming Hsing, *J. Electrochem. Soc.*, **146**, 2049 (1999).

Table I. Summary of membrane characteristics and properties, and experimental conditions

Reference	22	24	24
Temperature (°C)	80	50	60
p_s (bar)	0.467	0.122	0.197
bl (cm^2)	50	100	100
Membrane	Nafion® N115	Nafion® N112	Nafion® N112
D (cm^2/s)	1.98×10^{-5}	9.68×10^{-6}	1.25×10^{-5}
λ_{min} (water vapor, 100 % relative humidity)	11.0	12.9	12.3
λ_{max} (liquid water, normal form)	20.3	16.2	17.6
$\bar{\lambda}$	15.7	14.6	15
k (mol/cm^3 bar)	0.0377	0.137	0.0866
δ (cm)	0.0127	0.00508	0.00508
Measured Dk/δ (mol/s cm^2 bar)	0.0032	0.005	0.00337
Estimated Dk/δ (mol/s cm^2 bar)	5.88×10^{-5}	2.61×10^{-4}	2.13×10^{-4}

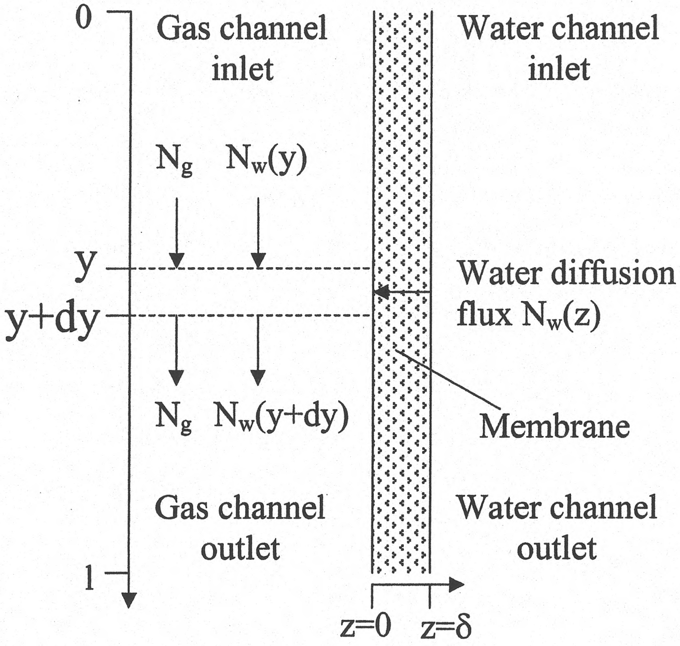

Figure 1. Schematic representation of the modeled water diffusion cell

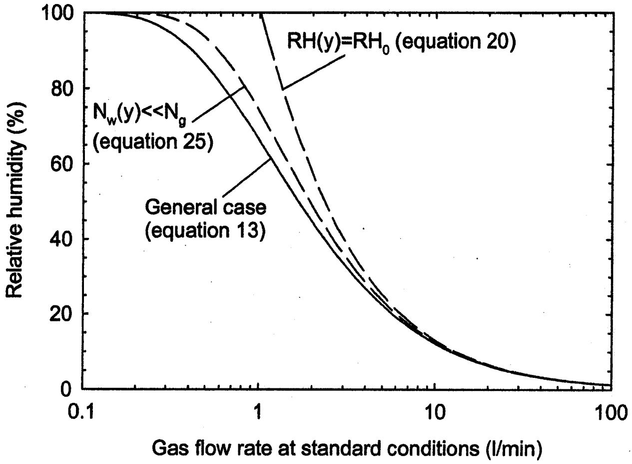

Figure 2. Comparison between the general relative humidity equation and two approximations

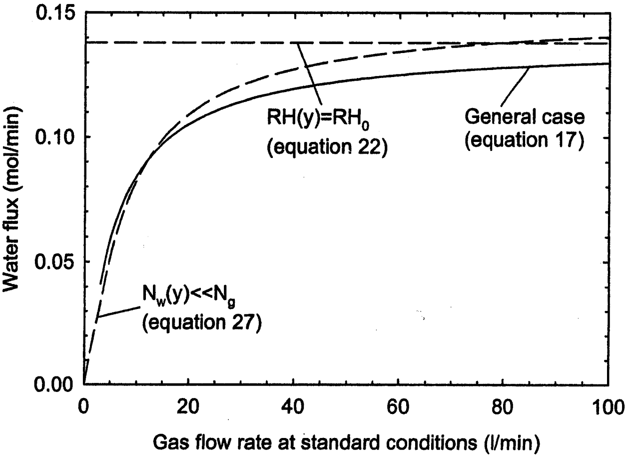

Figure 3. Comparison between the general water flux equation and two approximations

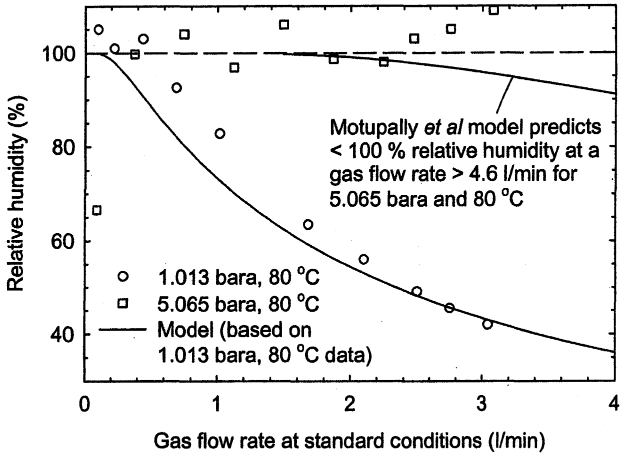

Figure 4. Comparison between the simple water diffusion model (relative humidity) and Motupally *et al* data

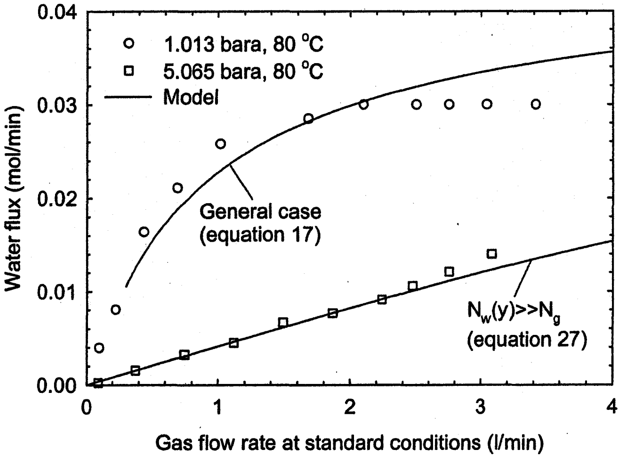

Figure 5. Comparison between the simple water diffusion model (water flux) and Motupally *et al* data

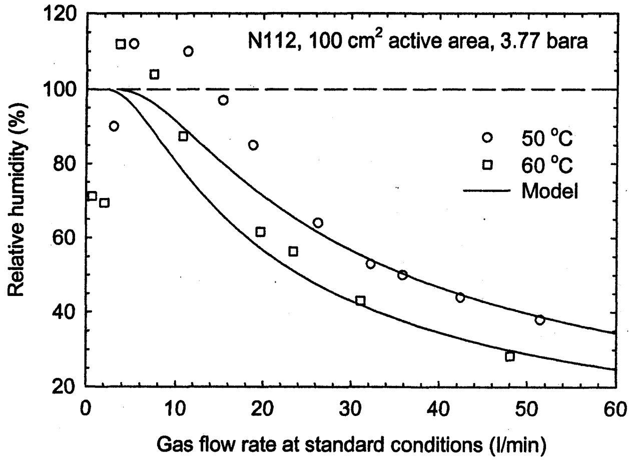

Figure 6. Comparison between the simple water diffusion model (relative humidity) and Sridhar *et al* data

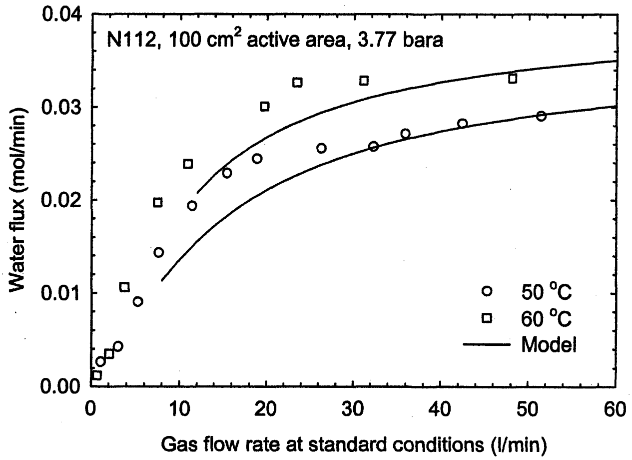

Figure 7. Comparison between the simple water diffusion model (water flux) and Sridhar *et al* data

Proceedings of The Electrochemical Society, PV 2002-31, 388-399 (2002)
DOI: 10.1149/200231.0388PV © The Electrochemical Society

A New Proton Conductive Membrane - Tungsten Peroxo Complex Doped Sol-Gel Organic/Inorganic Nanocomposite Polymer

Hitoshi NAKAJIMA and Itaru HONMA

National Institute of Advanced Industrial Science and Technology
Umezono 1-1-1, Tsukuba, Ibaraki, Japan 305-8568

ABSTRACT

New family of proton conducting organic/inorganic hybrid polymer electrolyte membrane was prepared by sol-gel processes. The method involves the stabilization of metastable acidic tungsten oxide cluster in the polymer composite membrane.

A free-standing, flexible and pale-yellowish transparent homogeneous membrane was formed from tungsten acidic homogeneous solution by sol-gel condensation with alkoxysilylated polyethylene oxide. The membrane showed very high protonic conductivity of 10^{-2}~10^{-3} S cm^{-1} from R. T. to 120°C, especially, 1.4 x 10^{-2} S cm^{-1} at 80°C under 100% R. H. The structure of tungsten cluster moieties was neither peroxo complex nor $WO_3.2H_2O$, shown by infrared red and powder X-ray spectra. It is suggested that nano-size clusters are dispersed homogeneously in polymer matrix without long-range ordering. Tungsten complexes with carboxylate ligands such as malonic acid could form similar homogeneous membrane. Thermal and ionic transport properties could be controlled by these families of organic derivatives.

INTRODUCTION

Protonic conductive membrane is very important elements for polymer electrolyte fuel cells, while it is also applicable for proton sensor, separation, acidic catalyst, and so on. Recently, incorporation of inorganic solid acids in organic polymer has been attempted for ionic conductive materials [1-4].

For example, hydrated acidic oxides, such as $WO_3.2H_2O$ and $Sb_2O_5.nH_2O$, are well known for high protonic conductive inorganic oxides. However, as these kinds of oxides have little solubility for water or organic solvents, homogeneous mixture into organic polymer is difficult, and the preparation of homogeneous membrane becomes also difficult.

A 12 phosphotungstic acid is known as a solid oxide cluster which has both high protonic conductivity and high solubility for water and alcohol, and many of groups used as doping inorganic solid acids. However, not so many of these kinds of crystals are obtained in protonic form until now. Many solid acid complex or oxide cluster are crystallized only in alkali-metal or (alkyl) ammonium salt and not crystallized in protonic form because of its charge balance, ionic radius, and so on, so that they are stable only in the solution.

In this work, we investigated the preparation of solid protonic conductive membrane by stabilizing metastable inorganic acidic clusters in the polymer membrane and investigated organic/inorganic hybrid structure and protonic conductivities of temperature range from R. T. to 160°C, which potentially provides more efficient high-temperature operation of PEM fuel cells.

EXPERIMENTAL SECTION

Tungstic acid (1 g) was dissolved in 30 wt % hydrogen peroxide (2 g) at 40°C. After 2 h, hydrogen peroxide was decomposed by Pt net (Pt black was supported) and this solution was filtered (**A**). Then 30 wt % hydrogen peroxide was added again to adjust the concentration of hydrogen peroxide to 5 wt %, and pale yellow clear solution was obtained (**B**). The whole species in this solution were not completely identified, though one of species was tungsten peroxo complex, $[W_2O_3(O_2)_4(H_2O)_2]^{2-}$, estimated by ^{183}W NMR [5]. For example, this cluster was crystallized only as Na salt and not obtained by H form crystal until now.

Tungstic acidic complex solution with carboxylate ligands was also prepared as follows: Oxalic acid dihydrate was dissolved in solution (**A**). Tungsten oxalate chelate complex was suggested to be formed in this solution by Raman spectroscopy [6]. Malonic acid, dimethylmalonic acid, and citric acid were also used to prepare chelate ligand metal complex.

Polyethylene oxide (PEO) or polytetramethylene oxide (PTMO) are able to be crosslinked with alkoxysilanes through isocyanato coupling (Scheme 1). These precursors, hereafter designated as "hybrid precursors", hydrolyze and condense to form macromolecules of flexible, glassy hybrid materials.

In this study, 3 g of "hybrid precursors" were dissolved in 10 ml of methanol. Solution (**B**) was added dropwise with ice-cooled bath. Adequate mount of water was added to the solution and casted into a polystyrene substrate and annealed at 60°C for 18-36 hours.

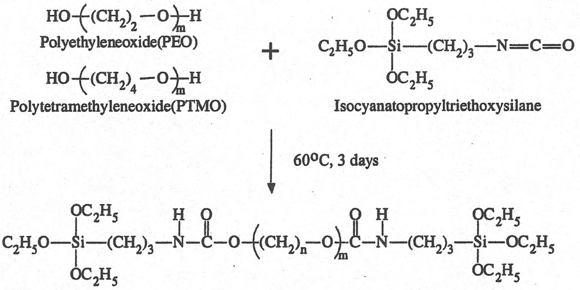

Scheme 1. Reaction Scheme of Alkoxysillylation of PEO or PTMO

Proton conductivity of these membranes was evaluated by the a.c. impedance method between 1 Hz and 1 MHz using an impedance analyzer (Solartron SI-1260 and Solartron SI-1287) in a stainless pressure resistant vessel from R. T. to 160°C. Water was previously introduced in the vessel and measurement was operated always under equilibrium water pressure at desired temperature.

RESULTS AND DISCUSSION

Conductivity of membrane from tungsten acidic homogeneous solution.

Fig. 1. Picture of Membrane.
(a) Homogeneous complex, (b) $WO_3.2H_2O$ direct addition.

First, we prepared membrane as following conditions: PEO600 was used as hybrid polymer, molar ratio of [W] / [PEO] = 0.25 and $[H_2O]$ / [PEO] = 2.6 x 10^2. Homogeneous organic/inorganic hybrid membranes of a free-standing, flexible and pale-yellowish transparent membrane (**1**) was formed from tungsten acidic homogeneous solution (**B**). Thickness of membrane was c.a. 0.3 mm. On the other hand, for comparison, the membrane prepared from the precursor $WO_3.2H_2O$ was directly added into methanol solution of hybrid precursor (**2**) was heterogeneous and not transparent.

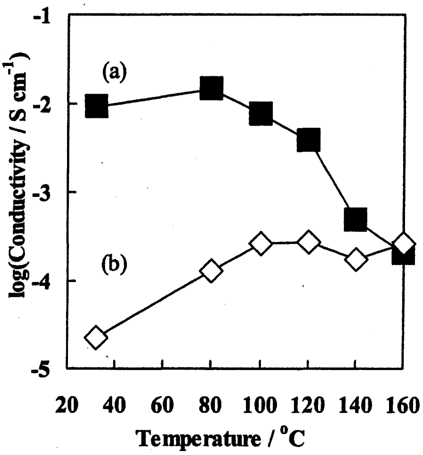

Fig. 2. Conductivity of membranes (R. H. =100%).
(a) prepared from tungsten homogeneous solution (**1**),
(b) prepared from $WO_3.2H_2O$ powder (**2**).

Conductivity of (**1**) and (**2**) from R. T. to 160°C were shown in Fig. 2. The hybrid membrane (**1**) showed very high protonic conductivity of 10^{-2}~10^{-3} S cm^{-1} from R. T. to 120°C, especially, 1.4 x 10^{-2} S cm^{-1} at 80°C. On the other hand, (**2**) did not show a conductivity excess of 10^{-3} S cm^{-1}. It was shown that the tungstic acidic cluster has been stabilized in the polymer matrix and the resulting membrane has good protonic conductivity, even 140°C, it has 10^{-4} S cm^{-1} conductivity. D. c. conductivity of (**1**) was under 10^{-4} S cm^{-1} from R. T. to 140°C (Fig. 3), indicating ionic transport number of (**1**) was more than 10^2 in this temperature region.

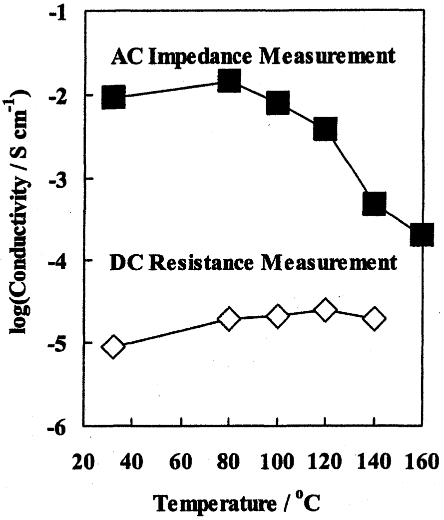

Fig. 3. AC / DC conductivity measurement of (1).

Structure of tungsten acidic clusters in membrane.

The infrared red spectra of (1) and (2) were shown in Fig. 4. The bands at 586, 816 and 976 cm^{-1} were observed only in (1) and not observed in the other membrane. These 3 bands are not assigned to polymer or silica matrix. The bands at 586 and 816 cm^{-1} are assigned to ν (W-O-W) due to corner-sharing WO_6 units and those at 976 cm^{-1} are assigned to ν (W=O) [7]. No band except weak bands due to polymer or silica matrix was observed in the region from 870 cm^{-1} to 900 cm^{-1}. Bands assigned to ν (O-O) due to peroxo group coordinated to metal and to ν (W-O-W) due to edge-sharing WO_6 units both to be strongly appeared in this wavenumber region. Peroxo complexes, formed in solution (**B**) as mentioned above, were transformed to non-peroxo tungsten cluster moieties during the synthesis process. The WO_6 octahedral units in these tungsten cluster moieties were not bonded by edge-shared but by corner-shared. Nevertheless, $WO_3.2H_2O$, known by corner-shared protonic tungsten oxide, showed IR bands at 1007, 945, 918 and 700 cm^{-1}, different from those of (1), indicating that these tungsten clustermoieties were not $WO_3.2H_2O$. In addition, the bands at 586, 816 and 976 cm^{-1} were sharp, suggesting that these clusters were molecularitic nano-size clusters rather than crystal.

The powder XRD pattern for (1) and (2) were shown in Fig. 5. No crystal signals were observed in (1), suggesting those tungsten cluster moieties was fixed in polymer matrix without long-range ordering.

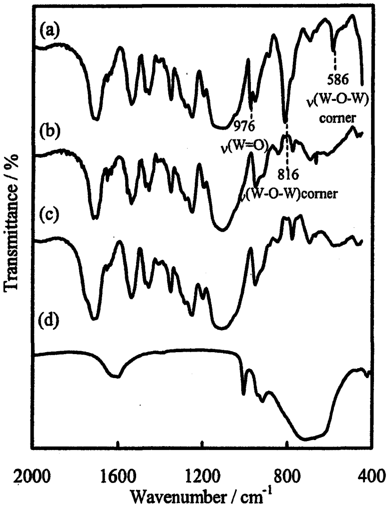

Fig. 4. IR spectra of (a) membrane prepared from tungsten homogeneous complex (1), (b) membrane prepared from $WO_3.2H_2O$ powder (2), (c) membrane without tungsten species, and (d) $WO_3.2H_2O$ powder.

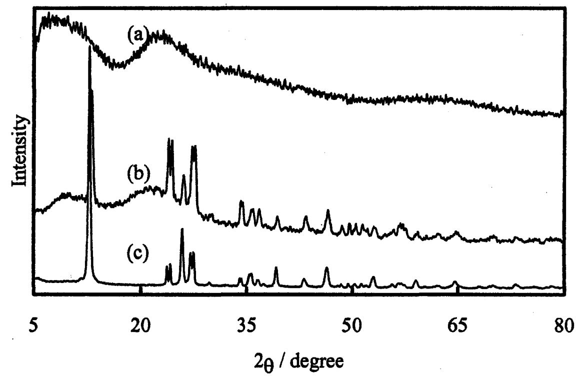

Fig. 5. XRD spectra of (a) membrane prepared from tungsten homogeneous complex (1), (b) membrane prepared from $WO_3.2H_2O$ powder (2), and (c) $WO_3.2H_2O$ powder.

Effect of polymer matrix.

Next, effects of polymer structure have been studied. To control inorganic/organic ratio and hydrophilicity of membrane, PEO200 and PTMO650 were used instead of PEO600.

In the case of PTMO650 and $[H_2O] / [PTMO] = 2.6 \times 10^2$, membrane was not formed properly and became white powderlike. PTMO was more hydrophobic than PEO; therefore, higher content of water prevented sol-gel polymerization and formation of membrane. In the case of PTMO650 and $[H_2O] / [PTMO] = 1.9 \times 10^1$, membrane (3) was successfully formed. In the case of PEO200, obtained membrane was harder than that of PEO600 due to higher ratio of inorganic components (4). Conductivity of (3) and (4) were shown in Fig. 6. Conductivity of (4) was lower than that of (1), probably the high-density and hardness of (4) prevented the formation of protonic conductive channel. Conductivity of (3) was lower than that of (4), probably due to a lower water uptake into membrane.

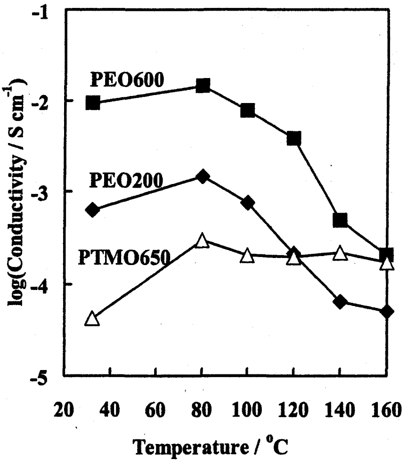

Fig. 6. Effect of polymer matrix on conductivity of membranes.

Effect of carboxylato ligands.

Next, we attempted some improvement of the membrane by producing organic derivatives of the tungsten acidic clusters and choosing the combination of polymer to acidic clusters. The thermal stability of the clusters was suggested to be improved by organic derivatives such as carboxylato ligands [8]. So, in the present study, we have checked the cluster stability and conductivity by systematic variation among carboxylic acid, oxalic acid, malonic acid, and so on.

First, five-member ring carboxylic ligands were chosen. All ligands could form transparent, homogeneous and flexible membrane in the case of [ligand] / [W] <= 1. The result of conductivity is shown in Fig. 7. Citric acid sample showed higher conductivity more than 140 °C.

Second, six-member ring carboxylic ligands were chosen. Also in this case, all ligands could form transparent, homogeneous and flexible membrane in the case of [ligand] / [W] <= 1, especially, in the case of malonic acid and dimethylmalonic acid, [ligand] / [W] <= 4. The result of conductivity is shown in Fig. 8. Malonic acid sample showed higher conductivity than the other, suggesting these kinds of ligand were effective for protonic conduction. Significant correlation between the structure of ligands and the conductivity of resulting membrane was not observed.

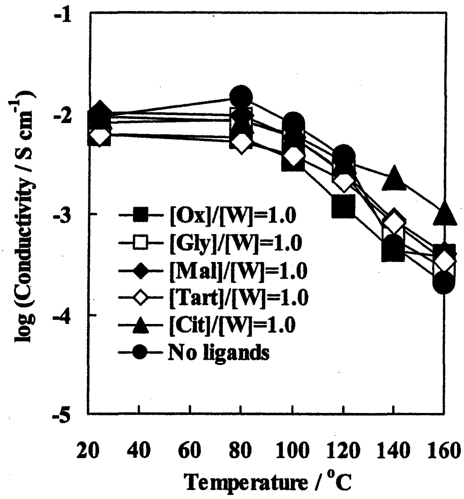

Fig. 7. Effect of the kind of Five-members ring carboxylic ligand.

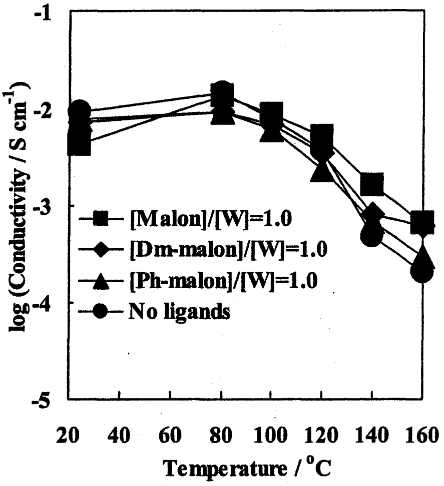

Fig. 8. Effect of the kind of Six-members ring carboxylic ligand.

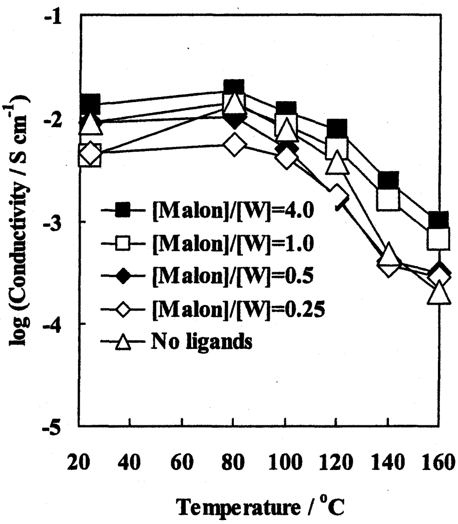

Fig. 9. Effect of [Malon] / [W].

The dependence of conductivity on the ratio of malonic acid to tungsten was examined. In the case of malonic acid to tungsten was less than or equal to 0.5, no significant increase of conductivity was observed. However, in the case of malonic acid to tungsten was 1, the conductivity at 140°C was about three times higher than that of the sample without ligands (Fig. 9), indicating that the effects of malonic acid to the conductivity in higher temperature range. The sample of malonic acid to tungsten was 4 showed a maximum conductivity at experimental temperature range.

The XRD pattern of these membrane showed that all samples can be assigned to the amorphous phase (Fig. 10). It indicates that even malonic acid to tungsten is 4, neither tungsten trioxide nor malonic acid are crystallized in the membrane.

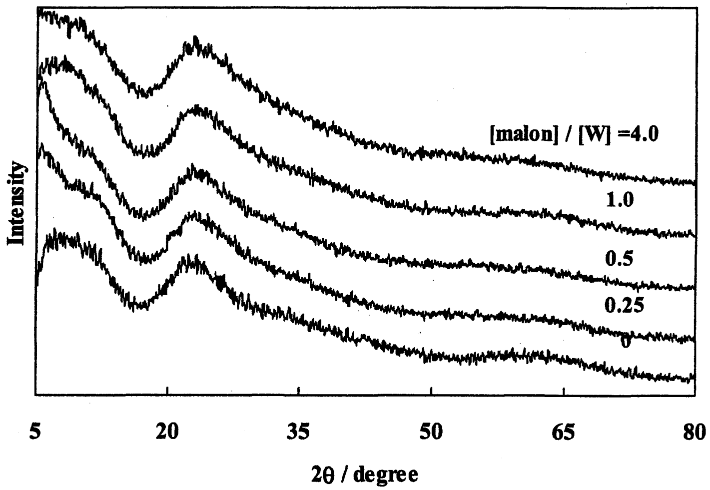

Fig. 10. XRD pattern of the membrane contained malonic ligand.

IR spectra of these membranes were shown in Fig. 11. In the case of malonic acid to tungsten was less than or equal to 0.5, the spectra were similar to that of the sample without malonic acid suggesting the release of malonic acid. In the case of malonic acid to tungsten was more than or equal to 1, the bands around 641, 913 and 1730 cm^{-1}, assigned to malonic acid were observed, indicating that malonic acid was incorporated in the membrane.

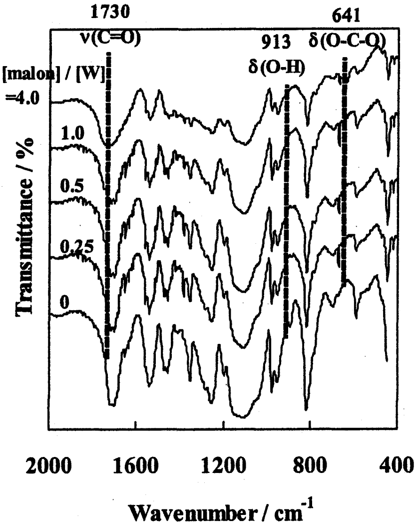

Fig. 11. IR spectra of membrane with malonic ligands.

CONCLUSION

A free-standing, flexible and pale-yellowish transparent membrane was formed from tungsten acidic homogeneous solution. The membrane showed very high protonic conductivity of 10^{-2}~10^{-3} S cm^{-1} from R. T. to 120°C, especially, 1.4 x 10^{-2} S cm^{-1} at 80°C. The structure of tungsten cluster moieties was neither peroxo complex nor $WO_3.2H_2O$. It is suggested that nano-size clusters are dispersed homogeneously in polymer matrix without long-range ordering. Thermal and ionic transport properties could be controlled by organic derivatives, such as malonic acid, to clusters.

REFERENCES

[1] S. Malhotra *et al.*, *J. Electrochem. Soc.* **144**, L23 (1997).
[2] J. M. Amarilla *et al.*, *Solid State Ionics* **127**, 133 (2000).
[3] N. Groselj *et al.*, *Solid State Ionics* **125**, 125 (1999).

[4] H. Nakajima *et al.*, *Chem. Lett.* 693 (1997).
[5] H. Nakajima *et al.*, *Chem. Mater.* **11**, 691 (1999).
[6] M. F. Daniel *et al.*, *J. Solid State Chem.* **67**, 235 (1987).
[7] I. Honma *et al.*, *J. Membrane science*, **185**, 83 (2001).
[8] M. Hibino *et al.*, *Solid State Ionics* **100**, 211 (1997).

Proceedings of The Electrochemical Society, PV 2002-31, 400-415 (2002)
DOI: 10.1149/200231.0400PV © The Electrochemical Society

Proton Transport Characteristics for Selected PEM's, Designed for Elevated Temperature Operation: Effect of Relative Humidity

Chengsong Ma, Lei Zhang and Sanjeev Mukerjee*
Department of Chemistry, Northeastern University
360 Huntington Avenue, Boston, MA 02115

David Ofer and Bindu Nair
Foster Miller Inc., 195 Bear Hill Road, Waltham, MA 02451

ABSTRACT

The proton conductivity of several new alternative proton exchange membranes *i.e* SPES-40 (a sulfonated poly arylene ether sulfone), SPSS-40 (sulfonated poly sulfide sulfone) and SPES-PS (a polyether sulfone post sulfonated) were studied using a four-probe ac-impedance method as a function of temperature and relative humidity (RH). Further, proton conductivity was also investigated for the same ionomers in the form of micro-aggregates such as those typically encountered in the reaction layer (the interfacial layer of the electrode containing the catalyst). For this a new configuration of the conventional reaction layer in a membrane electrode assembly (MEA) was used, which enabled the isolation of proton conductivity to be the principle contributor to the ac impedance. Conductivity of all membranes showed strong dependence on temperature and RH. The results under 100% relative humidity, showed that SPES-40 has similar proton conductivity as Nafion in the membrane within the range our experimental conditions. The values for the other membranes investigated were lower. Conductivity values increase with the increase of temperature and RH for all membranes investigated. However at lower relative humidity, all of the alternative membranes have lower conductivity performance comparing to Nafion 117. Attempts to correlate these observed differences with parameters such as EW (equivalent weight), λ, acidity (pK_a) etc., showed that the prime contributor was the difference in microstructure of the membranes. Activation energy for proton conduction in these different polymer membranes based on Arrhenius plots showed similar values. Conductivity of these polymeric ionomers when present as micro-aggregates in the reaction layer showed very different values as compared to the bulk membranes. There was a great divergence in conduction as a function of increase in temperature with Nafion® showed a far greater rate of increase of conductivity than SPES-50 and SPES-PS. Blends of these ionomers with Nafion showed intermediate values, albeit lower with characteristics closer to Nafion.

INTRODUCTION

Proton exchange membrane fuel cells (PEMFCs) are one of the most promising emerging power technologies in transportation and portable consumer applications. Central to this

---

* Person to whom correspondence should be addressed. Email: smukerje@lynx.neu.edu

technology are the proton exchange polymer membrane, the current state of the art for which is based on perfluorinated sulfonic acid chemistry, such as those from Dupont (Nafion®), Asahi Chemicals (Aciplex®) and others. These membranes possess very desirable properties such as good mechanical strength, chemical stability, and high conductivity [1]. However, these membranes remain expensive and have several limiting factors such as low conductivity at low relative humidity[2], high methanol permeability[3,4] and a low T_g (glass transition temperature)[5] which restricts its application to below 100°C.

Transitioning to temperatures above 100°C does provide for several attractive options which include higher CO tolerance[6,7] and heat management. Enabling elevated temperature proton conduction in a PEM fuel cell has to be examined in the context of either hydrated or non-hydrated membrane material. Recently, the use of non-volatile solvents as replacement for water have been attempted such as in the case of phosphoric acid, polybenzimidazole, butyl methyl imidazolium triflate, butyl methyl imidazolium tetrafluoroborate etc.,[8-12]. For proton conduction using hydrated membranes, there is an active interest in examining the role of additives to prevent the loss of water from ionic regions (pores) in the membrane. In this context, several hydrophilic inorganic gel materials such as SiO_2, $Zr(HPO_4)_2$, heteropolyacids etc., have been incorporated into conventional perfluorinated membranes such as Nafion®[13-19]. Alternative hydrated membranes to the perfluorinated sulfonic acid based systems (such as Nafion®) possessing high proton conductivity at lower relative humidity and stability at elevated temperatures are currently the focus of a lot of research and development. Most of these polymer systems are based on engineering polymers with high thermochemical stability[20], typically with a high degree of aromatic character, where the monomer consists of a variety of fused phenyl rings linked together with a number of bridging moieties [hereafter referred to as membranes with aromatic backbone]. There are however lingering concerns about their resistance to auto-oxidation in the fuel cell[21]. Several families of polymers have been developed in this context, these include poly ether (ether) ketone (PEEK)[22,23], polyether sulfone (PES)[24-26], poly sulfide sulfone (PSS)[27,28], poly phenyl quinoxaline (PPQ)[29], aryl oxyphosphazene (AOP)[30].

Proton conduction in polymer electrolyte membranes is an intimate function of equivalent weight (EW), water content (relative humidity, RH), crystallinity (cluster structure involving hydrophilic and hydrophobic components). Proton conduction in perfluorinated[31] and partially fluorinated membranes[31,32], with aliphatic chain backbone [hereafter referred to as aliphatic chain membranes] have been extensively studied in the context of all the above mentioned parameters. Prior studies[31] have included the BAM® (sulfonated *αββ* trifluorostyrene-*αββ* trifluorostyrene copolymers), DAIS® (sulfonated styrene-(ethylene butylenes)-styrene triblock copolymers) and ethylene-tetrafluoro-ethylene-*g*-polystyrene sulfonic acid (ETFE-*g*-PSSA) membranes. More recently, proton conduction has also been studied for the membranes based on a high degree of aromatic character[29]. This study[29] included sulfonated polyether (ether) ketone (SPEEK), a polyether sulfone (SPES) and polyphenyquinoxalene (SPPQ). It is well known that the transport of protons and associated water molecules is strongly dependent on the microstructure and acidity. A cluster network as proposed earlier by Gierke[33] for Nafion® involves the formation of inverted micelles (~ 50Å) comprising of solvent and ion exchange sites separate from the polymer backbone and connected by narrow channels (~10 Å). Prior report by Gavach *et al.*[34] have shown 6 water molecules are considered to form the primary hydration shell of the SO_3H group. Lower water content leads to narrowing of the channels and hence a hindrance to proton conduction. In a comparison of fluorinated and partially fluorinated aliphatic polymer backbone membranes[31] the complexities of correlating conductivity with water content has been pointed out. The cross influence of acid concentration and different elasticity of the aliphatic polymer backbone provides for very different proton conductivity, when comparing within the same range of EW and λ. These differences are also evident from the comparison of conductivity of Nafion® membrane with some membranes with aromatic based backbone[29]. In this comparison[29], it is evident that besides the influence of EW, λ and the tertiary structure of the membrane (nature of cluster formation), there are additional effect due to pK_a.

Besides the membrane, the membrane electrode assembly forms an important determinant to fuel cell performance especially in avoiding high interfacial resistance and onset of mass transport limited behavior at lower current densities[36]. The charge transfer interface with the membrane is called the 'reaction layer'. It is typically a thin layer of catalyst and ionomer (typically a solubilized form of the electrolyte membrane) with or without a binder such as Teflon, deposited on top of the teflonized carbon layer. This reaction layer therefore extends the charge transfer interface from the membrane surface deeper into the electrode structure in order to increase the interfacial area available to carry out the desired reactions. Drying out this reaction layer would negate any advantage of choosing a better-elevated temperature proton conductor. The reaction layer typically has a different ionomer structure from that of the membrane. Ionomer in the reaction layer is deposited from aggregates in solution. The size and morphology of these aggregates therefore determine the nature of the tertiary cluster structure of the hydrophilic and hydrophobic domains. Examining proton conduction in reaction layers is therefore an important component of enabling alternative membranes for elevated temperature PEM operation.

The performance of PEM fuel cell is strongly dependent of humidification of the membrane. Water content inside membrane electrolyte changes at different relative humidity, which cause conductivity of membrane changes drastically. Operation of PEM fuel cell at elevated temperature (above 100C) will result in dehydration of membrane, which in turn make Ohmic resistance increase. And high proton conductivity in the membrane electrolyte is the key for getting high power density of fuel cell. So analysis of performance of PEM fuel cell at elevated temperature needs accurate conductivity data for proton exchange membrane at different relative humidity in combination of water uptake. Proton conductivity of Nafion 117 was measured by Y.Sone et al[37] under various conditions of humidity and temperature using ac impedance method. They found at a given relative humidity conductivity decrease with increasing temperature from 21 to 45°C and while from 45 to 80°C it increased with temperature. A.V. Anantaraman [38]also studied the effect of humidity on the conductivity of Nafion using coaxial probe method. Studies on a new alternative membrane-bis[(perfluoroalkyl)sulfonyl]imide was performed by D.DesMarteau et al[2] under variable temperature and humidity conditions. They compared this membrane with Nafion 117 and found both materials exhibited a strong dependence of conductivity on temperature and humidity, with conductivity in both cases being strongly diminished with decreasing humidity(at constant temperature) and increasing temperature(at constant water partial pressure). Zawodzinski [39]studied the water uptake and transport properties of Nafion 117, they specifically determined the amount of water taken up by membranes immersed in liquid water and by membranes exposed to water vapor of variable water activity. The relationship of water sorption characteristics and proton conductivity were discussed. This studied was confirmed by J.Hinatsu [40] et al by study water uptake of Nafion membranes from liquid water and from water vapor over a range of temperature.

This investigation forms the second part of a series, examining a select group of promising alternative proton conducting membranes for elevated PEM fuel cell applications. The membranes used as part of this investigation are polyarylene-ether-sulfones (including polymers synthesized with sulfonated monomers and ones which were post-sulfonated), polyarylene-sulfide-sulfones and the control material, Nafion® (Dupont). The aim of this investigation was to compare the conductivity of these alternative membranes under fully hydrated conditions (akin to fuel cell operation) as a function of temperature as well as under lower relative humidity (RH) as a function of temperature. The performance of conductivity of alternative membranes was different with that of Nafion 117 at lower relative humidity as comparison at fully hydration condition. The difference of both cases was elucidated based on their chemistry, acidity (pK_a), chemical structure, equivalent weight etc. In addition, conductivity was investigated for these polymers in highly filled structures analogous to those they form in PEMFC electrode reaction layer interfaces.

EXPERIMENTAL

Choice of Membranes and Preparation:

All chemical structures of polymer membranes and nomination are described in our prior work[36].

Measurement of Membrane Properties:

In this study proton conductivity was measured using a four-probe conductivity cell. Detail description of the cell structure is reported in our prior study[36]. This cell was connected to humidification set up akin to a fuel cell humidification system as well as lower relative humidity with a conventional heated bubbler setup which included mass flow controlled wet and dry gas mixtures and the cell fixture in a constant temperature oven. By adjusting the carrier gas flow rates and bubbler temperature, different humidification levels could be adjusted at any temperature. In this investigation data at 100 % humidification and at lower relative humidity is reported. Humidification levels were measured using a sensor (Electronik, series EE-30), placed close to the fritted disk. Detailed experimental condition was reported in our earlier work[36]. Measurements were made at different temperatures keeping the constant relative humidity value. This allowed for the determination of activation energies using the standard Arrhenius plots.

Ion exchange capacities were measured using standard methods. Measurements of water uptake at fully hydration condition and at lower relative humidity were followed typical methods reported earlier.[44] Number of water molecules per sulfonic acid group was then calculated (λ=# moles of H_2O/SO_3^-).

The pK_a values of the polymers were measured according to procedure described in detail elsewehere[45]. With the control sample, Nafion® 117, the value of pK_a obtained was –3.09, which is in agreement with prior reports[46].

For measurement of conductivity of reaction layers a special setup was used. Detailed experimental condition was reported in our prior work[36]. The arrangement for this modified reaction layer is depicted in figure 6. For the reaction layer studies the choice of SPES material was one with a slightly higher sulfonation level (1:1, higher IEC), this is referred to as **SPES-50.** Details of its IEC (EW) and conductivity as published previously by Virginia Tech., group (Professor McGrath) are given in Table 1.

RESULTS AND DISCUSSION

Proton Conduction: Effect of λ, EW, acidity and tertiary structure of the membrane:

Proton conduction in polymer membranes under fully hydration:

Table 1 lists the values of proton conductivity for the various membranes measured at 100 % relative humidity along with the data for EW (IEC), # of moles of water molecules/SO_3^- (λ), and pK_a. As evident from Table 1, all the polymer membranes samples have similar levels of λ when compared at 85°C (within the levels of error, ± 5%, inherent in these measurements). The values for Nafion® 117 were in agreement with prior reports[31,44,47]. Results for SPES-40 are also in agreement with previously reported values[41] when compared at room temperature (see Figure 1). Normally water content of the membrane increases with decreasing equivalent weight, where the higher water content is consistent with the increased osmotic driving force for water sorption. However, water content does not necessarily correlate to proton conductivity for membranes, which have very different chemical structure. In that context, λ is a better measure, especially when comparing data under conditions of full hydration. Hence, when comparing these membranes with very different chemical structures and EW, it is important to note that their primary hydration shell around the proton as far as each acidic center is concerned is approximately the same.

Figure 1, shows the variation of water uptake expressed in terms of λ with temperature, for Nafion® 117, SPES-40 and SPES-PS membranes. The variation of λ for Nafion® 117 shows agreement with values reported earlier[39,40,47]. The variation of λ, exhibit very different slopes for the three membranes, however they start to merge at elevated temperature (close to 100°C). As evident from this figure, the trend in slope shown in descending order is Nafion® 117 > SPES-PS > SPES-40.

Figure 2, shows the variation of conductivity with temperature under fully hydrated conditions. Comparison of values at 85°C (Table 1) for Nafion® 117 shows very good agreement with those published earlier[22,29]. The value for SPES-40 when compared at 20°C also shows very good agreement with previously reported data[41].

Rationalizing proton conductivity with membrane parameters such as EW, λ, chemistry of the polymer backbone & sulfonation and acidity (pK_a) is complex, especially when comparing such a diverse group of membranes. This is amply evident from previous reports[29,31]. Beattie *et al.*,[31] compared the proton conductivity of several aliphatic chain membranes with different sulfonic acid end chains (both aliphatic and aromatic). Correlation of proton conductivity with parameters related to water uptake *i.e.*, EW, water content (%), λ, etc., showed very different relationships amongst the membranes investigated. Membrane with sulfonated styrene-(ethylene butylene)-styrene triblock copolymers (DAIS®) showed the smallest variation of conductivity for all the above mentioned parameters. However, a sulfonated *αββ* trifluorostyrene-*αββ* trifluorostyrene copolymer (BAM®, from Ballard) exhibited a volcano type behavior, showing maximum conductivity in the intermediate range of EW. In contrast to these the ethylenetetrafluoroethylene-*g*-polystyrene sulfonic acid (ETFE-*g*-PSSA) membrane exhibited an almost exponential increase in conductivity with lowering of EW (increased water content). A study[29]comparing membranes of sulfonated poly (ether-ether ketone) (SPEEK), a polyether sulfone (SPES) and polyphenyquinoxalene (SPPQ) provided a similar perspective. All the membranes in this prior study exhibited relatively little variation of proton conductivity as a function of EW (in the mid range of percent sulfonation), which was in contrast to the earlier work reported by Beattie *et al.*,[31] on aliphatic chain membranes.

Comparison of proton conductivity at 85°C (Table 1) with values related to water uptake, EW and λ, shows that while SPES-40 and Nafion® 117 have similar conductivity in the entire temperature range investigated (Figure 2), the EW for SPES-40 is half that of Nafion, and therefore it has twice the water content. On the other hand SPES-PS has a lower conductivity as compared to SPES-40 even though it has a larger IEC (or smaller EW) and hence greater water content. This is particularly interesting in light of the two polymers having very similar polymer backbone structure. Likewise, despite having close equivalent weights (a difference of approximately 8%) and λs (and hence water content) the proton conductivity of SPSS-40 is 40 % lower than SPES-40. These comparisons show that there is no apparent correlation between the proton conductivity and water uptake. In this context it is important to note that the variation of proton conductivity with temperature had no correlation with variation of λ in the same temperature range.

As pointed out in a review by Kreuer[48], proton conduction of ionomers has to be viewed in the context of phase formation and clustering between hydrophilic and hydrophobic moieties. Further, when comparing membranes with aromatic polymer chains, the issue of acidity (pK_a) becomes important as pointed out recently by Kopitzke *et al.*[29] The acidity of the various proton conducting membranes are reported in Table 1. As expected, Nafion® 117 has a negative value of pK_a (-3.09), this is broadly in agreement with earlier report[49] that have put its value somewhere in between that of methane sulfonic acid (pK_a=-1.0) and tri-flouro methane sulfonic acid (pK_a=-5.1). As mentioned in the introduction section, compared to perflouro sulfonic acids, which fall in the category of superacids, the simplest aromatic sulfonic acid, benzene sulfonic acid, has a reported pK_a of 0.7 [35], which implies that a 1M solution is only 36 % dissociated. However the polyaromatic ionomers in this study are considerably more acidic. The pK_a of SPSS-40 is measured at –1.25 and that of SPES-40 and SPES-PS are –2.04 and –1.24 respectively. These values, although different, indicate that all the polymer membranes are very strong acids and are completely dissociated in 100% relative humidity condition. Smaller variations in proton conduction may arise as a result of these different pK_a values when subject to very low humidification conditions.

The prime distinguishing parameter in comparing these membranes therefore is most likely their microstructure. This is a very important contributor to the overall proton conductivity value as explained in the introduction based in earlier work by Gierke[33]. This report was among the first to propose a cluster network formation with inverted micelles containing hydrophobic solvent and ion exchange sites as separate from the polymer backbone connected with narrow channels (~10 Å). As evident from the chemistry of these ionomeric polymer membranes, there are several important differences, (a) the polymer backbone (aliphatic flourinated vs. aromatic), (b) sulfonic acid groups bound directly to the aromatic polymer backbone vs. being bound by relatively long dangling fluorinated aliphatic moieties. Further comparisons between the aromatic polymer backbone membranes show very different ratios of groups with and without sulfonation. This difference is most prominent when comparing SPES-40 and SPSS-40 with SPES-PS. These differences appear to be the prime contributor to the observed differences in proton conductivity. A systematic study of these aromatic backbone membranes is expected to shed more lightly on their microstructure relative to Nafion® 117.

As expected, increase of temperature results in a concomitant increase in conductivity (Figure 2) based on the simplified diffusion mechanism and thermal motion of protons in channels within the membranes. The variation of proton conductivity for the various membranes showed very similar slopes with the differences in their respective conductivity remaining approximately the same in the range of temperatures studied. The order of decreasing conductivity was Nafion®117≈SPES-40>SPES-PS>SPSS-40. It was interesting to note that the variation of proton conductivity of SPES-40 followed exactly that of Nafion®117 in the entire temperature range of this investigation. Standard Arrhenius relationship between the proton conductivity (σ), and temperature (1/T(°K)), can be expressed as:

$$\sigma = Ae^{-E_a/RT}$$

where A is the frequency factor and R is the universal gas constant. Arrhenius plots for determination of the activation energy for proton conduction are plotted in figure 3. The values of the activation energies obtained are given in Table 1. The value for Nafion®117 agrees well with those published earlier[50] by Yeo *et al.,* (2.25 Kcal/mol). Comparison with values obtained for the other polymer membrane show similar values in the range of 8.6 to 10 KJ/mol. All the ionomers studied have very similar activation energy for proton conduction. This is consistent with the fact that they all have similar values of λ and all have very high acid dissociation constants, and it indicates that they all conduct protons by a similar mechanism under the fully hydrated conditions used for this study. The prime reason for different values of proton conductivity in these membranes is due to different values of the pre-exponential factor. This pre-exponential factor, to the simplest approximation, is comprised of orientation contribution and a frequency term, both of which ultimately depend on the microstructure.

Proton conduction in polymer membrane at lower relative humidity

Water uptake values of Nafion 117 and alternative membranes from water vapor were measured according to method described in reference [47]. At room temperature saturated $CaCl_2$ was used to produce 31% relative humidity environment and saturated $(NH4)_2SO_4$ produce 81% relative humidity[51]. 100% relative humidity was produced by deionized water. The water uptake data represent as λ (# moles of H_2O/SO_3^-) is shown in Table 2. From 100% RH water vapor λ value of Nafion 117 is similar with reference [39], but SPES 40, SPES-PS , SPSS 40 have lower λ value than Nafion 117. At lower relative humidity all of the membranes studied have similar λ values except SPSS 40 has slightly lower value at 31% RH. Water uptake from water vapor for all membranes is less from liquid water (compare with Table 1). This difference is because water sorption from liquid water is direct, all the ionic pores are filled with water and finally form the ionic channel[33,47]. From water vapor phase, water sorption occurs by adsorption of monolayers on pore walls, multilayer formation in addition to process of condensation of water onto the interior pore wall. The difficulty of sorption from water vapor phase due to poor wetting of the hydrophobic wall surface. At lower relative humidity this hydrophobic surface expel water than water hydration. , the only sorbed water is the water hydrating the ionic sulfonic acid in the polymer[47]. Fig. 4 presents the comparison of conductivity of different membranes at different relative humidity at room temperature. Conductivity values for all membranes decrease drastically with decrease of the relative humidity, this phenomena is in agreement with the results obtained by other researchers on Nafion membrane[2,37,38]. The strong dependence of conductivity on humidity can be explained by our water uptake experimental data at different relative humidity. At higher relative humidity polymer membranes absorb more water than at lower relative humidity, all ionic pore is filled with water, proton can transport easily as free ions through these water filled cluster or ionic channels inside of polymer membrane networks. With decrease of the relative humidity, polymer membranes absorb less water, so these ionic channels will shrink and collapse because the sorption water molecules only exist around the ionic sulfonic acid group not into the ionic pore. And at very low relative humidity, the sorption water is even not enough for the need of acid dissociation, proton transport became even more difficult, polymer membrane is getting close to insulator, proton conductivity is diminished. As we discussed before, Proton Conduction was effected by several parameters of the membrane. Since we determined the λ value are almost same for different membranes at low relative humidity. And we found pKa , EW of the polymer is not a main factor for proton conduction. The only reason accounts for the low conductivity value for alternative membranes comparing with Nafion 117 might be different of micro structure of polymer in the membrane. These alternative ionomeric polymer membranes have totally different chemistry structure with Nafion. Nafion has clear phase separate structure which it aliphatic backbone form hydrophobic phase while its long pendant sulfonic acid moieties form the hydrophilic phase. The alternative polymer membrane has aromatic rings linked together with a number of bridge and the sulfonic acid groups bound directly to the aromatic polymer, which do not have clear phase separation. These differences appear to be the prime contributor to the observed differences in proton conductivity at low relative humidity.

We also studied the relationship between conductivity of membrane and temperature at different fixed lower relative humidity. At all studied relative humidity range (20% -80% RH), conductivity shows the same trend with the change of temperature. Fig 5 shows the dependence of conductivity of all membranes on temperature at 60% RH. With increase of temperature, conductivity values of all alternative membranes and Nafion 117 increase. According to Arrhenius equation, conductivity has linear exponential relation with temperature, our experimental results of conductivity and temperature are in agreement with Arrhenius relation. Activation energy (Ea) of proton conduction for all membranes are calculated from Arrhenius equation, Ea values at different relative humidity (100% -20% RH) were shown in Table 3. From 100% to 40% RH, Ea values for all the membranes are similar. At 20% RH, Ea values are slightly higher. According to prior study[52,53], proton migration in polymer membrane follows Grothuss mechanism, for such mechanism, the activation energy for proton conduction is about 13-14KJmol^{-1}, our data follow in the range 8-12KJmol^{-1}, which are similar with other study[50] by Yeo *et al.*, (2.25 Kcal/mol). As discussed before, proton conduction depends on the relative humidity. At very low RH (20%), the conductivity decrease drastically, SPSS behaves like a pure insulator. The slight high Ea values at 20% RH might also due to the poor hydration of the polymer membranes.

Proton conduction in reaction layers:

It is well recognized that it is not only important to ensure good proton conduction within the membrane structure, but also within the reaction layer in order to extend the reaction zone deeper into the electrode substrate. It is also well recognized that when using these alternative membranes in an MEA, a different ionomer in the reaction layer such as the often-used 5 % solubilized Nafion® solution (Aldrich) can be deleterious. This could be due to (a) the possibility of a junction potential being set up at the electrode's interface with the membrane. (b)

Lower thermal stability of Nafion (the whole purpose of choosing a higher thermochemically stable polymer membrane being negated due to the use of Nafion® in the reaction layer). It is therefore imperative to attempt to measure the proton conduction of these solubilized ionomers in a reaction layer environment. Figure 6 shows the design of reaction layer analogs that we have used to study their proton conduction. Both the conventional and the modified reaction layer schematics are shown. In the modified reaction layer 5 % solubilized ionomer (pure or a blend) was mixed with α-Al_2O_3 and sprayed in top of a hydrophilic Nylon film (see experimental section for details). Blanks were run for this system without the presence of ionomer and values of conductivity were found to be below the measurable limits of our instrumentation. All conductivity values were measured in-plane. In order to ensure that we were not measuring erroneous effects due to a thin layer of ionomer on the top layer of this modified reaction layer, measurements were repeated with at least four different sets of samples for each case. All the measurements reported had variation in the range of 5-10%. The reported values are an average of these measured conductivity values. It is also important to note that the measured conductivity values were at least two orders of magnitude lower than those measured for polymer membranes. The invariance of the impedance within this range of frequency and the fact that the phase angle was zero for most of this frequency range shows that the modified reaction layer was behaving as a pure resistor. The resistance could then be determined using the corresponding Cole plot.

Based on the discussion presented so far, it is evident that proton conduction in polymer ionomeric membranes is a complex phenomenon. For the materials studied here, differences between their conductivity are not related to parameters such as EW, λ, pK_a etc. This leaves the microstructure differences between these materials as the most likely source of their differing conductivity. The bulk membrane microstructure environments may or may not be preserved within the domains of polymer aggregates. Not only were solubilized forms of the pure ionomer used in this study, but blends were made with Nafion in order to understand, albeit simplistically, the effect of close contact between these disparate polymer systems.

Figure 7 (a), shows the first set of comparisons between Nafion®, pure SPES-PS and blends of SPES-PS with Nafion (8:2) and (1:1). The ionomers show relatively close proton conduction in the reaction layer analog at 20°C. However as temperature is raised the proton conduction values diverge significantly, with Nafion conductivity showing far greater increases than that of the pure SPES-PS material. A blend of 8:2 (Nafion®: SPES-PS) has conductivity close to that of Nafion, while a 1:1 (Nafion®: SPES-PS) blend has conductivity that is almost exactly intermediate between that of the two components. This system appears to behave in a straightforward rule of mixtures. Figure 7 (b) shows data for conductivity of SPES-50 material in reaction layer analogs. Here the pure SPES-50 has a higher value of proton conductivity at 20°C than pure Nafion®. But the conductivity of Nafion surpasses that of SPES-50 for temperature above approximately 70°C. Due to this, blends of SPES-50 with Nafion exhibited more complex behavior than the Nafion/SPES-PS blends shown in Figure 7 (a). While the 1:1 Nafion: SPES-50 blend reaction layer analog has conductivity intermediate between that of the two constituent ionomers at 20 °C, at 70°C the conductivity is closer to the Nafion sample. The proton conductivity of pure SPES-50 reaction layer analogs was higher at all temperatures than that of SPES-PS, and the conductivity increase with temperature was greater. However the 1:1 blend of the two polymers had conductivity that was not very different from that of the pure SPES-50. These plots suggest that mixing ionomers in reaction layers can have unexpected consequences for protonic conduction in those electrodes, and may offer a useful route to optimizing their performance under particular fuel cell operational regimes.

It is likely that incorporation of highly sulfonated ionomers in reaction layers greatly magnifies the role that their microstructure plays in determining conductivity. In bulk membranes, the tendency for highly sulfonated ionomers to form sulfonate-rich segregated microstructures may not be as critical for achieving a conductivity percolation threshold as it is in the reaction layer, where the ionomer is present as a diluted phase with limited continuity. Nafion has clear and distinctive hydrophobic (the perfluorinated backbone) and hydrophilic ends (the pendant prefluorinated sulfonic acid groups), resulting in cluster formation. It is interesting to note that the SPES-PS is expected to have the least likelihood of a clear phase separation because it probably has the shortest average length of unsulfonated chain segment, and this may be why lower conductivity is observed at elevated temperature. It is clear however, that a lot more needs to be done to understand the effect of proton conduction in the reaction layer. This is especially important when considering the use of these alternative polymers under conditions of lower relative humidity.

Acknowledgements

The authors gratefully acknowledge the financial support from the U.S. Department of Energy, Office of Transportation Technology as well as from Foster-Miller Inc., Waltham, MA. Authors would like to express their deepest gratitude to Professor James McGrath and his graduate student Michael Hickner for useful discussions and samples of SPES-40 and solubilized form of the same (SPES-50) with higher IEC.

References

(1) Savadogo, O. *Journal of New Materials for Electrochemical Systems* **1998**, *1*, 47.

(2) Sumner, J. J.; Creager, S. E.; Ma, J. J. A.; DesMarteau, D. D. *Journal of the Electrochemical Society* **1998**, *145*, 107.

(3) Kauranen, P. S.; Skou, E. *J. Appl. Electrochem.* **1996**, *26*, 909.

(4) Jia, N.; Lefebvre, M. C.; Halfyard, J.; Qi, Z.; Pickup, P. G. *Electrochemical and Solid-State Letters* **2000**, *3*, 529.

(5) Samms, S. R.; Wasmus, S.; Savinell, R. F. *J. Electrochem. Soc.* **1996**, *143*, 1498.

(6) Kreuer, K. D. *Solid State Ionics* **1997**, *97*, 1.

(7) Malhotra, S.; Datta, R. *Journal of the Electrochemical Society* **1997**, *144*, L23.

(8) Wang, J. T.; Savinell, R. F.; Wainright, J.; Litt, M.; Yu, H. *Electrochim. Acta* **1996**, *41*, 193.

(9) Kreuer, K. D. *Solid State Ionics: Science and Technology, [Proceedings of the Asian Conference], 6th, New Delhi, Nov. 29-Dec. 4, 1998* **1998**, 263.

(10) Doyle, M.; Choi, S. K.; Proulx, G. *Journal of the Electrochemical Society* **2000**, *147*, 34.

(11) Bozkurt, A.; Ise, M.; Kreuer, K. D.; Meyer, W. H.; Wegner, G. *Solid State Ionics* **1999**, *125*, 225.

(12) Sakaguchi, Y.; Kitamura, K.; Nakao, J.; Hamamoto, S.; Tachimori, H.; Takase, S. *Polymeric Materials Science and Engineering* **2001**, *84*, 899.

(13) Adjemian, K. T.; Srinivasan, S.; Benziger, J.; Bocarsly, A. B. *Journal of Power Sources* **2002**, *109*, 356.

(14) Adjemian, K. T.; Lee, S. J.; Srinivasan, S.; Benziger, J.; Bocarsly, A. B. *Journal of the Electrochemical Society* **2002**, *149*, A256.

(15) Antonucci, V.; Arico, A. Polymeric membrane electrochemical cell operating at temperatures above 100.degree. In *Eur. Pat. Appl.*; (De Nora S.p.A., Italy). Ep, 1999; pp 6 pp.

(16) Costamagna, P.; Yang, C.; Bocarsly, A. B.; Srinivasan, S. *Electrochimica Acta* **2002**, *47*, 1023.

(17) Lin, J.-C.; Kunz, H. R.; Cutlip, M. B.; Fenton, J. M. *Hazardous and Industrial Wastes* **1999**, *31st*, 656.

(18) Miyake, N.; Wainright, J. S.; Savinell, R. F. *Journal of the Electrochemical Society* **2001**, *148*, A905.

(19) Miyake, N.; Wainright, J. S.; Savinell, R. F. *Journal of the Electrochemical Society* **2001**, *148*, A898.

(20) Kopitzke, R. W.; Linkous, C. A.; Nelson, G. L. *Polymer Degradation and Stability* **2000**, *67*, 335.

(21) Kovar, R. F.; Ofer, D.; Nair, B.; McGrath, J. E.; Laconti, A.; Kosek, J.; Hamdan, M. *Abstracts of Papers, 222nd ACS National Meeting, Chicago, IL, United States, August 26-30, 2001* **2001**, FUEL.

(22) Alberti, G.; Casciola, M.; Massinelli, L.; Bauer, B. *Journal of Membrane Science* **2001**, *185*, 73.

(23) Ise, M.; Kreuer, K. D.; Maier, J. *Solid State Ionics* **1999**, *125*, 213.

(24) Kopitzke, R. W.; Steckler, T. T.; Seurer, B. D. *Abstracts of Papers, 223rd ACS National Meeting, Orlando, FL, United States, April 7-11, 2002* **2002**, CHED.

(25) Kopitzke, R. W.; Seurer, B. D.; Steckler, T. T. *Abstracts of Papers, 223rd ACS National Meeting, Orlando, FL, United States, April 7-11, 2002* **2002**, CHED.

(26) Wang, F.; Hickner, M.; Ji, Q.; Harrison, W.; Mecham, J.; Zawodzinski, T. A.; McGrath, J. E. *Macromolecular Symposia* **2001**, *175*, 387.

(27) Lufrano, F.; Squadrito, G.; Patti, A.; Passalacqua, E. *Journal of Applied Polymer Science* **2000**, *77*, 1250.

(28) Lufrano, F.; Gatto, I.; Staiti, P.; Antonucci, V.; Passalacqua, E. *Solid State Ionics* **2001**, *145*, 47.

(29) Kopitzke, R. W.; Linkous, C. A.; Anderson, H. R.; Nelson, G. L. *Journal of the Electrochemical Society* **2000**, *147*, 1677.

(30) Allcock, H. R.; Hofmann, M. A.; Ambler, C. M.; Lvov, S. N.; Zhou, X. Y.; Chalkova, E.; Weston, J. *Journal of Membrane Science* **2002**, *201*, 47.

(31) Beattie, P. D.; Orfino, F. P.; Basura, V. I.; Zychowska, K.; Ding, J.; Chuy, C.; Schmeisser, J.; Holdcroft, S. *Journal of Electroanalytical Chemistry* **2001**, *503*, 45.

(32) Creager, S. E.; Sumner, J. J.; Bailey, R. D.; Ma, J. J.; Pennington, W. T.; DesMarteau, D. D. *Electrochemical and Solid-State Letters* **1999**, *2*, 434.

(33) Gierke, T. D.; Hsu, W. Y. *ACS Symp. Ser.* **1982**, *180*, 283.

(34) Pourcelly, G.; Lindheimer, A.; Pamboutzoglou, G.; Gavach, C. *J. Electroanal. Chem. Interfacial Electrochem.* **1989**, *259*, 113.

(35) *CRC Handbook of Chemistry and Physics*; CRC Press, Boca Raton, FL, 1983, pp p 167.

(36) Chengsong Ma, L. Z., Sanjeev Mukerjee, et al. *J.Membrane Science(submmitted)* **2002**.

(37) Sone, Y.; Ekdunge, P.; Simonsson, D. *J. Electrochem. Soc.* **1996**, *143*, 1254.

(38) Anantaraman, A. V.; Gardner, C. L. *Journal of Electroanalytical Chemistry* **1996**, *414*, 115.

(39) Zawodzinski, T. A., Jr.; Springer, T. E.; Davey, J.; Jestel, R.; Lopez, C.; Valerio, J.; Gottesfeld, S. *Journal of the Electrochemical Society* **1993**, *140*, 1981.

(40) Hinatsu, H. T., Mizuhata, M., and Takenaka, H. *Journal of Electrochemical Society* **1994**, *141*, 1493.

(41) Wang, F.; Hickner, M.; Kim, Y. S.; Zawodzinski, T. A.; McGrath, J. E. *Journal of Membrane Science* **2002**, *197*, 231.

(42) Formato, R. M.; Osenar, P.; Kovar, R. F.; Langrau, N. Novel ion-conducting materials suitable for use in electrochemical applications and methods related thereto. In *PCT Int. Appl.*; (Foster-Miller, Inc., USA). Wo, 2000; pp 53 pp.

(43) Wang, F.; Mecham, J. B.; Harrison, W.; McGrath, J. E. *Abstr. Pap. - Am. Chem. Soc.* **2000**, *220th*, POLY.

(44) Basura, V. I.; Chuy, C.; Beattie, P. D.; Holdcroft, S. *Journal of Electroanalytical Chemistry* **2001**, *501*, 77.

(45) Helfferich, F. *Ion exchange*; Dover Publications: Mineola, NY, 1995.

(46) P. Stang, a. V. Z. "Chemistry of Organic Fluorine Compounds II", 1995.

(47) Zawodzinski, T. A., Jr.; Derouin, C.; Radzinski, S.; Sherman, R. J.; Smith, V. T.; Springer, T. E.; Gottesfeld, S. *J. Electrochem. Soc.* **1993**, *140*, 1041.

(48) Kreuer, K. D. *Solid State Ionics* **2000**, *136-137*, 149.

(49) Smart, B. E.; American Chemical Society, Washington, DC; Vol. In Chemistry of Organic Flourine Compounds-II; pp p 988.

(50) Yeo, R. S. *J. Electrochem. Soc.* **1983**, *130*, 533.

(51) Lide, D. R. *CRC Handbook of Chemistry and Physics*, 75th ed.; CRC Press, 1995.

(52) Colomban, P.; Editor *Proton Conductors: Solids, Membranes and Gels - Materials and Devices. [In: Chem. Solid State Mater., 1992; 2]*, 1992.

(53) Agmon, N. *Chemical Physics Letters* **1995**, *244*, 456.

Table 1

Membrane	I E C (meq/g) [EW: mg/meq]	Conductivity (85°C)	Activation Energy (KJ/mol)	Water uptake (%wt)	λ $[H_2O]/SO_3^-$ (85°C)	pK_a
SPSS-40	1.47 [680]	0.126	9.082	47	18.2	-1.25
Nafion® 117	0.91 [1100]	0.205	9.568	29	17.7	-3.09
SPES-40	1.59 [628]	0.203	9.352	61	19.9	-2.04
SPES-PS	2 [500]	0.139	8.635	62.6	20.4	-1.24
SPES-50	1.8	0.284			-	-

Table 1. Comparison of proton conductivity (@ 85°C) under 100 % relative humidity with water uptake ($\lambda = [H_2O]/SO3^-]$), Ion exchange capacity (meq/g) or equivalent weight, and pK_a for select aromatic chain proton conducting membranes. Data for Nafion® 117 is included as a control.

Table 2.

	$\lambda(H_2O/SO_3H)$ at 31% RH	$\lambda(H_2O/SO_3H)$ at 81% RH	$\lambda(H_2O/SO_3H)$ at 100% RH	$\lambda(H_2O/SO_3H)$ from liquid water
Nafion 117	3.0	6.7	14.2(14[39])	20
SPES 40	3.1	6.3	11.2	20.8
SPES-PS	2.7	6.4	11.0	21.5
SPSS 40	2.2	6.2	11.4	20.5

Table 2. Water Uptake ($\lambda = [H_2O]/SO3^-]$) of different membrane at different relative humidity.

Table 3.

Ea (KJ/mol)	100% RH	80% RH	60% RH	40% RH	20% RH
Nafion 117	9.57	9.47	8.98	11.3	12.3
SPES 40	9.35	10.0	8.93	9.11	10.4
SPES-PS	8.63	8.43	8.24	10.8	1.17
SPSS 40	9.08	9.06	8.80	8.94	

Table 3. Activation energy of proton conduction of different polymer membrane at different relative humidity

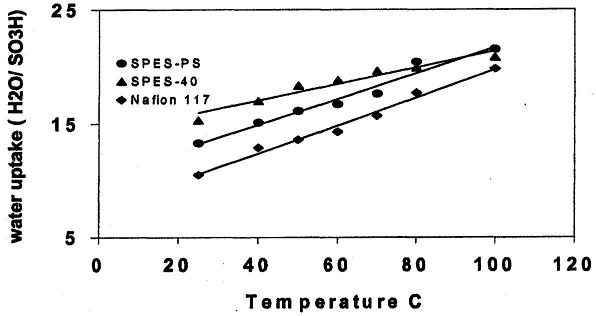

Figure 1. Water uptake, expressed as λ ($[H_2O]/SO_3^-$) as a function of temperature (°C) for SPES-PS (•), and SPES-40 (Δ). Data for Nafion® 117 (_) is also included as a control.

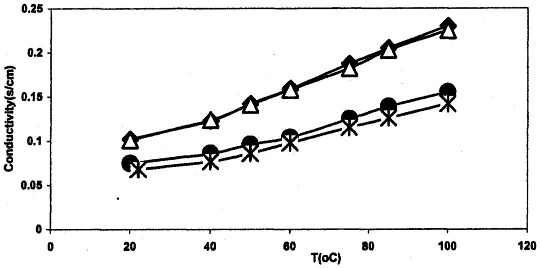

Figure 2. Variation of proton conductivity (S/cm) measured under conditions of 100 % relative humidity, as a function of temperature for SPES-40 (Δ), SPES-PS (•), SPSS-40 (✳). The data for Nation® 117 (_) is also reported as a control.

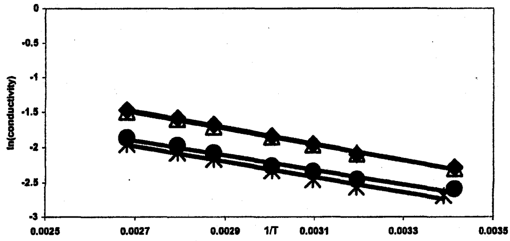

Figure 3. Arrhenius plot of the proton conductivity (Ln conductivity (S/cm) vs. 1/T (°K)), for determination of activation energy of proton conduction for various membranes, SPES-40 (Δ), SPES-PS (•), and SPSS-40 (X). Data for Nafion® 117 (_) is also included as a control.

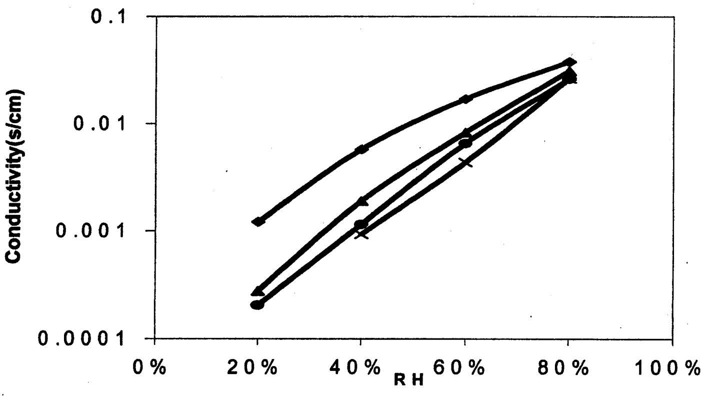

Figure 4. Variation of proton conductivity (S/cm) as a function of relative humidity at 24°C. SPES-40 (Δ), SPES-PS (•), and SPSS-40 (X). Data for Nafion® 117 (_) is also included as a control.

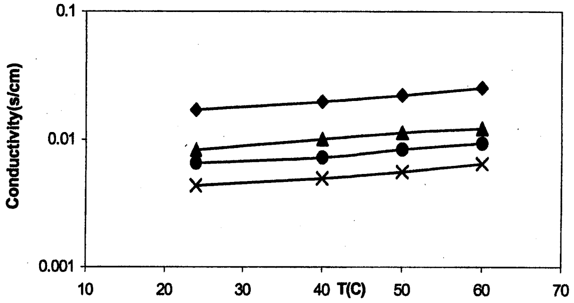

Figure 5. Variation of proton conductivity (S/cm) measured under conditions of 60 % relative humidity, as a function of temperature for SPES-40 (Δ), SPES-PS (•), SPSS-40 (✳). The data for Nation® 117 (_) is also reported as a control.

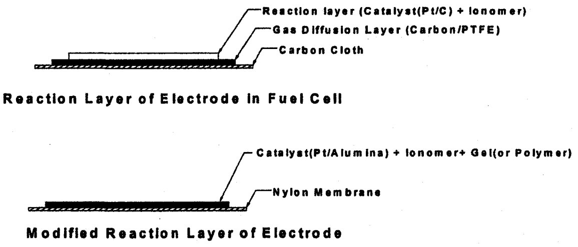

Figure 6. Schematic of the reaction layer showing (a) the arrangement in a conventional PEM fuel cell electrode and (b) the arrangement used to determine the proton conductivity of the solubilized ionomers.

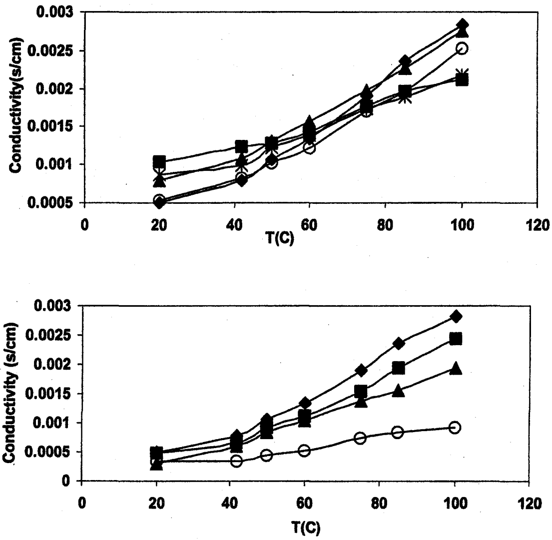

Figure 7. Proton conduction in modified reaction layers for solubilized ionomers and ionomer blends as a function of temperature (°C), comparing (a) Nafion (_), Nafion-SPES-PS (8:2) (◆), Nafion-SPES-PS (1:1) (‿) and pure SPES-PS (o) and (b) Nafion (_), SPES-50 (◆), Nafion – SPES-50 (1:1) (‿), Nafion-SPES-50 (2:8) (o) and SPES-50-SPES-PS (1:1) (Ж).

Proceedings of The Electrochemical Society, PV 2002-31, 416-425 (2002)
DOI: 10.1149/200231.0416PV © The Electrochemical Society

NOVEL COMPOSITE MEMBRANE-ELECTRODE ASSEMBLY FOR HIGH-TEMPERATURE PEMFC

Chao-Yi Yuh, Pinakin Patel, Ray Kopp, Sai Katikaneni
FuelCell Energy, Inc.
3 Great Pasture Road
Danbury, CT 06813

Stephen Grot
Ion Power, Inc.
102 East Scotland Dr.
Bear, DE 19701

ABSTRACT

For the clean and efficient proton exchange membrane fuel cell (PEMFC) to be commercially viable, the performance of critical components, membrane-electrode assembly (MEA) in particular, needs to be enhanced. Operating PEM fuel cell at 100-150°C can improve CO tolerance, mitigate water and thermal management challenges, and enhance electrode kinetics. Extensive literature survey has showed that new cathodes as well as new membranes need to be developed for operating PEMFC at this temperature range. The approach in this study is to develop composite MEA consisting of high-temperature proton conducting phases. A 2,000h 120°C endurance testing showed that both membrane durability and cathode polarization loss need to be enhanced for achieving reasonable performance and life. An advanced MEA showed ~600mV atmospheric-pressure performance at 120°C, atmospheric pressure and 400 mA/cm^2 for 500 hours, about 200mV performance improvement over the baseline.

INTRODUCTION

Fuel cells offer the best alternative to conventional fossil fuel combustion power generation technologies. They are inherently cleaner and more efficient. However, for fuel cells to be commercially viable, issues such as cost, size, and functionality need to be addressed. A natural-gas fueled PEMFC system for building application desires near atmospheric pressure operation, >35% HHV efficiency, >100°C operation for cogeneration, simple construction, reliable >40,000h life, and low system cost (<$1500/kW). A PEMFC system for transportation application requires <3 atm pressure operation, >5,000h life and <$10/kW MEA cost. Although research efforts so far have advanced PEMFC technology significantly, substantial improvements beyond the current state-of-the-art are required before the above goals can be achieved. The performance and durability of critical components, membrane-electrolyte assembly (MEA) in particular, needs to be improved.

At present, the state-of-the-art PEMFC is operated at ~60 to 80°C. CO poisoning of its anode precious metal catalyst at this temperature range is a major barrier for its commercialization utilizing hydrocarbon feedstock (1). The current state-of-the-art anode catalyst cannot tolerate even 50ppm CO. Various approaches to mitigate CO poisoning such as alternative anode catalysts, catalytic preferential oxidation (PROX), or air bleeding have not completely alleviate the issue.

Since the chemisorption of CO is exothermic and therefore weakens considerably with temperature, one approach to mitigate the CO poisoning issue is to operate PEMFC at higher temperatures. Additional advantages such as faster electrode kinetics and higher quality waste heat for cogeneration can also be realized. Operating at >100°C also mitigates cathode flooding by the liquid water reaction product and allows a greater ability to remove waste heat, a very important consideration for transportation application. With the current <100°C PEMFC, a complicated and expensive cooling system design (due to the small temperature difference between the stack and the ambient) is needed to avoid stack overheating. Such overheating can cause significant cell resistance increase and performance loss for the current baseline MEA, as will be discussed in detail below.

Most developers presently use perfluorosulfonic acid polymer membrane such as Nafion® made by DuPont. It is deficient in terms of ionic conductivity at temperatures above 100°C and at low relative humidity (R.H.). High-temperature operation dries out the membrane, drastically reducing proton conduction (by a factor greater than three). Water is needed in Nafion® to facilitate proton conduction (1). To operate Nafion® beyond 100°C, pressurization is needed to maintain high R.H., requiring compressor that complicates the system. Dried Nafion® is also more permeable to gases, resulting in increased cross-leakage. Furthermore, the loss of liquid water embrittles the membrane and could cause membrane cracking and poor electrode-membrane contact.

Another important observation for >100°C operation of the baseline Nafion®-base MEA is the significantly reduced cell voltage, only a minor portion (~20%) is explainable by the membrane ohmic resistance increase. In a typical PEMFC, the cathode is the major cell voltage loss contributor, due to an inherently slow ORR (oxygen reduction reaction) kinetics (1). The majority of the voltage loss increase at high temperatures is in fact due to cathode polarization increase. This increase is mainly caused by a loss of proton conductivity and catalyst utilization in the cathode catalyst layer. Therefore, further cathode performance enhancement is necessary in order to achieve the desired overall system efficiency goal of >35% HHV.

In summary, a high-temperature MEA operating above 100°C (preferably near 140-150°C) is highly desired for both stationary and transportation applications. The ultimate MEA goals for commercial use include:

- Higher membrane proton conductivity with negligible electronic conductivity, area specific resistance less than 200 mΩcm^2
- Improved humidification properties (minimal water transport and low hydration) and dimensional stability (low swelling)

- High mechanical strength
- Low gas permeability (less than 0.1 percent crossover of gases)
- Long life of 40,000h for stationary and 5,000h for transportation applications
- Cell performance >0.7 V at 400-500 mA/cm^2
- Low cost

LITERATURE SURVEY

Proton-conducting mechanisms have been extensively discussed by Kreuer (2,3). Literature survey has showed that a useable proton conducting membrane material with desired proton conductivity comparable to fully hydrated Nafion® (>0.1 S/cm) between 100-150°C is not yet available (4-6). In this temperature range the liquid H_3PO_4, having sufficient proton conductivity at low R.H., can induce high cathode polarization due to a strong adsorption of the phosphate anions on Pt that disrupts ORR. This is why phosphoric acid fuel cell is usually operated at much high temperatures (i.e., 200°C) to overcome the poor cathode kinetics.

Because useable 100-150°C proton-conducting materials are not yet available, many new high-temperature proton-conducting materials are being actively developed. In summary, the reported approaches include:

- <u>Mechanical Support</u> to enhance high-temperature mechanical strength
- <u>Solid Proton Conductor/Superacid</u> to enhance proton conductivity at low R.H.
- <u>New High-Temperature Proton-Conducting Ionomer</u>
- <u>Substitutes for Water in Nafion</u> to reduce humidity effect
- <u>Pt Doping for Self Humidification</u>

Thermally stable porous polymer supports (PTFE, PBO, PEO), to improve membrane durability and strength, have been included in many composite membranes under development. One important consideration is to maintain the bonding between the support and the proton-conducting phase at high temperatures. Separation of the bonding can result in membrane cross-leakage increase.

The solid proton conductors/superacid under evaluation include:

PTA (Phosphotungstic Acid) $H_3PO_4{\bullet}12WO_3{\bullet}xH_2O$
PMA (Phosphomolybdic Acid) $H_3PO_4{\bullet}12MoO_3{\bullet}xH_2O$
STA (Silicotungstic Acid) $SiO_2{\bullet}12WO_3{\bullet}xH_2O$
Sulfated Zirconia/Titania (S-ZrO_2 and S-TiO_2)
ZHP: $Zr(HPO_4)_2$
Zeolite, Silica, $CsHSO_4$

These materials are brittle inorganics and cannot be easily formed into a flexible thin film by itself. Therefore, they are generally incorporated into a composite structure containing flexible polymeric ionomer phases. The conductivities of PTA, PMA and STA are comparable to well-humidified Nafion® at Low Temperatures. However, although to a lesser extent than Nafion®, they also lose water at high temperatures, with reduced proton conductivity. Water also facilitates proton conduction in these materials. Furthermore, they easily dissolve in liquid water; therefore, water condensation must be avoided to prevent leaching out. $CsHSO_4$ does not rely on water but on superionic phase proton hopping for proton conduction (7). However, on the anode side, it is unstable and loses proton conductivity. Other similar types of materials (usually phosphate-containing) are still at early stages of development. ZHP, S-ZrO_2/S-TiO_2, zeolite, and silica do not dissolve in water but considerable modifications of their morphologies (such as fine nano-size) may be needed to effectively enhance proton conductivity.

New high-temperature iomomers are in general sulfonated/phosphonated polymers, usually containing aromatic backbone (8-10), including:

Sulfonated Polyimide (SPI)
Bis(perfluroalkyl) Sulfonyl Imide
Polyphosphazene
BPS (polyarylene ether sulfone)
Sulfonated PEEK, PES, PPO
Phosphonic Acid Functionalized Trifluorostyrene (TFS)

They all still require water to facilitate proton conduction. So far, long-term high-temperature proton conductivity and durability under low R.H. have yet to be demonstrated.

The liquid acid impregnated membranes include:

H_3PO_4 Doped PBI (Polybenzimidazole)
H_3PO_4 Doped Polyoxadiazoles
H_3PO_4 Doped SPSF(Sulfonated Polysulfone)+PBI
Sulfuric, Phosphoric, Triflic Acids Doped PVDF Bonded Ceramic Powders (Alumina, Silica, Titania, Zirconia)

These liquid acid (less volatile than water) impregnated membranes have sufficient proton conductivity at high temperature; however, the acids may decompose or adsorb at the Pt surface, resulting in high cathode polarization. Furthermore, the liquid acids may evaporate away slowly during long-term use, limiting their high-temperature durability.

Because water dry-out is the main cause of proton-conductivity loss in many materials at high temperatures, substitutes for water in the ionomers with high boiling-point proton-conducting liquid have been evaluated:

BMITf or $BMITF_4$ Doped Nafion
sPEEK+Pyrazole/Imidazole

However, these liquid proton conductors may adsorb on the Pt catalyst surface, interfering ORR and resulting in high cathode polarization. The liquid proton conductor may also slowly evaporate away.

Many composite membranes are under active development, including:

PTA, ZHP/Nafion®/(Teflon)
PTA/Silica-PBI
Nafion®/Ti Sulfonylphosphonate
PFSA/Silica
Sulfonated PEEK+Phosphate/Oxide
PEEK or SPES+Zeolite
Sol-Gel Silica+PEO,PPO,PTMO,HMG+Solid Acids (PTA,MDP)
Pseudo PEO+STA

Zr-Phosphate+PTFE and Silicophosphate Gel Glass Composite
Sol-Gel Silane+PEO+$HClO_4$
Silicophosphate Gel Composite+Porous Alumina Support+$HClO_4$
PPSU+PBO
$CsHSO_4$+PVDF

The composite approaches are adopted because few single-component monolithic materials have all the desired properties. So far, few composite materials have sufficient proton conductivity comparable to a fully hydrated Nafion®. In addition, very little cell performance and endurance data were reported.

Many of the membrane materials reported above were studied for their proton-conducting and mechanical properties. However, very little MEA performance data at high temperatures were reported. The reported performance data were usually obtained with non-system conditions (e.g., very high R.H. or stoichs). The electrode Pt catalyst loading level was also usually too high (such as using Pt black, >1mg/cm^2 per electrode), not practical for commercial use.

The structure of the cathode catalyst layer can be illustrated as in Figure 1. In order for the Pt catalyst to be utilized, its surface needs to be accessed by the proton-conducting phases and reactant oxygen. Therefore, an ionomer of high proton conductivity is not sufficient to guarantee a high cathode performance. The acid groups (ionic clusters) of the ionomers have to be situated right at the Pt for it to be active for the ORR. The water in the acidic ionic clusters is also needed to facilitate ORR (1). Furthermore, high oxygen permeability is needed to reduce mass-transfer loss. The baseline Nafion® ionomer if well humidified has a very high oxygen permeability (1). Any new proton-conducting phase in the cathode catalyst layer also needs to have similarly high oxygen permeability.

This paper detailed the MEA work performed at FCE focusing on improving high-temperature membrane durability and cathode catalyst layer activity.

MEA EVALUATION

A number of composite membrane and MEA have been developed to improve water retention and proton conduction at 120°C. The experimental MEA are all less than 75 μm thick. The composite membranes consist of ionomer and solid superacid. Fine additives/modifiers with high-proton conductivity have been incorporated into the MEA (membrane and/or cathode). The proton-conducting additives include: PTA, sulfated zirconia, ZHP ($Zr(HPO_4)_2$), and several types of zeolites. The ionomer phase under study in the composite MEAs include Nafion® of various EW as well as low EW experimental ionomers (800EW). Initial attempt to hot-press thin composite membrane with catalyst coated diffusion layers frequently result in shorting and membrane crossover due to penetration of the carbon fibers of the diffusion layers through the membrane, also reported by Lin, et al. (11). Therefore, coating catalyst layers directly to the composite membranes was chosen as the MEA fabrication method. The fabricated MEAs were characterized by SEM, XRD, and proton conductivity and tested in laboratory-scale 25cm^2 cells at 80-120°C to evaluate promising MEA formulations. Figure 2 shows SEM micrograph of a typical catalyst-coated MEA fabricated in this study. The total thickness of the MEA was only 50μm.

4,000h Endurance Testing of Baseline MEA

A baseline MEA with a <30μm membrane was tested for 4,000h, including 2,000h at 120°C. The electrodes contain Nafion®-impregnated Pt/C without additives. The Pt loading level was 0.5mg/cm^2 for each electrode. The test was performed at atmospheric pressure with hydrogen fuel and air oxidant. The endurance results are shown in Figure 3. The cell performance at 60°C (at 100% R.H.) was stable high for 2,000 hours (about 0.7V at 400mA/cm^2). After 2,000h 60°C operation, the cell temperature was raised to 120°C. The humidification temperature was also increased but the R.H. decreased below 40%. The cell performance at 120°C dropped below 400mV (>300mV cell performance decrease from 60°C) and the cell ohmic resistance increased to 300 from 100 mΩcm^2. This resistance increase can only account for about 80mV cell performance drop. Therefore, the majority of the cell performance drop is due to electrode polarization increase, presumably due to a significantly increased cathode performance loss at 120°C. The anode polarization is estimated small even at 120°C. The cell performance slowly decreased with time (under condition B), due to an increase of gas crossover. By increasing the humidification from condition B to C, the cell resistance decreased to ~220mΩcm^2. The cell performance was restored to 400mV, but then continued to decay with time, due to continued crossover increase. This test showed that a standard baseline MEA had insufficient cathode performance and membrane endurance under a high-temperature and low R.H. condition.

Advanced MEA:

Many selected candidate solid superacids were incorporated into the cathode or membrane layer. It is desired to have superacid phase with nanostructure well dispersed in the MEA for a more homogeneous proton conductivity. All the MEAs contained no special additives in the anode. For this study, the tested ionomer EW varied from 800 to 1100.

PTA was first studied as the additive to the membrane. Figure 4 showed endurance result of a MEA impregnated with 5wt% PTA. The catalyst loading level was 0.5mg/cm^2 for each electrode. The cell performance level was initially >700mV at 95°C, with hydrogen and air humidified at 80°C. Raising the temperature to 120°C increased the ohmic resistance to 150-200mΩcm^2 and decreased the cell performance to 400-450mV at 400mA/cm^2 under atmospheric condition. The cell performance appeared slightly higher and more stable than cell FCE-25-3 (Figure 3). Although the membrane durability appeared enhanced by the incorporation of PTA in the membrane, further significant improvements are still needed. Increasing the PTA content in the membrane and impregnating the cathode with PTA did not improve the MEA performance. Much of PTA is suspected to have adsorbed onto the catalyst carbon support and not enhanced protonic conductivity.

Due to the concern of possible leaching out of PTA during cell operation, other types of insoluble solid superacids were investigated. The anode and cathode catalyst loading levels for all the MEAs were 0.4mg/cm^2 each. Figure 5 showed typical polarization curves of two identical superacid-impregnated MEAs tested at 80°C under atmospheric condition. Good OCV of >900 mV can be achieved. The cell resistances were all very low at less than 100mΩcm^2. Slight increase of the ohmic resistance beyond 600mA/cm^2 can be explained by the slight dry-out of the membrane at the anode side due to osmotic drag of water. The anode-side polarization can be estimated by performing polarization measurement with both electrodes fed with humidified hydrogen. Figure 6 illustrated such as typical polarization curve at 80°C under atmospheric condition. After subtracting the ohmic loss, the total electrode polarization (anode hydrogen oxidation and cathode hydrogen evolution) was only about 15mV at 400mA/cm^2. Therefore, it is determined that the anode had negligible polarization loss (<15mV). The cathode polarization was estimated to be ~180mV at 400mA/cm^2 under atmospheric condition.

The performance of all the experimental MEAs decreased with increasing temperature. About 600mV performance at 120°C had been achieved (Figure 7). The total cell ohmic resistance increased to about 170mΩcm^2, corresponding to ~45mV loss at 400mA/cm^2. The anode polarization was measured by feeding humidified hydrogen to both electrodes (Figure 8). The anode polarization was estimated to be less than 20mV, after subtracting the ohmic loss. The cathode polarization was estimated to be about 285mV at 400mA/cm^2, the dominant performance loss factor. The test demonstrated the need to further modify the cathode structure to achieve a desired high performance. Diagnostic testing by AC-impedance showed an increase of ionic resistance in the cathode catalyst, explaining the decrease of the cathode catalyst utilization. In order to enhance the ionic conductivity in the cathode catalyst layer, a low-EW ionomer (800EW) was incorporated into the cathode. Preliminary test result did not showed cell performance improvement. Significant ionomer modification will be needed to achieve the desired structure as shown in Figure 1.

The effect of pressure was also evaluated. Figure 9 showed increasing cathode backpressure decreased ohmic loss and increased cell performance. Increasing the cathode-side pressure not only increased oxygen partial pressure for a faster kinetics, but also decreased membrane ohmic loss, implying improved back-diffusion humidification by the reaction product water. Figure 10 showed the effect of increasing total cell pressure on the cell performance. At 30 psig, a cell voltage beyond 750 mV can be achieved at 120°C. The cell resistance also decreased with the cell total pressure, implying the benefit of a better membrane hydration by the reaction product water at high pressures. The test concluded that to achieve the desired >750mV performance at high temperatures, pressurization is needed.

Membrane durability is important for long-term commercial stack operation. The tests at FCE revealed lower EW membrane all developed crossover within 100 hours, accompanied by a decrease of OCV and cell performance. Figure 9 showed the endurance results of two MEAs. The cell #68 had a lower EW membrane and cell #84 had a higher EW membrane. The higher EW membrane showed a better OCV and performance stability. About 500h stable endurance has been achieved. This represents a >200mV performance improvement over the baseline membrane tested for 4,000h (Fig. 3).

In the future, the research will focus on optimization of the promising membrane-electrode assembly, scale-up to bench-scale nominal 300cm^2 and validation in bench-scale single cells followed by short stack evaluation.

CONCLUSIONS

Extensive literature survey has showed that new cathodes as well as membranes need to be developed for high-temperature >100°C PEMFC. Single-cell testing identified that the high performance loss at elevated temperature was mainly due to cathode polarization increase, resulting from high ionic resistance and loss of catalyst utilization in the cathode catalyst layer. Endurance testing revealed the need to further enhance the membrane durability. An advanced MEA has achieved a near 600mV performance for 500h at 120°C and 400mA/cm^2. Improvements in membrane endurance and cathode activity are still required for achieving MEA commercial goals.

ACKNOWLEDGEMENTS

This study was supported by US DOE under Contract DE-FC02-99EE27567. The interest and guidance of DOE program managers R. Fiskum and J. Jonkouski are appreciated.

REFERENCES

1. S. Gottesfeld and T. Zawodzinski, "Polymer Electrolyte Fuel Cells," in *Electrochemical Science and Engineering*, R. Alkire, H. Gerischer, D. Kolb and C. Tobias, Editors, **5**, p.195-301, Wiley-VCG, New York (1997).
2. K. Kreuer, *Solid State Ionics*, **136-137**, 149 (2000).
3. K. Kreuer, *Solid State Ionics*, **94**, 55 (1997).
4. J. Roziere and D. Jones, in *1st European PEFC Forum*, F. Buchi, G. Scherer and A. Wokaun, Editors, p. 145 (2001).
5. T. Zawodzinski, et al., in *2002 US DOE Hydrogen and Fuel Cell Joint Program Review*, May 6-10, 2002.
6. N. Norby, *Solid-State Ionics*, **125**, 1 (1999).
7. N. Norby, *Nature*, **410**, 877 (2001).
8. J. Kerres, *J. Membrane Science*, **185**, 3 (2001)
9. D. Jones and J. Roziere, *J. Membrane Science*, **185**, 41 (2001)
10. K. Kreuer, *J. Membrane Science*, **185**, 29 (2001)
11. J. Lin, et al., Abstract, The Electrochemical Society, 2000 Fall Meeting, Phoenix, AZ.

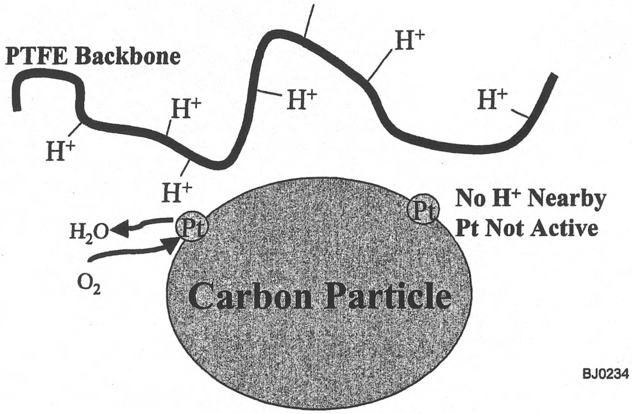

Figure 1. Schematics of cathode catalyst layer:
For Pt catalyst to be active and for a high cathode performance, high proton conductivity and oxygen permeability near the Pt surface are needed.

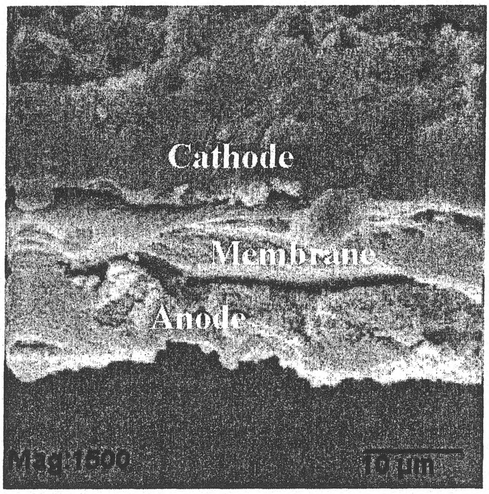

Figure 2. Fabricated ultra-thin composite MEA with a total thickness less than 50μm

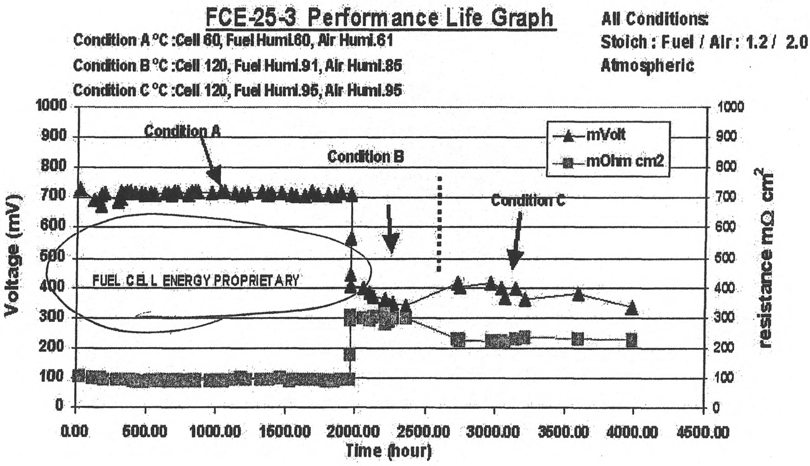

Figure 3. Endurance testing of a baseline MEA:
In addition to the need to improve membrane stability, cathode performance also needs substantial enhancement.

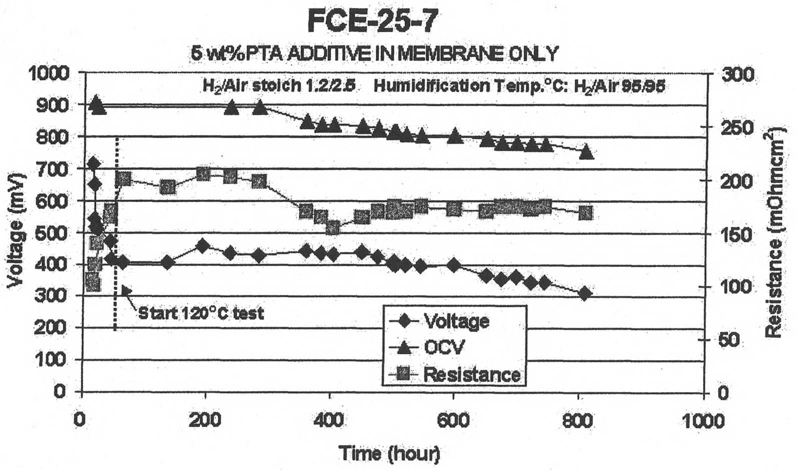

Fig 4. Endurance testing of MEA with PTA-impregnated membrane:
Crossover developed after 300 hours as indicated by the OCV decrease

Proceedings of The Electrochemical Society, PV 2002-31, 426-439 (2002)
DOI: 10.1149/200231.0426PV © The Electrochemical Society

PERFORMANCE OF HIGH TEMPERATURE PROTON EXCHANGE MEMBRANE FUEL CELLS UNDER OFF-DESIGN CONDITIONS

V. Ramani, A. Smirnova, H. R. Kunz, J. M. Fenton

Department of Chemical Engineering,
University of Connecticut, Storrs, CT 06269.

ABSTRACT

PEMFCs are well suited for transportation applications by virtue of their efficiency and high power densities. Several advantages result by operating a PEMFC at elevated temperatures (above 100°C). An important factor to be considered during such operation is the effect of exposure to adverse off-design conditions on fuel cell performance. In this study, cells were built that conform to a defined baseline performance (H_2/air; atmospheric pressure) at 120°C with reactant gases saturated at 90°C (38% exit relative humidity). The cells were then subject to harsh off-design conditions in a series of five increasingly challenging sequences, with temperatures going up to 150°C and reactant gas saturation temperature going down to 20°C (exit relative humidity going down to ~2%). The first and final run in each sequence were carried out at baseline conditions to determine the effect of exposure to off-design conditions on baseline performance. The results are discussed in this paper.

INTRODUCTION

Proton Exchange Membrane Fuel Cells (PEMFCs) are well suited for a variety of applications by virtue of their efficiency and high power densities. From an automotive application point of view, several advantages result by operating a PEMFC at elevated temperatures (above 100°C), such as easier and more efficient water management, higher reaction rates and better CO tolerance by the anode electrocatalyst leading to lower noble metal loadings, better system integration, higher quality waste heat and higher heat rejection rates. For other applications such as portable power and military use, the onus is on low relative humidity operation to obviate the need for saturating reactant gases – thereby reducing considerably the volume and complexity of the fuel cell system. Therefore, a significant economic incentive exists to develop and commercialize PEMFCs that operate at high temperatures and low relative humidities.

One of the most common PEMs in use today is the perfluorosulfonicacid based Nafion membrane. While this membrane performs very well in a saturated environment, its proton conductivity has a strong dependence on water content. Its water uptake, and consequently proton conductivity, decreases considerably at low relative humidities (1), leading to large resistive losses and a reduction in cell voltage. This drawback essentially means that the Nafion membrane cannot be used 'as is' for high temperature (>100°C) applications at ambient pressures. Nafion based organic / inorganic composite membranes with heteropolyacids additives have been shown (2, 3, 4) to maintain sufficient protonic conductivities for viable operation at temperatures above 100°C. In overpotential at elevated temperatures. We have recently carried out the optimization of the cathode structure for operation under these conditions (5). The objective of this work was to determine the effect of sudden adverse changes in operating conditions such as cell temperature and relative humidity on factors such as membrane integrity, membrane conductivity and cathode catalytic activity, all of which have been identified as key factors affecting long term endurance and stability of the cell (6). The results of a study conducted to this end are discussed below.

EXPERIMENTAL

In this study, cells were built that conform to defined baseline performance of 0.45 V or above at a current density of 400 mA/cm^2 for ambient pressure, H_2/air operation at a cell temperature of 120°C with reactant gases saturated at 90°C (defined as baseline conditions). The membrane electrode assembly (MEA) used for the experiments consisted of a modified 0.8 mil thick recast Nafion 1100 membrane impregnated with phosphotungstic acid, with 45% Pt/C (0.32 mg/cm^2 noble metal loading) and 54% Pt-Ru/C (0.4 mg/cm^2 noble metal loading) on the cathode and anode respectively. The electrolyte (Nafion 1100) loading in both catalyst layers was 25% by weight as determined in the optimization study (3). The active area of the MEA was 5 cm^2. Commercial gas diffusion layers obtained from SGL Carbon, LLC, were used in this study. The operation of the cell was characterized by linear sweep voltammetry, cyclic voltammetry, and cell voltage / current density performance testing.

Linear Sweep Voltammetry (LSV)

LSV experiments were performed at room temperature to evaluate and monitor fuel crossover and to check for the presence of electronic shorts. The experiments were done using a PAR potentiostat with a flow rate of 200 ccm of H_2 on the anode and 200 ccm of N_2 on the cathode. A scan rate of 4 mV/s was used in the range of 0-800 mV cell voltage with higher voltages being avoided to prevent Platinum oxidation. The experiments were performed regularly throughout the study.

Cyclic Voltammetry (CV)

CV experiments were carried out to determine and monitor the electrochemically active surface area (ECA) of the cathode catalyst. The experiments were done using a PAR potentiostat with a flow rate of 50 ccm of 4% H_2 (balance N_2) on the anode and 50 ccm of N_2 on the cathode. A lower concentration of H_2 was used to reduce H_2 evolution from the cathode at low potentials. A scan rate of 20 mV/s was used in the range of 0-800 mV cell voltage. The ECA was determined from the voltammogram using a technique described elsewhere (7). The experiments were carried out at room temperature to avoid uncertainties in the H_2 reference electrode potential at higher temperatures, and to minimize the effects of gas crossover.

Cell Performance

The performance of the cell was evaluated by obtaining polarization curves at 80°C (anode gas saturated at 80°C and cathode gas saturated at 73°C) and 120°C (both anode and cathode gases saturated at 90°C). The data was obtained using the Fuel Cell Test System (No. 890 B) manufactured by Scribner Associates. The system was connected to a home built flow loop, and controlled by the Fuel Cell software. H_2 was used at the anode, while both O_2 and air were used at the cathode. The cell was started up by increasing the cell temperature set point to 80°C and raising the saturator temperatures to their respective values. Care was taken to maintain a temperature differential between the cell and the saturators to prevent condensation inside the cell. Similarly, the fuel and oxidant line temperatures were also maintained 10°C higher than the saturators to prevent condensation in the lines. Once the operating conditions were attained, the voltage and cell resistance were monitored at a current density of 400 mA/cm^2 until they attained a constant value. At this point, cell performance was measured as a function of current density with each condition held over 5 minutes. The resistance was also monitored using the current interrupt technique. In this manner, 80°C and 120°C performance data were obtained for oxygen and air, and were repeated over a period of 6 days with several shut downs and start ups. Both LSV and CV experiments were carried out prior to each start up. All experiments were carried out at ambient pressure

Off-Design Testing

Once stable cell performance that confirmed to requirements at baseline conditions (as defined earlier) was attained, the cell was subject to harsh off-design conditions in a series of five challenging sequences with temperatures going up to 150°C and reactant gas saturation temperature going down to 23°C. The operating conditions for the runs carried out in each of the sequences are described in Table 1. At each off–design condition, the cell was equilibrated until steady state performance was attained. Performance was then measured as described earlier. The reactant gases were H_2 and air, and all runs were performed at ambient pressure. The first and final run in each sequence were carried out at baseline conditions to determine the effect of exposure to off-design conditions on baseline performance. The cell was equilibrated at 80°C between sequences. Finally, transient effects were determined by holding the cell at a current density of 400 mA/cm^2 and monitoring the membrane resistance and cell voltage as the exit relative humidity was first decreased and then brought back up to baseline. The voltage and resistance at each condition were noted on attaining a steady state value, which typically took about 20 minutes. The change in relative humidity was implemented both by increasing cell temperature while maintaing constant saturator temperatures, and by decreasing saturator temperatures for a given cell temperature. LSV and CV experiments were performed periodically between sequences.

Table 1

Operating conditions for the runs performed in each sequence.
120 – 90 – 90 refers to a cell temperature of 120°C, and anode gas saturation temperature of 90°C and a cathode gas saturation temperature of 90°C.

Sequence Number	Run 1	Run 2	Run 3	Run 4	Run 5	Run 6
1	120-90-90	120-80-80	120-60-60	120-40-40	120-90-90	-
2	120-90-90	120-80-80	120-60-60	120-40-40	120-23-23	120-90-90
3	120-90-90	140-90-90	120-90-90	-	-	-

4	120-90-90	140-90-90	150-90-90	120-90-90	-	-
5	120-90-90	140-90-90	140-80-80	140-60-60	140-40-40	120-90-90

RESULTS AND DISCUSSION

Linear Sweep Voltammetry

The cell maintained its integrity throughout the testing program despite the use of a thin membrane, with no internal shorting and a crossover current lower than 2 mA/cm^2 in all cases. The results of the LSV measurements are shown in Fig. 1.

Cyclic Voltammetry

A reproducible voltammogram was obtained after 4 days of operation. The voltammogram was well resolved, with a clearly distinguishable second inflection point. From this voltammogram, the ECA was determined to be 17 m^2/g-Pt by evaluating the area under the hydrogen reduction peak. The error in estimating the ECA was determined to be ± 2 m^2/g-Pt. This error arose due to small uncertainties in pinpointing the exact position of the bounds of the reduction peak, namely the point of onset of hydrogen reduction and the second inflection point prior to the onset of hydrogen evolution. Fig. 2 compares the initial voltammogram to those obtained during the program. This area was lower than would be expected for this catalyst. The difference could be due to the inability to measure the entire platinum surface area using this approach and due to part of the cathode platinum being electrochemically ineffective. Little change was observed until the end of the fourth sequence. However, the hydrogen oxidation peak was observed to have shifted to a more positive potential after the final sequence, and the resolution of the voltammogram was poorer. The area under the reduction peak, and hence the ECA, were found to be nearly constant in all cases (Fig. 3). The slight reduction observed after the final sequence was within the bounds of error. This suggested that the cathode platinum catalyst retained its area even when run at off-design conditions for this period.

Stability of Cell Performance

The cell performance stabilized after an operating period of 4 days at 80°C and 120°C. This finding was in agreement with the results of the voltammetry experiments. Typical polarization curves on oxygen and air at 80°C and 120°C are shown in Fig. 4. The membrane resistance at 80°C and 120°C were found to be 0.065 and 0.165 ohm-cm^2 respectively. The poor limiting currents observed were attributed to mass transport limitations arising from the gas diffusion layer used, which was not optimized for high temperature operation, and the fact that that the experiments were being run with a constant flow rate of reactant gases, leading to very high utilizations (approaching 100%) even at current densities of 1300 mA/cm^2 on air. Notwithstanding these limitations, the performance on air at 120°C and 400 mA/cm^2 was found to be 489 mV, which confirmed to baseline requirements.

Off-Design Testing

During the course of the first sequence, the cell experienced exit relative humidities of as low as 6 and 10% (down from 35% at baseline conditions) each for an hour or more. However, the performance at baseline conditions decreased only marginally from 480 mV to 450mV at 400 mA/cm^2 (all subsequent references to voltages correspond to a current density of 400 mA/cm^2 unless otherwise stated). This drop was due to losses in the cathode layer, as the membrane resistance was found to regain its original value during the retest. It was interesting to note that during 120-80-80 operation (24% exit relative humidity), the membrane resistance contributed to 92% of the total loss in performance. This could be due to the fact that the losses due to dehydration of ionomer in the catalyst layer and the resulting reduction in oxygen permeability and cathodic ionic conductivity were nearly compensated by the gains due to the increase in the partial pressure of oxygen and hydrogen. However, a further decrease in relative humidity to 10% and then down to 6% resulted in overwhelming cathodic losses. The second sequence was similar to the first, with an added run at 120-23-23, corresponding to an exit relative humidity of 2%, being the only difference. The results were found to mirror those observed in the first sequence, with a similar 25-30 mV difference in performance between the baseline test and retest. Once again, this difference was due to losses in the cathode layer, with the membrane resistance regaining its original value. Similar results were also obtained for the 120-80-80 run, and other subsequent runs. The results of the first two sequences are shown in Figs. 5 (a) and 5 (b).

Sequences 3 and 4 involved lowering relative humidity by increasing the cell temperature as opposed to the previous two sequences, where this was achieved by lowering the saturator temperatures. The results are shown in Figs. 6 (a) and 6 (b) respectively. In each case, a higher performance loss of about 40 mV between the baseline test and retest was noted. The loss was again due to the cathode layer, with the membrane resistance regaining its original value in both cases. Unlike the previous cases where a 10°C drop in saturator temperatures led to losses that were mainly due to membrane resistance, the increase in cell temperature resulted in losses due to both the membrane resistance and increased cathodic overpotential, with the split being nearly even. Besides, a near threefold increase in the magnitude of the loss occurred. While the absence of the beneficial effect of increased oxygen and hydrogen partial pressure in the latter case could account for some of the differences observed, the extent of losses incurred implied that an increase in cell temperature extracts a greater penalty from the cell when compared to a decrease in gas saturation temperature. Therefore, transients in increasing cell temperature would be expected to be particularly harmful.

Sequence 5 represented a combined approach to lowering relative humidity, with the cell temperature being increased to 140°C, and the saturator temperatures being progressively lowered all the way down to 40°C. The results are shown in Fig. 7. While the increase in temperature from 120 to 140°C produced results identical to those seen in earlier sequences, running the cell at 140°C and very low humidities during subsequent runs was found to have a detrimental effect on the activity of the cathode catalyst. A comparison between the baseline test and retest revealed a displacement of 50 - 60 mV in the Tafel region as opposed to the 15-25 mV displacement observed in earlier cases. Moreover, unlike in earlier sequences, subsequent equilibration at baseline conditions did not result in any improvement in performace. The effect of operation under such stringent conditions on the cathode was also observed in the cyclic voltammetry experiments as discussed earlier.

Finally, the transient studies yielded hysterisis curves for resistance and voltage measurements for both measurement techniques. The results are shown in Figs. 8 (a) – 8 (d). It was seen that the earlier trends in performance loss distribution were maintained to a certain extent in this experiment, with the membrane resistance contributing to approximately half the voltage loss when the cell temperature was increased with constant saturator temperatures.

CONCLUSIONS

This study revealed the ability of the MEA studied to provide reproducible performance at 120°C at a relative humidity of ~ 35% over a period of several days. Additionally, it showed that the MEA was not adversely affected by exposure to harsh off-design conditions of increased cell temperatures and greatly reduced relative humidities and displayed excellent recovery properties. While a performance loss was observed on retesting immediately at baseline conditions, this loss was recovered upon subsequent equilibration at baseline conditions and at more benign conditions. The membrane resistance at baseline conditions remained nearly constant throughout the program, and there was no evidence of crossover or internal shorting, which was commendable given the thickness of the membrane used. The cathode catalyst layer proved to be very stable, and only showed deterioration at the very end of the program after tens of hours of operation at off-design conditions. The deterioration was thought to be due to platinum recrystallization or carbon corrosion, though no conclusive evidence for either mechanism was found. The near constant ECA suggested that the contact between the ionomer and the catalyst was retained throughout the program. Overall the MEA demonstrated very good performance under testing conditions. It must be noted, however, that the entire testing sequence lasted only for a period of a few days. Even so some performance deterioration was evident towards the end. Long-term (1000s of hours) endurance of the MEA under baseline conditions remains very much a challenge, and is an issue we plan to address in our future endeavors.

FUTURE DIRECTIONS

Proposed research endeavors include a detailed study on the effect of membrane composition (additive type, concentration and size on performance under steady state and transient operation conditions at high temperature and determination of the effect of low exit relative humidities on the distribution of overpotentials using different diagnostic gases such as helium-oxygen and 4% O_2 (balance N_2) on the cathode. Endurance testing at constant current conditions for ambient pressure 120-90-90 operation is currently underway, and will be actively pursued over the next several months.

ACKNOWLEDGEMENTS

The authors would like to acknowledge Los Alamos National Laboratories for the financial support provided for this study under proposal subcontract number 25686-001-01-23, and SGL Carbon, LLC, for providing the gas diffusion layers used in this study.

REFERENCES

1. T. A. Zawodzinski, Jr., C. Derouin, S. Radzinski, R. J. Sherman, T. Springer, S. Gottesfeld, *J. Electrochem. Soc.*, 140, 1041 (1993)
2. S. Malhotra, R. Datta, *J. Electrochem. Soc*, 144, L23 (1997)

3. B. Tazi, O. Savadogo, *Electrochimica Acta*, 45, 4329 (2000)
4. A. Smirnova, C. Hawk, V. Ramani, H. R. Kunz, J. M. Fenton, *Abstracts of the 200th Meeting of the Electrochemical Society*, San Francisco, September 2001.
5. V. Ramani, A. Smirnova, H. R. Kunz, J. M. Fenton, Manuscript under preparation
6. S. Gottesfeld, T. A. Zawodzinski, Polymer Electrolyte Fuel Cells, Advances in Electrochemical Science and Engineering, R. C. Alkire, H. Gerischer, D. M. Kolb, C. W. Tobias ed. (1996)
7. M. Wakizoe, O. A. Velev, S. Srinivasan, *Electrochimica Acta,* 40, 2, 335 (1995)

Fig. 1

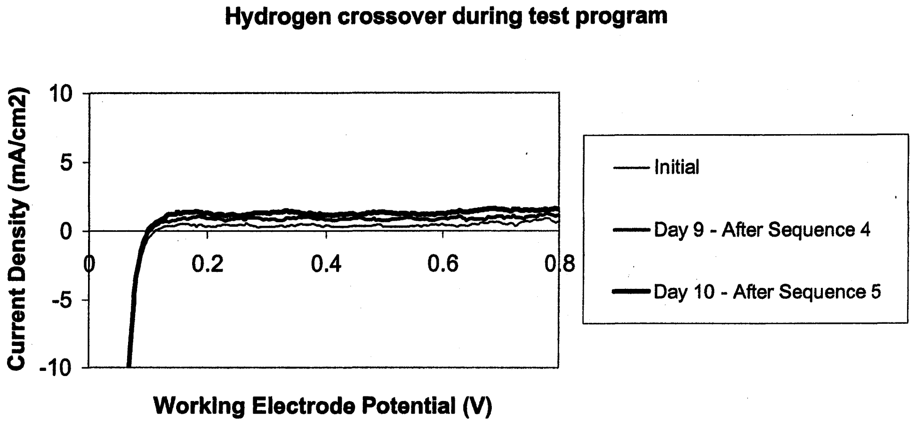
Hydrogen crossover during test program
Current Density (mA/cm2)
10
5
0
-5
-10
0
0.2
0.4
0.6
0.8
Working Electrode Potential (V)
Initial
Day 9 - After Sequence 4
Day 10 - After Sequence 5

Fig. 2

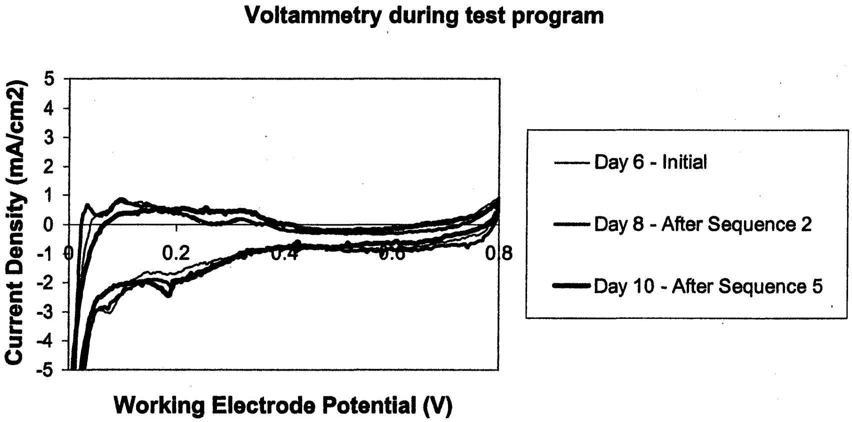
Voltammetry during test program
Current Density (mA/cm2)
5
4
3
2
1
0
-1
-2
-3
-4
-5
0
0.2
0.4
0.6
0.8
Working Electrode Potential (V)
Day 6 - Initial
Day 8 - After Sequence 2
Day 10 - After Sequence 5

Fig. 3

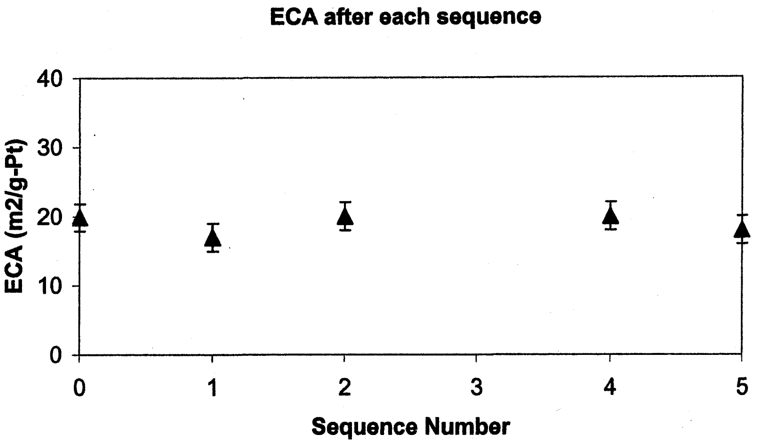
ECA after each sequence
ECA (m2/g-Pt)
40
30
20
10
0
0
1
2
3
4
5
Sequence Number

Fig. 4

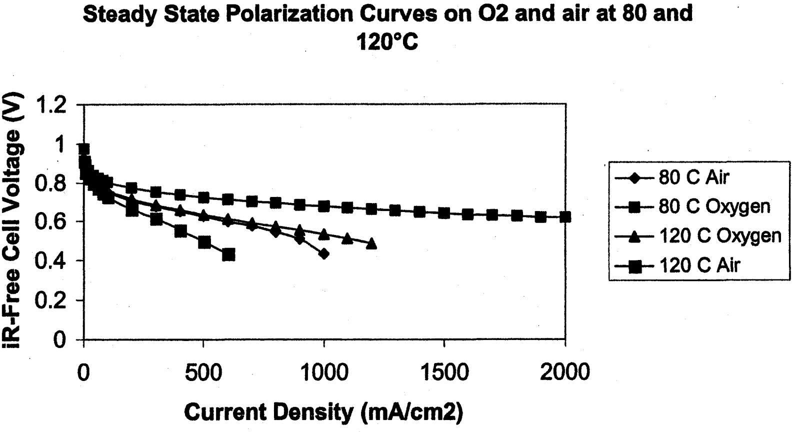
Steady State Polarization Curves on O2 and air at 80 and 120°C
iR-Free Cell Voltage (V)
1.2
1
0.8
0.6
0.4
0.2
0
0
500
1000
1500
2000
Current Density (mA/cm2)
80 C Air
80 C Oxygen
120 C Oxygen
120 C Air

Fig. 5 (a)

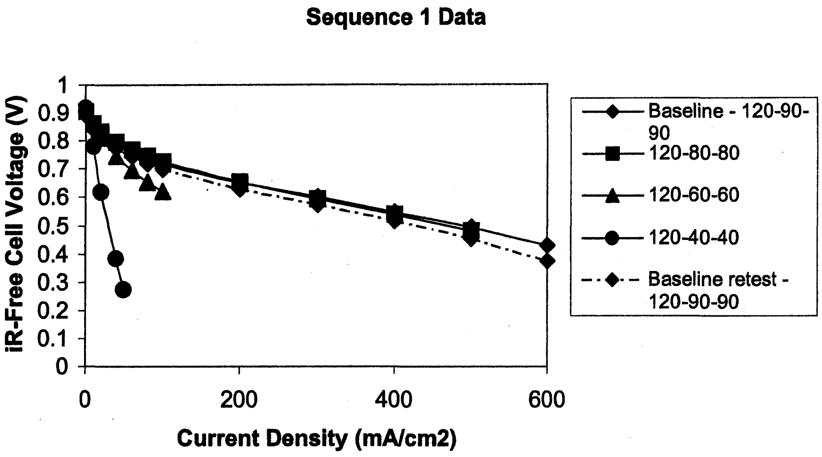
Sequence 1 Data
iR-Free Cell Voltage (V)
1
0.9
0.8
0.7
0.6
0.5
0.4
0.3
0.2
0.1
0
0
200
400
600
Current Density (mA/cm2)
Baseline - 120-90-90
120-80-80
120-60-60
120-40-40
Baseline retest - 120-90-90

Fig. 5 (b)

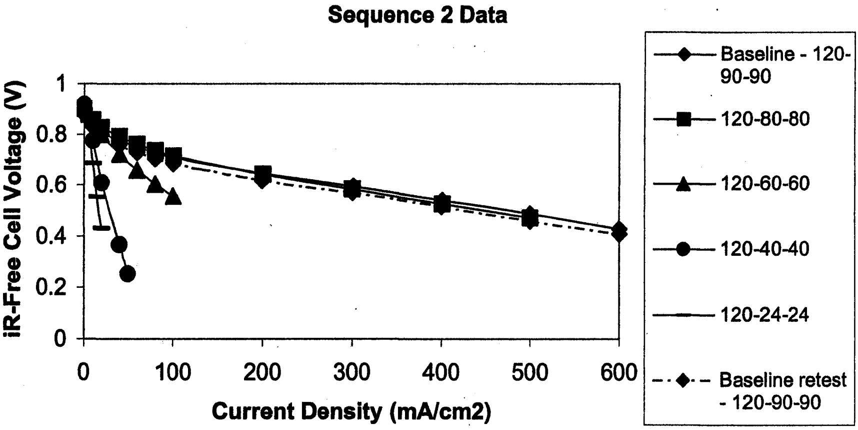
Sequence 2 Data
iR-Free Cell Voltage (V)
1
0.8
0.6
0.4
0.2
0
0
100
200
300
400
500
600
Current Density (mA/cm2)
Baseline - 120-90-90
120-80-80
120-60-60
120-40-40
120-24-24
Baseline retest - 120-90-90

Fig. 6 (a)

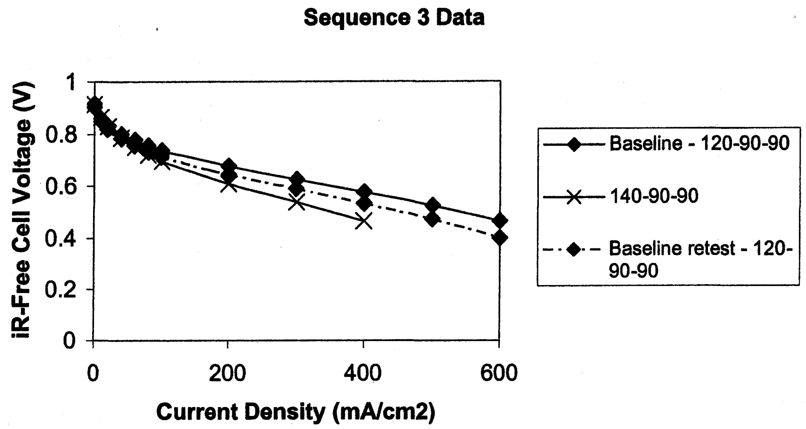
Sequence 3 Data
iR-Free Cell Voltage (V)
1
0.8
0.6
0.4
0.2
0
0
200
400
600
Current Density (mA/cm2)
Baseline - 120-90-90
140-90-90
Baseline retest - 120-90-90

Fig. 6 (b)

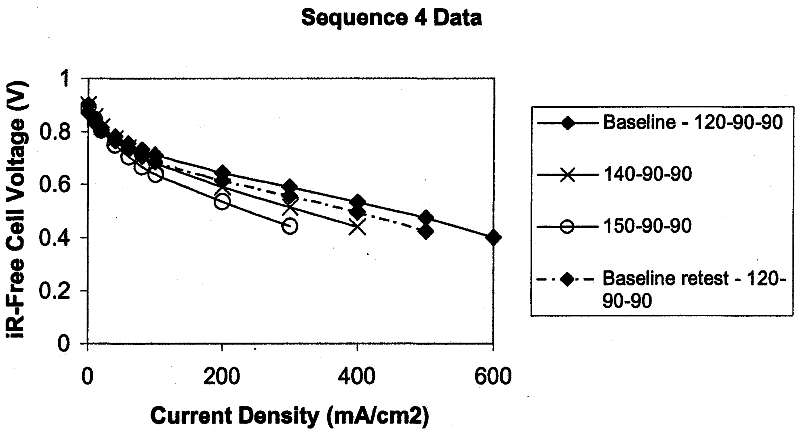
Sequence 4 Data
iR-Free Cell Voltage (V)
1
0.8
0.6
0.4
0.2
0
0
200
400
600
Current Density (mA/cm2)
Baseline - 120-90-90
140-90-90
150-90-90
Baseline retest - 120-90-90

Fig. 7

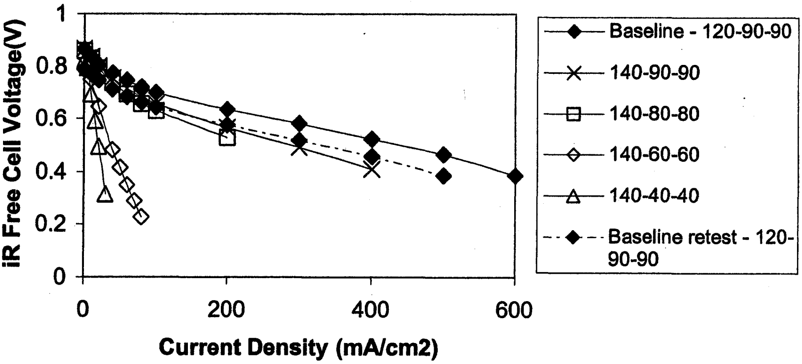
Sequence 5 Data
iR Free Cell Voltage(V)
1
0.8
0.6
0.4
0.2
0
0
200
400
600
Current Density (mA/cm2)
Baseline - 120-90-90
140-90-90
140-80-80
140-60-60
140-40-40
Baseline retest - 120-90-90

Fig. 8 (a)
Transient studies

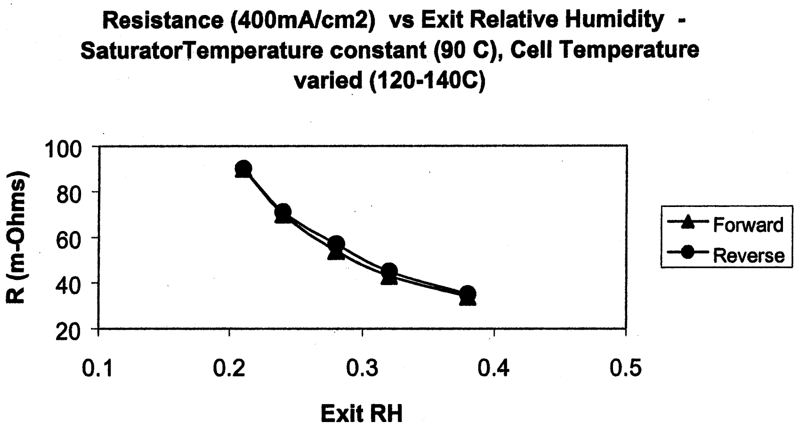

Fig. 8 (b)
Transient studies

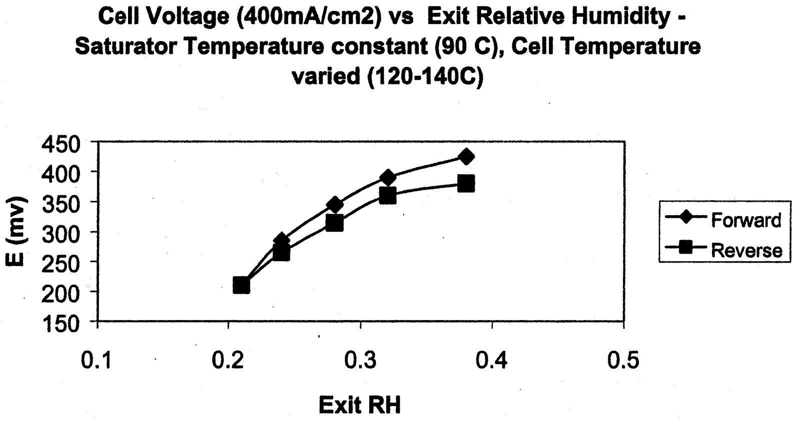

Fig. 8 (c)
Transient studies

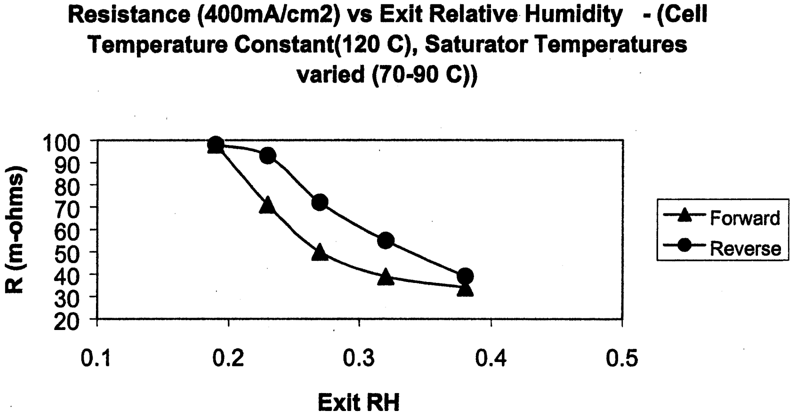

Fig. 8 (d)
Transient Studies

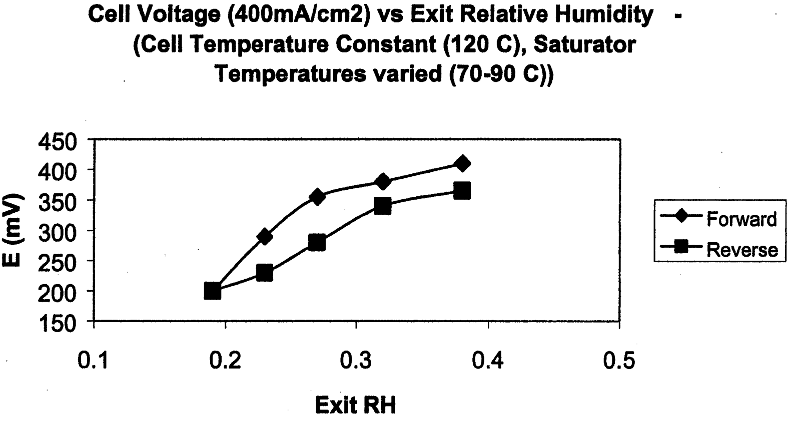

Proceedings of The Electrochemical Society, PV 2002-31, 440-449 (2002)
DOI: 10.1149/200231.0440PV © The Electrochemical Society

CO TOLERANCE IN PBI/H$_3$PO$_4$ POLYMER ELECTROLYTE FUEL CELLS

J. S. Wainright, J. Staser and R. F. Savinell
Department of Chemical Engineering
Case Western Reserve University
Cleveland OH 44106-7218

ABSTRACT

An extended study of the effects of CO on hydrogen anode performance has been carried out using PBI/H$_3$PO$_4$ fuel cells with Pt on XC-72 as a catalyst. Three different commercial electrode structures were considered. The charge transfer resistance for hydrogen oxidation for two different concentrations of CO in the hydrogen feed was determined for the three electrode structures at temperatures of 155, 175 and 195 °C. In order to achieve tolerance to 2%CO at 155 °C, an active Pt area on the order of 700 cm^2 per cm^2 of geometric area may be required.

INTRODUCTION

It is well known that there are several promising attributes associated with hydrogen fueled polymer electrolyte fuel cells; high efficiency and high power density, relatively simple, quiet and non-polluting operation, a non-corrosive electrolyte, and low operating temperatures. Together, these attributes provide a general suitability to a wide range of applications and power levels from watts to hundreds of kilowatts. These promising attributes have always been tempered by the difficulties associated with hydrogen as a fuel; poor energy density if hydrogen is stored as compressed gas or in a metal hydride, and intolerance to the ever-present carbon monoxide when hydrogen is produced from reformation of hydrocarbons. At the anode potential of a hydrogen-fueled device, carbon monoxide is a known poison on platinum, the electrocatalyst of choice. A theoretical calculation of CO coverage on Pt as a function of temperature and CO concentration has recently been presented [1]. The literature on CO adsorption is extensive, and a number of remedies have been developed, including use of alloy electrocatalysts such as Pt/Ru and Pt/Mo [2,3], bleeding air into the anode to chemically oxidize adsorbed CO [4] and moving to higher operating temperatures, where the equilibrium adsorbed CO content is lowered.

The development of polymer electrolytes capable of operating at temperatures in excess of 120 °C has been fairly recent and has been focused on two approaches, acid doping of basic polymers, such as polybenzimidazole (PBI) doped with phosphoric acid

[5], and electrolytes prepared by incorporating various hydrous oxides into perfluorosulfonic acid membranes, such Nafion/$ZrPO_4$ [6] or Nafion/SiO_2 [7].

Polybenzimidazole (PBI) is commercially manufactured by Hoechst-Celanese primarily for use in fabrics for fire protection clothing. The polymer is high temperature resistant and chemically stable. It has a glass transition temperature of about 450 °C because of its all-aromatic structure. The benzimidazole group has a pKa of about 5.5, which facilitates its absorption of acid, which can act as a plasticizer. Various aspects of the PBI/H_3PO_4 electrolyte have been previously presented, including conductivity investigations [8,9], hydrogen [10] and direct methanol fuel cell performance [11], thermal stability [12], and permeability and electro-osmotic drag determinations [13]. Examples of the CO tolerance of this system have also been reported as shown in Figure 1 [14]. In this figure, it can be seen that an electrode based on a Pt black catalyst, at a fairly high loading (2.6 mg Pt/cm^2) can achieve a high degree of CO tolerance - 30 mV loss (1%CO vs pure H_2) at 700 mA/cm^2 and 175 °C. In this paper the CO tolerance of platinum supported on Vulcan XC-72 in the form of three different commercial electrode structures will be examined.

EXPERIMENTAL

Polybenzimidazole films were prepared from PBI powder obtained from Hoechst-Celanese. In order to increase the average molecular weight of polymer to produce high quality films, the lower MW components were extracted by fractionation in dimethyl acetamide (DMAc). Typical extraction conditions and results for the yield of undissolved polymer are given in [15]. The higher molecular weight fraction of the polymer was then dissolved at higher temperatures in DMAc with 1-2 wt% LiCl added to maintain solution stability. Films were cast onto glass plates, the solvent evaporated, and the film washed in boiling water to remove the residual LiCl. Doping of the films was accomplished by immersion in 11M phosphoric acid solutions. This procedure yields a doping level of ≈500 mol% phosphoric acid, i.e., 5 H_3PO_4 molecules per polymer repeat unit. Film thicknesses after doping were typically 0.01 cm (4 mil).

Membrane electrode assemblies (MEA) were prepared using three different electrode materials obtained from E-tek; 1) “EFCG” electrode, Toray carbon paper backing (TGPH-120), 10%Pt on carbon, 0.35 mg Pt/cm^2, 2) “ELAT” V2.11 -single sided, carbon cloth backing, 20%Pt on carbon, 0.35 mg Pt/cm^2 and 3) “ELAT-HL”, carbon cloth backing, 40% Pt on carbon, 2 mg Pt/cm^2. In each case the carbon support is Vulcan XC-72 and the backing is wet-proofed. The EFCG electrode is typically used in liquid phosphoric acid fuel cells, while the ELAT and ELAT-HL are intended for use in polymer electrolyte (e.g. Nafion) fuel cells. In each case, the electrode was imbibed with phosphoric acid by soaking for five minutes in a solution of 1 part by volume 5M H_3PO_4 and 7 parts by volume ethanol. The imbibed electrodes were then dried at 120 °C in air for 15 minutes. Doped PBI membranes were dried at 95 °C under vacuum for one hour. The dried electrodes were pressed onto dried membranes at a temperature of 150 °C and a pressure of 0.9×10^7 N/m^2 (200 lb_f over 1 cm^2) [16]. No attempts were made to optimize the acid imbibing or hot pressing procedures for the different electrode types.

Membrane electrode assemblies with an active area of 1 cm^2 were placed in fuel cell hardware with 316 stainless steel flow field plates for testing. The fuel cell assembly was then placed in a forced convection oven for temperature control. Each cell was held at temperature for two hours before the hydrogen polarization and cyclic voltammetry data were collected. The flow rate of the reactant gases was controlled using mass flow controllers (MKS) and were typically 16 sccm for H_2, and 18sccm for N_2. The reactants were humidified by passing the gasses through temperature controlled bubblers, and were passed through several feet of coiled stainless steel tubing inside the oven to insure that the gasses were at the desired temperature before being introduced into the fuel cell.

The active platinum area for each electrode was estimated from hydrogen adsorption areas as determined by cyclic voltammetry. For these experiments the working electrode was fed a stream of humidified nitrogen, while the counter electrode (which also served as a reversible hydrogen reference electrode) was fed humidified hydrogen. Cyclic voltammetry of the working electrode was then obtained at 50 mV/s sweep rate, between 0.025 and 1.0 V vs RHE. Integrating the anodic sweep between 0.05 and 0.35 V vs RHE and correcting for the background charge due to double layer charging determined the hydrogen adsorption charge. The active area was then determined by dividing the hydrogen adsorption charge by 210 μC/cm^2 [17].

The charge transfer resistance for hydrogen oxidation (Rct) was determined using AC impedance spectroscopy on cells operating as hydrogen pumps, i.e., the anode oxidized hydrogen as in the fuel cell, while the cathode evolved hydrogen. For the hydrogen oxidation experiments the reactant gas was fed into one compartment of the fuel cell, and then in series to the other side of the cell. The measured impedance represents the combined impedance of the anode and cathode. The impedance spectrum was acquired at the open circuit potential, with an AC amplitude of 10 mV RMS over a frequency range of 20,000 Hz to 0.2 Hz, at five discrete frequencies per decade, equally spaced in log frequency. Under these small amplitude conditions it was assumed that the anode and cathode overpotentials were equal. The anode charge transfer resistance was then taken to be 50% of the total charge resistance measured.

RESULTS AND DISCUSSION

Determination of Active Pt Area

Estimated active Pt areas (given as a roughness factor - Pt area per unit geometric area) obtained from the hydrogen adsorption region in the cyclic voltammetry are listed in Table I for the three types of electrodes used. The total Pt area is calculated from the product of the Pt loading and the specific Pt area for each catalyst; these values are based on information available from the manufacturer. The effective Pt utilization is calculated by dividing the active area by the total Pt area.

It is clear from Table I that the procedure used to imbibe electrolyte into these electrode structures is not optimal; achieving optimal performance was not the goal of this project. However, it should be possible to take the results presented below and predict the degree of CO tolerance under a given set of conditions and a known active platinum area. The probable explanation for the low utilization observed is that the phosphoric acid that is imbibed into the electrode structures equilibrates with the acid doped into the PBI membrane. The acid in the electrodes, being more highly concentrated than the 11M solution used to dope the membranes, will be taken up by the membrane, increasing the membrane doping level slightly, while lowering the amount of acid within the electrode structure. As a result, the ionic conductivity within the electrode structure is low, and the Pt utilization is also low.

TABLE I

Estimated Active Pt Area and Pt Utilization for the Three Electrode Types

Electrode Type	Estimated Active Area cm^2/cm^2	Pt Loading mg /cm^2	Specific Pt Area m^2/g	Total Pt Area cm^2/cm^2	Pt Utilization
EFCG	67	0.35	140 (10% Pt on C)	490	13.6%
ELAT V2.1	24	0.35	112 (20% Pt on C)	390	6.1%
ELAT-HL	143	2.0	72 (40% Pt on C)	1440	9.9%

CO Poisoning - Effect of Temperature

Examples of typical impedance spectra are shown in Figure 2 (Nyquist and Bode formats) for hydrogen with 0.1 and 2% CO. These spectra were obtained with the EFCG electrodes at a temperature of 175 °C, and with the reactant gas humidified at 60 °C. As can be seen in the figure, nearly perfect semi-circles are obtained in the Nyquist representation, indicating that spectra can be simply modeled in terms of the membrane resistance (high frequency intercept of the real axis), double layer capacitance and a single charge transfer resistance - both electrodes are essentially identical. There is no apparent dispersion from distributed impedance effects or from mass transfer limitations. The high frequency intercept with the real axis, ca. 0.3 Ωcm^2, is consistent with the known conductivity of the PBI/H_3PO_4 electrolyte under these conditions and the membrane thickness of 0.01 cm.

Results for the anode charge transfer resistance, based on geometric area, are given in Tables II and III for the three different electrode types and for CO levels of 0.1% and 2% in H_2 at temperatures of 155, 175 and 195 °C. The reactant gas was humidified at 25 °C. The tables also list the values for the charge transfer resistance when scaled by the active Pt area as given in Table I.

Table II

H_2 Oxidation Charge Transfer Resistance (Rct) as a Function of Temperature
0.1%CO in H_2

Electrode Type	155 °C	175 °C	195°C
EFCG	0.38 / 25.5	0.15 / 10.1	0.065 / 4.4
ELAT V2.1	0.80 / 19.2	0.47 / 11.3	0.17 / 4.1
ELAT-HL	0.17 / 24.3	0.11 / 15.7	0.045 / 6.4

in each field - the first value is Rct in Ωcm^2 based on geometric area.
the 2nd value in each field is Rct scaled by the active Pt area

Table III

H_2 Oxidation Charge Transfer Resistance (Rct) as a Function of Temperature
2%CO in H_2

Electrode Type	155 °C	175 °C	195°C
EFCG	1.2 / 80.4	0.60 / 39.9	0.26 / 17.4
ELAT V2.1	3.0 / 72.0	0.95 / 22.8	0.46 / 11.0
ELAT-HL	0.67 / 95.8	0.23 / 32.9	0.10 / 14.3

in each field - the first value is Rct in Ωcm^2 based on geometric area.
the 2nd value in each field is Rct scaled by the active Pt area

For purposes of discussion, we will arbitrarily define 'CO tolerance' as a charge transfer resistance (based on geometric area) of $<0.1\ \Omega cm^2$, e.g., 30 mV loss in the presence of CO at 300 mA/cm^2. For the 2%CO case, the active Pt area required to achieve tolerance is then 100-200 cm^2/cm^2 at 195 °C, 200-400 cm^2/cm^2 at 175 °C, and 700-1000 cm^2/cm^2 at 155°C. The roughness factors required at the higher temperatures should be easily achievable, and indeed a higher level of tolerance is shown in Figure 1. At lower temperatures a far more effective electrode structure is required than is considered here.

If it can be assumed that the intrinsic activity of the 10, 20 and 40 wt% Pt on XC-72 catalysts is similar, than the scaled Rct values for each combination of temperature and CO content should be the same for each electrode. In several cases there is such agreement between two of the three electrodes, but the value for the third electrode is somewhat different. However, the identity of the differing electrode, and the nature of the difference (higher or lower) is apparently random. It should be noted that repeated measurements for samples under the same conditions were reproducible. For example, the value given for the EFCG electrode at 175 °C and 2%CO is the average of two samples, with two measurements from each sample. The individual values for Rct were 0.56, 0.6, 0.61 and 0.61 Ωcm^2.

For comparison with Table III, Table IV presents charge transfer resistance for hydrogen oxidation as derived from Dhar et al. [17] for 1 and 3 %CO at 150, 170 and 190 °C. These values were obtained in liquid phosphoric acid electrolyte, using Pt on XC-72 (40 wt% Pt) as a catalyst. Dhar et al. stated that their electrochemically active Pt area was 150 m^2/g, giving a total Pt area of 600 cm^2/cm^2. The values for Rct scaled by the active Pt area are in rough agreement in Tables III and IV. This suggests that the intrinsic activity of the catalyst is similar in the two different electrolytes.

Table IV
Hydrogen Oxidation Charge Transfer Resistance in Liquid H_3PO_4
estimated from Figures 4 and 5 in ref [x].

1%CO				3%CO		
150 °C	170 °C	190 °C		150 °C	170 °C	190 °C
0.083 / 50.0	0.033 / 20.0	0.02 / 12.5		0.13 / 79.8	0.054 / 32.5	0.033 / 20.0

in each field - the first value is Rct in Ωcm^2 based on geometric area.
the 2nd value in each field is Rct scaled by the active Pt area

In Figure 3, the data from Tables II and III are presented in the form of ln(Rct) vs 1/T in order to estimate the activation energy for hydrogen oxidation. Given the relatively narrow range of temperatures and the scatter in the data, the activation energy can only be estimated to lie in the range from 55 to 80 kJ/mol. The data given in Table IV for liquid phosphoric acid are consistent with an activation energy in the low end of this range, ≈56-58 kJ/mol.

CO Poisoning - Effect of Humidification

It might be expected that increasing the humidity content in the hydrogen/CO stream would lessen the effects of CO poisoning due to 1) increased conductivity within the electrode structure leading to increased Pt utilization and/or 2) conversion of some of the CO to CO_2 via the water gas shift reaction. To test this hypothesis, the reactant stream was saturated at either 25 or 60 °C. However, repeated experiments with these humidification conditions showed that there was not a significant effect of humidification on the hydrogen oxidation charge transfer resistance.

SUMMARY

Three commercial electrode structures, each containing Pt on Vulcan XC-72 as a catalyst, were imbibed with phosphoric acid and hot pressed to PBI/H_3PO_4 electrolyte membranes. In each case the active Pt area was ca. 10% of the total Pt area present. This resulted in relatively poor CO tolerance. However, when the results were normalized to the active area, the intrinsic catalytic activity was similar to that found in liquid H_3PO_4 electrolyte. Increasing the reactant humidification did not have a significant effect on the CO tolerance. In order to achieve tolerance to 2%CO at 155 °C, an active Pt area on the order of 700 cm^2 per cm^2 of geometric area may be required.

ACKNOWLEDGEMENTS

This material is based on research sponsored by DARPA under agreement DABT63-99-C-0039 via a subcontract from Battelle. The U.S. Government is authorized to reproduce and distribute reprints for Governmental purposes notwithstanding any copyright notation thereon. The views and conclusions contained herein are those of the authors and should not be interpreted as necessarily representing the official policies or endorsements, either expressed or implied of Battelle, DARPA, or the U.S. Government.

REFERENCES

1. C. Yang, P. Costamagna, S. Srinivasan, J. Benziger and A. B. Bocarsly, *J. Power Sources,* **103,** 1 (2001).
2. B. N. Grgur, G. Zhuang, N. Markovic, and P. N. Ross, *J. Phys. Chem. B*, **102,** 2494 (1998).
3. H. F. Oetjen, V. M. Schmidt, U. Stimming and F. Trila, *J. Electrochem. Soc.*, **143,** 3838 (1996).
4. a)S. Gottesfeld and J. Pafford, *J. Electrochem. Soc.*, **135,** 2651 (1988).
   b) F. Uribe and T. A. Zawodzinski, in *Extended Abstracts of the 201st Electrochemical Society Meeting*, Abstract #806, (2002).
5. J.S. Wainright, J-T. Wang, R. F. Savinell, and M. Litt, *J. Electrochem. Soc.*, **142,** L121 (1995).
6. C. Yang, S. Srinivasan, A. S. Arico, P. Creti, V. Baglio, and V. Antonucci, *Electrochemical and Solid-State Letters*, **4,** A31 (2001).
7. N. Miyaki, J. S. Wainright, and R.F. Savinell, *J. Electrochem. Soc.*, **148,** A898 (2001).
8. J. J. Fontanella, M.C. Wintersgill, J.S. Wainright, R.F. Savinell and M. Litt, *Electrochimica Acta*, **43,** 1289 (1998).
9. R. Bouchet and E. Siebert, *Solid State Ionics*, 118, 287 (1999)
10. J. -T. Wang, R. F. Savinell, J. Wainright, M. Litt and H. Yu, *Electrochimica Acta*, **41,** 193 (1996).
11. J. -T. Wang, J. S. Wainright, R. F. Savinell and M. Litt, *J. Appl. Electrochem.,* **26,** 751 (1996).
12. S. R. Samms, S. Wasmus, and R. F. Savinell, *J. Electrochem. Soc.*, **143,** 1225 (1996).
13. D. Weng, J. S. Wainright, U. Landau, and R. F. Savinell, *J. Electrochem. Soc.*, **143,** 1260 (1996).
14. J. S. Wainright, R. F. Savinell and M. H. Litt, in *Proceedings of the 2nd International Symposium on New Materials for Fuel Cells and Modern Battery Systems*, O. Savadogo and P. R. Roberge, eds., p. 808, Montreal, (1997).
15. M. Litt, R. Ameri, Y. Wang, R. Savinell and J. Wainright, *Mater. Res. Soc. Symp. Proc.,* **548,** 313 (1999).
16. S. R. Samms, Ph.D. Dissertation, Case Western Reserve University, (2001).
17. S. K. Zecevic, S. Gojkovic, J. S. Wainright, and R.F. Savinell, *J. Electrochem. Soc.,* **144,** 2973 (1997).
18. H. P. Dhar, L. G. Christner and A. K. Kush, *J. Electrochem. Soc.*, **134,** 3021 (1987).

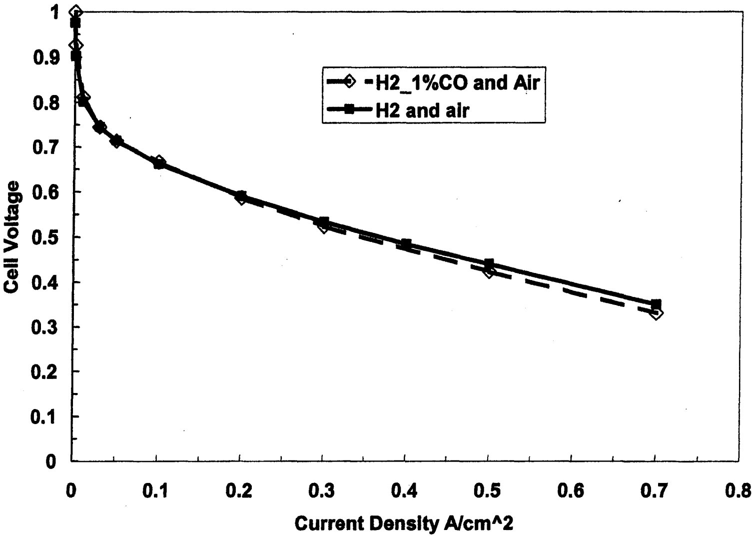

Figure 1: PBI Fuel Cell Polarization Curves on H_2 and H_2 with 1%CO. Temperature: 175 °C, cathode reactant: air, humidified at room temperature, Anode loading: 2.6 mg Pt/cm^2. Reprinted from ref. [14].

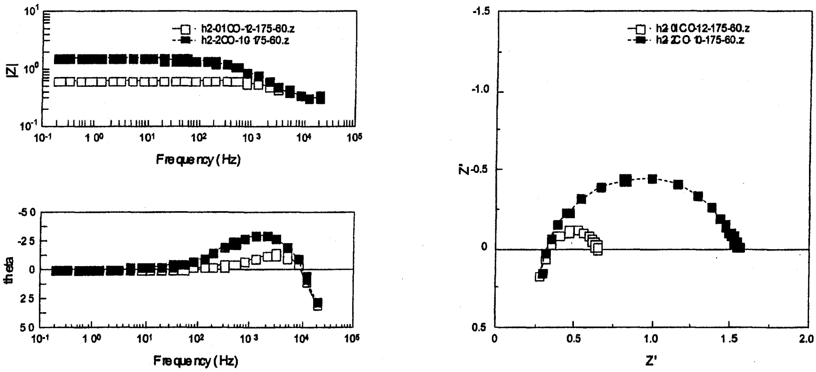

Figure 2: Impedance spectra (Bode and Nyquist formats) for EFCG electrodes exposed to 0.1 %CO (open symbols) and 2%CO (filled symbols) at 175 °C. Reactant gas humidified at 60 °C. Hydrogen pump operation, DC potential = open circuit, AC perturbation 10 mV RMS.

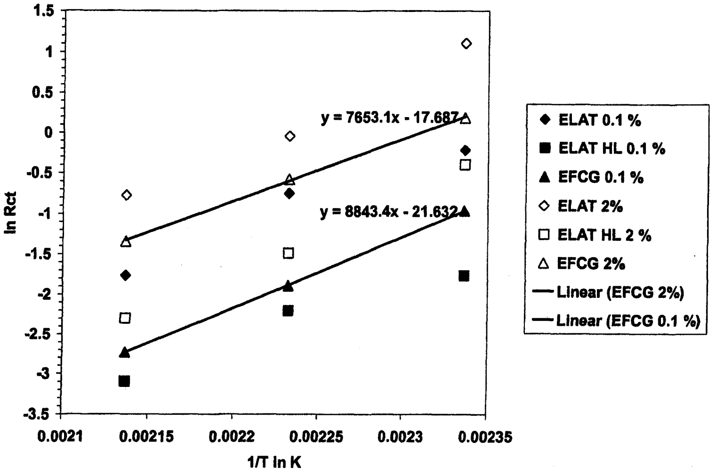

Figure 3. Arrhenius plot of charge transfer resistance for hydrogen oxidation for the three electrode types and 0.1% CO (filled symbols) and 2%CO (open symbols). Two examples of the linear fits used to obtain the activation energy (E_A = slope*8.314 J/mol K) are shown.

Proceedings of The Electrochemical Society, PV 2002-31, 450-467 (2002)
DOI: 10.1149/200231.0450PV © The Electrochemical Society

ELECTROCHEMICAL AND XRD CHARACTERIZATION OF Pt-Ru BLACKS FOR DMFC ANODES

Christian Eickes, Eric Brosha, Fernando Garzon, Gerie Purdy and Piotr Zelenay
Materials Science and Technology Division (MST-11)
Los Alamos National Laboratory, Los Alamos, New Mexico 87545, USA

Takanari Morita and David Thompsett
Fuel Cell Research, Johnson Matthey Technology Centre, Reading, RG4 9NH, UK

ABSTRACT

It is generally accepted that Pt-Ru alloy catalysts with an atomic Pt-to-Ru ratio of 1:1 generate the best anode performance in the direct methanol fuel cell (DMFC). However, at near-ambient cell operating temperatures, Gasteiger *et al.* [1] reported that a catalyst with significantly lower Ru content, ~10 at %, offers the highest activity towards methanol. Recently, Dinh *et al.* [2] demonstrated that the activity of different Pt-Ru catalysts with the same Pt-to-Ru atomic ratio in the bulk might vary depending on the actual surface composition, which is often significantly different from that in the bulk phase. In this work, we study several experimental Pt-Ru catalysts (Johnson Matthey) with Pt-to-Ru atomic ratio ranging from 9:1 to 1:2. Electrocatalytic activity of these catalysts in methanol oxidation reaction is investigated in a regular DMFC and probed using voltammetric stripping of surface CO.

INTRODUCTION

Direct methanol fuel cells (DMFCs) are generally perceived as the most promising fuel cells for portable power applications at low temperatures. The bi-functional mechanism of methanol oxidation, postulated by Watanabe (e.g. [3]), is universally accepted, with unsupported Pt-Ru alloys remaining the best performing anode catalysts to date. According to the bi-functional mechanism, the methanol molecule is first adsorbed on two or three free Pt sites, before undergoing gradual dehydrogenation to form surface CO. Chemisorbed carbon monoxide, which in the absence of Ru would irreversibly block active Pt sites, is then oxidized to CO_2 by the ruthenium oxide species and removed from the surface. In the final stage of the anodic process, ruthenium oxide (and or hydroxide, hydrous oxide) is rebuilt at the surface in a reaction involving bulk water.

While the above mechanism seems to well describe the oxidation process, it is not yet clear what atomic Pt-to-Ru ratio in the bulk of the alloy leads to the highest activity towards methanol. A bulk Pt-to-Ru atomic ratio of 1:1 is often reported to generate the best anode performance, however, Gasteiger *et al.* [1] reported that at 25°C a catalyst with a surface concentration of 10 at% Ru exhibits the highest activity. The same authors found that an alloy with 30% Ru atoms on the surface is the most active at a somewhat elevated temperature of 60°C. Iwasita *et al.* [4] investigated Pt-Ru catalysts prepared by various methods and concluded that alloys with surface composition between 10% and 40% Ru lead to the highest activity in methanol oxidation.

In this paper, we present results from a study involving eight unsupported Pt-Ru catalysts with the atomic Pt-to-Ru ratio ranging from 9:1 to 1:2. The catalyst activity was determined directly under actual DMFC operating conditions in a temperature interval from 40°C to 80°C. The active surface area of the samples was probed with CO chemisorbed from either the gas phase or derived from aqueous solution of MeOH, as in an actual fuel cell. The catalyst morphology and composition were also investigated by the X-ray diffraction (XRD), X-ray fluorescence (XRF) and thermogravimetry (TGA).

EXPERIMENTAL

MEA Preparation and Fuel Cell Testing

Unsupported Pt-Ru anode catalysts were manufactured by Johnson Matthey, specifically for the purpose of this study except for Ru-55, which is a commercial DMFC Pt-Ru catalyst from Johnson Matthey, offered under a name of HiSPEC™ 6000. The cathode catalyst was a commercial unsupported Pt black catalyst (HiSPEC™ 1000, Johnson Matthey). Both the anode and the cathode catalysts were applied directly to the membrane at 60°C, according to the standard membrane-electrode assembly (MEA) fabrication procedure adopted at LANL [2,5]. Each 5-cm^2 MEA was conditioned in a hydrogen-air fuel cell at 80°C for several hours. The H_2-air polarization plots were then recorded, followed by extensive testing in the DMFC operating mode with 1.0 M MeOH at 40°C, 60°C and 80°C. As a part of the DMFC testing, the anode activity was examined directly by recording anode polarization plots. For that purpose, the fuel cell was operated in a driven mode, in which the cathode acted as a hydrogen quasi-reference/counter electrode.

CO and MeOH Stripping

After fuel cell testing, the cell was cooled down to 25°C and the temperature of the gas humidification bottles lowered to 30°C. In the CO-stripping experiments the cathode was fed with hydrogen (0.14 L min^{-1}, 0.76 atm) to work as a quasi-reference/counter electrode. Carbon monoxide was adsorbed from a 99.3 % gaseous CO for 10 minutes and at an anode potential of 0.1 V. In order to remove excess CO from the system, the cell was then purged for 30 minutes with nitrogen gas (1.0 L min^{-1}, 0.76 atm). The electrode potential was maintained at 0.1 V throughout the purging. A cyclic voltammogram (CV) was then recorded from 0.1 V to 0.8 V at a scan rate of 5 mV s^{-1}. The experimental conditions for adsorption and purging were carefully optimized in earlier experiments.

CO was also chemisorbed from 1.0 M MeOH solution, fed to the anode for 60 min at a rate of 2 mL min^{-1}. After the chemisorption, the anode was purged with nitrogen (1.0 L min^{-1}, 0.76 atm) to remove excess methanol. The stripping voltammogram was then recorded at a scan rate of 5 mV min^{-1}, the same as for the stripping of CO chemisorbed from the gas phase. Extending the adsorption time to 180 min led to the same results as those obtained in one-hour experiments.

XRD

X-ray diffraction methods were used to characterize the crystal structure, phase purity, degree of alloying, and particle size. The measurements were made with a Siemens D5000 diffractometer fitted with an incident-beam monochrometer. The single crystal Ge (220) provided a monochromatic source of $CuK_{\alpha 1}$ radiation. The operating conditions were 50 kV accelerating voltage and 40 mA of beam current. The analysis of the XRD data was carried out using the SHADOW™ full profile refinement package written by Materials Data Corporation. Full profile or whole-pattern analysis methods model the entire X-ray pattern rather than simply determining the d-spacings from peak maxima. The measured peak profile function was modeled by a convolution of an experimentally-determined instrument function and a Lorentzian peak profile sample function. The average crystallite size of the catalyst powder was determined using a Scherrer crystallite size broadening model after de-convoluting the sample profile from the instrument function. Full-profile refinement also yielded FCC unit cell size. The degree of alloying was thus determined by measurement of the d-spacing in the (111) plane of the unit cell. The measured $d_{(111)}$ spacings of the catalyst powders studied in this work were then compared with literature values for Pt-Ru alloys [6]. Vegard's law was used to determine the atomic percentage of alloying.

XRF

A Spectrace QuanX Energy Dispersive X-ray Fluorescence Analyzer (XRF) equipped with a LN_2-cooled Si(Li) detector was used to independently measure the Pt and Ru composition and mass loading. The weight-percentages of Pt and Ru were calculated using a fundamental parameter method included in the QuanX™ analysis software. An advantage of the fundamental parameter method over older empirical standards method is the elimination of the many calibration standards typically required to accurately model a wide range of Pt-Ru stoichiometry. The fundamental parameter method only requires a single calibration standard per element. The XRF cannot detect elements lighter than sodium hence, only Pt to Ru ratios and mass loadings were determined.

Thermogravimetric Analysis

In order to accurately determine the metal content in the samples containing Ru-hydrates, thermogravimetric analysis was used. A Perkin Elmer TGA-7 with flowing forming gas (6% H_2/Ar balance) to reduce the hydrated Ru component to Ru metal was employed. The weight percentage of oxygen and water was calculated from the resulting weight loss at 400-500°C.

RESULTS AND DISCUSSION

Before evaluating the anode catalyst activity in a DMFC, it was necessary to make sure that the cathode properties remain the same in all cells tested with different anode catalysts. Since hydrogen oxidation at the anode is very fast compared with the oxygen reduction at the cathode, the cathode performance was determined from the hydrogen-air polarization plots recorded with each cell. Such H_2-air polarization plots from 1.0 V to

0.4 V are shown in **Figure 1** for MEAs with three different anode catalysts and identical cathode in each case. As expected, in spite of different anodes, all three V-i plots are very similar, with slight deviations occurring only in the voltage range, where the cell performance becomes limited by the mass transport. At a "DMFC-relevant" current density of 0.2 A cm^{-2} the cell voltage was measured at 0.85 V in all three cases while at a significantly higher current density of 0.6 A cm^{-2} the cell voltage was 0.7 V, again the same for all cells.

Cathode reproducibility is further demonstrated in **Figure 2,** in which the H_2-air performance at 0.7 V is shown for cells with the anodes made from all eight Pt-Ru catalysts investigated in this work. As expected, the recorded cell current is very similar for all eight cells, with the most extreme values being no more than 10% apart.

After conditioning and making sure that a well-defined cathode "reference" has been established, all eight anode catalysts with different Pt-to-Ru atomic ratios were studied under an assumption that changes in the performance of individual cells are only due to differences in the anode activity. **Figure 3** shows polarization plots obtained with three different Pt-Ru catalysts using 1.0 M MeOH anode feed stream at 80°C. The data demonstrate that Ru-55 with an intermediate a bulk Ru content of 55 at% shows better performance than catalysts with either higher (Ru-65, 65 at% Ru) or substantially lower (Ru-09, 9% Ru) content of ruthenium. This comparison is extended over all eight Pt-Ru catalysts and three temperatures in **Figure 4** shows. Based on the current density values at a typical DMFC voltage of 0.5 V, it turns out that, initially, the cell performance improves with increasing Ru-to-Pt ratio. The best performance is obtained with the bulk atomic content of Ru between 50% and 60 %. Further increase in the ruthenium content results in a decrease in the catalyst activity. In spite of previous reports implying that an optimum Pt-to-Ru ratio could depend on the cell operating temperature, especially at near-ambient conditions [1], in this work, the same pattern of catalyst activity was observed at all studied temperatures: 40°C, 60°C and 80°C (Figure 4).

Catalytic activity of a DMFC anode can also be measured directly by recording anode polarization plots in a driven cell configuration, with the fuel cell cathode being used in this case as a hydrogen quasi-reference/counter electrode. Anode polarization plots for the same three different Pt-Ru catalysts as those shown in Figure 3 are given in **Figure 5.** While the DMFC data in Figure 3 were taken "as is", without applying any *iR* correction, the anode performance data in Figure 5 have been *iR*-corrected to allow true comparison of the relative activity of the catalysts. As expected from the DMFC performance shown above, Ru-55 performs considerably better than the catalysts with either lower or higher content of ruthenium. At a potential of 0.35 V, often used for comparing activity of different anode catalysts, the performance of Ru-55 is approximately six times better than that of the other two catalysts. When current density at 0.35 V is plotted at three temperatures as a function of the ruthenium content for all eight catalysts tested (**Figure 6**), a dependence similar to that already shown in Figure 4 is obtained. This clearly indicates that the earlier observed difference in the DMFC performance (Figure 4) did indeed result from significant differences in the catalytic activity of Pt-Ru towards methanol.

We demonstrate here a strong correlation between the composition of Pt-Ru anode catalyst and its activity in methanol oxidation. The highest catalytic activity has been obtained with samples having bulk atomic content of ruthenium between 50% and 60%.

CO stripping data, peak potential in particular (see below), indicate that the surface concentration of these most active catalysts is close to 30 at% of Ru, in agreement with Gasteiger *et al.*[1] and Iwasita *et al.* [4].

CO Stripping

The CO stripping data recorded at 25°C and normalized to the *BET* surface area are shown in **Figure 7**. Stripping from the surface of a catalyst with the lowest content of ruthenium (Ru-09, solid line) results in a narrow peak at 0.45 V and a shoulder at around 0.52 V. They most likely originate from the CO chemisorbed on the Pt-Ru alloy and islands of pure Pt, respectively. CO stripping from Ru-55, the most DMFC-active catalyst tested, gives rise to a much broader peak and, consequently, significantly higher oxidation charge. The onset potential of CO stripping is noticeably lower on Ru-55 than on Ru-09, which reflects its superior activity in methanol oxidation. Unlike Ru-09 and Ru-55, the ruthenium-rich Ru-65 exhibits virtually no activity in CO adsorption.

The dependence of a total CO stripping charge density, *Q*, on the catalyst composition is shown in **Figure 8** with a solid line. With increasing Ru content, the CO charge initially decreases and later increases reaching maximum at a point corresponding to 55 at% of Ru (Ru-55 catalyst). Interestingly, the CO stripping charge recorded for relatively inactive Ru-09 is high compared with Ru-50 and Ru-55, which are found to much more active towards methanol in a DMFC testing (*cf.* Figure 4 and Figure 8, fine dashed line). However, if the charge ascribed above to CO stripping from pure Pt sites is subtracted from the total stripping charge for Ru-09, the resulting charge of CO stripping from the alloyed part of the Ru-09 decreases quite significantly. The shape of the thus corrected Q_{CO} *vs.* $x_{Ru,bulk}$ dependence (Figure 8, thick dashed plot) becomes very similar to the plot of j_{AP} *vs.* $x_{Ru,bulk}$, representing the actual change in the catalyst activity as a function of the catalyst composition (Figure 8, fine dashed line). In other words, there is a direct relationship between the activity of a catalyst and the tendency for the CO to chemisorb on the alloyed part of that catalyst surface. Furthermore, the CO bound to the pure Pt islands represents those surface sites that get fully blocked by CO under DMFC operating conditions. In the absence of Ru sites anywhere near, such Pt-bound CO cannot be removed from the surface at potentials low enough to be practical for the DMFC operation and remains chemisorbed, thereby rendering that part of the surface inactive in the methanol oxidation reaction. Not surprisingly, the contribution of Pt islands to the overall CO stripping charge is more pronounced for catalysts with relatively high Pt content, *e.g.* Ru-09. Such catalysts show poor DMFC performance in spite of a relatively high total CO stripping charge.

Another interesting case is that of Ru-61. In spite of showing high activity towards methanol (Figure 8, dashed line) this catalyst tends not to get significantly covered by the surface CO (Figure 8, thin dashed line). Characteristic of this catalyst is high content of ruthenium oxides (hydroxides) in the bulk, which are not known to adsorb CO to a significant degree (*e.g.*, [7]). XRD evidence that confirms the presence of ruthenium oxides will be shown below in the next section. However, the oxides (hydroxides) may affect the surface the properties of the catalyst, possibly through electronic effects from the layers immediately below the surface layer. Although no explanation of a good DMFC performance of Ru-61 can be given at this time, this case clearly shows the limits of CO stripping as an activity probe for the Pt-Ru anode catalysts.

One way of possibly making the CO probe more relevant to DMFC operation is to generate surface CO from methanol rather than adsorb it from a gas phase. Unlike in the case of CO adsorbed from the gas phase, stripping methanol-generated carbon monoxide is expected to be specific to Pt-sites for it is known that MeOH only adsorbs on platinum and not on ruthenium (*e.g.*, [1, 8]). In this work, the methanol-generated CO was used to determine the nature of the shoulder in CO stripping peaks on Ru-09 and Ru-18. Comparison of the stripping scans of CO formed on Ru-09 from the gas phase and from 1.0 M aqueous MeOH are shown in **Figure 9** with solid line and dashed line, respectively. Based on the comparison of stripping charges and peak locations it becomes immediately clear that the CO-stripping shoulder does indeed arise from the CO stripping from Pt islands. The difference in the CO stripping charge measured on Ru-09 after adsorption form the gas phase and from aqueous solution of methanol is about 70 $\mu C\ cm^{-2}$, *i.e.* close to 30% of the total charge for stripping of the gas-phase CO. Work is in progress to reproducibly correlate the charge difference with surface activity of different unsupported Pt-Ru catalysts towards methanol.

XRD and TGA analysis

In **Figure 10**, the X-ray diffraction pattern is presented for two "as-received" catalysts: Ru-09 and Ru-65. While the low ruthenium content catalyst exhibits sharp diffraction peaks, a pronounced background can be seen for the catalyst with the highest Ru content. This indicates the presence of amorphous Ru oxides and/or hydroxides in the Ru-65 sample. Diffraction peaks belonging to crystalline RuO_2 can also be found in the pattern as shown in Figure 11b. Full-profile fitting of the XRD data show an average crystallite size of 5.2 nm for the Pt-Ru alloy of Ru-09 and 2.9 nm and 1.0 nm for the Pt-Ru alloy and RuO_2, respectively, in the Ru-65 sample. Thermogravimetric analysis (TGA) under reducing conditions (6%H_2/Ar balance) confirms the presence of possible oxides and/or hydroxides. Analysis of the Pt unit cell lattice parameter in the alloy suggests that all samples displayed incomplete alloying; the FCC phase was typically Ru deficient. No HCP phase material was observed in high Ru content samples. These data are summarized in **Table 1**.

Table 1: XRD, XRF and TGA Summary

Catalyst[1]	Ru Content[2] (at%)	Surface Area[3] ($m^2 g^{-1}$)	Average Crystallite[2] Size (nm)	XRF Composition (at%)		TGA Weight Loss (%)
				Pt	Ru	
Ru-09	10	34	5.2	89	11	*n.m.*[4]
Ru-18	10	46	4.3	79	21	*n.m.*
Ru-33	20	61	2.9	63	37	*n.m.*
Ru-50	40	86	1.8	46	54	*n.m.*
Ru-52	35	86	2.0	46	54	10
Ru-55	35	67	1.8	46	54	12
Ru-61	20	115	1.6	35	65	18
Ru-65	15	122	2.9	30	70	20

[1] *Total Ru content determined by "wet chemistry" method;* [2] *XRD data for alloyed Pt-Ru phase only*
[3] *By N_2 BET;* [4] *Not measured*

In spite of vast effort invested into making all eight catalysts well alloyed and therefore differing from one another by only the Pt-to-Ru atomic ratio, the relative content of the Pt-Ru alloy in the samples changes significantly as the ruthenium content increases from as low as 9 at% to as high as 65 at%. Even before completing the ongoing XRD study of the "as-received" samples, there is a strong indication that the catalysts in this study can be divided into two groups: (i) "true" Pt-Ru alloys and (ii) catalysts of the Pt/"RuO_x•$(H_2O)_y$" type, with a relatively low content of the Pt-Ru alloy. More work is currently underway at Los Alamos to better correlate electrocatalytic activity of Pt-Ru catalysts in these two groups with the average particle size, degree of alloying and the content of amorphous Ru oxide/hydrous oxide/hydroxide. Also, to make XRD data as relevant as possible to the actual DMFC operating conditions, X-ray diffraction experiments with reduced catalyst samples will be carried out.

CONCLUSIONS

It is very difficult to prepare a series of Pt-Ru alloys with differing atomic ratios while maintaining similar crystallite sizes, surface areas and phase homogeneity. Comprehensive catalyst materials analysis is required for all samples before conclusions can be drawn about what factors influence anode catalytic activity. For our series the optimum bulk composition of a binary Pt-Ru catalyst for methanol oxidation at the DMFC anode is between 50 and 60 at% of Ru, which typically corresponds to ~30 at% of Ru on the surface. The best-performing catalyst composition is temperature independent in the temperature range investigated in this work, from 40°C to 80°C.

The stripping charge of carbon monoxide chemisorbed from the gas phase or from an aqueous solution of methanol gives an indication of the catalyst activity, yet it can only be used as a first approximation of the total number of free catalyst sites available to methanol oxidation. Stripping of a methanol-derived CO appears to be an effective tool for identifying two different adsorption sites for catalysts with high Pt content, namely, Pt-Ru alloy sites and pure Pt islands.

ACKNOWLEDGMENTS

This work was supported by the Defense Advanced Research Projects Agency through the Defense Sciences Office and by the U.S. Department of Energy through the Office of Advanced Automotive Technologies.

FIGURES

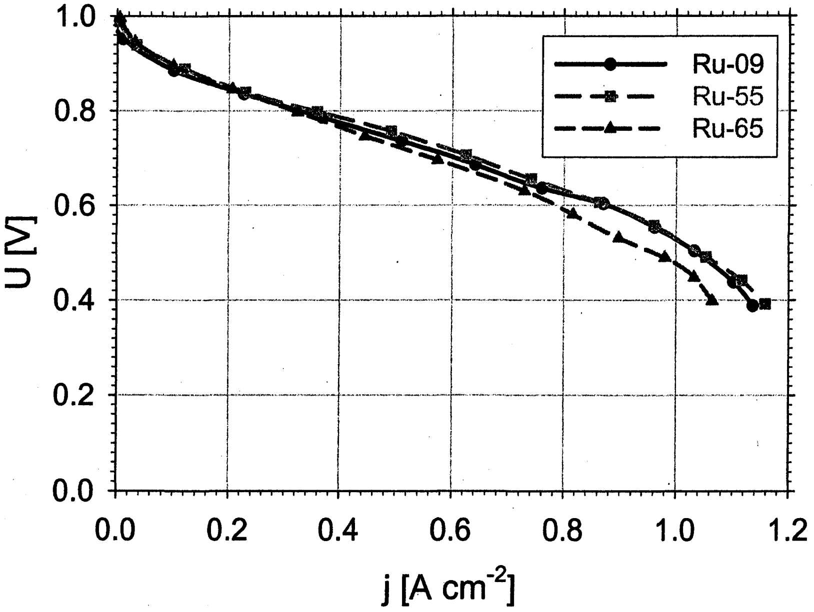

Figure 1 Hydrogen air performance of MEAs with three selected Pt-Ru anode catalysts at 80°C. Pt-Ru anode: H_2, 2.8 atm, ~9 mg cm^{-2} Pt-Ru; Pt cathode: air, 2.8 atm, ~6 mg cm^{-2} Pt.

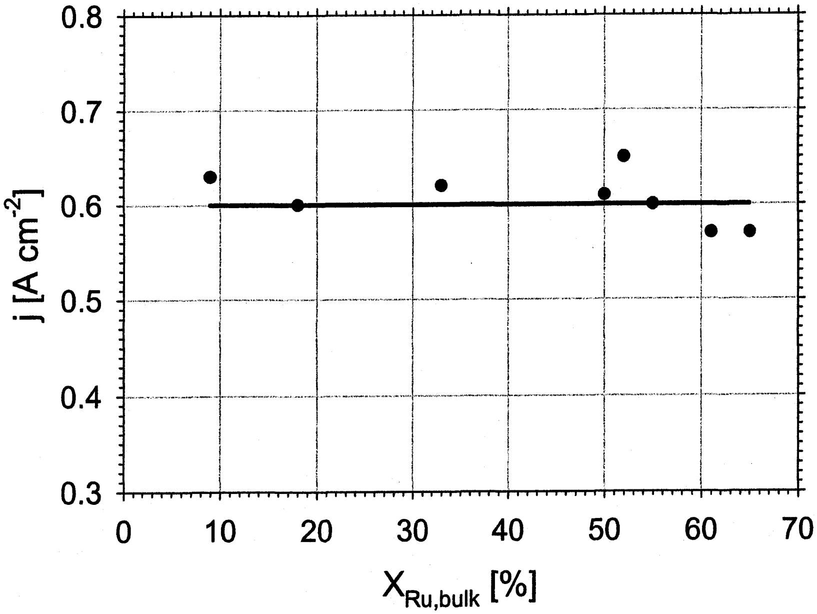

Figure 2 H_2-air performance at 0.7 V *vs.* bulk atomic percent of Ru in the anode catalyst. Test conditions as in Figure 1.

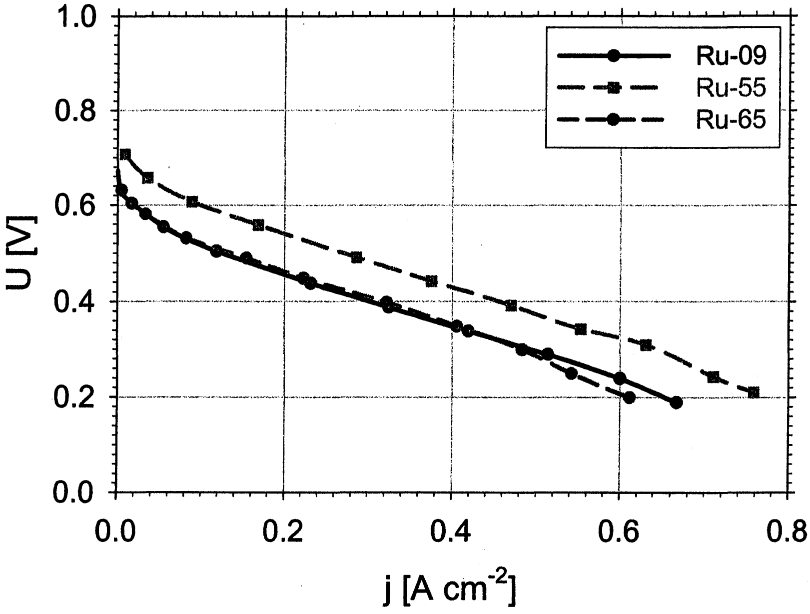

Figure 3 DMFC polarization plots for MEAs with three selected Pt-Ru anode catalysts at 80°C. Pt-Ru anode: 1.0 M MeOH, ~9 mg cm^{-2} Pt-Ru; Pt cathode: air, 2.8 atm, ~6 mg cm^{-2} Pt.

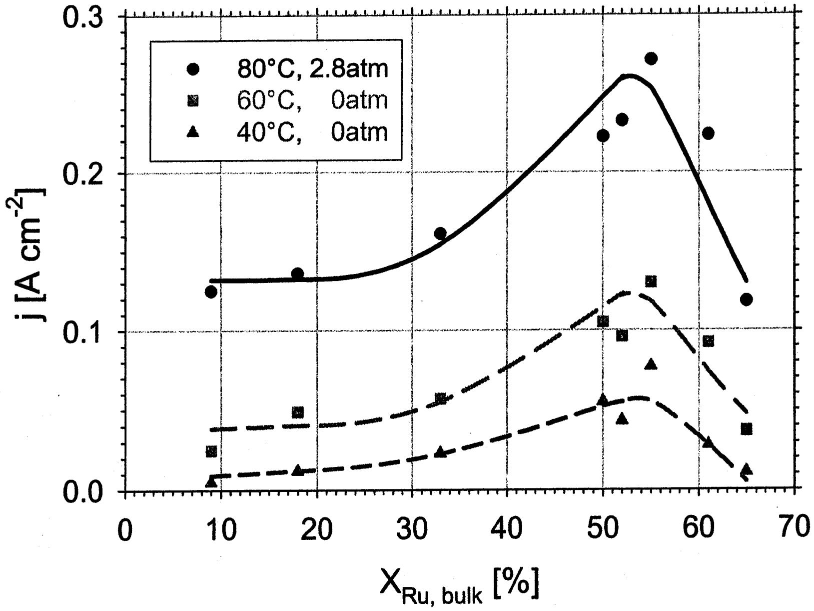

Figure 4 DMFC performance at 0.5 V *vs.* bulk atomic percent of Ru in the anode catalyst. Test conditions as in Figure 3.

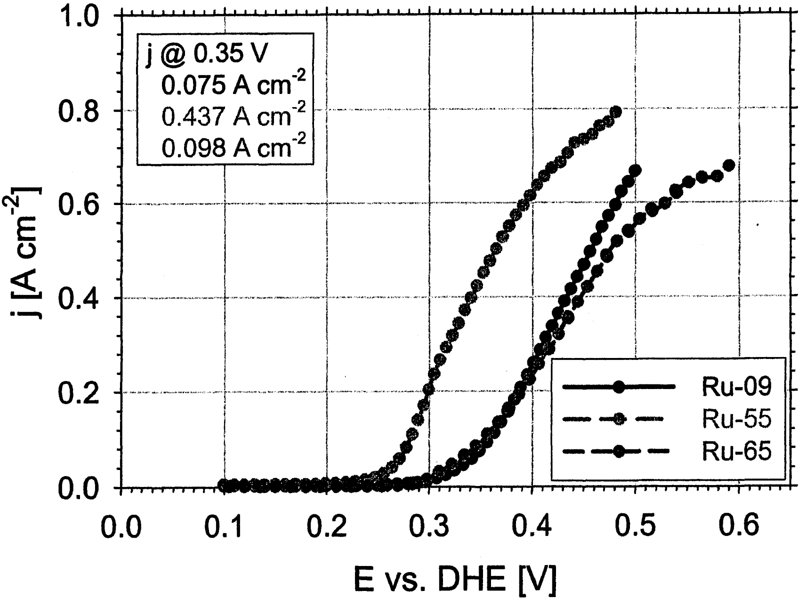

Figure 5 *iR*-corrected anode polarization plots at 80°C; 1.0 M MeOH.

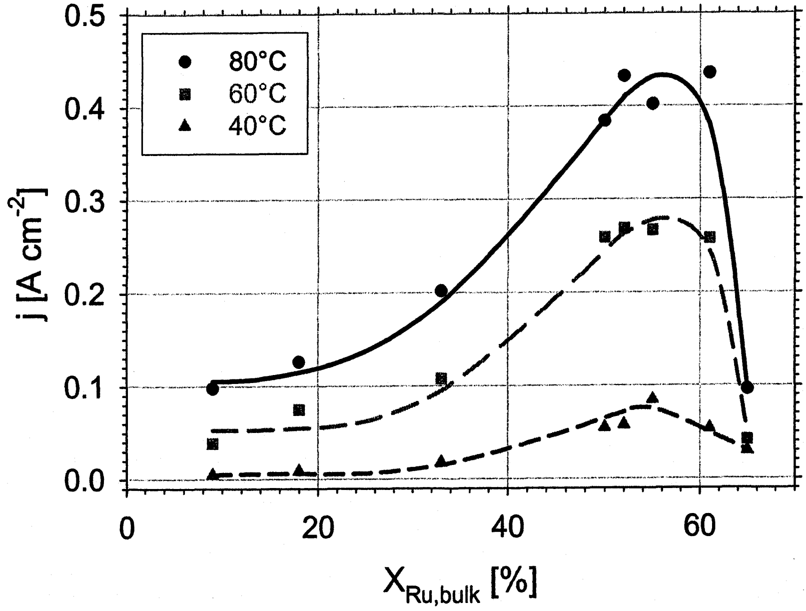

Figure 6 Anode activity at 0.35 V *vs.* bulk atomic percent of Ru in the anode catalyst at three different cell temperatures; *iR*-corrected data; 1.0 M MeOH.

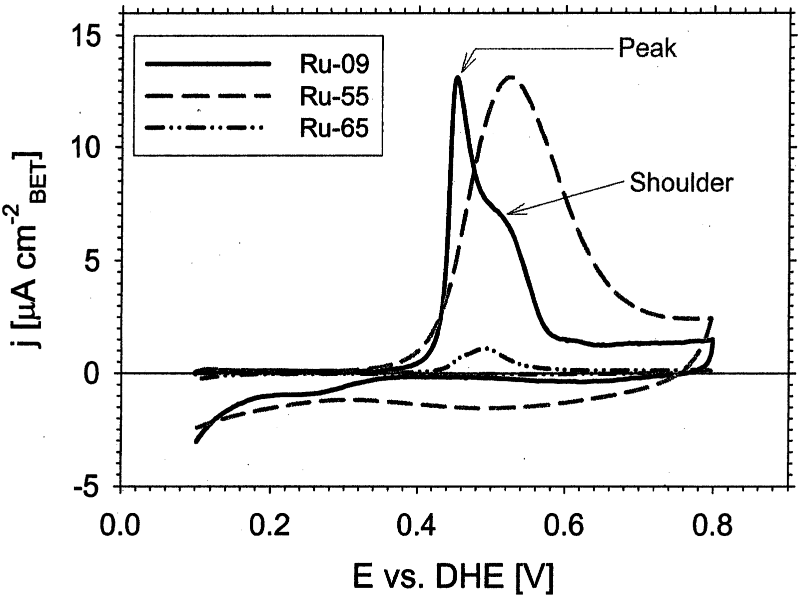

Figure 7 Voltammetric stripping of CO chemisorbed from the gas phase on three selected Pt-Ru catalysts at 0.1 V for 10 min; temperature 25°C; scan rate 5 mV s^{-1}.

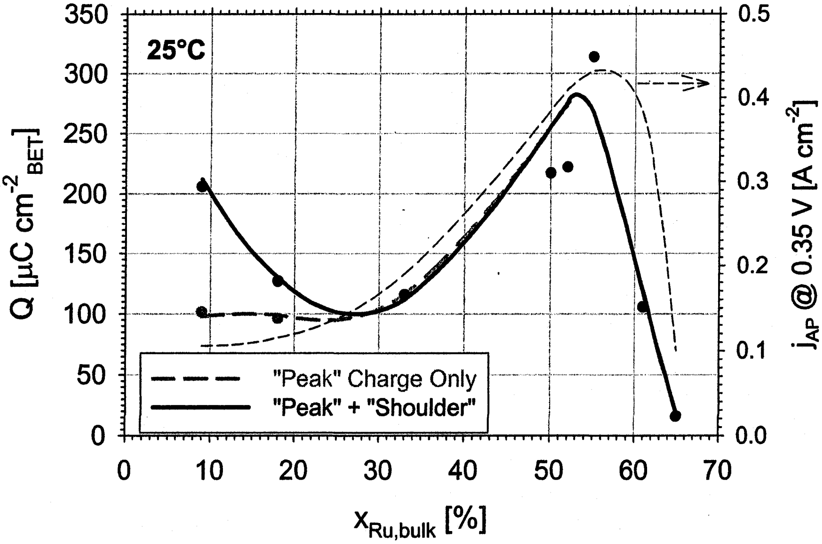

Figure 8 CO stripping charge *vs.* bulk atomic percent of Ru in the anode catalyst; test conditions as in Figure 7.

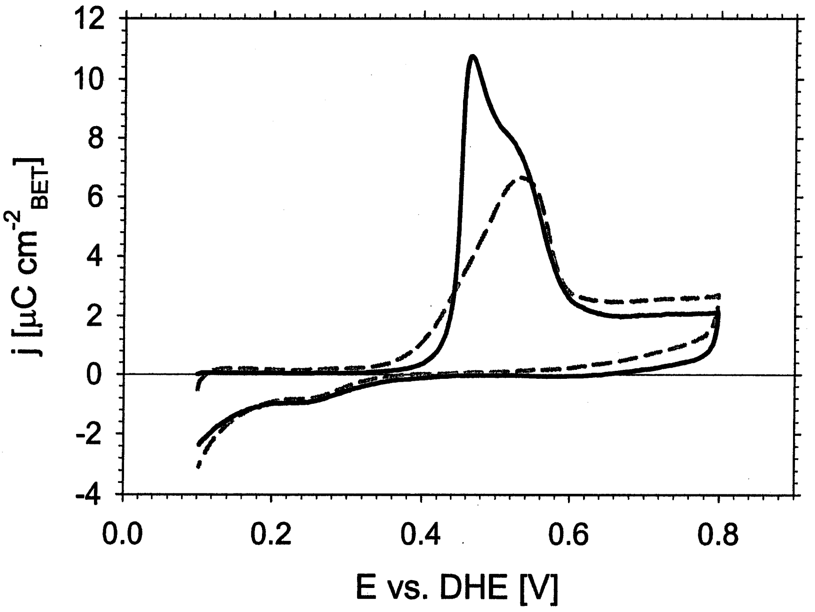

Figure 9 Comparison of stripping voltammetry (*iR*-corrected) of CO chemisorbed from the gas phase at 0.1 V for 10 min (solid line) and from 1.0 M aqueous MeOH at 0.1 V for 60 min (dashed line); temperature 25°C; scan rate 5 mV s^{-1}.

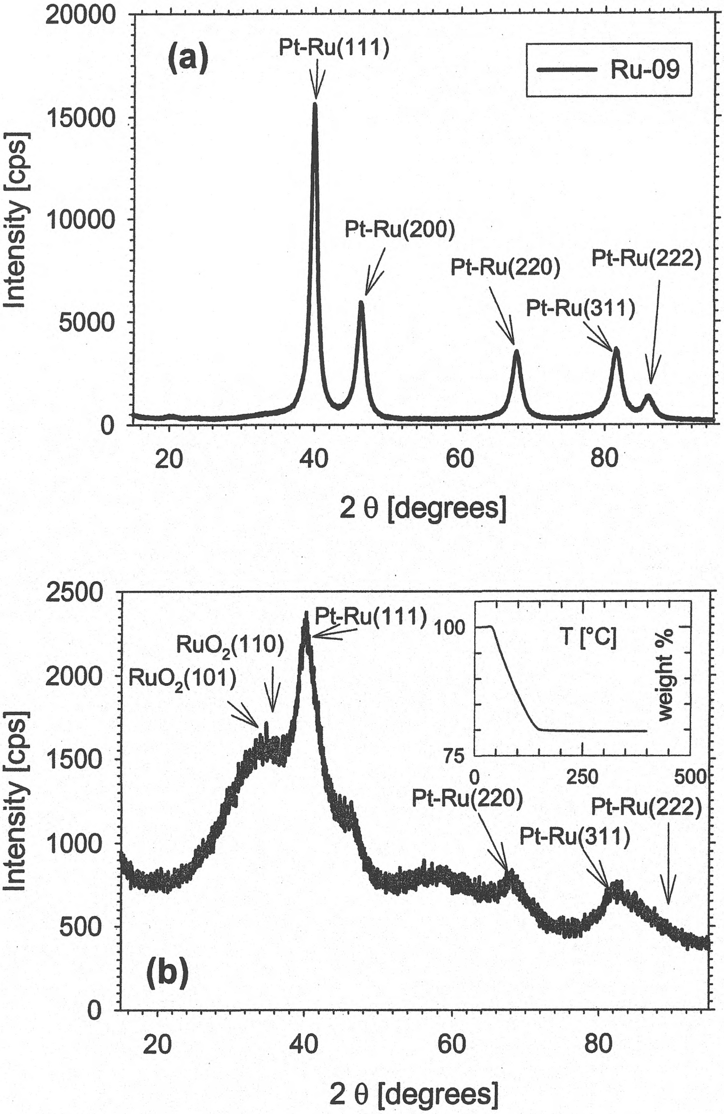

Figure 10 XRD traces from 15 to 96 degrees two-theta using Cu$K_{\alpha 1}$ radiation of the "as-received" Johnson Mattey Ru-09 and Ru-65 catalysts. The indexed FCC alloy peaks and those for RuO_2 are labeled accordingly; **(a)** Ru-09, **(b)** Ru-65 with a TGA spectrum shown as an insert.

REFERENCES

1. H. A. Gasteiger, N. Marković, P. N. Ross, Jr. and E. J. Cairns, *J. Phys. Chem.* **97**, 12020 (1993).
2. H. N. Dinh, X. Ren, F. H. Garzon, P. Zelenay and S. Gottesfeld, *J. Electroanal. Chem.* **491**, 222 (2000).
3. M. Watanabe and S. Motoo, *J. Electroanal. Chem.* **60**, 275 (1975).
4. T. Iwasita, H. Hoster, A. John-Anacker, W. F. Lin and Vielstich; W., *Langmuir* **16**, 522 (2000).
5. S. C. Thomas, X. Ren, S. Gottesfeld and P. Zelenay, *Electrochim. Acta*, in press.
6. M. Watanabe, M. Uchida and S. Motoo, *J. Electroanal. Chem.* **229**, 395 (1987).
7. W. B. Wang, M. S. Zei and G. Ertl, *Phys. Chem. Chem. Phys.* **3**, 3307 (2001).
8. H. A. Gasteiger, N. Marković, P. N. Ross, Jr. and E. J. Cairns, *J. Electrochem. Soc.* **141**, 1795 (1994).

Proceedings of The Electrochemical Society, PV 2002-31, 468-480 (2002)
DOI: 10.1149/200231.0468PV © The Electrochemical Society

NOVEL METHOD FOR THE ESTIMATION OF THE ELECTRO-ACTIVE Pt AREA

C. Bock and B. MacDougall
National Research Council Canada, Montreal Road, Ottawa, Ontario K1A 0R6

ABSTRACT

The $(COOH)_2$ oxidation reaction was studied at potentials below which the oxygen evolution reaction (oer) takes place. Pt was found to catalyze the $(COOH)_2$ oxidation reaction more strongly than Au, while Ru did not display any activity towards the $(COOH)_2$ oxidation reaction. Furthermore, under rapid stirring conditions, the $(COOH)_2$ oxidation reaction using Pt electrodes was shown to be purely activation controlled. Therefore, the $(COOH)_2$ oxidation currents can be related to the electro-active Pt area, as shown for a range of polycrystalline, bulk metal Pt and Pt powder electrodes. The Pt surface area for multi-component catalyst systems can also be estimated by combining $(COOH)_2$ oxidation data with the charge needed to oxidize adsorbed CO to CO_2 (CO_{ads} charge), as shown for a range of Pt and Ru containing powder electrodes. In fact, the combination of the two methods ($(COOH)_2$ oxidation current and CO_{ads} charge) can be used as an *in-situ* probe to estimate the fraction of Ru in the metallic state in the potential region where CO is adsorbed provided that the surface ratio of Pt vs. Ru is known.

INTRODUCTION

Pt and Pt-Ru catalysts have attracted much attention due their promising use in fuel cell technologies (1,2). The estimation of the true electro-active surface area of these catalysts remains a challenge. Anodic stripping voltammetry of adsorbed CO (CO_{ads}) has been suggested as a possible *in-situ* probe for these catalyst systems yielding information about catalyst composition and surface areas (3,4). This method involves the adsorption of CO on the catalyst at negative potentials, followed by oxidizing the CO_{ads} to CO_2 in a subsequent positive potential scan. On Pt surfaces, ca. one monolayer of CO is adsorbed at sufficiently negative potentials (3). The CO stripping method can also be employed to estimate the electro-active Pt area for multi-component catalyst systems provided that CO is not adsorbed on the non Pt catalyst components. However, it is known that CO also adsorbs on metal surfaces other than Pt, such as Au, Hg, and Ru (5,6). The case of CO adsorption onto surfaces that contain Ru has received some attention and some researchers suggested that up to two moles of CO per Ru sites may adsorb, while the general view exists that CO does not adsorb onto oxide covered Ru sites (4,5). Frequently, the Ru component of the Pt-Ru catalyst is in the form of one or more of the many possible Ru oxides. Ru oxides, particularly in the presence of Pt, can be partially or possibly completely reduced to metallic Ru in the potential region where CO is typically adsorbed (5). Based on these results, it is clear that the estimation of the Pt surface area for Pt-Ru systems using the CO_{ads} stripping method may be difficult.

In this work, the electrochemical oxidation reaction of $(COOH)_2$ to CO_2 is tested for its potential use for the estimation of the electro-active Pt area for bulk metal Pt and Pt powder electrodes. The method is also applied to a range of Pt-Ru powder electrodes.

EXPERIMENTAL

Pt, Ru and Pt-Ru powder preparation

A range of Pt, Ru and Pt-Ru powders were synthesized. The atomic (at) Pt to Ru ratio of the starting, i.e., the total bulk powder, composition for the Pt-Ru powders was generally maintained constant, namely 70 to 30 (Pt to Ru) at %. The following powders were prepared: Powder 1: Pt powder: Formed by the reduction of 3.2 g of $H_2PtCl_6 \cdot 6\ H_20$ (Alfa Aesar) dissolved in 150 mL H_2O with 75 mL of 0.2 M $NaBH_4$ (Anachemia); Powder 2: Ru powder: Formed as Pt powder 1, but using 1.6 g $RuCl_3$ (Alfa Aesar) instead of $H_2PtCl_6 \cdot 6\ H_2O$; Powder 3: PtRu alloy: Formed by the simultaneous reduction of 3.256 g $H_2PtCl_6 \cdot 6\ H_2O$ and 0.5603 g $RuCl_3$ dissolved in 150 mL H_2O with 75 mL 0.2 M $NaBH_4$. Powder 4: Pt/RuO_2 (thermal): Formed by the reduction of 3.256 g $H_2PtCl_6 \cdot 6\ H_2O$ dissolved in 150 mL H_2O with 75 mL 0.2 M $NaBH_4$, after excessive washing with H_2O, filtering and drying in an air oven at 100 °C, 0.5603 g of $RuCl_3$ was distributed (using a mortar) within the Pt powder. This powder mixture was subsequently heated at 500 °C under O_2 flow in a tube furnace for 2 h; Powder 5: Pt/RuO_2 (ball-mill): 2.83 g Pt powder (-200 mesh, 99.98 %, Alfa Aesar) and 0.85 g RuO_2 (Electronic Grade, Premion, 99.95 %, Alfa Aesar) were ball milled using a Spex2000 ball mill mixer, as described in detail elsewhere (7); Powder 6: Pt/Ru: The Pt/RuO_2 (thermal) powder 4 was reduced in a H_2 atmosphere at 100 °C for 2 h. After preparation, powders 1-3 were washed thoroughly with H_2O, filtered and dried in an air oven at 100 °C. A PtRu alloy powder of Pt to Ru at % composition of 54:46 was also prepared in the same manner as powder 3 by the simultaneous reduction of 3.256 g $H_2PtCl_6 \cdot 6\ H_20$ and 0.8591 g $RuCl_3$. This powder catalyst is referred to as powder 3a.

All powders synthesized in this work were characterized using X-ray diffraction (XRD), X-ray photon electron spectroscopy (XPS) and transmission electron microscopy (TEM). The results are discussed and presented in detail elsewhere (7). The XPS studies indicated that a significant fraction of Ru metal was present for the Ru powder (7).

Working electrode preparation

The catalyst powders were formed into anodes by sonicating 13 mg of a particular powder in 5 to 20 mL of H_2O for 30 min. Appropriate amounts (1-2 μL's) of the suspension were then pipetted onto and well spread out on 0.2 cm^2 (geometrical area) glassy carbon disc electrodes (Pine). In some cases, as stated in the appropriate section of the text, catalyst powder suspensions were also pipetted onto ca. 0.35 cm^2 Au foil electrodes (99.9 % Au, 0.1 mm thick (Goodfellow)). The electrodes were dried in air and at room temperature (ca. 30 min.) and subsequently washed thoroughly with H_2O. The Au foils were firmly attached to Au wire electrodes. All Au electrodes were carefully wrapped with Teflon tape to mask Au not covered with the catalyst powder and expose a geometrical area of ca. 0.12 cm^2 in all cases. All Au electrodes In some cases, a polycrystalline Pt rotating disc electrodes (RDE's) (0.2 cm^2 geometrical area, Pine) were also used as working electrode. All $(COOH)_2$ oxidation studies were carried out using the powder electrodes prepared without the typically used Nafion solution (8), as preliminary studies showed that Nafion slows down the transport of $(COOH)_2$ to the catalyst sites.

Cells and Electrodes

Three compartment cells, in which the reference electrode was separated from the working and counter electrode compartment by a Luggin capillary, were employed for the electrochemical studies. A saturated calomel electrode (SCE) was used as reference electrode. All potentials reported in this paper are vs. the SCE unless otherwise stated. Large surface area Pt gauzes served as counter electrodes.

Techniques and Instrumentation

Electrochemical experiments were performed using either an EG&G 273 potentiostat or a Solarotron SI 1287 electrochemical interface (Solarotron Group, Ltd.) both driven by Corrware software program (Scribner, Assoc.). A PINE RDE Rotator controlled by a MSR speed control system (PINE Instrument Company) was employed for the electrochemical oxidation studies carried out under controlled stirring conditions. The RDE Rotator was calibrated using a 5 mM $K_4Fe(CN)_4$ in 1 M KCl solution, as discussed in the text.

CO_{ads} stripping voltammetry

CO was adsorbed onto the Pt based powder electrodes at –0.1 V by bubbling CO gas (Matheson purity, Matheson gas) through the 0.5 M H_2SO_4 solution for 20 min. Solution CO was subsequently removed by bubbling Argon gas (Air products) for 40 min., holding the potential at –0.1 V. The potential was then cycled at 20 mV s^{-1} between –0.1 V and a specific upper limit (E+) for two complete oxidation/reduction cycles.

Solutions

All $(COOH)_2$ oxidation studies were carried out using 10^{-2} M $(COOH)_2$ + 0.5 M H_2SO_4 solutions. The solutions were deoxygenated using high purity Argon gas prior to the electrochemical studies. All electrochemical experiments were carried out at room temperature. A.C.S. grade chemicals and high resistivity 18 MΩ water were used. The $RuCl_3$ powder was dried in air at 135 °C prior to its use for the catalyst powder synthesis.

RESULTS AND DISCUSSION

$(COOH)_2$ oxidation reaction: Cyclic Voltamogram (CV) characteristics

Fig. 1 shows typical CV characteristics recorded at 20 mV s^{-1} in 10^{-2} M $(COOH)_2$ + 0.5 M H_2SO_4 solutions using a Au foil, Pt and Ru powder electrodes. The Pt and Ru powders were supported using Au foil electrodes, as described in the experimental section. Steady-state CV characteristics were generally obtained within 5 to 7 complete oxidation/reduction cycles for all $(COOH)_2$ oxidation studies reported in this work. For the Pt powder and Au foil electrodes, a significant $(COOH)_2$ oxidation current is observed, while the Ru powder electrode does not show any activity for the $(COOH)_2$ oxidation reaction within the potential range investigated. (It should be noted that the exact amount of Ru powder on Au foil support electrode was not estimated, but a Ru powder layer was clearly visible, indicating the presence of a significant amount of Ru.) As found for the Ru powder electrode, the glassy carbon RDE was also found not to display activity for the $(COOH)_2$ oxidation reaction, thus justifying the use of this electrode as support for the Pt and Pt-Ru powders. The $(COOH)_2$ oxidation reaction is seen to take place at more negative potentials (ca. 80 mV roughly estimated by extrapolation as shown in fig. 1) for the Pt powder than for the Au electrode. This result suggests that Pt catalyzes the $(COOH)_2$ oxidation reaction more strongly than Au and clearly much more effectively than Ru. The fact that the $(COOH)_2$ oxidation reaction takes place at more negative potentials than Au and not at all on Ru suggests that the $(COOH)_2$ oxidation currents observed for Pt containing electrodes are directly related to the Pt area, particularly for electrodes exposing no or little Au to the electrolyte solution.

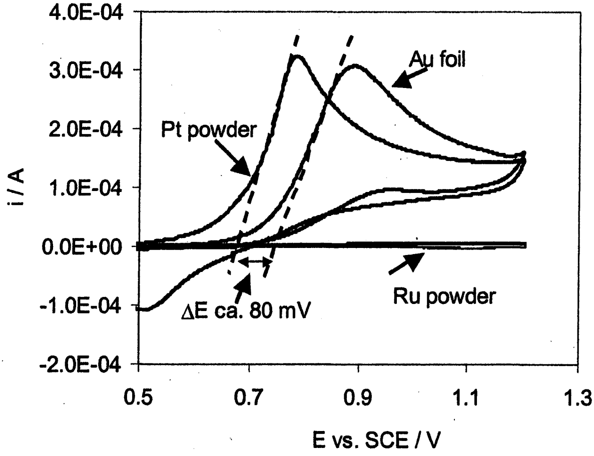

Fig. 1 Typical cyclic voltammograms for Au foil, Pt and Ru powder electrodes recorded at 20 mV s^{-1} in quiescent 10^{-2} M $(COOH)_2$ + 0.5 M H_2SO_4 solutions.

The faradaic $(COOH)_2$ oxidation at potentials below the oxygen evolution reaction (oer) using polycrystalline Pt has been studied previously (9). It has been shown that undissociated $(COOH)_2$, i.e., $(COOH)_2$ in acidic, aqueous solution, is oxidized to CO_2 according to the following net reaction (9):

$$(COOH)_2 = 2CO_2 + 2H^+ + 2e^- \qquad [1]$$

Three possible reaction pathways for the oxidation reaction of $(COOH)_2$ using Pt electrodes, have been suggested (9). All three reaction pathways involve adsorptive interactions of the oxalic acid with the Pt surface (according to a Temkin isotherm), thus emphasizing the importance of the electrode type.

RDE $(COOH)_2$ oxidation studies using Pt electrodes

Sweep rate studies and limiting current calculations using unstirred solutions showed that the electrochemical $(COOH)_2$ oxidation reaction observed using Pt catalyst electrodes takes place under mass transport controlled conditions (10). However, the $(COOH)_2$ oxidation reaction needs to take place under activation controlled conditions in order to relate the $(COOH)_2$ oxidation current to the total Pt area. Hence, in this work, the $(COOH)_2$ electrolyte solutions were rapidly stirred employing a rotating disc electrode arrangement to ensure that the $(COOH)_2$ oxidation reaction takes place under activation controlled conditions. Furthermore, the powder electrodes were prepared as thin layers of small total surface areas (< 0.2 cm^2) to allow all Pt catalyst sites to be involved in the activation controlled $(COOH)_2$ oxidation reaction, as discussed in the following sections.

Fig. 2 shows a plot for the $(COOH)_2$ oxidation currents (◇), $i_{p,a}$, extracted from raw i-E curves at 1.1 V as a function of the square root of the rotation rate ($\omega^{1/2}$) using a polycrystalline (0.2 cm^2, geometrical area) Pt RDE. (The i-E curves were recorded at 20 mV s^{-1}.) It is seen that the $i_{p,a}$ values are independent of the rotation rate provided that sufficiently high rotation rates (≥ 2000 rotations per minute (rpm)) are employed. The $i_{p,a}$ values measured at higher rpm's (≥ 2000 rpm) were found to vary by $\pm 2 \cdot 10^{-4}$ A cm^{-2}, thus accounting for the scatter in the experimental $i_{p,a}$ data. At lower (≤ 1000) rpm's, a decrease of the $i_{p,a}$ value with decreasing $\omega^{1/2}$ is observed, indicating that elements of mass transport control are present at these lower rotation speeds. The result indicate that by operating at rotation rates larger than 2000 rpm's, it is possible to study the $(COOH)_2$ oxidation reaction under activation control.

It is well known that the mass transport limited current (i_L) is proportional to $\omega^{1/2}$, according to the Levich equation (11), as follows:

$$i_L = B\varpi^{1/2} = 0.20nFAD^{2/3}v^{-1/6}\varpi^{1/2}c^o \qquad [2]$$

In eq. (2), n is the number of electrons (in the case of the $(COOH)_2$ oxidation reaction studied here n equals 2); F is Faraday's constant, A the surface area, D the diffusion coefficient ($5 \cdot 10^{-6}$ cm^2s^{-1} (10)), ν the kinematic viscosity (0.01 cm^2s^{-1} (12)), ω the rotation rate in rpm and c^o the concentration (this case: 10^{-5} mol cm^{-3}). B is the slope of a plot of i_L vs. $\omega^{1/2}$ and is defined as shown in eq. (2). Therefore, for a 0.2 cm^2 electrode, a theoretical slope of $4.8 \cdot 10^{-5}$ A $rpm^{-1/2}$ is calculated using this relationship and a D value of $5 \cdot 10^{-6}$ cm^2s^{-1}. This value is of the same order of magnitude as the experimentally obtained slope value of $3 \cdot 10^{-5}$ A $rpm^{-1/2}$ for the $(COOH)_2$ oxidation data observed at lower (≤ 1000) rpm's, although only two data points are used in this experiment. The i_L dependence for the Fe^{2+} oxidation reaction (△) on $\omega^{1/2}$ is also shown in fig. 2. An experimental slope of $1.2 \cdot 10^{-5}$ A $rpm^{-1/2}$ is found for this one electron reaction using a 5 mM $Fe(CN)_4^{2-}$ in 1 M KCl solution. The experimental slope for the Fe oxidation reaction is very close to the theoretical slope of $1.4 \cdot 10^{-5}$ A $rpm^{-1/2}$, calculated using a D value of $6.5 \cdot 10^{-6}$ $cm^2 s^{-1}$ (13).

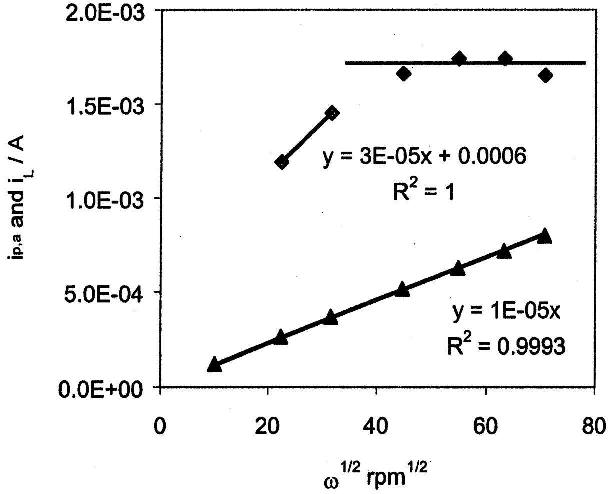

Fig. 2 $i_{p,a}$ (◇) and i_L (△) dependence for the $(COOH)_2$ and Fe^{2+} oxidation reaction, respectively on $\omega^{1/2}$ using a 0.2 cm^2 (geometrical area) Pt rotating disc electrode. 10^{-2} M $(COOH)_2$ in 0.5 M H_2SO_4 (◇) and 5 mM $Fe(CN)_4^{2-}$ in 1 M KCl (△) solutions were used. The solid lines represent the best fit to the experimental data.

Fig. 3 shows a typical current-potential (i-V) curve recorded at 20 mV s^{-1} in a 10^{-2} M $(COOH)_2$ + 0.5 M H_2SO_4 solution using a polycrystalline (0.2 cm^2, geometrical area) Pt RDE rotated at 2000 and 5000 rpm's. It is seen that the i-V curves are essentially the same (within an experimental current density variation of $\pm 2 \cdot 10^{-4}$ A estimated at the peak maxima ($i_{p,a}$)), i.e., i-V curves are independent of the rotation rate consistent with an activation controlled reaction. Consistent with this view of an activation controlled mechanism, the experimentally observed peak currents are also smaller than the i_L currents predicted for this oxidation reaction, as a i_L value of $2.2 \cdot 10^{-3}$ A is predicted by eq. (2) for 2000 rpm and a 0.2 cm^2 electrode. Sweep rate studies carried out at high rpm's provided further support for an activation controlled reaction mechanism, as i-V curves recorded for the same electrode and conditions, but employing different sweep rates (10 - 30 mV s^{-1}), were essentially the same. However, the shape of the experimentally observed i-V curve for the $(COOH)_2$ oxidation reaction is unusual for a classical activation controlled charge transfer reaction. For an activation controlled reaction, a steady increase in current with increasing potential in an exponential manner is predicted, unlike the decrease in current, and hence current maxima, observed here. The experimentally observed current maxima and decrease in the $(COOH)_2$ oxidation current is believed to be related to a continuous passivation of the Pt surface, taking place with increasingly positive potentials (14). The passivation process is thought to involve the formation of higher Pt oxides that are known to form at potentials more positive than 1.3 V vs. RHE, i.e, ca. 1.06 V vs. SCE (14). Consistent with this view, it has also been observed that preformed, thick Pt oxide films display little or no activity towards the oxidation of $(COOH)_2$ in the more positive potentials region where O_2 is evolved (15).

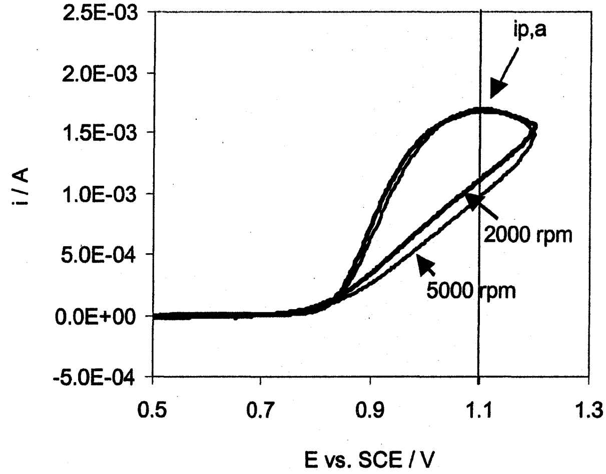

Fig. 3 Experimental i-V curves recorded at 20 mV s^{-1} for the oxidation of 10^{-2} M $(COOH)_2$ in 0.5 M H_2SO_4 using a 0.2 cm^2 (geometrical area) Pt rotating disc electrode. Different rotation rates, as indicated in the figure, were employed. The seventh, steady-state cycles recorded at a particular rotation rate are shown.

Conversion of the $(COOH)_2$ oxidation currents to the Pt surface area

The following relationship between the oxidation current (i_a) and potential, E, applies for the activation controlled $(COOH)_2$ oxidation reaction at sufficiently high over-potentials (12):

$$i_a = nFAk_o c_{(COOH)_2} \exp^{\alpha_a \frac{nF}{RT}(E-E^o)} \qquad (3)$$

In eq. (3), n is the number of electrons (i.e., 2 for the $(COOH)_2$ to CO_2 oxidation), F Faradays constant, α_a the transfer coefficient, R the gas constant, T the temperature and E^o the standard potential. Eq. (3) shows that the activation controlled oxidation current, i_a, is proportional to A, and hence this equation can be used to relate the ratio of the experimentally observed i_a values to the real Pt area, A_{Pt}. It follows from eq. (3) that this ratio, R_{APt}, is defined as follows:

$$R_{APt} = \frac{i_a}{A_{Pt}} = nFk_o c_{(COOH)_2} \exp^{\alpha_a \frac{nF}{RT}(E-E^o)} \qquad (4)$$

Eq. (4) predicts the R_{APt} ratio to be constant for a particular $(COOH)_2$ concentration and potential, even if the Pt electrodes have different areas. Table I, summarizes the experimentally observed $i_{p,a}$and A_{Pt} values for Pt RDE and Pt powder electrodes (i.e., all electrodes contain only Pt and no Ru). The ratio of the $i_{p,a}$ to A_{Pt} values, i.e., the value of the R_{APt} factor at 1.1 V, is also given in Table I. The A_{Pt} values were estimated from the CO_{ads} charge using a charge to area conversion factor of 420 $\mu C\ cm^{-2}$ (3). Average R_{APt} values of 100 ± 5 cm^2A^{-1} are found for the Pt powder and polycrystalline Pt electrodes tested. The R_{APt} ratios are essentially the same for the Pt powders and the Pt RDE's indicating that the $(COOH)_2$ oxidation reaction is not influenced by the particle size of the Pt powders studied here.

Table I

$(COOH)_2$ oxidation currents and R_{APt} factors for a range of Pt electrodes

	$i_{p,a}$ $(COOH)_2^{\#}$ / A	$A_{Pt}^{\#\#}$ / cm^2	R_{APt} (=$A_{Pt}^{\#\#}/i_{p,a}$) /cm^2A^{-1}
Pt RDE's	$1.65 \pm 0.2 \cdot 10^{-3}$	0.16 ± 0.01	100 ± 5
1st Pt powder	$1.02 \pm 0.1 \cdot 10^{-3}$	0.104 ± 0.005	102 ± 5
2nd Pt powder	$1.8 \pm 0.2 \cdot 10^{-4}$	0.018 ± 0.0001	100 ± 5
3rd Pt powder	$1.65 \pm 0.1 \cdot 10^{-3}$	0.173 ± 0.009	105 ± 5
4th Pt powder	$7.9 \pm 0.8 \cdot 10^{-4}$	0.073 ± 0.004	92 ± 5

#: Steady-state $i_{p,a}$ values extracted at 1.1 V vs. SCE from raw i-V curves recorded at larger than 3000 rpm's and 20 $mV\ s^{-1}$ in 10^{-2} M $(COOH)_2$ + 0.5 M H_2SO_4 solutions. Experiments were carried out at different rpm's confirming that the $i_{p,a}$ value is independent of the rotation rate;

##: Pt surface area (A_{Pt}) estimated from CO_{ads} stripping voltammetry using a charge to area conversion factor of 420 $\mu C\ cm^{-2}$ (3).

The relationship between the electro-active Pt area and the CO_{ads} charge: The conversion factor (f_{APt})

The electro-active Pt area can be related to the experimentally obtained CO_{ads} stripping charge using a conversion factor, f_{Apt}, as follows:

$$A_{Pt} = \frac{Q_{COads}}{420\mu Ccm^{-2}} * f_{APt} \tag{5}$$

In this work, the f_{APt} factor is taken as unity for Pt only (i.e., Ru free) electrodes, i.e., assuming that each Pt surface atom adsorbs one CO molecule. However, it should be noted that the ratio of CO adsorbed atoms vs. Pt surface atoms is often less than unity, (namely ca. 0.8-0.9 (3)), and hence, Pt areas estimated using the CO_{ads} stripping charge, and an f_{APt} factor of one, are somewhat lower than the true electro-active Pt areas. Despite this fact, a f_{APt} factor of unity is used here, as this error is eliminated in the Pt area estimation for the Pt-Ru powders using the $(COOH)_2$ method introduced in this work.

As discussed above, the f_{APt} factor for the Pt electrodes is expected to be unity, while the f_{APt} value for Pt-Ru electrodes is likely less than unity and expected to be influenced by the electrode composition. Metallic Ru contributes to the CO_{ads} charge, however, it is inactive towards the $(COOH)_2$ oxidation reaction (as shown above), thus reducing the f_{APt} value. With increasing surface fraction of metallic Ru vs. Pt the contribution of the Ru sites to the CO_{ads} charge increases, and hence, the f_{APt} value is predicted to decrease. In fact, the value of the f_{APt} factor for a particular catalyst yields the fraction of the CO_{ads} molecules that adsorb onto Pt sites, and vice versa, the value of $1\text{-}f_{APt}$ yielding the fraction of CO_{ads} molecules on the other catalyst components (i.e., Ru in the present study). It is clear that the f_{APt} value needs to be estimated for each individual powder. The f_{APt} value for Pt-Ru powders can be obtained from the experimentally determined Pt area values estimated from $(COOH)_2$ oxidation experiments, e.g., using the R_{APt} value of 100 ± 5 cm^2A^{-1} estimated at $i_{p,a}$, i.e., 1.1 V for 10^{-2} M $(COOH)_2$ in 0.5 M H_2SO_4 solutions, and combining eqs. 4 and 5, as follows:

$$f_{APt} = \frac{\dfrac{i_a}{R_{APt}}}{\dfrac{Q_{COads}}{420\mu Ccm^{-2}}} = \frac{A_{Pt}}{\dfrac{Q_{COads}}{420\mu Ccm^{-2}}} \tag{6}$$

It should be noted that any $(COOH)_2$ oxidation current can be used for the Pt area estimation carried out in such a manner provided that the R_{APt} factor is estimated for the corresponding potential. Using additional $(COOH)_2$ oxidation current data and R_{APt} values found and estimated for a range of potentials clearly increases the accuracy of the method. Furthermore, it is possible to estimate the $(COOH)_2$ oxidation currents at potentials less positive than 1.1 V. This is particularly important for catalysts that may corrode at such positive potentials, as is often observed for catalysts containing Ru. In this work, CO_{ads} stripping voltamogramms were also recorded before and after $(COOH)_2$

oxidation studies were carried out for a particular catalyst. A decrease in CO_{ads} charge would indicate a loss of catalyst due to either catalyst detachment from the support and/or partial dissolution of the catalyst, while changes in the shape of the CO_{ads} stripping peak (typically a shift of the oxidation wave to more positive potentials) likely indicates the preferential dissolution of Ru from the catalyst system. In this work, it was found that all Pt powders 1 and the Pt/RuO_2 (thermal) powder 4 electrodes did not dissolve or detach from the glassy carbon support, as a result of the $(COOH)_2$ oxidation studies carried out involving potentials as high as 1.2 V. However, it was necessary to restrict the potential range of the other Pt-Ru electrodes (powders 3, 3a, 5 and 6), to potentials less negative than 0.8 V to avoid changes in the catalyst area as well as dissolution of the Ru component.

It is noteworthy that the shape of the experimentally observed current density (J)-V curves for the individual Pt and Pt-Ru powders were found to be essentially the same for all powders investigated in this work. This is shown in fig. 4 for Pt powder 1 and Pt/RuO_2 (thermal) powder 4 electrodes. The experimentally observed currents were normalized using the CO_{ads} charges and f_{APt} factors of unity and 0.55 for the Pt powder 1 and the Pt/RuO_2 (thermal) powder 4, respectively. The meaning of the value of these f_{APt} factors is further discussed below.

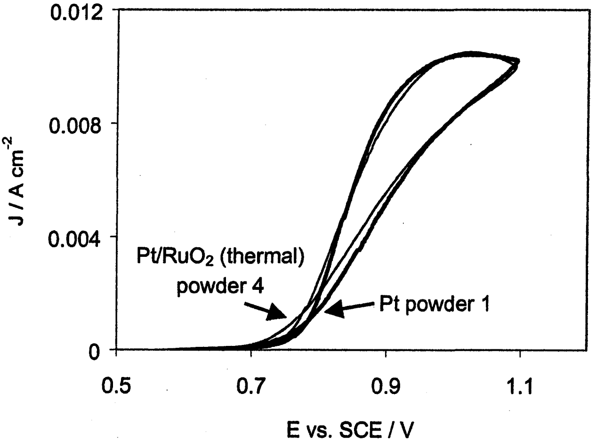

Fig. 4 Typical J-V curves for Pt powder 1 (thick line) and Pt/RuO_2 (thermal) powder 4 (thin line) electrodes recorded at 8000 rpm's and 20 mV s^{-1} in 10^{-2} M $(COOH)_2$ + 0.5 M H_2SO_4 solutions. The currents were normalized using the experimentally observed CO_{ads} charge and a f_{APt} factor of unity and 0.55 for the Pt powder and $PtRuO_2$ (thermal) powder 4 electrodes, respectively.

The f_{APt} values for the individual Pt and Pt-Ru powders estimated in this work are listed in Table II. These f_{APt} values represent the average value extracted from the experimental data for at least five electrodes prepared using a particular powder. The Pt at. % values for the individual powders obtained from XPS measurements are also given in Table II (7). Generally, XPS data yield surface concentrations. However, the estimation of the Pt and Ru surface concentrations for the powders investigated in this work may be complicated due to possible inhomegenities within the Pt and Ru phases, and/or the presence of multilayers of Ru on the surface of the catalyst particles. Therefore, the XPS data shown in Table II need to be used with caution. In the case of the PtRu alloys (powders 3 and 3a) the Pt surface concentration corresponds to the bulk concentration, namely 70 and 55 at % Pt, respectively. This likely indicates that the Pt and Ru components of this PtRu alloys are uniformly distributed within the particle and it is believed that the XPS data yield the true surface concentrations. However, a lower Pt surface concentration than bulk Pt concentration, i.e., a surface enrichment in Ru, is suggested by the XPS data for the Pt-Ru powders 4, 5 and 6. The surface enrichment of Ru for the catalyst particles prepared involving the thermal decomposition of $RuCl_3$ (powders 4 and 5) is easily understandable, as the $RuCl_3$ precursor is distributed among preformed Pt particles. The data for these particular powders suggest that Pt and Ru are not uniformly distributed within a particular catalyst particle, thus likely resulting in a discrepancy between the true Pt surface concentration and the Pt concentration estimated by XPS (shown in Table II). A similar argument can be used to explain the data for the ball-milled Pt/RuO_2 powder 6.

Table II

f_{APt} values and XPS data for a range of Pt and Pt-Ru powder electrodes

Pt based powder type	f_{APt} ##	Pt / atomic % #
Pt (1)	1 ± 0.05	1
PtRu alloy (3)	0.7 ± 0.05	0.7
PtRu alloy (3a)	0.54 ± 0.03	0.55
$PtRuO_2$ (thermal) (4)	0.55 ± 0.03	0.36
PtRu (H_2 reduced) (5)	0.45 ± 0.02	0.44
$PtRuO_2$ (ball-mill) (6)	0.5 ± 0.03	0.54

#: Atomic fraction of Pt (atomic Pt concentration divided by the total atomic concentration of Pt and Ru) obtained from XPS data, as discussed in detail elsewhere (7). The atomic fraction of Pt data indicated in the 3rd column for the powders 4, 5 and 6 are thought to be lower than the actual values due to possible inhomogeneities of the Pt and Ru phase within the catalyst particles that could complicate the XPS analyzes;

##: The f_{Apt} factors are estimated from $(COOH)_2$ oxidation studies and CO_{ads} stripping voltammetry, as described in the text.

Meaning of the f_{APt} conversion factor

These f_{APt} factors listed in Table II can be used to calculate the Pt area from the experimentally observed CO_{ads} charge for any electrode made up of the corresponding Pt based catalyst and using eq. (5). Furthermore, the value of the f_{APt} factor indicates the fraction of CO that is adsorbed on Pt sites, and hence, this factor also yields information about the fraction of CO adsorbed on the Ru sites of the catalysts studied here. This is clearly seen for the PtRu alloy catalyst powders 3 and 3a. The f_{APt} factor of 0.7 found for the PtRu powder 3 suggests that 70 % of the adsorbed CO molecules adsorb on Pt sites, while 30 % are adsorbed on other sites, i.e., Ru. Similarly, the f_{APt} factor of 0.54 estimated for the PtRu alloy powder 3a suggests that 54% of the adsorbed CO molecules are adsorbed on Pt sites, while 46% are adsorbed on Ru sites. This, and the fact that the surface atomic fraction of Pt to Ru for these two PtRu alloy powders 3 and 3a is 0.3:0.7 and 0.54:0.46, respectively, suggests that one CO molecule adsorbs per Pt as well as Ru site. These results further suggest that the Ru sites are likely present in their metallic state at the potential of –0.1 V where CO is adsorbed, as CO adsorption onto the oxide covered Ru surface is generally not observed.

The f_{APt} factors for the $PtRuO_2$ (thermal) powder 4, PtRu (H_2 reduced) powder 5 and $PtRuO_2$ ball-milled powder 6 are less than unity indicating that CO also adsorbs onto Ru sites. In fact, 45 (powder 4), 55 (powder 5) and 50 (powder 6) % of the CO_{ads} molecules adsorb onto Ru sites, thus further suggesting that a significant fraction of the Ru sites of these powders are in the reduced Ru metal state.

CONCLUSIONS AND SUMMARY

It has been shown that the activation controlled $(COOH)_2$ oxidation current can be related to the electro-active Pt area for Pt based catalysts. The combination of the CO_{ads} stripping voltammetry and the activation controlled $(COOH)_2$ current was applied to estimate the Pt surface area for a range of Pt-Ru powder electrodes. It was also found that the combination of these two methods can yield *in-situ* information about the fraction of CO molecules that adsorb on Pt vs. the ad-metal (i.e., Ru in this work) catalyst sites. For the case of PtRu alloy electrodes, it was found that one mole of CO adsorbs per Pt as well as Ru sites at –0.1 V, i.e., the potential used for CO adsorption in this work. However, care must be taken to apply this method for the estimation of the electro-active Pt area and possible extraction of the fraction of CO molecules that adsorb on the individual catalyst sites. The catalysts must be stable within the potential range used to measure the $(COOH)_2$ oxidation current. Furthermore, a thin layer of catalyst particles must be applied to the electronically conductive support and the $(COOH)_2$ oxidation reaction must be carried out under controlled and rapid stirring conditions. It is also noteworthy that activation controlled currents are more susceptible to impurities and electrode poisoning effects than mass transport limited currents. This is due to the fact that for mass transport controlled conditions, the electrode area collapses to the geometrical area, while the real electro-active area determines the activation controlled currents.

ACKNOWELEGEMENTS

The authors like to thank P. L'Abbe (National Research Council Canada) for making the electrochemical cells used in this work and G. Pleizier (National Research Council Canada) for the XPS analyzes. Helpful discussions with Dr. E. Gileadi (Tel-Aviv University, Isreal) are also greatly appreciated.

REFERENCES

1. J. O'M. Bockris and H. Wroblowa, *J. Electroanal. Chem.*, **7**, 428 (1964)
2. M. Watanabe and S. Motoo, *J. Electroanal. Chem.,* **60**, 267 (1975)
3. H. Gasteiger, N. Markovic, P. Ross and E. Cairns, *J. Electrochem. Soc.,* **141**, 1795 (1994)
4. H.N. Dinh, X. Ren, F.H. Garzon, P. Zelenay, S. Gottesfeld, *J. of Electroanal. Chem.*, **491**, 222 (2000)
5. K. Kinoshita and P.N. Ross, *J. Electroanal. Chem.*, **78**, 313 (1977)
6. K.A. Friedrich, F. Henglein, U. Stimming and W. Unkauf,
7. C. Bock, M-A. Blackely and B. MacDougall, *in preparation*
8. T.J. Schmidt, H.A. Gasteiger and R.J. Behm, *J. Electrochem. Soc.,* **146**, 1296 (1999)
10. C. Bock, A. Smith and B. MacDougall,
11. E. Gileadi, Electrode Kinetics for Chemists, Chemical Engineers, and Material Scientists, VCH Publishers Inc (1993) New York
12. A. J. Bard and L. R. Faulkner, *Electrochemical Methods, Fundamentals and Applications*, John Wiley & Sons, Inc. (1980) New York
13. L. Lipp and D. Pletcher, *Electrochim. Acta*, **42**, 1091 (1997)
14. X. Giner, *Electrochim. Acta*, **4**, 42 (1961)
15. C. Bock, A. Smith and B. MacDougall in *Energy and Electrochemical Processes for a Cleaner Environment 2001*, Editors, C. Comninellis, PV-2001-23, p. 23, The Electrochemical Society Proceeding Series, Pennington, NJ (2001)

Proceedings of The Electrochemical Society, PV 2002-31, 481-489 (2002)
DOI: 10.1149/200231.0481PV © The Electrochemical Society

A Six-Cell 'Single-Cell' Stack for Stack Diagnostics and Membrane Electrode Assembly Evaluation

B. Pivovar, F. Le Scornet, C. Eickes, C. Zawodzinski, G. Purdy, M. Wilson, P. Zelenay

MST-11 Fuel Cells and Electrochemistry
Los Alamos National Laboratory
Los Alamos, NM 87544

ABSTRACT

Polymer electrolyte fuel cells are promising candidates as energy conversion devices in applications from portable power to stationary applications or electric vehicles. In order to achieve practical voltage, power and energy density, stacks are employed for almost all applications. Here, we present a six-cell 'single cell' stack in which individual cells can be isolated from the stack by current carrying leads found within each of the bipolar plates. The current carrying leads allow individual cells to be isolated from the rest of the stack, so that cells can either be tested together or independently. The design of the stack, utility for specific applications, including stack diagnostics and membrane electrode assembly (MEA) testing, and some experimental results, obtained using the stack, are presented. Special focus is given in this paper to the area of direct methanol fuel cell (DMFC) stacks, however the equipment and many of the experimental results presented are appropriate for other fuel cell systems.

INTRODUCTION

Polymer electrolyte fuel cells are currently being investigated for a number of applications with milliwatt to kilowatt power requirements. However, single cells are rarely adequate for specific applications so that stacks are typically employed to achieve the voltage, power, and energy density requirements necessary to compete in given applications. The cells in such stacks are usually placed in series with the same current passing through each of the individual cells.

A drawback of such a setup is that under normal conditions, the cell that reaches its mass transport limit first limits the performance of the entire stack. Further compounding this problem, optimized systems tend to operate near mass transport limits (relatively low stoich) because this lowers the balance of plant losses associated with pumps and compressors, and in the case of DMFCs, methanol crossover. In order to ensure optimum stack performance, even flow distribution through the cells is a critical concern in stack design.

While it is possible to monitor and control the flows through individual cells for some externally manifolded stacks, internally manifolded cells are often preferred due to the decreased number of individual parts and ease of assembly. Unfortunately, monitoring or controlling individual flow rates directly in internally manifolded stacks is usually impractical. Modeling of flow through stacks can yield insight, but tolerances of parts and components as well as issues involved with assembly can lead to significant errors. For MEA evaluation using stacks, this can make data interpretation difficult. For example, distinguishing the difference between performance losses due to uneven flow distribution versus individual MEA performance may not be possible. If more information were available on individual cell flow rates, it would lend insight into the performance loss mechanisms of the stack and be a useful tool for designing stacks with more equal flow distribution. Furthermore, if the flow rates through the individual cells can be accurately measured, evaluating individual MEA within a stack configuration becomes much more accurate, offering advantages in the number of MEAs that can be tested (throughput) and the number of test stations required (capital cost).

Here, we present a six-cell 'single cell' stack in which individual cells can be isolated from the stack by individual leads connected to each of the bipolar plates. The primary limitation of such a system is that the leads from each individual cell be capable of carrying the maximum current that the cells were designed for. For this system, the individual bipolar plates have been specially constructed to allow for high currents to be carried through each individual cell. This allows us to test individual cells over a much wider range of operating conditions, operate the stack with some cells removed from operation, and perform diagnostic experiments that are not otherwise possible.

EXPERIMENTAL

Six –celled 'single-cell' stack design

The stack, shown in Figure 1, consisted of six cells each of active area 22cm^2. The unique character of this stack comes from the bipolar plates, shown in Figure 2. The bipolar plates are not a single plate, but rather three components: a 0.036" thick 316 stainless steel current collector and two 0.125" thick graphite plates. Flow fields were machined into the outer faces of the graphite plates, and o-ring grooves were machined near the manifold channels and o-rings were used to isolate the stainless steel current collector from the reactant flow.

Two tabs were on opposite sides of the stainless steel current collectors and connected by spade connectors, one to act as voltage monitor and the other as a current carrier (in Figure 1, the current carrying spade connectors are visible on the left hand side of the Figure). These connections were capable of carrying currents greater than 10 Amps, so testing was limited to less than 0.5 Amps/cm^2. The focus of this work was DMFC testing so this current limit was sufficient, but for hydrogen fuel cell testing it might be desirable to work at higher current densities. This could be accomplished by moving to a thicker current collector and a higher rated spade connection or by decreasing the active area of the cells. All the spade connections were made at the same location along the length of the stack (see Figure 1), allowing for easier handling of the stack during testing. However, a high cell pitch (0.310") was necessary to allow adequate space for the connectors, leading to bipolar plates that are much thicker than those used in practical stacks. Thinner plates could be used if one were to stagger the leads.

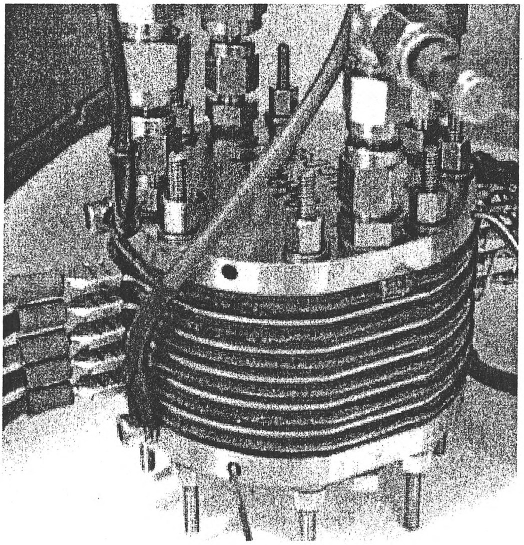

Figure 1: Six-celled 'single cell' stack with current carrying leads attached to left.

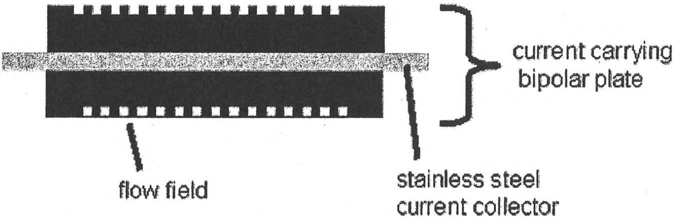

Figure 1: Current carrying bipolar plate for six celled 'single cell' stack.

A six-cell stack was chosen as a balance between having enough cells to determine reproducibility, being able to isolate issues associated with stack location (end cells vs. interior cells), and ease of data acquisition and manufacture. Six cells allowed us to test either three sets of two identical MEAs or two sets of three identical MEAs and isolate these MEAs from each other. The typical arrangements were cells 1 & 4, 2 & 5, 3 & 6 for the three sets of two identical MEAs and cells 1 & 3 & 5, 2 & 4 & 6 for the two sets of three identical MEAs.

Fuel cell experiments

MEA fabrication - MEAs were prepared from standard catalyst inks containing either unsupported platinum or platinum-ruthenium, water, and Nafion 1100 solution. These inks were mixed by sonication and then applied to the membranes by direct painting. All the membranes tested had identical electrodes. Nafion 117 films were pretreated by boiling for 1.5 hours in each step in 3% H_2O_2, deionized water, 0.5 M H2SO4, and again in deionozed water.

Polarization curves – Current versus voltage performance of the stacks on MeOH/air or H_2/air were obtained. One significant advantage of this stack was the ability to obtain performance of individual cells, thereby extending the current range and learning about the mass transport limits of individual cells.

Anode polarization - Current versus voltage performance of the stacks on MeOH/H_2 were obtained. For DMFCs, this data yields quantitative data about the anode performance(1). One significant advantage of this stack was the ability to obtain performance of individual cells, thereby extending the current range and learning about the mass transport limits of individual cells.

CO stripping – CO (99.3% purity, 1.8 L min^{-1}) was adsorbed at 0.1 V versus H_2 for 15 minutes at 25°C. The gaseous CO was removed with purging N_2 (6.0 L min^{-1}) for 30 minutes. The beauty of the 'Single Cell' stack configuration is the possibility of stripping off the adsorbed CO for one cell while keeping the CO adsorbed in the remaining five cells at 0.1 V. The CO could then be consecutively removed for each catalyst surface by a linear potential sweep from 0.1 to 0.8 V with a scan rate of 2.3 mV s^{-1}. The stripping charge was determined from the peak area under the peak associated with CO adsorption and the scan rate(2,3). This measurement was not possible using a traditional stack.

Limiting current methanol crossover - Current versus voltage performance of the stacks on MeOH/N_2 were obtained. From this data open circuit methanol crossover through each individual cell could be measured(1). Because the MEAs presented here were identical, the data obtained were approximately equal and will not be discussed, but it is another example of a measurement not possible using a traditional stack.

High frequency resistance – High frequency resistances were also measured. While these can also be measured in traditional stacks, even cells that have been short-circuited still give meaningful resistances.

Lifetime studies – Stacks were held at a constant current and the voltage change of the individual cells over time was recorded. This is a traditional stack test, however, because of the addition of the current collecting bipolar plates, some of the aforementioned fuel cell tests could be run periodically during the life test to isolate the loss mechanisms associated with declining performance.

RESULTS AND DISCUSSION

For purposes of illustration, a specific six-cell 'single-cell' test case is presented here. In this case, three sets of two identical cells (1 & 4, 2 & 5, 3 & 6) were prepared. This arrangement allowed us to test duplicate cells and decouple issues associated with cell location. The MEAs were of the same catalyst loading and all were on Nafion 117. At the beginning of our testing, cells 2 & 5 had developed severe flow problems due to specific differences in processing. While even single cell failure is catastrophic for MEA testing within traditional stacks, due to the construction of our stack we were still able to test cells 1, 3, 4 & 6, by short-circuiting cells 2 & 5. Thereby salvaging the time and effort needed to prepare and assemble the stack.

The purpose of this stack was to understand DMFC MEA degradation for MEAs prepared by different processing routes. Therefore, a DMFC lifetime experiment was run at 2 amps for 360 hours and the voltage response of the cells was recorded as a function of time, see Figure 3. The operating conditions for the stack are 1M methanol at a flow rate of 18 mL/min preheated to 80C for the anode, and 2.14 L/min air humidified to 90C without backpressure inside an oven at 80C. The first 20 hours of the lifetest were used as a 'break-in' period and data were not recorded. The lifetest was stopped periodically, after 20, 120 and 339 hours, so that the cell performances could be evaluated as a function of time. These breaks are visible in Figure 3 as cell performance is recovered following the intermittent testing. It is worth noting that the cathode humidifying bottle in the test station affected cell performance between 20 and 120 hours. After the faulty bottle was replaced (120 hours), the performance of the cells improved significantly and performance was much more even.

High frequency resistances (HFR) were also recorded during the lifetest, see Figure 4. The cells showed little change in resistance, except for cell 6, which showed a slightly elevated HFR between 20 and 120 hours. This elevated HFR was likely related to the cathode humidifying bottle and because cell 6 faced the cathode endplate it would tend to be more susceptible to cathode flow effects.

During breaks in the lifetest, various single cell and stack measurements were performed to evaluate the performance of the individual MEAs. Here, we will focus on anode polarization and CO stripping on the anode.

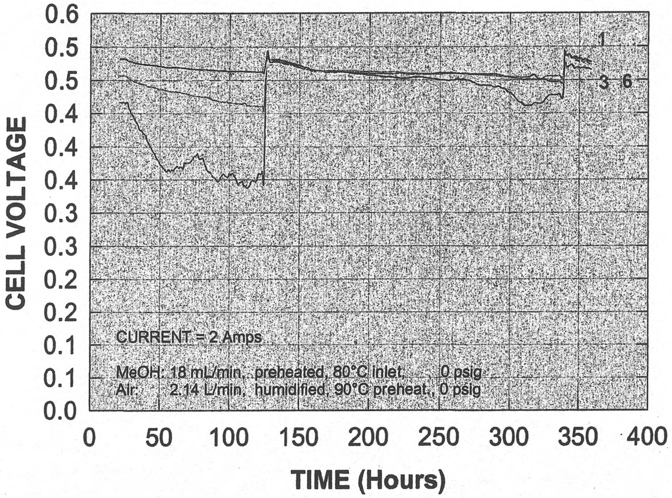

Figure 3: Voltage response of cells 1, 3, 4 and 6 at 2 amps for a 360-hour lifetest

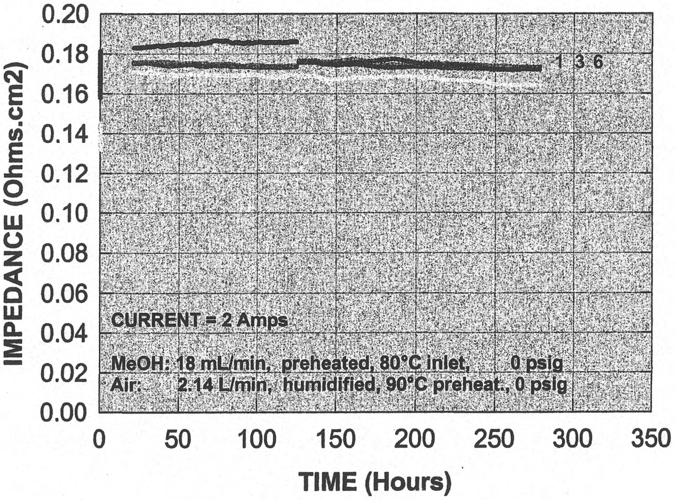

Figure 4: High frequency resistance of cells 1, 3, 4 and 6 at 2 amps

Figure 5 shows a typical CO stripping response for a CO-free DMFC anode versus a DMFC anode that has been saturated with adsorbed CO. The area under the peak is proportional to the amount of CO that has been adsorbed by the surface, or in other words, the active catalyst surface area. By quantifying the changes in active surface area as a function of lifetime in the stack, the degradation mechanisms associated with declining performance can be better understood.

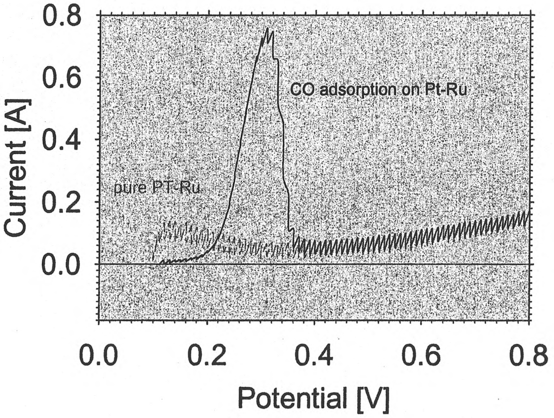

Figure 5: Typical anode CO stripping responses for a DMFC anode exposed to CO and a CO-free surface at 80°C. CO (99.3%) was adsorbed for 15 min and 1.8 L min^{-1}. Gaseous CO was removed with purging N_2 (6.0 L min^{-1}) for 30 min. The adsorbed CO was oxidatively removed with a single potential sweep from 0.1 V to 0.8 V, scan rate 2.3 mV s^{-1}

The changes in the anode CO stripping charge as a function of time are shown in Table 1. A significant decrease in the total stripping charge was shown for each of the electrodes, with an average decrease of an 8% after 120 hours and 13% after 339 hours. The numbers presented in these tables represent the average of two separate stripping experiments. Interestingly, the numbers from cell to cell and between scans show good consistency and reproducibility. The data suggest that one possible loss mechanism in the system is loss of active catalyst surface area on the anode as a function of time.

Anode polarization data complements the CO stripping data presented above. Figure 6 represents the average anode polarization of cells 1, 3, 4 and 6 as a function of time. From Figure 6, it is obvious that over time a higher potential is required to give the same current density at earlier times. These results are tabulated for single cells in Table 2 in terms of current density at 0.3 volts. The results in Table 2 show qualitative agreement with those shown in Table 1 for CO stripping, with the current density associated with the anode polarization at 0.3 V decreasing on average 14% after 120 hours and 19% after 339 hours. While the decreases in current density are not as uniform for cell to cell as the decrease in active surface area, this might not be surprising because interpreting losses in current density at a specific voltage are not as straight forward as interpreting losses in active surface area.

	Charge [C]			S.C. (C)	
cell #	20 h	120 h	% loss	339 h	% loss
1	47.6	43.4	9	41.2	13
4	42.3	38.7	9	36.8	13
3	42.4	40.0	6	36.6	14
6	45.1	41.6	8	39.1	13
Average	44.4	40.9	8	38.4	13

Table 1: Anode CO stripping charge for cells 1, 3, 4 and 6 as a function of time

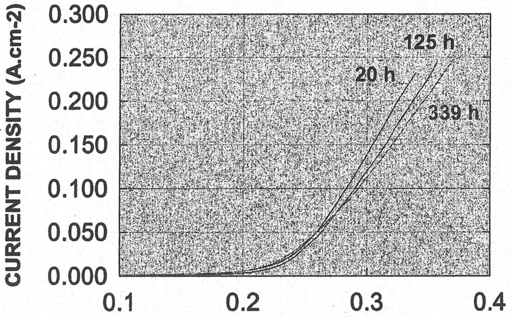

Figure 6: Average anode polarization of cells 1, 3, 4 and 6 as a function of time.

	Curr.Dens. @ 0.3V			C.D. (0.3V)	
cell #	20 h	120 h	% decrease	339 hr	% decrease
1	132	116	12	107	19
4	136	115	15	105	23
3	145	121	17	113	22
6	140	125	10	124	11
Average	138	119	14	112	19

Table 2: Anode polarization for cells 1, 3, 4 and 6 as a function of time

CONCLUSIONS

The six-cell 'single cell' stack in which individual cells could be isolated from the stack by current carrying leads found within each of the bipolar plates was found to be useful in the lifetime testing of DMFC stacks presented here. The stack has shown utility in screening multiple MEAs without requiring multiple test stations, and can also be used as a diagnostic tool in stack design.

ACKNOWLEDGEMENTS

Expressed appreciation to the U.S. Department of Energy and the Defense Advanced Research Project Agency (DARPA) for support.

REFERENCES

1. X. Ren, T.E. Springer, and S. Gottesfeld, in Proton Conducting Membrane Fuel Cells II/1998, Gottesfeld, S. and Fuller, T.F., Editors, PV98-27, 341-357, The Electrochemical Society Proceedings Series, Pennington, NJ (1998).
2. H. N. Dinh, X. Ren, F. H. Garzon, P. Zelenay and S. Gottesfeld, *J. Electroanal. Chem.* **491**, 222 (2000).
3. H. A. Gasteiger, N. Marković, P. N. Ross, Jr. and E. J. Cairns, *J. Phys. Chem.* **98**, 617 (1994).

Proceedings of The Electrochemical Society, PV 2002-31, 490-505 (2002)
DOI: 10.1149/200231.0490PV © The Electrochemical Society

OPTIMIZATION OF CARBON-SUPPORTED PLATINUM CATHODE CATALYSTS FOR DMFC OPERATION

Yimin Zhu, Eric Brosha and Piotr Zelenay

Materials Science and Technology Division (MST-11)
Los Alamos National Laboratory
Los Alamos, New Mexico 87545, USA

ABSTRACT

In this paper, we describe performance and optimization of carbon-supported cathode catalysts at low platinum loading. We find that at a loading below 0.6 mg cm^{-2} carbon-supported platinum outperforms platinum black as a DMFC cathode catalyst. A catalyst with a 1:1 volume ratio of the dry Nafion^{TM} to the electronically conducting phase (platinum plus carbon support) provides the best performance in oxygen reduction reaction. Thanks to improved catalyst utilization, carbon-supported catalysts with a platinum content varying from 40 wt% to 80 wt% deliver good DMFC performance, even at relatively modest precious metal loadings investigated in this work.

INTRODUCTION

Until alternative catalysts are developed, the most active anode and cathode catalysts for polymer electrolyte fuel cells (PEFCs), including the direct methanol fuel cell (DMFC), are likely to be platinum-based (1,2). Consequently, the need for limiting precious metal loading while maximizing catalyst utilization, with the emphasis on the optimization of electrode structure, may remain one of the primary goals of PEFC research for the foreseeable future. Thanks to significant progress in electrocatalysis and membrane-electrode assembly (MEA) research over past 10-15 years, the total Pt loading required by the H_2/air fuel cells has been reduced by more than an order of magnitude, from *ca.* 4.0 mg cm^{-2} (with unsupported Pt blacks) to as low as 0.2 mg cm^{-2} (with well-dispersed carbon-supported Pt catalysts) (3,4,5). In most cases, this impressive decrease in the required precious metal loading has been achieved with catalyst formulations containing no more than 20 wt% of Pt.

DMFCs suffer from the methanol permeation (crossover) through the polymer electrolyte membrane that kinetically burdens the cathode catalyst (5,7,8). As a consequence, the cathode loading needs to be much higher than that of an H_2/air fuel cell, reaching levels quite comparable to that of the anode loading and bringing the total cell Pt loading to ~10 mg cm^{-2} or even more.

In this work, we demonstrate that respectable DMFC cathode activity can be achieved with carbon-supported platinum catalysts having Pt-to-C ratios higher than used for the cathode in H_2/air fuel cells. Good performance will be demonstrated with cathode Pt loading not exceeding 0.6 mg cm^{-2}. It will also be shown that careful optimization of platinum content in the cathode catalyst can offer substantial improvements in DMFC performance at the low catalyst loading.

EXPERIMENTAL

All cathode catalysts used in this work were supported on carbon black, with the platinum content varying from *ca.* 30% to 80% by weight. The anode catalyst was a Pt-Ru black from Johnson Matthey, UK, used at a high loading of *ca.* 9.0 mg cm^{-2}. The anode and the cathode catalyst inks were made by dispersing appropriate amount of the catalyst powder in water with added 5 wt% suspension of Nafion™ in a mixture of alcohols (Solution Technology Inc., USA). The inks were then applied to Nafion™ 117 membranes. The experimental techniques employed in this work for measuring fuel cell performance and high-frequency membrane resistance have been described in detail elsewhere (9). In this study, both upward and downward voltage scans were used for each polarization curve measurement. Polarization plots were taken using a voltage interval of 50 mV and 25 s waiting time between points. The curves in the two scan directions were averaged and presented here as a single curve. To measure the high-frequency cell resistance, a sinusoidal wave perturbation at 2.4 kHz was applied to the fuel cell load, resulting in a few millivolt cell voltage variation and the associated cell current variations. At such a high frequency, the imaginary part of the impedance was verified to be negligible.

MEAs with different Pt/C catalysts were typically conditioned in an H_2/air operating mode for 2-5 hours. Hydrogen-air cell polarization plots were then recorded as an initial test of cathode activity, followed by DMFC tests. In all DMFC experiments, 1.0 M methanol solution was pumped through the anode flow field at 2 mL min^{-1} against a zero backpressure. The cathode air was humidified at 95°C, and flown through the cathode at 460 mL min^{-1} (standard flow conditions). Cathode back-pressurize was ~2.0 atm,resulting in a total cathode pressure of 2.8 atm (exactly, 2.04 atm back pressure plus 0.76 atm, the atmospheric pressure at the altitude of Los Alamos). When required, *e.g.* for cell conditioning, hydrogen-air fuel cell operating mode was used. In such cases hydrogen gas was humidified at 105°C and flown at a rate of 150 mL min^{-1} against a backpressure of ~2.0 atm. The cell operating temperature was 80°C and the geometric active area of the MEAs used in this work was 5 cm^2.

In order to make sure that the cathode catalyst comparison was not affected by the individual anode performance, all anodes had the same loading of the Pt-Ru black catalyst. The anode activity was independently verified by measuring anode polarization plots. In these experiments, 1.0 M methanol was flown through the anode at a rate of 2.0 mL min^{-1}, with the fuel cell cathode serving as a combined reference/counter electrode (a dynamic hydrogen electrode, DHE). The rate of hydrogen gas flow through the cathode was 110 mL min^{-1} at a backpressure of 0.7 atm (1.4 atm total pressure). The hydrogen was humidified at a temperature 10°C higher than the cell temperature. The potential scan rate was 2.0 mV s^{-1}.

RESULTS AND DISCUSSION

Low Loading Operation of the Pt Black and 40% Pt/C Cathodes

In the first part of this work, the performance of a 40% Pt/C catalyst (De Nora E-Tek, USA) and unsupported Pt black catalyst (HiSPEC 1000, Johnson Matthey) was compared as a function of Pt loading. A series of fuel cell tests were conducted by using different cathode Pt loading. H_2/air fuel cell performance as a function of the catalyst loading is shown for the Pt black and 40% Pt/C catalysts in **Figure 1**. The performance was determined at 0.8 V, often used as a reference voltage in the PEFC technology. The two plots cross at a point corresponding to a cathode Pt loading of 0.6 mg cm^{-2}. Carbon supported catalyst performs better at lower loadings while the Pt black catalyst provides an overall performance advantage at higher loadings. At the Pt loading higher than 2.0 mg cm^{-2}, the performance of the carbon-supported catalyst begins to decrease, likely due mass transport limitations in the carbon-rich – and therefore relatively thick – layer of the catalyst material.

The DMFC performance of the two cathode catalysts was compared at a selected cell voltage of 0.45 V. As shown in **Figure 2**, once again the carbon-supported Pt performs better at the lowest catalyst loading, below 0.6 mg_{Pt} cm^{-2}. Both catalysts allow to generate similar cell current density in the loading range from ~0.8 to ~1.6 mg_{Pt} cm^{-2}, with the unsupported catalyst beginning to outperform the carbon-supported material at higher loadings. There may be several possible reasons for the better H_2/air and DMFC performance of the carbon supported than the Pt black catalyst at low loadings, with the most likely being (i) smaller catalyst particle size, (ii) better catalyst utilization, and (iii) reduced tendency to particle agglomeration.

The results presented so far in Figures 1 and 2 were obtained at a high flow rate ("stoichiometry") and a high total pressure of the air, 460 mL min^{-1} and 2.8 atm, respectively. In the case of Pt black catalysts, a reduction in the flow rate from 460 to 51 mL min^{-1} at a constant total pressure of 2.8 atm leads to a significant performance drop (**Figure 3**). The cell current density drops further upon lowering of the cathode air pressure (from 2.8 atm to ~1.4 atm, Figure 3). The performance of the carbon-supported cathode is even more sensitive to the changes in the flow rate and pressure of the air (**Figure 4**). While relatively little effect of the cathode feed conditions can be seen at ultra-low loadings of Pt, 0.2-0.3 mg cm^{-2}, the situation changes as the loading increases. For example, at 1.6 mg_{Pt} cm^{-2}, the DMFC current density measured at a high flow and pressure of the air, 460 mL min^{-1} and 2.8 atm, respectively, is nearly twice that measured at a low flow and pressure of the air (50 mL min^{-1} and 1.4 atm, respectively). Lowering the flow and pressure of the air possibly results in an increased flooding and in a drop of the mixed potential of the cathode. The mixed potential, a direct result of methanol crossover, is strongly dependent on the air flow and tends to become more apparent under conditions of a limited supply of the air to the cathode catalyst layer (5,7,8,10). Both the catalyst flooding and mixed-potential effects could be augmented as the layer of the carbon-supported catalyst becomes thicker.

Cathode Performance *vs.* Nafion™ Content in the Catalyst Layer

Traditionally, the reason for replacing Pt black with a carbon-supported Pt catalyst was to extend the three-dimensional reaction zone, raise catalyst utilization and, effectively, reduce the amount of the precious metal needed to generate practically viable currents (11,12,13). One important parameter to be optimized is the content of a proton-conducting ionomer, typically Nafion™, in the catalyst layer. This is done to minimize ohmic losses, facilitate mass transport to and from the reaction site, preserve good electronic and ionic conductivity in the catalyst layer and, ultimately, achieve the highest possible utilization of the Pt catalyst. The effect of the Nafion™ content on DMFC performance of the 40% Pt/C cathode catalyst is shown in **Figure 5**. The cell performance improves until Nafion™ content in the cathode reaches ~41 wt%. At an even higher ionomer content the performance drops, likely due a gradual loss in the electronic conductivity in the catalyst layer as the individual catalyst particles become electronically isolated from one another and cease to participate in the electrode process. Interestingly, the optimum weight percent of the Nafion™ ionomer in the catalyst layer (~41 wt%) corresponds to approximately 52% by volume. This may suggest that the best performing formulations of the cathode catalyst are those with a balanced content of ionic (recast ionomer) and electronic (Pt, carbon support) conductors.

Cathode Catalysts with Different Pt-to-C Ratios

Even with low Pt cathode loading of *ca.* 0.6 mg cm^{-2}, the H_2/air cell voltage measured with the 56% Pt/C catalyst at a current density of 0.2 A cm^{-2} is *ca.* 0.84 V, indicating high activity of the catalyst in the oxygen reduction reaction, ORR (**Figure 6**). For a comparison, the cell voltage obtained with 40% Pt/C catalyst at a similar loading is no more than 0.78 V under identical H_2/air test conditions. The 60% Pt/C catalyst performs similarly to 80% Pt/C but not as good as 56% Pt/C. By comparison with other catalysts, 30% Pt/C does not show good H_2/air performance.

In order to make sure that the cell performance is affected by the cathode performance only, anode polarizations were recorded for the cells with different Pt-to-C cathode ratios. In this case, the cells were operated in a 'driven mode', with methanol being oxidized at the fuel cell anode and the fuel cell cathode acting as a counter/quasi-reference hydrogen-evolving electrode (a dynamic hydrogen electrode, DHE). As demonstrated in **Figure** 7, the anode performance is very similar in all five tested cells.

The DMFC performance plots obtained with different Pt/C catalysts at 80°C are shown in **Figure 8**. Polarization plots shown in this figure, recorded for the same Pt loading and cell operating conditions, reveal that 56% Pt/C and 60% Pt/C provide the best performance at the cathode loading of 0.6 mg_{Pt} cm^{-2}. The DMFC performance recorded with 80% Pt/C is not as good as that of 56% Pt/C and 60% Pt/C, yet better than that of 40% Pt/C and 30% Pt/C. The difference between two best performing catalysts and the 80% Pt/C catalyst is more significant in DMFC operation than H_2/air operation (Figure 6). This may indicate that, in addition to somewhat lowered activity in ORR, the high-Pt-content catalyst may be less effective in handling methanol crossover.

The performance of a DMFC cathode catalyst for a specific application is often a compromise between required precious metal loading and acceptable cost. For certain cost-sensitive applications, the Pt-to-C ratio in a cathode catalyst may depend on the Pt loading that can be afforded. As already demonstrated above, at a cathode loading of 0.6 mg_{Pt} cm^{-2}, 60% Pt/C is potentially a good choice. Earlier presented data on the loading dependence of the DMFC performance obtained with 40% Pt/C (Figure 2) indicate a decrease in the catalyst performance at loadings in excess of 1.6 mg_{Pt} cm^{-2}, which is likely to result from mass transport limitations as the catalyst layer gets thicker. A comparison of the data obtained with cathode catalyst of different Pt-to-C ratios implies that at higher required Pt loadings better performance may be generated by catalysts with a higher Pt content.

Once the Pt loading is increased to 2.0 mg cm^{-2}, the H_2/air fuel cell voltage obtained with the 80% Pt/C cathode raises to *ca.* 0.84 V at 0.2 A cm^{-2}, attesting to good overall cell performance (**Figure 9**). Thus, at a higher Pt loading, the performance offered by 80% Pt/C becomes very similar to that of 60% Pt/C and Pt black and approaches that of the best-performing 56% Pt/C (0.86 V at 0.2 A cm^{-2}). The performance advantage offered at a higher loading by the higher Pt-content catalyst in H_2/air operation is also seen in the DMFC (**Figure 10**). For example, the DMFC current density measured with 56% Pt/C cathode catalysts reaches 0.34 A cm^{-2} at 0.45 V, not much below the current density obtained with a Pt black catalyst at a very high loading (greater than 5 mg_{Pt} cm^{-2}). This result demonstrates that, thanks to the right dispersion of the catalyst particles, a very promising DMFC performance can be accomplished with high-Pt content Pt/C catalysts at a relatively low platinum loading.

As stated earlier, a practically viable approach to lowering precious metal loading in fuel cells is to support electrocatalysts on high surface area graphitic carbons. Generally, this approach allows for making effective membrane-electrode assemblies with low and moderate catalyst loadings. At high loadings, like those required for DMFCs under development for portable applications, the condition of maintaining catalyst layers thin is impossible to meet with most commercially available carbon-supported catalysts. These catalysts, developed for H_2/air fuel cell operation, typically contain ~20 wt% of platinum. Based on the experimental evidence presented above, this is far too low a Pt-to-C ratio for DMFCs. In order to effectively operate, direct methanol fuel cells need much higher catalyst content, not in the cathode but also in the anode (14). Unfortunately, achieving a good dispersion of the metal nanocrystallites in catalyst materials with high Pt content catalysts has remained a big challenge. Designing a good cathode catalyst becomes more complex at the presence of methanol crossover that significantly raises the demand for the active catalyst sites and makes the task of lowering the cathode catalyst loading even more difficult. Clearly, the most effective approach to lowering the cathode catalyst loading in today's DMFCs would be to either lower the methanol crossover through advances in the membrane technology or to develop a well-performing methanol-tolerant cathode catalyst. In spite of a very significant effort invested in these two areas of the DMFC research, the progress to date on the way to replacing the Nafion™ membrane and the Pt cathode catalyst with a better performing and/or less expensive materials has been rather limited. For as long as practically viable replacements of the presently used materials are not available, improving the electrode structure will remain a prudent and perhaps the most promising approach to boosting the cathode performance.

CONCLUSIONS

Operating the DMFC cathode with loadings lower than 0.6 mg_{Pt} cm^{-2} is possible at the expense of loss in maximum achievable initial cathode activity of about 50%. (Beyond that loss of initial activity, there is a remaining question on a possibly stronger loss of cathode performance with operation time when low loadings are being used.) When such lower cathode catalyst loadings are the choice, carbon-supported catalysts have an advantage over Pt black catalysts, whereas at any loading in excess of 0.6 mg_{Pt} cm^{-2}, Pt black catalysts provide higher activity per mg of Pt.

Depending on the total required cathode loading, a Pt content between 40 and 60 percent by weight is the best suited for DMFC operation. Regardless of catalyst used, the best performing cathode formulations appear to be those with a balanced content of ionic (recast ionomer) and electronic (Pt, carbon support) conductors.

ACKNOWLEDGEMENTS

This work was supported by the Defense Advanced Research Projects Agency through the Defense Sciences Office and by the U.S. Department of Energy through the Office of Advanced Automotive Technologies.

REFERENCES

1. A. S. Aricò, S. Srinivasan and V. Antonucci, *Fuel Cells*, **1**, 133 (2001).
2. N. M. Marković, T. J. Schmidt, V. Stamenković and P. N. Ross, *Fuel Cells*, **1**, 105(2001).
3. G. J. K. Acres, J. C. Frost, G. A. Hards, R. J. Potter, T. R. Ralph, D. Thompsett, G. T. Burstein, G. J. Hutchings, *Catal. Today*, **38**, 393(1997).
4. M. S. Wilson, J. A. Valerio and S. Gottesfeld, *Electrochim. Acta*, **40**, 355 (1995).
5. S. Gamburzev, A. J. Appleby, *J. Power Sources*, **107**, 5 (2002).
6. X. Ren, P. Zelenay, S. C. Thomas, J. Davey and S. Gottesfeld, *J. Power Sources*, **86**, 111 (2000).
7. D. Chu and S. Gilman, *J. Electrochem. Soc.*, **141**, 1770 (1994).
8. P. S. Kauranen and E. Skou, *J. Electroanal. Chem.*, **408**, 189 (1996).
9. T. E. Springer, M. S. Wilson, and S. Gottesfeld, *J. Electrochem. Soc.*, 40, 3513 (1993).
10. J. H. Hirschenhofer, D. B. Stauffer, R. R. Engleman, and M. G. Klett, *Fuel Cell Handbook*, Fourth Edition, (1998).
11. E. Passalacqua, F. Lufrano, G. Squadrito, A. Patti and L. Giorgi, *Electrochim. Acta*, **43**, 3665(1998).
12. E. A. Ticianelli, J.G. Berry, S. Srinivasan, *J. Appl. Electrochem.*, **21**, 597 (1991).
13. E. A. Ticianelli, C. R. Derouin, A. Redondo, S. Srinivasan, *J. Electrochem. Soc.*, **135**, 2209 (1988).
14. P. Zelenay, F. Guyon and S. Gottesfeld, in *Direct Methanol Fuel Cells*, S. R. Narayanan, S. Gottesfeld and T. Zawodzinski (Eds.), ECS Proceedings, Electrochemical Society, Pennington, New Jersey, **2001-4**, 123 (2001).

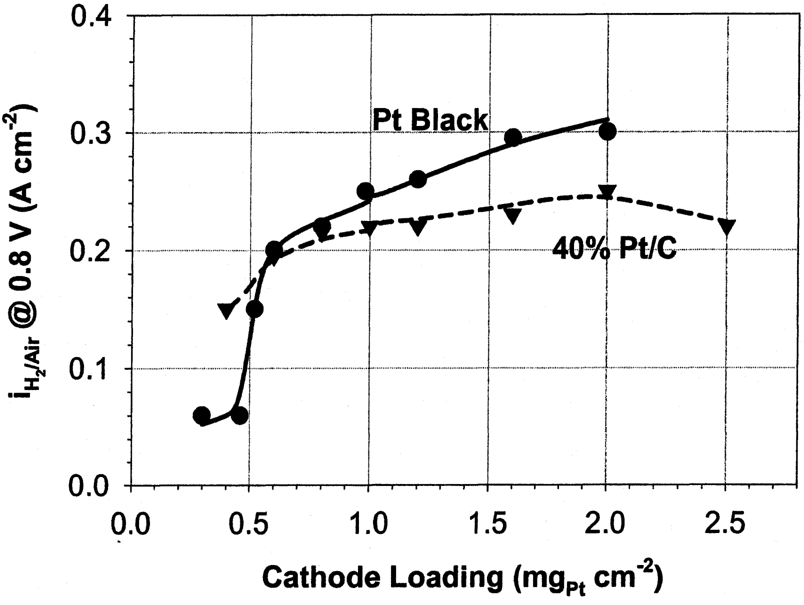

Figure 1 H_2/air fuel cell performance at low cathode Pt and Pt/C loadings at 80°C. Pt-Ru black anode: H_2, 300 mL min^{-1}, 2.8 atm total pressure. Pt black or 40% Pt/C cathode: Air, 460 mL min^{-1}, 2.8 atm total pressure.

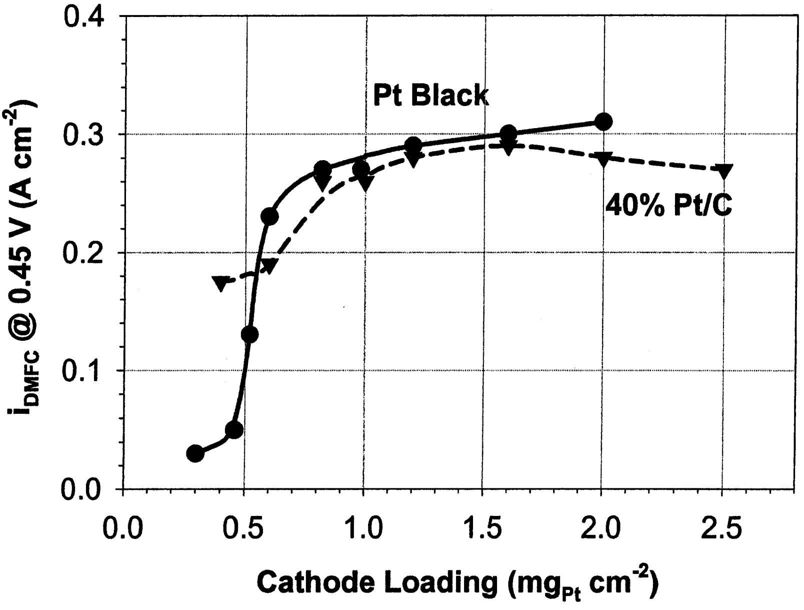

Figure 2 DMFC performance at low loading of Pt black and Pt/C cathode catalysts at 80°C. Pt-Ru black anode: 1.0 M MeOH. Pt black or 40% Pt/C cathode: Air, 460 mL min^{-1}, 2.8 atm total pressure.

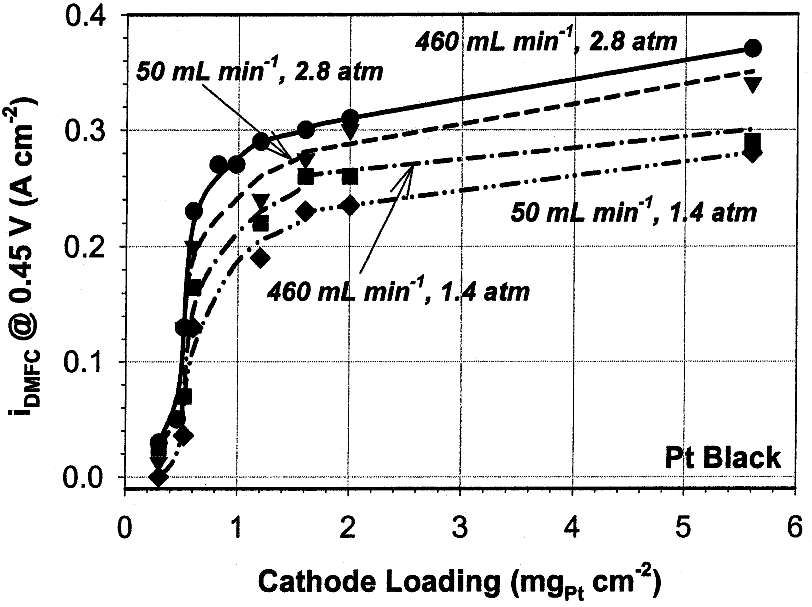

Figure 3 DMFC performance with different Pt black cathode loadings at 80°C. Pt-Ru black anode: 1.0 M MeOH. Pt black cathode: Air (flow and total pressure indicated on the graph).

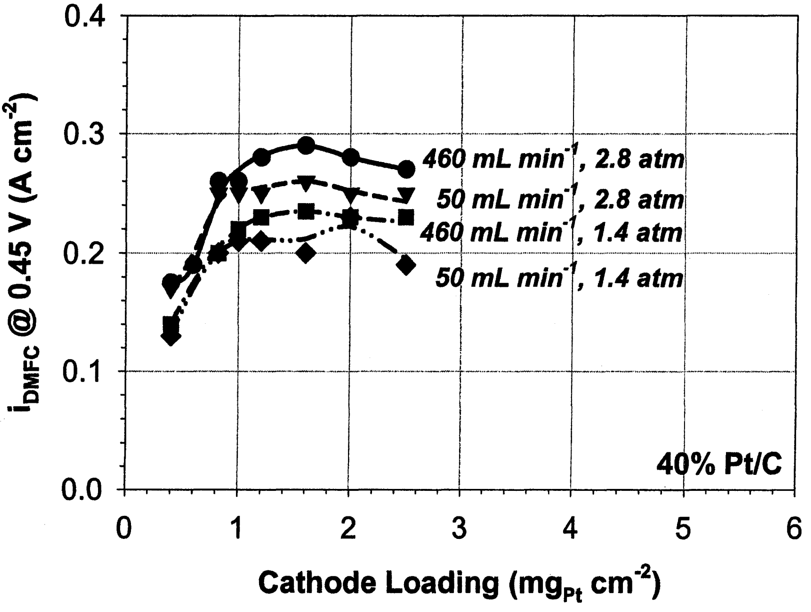

Figure 4 DMFC performance with different 40% Pt/C cathode catalyst loading at 80°C. Pt-Ru black anode: 1.0 M MeOH. 40% Pt/C cathode: Air (flow and total pressure indicated on the graph).

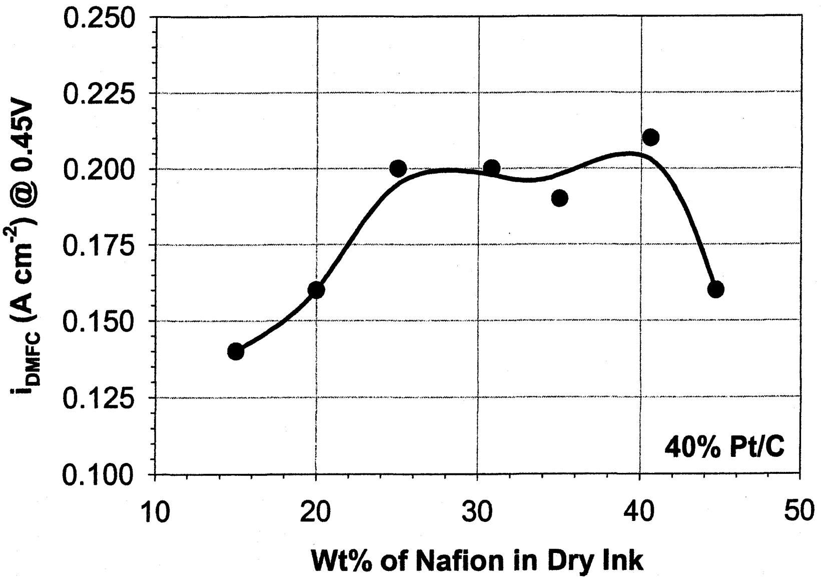

Figure 5 Relationship between DMFC performance at 0.45 V and the weight percent of Nafion^{TM} in the cathode catalyst layer. Pt-Ru black anode: 1.0 M MeOH. 40% Pt/C cathode: Air, 460 mL min^{-1}, 2.8 atm total pressure, 0.6 mg$_{Pt}$ cm^{-2}.

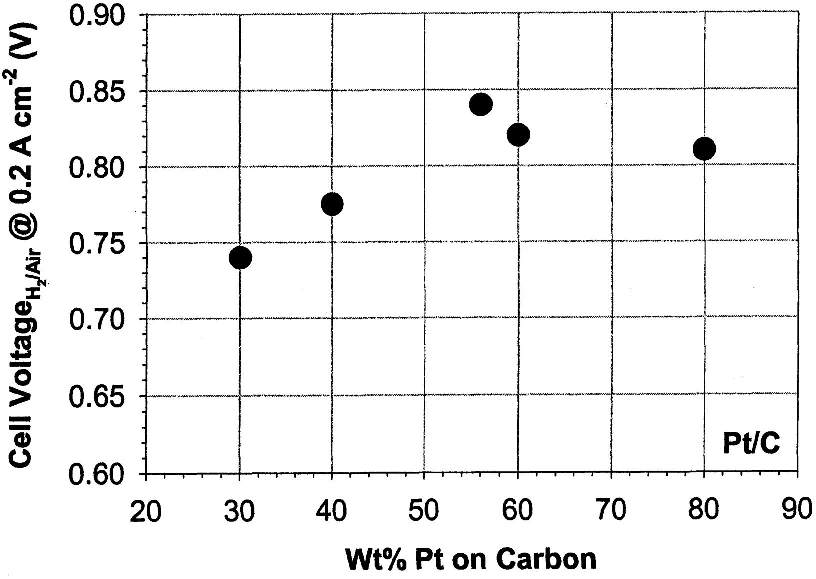

Figure 6 H_2/air performance of fuel cells with different Pt/C cathode catalysts at 80°C. Pt-Ru black anode: H_2, 150 mL min^{-1}, 2.8 atm total pressure. Pt/C cathodes: Air, 460 mL min^{-1}, 2.8 atm total pressure, 0.6 mg$_{Pt}$ cm^{-2}.

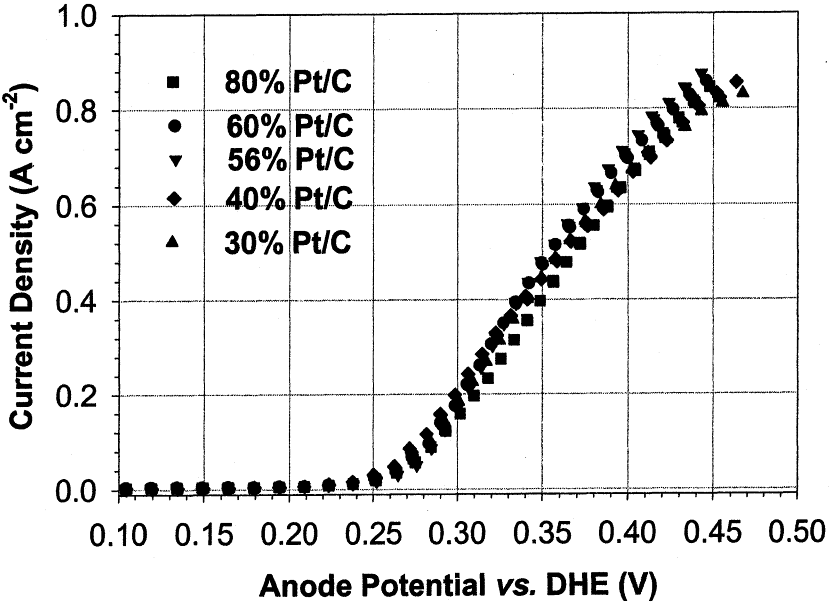

Figure 7 Anode polarization plots with cells using different Pt/C cathode catalysts at 80°C. Pt-Ru black anode: 1.0 M MeOH. Pt/C "cathodes": H_2, 110 mL min^{-1}, 1.4 atm total pressure, 0.6 mg$_{Pt}$ cm^{-2}.

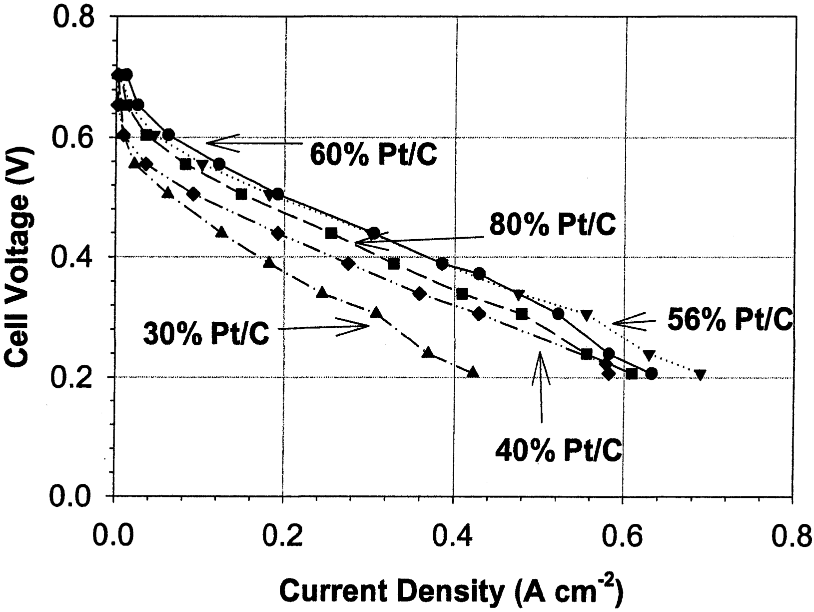

Figure 8 DMFC performance of different Pt/C cathode catalysts at 80°C. Pt-Ru black anode: 1.0 M MeOH. Pt/C cathodes: Air, 460 mL min^{-1}, 2.8 atm total pressure, 0.6 mgPt cm^{-2}.

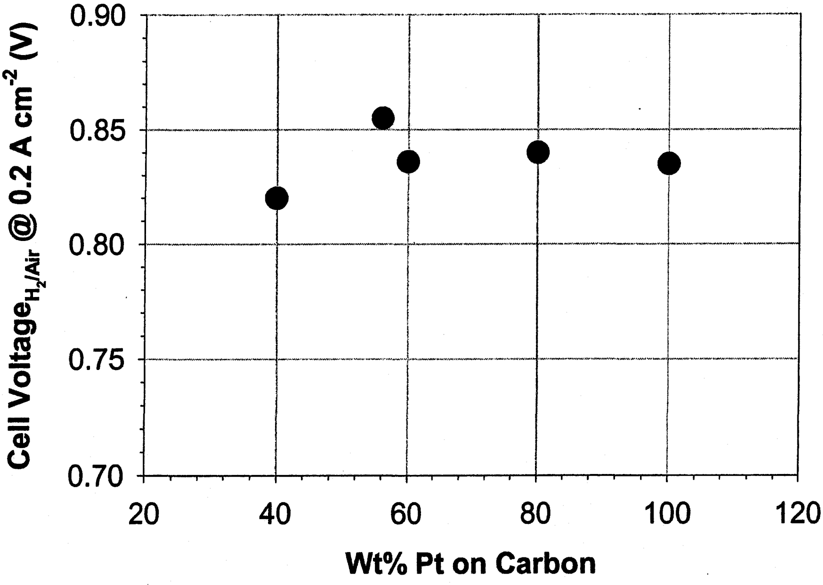

Figure 9 H_2/air performance of cells with different Pt/C cathode catalysts at 80°C. Pt-Ru black anode: H_2, 150 mL min^{-1}, 2.8 atm total pressure. Pt/C cathodes: Air, 460 mL min^{-1}, 2.8 atm total pressure, 2.0 mg$_{Pt}$ cm^{-2}.

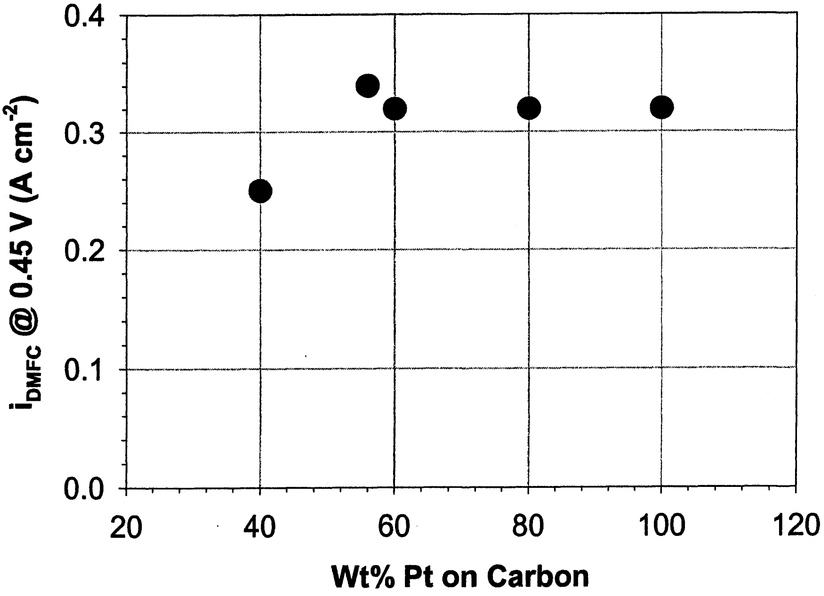

Figure 10 DMFC performance of different Pt/C cathode catalysts at 0.45 V and 80°C. Pt-Ru black anode: 1.0 M MeOH. Pt/C cathodes: Air, 460 mL min^{-1}, 2.8 atm total pressure, 2.0 mg$_{Pt}$ cm^{-2}.

Proceedings of The Electrochemical Society, PV 2002-31, 506-517 (2002)
DOI: 10.1149/200231.0506PV © The Electrochemical Society

EFFECT OF FABRICATION TECHNIQUE ON DIRECT METHANOL FUEL CELLS DESIGNED TO OPERATE AT LOW AIRFLOW

T. I. Valdez and S.R. Narayanan

Jet Propulsion Laboratory,
California Institute of Technology,
4800 Oak Grove Drive, Pasadena, CA 91109

ABSTRACT

Various fabrication techniques for Direct Methanol Fuel Cell (DMFC) Membrane Electrode Assemblies (MEAs) have been studied. The addition of hydrophobic particles to the cathode improves the cathode water rejection characteristics and thus mitigates the effects of crossover. A DMFC with hydrophobic particles concentrated at the gas diffusion backing is capable of producing a cell power density of 70 mW/cm^2 and a cell efficiency of 29% while operating at 60 °C, 0.5 M methanol, 1.76 times stoichiometric airflow. The addition of hydrous RuO_2 to the anode catalyst/ proton exchange membrane (PEM) interface reduces the anodic overpotential and improves catalyst utilization. The anode potential of a cell with 4mg/cm^2 loading and a hydrous RuO_2 enhanced catalyst/ membrane interface is 0.224 V versus NHE at 100 mA/cm^2 operating with 90 °C 1M methanol which is comparable to the anode performance of an MEA with 8 mg/cm^2 anode loading.

INTRODUCTION

Direct Methanol Fuel Cell (DMFC) technology has matured to a level that has allowed complete fuel cell systems to be fabricated [1]. The airflow rate at which a DMFC operates is a key parameter that determines the fuel cell system water balance, efficiency, and total mass [2,3]. Methanol crossover increases the airflow rate requirements of the DMFC system [4]. Thus, one of the solutions to minimizing the airflow rate requirements of a DMFC system is to curb methanol crossover. The addition of hydrophobic particles to the cathode has been demonstrated to mitigate the effects of crossover and decrease the airflow required [4]. The motivation of this paper was to develop high performance membrane electrode assemblies (MEAs) that require a minimum airflow to operate. This study investigates the effects of catalyst ink constituents and MEA fabrication techniques on improving cell performance. Particular attention was focused on increasing the overall cell efficiency.

EXPERIMENTAL

MEAs

Several MEAs were fabricated by variants of the Jet Propulsion Laboratory Direct Deposit Technique [5]. This technique involved the brush painting and spray coating of catalyst layers on the membrane and the gas diffusion backing followed by drying and hot pressing and is to be distinguished from other widely used techniques such as the "decal technique" used to prepare MEAs. Each of these MEAs consisted of a Pt-Ru-black (50:50) anode, a Pt-black cathode, and Nafion 117® as the polymer electrolyte membrane (PEM). The catalyst used to fabricate these MEAs was purchased from Johnson Matthey. The MEAs studied in this paper had an active electrode area of 25 cm^2. The catalyst loadings for both the anode and the cathode were in the range of 8 to 12 mg/cm^2 unless noted otherwise. The gas diffusion backings and current collectors for all MEAs were made of Toray 060® carbon paper with approximately five to six weight percent Teflon content.

Fabrication Techniques

Variations in fabrication technique included mechanical roughening of the membrane, modifications to the catalyst layer, and changes to the catalyst application process. The catalyst constituents studied included hydrophobic particles and proton-conducting substances added to the catalyst mix. The four MEA fabrication techniques studied are schematically shown as figure 1.

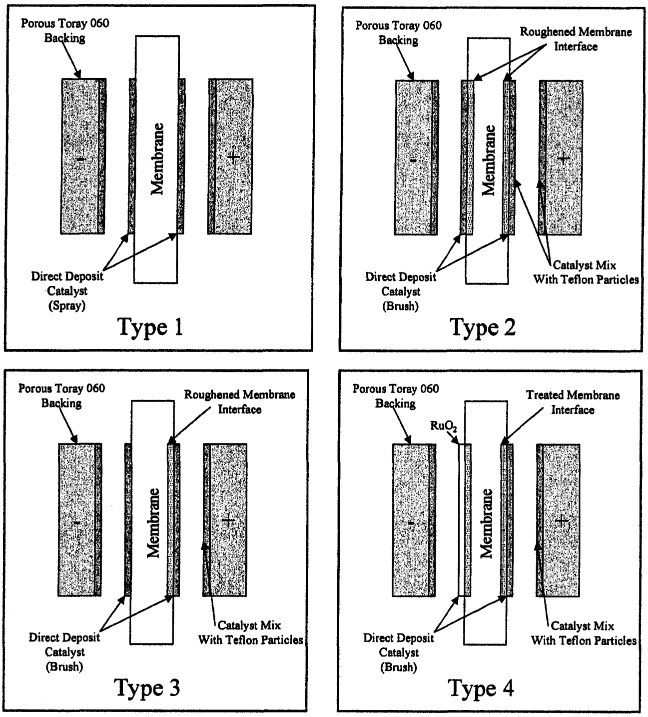

Figure 1. A schematic of the MEA fabrication techniques explored in this paper.

In fabrication technique Type 1, anode and cathode catalyst are deposited on the membrane; the anode is spray-coated and no hydrophobic particles are dispersed in the cathode catalyst layer. In fabrication technique Type 2, the PEM was mechanically roughened on both the anode and cathode sides prior to the application of catalyst. In a Type 2 MEA, the anode is brush-painted and the hydrophobic particles are evenly dispersed within the cathode structure. In fabrication technique Type 3, only the cathode side of the PEM is roughened and the hydrophobic particles are concentrated only at the gas diffusion backing of the cathode structure. The anode of a Type 3 MEA is brush-painted. In fabrication technique Type 4, a layer of hydrous RuO_2 is brush-painted on to a roughened anode side of the PEM prior to the brush-painting of Pt-Ru catalyst; the cathode is prepared as in a Type 3 MEA.

Test System

The fabricated cells were then characterized in an in-house developed DMFC test system. The DMFC test system consisted of a fuel cell test fixture, a temperature controlled circulating fuel solution loop and an oxidant supply from a compressed gas tank. The fuel cell test fixture, supplied by Electrochem Inc., accommodated electrodes with a 25-cm^2 active area and had pin-cushion flow fields for both the anode and cathode compartments. Crossover rates were measured using a Horiba VIA-510 CO_2 analyzer and are reported as an equivalent current density of methanol oxidation.

Methodology

The electrical performance of DMFCs has been characterized by the evaluation of full cell performance, anode polarization, cathode polarization, and methanol crossover. Electrical performance and cell efficiency are characterized by techniques described earlier [4,6].

RESULTS AND DISCUSSION

Cathode Performance

The results in figures 2 and 3 suggest that the hydrophobic particles have a beneficial effect on cell performance at low airflow rates. Also, the location of the hydrophobic particles in the gas diffusion backing appears to be particularly beneficial in realizing high performance. As summarized in table 1, modifying the MEA electrode structures results in an 80% increase in peak power density and substantially improved cell efficiency.

The relative effects of anode and cathode modifications on performance can be analyzed by determining the contributions from the anode and cathode using anode polarization analysis [7]. The effect of methanol crossover on the cathode performance in a DMFC has been studied [4]. Crossover places an additional load on the cathode of having to oxidize the methanol that has crossed over. The mixed potential so arising at the cathode lowers the total cell efficiency. Figure 4 is a plot of electrode potential versus the NHE as a function of applied current density for a Type 1, 2 and 3 MEA. The improvement in cell performance from the Type 1 to Type 2 MEAs can be seen as an increase in cathode performance for applied current densities lower than 100 mA/cm^2 and increase in anode performance for current densities greater than 40 mA/cm^2. The average increase in cathode performance between the Type 1 and Type 2 MEAs is 16 mV. The

Table 1. Cell performance of a Type 1, 2 and 3 DMFC at 60 °C, 0.5M MeOH, 0.1 LPM ambient pressure air.

	MEA Type		
Peak Efficiency	**1**	**2**	**3**
Cell Efficiency (%)	23	27	29
Cell Voltage (V)	0.44	0.43	0.49
Applied Current Density (mA/cm^2)	80	120	120
Cell Power Density (mW/cm^2)	35	52	59
Peak Power			
Cell Efficiency (%)	23	25	27
Cell Voltage (V)	0.31	0.34	0.37
Applied Current Density (mA/cm^2)	120	140	180
Cell Power Density (mW/cm^2)	37	47	66

improvement in cathode performance observed between the Type 1 and Type 2 MEAs can be attributed to the hydrophobic particles allowing the oxidant easier access to the catalytic surfaces as well as increasing the water rejection rate in the Type 2 cathode structure. The average decrease in the anode overpotential between the Type 1 and Type 2 MEAs is 40 mV versus the NHE. The increase in anode performance from the Type 1 to Type 2 is attributed to the anode fabrication technique. It has been observed that anodes fabricated by the spray processes exhibit higher anodic over potentials as compared to anodes fabricated by the brush technique. This change in anode performance is attributed to possible changes in ionomer/ catalyst distribution within the anode structure as a result of the spraying technique.

Results in figure 4 suggest that the improvement in cell performance from the Type 2 to Type 3 MEAs is attributed to improved cathode and anode performance. The anode potentials at the peak efficiency and peak power were 0.336, 0.29, 0.37, and 0.33V versus NHE for the Type 2 and Type 3 MEAs respectively. Mechanical roughening of the PEM prior to deposition of the catalyst results in a very dense anode. The denser or the higher tortuosity of the anode can render catalyst sites inaccessible and thus manifest itself as lower anode performance. The increase in anode performance between the Type 2 and Type 3 MEA thus could be attributed to the density changes in the anode coating. For current densities less than 140 mA/cm^2 the performance of the cathode is lower for the Type 3 versus Type 2 MEA. However the cathode of the Type 3 MEA can sustain much higher currents than the cathode of the Type 2 MEA. The initial decrease in cathode performance observed for the Type 3 MEA may be attributed to catalyst variation and perhaps a minimal increase in crossover current density. Based on the results, the hydrophobic particles should be placed near the gas diffusion/ oxidant interface to allow for increased water rejection at the cathode.

Figure 5 is a plot of crossover current density versus applied current density for a DMFC fabricated with a mechanically roughened and un-roughened PEM. One of the factors that control crossover current density is membrane thickness [8]. One would expect that the mechanical roughening of the membrane can lead to a thinner membrane and thus increased crossover. The average increase in crossover current density for a roughened and an un-roughened PEM is on the order of 5 - 10 mA/cm^2 over a wide range of current densities.

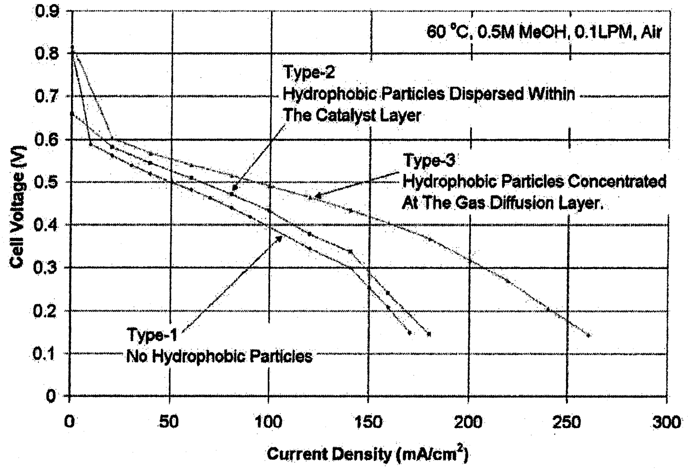

Figure 2. A plot of the effect of fabrication technique on DMFC performance for cells operating at 60 °C, 0.5M MeOH, 0.1 LPM ambient pressure air.

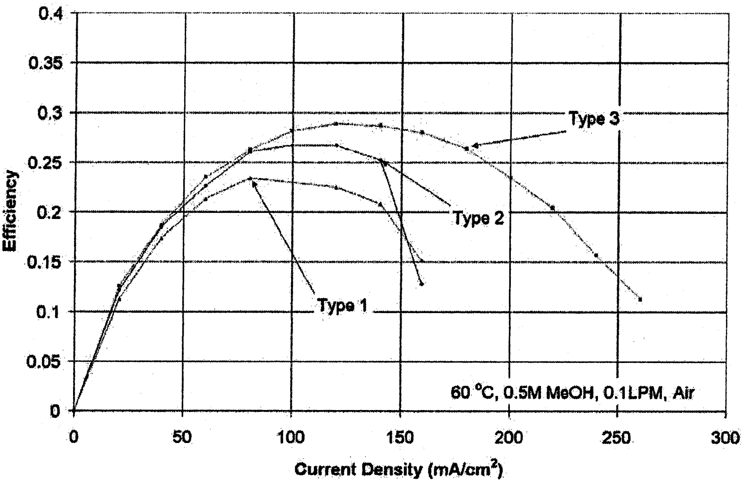

Figure 3. A plot of cell efficiency as a function of applied current density for a Type 1, 2 and 3 DMFC operating at 60 °C, 0.5M MeOH, 0.1 LPM ambient pressure air.

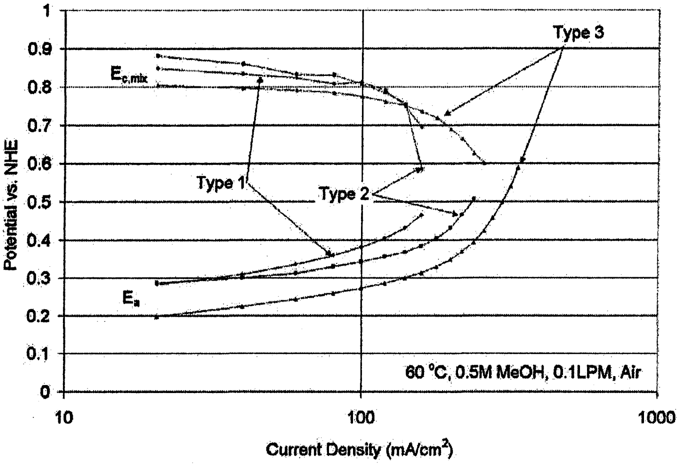

Figure 4. A Tafel plot of electrode potential as a function of applied current density for a Type 1, 2 and Type 3 DMFC operating at 60 °C, 0.5M MeOH, 0.1 LPM ambient pressure air.

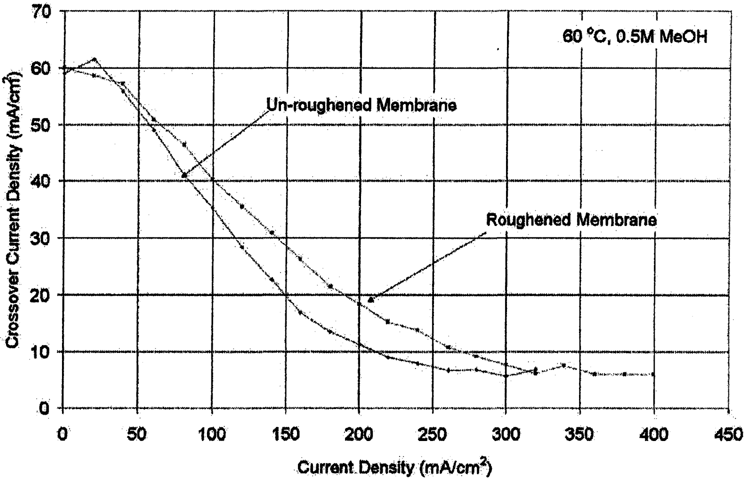

Figure 5. A plot of effective crossover rate as a function of applied current density for a DMFC fabricated with a mechanically roughened and un-roughened PEM operating at 60 °C on 0.5M MeOH.

Type 3 MEA

Figures 6, 7, and 8 are plots of cell performance, cell power density and cell efficiency versus applied current density respectively for a Type 3 MEA operated at 60 °C, 0.5M MeOH, with ambient pressure air. Table 2 is a summary of the data in figures 6,7, and 8. The plots and table show that as the airflow to a DMFC is increased the cell performance, peak power, and efficiency all increase. The question then becomes, why not run the cells at the highest flow rate possible? The answer is that the cells should be operated at the highest airflow possible in which a system water and thermal balance is maintained [2]. It has been shown that for a stack operating at 55 °C in a 42 °C environment, the airflow rate should be in the range of 1.75 stoich to avoid water vapor recovery [9].

Table 2. Cell performance of a Type 3 DMFC as a function of airflow rate.

	Airflow Rate (LPM)			
Peak Efficiency	**0.1**	**0.15**	**0.3**	**0.5**
Cell Efficiency (%)	29	32	33	34
Cell Voltage (V)	0.44	0.45	0.47	0.49
Applied Current Density (mA/cm^2)	120	140	140	140
Air Stoichiometry (X x Stoich)	1.54	2.11	4.23	7
Cell Power Density (mW/cm^2)	53	63	66	69
Peak Power				
Cell Efficiency (%)	26	29	28	30
Cell Voltage (V)	0.37	0.39	0.38	0.40
Applied Current Density (mA/cm^2)	160	180	200	200
Air Stoichiometry (X x Stoich)	1.27	1.76	3.22	5.37
Cell Power Density (mW/cm^2)	59	70	75	80

As shown in table 2, for a 50% increase in airflow to the cell, from 0.1 to 0.15 LPM, a 19% increase in cell power density can be observed. Overall, for a five-fold increase in airflow a 37% increase in peak power density is observed. Similarly, the overall gains for in peak efficiency for the airflow range of 0.1 to 0.5 LPM are 30%. The gains in peak efficiency with increase in airflow are not as large as the gains observed for peak power. This is because the air stoichiometry (including crossover) at peak efficiency is in the range of 1.5 to 7 versus 1.3 to 5.4 times stoich in the case of peak power. The change in oxygen demand for the cell operating at peak power is greater than that for a cell operating at peak efficiency, leading to greater impact of airflow rate.

The effect of airflow rate on cathode performance can be best understood by separating the cathode from the full cell performance through the technique of anode polarization as shown in figure 9. The cathode potentials, $E_{c,mix}$, at varied airflow rates can be compared. The effects of air stoichiometry at the cathode manifest themselves as mass transfer limitations at high current densities. As can be seen in figure 9, the cathode potentials are steady for all airflow rates at current densities less than 60 mA/cm^2. At applied current densities of 100 mA/cm^2, a cell operating at 0.1 LPM airflow begins to operate in a mass transfer limited regime. The air stoichiometry at 0.1 LPM airflow and 100 mA/cm^2 applied current density is 1.54 time stoic (including crossover). The cathode potentials are steady at 100 mA/cm^2 for airflow rates of 0.15 LPM or greater. The air stoichiometery at an airflow of 0.15 LPM and at an applied current density of 100 mA/cm2 is 2.56 times stoic (including crossover). There is little variation in cathode potentials for airflow rates above 0.15 LPM for all applied current densities.

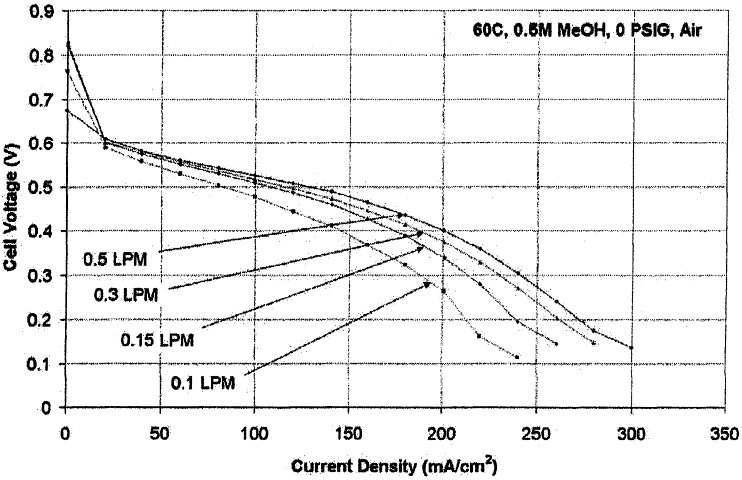

Figure 6. A plot of a cell performance as a function of airflow rate and applied current density for a Type 3 DMFC operated at 60 °C, 0.5M MeOH, ambient pressure air.

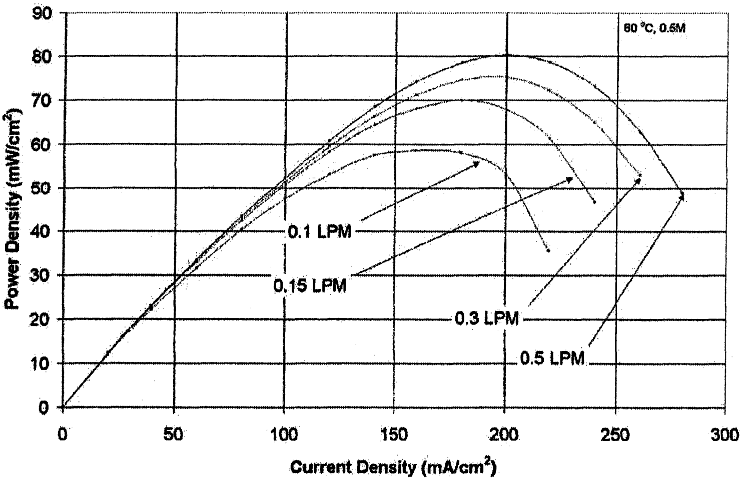

Figure 7. A plot of cell power as a function of airflow rate and applied current density for a Type 3 DMFC operated at 60 °C, 0.5M MeOH, ambient pressure air.

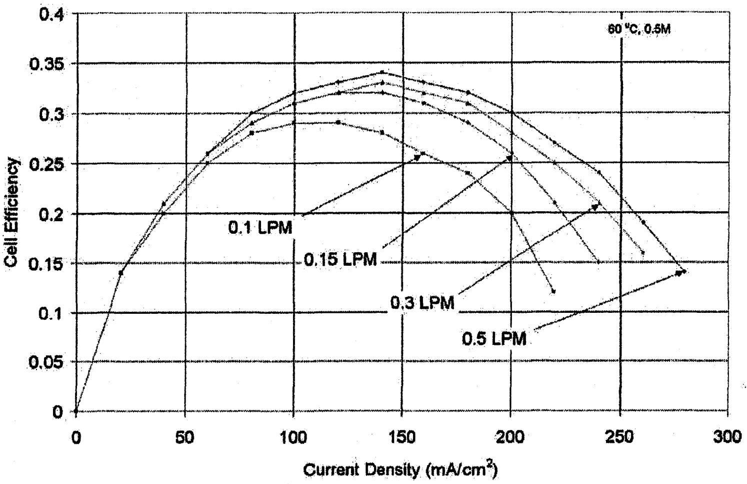

Figure 8. A plot of cell efficiency as a function of airflow rate and applied current density for a Type 3 DMFC operated at 60 °C, 0.5M MeOH, ambient pressure air.

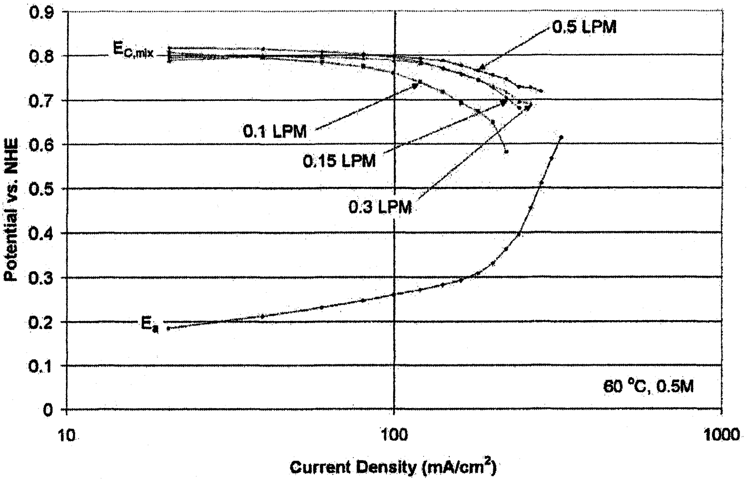

Figure 9. A Tafel plot of cathode performance as a function of airflow rate and applied current density for a Type 3 DMFC operating at 60 °C, 0.5M MeOH, ambient pressure air.

Hydrous RuO_2

The impact of hydrous ruthenium oxide as a proton conductor for fuel cell applications is a topic of recent interest [10-12]. Figure 10 is an anode polarization experiment performed with 90 °C 1M methanol. MEAs 1 and 2 are of the Type 3, MEA 3 is of the Type 4. The anode of MEA 1 has a catalyst loading of 4 mg/cm^2, the anode of MEA 2 has a catalyst loading of 8 mg/cm^2, and the anode of MEA 3 has a catalyst loading of 4 mg/cm^2 brush coated on top of a layer of hydrous RuO_2. As can bee seen from in figure 10, the addition of hydrous RuO_2 to the catalyst interface improves anode performance. At an applied current density of 100 mA/cm^2 the anode over potential decrease from 0.26 to 0.22 V versus NHE for MEA 1 versus MEA 3. The performance of the MEA 3 is comparable to MEA 2 for current densities less than 500 mA/cm^2. Another property that was noticed was that the internal cell resistance was lower for the MEA 3 as compared to MEA 1. The internal resistance for the cells at 90 °C, averaged over the range of current densities, is 7.5 and 4.6 mΩ for MEA 1 and MEA 3 respectively. As shown in figure 10, and elsewhere [12], an electrically conducting/ proton conducting interface is a key to improved catalysis in PEM based fuel cells. At current densities higher than 500 mA/cm2, the higher catalyst-loading anode of MEA 2 exhibits better characteristics of methanol oxidation since the turnover rates on the catalyst become important.

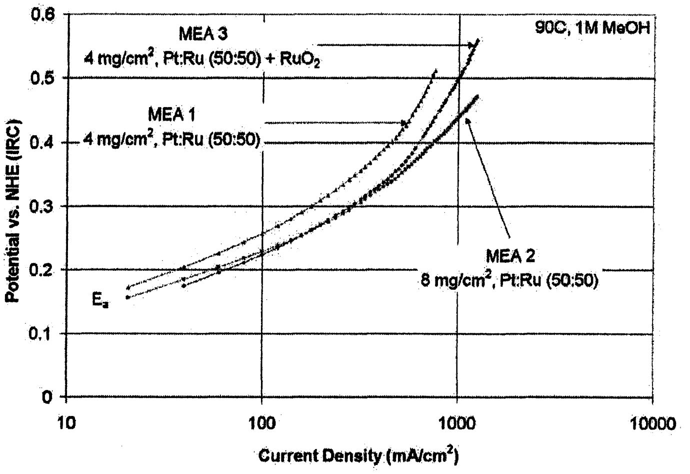

Figure 10. Internal resistance corrected anode potential as a function of applied current density for a DMFC with and without Hydrous RuO_2. (90 °C, 1M MeOH)

CONCLUSIONS

The increase in cell performance from the Type 1 to Type 2 and Type 2 to Type 3 DMFC can be attributed to improvements at the anode and cathode of the respective MEAs. The Type 3 DMFC achieved the highest peak operating efficiency, current density at peak efficiency and peak power of 29 %, 56 mW/cm^2 and 66 mW/cm^2 respectively operating on 60 °C 1M MeOH at 1.6 times air stoichiometry.

The effects of crossover on the cathode of a DMFC can be mitigated by the addition of hydrophobic particles. The location of the hydrophobic particles in the cathode structure determines the ability of the cathode to sustain higher current densities. Anode structure has a strong effect on anode polarization in DMFCs. The denser anodes of the Type 1 and Type 2 MEAs exhibited higher overpotentials as compared to that of the Type 3 MEA. The anode potentials at an applied load of 100 mA/cm^2 are 0.379, 0.342, and 0.273 V versus NHE for the Type 1, 2, and 3 MEAs respectively. The Type 3 MEA has the best characteristics for low airflow rates. Power densities as high as 70 mW/cm^2 can be attained at 1.76 stoich and 80 mW/cm^2 at 5.4 stoich at 60 °C. The use of hydrophobic particles in the gas diffusion backing is key to attaining high cell performance at low airflow.

The addition of hydrous RuO_2 to the anode/ membrane interface lowers the anode overpotential and allows for improved utilization of the catalyst. The addition of hydrous RuO_2 can also decrease the internal cell resistance of a DMFC. Electrically conductive proton conducting additives enhance the utilization of the catalyst and thus offer an alternative path to catalyst reduction.

ACKNOWLEDGEMENT

The work presented here was carried out at the Jet Propulsion Laboratory, California Institute of Technology for the National Aeronautics and Space Administration. TechSys Inc., through the Jet Propulsion Technologies Affiliate Program, sponsored this research.

REFERENCES

1. A. Kindler, T.I. Valdez, C. Cropely, S. Stone and E Veksler, in Methanol Fuel Cells/ 2001, S.R. Narayanan, S. Gottesfeld and T. Zawondzinski, Editors, PV 2001-4, p. 231 The Electrochemical Society Proceeding Series, Pennington, NJ. (2001)
2. S.R. Narayanan, T. Valdez, N. Rohatgi, J. Christiansen, W. Chun, G. Voecks, and G. Halpert, in Proton Conducting Membrane Fuel Cells II/ 1998, S. Gottesfeld and T Fuller, Editors, PV 98-27, p. 316 The Electrochemical Society Proceeding Series, Pennington, NJ. (1998)
3. T.I. Valdez, S.R. Narayanan, H. Frank, and W. Chun, Proceedings of the 11th annual Battery Conference on Applications and Advances, Long Beach, CA., Jan 9-12, 1997. IEEE pg. 239 – 244 (1996)
4. T.I. Valdez and S.R. Narayanan, in Proton Conducting Membrane Fuel Cells II/ 1998, S. Gottesfeld and T Fuller, Editors, PV 98-27, p. 380 The Electrochemical Society Proceeding Series, Pennington, NJ. (1998)
5. Narayanan *etal,* Patent No: 6221,523, Direct Deposit of Catalyst on the Membrane of Direct Feed Fuel Cells.
6. B.S. Pivovar, M. Hickner, T.A. Zawodzinski, X. Ren, S. Gottesfeld, in Direct Methanol Fuel Cells/ 2001, S.R. Narayanan, S. Gottesfeld, T. Zawodzinski, Editors, PV 2001-04, p. 221, The Electrochemical Society Proceeding Series, Pennington NJ. (2001)

7. S.R. Narayanan, A. Kindler, B. Jeffries-Nakamura, W. Chun, H. Frank, M. Smart, S. Surampudi, and G. Halpert, in Proton Conducting Membrane Fuel Cells I/ 1995, S. Gottesfeld, G. Halpert, and A Landgrebe, Editors, PV 95-23, p. 261 The Electrochemical Society Proceeding Series, Pennington, NJ. (1995)
8. S.R. Narayanan, H. Frank, B. Jeffries-Nakamura, M. Smart, W. Chun, G. Halpert, J. Kosek, C. Cropley, in Proton Conducting Membrane Fuel Cells I/ 1995, S. Gottesfeld, G. Halpert, and A Landgrebe, Editors, PV 95-23, p. 278 The Electrochemical Society Proceeding Series, Pennington, NJ. (1995)
9. T.I. Valdez, S.R. Narayanan, and N Rohatgi, Proceedings of the 15th annual Battery Conference on Applications and Advances, Long Beach, CA., Jan 11-14, 2000. IEEE pg. 37 – 40 (2000)
10. J.W. Long, R.M. Stroud, K.E. Swider-Lyons, and D.R. Rolison, *Journal of Physical Chemistry B*, Vol. 104, p. 9772. (2000)
11. K.E. Swider-Lyons, C.T. Love, and D.R. Rolison, in Direct Methanol Fuel Cells/ 2001, S.R. Narayanan, S. Gottesfeld, T. Zawodzinski, Editors, PV 2001-04, p. 42, The Electrochemical Society Proceeding Series, Pennington NJ. (2001)
12. K.-W. Park, B.-K. Kwon, J.-H. Choi, I.-S.Park, Y.-M. Kim, Y.-E. Sung, *Journal of Power Sources*, Vol. 109, p. 439. (2002)

Proceedings of The Electrochemical Society, PV 2002-31, 518-529 (2002)
DOI: 10.1149/200231.0518PV © The Electrochemical Society

PREPARATION OF PLATINUM CATALYST LAYERS FOR DMFC CATHODES BY PULSED ELECTRO-DEPOSITION

K. Wippermann[a], K. Klafki[a], J. Mergel[a], M.-S. Löffler[b], H. Natter[b] and R. Hempelmann[b]
[a]Institute for Materials and Processes in Energy Systems (IWV-3),
Forschungszentrum Jülich GmbH, D-52425 Jülich, Germany
[b]Physikalische Chemie, University of Saarbrücken, D-66123 Saarbrücken, Germany

ABSTRACT

DMFC cathode catalyst layers as part of MEA's are prepared by pulsed electro-deposition (PED). A mixture of hexachloroplatinic acid dissolved in Nafion solution and carbon Vulcan XC 72 is used as a precursor and the platinum particles are deposited in the Nafion/carbon interface. The deposition is optimized by varying the pulsing parameters: pulse current density ('j_{pulse}'), pulse duration ('t_{on}') and pulse interval duration ('t_{off}'). In dependence on the pulsing conditions, the performance of the electro-deposited catalyst layers differs by more than one order of magnitude. The best cathode performance is obtained at high pulse current density and low 'on'- and 'off-time' (j_{pulse} = 1000 mA/cm², t_{on} = 2 ms, t_{off} = 10 ms). A second maximum is obtained at low current density and high 'on'- and 'off-time' (j_{pulse} = 100 mA/cm², t_{on} = 200 ms, t_{off} = 500 ms). In comparison with commercial platinum catalyst (E-TeK), the size of the electro-deposited catalyst particles is three times larger (about 11 nm) and thus the platinum surface accordingly smaller, but the utilization is probably 3-4 times higher. As a result, the average performance of both catalysts is similar. If the size of the electro-deposited platinum particles can be reduced by further optimization of the PED process, an improvement of the cathode performance by a factor of three is expected.

INTRODUCTION

A disadvantage of commercial fuel cell electrodes prepared by common preparation techniques is the low catalyst utilization [1,9]. This is caused by a considerable amount of the catalyst, which is not in direct contact with the ionomer phase and therefore is unable to contribute to electrochemical reactions. Consequently, a substantial reduction of the catalyst loading can be realized by preparing the catalyst particles in the ionomer/carbon interface. This goal can be achieved by electrochemical deposition of the catalyst particles by using plating baths containing a soluble noble metal salt (see e.g. [2,3]).

We have developed a new preparation method [12], where in the first step, a precursor layer is fabricated by spraying a suspension of the soluble catalyst salt dissolved in a Nafion solution and carbon particles, which is either the Nafion membrane or the backing layer. In the second step, the catalyst particles are deposited onto the carbon particles by pulsed electro-deposition [4,5]. This method allows to control the size of the crystallites depending on the deposition parameters.

In the present work, we have prepared platinum catalyst layers by pulsed electro-deposition. These catalyst layers are part of DMFC cathodes in MEA's with an electrode area of about 2 cm². The deposition was optimized by varying the pulsing parameters, i.e. pulsed current density, pulse duration ('ton') and pulse interval duration ('toff'). The optimum pulsing conditions are obtained by means of a statistical method.

EXPERIMENTAL

Preparation of MEA's / electrode geometry and compositions:

At first, anode catalyst layers are prepared by spraying a mixture of unsupported Pt/Ru (1:1)black (Johnson Matthey), an appropriate amount of 15 % Nafion solution (Ion Power, Inc.) and isopropanol onto a backing layer made of 60 wt% carbon black (XC 72) and 40 wt% PTFE (Dyneon GmbH, TF 5032) supported by carbon cloth (E-Tek, Inc., "A" cloth). The catalyst loading was about 4 mg/cm². The disk-shaped anodes are hotpressed (T = 130 °C, p = 0.5 kN/cm²) onto a Nafion 117 membrane. They have an electrode area of 1.8 cm² and act as a counter electrode. Half cell measurements can be performed by means of a ring-shaped reference electrode with the same composition as the counter electrode.

In the second step, precursor layers of the cathode catalyst layers are fabricated by spraying a suspension of solubilized Nafion (15 %, Ion Power, Inc.), carbon support (Vulcan XC72) and hexachloroplatinic acid as soluble catalyst salt homogeneously dispersed in i-propanol on the opposite side of the Nafion membrane. The geometry and size of the precursor layer is alike the counter electrode. The precursor layer is baked in an oven until dry. The composition of the precursor layer is adjusted in such way, that after the electro-deposition, the catalyst layer consists of 10 wt% Nafion and 90 wt% carbon supported catalyst. The latter consists of 40 wt% platinum and 60 wt% carbon Vulcan XC72. The amount of hexachloroplatinic acid corresponds to a platinum loading of about 0.5 mg/cm².

Finally, the platinum(IV) ions in the Nafion phase of the MEA cathode precursor layer are electrochemically reduced by formation of platinum catalyst particles. The pulsed electrochemical deposition is carried out in a thermostated vessel, which is schematically shown in Fig.1. The vessel is partially filled with water, which is kept at a temperature of 40 °C and purged with nitrogen. The MEA is placed in the upper part of the vessel with the precursor cathode layer on top. On the one hand, this arrangement avoids contact of the precursor layer with liquid water and a subsequent leaching of the platinum salt. On the other hand, the water vapor ensures a sufficient swelling and thus proton conductivity of the Nafion phase. The pulsed electrochemical deposition of platinum is performed by applying an appropriate current between the cathode (precursor layer) and the anode (counter electrode). For this purpose, negative rectangular voltage pulses are generated by a Wavetek Model 39 Generator. These voltage pulses are transformed into current pulses and amplified by a Kepco Bipolar Operational Power Supply (BOP 20-10M), with a maximum output current of 20 A. The resulting voltage pulses are recorded by a

Tektronix TDS 3012 B oscilloscope. A scheme of the pulsing process and the electrochemical reaction are shown in Fig.2. The overall charge during each pulsing process was set five times higher than the theoretical charge calculated from Faraday's law, to avoid incomplete reduction of the platinum salt caused by capacitive effects and side reactions like hydrogen evolution. Thus, the pulsing period was five times longer than the calculated value and ranged from 5 seconds (Exp. No.9) to 4 hours (Exp. No.2), depending on the pulsing conditions. The complete reduction of the platinum was proved by elementary analysis. The pulsing parameters used for the PED process are described in the next section.

Experimental Design:

The optimization of the pulsed electrochemical deposition was achieved by means of a factorial 2^3 experimental design using the STATGRAPHICS® Software (Umex GmbH, Dresden, Germany). The factorial 2^3 experimental design demands a variation of three parameters, here: a. pulsed current density, b. pulse duration ('ton'), c. pulse interval duration ('toff'). For each of these parameters, two values, i.e. a lower value and a higher value, are defined (see table 1). Therefore, $2^3 = 8$ experiments have to be performed. Additionally, a measurement of the centerpoint is useful to check the linearity of the system within the limits of variation. Hence, nine parameter combinations were investigated, as listed in table 2.

Table 1: Variation of the pulsing parameters

parameter	**lower value**	**higher value**	**medium value**
j_{pulse} / mA * cm^{-2}	100	1000	550
t_{on} / ms	2	200	101
t_{off} / ms	10	500	255

Table 2: Factorial 2^3 experimental design for the optimization of the pulsing parameters

Experiment No.	**j_{pulse} / mA * cm^{-2}**	**t_{on} / ms**	**t_{off} / ms**
1 (centerpoint)	550	101	255
2	100	2	500
3	100	200	500
4	100	2	10
5	1000	2	500
6	100	200	10
7	1000	200	500
8	1000	2	10
9	1000	200	10

The platinum catalyst layers prepared with the nine pulsing parameter combinations were characterized by quasi-stationary current potential measurements of oxygen reduction. In order to obtain reliable results, three samples were prepared and characterized for each of the nine parameter combinations.

Electrochemical characterization:

The performance of the cathodes prepared by PED was characterized by quasi-stationary current/potential measurements of oxygen reduction (scan rate: 20 mV/s) and impedance spectroscopy ($\tilde{U}$ = 10 mV). All the electrochemical measurements were performed with a three electrode arrangement. The electrode potential, U (RE_A), is measured vs. the reference potential of the methanol reaction established at the anode ring. Because the platinum loading of the cathodes is slightly different (0.4 – 0.6 mg/cm²), the current density is normalized to the platinum loading. A more detailed description of the electrochemical apparatus as well as the geometry of the MEA's and the measuring cell is to be found in /10/.

RESULTS AND DISCUSSION

Fig.3 shows current/potential curves of oxygen reduction on DMFC cathodes prepared by the nine different pulsing conditions described in the experimental section. It is evident from these curves, that the performance of the cathodes is strongly affected by the pulsing conditions. The highest current densities reached with pulsing condition No. 8 (j_{pulse} = 1000 mA/cm², t_{on} = 2 ms, t_{off} = 10 ms) are about one order of magnitude higher than the current densities e.g. obtained with pulsing condition No. 5 (j_{pulse} = 1000 mA/cm², t_{on} = 2 ms, t_{off} = 500 ms). It should be stressed, that because of the methanol permeation through the Nafion membrane, the cathode potential is rather a mixed potential with a dominating oxygen reduction than the overpotential of oxygen reduction. The combination of methanol permeation and the small platinum loading of the cathode induces relatively low potentials. In some cases, steep current/potential curves (see e.g. Exp. No 8 !) are obtained, which may be interpreted by a decreasing methanol permeation with rising current density. As a result, the mixed potential shifts to more positive values and the current/potential curve seems to be 'overcorrected'.

As mentioned in the experimental section, the experiments shown in Fig.3 were repeated twice with new samples. The resulting three blocks of experimental data were analyzed by using the STATGRAPHICS® Software. The goal of this analysis is to find the optimum pulsing conditions in the parameter field investigated. More precisely, it means to search for the highest current density of oxygen reduction at a constant cathode potential. We have commited a cathode potential of 0.4 V as a representative value. In Figs.4-6, the calculated current density of oxygen reduction at U = 0.4 V for different pulsed current densities is shown in dependence on the pulse duration and pulse interval duration. Within the parameter field investigated, the maximum current density of 290 mA/mg is obtained at a pulsed current density of 1000 mA/cm², a pulse duration of 2 ms and a pulse interval duration of 10 ms (see Fig.4). These pulsing parameters are identical with the parameter combination No.8 and thus in accordance with the results presented in Fig.3. As seen from Fig.4, high t_{on}- and t_{off}-values are unfavorable at high pulsed current density. For example, by increasing t_{off} from 10 ms to 500 ms, the current density drops from 290 mA/mg to a value of about 30 mA/mg. With decreasing pulsed current density, the picture changes: high t_{on}- and t_{off}-values are more and more favorable. At a pulsed current density of 100 mA/cm², the maximum current density of 240 mA/mg is obtained with t_{on} = 200 ms and t_{off} = 500 ms (see Fig.6). It is interesting to note, that the maximum performance obtained at medium pulsed current density of 550 mA/cm² is lower than the maxima obtained at higher and lower pulsed current density (see Fig.5).

Generally, the influence of the pulsing parameters on the performance of the DMFC cathode can be interpreted in terms of nucleation processes, crystal growth and mass transport limitations caused by a depletion of the platinum salt. The nucleation rate, $v_{nucl.}$, increases exponentially with the overpotential of electrochemical reduction according to the following equation [6]:

$$v_{nucl.} = k_1 * \exp(-k_2 / |\eta|) \ s^{-1}cm^{-2} \qquad (1)$$

where k_1 is a proportionality constant and k_2 is related to the amount of energy needed for the two-dimensional nucleation. If the pulsed current density is increased, the overpotential also increases, which induces a higher nucleation rate and thus a larger number of nuclei. During the 'on-time', a grain growth takes place. Therefore, the combination of a high pulsed current density and a short 'on-time' is expected to yield a large number of small catalyst particles with a high active surface, whereas a low pulsed current density and a long 'on-time' should produce a small number of large particles with a small active surface. During the 'off-time', mostly grain growth is observed which is caused by a recrystallization of the particles. Nevertheless, also grain refinement can occur in the 'off-time', if inhibiting species are blocking growth centers by adsorption [11]. If we assume a progressing grain growth during the pulsing process, low t_{on}- and t_{off}-values combined with a high pulsed current density should be favorable to obtain small catalyst particles, a high active surface and high performance. This consideration is confirmed by the current maximum achieved with parameter combination No.8 (see table 2 / Fig.4). However, an increasing depletion of the platinum salt in the Nafion / carbon interface during the 'on-time' has to be considered, which is even more critical at high pulsed current density. The resulting diffusion overpotential causes a shift of the cathode potential to more and more negative values. In worst case, the reduction current is dominated by hydrogen evolution instead of platinum deposition and it is not possible to control the platinum particle size anymore. Therefore, a high pulsed current density combined with a high 'on-time' is unfavorable. During the 'off-time', the $[PtCl_6]^{2-}$ ions diffuse to the Nafion / carbon interface and their concentration increases. In this regard, a high 'off-time' may be favorable. The positive effect of an increasing 'off-time' at low pulsed current density and high 'on-time' is to be seen in Fig.6. However, in most cases, a rising 'off-time' is unfavorable probably due to recrystallization processes.

It is also the so-called 'duty cycle', which is important for the electrodeposition process. The duty cycle is a measure for the ratio of t_{on} and t_{off} and is defined as

$$\text{duty cycle (\%)} = \frac{t_{on}}{t_{on} + t_{off}} \times 100 \qquad (2)$$

As shown by Cheh [7] and Ibl [8], the pulse limiting current density, which is the pulse current density at which the surface concentration reaches zero at the end of the pulse, increases with decreasing 'on-time' and duty cycle. To avoid dendrite and powder formation, the pulsed current density should stay well below the limiting current density. Especially at high pulsed current densities, the duty cycle should not be too high. In our experiments, the duty cycle ranges from 0.4 % (Exps.No. 2/5) to 95 % (Exps.No. 6/9).

We have roughly estimated, that more than 90 % of the platinum salt is reduced in most of our experiments, until the pulse limiting current density is exceeded. Only in the case of the experiments No. 6 and 9, where the duty cycle is 95 %, the pulse limiting current density is already exceeded after deposition of only 20 % (Exp. No 9) or 70 % (Exp. No 6) of the platinum salt. Independent on the pulsing conditions, in the final period of deposition, the concentration of hexachloroplatinic acid in the Nafion phase tends to zero. Then, the pulsing current will be higher than the limiting current and hydrogen evolution will take place as additional, undesired reduction process. An exact calculation of the pulse limiting current density especially in the final period is difficult, because hydrogen evolution may induce a convective diffusion inside the Nafion phase, which is impossible to determine. An accelerated diffusion of $[PtCl_6]^{2-}$ ions to the Nafion / carbon interface will decrease the thickness of the Nernst diffusion layer and increase the limiting current. Regarding the current maxima obtained in Figs.4-6, duty cycles in the range of 20 – 30 % seem to be most favorable, whereas catalyst layers prepared with very high or low duty cycles exhibit an inferior performance. This result is in accordance with data from Choi et al. [3], which reported a duty cycle of 25% to yield the best performance.

A comparison of the performance of the best cathode prepared by pulsed electrodeposition and a conventional cathode with a commercial catalyst (E-TeK) is shown in Fig.7. It can be seen, that the cathode catalyst layer prepared by PED yields the highest current densities, that is the pulsed catalyst shows the best performance at high overpotentials of oxygen reduction. On the other hand, the commercial catalyst gives the better performance at low overpotentials. The true reason for the different slopes of the current/potential curves is not yet clear. From first XRD measurements it turns out, that the electrodeposited platinum particles are about three times larger than the platinum particles of commercial catalysts with 40 wt % platinum and 60 wt% carbon phase (12 nm vs. 4 nm). This means, that in comparison with commercial catalyst, the performance of the catalyst layers prepared by PED could be better at low overpotentials as well, if the grain size of the platinum particles could be further reduced. At the example of unsupported platinum black catalyst we have recently demonstrated, that 70 – 100 % of platinum catalyst particles prepared by electro-deposition are electro-active, whereas commercial catalyst only yields a utilization of 25 % [13]. If the same prediction holds for supported catalyst, a potential improvement of the cathode performance by a factor of 3-4 can be expected.

CONCLUSIONS

We have prepared DMFC cathode catalyst layers by a new preparation method based on the electro-deposition of the catalyst [12]. This technique circumvents the use of expensive galvanic baths. Instead of this, the catalyst particles, here: platinum, are deposited inside a precursor cathode catalyst layer as part of a MEA. The precursor layer consists of a mixture of hexachloroplatinic acid, Nafion solution and carbon XC 72. The hexachloroplatinic acid is dissolved in the Nafion phase and the platinum particles are deposited onto the carbon particles in the Nafion / carbon interface. This technique allows a considerable enhancement of the utilization of the catalyst, as shown in [13]. To control the size of the platinum particles, the method of pulsed electro-deposition (PED) was used [4,5]. The deposition was optimized by varying the pulsing parameters: pulse current density ('j_{pulse}'), pulse duration ('t_{on}') and pulse interval duration ('t_{off}'). The performance of the DMFC cathodes was characterized by quasi-stationary current/potential measurements of oxygen reduction.

It turns out, that the performance of the electro-deposited catalyst layers differs by more than one order of magnitude, depending on the pulsing conditions. Within the parameter field investigated, the best cathode performance is obtained at high pulse current density and low 'on'- and 'off-time' (j_{pulse} = 1000 mA/cm², t_{on} = 2 ms, t_{off} = 10 ms). A second maximum is obtained at low current density and high 'on'- and 'off-time' (j_{pulse} = 100 mA/cm², t_{on} = 200 ms, t_{off} = 500 ms). These maxima are explained as the result of nucleation and grain growth effects, depletion of platinum salt nearby the reaction zone and undesired side reactions like hydrogen evolution. The 'duty cycle', which is proportional to the ratio of t_{on} and t_{off}, is also important for the electrodeposition process. The best performance is obtained with duty cycles of 20 – 30 %, which is in accordance with literature data [3].

Compared with commercial E-TeK platinum catalyst, the electro-deposited catalyst shows a higher current density at high overpotentials of oxygen reduction, but a lower performance at low overpotentials. In average, the performance of both catalysts is similar. We assume, that this result is due to contradicting effects, which approximately compensate each other: On the one hand, the size of the electro-deposited platinum particles (11 nm) is about three times larger compared to the size of commercial catalyst particles, which comes out from X-Ray diffraction measurements. Considering the same catalyst loading, the overall platinum surface should be lower by the same factor. On the other hand, the utilization of the electro-deposited particles is assumed to be 3-4 times higher than the platinum particles in a catalyst layer prepared by conventional technique. This assumption is based on results obtained with platinum black catalyst layers prepared by pulsed electro-deposition [13]. However, this has to be proved also for supported catalyst layers by determination of the platinum particle size (XRD and TEM measurements) as well as the active surface (cyclic voltammetry). If the assumption is true, a further optimization of the electro-deposition process regarding a reduction of the particle size should considerably improve the DMFC cathode performance.

ACKNOWLEDGEMENTS

We gratefully acknowledge the financial support of this work by the MSWWF of North-Rhine-Westfalia.

REFERENCES

Journals

1. J. Mc Breen, J. Electrochem. Soc. **132,** 112 (1985)
2. E.J. Taylor, E.B. Anderson and N.R.K. Vilambi, J. Electrochem. Soc. **139,** L45 (1992)
3. K.H. Choi, H.S. Kim and T.H. Lee, J. of Power Sources **75,** 230 (1998)
4. H. Natter, T. Krajewski and R. Hempelmann, Ber. Bunsenges. Phys. Chem. **100,** 55 (1996)
5. H. Natter and R. Hempelmann, J. Phys. Chem. **100,** 19525 (1996)
6. B.R. Kaischew, E. Budewski and J. Malinowski, Zeitschrift für Physikalische Chemie **204,** 348 (1955)
7. H.Y. Cheh, J. Electrochem. Soc. **118,** 551 (1971)
8. N. Ibl, Surface Technology **10,** 81 (1980)

Society Proceedings Series

9. S. Srinivasan, O.A. Velev, A. Parthasarathy, D.J. Manko and A.J. Appleby, NASA Conf. Publication 3125, April 11-13, 1989
10. A. Havránek, K. Klafki and K. Wippermann, Proc. of the Symposium 'Direct Methanol Fuel Cells', 199th ECS meeting, Eds.: S. Narayanan, S. Gottesfeld and T. Zawodzinski, The Electrochemical Society Proceedings, Pennington, NJ, 2002

Books

11. J.-C. Puippe, F. Leaman (Eds.), 'Theory and practice of pulse plating', American electroplaters and surface finishers society, Orlando, Florida / USA

Patents

12. J. Divisek, H.-F. Oetjen and V.M. Schmidt, DE No. 19720688, May 16, 1997

Diploma thesis

13. B. Ćudina, Diploma thesis, Forschungszentrum Jülich / Fachhochschule Aachen – Abteilung Jülich, July 2001

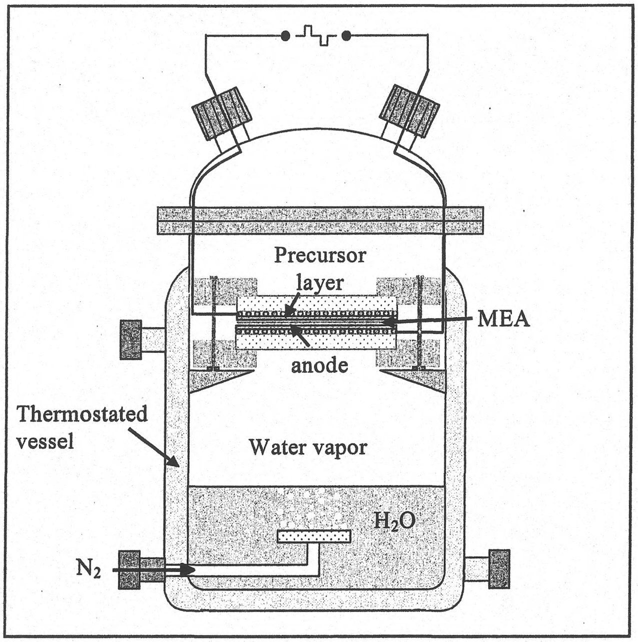

Fig. 1: Scheme of the thermostated vessel used for the electrochemical deposition of platinum in the cathode precursor layer of a DMFC MEA

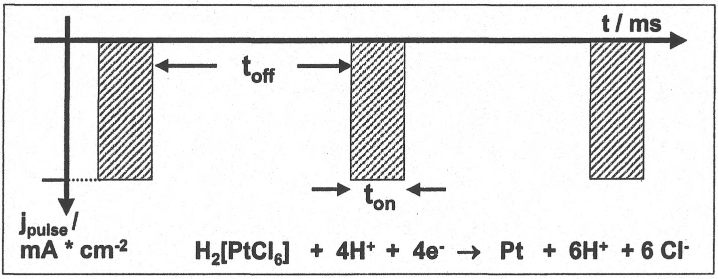

Fig. 2: Scheme of the pulsed current density vs. time

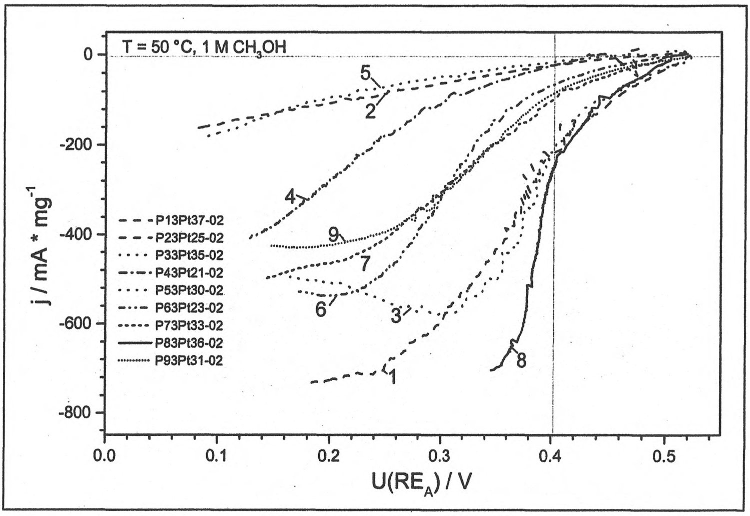

Fig. 3: Quasi-stationary current/potential curves (dU/dt = 0.5 mV/s) of oxygen reduction on Pt prepared by PED with nine different pulsing conditions (see table 1), T = 80 °C, oxygen

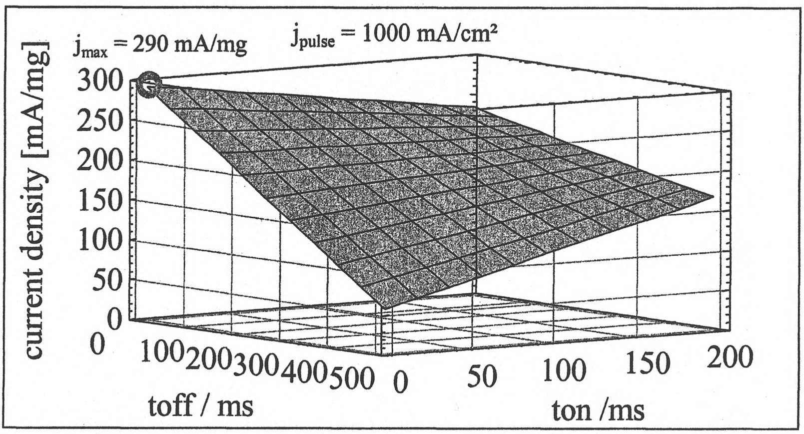

Fig. 4: Calculated current density of oxygen reduction in electro-deposited Pt catalyst layers as a function of the pulsing parameters t_{on} and t_{off}, j_{pulse} = 1000 mA/cm²; measuring conditions: dU/dt = 0.5 mV/s, U = 0.4 V, pure oxygen

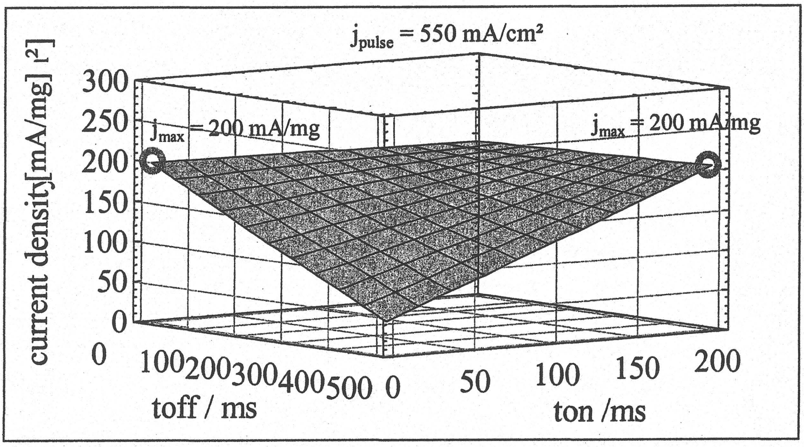

Fig. 5: see Fig.4, j_{pulse} = 550 mA/cm²

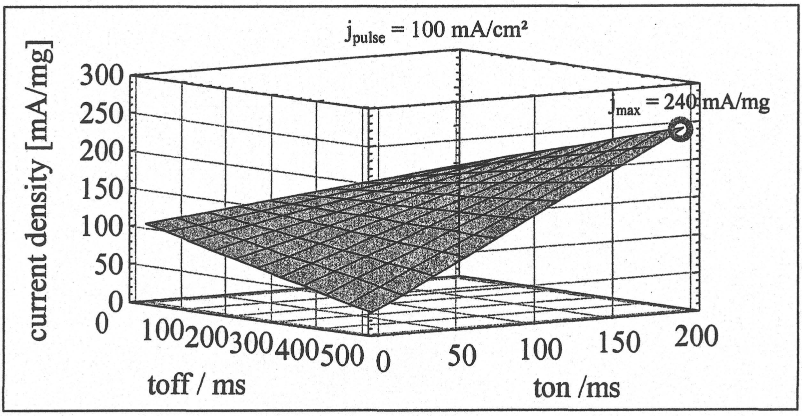

Fig. 6: see Fig.4, j_{pulse} = 100 mA/cm²

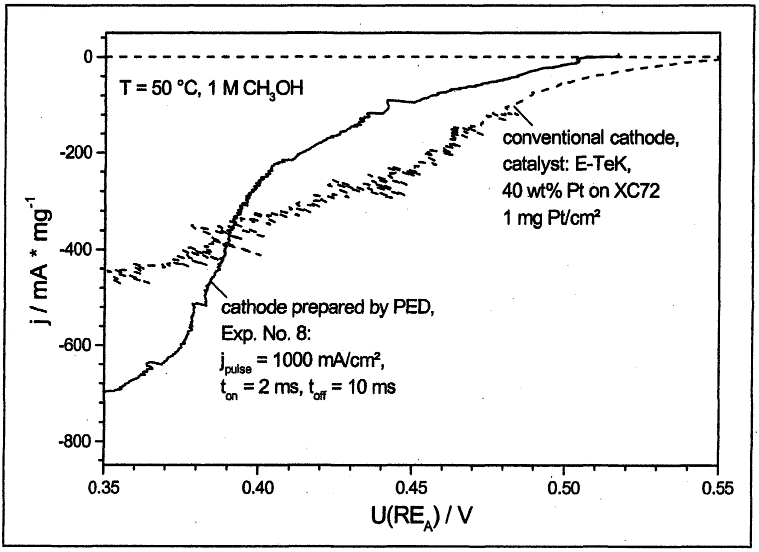

Fig. 7: Quasi-stationary current/potential curves (dU/dt = 0.5 mV/s) of oxygen reduction, comparison of DMFC cathode catalyst layers prepared by PED and with commercial E-TeK catalyst, T = 50 °C, oxygen

Proceedings of The Electrochemical Society, PV 2002-31, 530-540 (2002)
DOI: 10.1149/200231.0530PV © The Electrochemical Society

The Effect of BPSH Post Treatment on DMFC Performance and Properties

M. Hickner,[1,2] Y. Kim,[2] J. McGrath,[2] P. Zelenay,[1] and B. Pivovar[1]

[1]MST-11 Fuel Cells and Electrochemistry
Los Alamos National Laboratory
Los Alamos, NM 87544

[2]Department of Chemistry
Virginia Polytechnic Institute and State University
Blacksburg, VA 24061

ABSTRACT

Direct methanol fuel cells (DMFCs) are being investigated for applications ranging from milliwatt (cell phones) to kilowatt (APUs) size scales. A common pitfall for DMFCs has been the inability of the electrolyte, typically Nafion, to act as an effective methanol barrier. Methanol crossover adversely affects the cell by lowering the cell voltage due to a mixed potential at the cathode and lower fuel utilization.

Improved DMFC performance was demonstrated with sulfonated poly(arylene ether sulfone) copolymer membranes (1). Another study has shown the dependence of polymer properties and morphology on the post treatment of such membranes (2). In agreement with measurements on free-standing films, the fuel cell characteristics of these membranes have been found to have a strong dependence on acidification treatment. Methanol permeability, proton conductivity, and electro-osmotic drag coefficient all were found to increase when the membranes were acidified under boiling conditions versus a low-temperature process.

INTRODUCTION

Direct methanol fuel cells (DMFC) have become an increasingly attractive alternative to other energy storage/conversion technologies for portable power applications. Current fuel cell membrane materials, particularly perfluoronated ionomers such as Nafion, have too much methanol permeation or "crossover" from anode to cathode for efficient cell operation. Unoxidized methanol at the anode travels through the membrane and reacts at the cathode causing lower cell voltages and decreased efficiency. Fuel cell engineering strategies exist for combating the effects of methanol crossover such as lowering the feed concentration, modifying the gas diffusion layers, increasing the thickness of the membrane, or increasing the cathode catalyst loading, but these solutions have their drawbacks and limitations. To make large gains in DMFC performance new membranes with lower intrinsic methanol crossover are needed. There has been and continues to be research on other types of membrane polymers with lower methanol permeability, but this lower methanol permeability often comes at the expense of conductivity. Both conductivity and methanol permeability must be taken into account when designing a new DMFC membrane.

The synthesis and characterization of a new class of sulfonated poly(arylene ether sulfone) proton conducting copolymers for use in DMFCs has been reported previously (2). Generally, these materials display low methanol permeability and high proton conductivity. Of note is that the selectivity of these copolymers is greater than that of Nafion. Selectivity is a measure of a membrane's proton transport (conductivity) relative to the membrane's methanol permeability, and has been used as a gauge of the potential for DMFC electrolytes (3). Sulfonated poly(arylene ether sulfone) copolymers with sulfonation levels between 30 and 50 % are attractive candidates for use in DMFCs because of their increased selectivity compared to Nafion. The nomenclature for these copolymers is BPSH (biphenol sulfone $\underline{H}^+$ form) to denote the backbone chemical structure followed by a number to indicate the molar ratio of sulfonated sulfone monomer. Therefore, BPSH-40 is a biphenol sulfone based poly(arylene ether) in the acid form with 40% of the sulfone monomer in the disulfonated form.

As fuel cell performance studies of these copolymers have progressed, the processing of the membrane has become a key variable in determining the membrane properties. Specifically, the temperature of acidification affects the methanol permeability and the conductivity, thereby affecting the selectivity of the membrane. In addition, the treatment of the membrane has an influence on its electro-osmotic drag coefficient. The electro-osmotic drag of a membrane has a large effect on the water management requirements of a DMFC. These property changes can be correlated to microstructural information obtained by atomic force microscopy (AFM).

While the properties of BPSH-40 and other sulfonation levels of the sulfonated poly(arylene ether sulfone) copolymers seems to be affected by the membrane processing temperature during acidification, Nafion is relatively insensitive to acidification temperature.

EXPERIMENTAL

Atomic Force Microscopy

Tapping mode atomic force microscopy (TM-AFM) was performed with a Digital Instruments Dimension 3000, using the micro-fabricated cantilevers with a force constant of approximately 40 N/m. The samples were imaged in relative humidity of about 35%.

Membrane Conductivity

Conductivity at room temperature under full hydration conditions was determined using a Solatron 1260 Impedance/Gain-Phase Analyzer over the frequency range of 10 Hz - 1 MHz. The "window cell" or in-plane geometry was chosen to ensure that the membrane resistance dominated the response of the system (4). The geometry of the cell is shown in Figure 1.

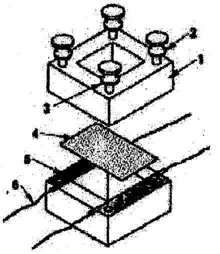

1. Kel-F support block
2. thumbscrew
3. open area to allow equilibration
4. membrane sample
5. blackened Pt foil
6. Pt ribbon lead

Figure 1: Conductivity Cell Geometry

The resistance of the film was taken at the frequency that produced the minimum imaginary response. The conductivity of the membrane could then be calculated from the measured resistance and the geometry of the cell.

Membrane Permeability

Stand-alone methanol permeability was determined using a membrane-separated diffusion cell. The experimental apparatus is shown in Figure 2.

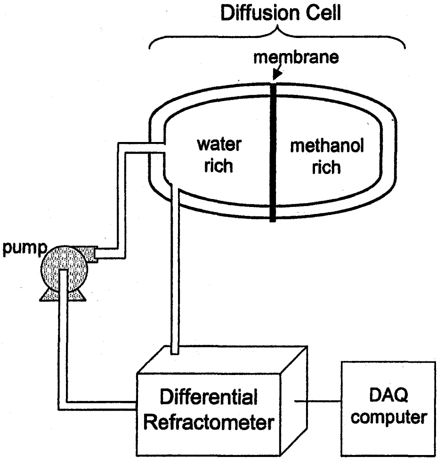

Figure 2: Membrane Separated Diffusion Cell Apparatus

At the outset of the experiment, the membrane of interest is placed between two compartments: one filled with DI water, and the other filled with a methanol/water solution. The rate of methanol diffusion through the membrane can be computed by measuring the change in methanol concentration in one side of the cell versus time using a differential refractometer and a recirculating pump. The permeability data were calculated using equation [1]

$$\frac{c_{1,R} - c_{1,L}}{c^{o}_{1,R} - c^{o}_{1,L}} = e^{-D_1 H_1 \chi t} \qquad [1]$$

A plot of $\ln[(c_{1,R}-c_{1,L})/ (c^{o}_{1,R}-c^{o}_{1,L})]$ versus t should yield a straight line with slope $-D_1H_1\chi$. Once χ is determined by measuring the geometry of the cell, the permeability of methanol through the membrane (D_1H_1) can be calculated. The specifics of the data analysis have been outlined by Cussler (5).

Synthesis of Membrane Electrode Assemblies (MEAs)

MEAs were prepared from standard catalyst inks containing either unsupported platinum or platinum-ruthenium, water, and Nafion 1100 solution. These inks were mixed by sonication and then applied to the membranes by direct painting. All the membranes tested had identical electrodes. Nafion 117 films were pretreated by boiling for 1.5 hours in each step in 3% H_2O_2, deionized water, 0.5 M H2SO4, and again in deionozed water.

BPSH-40 polymer in the potassium neutralized form were solution cast from N,N,-dimethylacetamide under vacuum at 150°C. Two different treatment methods were applied to convert the sulfonated poly(arylene ether sulfone) random copolymer membranes to the acid form. Method 1 will refer to converting the membranes to acid form by soaking in 1.5 M H_2SO_4 for 24 hours, then soaking in DI water for 24 hours. Conversion method 2 involves boiling the cast membrane in 0.5 M H_2SO_4 for 2 hours, then boiling in DI water for 2 hours to remove the excess H_2SO_4.

Fuel Cell Experiments

The resulting MEAs were tested in fuel cell hardware to determine membrane properties and DMFC performance. Relevant DMFC membrane properties such as methanol permeability, proton conductivity and electro-osmotic drag were obtained from these experiments.

Fuel cell test results reported here are for tests run in 5 cm^2 cells at 60°C with 1M methanol at a flow rate of 2 mL/min, and an air flow rate (humidified to a dew point of 60°C) of 250 sccm at 0 psig backpressure. Polarization curves were obtained under these conditions, and proton conductivities were determined from high frequency resistance measurements.

By operating the cell at a constant current, the water flux through the membrane and the methanol crossover as a function of current density could be obtained from an analysis of the cathode effluent. In this experiment, the water in the cathode exhaust was collected in a Drierite filled U-tube, and the CO_2 content of the dry effluent was determined using a nondispersive linearized CO_2 sensor. The details of this experiment are described in greater detail elsewhere (6). The electro-osmotic drag coefficient of the membrane was also extracted from the constant current data.

RESULTS AND DISCUSSION

Three types of membrane were included in this study. Nafion 117 processed in the usual fashion, BPSH-40 acidified by soaking (Method 1), and BPSH-40 acidified by boiling (Method 2). Both stand-alone membrane properties and DMFC performance is reported in this work.

Effect of Processing Method on Morphology and Membrane Properties

The morphological change induced by the method of acidification can be observed using atomic force microscopy. Figure 3 shows the morphology of BPSH-40 processed using the two different acidification methods.

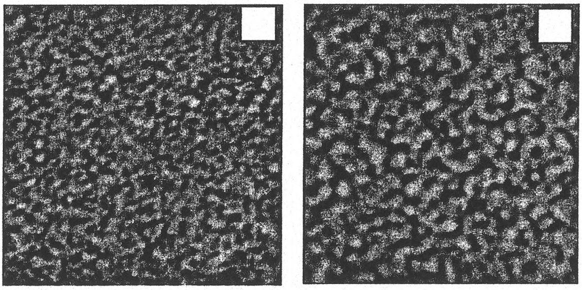

Figure 3: Influence of treatment Method upon Tapping Mode AFM Phase Image (a) BPSH-40 Method 1 (b) BPSH-40 Method 2

The dark areas represent hydrophilic sulfonic acid rich domains whereas the lighter areas are primarily unsulfonated polymer. The micrograph on the left where the membrane was acidified by soaking shows a finer domain structure than that on the right where the membrane was acidified by boiling. The higher temperature treatment may cause swelling of the existing domains, reorganization of the morphological structure into larger features, or a combination of the two, both reorganization and swelling.

The morphological change due to acidification treatment is accompanied by a corresponding change in membrane properties. Generally, an increase in water uptake, conductivity, and methanol permeability are observed for the higher temperature treatment of BPSH-40. Nafion 117 has proven to be relatively insensitive to acidification treatment. Table I provides a comparison membrane properties between Nafion 117 and the BPSH-40 membranes after Method 1 and Method 2 processing.

Table I: Effect of Treatment Process on Membrane Properties

	Water Uptake (weight %)	Conductivity (S/cm)	Methanol Permeability (cm^2/s)	Electro-osmotic Drag Coefficient ($N\ H_2O/H^+$)
Nafion 117	19	0.113	$16.7 * 10^{-7}$	3.6
BPSH-40 (M1)	39	0.077	$3.6 * 10^{-7}$	1.5
BPSH-40 (M2)	58	0.104	$8.1 * 10^{-7}$	1.9

Conductivity at 30°C, Methanol Permeability at 25°C and Electro-osmotic Drag at 60°C
M1 – acidification by Method 1: low temperature soaking
M2 – acidification by Method 2: high temperature boiling

The methanol permeability and electro-osmotic drag coefficient of BPSH-40 greatly reduced as compared to Nafion no matter which processing method is used. Additionally, the conductivity of the BPSH-40 membranes is close to that of Nafion indicating that the BPSH-40 membranes have a greater selectivity and could potentially show superior performance in direct methanol fuel cells.

Comparison of Fuel Cell Performance

The change in membrane properties according to treatment method can be observed in the direct methanol fuel cell behavior of the membrane. Membrane conductivity and methanol permeability have a direct effect on two distinct regions of the polarization curves. In the low current region (0 to 100 mA/cm^2), methanol crossover plays a large role in determining the voltage achieved at a given current. Higher voltages for a given current are an indication of lower methanol crossover. Above 100 mA/cm^2 as the methanol becomes depleted at the anode, membrane conductivity has a large influence on the voltage generated for a given current density. The slope of the nearly linear, ohmic region of the polarization curve is determined primarily by the bulk resistance of the membrane. Large ohmic losses result in increased slopes, which in turn suggest decreased membrane conductivity.

Fuel cell polarization curves for Nafion 117, BPSH-40 processed by method 1, and BPSH-40 processed by method 2 are shown in Figure 4.

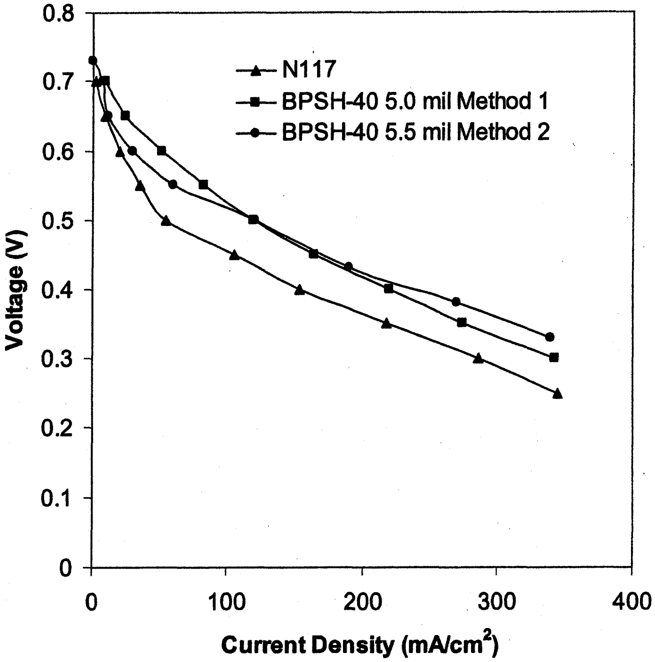

Figure 4: Comparison of Polarization Curves at 60°C with 1M Methanol

The general shift of both the BPSH-40 polarization curves to increased voltages over Nafion is a result of the dramatically reduced methanol permeation of BPSH-40 no matter what processing method is used to acidify the membrane. The open circuit voltages (OCVs) shown in Figure 4 are sensitive to test conditions, particularly the amount of time left at open circuit conditions. While care was not taken in these polarization curves to obtain true OCVs, the qualitative trend to higher OCVs with BPSH-40 (method 1), followed by BPSH-40 (method 2) and finally Nafion 117 agrees with expected changes in methanol permeability of the three membranes.

In the high current region of the performance curves, the ohmic slopes of Nafion 117 and BPSH-40 processed by Method 2 are very similar. This is not surprising given that the stand-alone membrane conductivities of the two are also similar. An increased ohmic slope is observed for BPSH-40 processed by Method 1, which is a reflection of its lower membrane conductivity. The high frequency resistances (HFR) of the MEAs also agreed with the trend in membrane conductivity shown in Table I for the three materials. Nafion 117 had an HFR of 0.21 Ω–cm^2, which is indicative of the highest membrane conductivity. BPSH-40 had HFRs of 0.33 Ω–cm^2 and 0.27 Ω–cm^2 for method 1 and method 2 processing, respectively which follows the conductivity trend established in Table I.

If the Nafion curve is omitted for clarity and just the BPSH-40 polarization curves are plotted, the same effects as discussed above can be observed when comparing the acidification methods. Figure 5 shows only the two BPSH-40 polarization curves processed by Method 1 and Method 2.

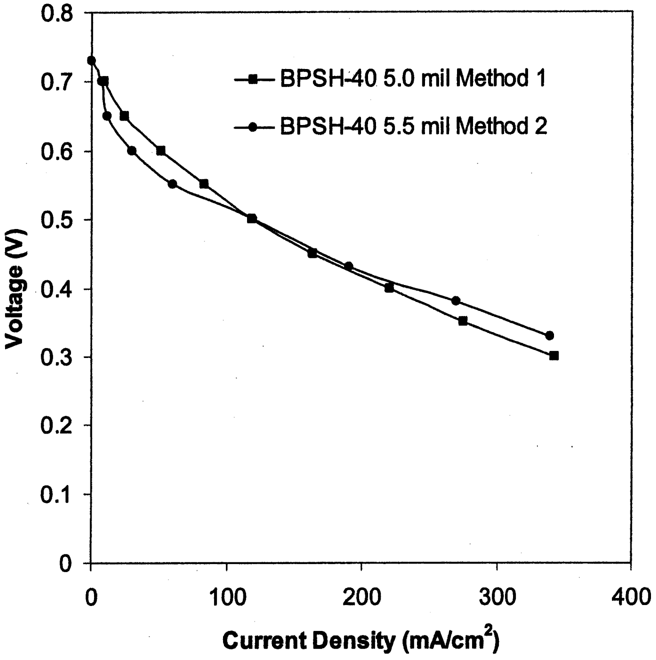

Figure 5: BPSH-40 Polarization Curves – Effect of Acidification Method on DMFC performance

The membrane processed by Method 1 has a lower methanol permeability and therefore, generated higher voltages for a given current density due to decreased methanol crossover in the low current region of the polarization curve. However, because Method 1 processing yields a BPSH-40 membrane with lower conductivity, the ohmic slope of the curve is larger than that of the curve generated using a membrane with Method 2 processing. The point where the two curves cross is the current density for these systems where the tradeoffs between methanol crossover and ohmic losses become equivalent. At higher current densities the membrane with higher conductivity processed by Method 2 shows better performance than the Method 1 processed membrane.

The methanol crossover of the MEAs in a DMFC was evaluated by measuring the amount of CO_2 generated at the cathode. The results can be expressed as an equivalent current density for the methanol molecules lost to crossover. Figure 6 shows the cell current versus the equivalent crossover current for the three membranes.

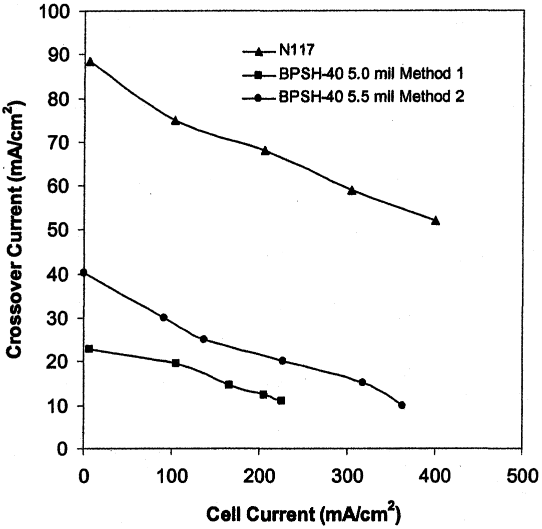

Figure 6: Methanol Crossover expressed as Crossover Current Density versus Cell Current

As can be seen from the figure, the methanol crossover of Nafion is much greater than BPSH-40 accounting for the shift to higher voltages in the polarization curves. Between the BPSH-40 membranes, Method 1 yields a membrane with lower methanol crossover over all current densities. The relative differences between these curves are mirrored in the stand-alone membrane methanol permeability experiments, the trend in open circuit voltages, and the increased performance shown in the polarization curves due to lower overpotentials at the cathode.

CONCLUSIONS

Sulfonated poly(arylene ether sulfone) copolymers have proven to consistently outperform Nafion in DMFCs principally because of their decreased methanol crossover without sacrificing protonic conductivity. However, the properties of the BPSH-40 membranes are highly influenced by the acidification process whereas Nafion is relatively insensitive to acidification temperature.

A relationship between the domain structure of the polymer and the resulting membrane properties has been established. Increased sulfonic acid domain size brought about by high temperature acidification causes an increase in electro-osmotic drag, conductivity, and methanol permeability. These properties were measured in both stand-alone membrane and in fuel cells.

The differences in methanol permeability and conductivity between the three types of membranes have a notable effect on the membranes' DMFC performance. At a given current density, shifts to higher voltages are observed for both BPSH-40 MEAs versus Nafion 117 because of the large difference in methanol crossover. When comparing the two BPSH-40 membranes processed by different acidification routes, behavior in the low current region is dominated by decreased methanol permeability, whereas the conductivity controls the performance at higher currents. The result is that the two BPSH-40 curves intersect with Method 1 processing showing advantages at low current, and Method 2 displaying higher performance at higher currents.

A likely cause for Nafion's insensitivity to processing may arise from the small amount of crystallinity that exists in the non-sulfonated part of the polymer. This crystallinity prevents swelling or reorganization of the sulfonated domains. No crystallinity exists in BPSH polymers resulting in the potential for morphological reorganization depending on how the membrane is processed. Additionally, the ion exchange capacity of Nafion is much lower than that of BPSH-40 (0.91 meq/g vs 1.72 meq/g, respectively). Less ions in the polymer leaves more unsulfonated matrix to stabilize the ionic domains. Nafion's unsulfonated tetrefluoroethylene regions – with or without crystallinity - may contribute to its behavior during processing.

REFERENCES

1. B. Pivovar, M. Hickner, J.E. McGrath, P. Zelenay, and T.A. Zawodzinski, *Meeting Abstracts, Joint International Meeting of the ECS and ISE*, San Francisco, CA, September 2-7, 420, (2001); B. Pivovar, M. Hickner, J.E. McGrath, P. Zelenay, and T.A. Zawodzinski, *Fuel Cell Technology: Opportunities and Challenges Topical Conference Proceedings, 2002 AIChE Spring National Meeting*, New Orleans, LA, March 10-14, 535, (2002).

2. Y. Kim, F. Wang, M. Hickner, T. Zawodzinski, and J. McGrath, *Meeting Abstracts, 201st Meeting of the Electrochemical Society*, Philadelphia, PA, May 12-17, 2002, Abstract #182.

3. F. Wang, M. Hickner, Y.S. Kim, T.A. Zawodzinski, and J.E. McGrath, *J. Membrane Sci.*, **197**, 231 (2001).

4. B.S. Pivovar, Y. Wang, and E.L. Cussler, *J. Membrane Sci.*, **154(2)**, 155 (1999).

5. T.A. Zawodzinski, M. Neeman, L. O. Sillerud, and S. Gottesfeld. *J. Phys. Chem.*, **95**, 6040 (1991).

6. E.L. Cussler, *Diffusion: Mass Transfer in Fluid Systems*, 2nd Ed. Cambridge University Press, New York (1997).

7. Ren, X., Henderson, W., and Gottesfeld, S., J. Electrochem. Soc., **144**, L267, 1997.

Proceedings of The Electrochemical Society, PV 2002-31, 541-549 (2002)
DOI: 10.1149/200231.0541PV © The Electrochemical Society

MICROREACTOR STUDIES ON THE EFFECT OF TEMPERATURE ON THE REACTION PATHWAYS OF METHANOL OXIDATION ON PT CATALYSTS

Nallakkan S. Arvindan and Eric M. Stuve
Department of Chemical Engineering,
University of Washington, Box 351750, Seattle, WA 98195-1750.

ABSTRACT

We report on the effects of high temperature (60–95 °C) temperature on the reaction pathways for methanol electro-oxidation. The studies were performed in a silicon-based microreactor system that enables effective instantaneous control of reaction temperature in the range of 20–100 °C. Methanol oxidation is measured at constant potential following a step from a non-reacting potential. Accumulation of surface species like CO is subsequently measured by linear sweep voltammetry. These two measurements enable the overall oxidation rate of methanol to be compared with the CO oxidation rate. Initial results demonstrate clean voltammetry of polycrystalline platinum electrodes for all temperatures. At 95 °C turnover rates vary from 0.1 to 1 s^{-1} for the respective potential range of 400 to 600 mV_{rhe}. These results show that unmodified polycrystalline platinum is an effective catalyst for methanol oxidation at 95 °C and support the feasibility of high temperature direct methanol fuel cells.

INTRODUCTION

Direct methanol fuel cells (DMFC) provide a versatile option for clean and efficient power production for a wide spectrum of energy requirements from stationary applications to automobiles and portable electronics. However, poor electrode kinetics combined with poisoning of the electrocatalyst by CO (1) at low temperatures (< 60 °C) has hampered the development of DMFCs. Few half-cell studies of well-characterized electrocatalysts for methanol oxidation have been reported at temperatures greater than 60 °C (2-5), and little information is available on the reaction rates and reaction pathways for methanol oxidation at higher temperatures.

One of the reasons for the lack of information at higher temperatures is the difficulty involved in performing clean electrochemistry involving volatile species like methanol and highly reactive chemicals like perchloric and sulphuric acids, in an oxygen-free environment. Experiments with single crystals are more difficult in comparison to polycrystalline samples because the meniscus configuration typically used in single crystal electrochemistry fails at higher temperatures. Moreover, the problems involved in pre-treatment (usually flame annealing or sputtering), mounting and masking of the electrodes (so that only the facet of interest contacts the electrolyte) without contaminating them have made it difficult for single crystal work to be carried out at high temperatures using conventional electrochemical setups. This paper describes a new experimental approach using a microreactor system to perform fundamental electrocatalytic studies on methanol electro-oxidation at high temperatures on polycrystalline, single crystal, and supported catalysts. Preliminary results from high temperature studies on polycrystalline samples are discussed as proof of concept for the new experimental approach.

Microchemical systems or microreactors are chemical reactors of extremely small dimensions with integrated sensors and control elements. The advantages of microreactors arise by virtue of process intensification (6), a strategy for reduced reactor size to achieve a number of different objectives. Micromachined reactors have been used to study catalytic partial oxidation reactions (7) at high temperatures and to study low surface area model catalysts (8) at atmospheric pressure.

EXPERIMENTAL APPARATUS AND PROCEDURE

The microreactors were 3 cm long and 1.5 cm wide and consisted of two halves bonded together. One half was made from a silicon wafer while the other half was made from pyrex. The silicon half of the microreactor had etched fluid channels 0.25 mm deep, 1.2 mm wide, and 20 mm long. A small opening or via was etched away on the bottom wall of the channel for introduction of external electrodes. The silicon wafer was finally subjected to a thermal wet oxidation process to form a 500 nm thick oxide layer over the entire surface of the silicon. The silicon wafers (obtained from Wafer World, Inc.) used in our process were 0.45–0.5 mm thick, 4 in. in diameter, N-type, (100) oriented, double side polished, and prime grade with a resistivity of 1-10 ohm-cm.

The pyrex wafers were Corning pyrex 7740, 0.5 mm thick, and 4 in. in diameter. The pyrex half contained the electrodes, temperature sensors, and heaters. Photolithography, followed by e-beam metal deposition and photo-resist lift-off was used to form the metal patterns on the pyrex substrate. The working and counter electrodes along with the heaters and temperature sensors were made of 100 nm thick platinum lines. A 10 nm titanium layer was used as an adhesion layer between the platinum and the pyrex. The reference electrodes were made of a 250 nm thick palladium layer deposited over 50 nm of platinum and 10 nm of titanium. The electrodes and temperature sensors were deposited on one side of the pyrex wafers facing the channels on the silicon, while the heaters were deposited on the other side so that they did not contact the electrolyte directly.

The wafers were diced into individual chips (Fig.1.) and cleaned in an oxygen plasma. The bonding side of each chip was carefully coated with Teflon AF® solution exposing only the electrode surfaces. The teflon coated chips were subjected to a heat treatment procedure to remove the solvent from the teflon. Upon cooling, each silicon chip was aligned with a corresponding pyrex chip and heat treated at 300 °C to bond them together.

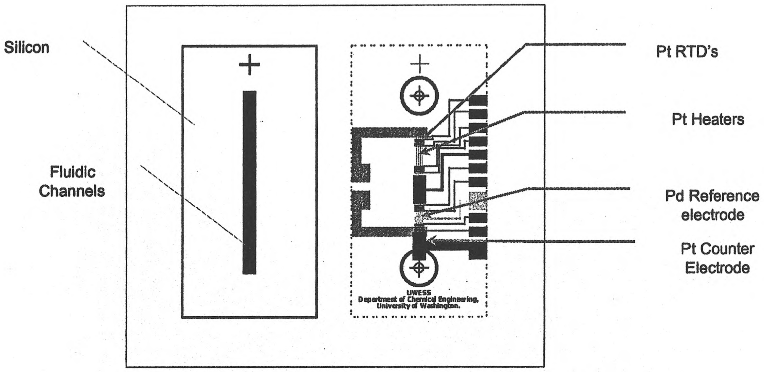

Figure 1: Layout of the two halves of the microreactor

The temperature sensors on the microreactor were made of thin, serpentine platinum lines 30 μm wide and 100 nm thick. The resistance of the platinum RTD (resistance temperature device) was between 1300 and 1600 ohms. The RTDs were calibrated by placing the microreactor in a constant temperature bath and measuring the resistance as a function of bath temperature.

A plot of the resistance of the RTD Vs bath temperature is shown in Fig 2, which shows a linear variation of resistance with temperature. The coefficient of resistance is calculated from the graph using equation 1.

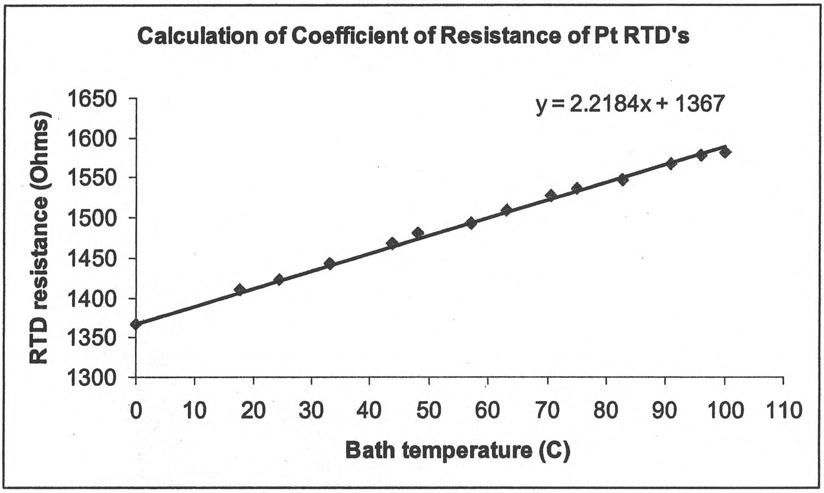

Figure 2: Plot of RTD resistance versus bath temperature

$$R = R_0[1+\alpha(T-T_0)] \qquad [1]$$

Where, R = resistance of RTD at temperature T; R_o and T_o are the resistance and temperature of the RTD at 0 °C; and α is the temperature coefficient of resistance. The average value of the temperature coefficient of resistance of the RTDs on the microreactor was found to be: $\alpha = 1.58 \times 10^{-3}\ K^{-1}$. During electrochemical experiments, the resistance of the RTDs was measured and the above value of α used to calculate the temperature of the RTD. The working electrode temperature was measured by the RTD located very close to the working electrode. The heaters were 50 μm wide and 100 nm thick platinum lines. The heaters were connected to a DC power supply.

The cleanliness of the system was determined from cyclic voltammograms obtained in 0.1 M $HClO_4$ solution. Thin film platinum electrodes on the microreactors were used for the working electrode and counter electrode. Thin film palladium was used as a Pd/H reference electrode. Before recording the cyclic voltammograms, the palladium reference electrode was charged for 30 minutes by applying a constant current of –50 μA in 0.1 M $HClO_4$. A steady state cyclic voltammogram of the thin film Pt electrode obtained after several sweeps is shown in Fig. 3. All potentials are reported with respect to the Pd/H electrode. At room temperature the potential of a Pd/H is 50 mV with respect to the reversible hydrogen electrode (RHE).

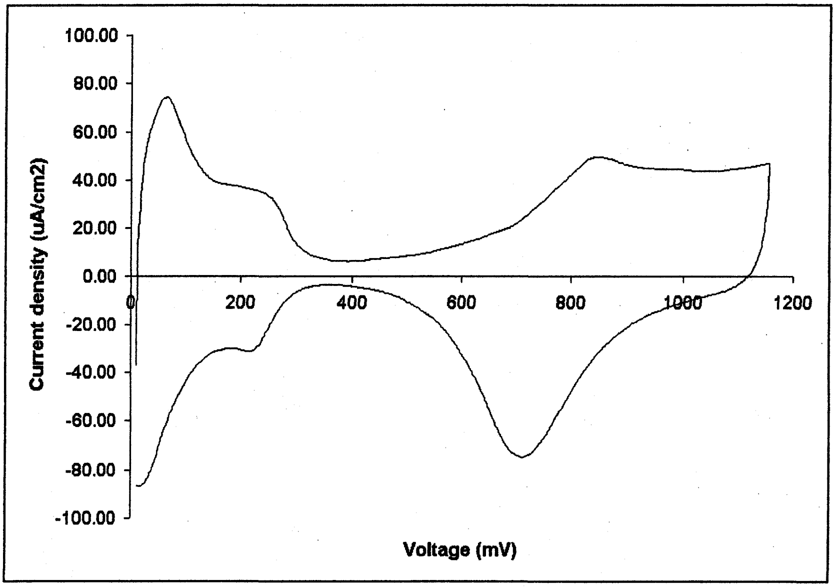

Figure 3: Cyclic Voltammogram of thin film Pt in 0.1M $HClO_4$ at a sweep rate of 50 mV/s

RESULTS

Qualitative information regarding methanol oxidation at high temperature was obtained from steady state cyclic voltammograms of 0.1 M methanol in 0.1 M perchloric acid and are shown at different temperatures in Fig. 4.

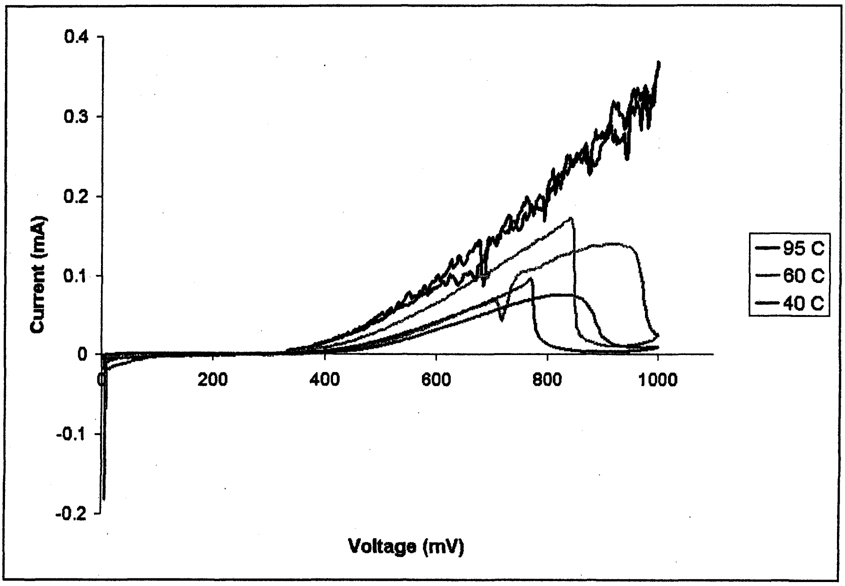

Figure 4 Cyclic voltammograms of 0.1M methanol in 0.1M perchloric acid

Potential step experiments

Before the start of each experiment, the working electrode was subjected to several cyclic voltammetric sweeps between the potentials of 0 and 1400 mV. All experiments were carried out at stopped flow conditions unless otherwise mentioned. At the beginning of an experiment, a cyclic voltammogram (blank CV) was recorded in blank electrolyte (0.1 M $HClO_4$). The blank CV was used to calculate the active area of the electrode and to ensure cleanliness. The electrode was then maintained at a constant potential of 5 mV for 60 s. The heaters were turned on and controlled to raise the temperature of the working electrode to the desired reaction temperature T_r. Once the temperature reached steady state, the potential of the working electrode was stepped to a value E_r and the resulting current transient recorded by the potentiostat. At the end of the reaction period, the potential was stepped back to 5 mV and the heaters turned off. The charge passed during the potential step was calculated by integrating the current transient. This charge is designated as q_{dlr}. A valve was activated to engage the methanol syringe pump and 2 ml of methanol containing electrolyte was flowed through the microreactor at a rate of 0.5 ml/min to replace the blank electrolyte. After the blank electrolyte was replaced with methanol, the temperature of the working electrode is raised to T_r. The potential of the working electrode was stepped to E_r and the resulting current transient recorded by the potentiostat. At the end of the reaction period, the potential was stepped aback to 5 mV and the heaters turned off. The charge passed during this step is calculated to be q_{meoh}. The reaction charge is given by equation 2.

$$q_r = q_{meoh} - q_{dlr} \qquad [2]$$

The main valve was activated to engage the blank electrolyte and 2 ml of blank electrolyte was flowed through the microreactor at a rate of 0.5 ml/min to wash away the methanol from the reactor. Another 1 to 2 ml of blank electrolyte was flowed through the reactor at 0.25 ml/min to make sure that the last traces of methanol were completely removed from the reactor. Following this, a linear sweep voltammogram was recorded in which the potential was ramped to 1150 mV at a sweep rate of 50 mV/s. During this sweep, the adsorbed intermediates were oxidized in a single peak. The charge under this peak minus the charge under the same potential region in the following scan gives the stripping charge q_s.

Figure 5 shows an example of a potential step experiment carried out in the microreactor. The potential was stepped up to E_r = 600 mV for a period of 20 s at 52 °C. The net reaction current density was obtained by subtracting the blank current density from the methanol current density. The charges were calculated and found to be: q_{dlr} = 29.9 μC and q_r = 1061.3 – 29.9 = 1031.4 μC. The adsorbate stripping voltammogram and the second sweep immediately following the stripping sweep for this example are shown in Fig. 6. The stripping charge was calculated to be: q_s = 1.7 μC.

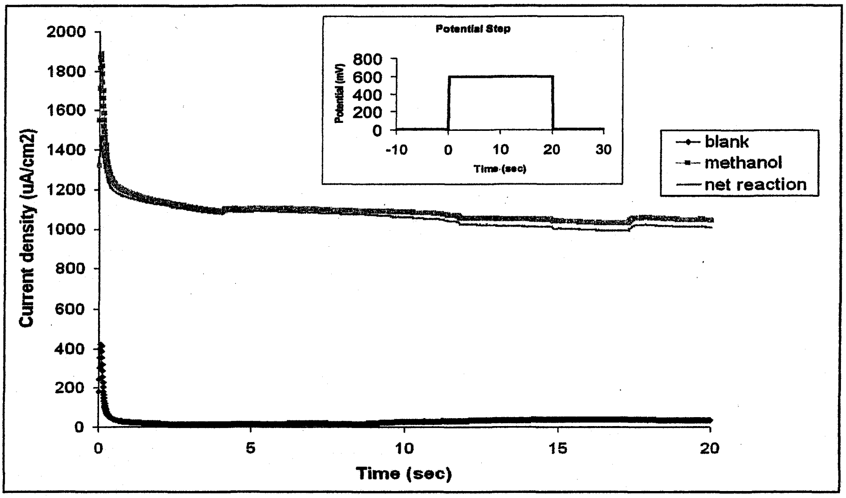

Figure 5: Current transients at 52 °C for a potential step (shown in inset) to 600 mV for a duration of 60 seconds in 0.1 M methanol and 0.1M perchloric acid.

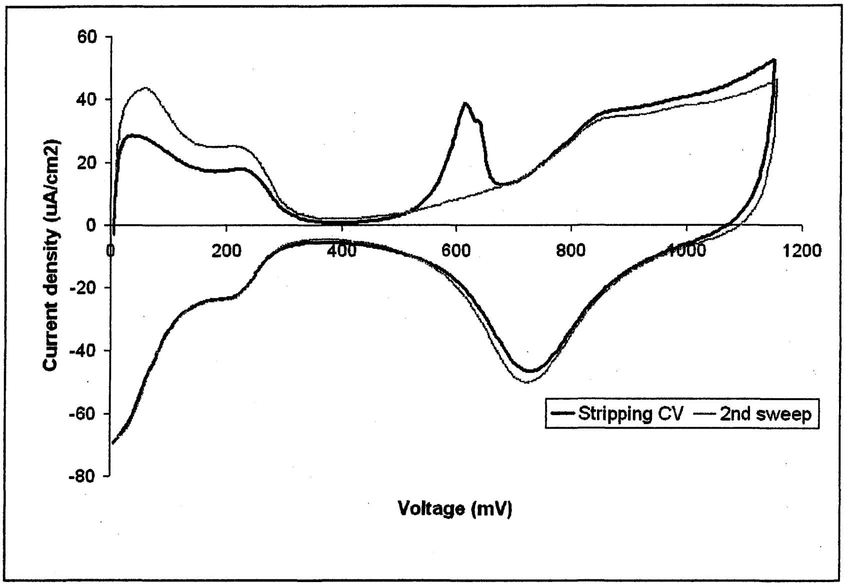

Figure 6: Adsorbate stripping voltammogram

Potential step experiments similar to that described above were performed at different temperatures as a function of reaction potential. The temperature dependence of the reaction rates is shown in the Arrhenius plots of Fig. 7.

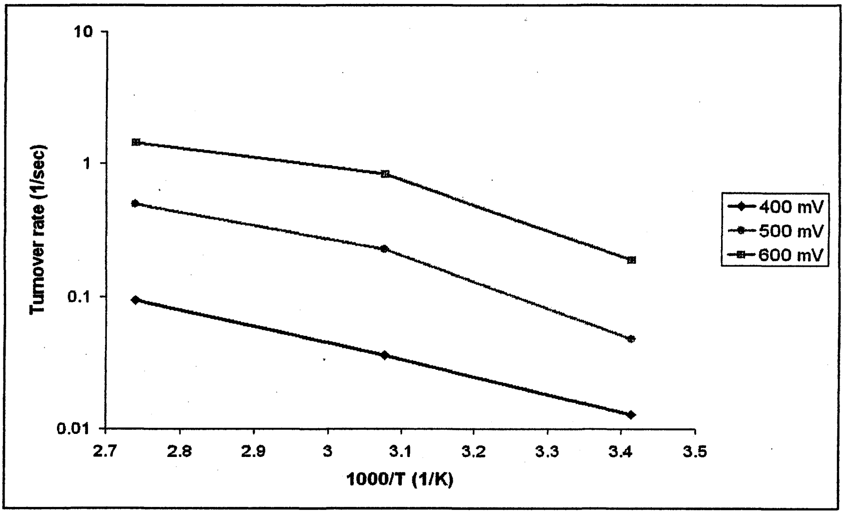

Figure 7: Arrhenius plots for methanol electro-oxidation in 0.1M methanol and 0.1 M perchloric acid

DISCUSSION

From the cyclic voltammograms shown in Fig. 4, we see that there is a negative shift in the onset of methanol oxidation with an increase in temperature. The oxide formation on platinum inhibits the methanol oxidation at potentials greater than 800 mV at room temperature. This gives rise to the current peak observed in the cyclic voltammograms. On the reverse sweep, the oxide reduction reaction usually takes place at a potential negative to oxide formation, giving rise to a hysterisis loop in the CV. However, as the temperature increases the oxide formation on platinum is shifted to potentials that are more positive. At 95 °C, no hysterisis is observed at potentials up to 1 $V_{Pd/H}$. At 95 °C turnover rates vary from 0.1 to 1 per second for the respective potential range of 400 to 600 mV_{rhe} as shown in Fig. 7. These results show that unmodified polycrystalline platinum is an effective catalyst for methanol oxidation at 95 °C and support the feasibility of high temperature direct methanol fuel cells.

CONCLUSION

Microreactors provide a new experimental approach to study high temperature electrocatalysis. It has been shown in this paper that high temperature electrochemical experiments can be successfully performed in a clean manner in the microreactor configuration. The microreactor is a useful tool to study polycrystalline, single crystal and supported catalysts. Preliminary results on polycrystalline electrodes suggest that platinum is an effective catalyst for direct methanol fuel cells at 95 °C.

ACKNOWLEDGEMENTS

We would like to thank the National Science Foundation (CTS-9876905) and the Center for Nanotechnology at the University of Washington for the funding for this work. We would also like to thank Professor Karl Böhringer, Department of Electrical Engineering, University of Washington and the staff at the Washington Technology Center (WTC) for their help with the microfabrication process.

REFERENCES

1. T. D. Jarvi and E. M. Stuve, *Electrocatalysis*, P. N. Ross, Editor, p.75-153 Wiley - VCH. Inc., New York, 1998.
2. D. Kardash and C. Korzeniewski, *Langmuir*, **16**, 8419-8425 (2000).
3. D. Kardash, J. M. Huang and C. Korzeniewski, *Langmuir*, **16**, 2019-2023 (2000).
4. H. A. Gasteiger, N. Markovic, P. N. Ross and E. J. Cairns, *Journal of the Electrochemical Society*, **141**, 1795-1803 (1994).
5. T. H. Madden, N. S. Arvindan and E. M. Stuve, *J. Electrochem Soc.*, accepted for publication (2002).

6. A. I. Stankiewicz and J. A. Moulijn, *Chemical Engineering Progress*, **96**, 22-34 (2000).
7. R. Srinivasan, I. M. Hsing, P. E. Berger, K. F. Jensen, S. L. Firebaugh, M. A. Schmidt, M. P. Harold, J. J. Lerou and J. F. Ryley, *Aiche Journal*, **43**, 3059-3069 (1997).
8. S. Johansson, E. Fridell and B. Kasemo, *Journal of Vacuum Science & Technology a-Vacuum Surfaces and Films*, **18**, 1514-1519 (2000).